

COHERENCE OF E-BEAM RADIATION SOURCES AND FELS – A THEORETICAL OVERVIEW

Avi Gover, Egor Dyunin, Tel-Aviv University, Ramat Aviv, Israel.

GENERAL FORMULATION FOR RADIATION EMISSION FROM MICROSCOPIC CHARGES

This publication is mostly tutorial. It presents a general time-frequency modal-expansion linear formulation for radiation excitation from charges. This, however, can be employed to analyze front-line FEL research problems. Starting from description of synchrotron undulator radiation, the model is extended to describe the coherence characteristics of stimulated emission devices (FEL amplifiers and oscillators), and then further extended to the SASE regime. It is then employed to point out directions for development of coherent X-UV FEL sources.

The starting point of our formulation is the general Maxwell Equations driven by particulate point charge sources (the source dimension is smaller than the emission wavelength):

$$\begin{aligned}\nabla \times \mathbf{E} &= -\mu \frac{\partial \mathbf{H}}{\partial t} - \mu_0 \frac{\partial \mathbf{M}}{\partial t} \\ \nabla \times \mathbf{H} &= \varepsilon \frac{\partial \mathbf{E}}{\partial t} + \mathbf{J} + \frac{\partial \mathbf{P}}{\partial t}\end{aligned}\quad (1)$$

where in general the point sources may be free electrons, atomic electric dipoles or atomic magnetic dipoles and spins [1]:

$$\begin{aligned}\mathbf{J} &= \sum_{j=1}^N -e \mathbf{v}_j \delta(\mathbf{r} - \mathbf{r}_j(t)) \\ \mathbf{P} &= \sum_{j=1}^N \mathbf{p}_j \delta(\mathbf{r} - \mathbf{r}_j(t)) \\ \mathbf{M} &= \sum_{j=1}^N \boldsymbol{\mu}_j \delta(\mathbf{r} - \mathbf{r}_j(t))\end{aligned}\quad (2)$$

In this article we focus on free electrons.

Maxwell Equations can be exceedingly simplified in the frequency domain. In the frequency domain it is possible in many structures to expand the radiation field in terms of a complete set of eigenmodes $\{\tilde{\mathbf{E}}_q\}$:

$$\tilde{\mathbf{E}}(\mathbf{r}, \omega) = \sum_q C_q(z, \omega) \tilde{\mathbf{E}}_q(\mathbf{r}) \quad (3)$$

This certainly can be done in a waveguide, but also in free-space, where one can use a discrete set of modes like Hermit-Gaussian modes, commonly used in laser physics, or continuous modes – like plane waves. In this latter case the summation of q degenerates into integration over transverse wave numbers.

After modal expansion it is possible to simplify Maxwell's set of 3-D differential equations into a simple infinite set of first order ordinary differential equations for the complex amplitudes $C_q(z, \omega)$ [2,3]. These can be solved for each mode at steady state, if the initial condition $C_q^{in}(\omega)$ (the complex amplitudes at the entrance to the interaction region) is given (see Fig.1). The formal solution for the increment of the complex amplitudes in the case of *free electron* microscopic charges is:

$$\begin{aligned}C_q^{out}(\omega) - C_q^{in}(\omega) &= \sum_{j=1}^N \Delta C_{qj} = \\ &= -\frac{1}{4} \sum_{j=1}^N \left\{ -e \int_{-\infty}^{\infty} \mathbf{v}_j(t) \cdot \tilde{\mathbf{E}}_q^*(\mathbf{r}_j(t)) e^{i\omega t} dt \right\}\end{aligned}\quad (4)$$

For any charges in the interaction volume the output amplitudes C_q^{out} can be calculated. Thus the entire output radiation field can be calculated then by substituting $\{C_q^{out}\}$ back into the expansion series (3), or using it otherwise to calculate optical parameters.

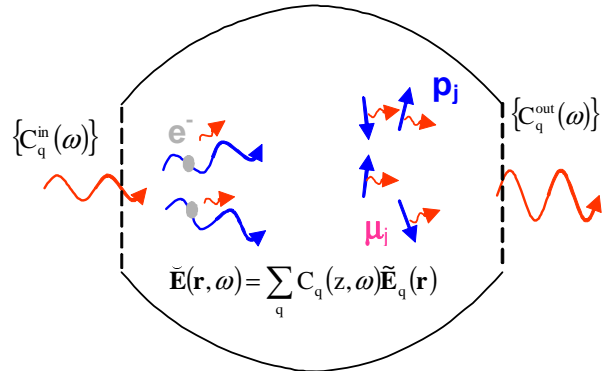


Fig.1: Excitation of radiation modes by particulate charges (Frequency Domain).

This suggests the following picture for modal excitation: the field amplitude increment of each mode is composed of the sum of contributions from the individual electrons, which correspond to the “wavepackets” emitted by the individual electrons. To calculate the increment to the radiation mode amplitude, one must solve a contour integral along the trajectory of each electron and sum up the wavepacket contributions.

In principle, the trajectories can be expanded in series in terms of the field amplitudes C_q . To zero order, the trajectories of the electrons are not modified by the radiation field and we know them explicitly. In this case the contour integrals can be performed straightforwardly. If all the electrons have the same trajectories (a narrow beam), then their wavepacket amplitudes are identical, except for a “start oscillation” or “entrance time” phase factor [3]:

$$C_q^{out}(\omega) = C_q^{in}(\omega) + \Delta C_{qe}^{(0)}(\omega) \sum_{j=1}^N e^{i\alpha_{oj}} + \sum_{j=1}^N \Delta C_{qj}^{st} \quad (5)$$

The contribution of the electrons to the total field depends to *zero order* in the fields on the phase relation between the wavepackets. These contributions (second term in (5)) give rise to the *spontaneous* or *superradiant* emission of the electron beam [3]. At higher order of expansion in terms of the fields, the modification of the electron trajectories by the fields, gives rise to *stimulated emission* or *stimulated absorption*, represented by the last term of (5).

Once one calculated the mode amplitudes (5) it is possible to substitute them in (3) to find the total field. Alternatively, one can use them to calculate optical parameters as radiation mode power or spectral energy (both are quadratic forms of C_q):

$$P_q = |C_q^{out}(\omega)|^2 \quad \text{or} \quad \frac{dW_q}{d\omega} = \frac{2}{\pi} |C_q^{out}(\omega)|^2 \quad (6)$$

Several physical situations can be distinguished, corresponding to the manner the amplitudes in (5) combine in the complex $C_q(\omega)$ plane to produce the total radiation field. These are shown graphically in Fig.2 [3]. Let us now neglect the stimulated emission terms, and assume no input field $C_q^{in}(\omega) = 0$. When one absolute value square the second term in (5) and then average over the electron phases j , one can distinguish two cases, corresponding to two different emission processes:

(1) The electron entrance times are random (Fig.2a). In this case only the non-mixed terms in the square of the sum do not average down to zero

$$\left\langle \left(\sum_{j=1; j \neq i}^N e^{i\alpha_{oj}} \cdot e^{i\alpha_{oi}} \right)_j \right\rangle = 0$$

consequently the spectral energy is proportional to the number of particles N . This process is referred to as *spontaneous emission* or *shot noise emission*, and radiation spectral energy (6) is proportional to:

$$\left\langle \left| \sum_{j=1}^N e^{i\alpha_{oj}} \right|^2 \right\rangle_j = N \quad (7)$$

(2) The electron entrance times are correlated (Fig.2b): either they enter in a bunch of duration shorter than the radiation period, or periodically at the radiation frequency. In these cases the wavepackets emitted by the individual electrons interfere in phase with each other, and the spectral power is proportional to N^2 :

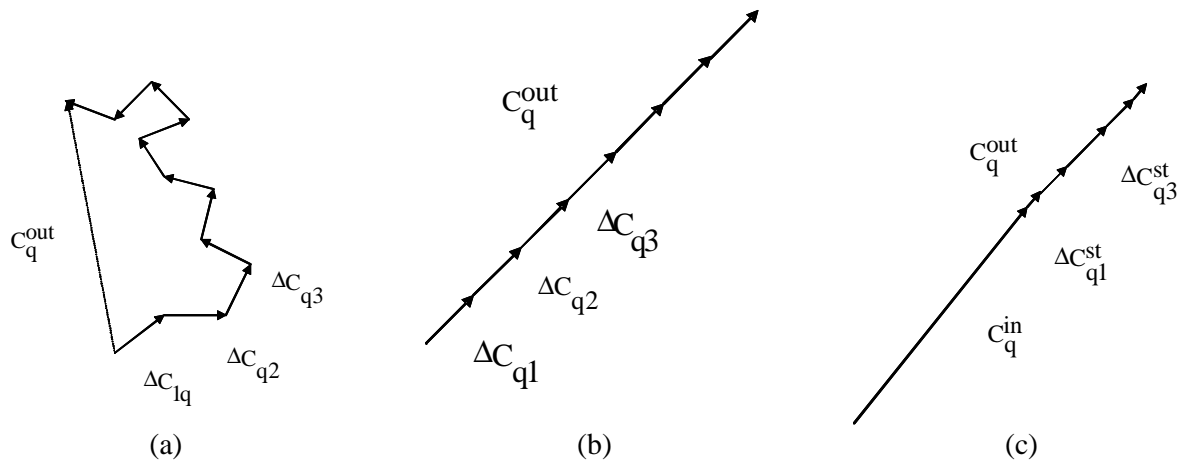


Fig.2: Superposition of mode wavepacket amplitudes of electrons C_{qj} in the complex plane: a) spontaneous emission, b) superradiant emission, c) stimulated emission.

$$\left\langle \left| \sum_{j=1}^N e^{i\omega t_{0j}} \right|^2 \right\rangle_j = N^2 \quad (8)$$

We term this emission process “superradiance”, following Dicke [4], who analyzed this case for an ensemble of molecules having electric or magnetic dipoles, employing a full quantum formulation (note though that the superradiance effect is classical even in Dicke’s problem [1]). Superradiant emission is also termed *coherent emission*, as in CSR [5].

(3) When the mode field amplitudes at entrance do not equal to zero ($C_q^{in} \neq 0$) (Fig.2c), the electron trajectories may be modified by the presence of the radiation field, and the integral (4) will result in, beyond the zero order expansion approximation, a field-dependent radiation term (third term in (5)). This is the *stimulated Emission* term. In first order expansion in the fields (linear regime), neglecting inter-mode scattering, and this term is proportional to the mode field amplitude:

$$\sum_{j=1}^N \Delta C_{qj}^{st} \propto C_q$$

and therefore produces radiation wavepackets in phase with the incoming wave of amplitude C_q^{in} , and the total radiation is coherent.

UNDULATOR RADIATION OF A SINGLE ELECTRON

The formalism and classification described in the previous section can be applied to any kind of radiation mechanism: undulator, synchrotron, Smith-Purcell etc. [3, 6]. We now concentrate on the case of radiative emission in an undulator. Expressing the radiation field both in frequency domain and time domain, helps to understand the coherence characteristics of undulator radiation and FEL devices. We therefore will employ on occasions inverse Fourier transform on the radiation expressions which are generally derived in this formulation in the frequency domain.

The frequency domain amplitude of a wavepacket

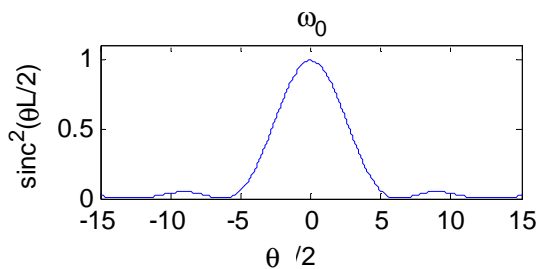


Fig.3 The spectral emission curve of undulator radiation of single electron emission.

emitted into transverse mode q by a single electron traversing through an undulator is calculated from (4):

$$C_q^{out}(\omega) = -\frac{1}{4} \left\{ -e \int_{-\infty}^{\infty} \mathbf{v}_j(t) \cdot \tilde{\mathbf{E}}_q^*(\mathbf{r}_j(t)) e^{i\omega t} dt \right\} \quad (9)$$

$$\mathbf{v}_j(t) = \text{Re} \left\{ \tilde{\mathbf{v}}_w e^{-ik_w z_j(t)} \right\} + v_z \hat{\mathbf{e}}_z$$

The result is:

$$C_{qj}^{out}(\omega) = e^{-\frac{\mathbf{v}_w \cdot \mathbf{E}_q^*(\mathbf{r}_{\perp 0})}{8v_z}} L \text{sinc}(\theta(\omega)L/2) e^{i\theta(\omega)L/2} e^{i\omega t_{0j}} \quad (10)$$

where $\theta(\omega)L \equiv \left(\frac{\omega}{v_z} - k_z(\omega) - k_w \right) L = (\omega - \omega_0) t_{sl}$ is the detuning parameter); $t_{sl} = \frac{2\pi}{\Delta\omega} = \frac{L}{v_z} - \frac{L}{v_g}$ is the slippage

time, and ω_0 , the synchronism frequency, is defined from $\theta(\omega_0) = 0$. Substituted in (6), this is a resonant emission linewidth function, centered on the synchronism frequency, and having a frequency bandwidth equal to the inverse of the slippage time (Fig.3):

Note that the amplitudes (10) of the wavepackets C_{qj}^{out} of different electrons differ only by a phase factor (as in (5))!

One can describe the wavepacket field in the time domain by performing an inverse Fourier transform over the complex amplitude function (10):

$$\begin{aligned} \mathbf{E}(\mathbf{r}, t) &= \mathbf{F}^{-1} \left\{ C_q(z, \omega) \mathbf{E}_q(\mathbf{r}_{\perp}) e^{ik_z(\omega)z} \right\} = \\ &= \sum_{i=1}^2 A_i \mathbf{E}_q(\mathbf{r}_{\perp}) \cos(k_z(\omega_i)z - \omega_i t) \text{rect} \left[\frac{t - z/v_z + t_{sl_i}/2}{|t_{sl_i}|} \right] \end{aligned} \quad (11)$$

In the time domain, the wavepacket is composed of two simple truncated sinusoidal waveforms (Fig.4). The *high frequency* radiation wavepacket of slippage time duration t_{sl1} arrives first after a retardation time L/v_{g1} ; then the electron arrives after time L/v_z and at the end the *low frequency* wavepacket, corresponding to backward emission in the electron rest-frame, arrives with a radiation (back-slippage) time L/v_{g2} [7]. Here v_{g1}, v_{g2} are the group velocities of the waves propagation in a waveguide enclosure [7]. In free space $v_{g1} = c, v_{g2} = -c$ and the low frequency wavepacket is actually emitted backward also in the lab frame. In any case this low frequency wavepacket is not important for the present discussion and will be neglected in the subsequent discussion.

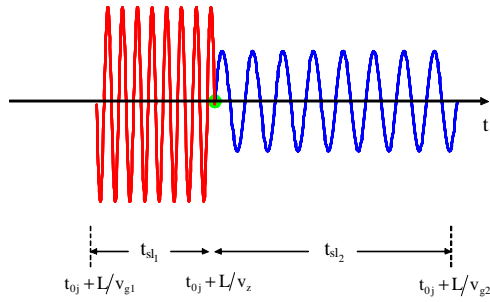


Fig.4: Time domain waveform of a single electron emission wavepacket.

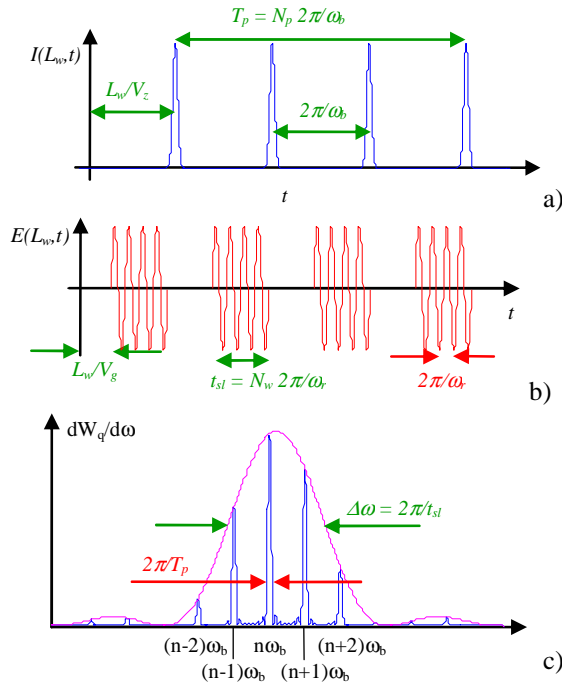


Fig.5: Superradiant (coherent) radiative emission from a macropulse train of e-beam bunches:

- a) current waveform; b) time domain picture of the train of phase coherent radiation wavepackets;
- c) spectral power of the radiation field waveform (b).

UNDULATOR RADIATIVE EMISSION OF A BUNCH OF ELECTRONS

If we consider now emission from a bunch of N electrons, its resultant radiative emission field will be composed of a superposition of wavepackets like the one in Fig.4 [3]. In the frequency domain the emission amplitude from all electrons (10) is the same except for a phase factor. Therefore the spectral emission curve is the same function as of a single electron (Fig.3). It is multiplied by N in the case of spontaneous emission (when t_{0j} is random - see Eq.7) or by N^2 in the case of superradiant emission (when $|t_{0j}-t_{0l}| < 2\pi/\omega$ - see Eq.8).

EMISSION OF A PERIODIC TRAIN OF ELECTRON BUNCHES

Examine now superradiant radiative emission from a train of electron bunches, for example a macropulse of an RF accelerator (Fig.5a).

The periodic bunches radiate independently of each other. The resultant radiation waveform (Fig.5b) is a temporal periodic sequence of the single bunch wavepackets of Fig.4 (only the high frequency wavepackets are considered). The duration of the electron beam macropulse is $T_p = N_p * 2\pi/\omega_b$: the number of electron bunches N_p times the bunching period. The duration of the wavepacket is $t_{sl} = N_w * 2\pi/\omega_r$: the number of wiggles N_w times the optical radiation period. The Fourier transform of the wave is dominated by these two time constants. Fig.5c displays the spectral power of this waveform (frequency domain) for the common case where $t_{sl} \ll 2\pi/\omega_b$. In this case there is no overlap between the wavepackets, and consequently there are several harmonics under the emission curve.

In the frequency domain, the macropulse spectral emission curve is the product of the single electron emission curve (the absolute value square of (10) - Fig.3) and the macropulse "form factor" [3]:

$$M_M(\omega) = \left[\frac{\sin(N_P \pi \omega / \omega_b)}{N_P \sin(\pi \omega / \omega_b)} \right]^2 \quad (12)$$

The emission is wide band ($2\pi/t_{sl}$), but if one can filter out one harmonic, or if $\omega_b > \Delta\omega_{sl}$, it will have a narrow linewidth corresponding to the macropulse duration (under the condition of *stability* of the bunching frequency during the entire macropulse duration). This observation will be important also for the later discussion on the case of FEL oscillator and SASE.

A nice verification of this concept was demonstrated by the MIT research group [8] who measured superradiant Smith-Purcell coherent emission using an RF Linac beam. Carefully filtering out the radiation emission at the 14th harmonic of the microbunch repetition rate within the macropulse by *heterodyne detection techniques*, they measured the exceedingly narrow linewidth of the total waveform of the macropulse radiation. It was indeed $2\pi T_p$, corresponding to the duration T_p of the e-beam macropulse.

If the electron bunch has a finite duration t_b , then the expression for radiation spectral energy includes also a "bunch-form factor"

$$|M_B(\omega)|^2 = \left| \frac{1}{Q} \int_{-\pi/\omega_b}^{\pi/\omega_b} I(t) e^{i\omega t} dt \right|^2 \quad (13)$$

(which is equal to unity as long as $t_b \ll 2\pi/\omega$). This, in practice, limits the harmonic number n_H , that can have appreciable amplitude out of the infinite numbers of harmonics that the macropulse form factor (12) admits, to

$$n_H \ll 2\pi/\omega t_b \quad (14)$$

If the waveform of the electron-beam current does not contain high harmonics (e.g. it is sinusoidally modulated) then there will be no harmonics under the spectral energy curve in Fig.5b except the fundamental ($n_H=1$), and its amplitude will be appreciable only within the bandwidth of the single electron emission spectrum $(\omega-\omega_b) < \Delta\omega = 2\pi/t_{sl}$. The narrow linewidth ($\delta\omega \sim 2\pi T_p$) radiation of the prebunched FEL follows the detuning curve of Fig.3 as demonstrated experimentally in [22].

Single harmonic radiative emission can take place also at high harmonic n_H of the bunching frequency ω_b . This will happen (under the condition (14)) if the spacing between the harmonics exceeds the emission bandwidth:

$$\begin{aligned} \omega_b > \Delta\omega_{sl} = 2\pi/t_{sl} \\ \text{or} \quad n_H < 2\pi/\omega_0 t_{sl} \equiv N_w \end{aligned} \quad (15)$$

In this case, the wavepackets train of Fig.5b merges into an harmonic wave of the macropulse duration T_p .

FEL AMPLIFIER

Our main interest is in stimulated emission. Many of the spectral features of superradiant emission discussed above apply quite closely also to stimulated emission in an amplifier configuration. The derivation of the increments ΔC_q^{st} in the wavepacket amplitudes (third term in Eq.5) in the amplifier case is more involved, since it requires the calculation of the modification of the electron trajectories by the input radiation field. When this is done, it is found that also in this case the electron beam is bunched. The classical stimulated emission from an electron beam, always involves electron beam density

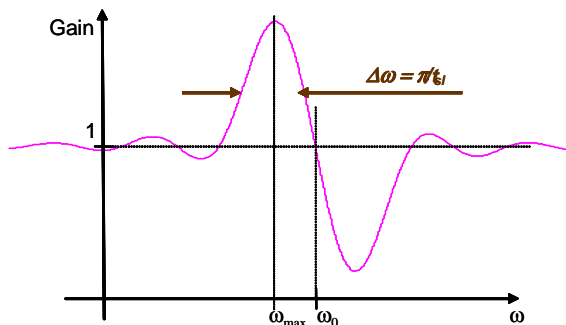


Fig.6: The FEL Linear regime small-gain curve.

bunching. Contrary to superradiance the bunching is not set *ab-initio*, before entrance into the interaction region, but it is created by the input radiation signal, at the signal frequency, in the first part of the wiggler.

As well known, in a CW (or long pulse) FEL amplifier the single mode (1-D) incremental power gain is given in the linear (small signal) small gain regime by (see Fig.6) [6, 16]:

$$\frac{\Delta P}{P} = \bar{Q} \frac{d}{d\theta} \text{sinc}^2(\bar{\theta}(\omega)/2) \quad (16)$$

The frequency ω of the electron bunching and the consequent radiation is determined by the input radiation signal. Thus the bandwidth of emitted radiation is determined by the bandwidth of the input signal, and if it is monochromatic then the output radiation is temporally coherent (except for admixture of noise (spontaneous undulator radiation) power emitted in the wiggler. Note however that the gain curve (16) (Fig.6, which is the derivative of the spontaneous emission spectral curve Fig.3) is quite wide still – about one half the width of the spontaneous emission curve $\Delta\omega_{sl} = \pi/t_{sl}$.

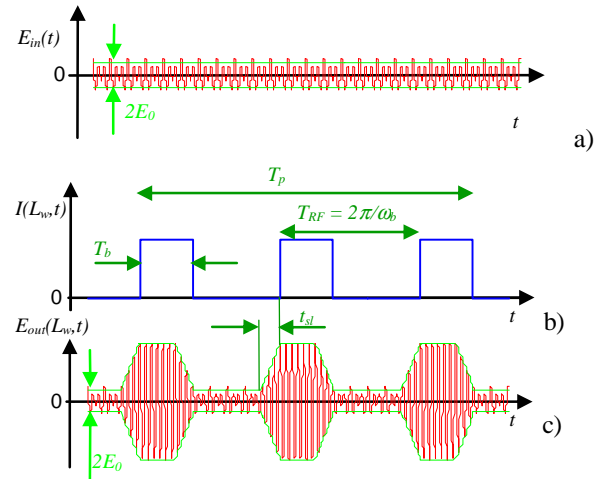


Fig.7: RF-Linac FEL Amplifier in the time domain. a) multi-frequency coherent input signal b) Electron beam macropulse current waveform c) Amplified signal.

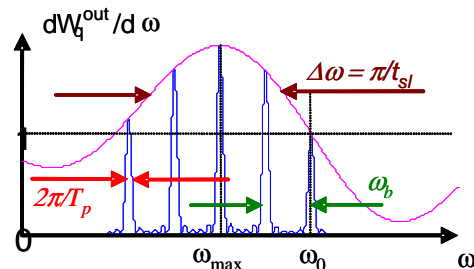


Fig.8: Spectral power of the amplifier output radiation waveform of Fig.7c.

If the electron beam is not continuous, of course, its temporal wave-form will modify the spectrum of the amplifier radiation output. Let us consider an FEL amplifier fed by a train of electron beam pulses (microbunches) from a continuously operating RF-LINAC (see Fig.7b). The electron macropulse duration, micropulse duration and repetition period are typically $T_p = 10 \mu\text{s}$, $T_b \sim \text{ps}$, $T_{RF} \sim \text{ns}$ respectively. The radiation signal period (say is the visible spectral region) $2\pi/\omega_b \sim \text{fs}$ and the slippage time $N_w 2\pi/\omega_b \sim 10 - 100 \text{ fs}$, are both much shorter than the pulse duration T_b .

Fig.7 depicts this case in the time domain. For didactic reasons we assume that the input radiation (Fig.7a) is a *coherent* multi-frequency wide spectrum signal, wider than the gain bandwidth of the FEL ($\Delta\omega_{sl} \sim \pi/t_{sl}$). The output signal (Fig.7c) is time gated by the waveform of the electron beam (Fig.7b) and also frequency filtered by the gain bandwidth of the FEL during the pulse duration.

The same case is displayed in the frequency domain in Fig.8. Only radiation frequencies within the gain bandwidth π/t_{sl} of the gain curve Fig.6 are amplified. Among the amplified frequencies only the ones which are harmonics of the bunching frequency ω_b , within a

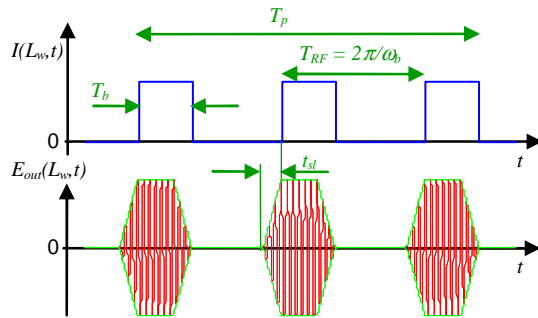


Fig.9: The time domain waveform of the radiation wavepackets emitted at saturation by an RF-Linac FEL oscillator during the electron beam macropulse.

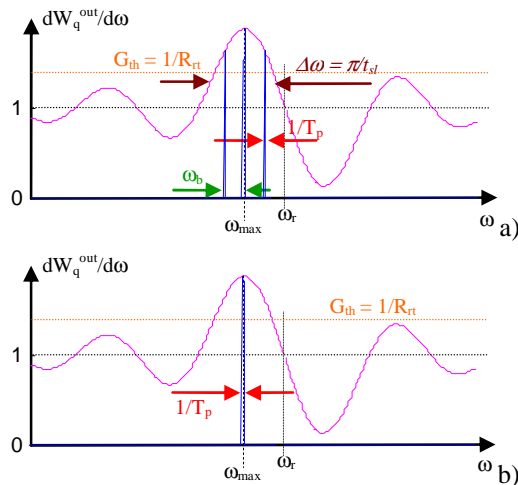


Fig.10: The spectral power and modes structure of saturated FEL oscillator – a) multiple modes, coherently mode-locked in an RF-Linac FEL, b) Single mode operation in a quasi-CW or long pulse (electrostatic accelerator) FEL.

frequency deviation $\Delta\omega \sim 2\pi/T_p$ will contribute coherently to a Fourier transformation of the waveform in Fig.7c (carried out over the entire macropulse). Consequently the amplified signal spectrum will contain harmonics of ω_b of linewidth $2\pi/T_p$.

RF – LINAC FEL OSCILLATOR

In laser physics it is customary to present an oscillator as an amplifier with feedback. In each round-trip a radiation wave-packet synchronous with an overlapping e-beam bunch gets amplified and is reflected back by mirrors into the entrance to the interaction region. It is assumed that the bunching frequency is commensurate with the round-trip frequency of the resonator: a new e-beam bunch arrives together with the radiation pulse, and the amplification process continues up to steady state saturation.

How does the saturation of an RF Linac FEL look in the time domain? Fig.9 displays the steady state waveform of the oscillator radiation in the time domain. It displays radiation pulses emitted synchronously with the RF bunches, somewhat modified by the slippage effect (as in the amplifier case – compare to Fig.7c).

In the frequency domain (Fig.10a), the single path gain curve is the same as in the amplifier (Fig.8), and the RF frequency of the e-beam bunches is synchronized (by cavity length detuning) with the round-trip frequency of the radiation pulses – namely the longitudinal modes of the resonator. In addition, in the oscillator there is a gain threshold condition: $P_{out}/P_{in} > 1/R_{rt}$. In the oscillation build-up process all modes (harmonics) are initially excited. But at saturation only modes with gain higher than the threshold are filtered in, and have a chance to survive the oscillation build-up process (Fig.10a).

The steady state output is as in the superradiant emission case (Fig.5) a finite coherent sum of longitudinal modes that lie within the gain bandwidth π/t_{sl} of the FEL. This finite sum of harmonic frequencies looks in the time domain as a periodic train of radiation pulses synchronous and with good overlap with the macropulses of e-beam bunches train that provides the gain. This is an exact analogue of an actively locked conventional "mode locked laser". Also in this case, if the RF frequency is stable over the macropulse, the coherence of the harmonics is very high (if they are filtered out), and is determined by the duration of the macropulse $\Delta\omega \sim 2\pi/T_p$. Namely, the consecutive radiation wavepackets are coherent with each other throughout the macropulse (assuming a single bunch per round-trip).

It is worth noting that high coherence between the radiation wavepackets emitted by consecutive microbunches was measured in a long-wavelength FEL oscillator [19]. This was measured both for the spontaneous and stimulated emission of the FEL. It is remarkable that this coherence was observed when there are several microbunches in the resonator at the same time (RF bunching period shorter than the cavity round-trip time). This is explained there as the result of high

stability of the e-beam RF frequency and the microbunches envelop shapes. It is argued that in the parameters regime of the FELIX FEL [19], the microbunch formfactor (16) is appreciable of the emission frequency, and the superradiant (coherent) undulator radiation related to the stable shape of the micropulse current waveform dominates the random shot noise radiation, and consequently determines the phase of all wavepackets. This happened both under conditions of saturated stimulated emission (oscillator lasing) and absence of stimulated emission (no overlap of the recirculating wavepackets).

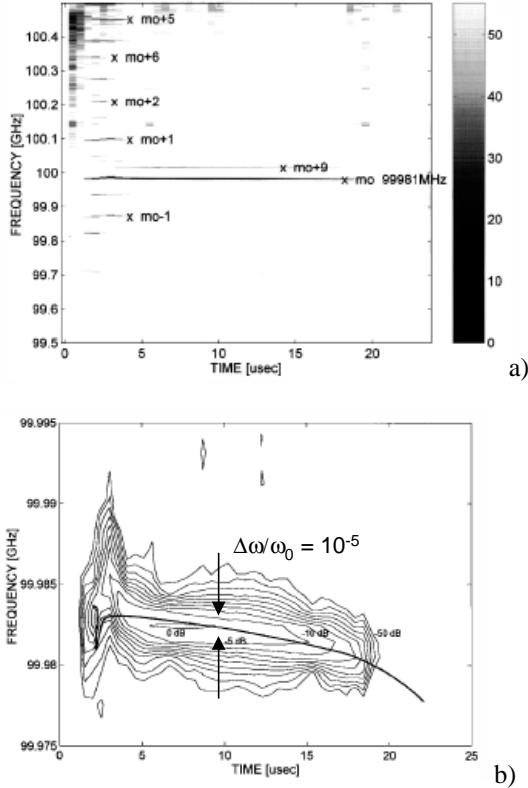


Fig.11: Spectrogram of the radiation output from an electrostatic accelerator FEL oscillator [9].

a) Multimode spectrum evolving into single mode operation during the oscillation build-up periods.

b) Fourier transform limited spectrum of the surviving single mode.

Maser	$\Delta\nu_{maser} = 2\pi kT \frac{(\Delta v_{sp})^2}{P_{gen}}$	Gordon, Zeiger, Townes [11]
Laser	$\Delta\nu_{laser} = 2\pi\hbar\nu \frac{(\Delta v_{1/2})^2}{P_{gen}}$	Schawlow, Townes [12]
FEL	$\Delta\nu_{FEL} = \frac{(\Delta v_{1/2})^2}{I_0/e}$	Gover, Amir, Elias [13]

CW (ELECTROSTATIC ACCELERATOR) FEL OSCILLATOR

What would happen in a CW or a long pulse FEL oscillator (like an electrostatic accelerator FEL)? In this case, there are longitudinal modes due to the round-trip periodicity, but there is no active mode locking. In principle, many longitudinal modes can co-exist within the gain bandwidth, and there is no external cue that can phase-lock them.

The oscillation build-up stage involves in this case a mode competition process, which arises when the oscillator approaches saturation and arrives to the non-linear regime. In the FEL, as in other "homogeneously broadened lasers", this process ends with single mode operation (see Fig.10b). The single mode laser radiation linewidth is very narrow corresponding to the pulse duration. It is given by the Fourier transform limit $\Delta\omega_{line} \sim 2\pi/T_p$, and it tends to zero as $T_p \rightarrow \infty$ (CW operation). An experimental confirmation for the mode competition process and the Fourier transform limited linewidth of the single-surviving mode in an Electrostatic Accelerator FEL was provided in the Israeli FEL [9] (see Fig.11). In [9] a relative linewidth $\Delta\omega_{line}/\omega_0 = 10^{-6}$ was measured at frequency $f_0 = 100$ GHz corresponding to a pulse duration $T_p \sim 10$ μ s.

What determines the linewidth in the limit $T_p \rightarrow \infty$? This fundamental problem was addressed already in the early days of conventional masers [11] and lasers [12]. In principle the oscillator line breadth is determined by a process of admixture of incoherent radiation with the coherent stored radiation field in the cavity. This process leads to random phase drift of the radiation mode amplitude C_q at the saturation stage (the amplitude is locked by the saturation process). In a maser the intrinsic linewidth results in from incoherent black body radiation emission into the cavity [11]. In a conventional laser, the limiting factor is the quantum spontaneous emission [12]. In the FEL the limiting factor is the spontaneous undulator radiation emission (or the electron beam shot noise) [9, 13]. The three intrinsic linewidth expressions are listed in Table 1.

HIGH GAIN FEL AMPLIFIER

Our analysis of the FEL in the linear regime is based on the Pierce TWT model for TWT [14, 6]. It is found that the amplitude of the radiation mode $C_q(L)$ in an FEL amplifier of interaction length L , depends on the input field amplitude $C_q(0)$ (regular FEL), but also on the amplitudes of the e-beam velocity and current (density) pre-modulation [15, 16]:

$$C_q(L, \omega) = H^E(\omega) C_q(\omega, 0) + H^v(\omega) v(\omega, 0) + H^I(\omega) I(\omega, 0) \quad (17)$$

where the transfer functions are:

$$H^E(\omega) = \sum_{j=1}^3 \text{Res} \left(\frac{(\delta k_j - i\theta)^2 + \theta_{pr}^2}{\Delta} \right) e^{i(k_{zq} + \delta k_j)L} \quad (18.1)$$

$$H^V(\omega) = \sum_{j=1}^3 \text{Res} \left(\frac{ik_z L / v_{0z} \cdot P_b^{1/2}}{\Delta} \right) e^{i(k_{zq} + \delta k_j)L} \quad (18.2)$$

$$H^I(\omega) = \sum_{j=1}^3 \text{Res} \left(\frac{(\delta k - i\theta)}{\Delta} \cdot P_b^{1/2} / I_b \right) e^{i(k_{zq} + \delta k_j)L} \quad (18.3)$$

$$P_b = \frac{I_b^2 \sqrt{\frac{\mu_0}{\epsilon_0}}}{32} \cdot \left(\frac{a_w}{\gamma \beta_z} \right)^2 \cdot \frac{L^2}{A_{em}} \quad (18.4)$$

$$\Delta = \delta k (\delta k - \theta - \theta_{pr}) (\delta k - \theta + \theta_{pr}) + \Gamma^3 \quad (18.5)$$

In these formulas we use the “conventional” parameters: θ – detuning parameter; Γ – gain parameter; θ_{pr} – space-charge parameter with reduction factor; L – interaction length; I_b – electron beam current, A_{em} – effective mode area. Here $\delta k = k_z - k_{zq}$ is the modification to the wavenumber of mode q (at fixed frequency ω) due to the interaction. Solution of the Pierce cubic dispersion equation 18.5 and substitution into (17, 18.1-18.3) results in the output radiation field amplitude for all gain regimes and any initial conditions.

In the high gain tenuous beam regime ($\Gamma^3 \gg \theta, \theta_{pr}, I$) one gets for an FEL amplifier:

$$P_q(L, \omega) = \left| \tilde{H}^{FEL} \right|^2 \cdot \left| \tilde{C}_q(0, \omega) \right|^2 = \left| \tilde{H}^{FEL} \right|^2 P_q(0, \omega) \quad (19.1)$$

for a current (density) pre-bunched FEL:

$$P^{pb-I}(L, \omega) = \left| \tilde{H}^{FEL} \right|^2 \cdot P_b \left(\frac{1}{I_b \Gamma L} \right)^2 \left| \tilde{I}(0, \omega) \right|^2 \quad (19.2)$$

for a velocity pre-bunched FEL:

$$P^{pb-v}(L, \omega) = \left| \tilde{H}^{FEL} \right|^2 \cdot P_b \left(\frac{k_z L}{v_{0z} (\Gamma L)^2} \right)^2 \left| \tilde{v}_z(0, \omega) \right|^2 \quad (19.3)$$

Here

$$\left| \tilde{H}^{FEL} \right|^2 = \frac{1}{9} e^{\sqrt{3} \Gamma L} \cdot e^{-(\omega - \omega_0)^2 / (\Delta \omega_{HG})^2} \quad (19.4)$$

is the power transfer function of the high gain FEL, and

$$\Delta \omega_{HG} = \frac{3^{3/4}}{2\pi} \lambda_w \sqrt{\frac{\Gamma}{L}} \omega_0 \quad (19.5)$$

is the full width of 1/e of maximum of the high gain FEL gain curve and

SASE FEL

The current and velocity modulation amplitudes in (19.2, 19.3) may be deterministic (prebunching) or random (noise). The video presentation in the transparencies demonstrates the meaning and significance of the current and velocity coherent modulation and noise processes.

The SASE FEL is based on amplification of electron beam noise in the FEL high gain regime. To analyze this case it is proper to calculate spectral energy and spectral power parameters instead of the single frequency gain and radiative power parameters (19.1-19.3):

$$\frac{dW_q}{d\omega} = \frac{2}{\pi} \left\langle \left| \tilde{C}_q(\omega) \right|^2 \right\rangle \quad (20.1)$$

$$\frac{dP_q}{d\omega} = \frac{1}{T} \left\langle \frac{dW_q}{d\omega} \right\rangle \quad (20.2)$$

where the averaging is over the electrons random entrance times and T is an averaging time duration longer than the slippage time t_{sl} .

The SASE FEL is nothing but a single path high gain FEL with an effective beam-prebunching input signal due to current shot noise and velocity shot noise. Near the synchronism frequency its spectral power is a sum of the amplified current and velocity shot noise sources:

$$\frac{dP_q^I}{d\omega} = \frac{2}{\pi} H^{FEL} \cdot P_b \left(\frac{1}{I_b \Gamma L} \right)^2 \frac{\left\langle \left| \tilde{I}(0, \omega) \right|^2 \right\rangle}{T} \quad (21.1)$$

$$\frac{dP_q^v}{d\omega} = \frac{2}{\pi} H^{FEL} \cdot P_b \left(\frac{k_z L}{v_{0z} (\Gamma L)^2} \right)^2 \frac{\langle |\tilde{v}_z(0, \omega)|^2 \rangle}{T} \quad (21.2)$$

where

$$\frac{\langle |\tilde{I}(0, \omega)|^2 \rangle}{T} = e I_b \quad (22.1)$$

$$\frac{\langle |\tilde{v}_z(0, \omega)|^2 \rangle}{T} = \frac{e}{I_b} |\delta v_z|^2 \quad (22.2)$$

Here δv_z is the axial velocity spread of the electron beam.

Usually the current shot noise is considered the main source for SASE input power and the velocity noise is neglected. This is not self evident. For this assumption to be valid (21.1) should exceed (21.2). Considering (22.1, 22.2) this leads to the condition

$$\frac{\delta v_z}{v_{oz}} < \frac{\Gamma}{k_z} \quad (23)$$

SPIKING IN SASE-FEL AND THE IMPULSE RESPONSE FUNCTION

Since the SASE-FEL is a wide band amplifier of a wide band incoherent signal (the shot noise), it is no wonder that the spectrum of its radiation output is relatively wide and its temporal waveform is characterized by a random sharp structure (spiky). Fig.12 [10, 17] displays the typical spectrum of a single SASE radiation pulse (Fig.12a), the averaged spectrum over many pulses (Fig.12b) and the spiky time-domain waveform of a single radiation pulse (Fig.12c). One should note that the

relatively high bandwidth of the averaged radiation spectrum ($1/T_{coh}$) is related to the characteristic duration of the spikes (T_{coh}). It is also noteworthy, that the single pulse spectrum contains spectral lines that are very narrow ($1/T_b$) – corresponding to the duration of the e-beam micro bunch - but appear at random centre frequencies.

Since the shot noise spectrum is uniform, the average spectrum of the SASE is determined merely by the transfer functions (18.2, 18.3). Consider now only the current shot noise. It is useful to expand the logarithm of the exponentially growing term in (18.3) (including the phase, namely the imaginary part) to second order in terms of frequency ω around the *synchronism* frequency ω_0 . In the high gain (tenuous beam limit) this results in:

$$\begin{aligned} \tilde{H}^I(z, \omega) \cong & \frac{P_b}{3I_b \Gamma z} e^{-i\pi/12} e^{(\sqrt{3}+i)\Gamma z/2} \times \\ & \times e^{-(1+i/\sqrt{3})(\omega-\omega_0)^2/2(\Delta\omega_{HG})^2} e^{ikz} \end{aligned} \quad (24)$$

where $\Delta\omega_{HG}$ is the width of the high gain FEL gain curve. Indeed this spectral width is the linewidth $\Delta\omega_{HG} \sim 1/T_{coh}$ of the SASE average spectrum shown in Fig.12b.

It is instructive now to calculate the "impulse response function" corresponding to the complex transfer function (24). This is straightforwardly found by applying an inverse Fourier transformation on (24):

$$\begin{aligned} E(z, t) = \text{Re} \{ & \left(P_b \Delta\omega_{HG} / 3^{3/4} \sqrt{2\pi(i+\sqrt{3})} I_b \Gamma z \right) \cdot \\ & \exp[-i\pi/12 + (\sqrt{3}+i)\Gamma z/2] \cdot \\ & \exp \left[+i \left(\omega_0 \left(t - \frac{z}{c} - t_0 \right) - (\Delta\omega_{HG})^2 \left(t - \frac{z}{c} - t_0 \right)^2 / 8 \right) \right] \cdot \\ & \exp \left[-(\Delta\omega_{HG})^2 \left(t - \frac{z}{c} - t_0 \right)^2 / 8 \right] \} \end{aligned} \quad (25)$$

This function is displayed in Fig.13. It depicts (within the quadratic expansion approximation a Gaussian wave form envelope of width $T_{coh} \sim 1/\Delta\omega_{HG}$. It also reveals an

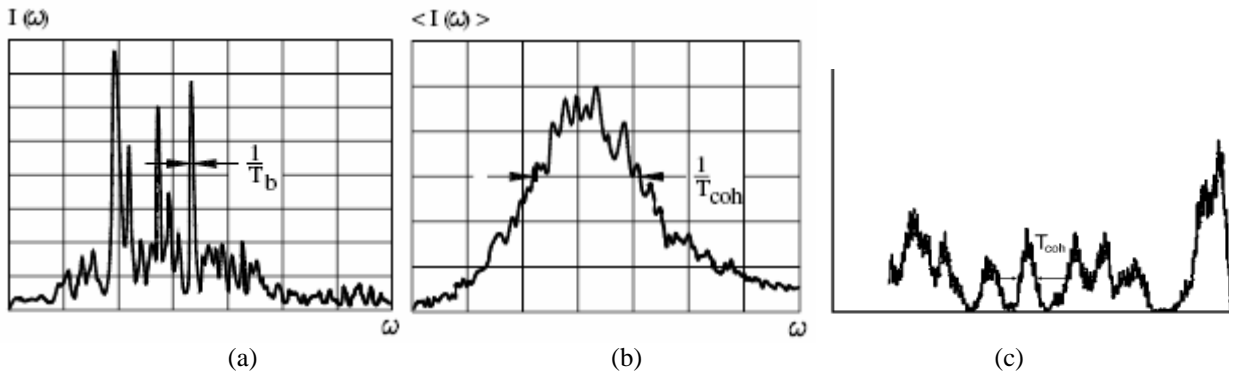


Fig.12: Simulation data of SASE radiative emission [9, 16]:

a) Single pulse spectral power, b) Spectral power averaged over many pulses, c) Time domain "Spiky" intensity distribution of a single pulse.

inherent (negative) chirp of the centre frequency

$$\frac{d\omega}{dt} = \frac{d^2\varphi}{dt^2} = -(\Delta\omega_{HG}/2)^2 \quad (26)$$

The impulse response function (25) is the coherent field wave-form created by an impulse of charge (of duration much shorter than the radiation wavelength), which is

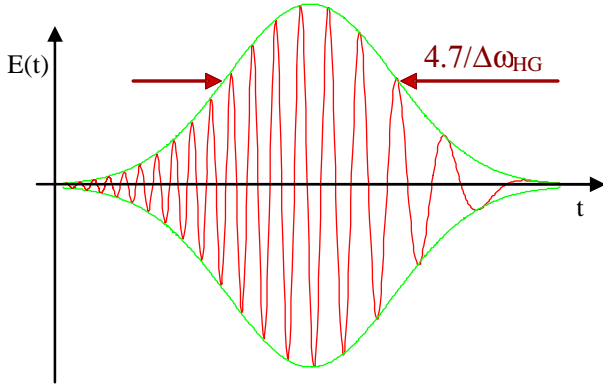


Fig.13: The time domain charge-impulse response function of an FEL in the high gain regime (Eq. 20).

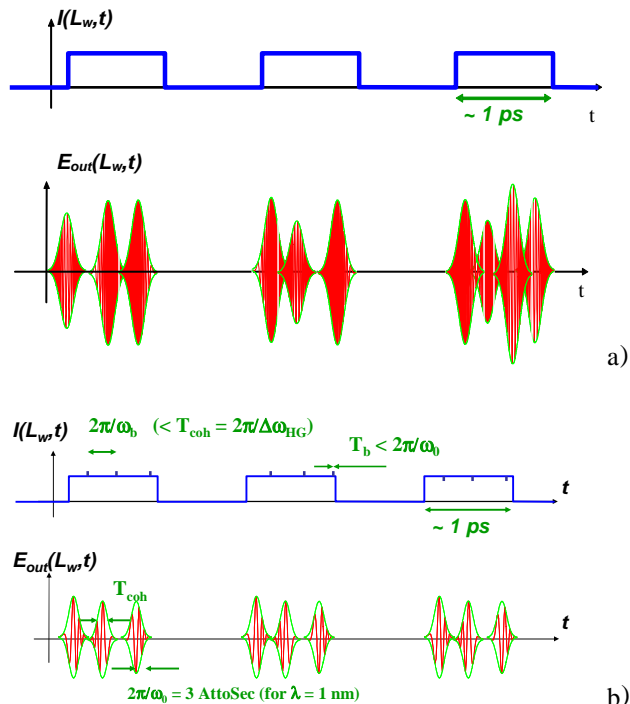


Fig.14: Spikes emission in SASE FEL within the micropulses duration: a) Random emission
b) Phase-locked coherent spikes emission initiated by subharmonic current prebunching.

Prebunching can be produced by a train of superimposed positive or negative current impulses or any stable periodic current waveform of high harmonic contents.

superimposed at entrance over a uniform e-beam current I_b . It is quite natural to identify it with the spikes phenomenon shown in Fig.12c. The physical picture of the phenomenon is based on appearance of random electron bunches (current fluctuation) on the electron beam current entering the interaction region. This current is uniform on the average, but fluctuates because of the randomness of electrons generation in the cathode ("shot noise"). The random electron bunches start radiating *superradiantly* right at start, and their radiation wavepackets dominate over the spontaneous radiative emission from the other uniformly (but randomly) injected electrons. Due to the forward slippage effect of the radiation wavepacket and the high gain stimulated emission process, the random electrons, that are flowing within a cooperation length $v_z T_{coh}$ ahead of the initial radiating random bunch, are induced to emit at the same frequency and phase (except for the inevitable chirp effect), and consequently a coherent wavepacket (Fig.13) is emitted. The output wavepacket duration $T_{coh} = \pi/\Delta\omega_{HG}$ (determined by the high gain FEL bandwidth 19.4) is the minimal width of the spike. Spikes that are excited by random bunches in time always shorter than T_{coh} merge into one spike. Assuming there are always enough random bunches to negate presence of long "silent" spaces between the spikes; one can estimate that the average number of spikes in a bunch of duration T_b is T_b/T_{coh} [10]. Fig.14a displays the spikes waveforms of this physical model. It should be compared to the simulation spiky pattern of Fig.12c. If $T_b \approx T_{coh}$ then there is only one spike in the macropulse duration [17]. In this case the SASE radiation is as coherent as can be (Fourier transform limited). Its spectral width is $\approx \pi/T_{coh} = \pi/T_b$. It can be narrowed down only if pulse stretching techniques can be employed.

CONDITIONS FOR COHERENT X-UV FEL

It is well known that the radiation output of SASE FEL is spatially coherent (due to the optical guiding effect). This is the reason why SASE FELs can be so much brighter than any other existing radiation source in this spectral regime. However there will be even greater interest in this source if it would be also temporally coherent and stable (pulse to pulse). How can a SASE FEL be turned into a coherent radiation source?

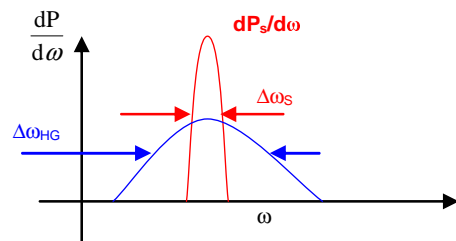


Fig.15: Spectral power of the coherent radiation output of the FEL amplifier (red) and the SASE (shot noise) radiation (blue).

Realizing that the SASE-FEL is an amplifier of noise, it is evident that what is required is a coherent input signal. The input signal can be a coherent radiation wave (this is sometimes called seed radiation injection), and there has been intensive studies of developing an appropriate coherent seed radiation sources based on high harmonic multiplication of intense laser pulses in gas. Another scheme is based on filtering the undulator synchrotron radiation after a few sections of the undulator, and reinjecting the narrower bandwidth radiation into the undulator for high gain amplification.

Another approach for attaining coherent emission from SASE-FEL is based on coherent prebunching of the electron beam (within the duration of its pSec microbunches) at the radiative emission frequency of a high power optical laser or its subharmonics. This process can be repeated in several steps, in which the bunched radiation is amplified at high gain, and then high harmonics of the electron bunching are filtered out and amplified again, and so on (High Gain High Harmonic Generation – HGHG [21]).

In all of these schemes the condition for attaining coherent high power output radiation is that the coherent input signal will be significantly larger than the noise. In the first case of *seed radiation injection* (coherent amplification) a simple criterion can be inferred by comparing (19.2) to (21.1-22.2). Assuming the current shot noise is dominant, this condition is:

$$P_s(0) \gg P_b \frac{e}{I_b (\Gamma L)^2} \Delta\omega \quad (27.1)$$

Here $\Delta\omega$ is the frequency bandwidth of the detection system in which inevitable (now undesirable) SASE radiation is collected. If there are no means of filtering available, then $\Delta\omega = \Delta\omega_{HG}$ - the SASE radiation bandwidth. In any case $\Delta\omega_s, \pi T_b < \Delta\omega < \Delta\omega_{HG}$, where $\Delta\omega_s$ is the linewidth of the injected input radiation and πT_b is the Fourier limited bandwidth of the finite pulse. Similar condition can be derived for the required prebunching current required to dominate the current shot-noise by comparing (19.2) to (21.1, 22.1):

$$|\tilde{I}(0, \omega)|^2 \gg \frac{2}{\pi} e I_b \Delta\omega \quad (27.2)$$

PHASE LOCKING THE SPIKES

If sufficient coherent seed radiation input power is attainable it makes the output power of the FEL amplifier coherent as well. But other aspects of the *seed radiation injection* approach, as tunability and operating wavelengths range still need to be addressed. The *current prebunching* approach may provide more options of frequency tunability and short wavelengths availability.

But its realization requires more intricate conceptual schemes.

Much insight into this problem may be gained from the physical description of the radiation processes in the previous section. In particular it is worth noting the striking correspondence between the emission of single mode undulator radiation wavepackets by a single electron (or single bunch) (10) (in the frequency domain) and (11) (in the time domain) and the corresponding expressions of spectral transfer function (24) and impulse response function (25) in the case of FEL in the high gain regime. In the first case the wavepackets emission process is spontaneous (or superradiant in the case of a bunch) and no supporting medium is required for the wavepacket emission. In this case Eq.11 (Fig.4) is the explicit time-domain expression of the wavepacket emitted in the undulator from a particulate charge of *one electron* (e). In the second case, (Eq.25) (Fig.13) is the radiation wavepacket emitted by a *current impulse of a unit charge*, and the excitation of this wavepacket is conditioned on the presence of an electron beam medium (assumed uniform) in front of the beam current impulse. Its emission process involves stimulated emission and bunching of the e-beam, in contrast to the first case.

In both cases the coherence of the total radiation of the e-beam depends on the phase relation between the emitted respective wavepackets by the charged particles or by the bunches. In the first case, when the electrons enter into the undulator at random, the superposition of the radiation wavepackets (11) in (5) produces incoherent radiation (or more correctly - partially coherent radiation with coherence time t_{st}). Analogously, in the SASE case, the superposition of the impulse response waveforms (23) from random bunches (the “spikes”) produces partially coherent radiation of coherence length $T_{coh} \sim 1/\Delta\omega_{HG}$.

How can we turn the SASE radiation to be coherent? In analogy to the case of superradiant emission from a periodic train of bunches it is suggested that periodic superposition of current impulses on top the uniform current of the microbunch will phase-lock the spikes into a coherent train of wavepackets with distinct phase relation of the “carrier” radiation waves along the entire microbunch (see Fig.14b as opposed to Fig.14a). This situation is analogous to the one described by Fig.5.

How to create the sub optical period current impulses is still an open challenge. It is important to note that the current perturbation does not have to be positive (see third pulse in Fig.15b). It can be of any shape, as long as it is kept periodic along the pulse with accuracy (stability) better than one optical period (which may be AttoSeconds in the X-UV regime!), and as long as it is “sharp” enough to produce significant current amplitude of Fourier harmonics to satisfy (27.2).

It is noteworthy that the prebunching frequency does not need to be equal to the radiation emission frequency and it can be a high sub-harmonic of this frequency. In this case the coherent spectrum may contain several harmonics as in Fig.5c, however as discussed in that context, each harmonic would be coherent throughout the

entire duration of the pulse, and its linewidth is Fourier transform limited ($2\pi T_p$). In principle the harmonics can be filtered out by physical means or by numerical processing of the data acquired by a coherent detection system data in a spectroscopic application.

Note that if single harmonic operation is desired it is not necessary that the prebunching frequency be equal to the radiation frequency. It is only required that the bunching frequency ω_b (sub-harmonic n_H of the radiation frequency ω_0) will be larger than the FEL high gain bandwidth (compare to (15)):

$$\omega_b = \frac{\omega_0}{n_H} > \Delta\omega_{HG} = \frac{3^{3/4}}{2\pi} \lambda_w \sqrt{\frac{\Gamma}{L}} \omega_0 \quad (28)$$

$$\text{or } n_H < \frac{2\pi}{3^{3/4}} \sqrt{\frac{\Gamma}{L}} / \lambda_w$$

The spectrum will look then as in Fig.5b, but with a single harmonic frequency of linewidth $2\pi T_p$ under the amplifier gain curve. In time domain the radiation waveform will look then as in Fig.14, without spacing between the overlapping phase locked spikes. In the extreme limit of (25) the waveform would be a single coherent wavepacket along the entire pulse (microbunch) duration T_p .

As mentioned above, realization of the high harmonic bunching schemes is still a challenge. We examine in principle (Fig.16) a scheme of optical laser bunching, employed on a uniform electron beam, which is trapped by the ponderomotive wave of a wiggler and an external coherent bunching laser. Fig.16a displays the $\theta-\psi$ phase-space electron distribution of one ponderomotive period exactly after one quarter period of synchrotron oscillation [16]. The current distribution along one bunching period is shown in Fig.16b and its Fourier harmonic amplitudes are shown in Fig.16c. Notice that significant amplitudes can be attained even at very high harmonics. However, in practice realizing the sharp current waveform structure of Fig.16b may be difficult, because of the electron beam energy spread and finite emittance. One should also bear in mind that in this scheme also velocity (energy) modulation of the beam is generated collaterally, and this contribution of to the radiation power (18.2) should be taken into account, including the consideration of the relative phase between the velocity and the current modulation.

A third scheme that should be considered for phase locking and increasing the coherence of the radiation in a SASE FEL consists of imposing periodic perturbation on the wiggler (e.g. periodic dispersive sections) [20]. The filtering effect of the periodic structure may be viewed as the analogue of linewidth narrowing of radiation emitted in a Fabri-Perot resonator. It is speculated (but needs further study) that if the SASE FEL in such a structure arrives to saturation within the wiggler length, nonlinear process of mode competition between the filtered spikes will lead to further increase of coherence and stability in

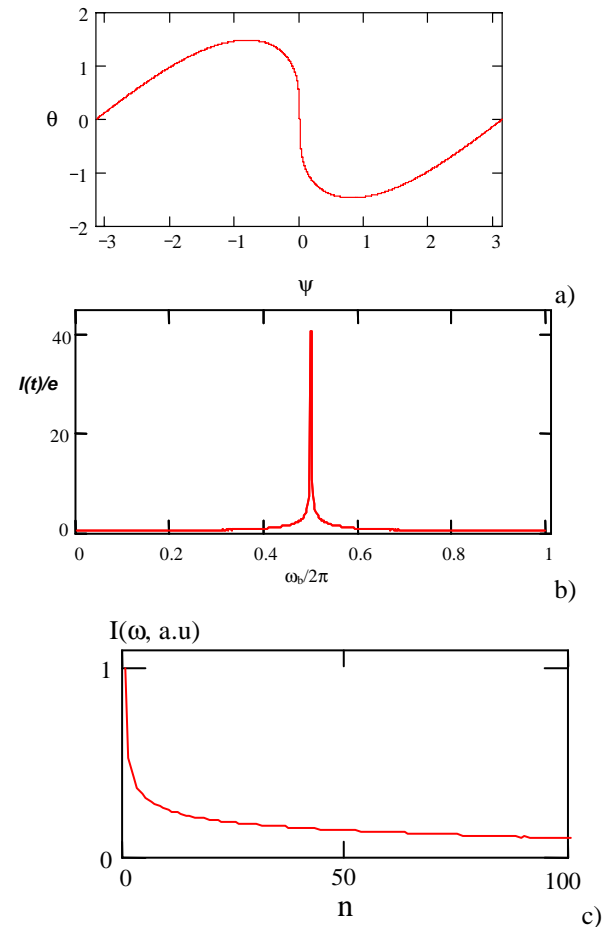


Fig.16: Bunching of a cold beam by the ponderomotive wave (pendulum equation model [15]):

- Electron detuning phase distribution in one period after one quarter period of synchrotron oscillation
- Corresponding current waveform in one bunching period
- Fourier harmonic amplitude of the waveform in (b).

analogy to the CW FEL oscillator case discussed previous.

Acknowledgement: This presentation was dedicated to the memory of Josef and Sofia Pietrowski (Yad-Vashem Righteous among Nations awardees) who saved the life of the parents of A.Gover during the Holocaust.

REFERENCE

- A. Gover, PRL, 96, 124801 (2006); A. Gover, Phys.Rev ST-AB, 9, 060703, (2006).
- A.A. Barybin, "Modern electrodynamics and coupled-mode theory: application to guided-wave optics", Rinton Press, (2002).
- A. Gover, Phys.Rev. ST-AB, 8, 030701 (2005).
- R.H. Dicke, Phys.Rev., 93, 99 (1954).
- G.L. Carr et al, Nature, 420, 153 (2002).
- A.Gover, P. Sprangle, QE-17, 1196 (1981).
- A. Gover et al, Phys.Rev.Lett., 72 1192 (1994).

8. S.E. Korbly et al, PRL, 94, 054803/1 (2005).
9. A. Abramovich et al, Phys.Rev.Lett., 82, 5257 (1999).
10. S. Krinski and R.L. Gluckstern, Phys.Rev. ST-AB, 6, 050701, (2003).
11. Gordon, Zeiger, Townes, Phys.Rev., 99, 1264 (1955).
12. Schawlow and Townes Phys.Rev., 112, 1490 (1958).
13. A. Gover A. Amir, L. Elias, Phys.Rev.-A, 35, 164 (1987).
14. J.R. Pierce, “*Traveling-Wave tubes*”, Toronto, Van Nostrand, (1950).
15. I. Schnitzer, A. Gover, NIMPR A237, 124 (1985).
16. A. Gover, “Lasers: Free Electron Lasers” *Encyclopedia of Modern Optics*, Ed. R. D. Guenther, D. G. Steel and L. Bayvel, Elsevier, Oxford (2005).
17. R. Bonifacio et al, PRL, 73, 70 (1994).
18. E. L. Saldin, E. A. Schneidmiller, and M.V. Yurkov, *The Physics of Free Electron Lasers*, Chap. 6 (Springer-Verlag, Berlin, 2000).
19. H.H. Weits, D. Oepts, IEEE QE, 35, 15, 1999.
20. Y.C. Huang – private communication.
21. L.H. Yu et al, Phys.Rev.Lett., 91, p 74801/1, 2003.
22. M. Arbel et al, Nucl.Inst.Meth.Phys.Res., A445, 247 (2000).

EVOLUTION OF FELS OVER THE LAST 34 YEARS

W.B. Colson, NPS, Monterey, California

Abstract

The concept of the free electron laser (FEL) started 34 years ago with Madey's 1972 paper. The basic mechanism which employs a beam of free electrons to amplify co-propagating light has remained essentially the same as further developments have demonstrated high peak power, high average power, high gain, optical guiding, continuous tunability and reliability. FELs have operated at wavelengths from the far infrared, infrared, visible and down to the ultraviolet. The realization of high gain has led to the generation of soft x-rays and soon hard x-rays where there are no mirrors. About a hundred FELs and user facilities are distributed around the world, and in many ways the FEL has become a "perfect" source of coherent electromagnetic radiation. FELs are in encyclopedias, in laser textbooks, with several textbooks specifically on FELs, and have clarified several physical principles for stimulated emission and laser physics. Today a Google search on "free electron lasers" produces nearly 13 million hits. The accomplishments during this time have been many, but none so important as establishing a community. Prospects for future directions are also briefly considered.

**PAPER NOT
AVAILABLE**

LASING AT 13 NM OF THE SASE FEL AT FLASH

E. Schneidmiller, M.V. Yurkov, DESY, Hamburg

Abstract

We present the recent result from FLASH (VUV FEL at DESY): lasing at 13 nm, the shortest wavelength ever generated in free electron lasers.

**PAPER NOT
AVAILABLE**

FIRST LASING AT SCSS

Tsumoru Shintake[#] and SCSS Team
RIKEN/JASRI/SPring-8, Hyogo 679-5148 Japan.

Abstract

On 20 June, the first lasing was observed at 49 nm in SCSS prototype accelerator for Japanese XFEL project. A challenging approach: 500 kV gun using CeB₆ single crystal thermionic cathode generates low emittance beam from 500 kV gun, followed by velocity bunching, and magnetic chicane bunch compression, the measured emittance at 50 MeV was 3π .mm.mrad normalized. When we firstly closed undulator, we observed narrow spectrum of amplified SASE signal. Radiation energy per pulse is around 1 μ J/pulse at moment.

INTRODUCTION

Unique combination of three key technologies: the in-vacuum short period undulator, the C-band high gradient accelerator and low emittance injector using thermionic electron source make possible to realize SASE-FEL at 1 Å within available site length at SPring-8 less than 800 m. It was named as SCSS: SPring-8 Compact SASE Source [1]. From year of 2001, we have been carrying out R&D on the key components: the electron gun, injector, C-band klystron modulator with oil-filled compact design, high resolution beam position monitor, digital rf signal processing system, etc.

TEST ACCELERATOR

In order to test this challenging scheme, and check all hardware components developed in our R&D [2], we constructed prototype accelerator in 2004-2005 as shown in Fig. 1. Beam line layout is shown in Fig. 4. We use four C-band accelerating structures, 1.8 m long each, energy gain 32 MV/m maximum. With maximum beam energy

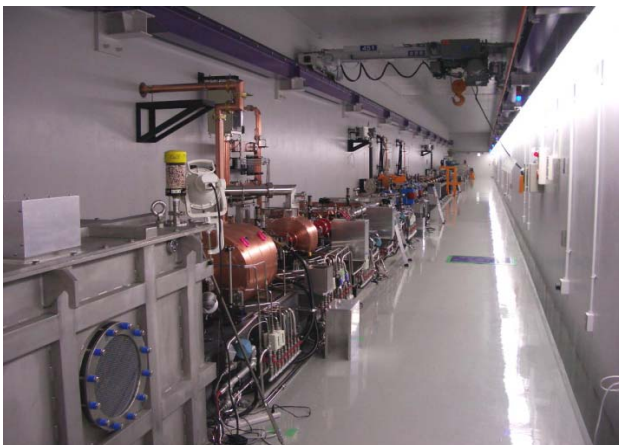


Fig. 1 Tunnel view in SCSS prototype accelerator.

[#]shintake@spring8.or.jp

of 250 MeV, the shortest wavelength of VUV-radiation at 50 nm can be obtained.

We commissioned beam operation in November 2005 and spent a few months to repair some hardware and software. From May 2006, we started dedicated beam tuning to demonstrate first lasing.

FIRST LASING EVENT

Two in-vacuum undulators were installed, whose undulator period is 15 mm, minimum gap is 3.5 mm, nominal K value is 1.3 and one undulator length is 4.5 m. In the beam tuning, we firstly opened the gap to 20 mm and passed the e-beam through gap and transported into the beam dump. We tuned the beam optics upstream of the undulator. We setup the optics, in coming beta-matching and focusing Q-magnet in between two undulators.

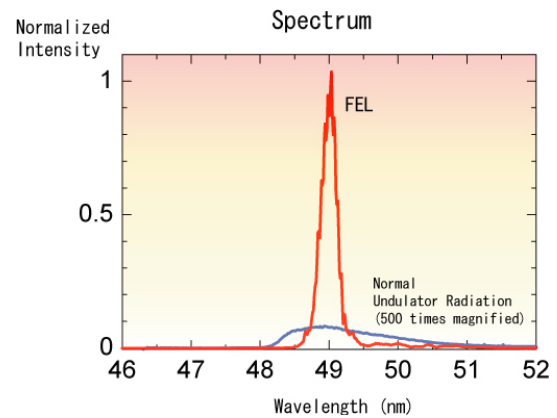


Fig. 2 Radiation spectrum at the lasing condition, 0.25 nC per bunch and 250 MeV. Peak at 49 nm is the coherently amplified signal (6000 times) from the spontaneous undulator radiation (blue line).

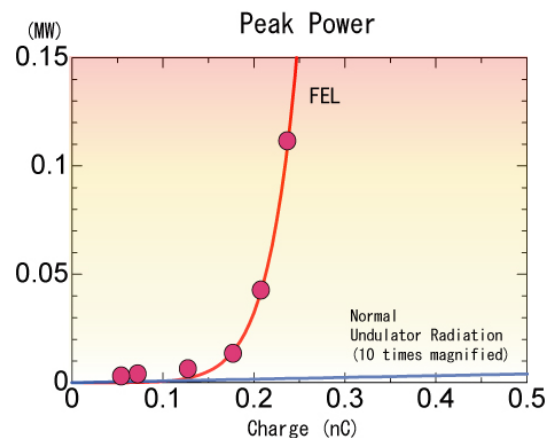


Fig. 3 Peak output power v.s. bunch charge. Using photo diode, peak height was detected from averaged pulses.

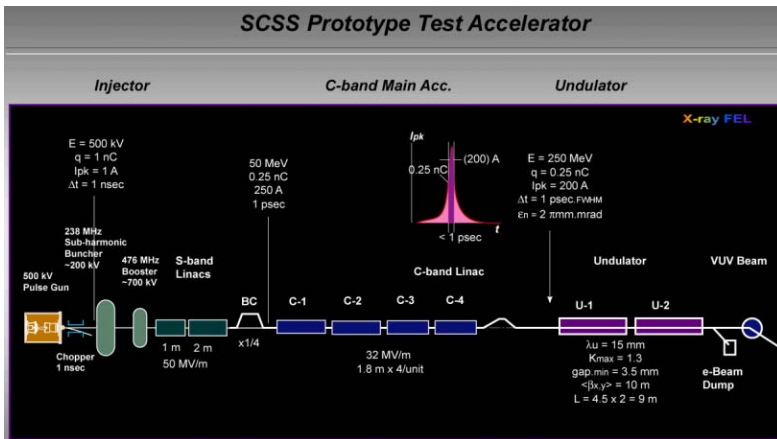


Fig. 4 SCSS prototype accelerator, two undulators of 15 mm pitch, 250 MeV e-beam, generates VUV-radiation.

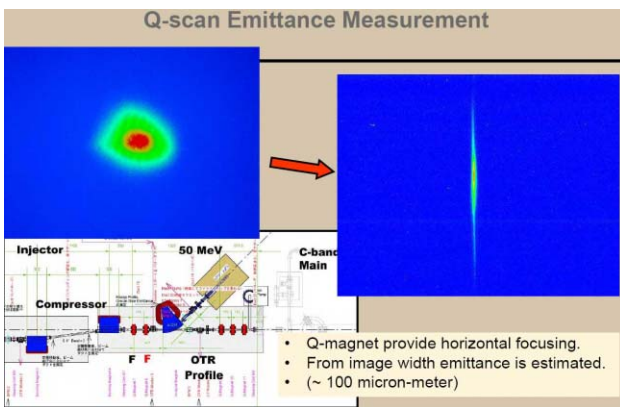


Fig. 5 Beam profile during Q-scan emittance measurement. Transition radiation from Au coating of optical mirror was monitored by CCD camera.

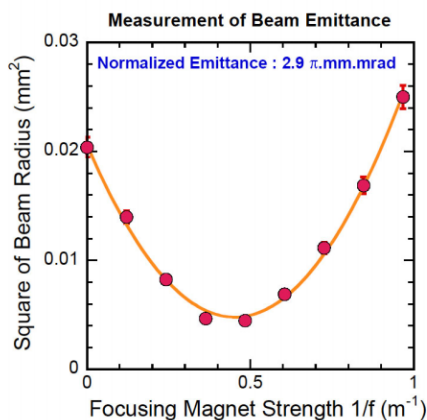


Fig. 6 Beam width as a function of focusing power. At beam energy 50 MeV, charge 0.25 nC, length $< 1 \text{ psec}$.

On 15 June, evening, we firstly closed the gap in the upstream undulator, and measured radiation spectrum, where the spectrum width was already quite narrow peaked at 49 nm, and totally different from the natural spontaneous radiation, as shown in Fig. 2. The spectrum width is around 1% FWHM, which is much narrower than the spontaneous undulator radiation, while it is dominated by e-beam energy fluctuation, at moment.

As shown in Fig. 3, when we varied the bunch charge, the lasing power drastically changed. This threshold phenomenon indicates high FEL amplification. The power has not yet reached the saturation. Further tuning is required. Detail analysis is now undertaken.

EMITTANCE MEASUREMENT

At the injector end, the velocity bunching and chicane bunch compression have been completed, where the beam energy reaches to 50 MeV, bunch charge is 0.25 nC and the bunch length is 1 psec or less, which depending on operation condition, specifically phase & amplitude tuning of 238 MHz and 476 MHz cavities.

We measured projected emittance right before the C-band accelerators, using Q-scan method. By reversing polarity of one of the Q-magnets to provided strong focusing in X- and Y-direction, and measured the minimum beam width. By varying focusing power, the beam width response was measured as Fig. 5. By fitting the beam size data as a function of the Q-magnet focusing strength as shown in Fig. 6, we found the normalized projected emittance of around $3 \pi \text{ .mm.mrad}$ for both X- and Y- directions. The slice emittance was also measured at 50 MeV beam dump, it was $2 \pi \text{ .mm.mrad}$, where the measurement was limited by spatial available resolution of profile monitor. Probably, the slice emittance is still lower than $1 \pi \text{ .mm.mrad}$ [3], but we do not have instrument to measure it at moment.

We repeated many measurements in this kind, always observed emittance around $3\sim 4 \pi \text{ .mm.mrad}$. This experimental data indicates that the velocity bunching in our system does not largely deteriorate the projected emittance for compression ratio exceeding 100 times.

CONCLUSION & SCHEDULE

We measured the e-beam emittance and observed first lasing in the SCS prototype accelerator. From this experiment, superior performance of the thermionic gun and injector system has been demonstrated.

Analysing the experimental data carefully, we refine hardware design, and start XFEL construction this year.

REFERENCES

- [1] T. Shintake, et. al, "SPRING-8 Compact SASE Source", SPIE2001, San Diego, USA, June 2001.
- [2] T. Shintake, Status of SCSS Project, 3rd Asian Particle Accelerator Conference, APAC2004, Gyeongju, Korea, March 2004.
- [3] K. Togawa et.al., "Emittance Measurement on the CeB6 Electron Gun for the SPRING-8 Compact SASE Source", FEL2004, Trieste Italy.

THE FIRST LASING OF 193 NM SASE, 4TH HARMONIC HGHG AND ESASE AT THE NSLS SDL*

X.J. Wang, Y. Shen, T. Watanabe, J.B. Murphy, J. Rose and T. Tsang, BNL, Upton, NY 11973, USA

Abstract

The first lasing of three types of single-pass high-gain FELs, SASE at 193 nm, 4th harmonic HGHG at 199 nm and ESASE at the Source Development Lab (SDL) of Brookhaven National Laboratory (BNL) is reported. The saturation of 4th harmonic HGHG and ESASE FELs was observed. We also observed the spectral broadening and instability of the 4th harmonic HGHG.

INTRODUCTION

After the successfully experimental demonstration of Self-Amplified Spontaneous Emission (SASE) and High-Gain Harmonic Generation (HGHG) around the world[1-4], great progress was made recently in reducing the SASE wavelength [5-6]. We present recent progress in both SASE and HGHG at the the National Synchrotron Light (NSLS) Source Development Lab (SDL). The new lasing of three types of the single-pass high-gain FELs at the NSLS SDL, SASE at the 193 nm, the first lasing of the 4th harmonic HGHG and ESASE is reported in this paper.

After a short description of the SDL facility, we will present the preliminary experimental characterization of new lasing of three types of single-pass high-gain FELs. We will first discuss the experimental characterization of the new lasing of a SASE FEL at 193 nm. The first lasing and saturation of the 4th harmonic HGHG at 199 nm with a 795 nm seed laser is presented. With the same experimental setup of the 4th harmonic HGHG, we observed first lasing of the laser enhanced SASE at 210 nm after detuning the electron beam energy. The first successful demonstration of ESASE [7-8] not only will open a new avenue to improve the performance of a SASE FEL, but will also greatly expand the HGHG tunability.

THE NSLS SDL

The SDL is a laser linac facility dedicated for linac based light source technology R&D and applications. The main components of the SDL are a high-brightness electron accelerator, an RF synchronized Ti:Sapphire laser system, a High Gain Harmonic Generation (HGHG) FEL, together with sophisticated electron and photon beam instrumentation. The accelerator system of the SDL consists of a 1.6 cell BNL photo-injector driven by the Ti:Sapphire laser system and a S-band traveling wave linac. After the recent electron beam energy upgrade [9], the maximum electron beam at the SDL is about 250 MeV. The magnetic chicane bunch compressor at the SDL produces sub-ps long electron bunches with a peak

current of a few hundred amperes. The high brightness electron beam transits the three magnets used for the HGHG and laser seeded FEL amplifier (Fig.1): a modulator undulator, a dispersion magnet and the 10 m long radiator undulator (named NISUS) (Table 1).

One of the unique features of the SDL laser system is that it was designed in such a way that a single laser system is used to drive both the photocathode RF gun and to provide a seed laser pulse. This setup make it possible to achieve sub-ps timing jitter between the seed laser and the electron beam. The seed laser used for the experiment has a bandwidth of 7 nm (FWHM), the pulse length can be adjusted from 100 fs to 6 ps (FWHM). Table 1 lists the undulators, seed laser and electron beam parameters used for the single-pass high-gain FELs presented here. The matching optics for the seed laser focuses the seed laser into the HGHG modulator on axis while a mini-chicane is used to manipulate the electron beam to by-pass the seed laser mirror. There are 16 beam profile monitors (BPM) uniformly distributed along the NISUS and they have been used both for e-beam matching and trajectory studies. There is a dipole magnet after the NISUS undulator which bends the electron beam to the beam dump. The beam profile monitor in front of the beam dump was used to monitor the electron beam energy and energy modulation. The FEL radiation can also be transported by a periscope to the diagnostic station for characterization. The diagnostics station allows us to characterize the FEL output.

Table 1: the SDL accelerator, seed laser and HGHG magnet parameters.

e-beam Energy (MeV)	180 - 210
e-beam peak current (A)	300 - 400
e-beam bunch length (FWHM, ps)	~ 1
Emittance (rms, mm-mrad)	2 - 4
Seed laser wavelength (nm)	795
Seed laser pulse length (FWHM, ps)	~ 2 - 3
HGHG modulator period (cm)	8
HGHG modulator length (m)	0.8
HGHG modulator K	1.67 - 3.02
HGHG dispersion magnet R_{56} (mm)	0 - 5
HGHG radiator period (cm)	3.89
HGHG radiator length (m)	10
Undulator parameter of the radiator	1.1

*xwang@bnl.gov



Figure 1: The SDL HGHG magnets and schematic of the 4th harmonic HGHG.

FEL CHARACTERIZATION

The major steps of the single-pass FEL experiment are electron beam and trajectory optimization, seed laser and e-beam synchronization, and FEL output characterization.

193 nm SASE Characterization

We first present the experimental characterization of a SASE FEL generated by the HGHG radiator – NISUS undulator. SASE was first used to optimize the electron beam and its trajectory inside the NISUS undulator. For the NISUS undulator, the shortest SASE FEL wavelength at the SDL should be about 150 nm when the electron beam energy chirped is taken into consideration. The UV Ocean Optics spectrometer and joulemeter used for characterizing the FEL are in the open air, which limits the minimum observable SASE wavelength to about 193 nm. Fig.2 is the shortest single-shot SASE spectrum obtained. The spectrometer resolution is about 0.7 nm. The maximum SASE energy is about 1 μJ when 5% transmission is assumed.

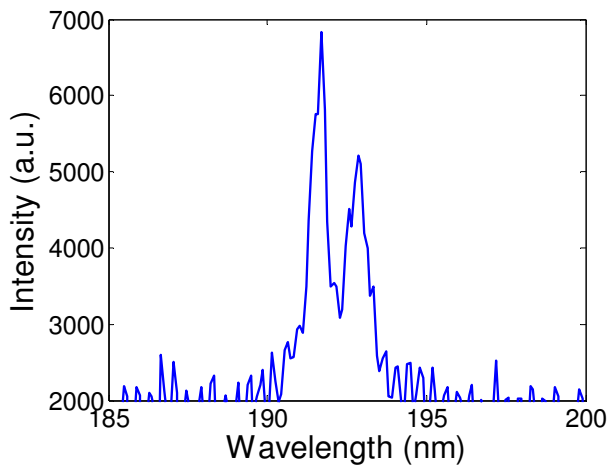


Figure 2: The shortest SASE spectrum at the SDL.

The First Lasing of the 4th Harmonic HGHG

To improve the performance of the SASE FEL, BNL has been performing R&D on laser seeded and HGHG FELs. Prior to April 2006, the shortest wavelength achieved is the 3rd harmonic HGHG at 266 nm [4].

As part of the recent electron beam energy upgrade [9], extensive modification of the HGHG modulator was done to make it possible to achieve HGHG at harmonics as high as seven. A new vacuum chamber and a stronger motor drive were installed. After the successful lasing of SASE at 193 nm, the electron beam energy was tuned to 202.5 MeV for the 4th harmonic HGHG with the seed laser at 795 nm. The synchronization of the seed laser and electron beam was realized in two steps. First we observed the SASE and seed laser using a fast photodiode at the diagnostics station to make the two of them within 100 ps. The final synchronization was realized by observing the electron beam energy modulation while adjusting the seed laser delay line. With the seed laser pulse length at about 2 ps (FWHM) and a peak power of 50-100 MW, we successfully observed the first lasing of the 4th harmonic HGHG at 199 nm (Fig. 3). The slight difference of the measured central spectrum from the 199 nm could be explained by the seed laser bandwidth, and that will be discussed in more detail later.

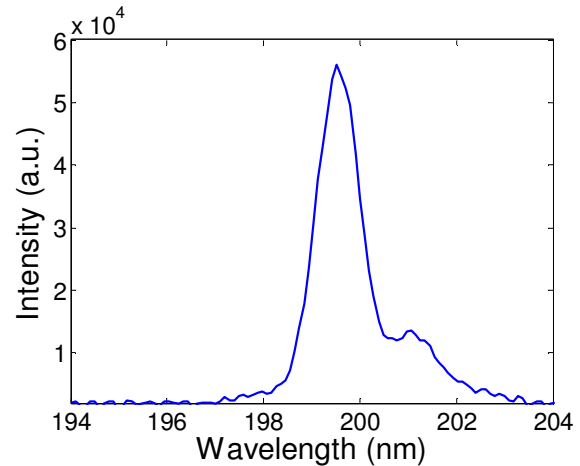


Figure 3: The 4th harmonic HGHG spectrum.

The HGHG dispersion magnet was adjusted to optimize the output of the 4th harmonic HGHG. The HGHG energy was measured at the diagnostics station while the electron beam was steered off the trajectory along the NISUS undulator. Fig. 4 plots the maximum energy of the 4th harmonic HGHG along the NISUS using the techniques just described. It can be clearly seen that the energy growth of the HGHG deviates from the exponential

growth which indicates the saturation of the 4th harmonic HGHG.

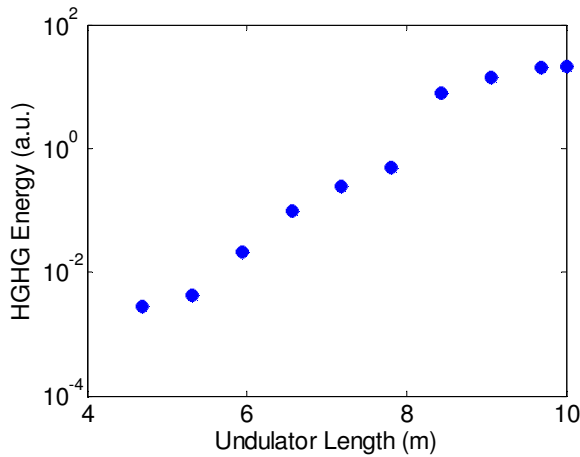


Figure 4: The log plot of the 4th harmonic HGHG energy along the NISUS undulator.

Experimental Characterization of the HGHG Spectrum Broadening and Instability

As we pointed out earlier, the HGHG spectra stability and width are not as stable and narrow as we expected. We decided to explore this more by taking hundreds of single-shot HGHG spectra using the UV spectrometer with 0.7 nm resolution. Fig. 5 plots four of the typical HGHG spectra obtained. The electron beam energy stability is one of the first considerations for the source of this instability. We measured the shot-to-shot electron beam energy fluctuation to be about 0.2% (Full width), which could contribute to about 0.4% fluctuation in the HGHG spectrum. But we observed as large as a 2% fluctuation of the HGHG spectrum. After carefully analyzing the data, we concluded that the dominant source of the HGHG spectrum fluctuation is the seed laser bandwidth.

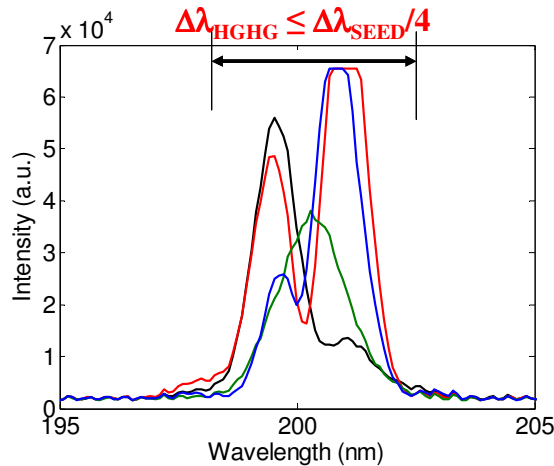


Figure 5: The 4th harmonic HGHG spectra.

In all of the previous HGHG experiments [4], the seed laser pulse length is much longer than the electron beam

bunch length. The effective seed laser bandwidth sampled by the electron beam is much narrower than the seed laser bandwidth. So the HGHG bandwidth observed in earlier experiments is dominated by the electron beam bunch length. In our 4th harmonic HGHG experiment, to increase the seed laser power, the seed laser pulse length employed is comparable to the electron beam bunch length (2 ps vs. 1 ps). When timing jitter and drifting are taken into consideration, the electron beam will sample the full range of the seed laser bandwidth. Fig. 5 shows the HGHG spectral fluctuation is about 2%, which is comparable to the seed laser bandwidth. The spectral broadening shown in Fig. 5 is well above the spectrometer resolution, which could be explained by the electron beam distribution and mismatch between the electron beam energy and the seed laser [10].

The First Lasing of ESASE at 210 nm

We also explore the tuning range of the HGHG modulator undulator. For this study the seed laser wavelength and power were kept constant while the electron beam energy was adjusted. We observed no significant change in electron beam energy modulation as the electron beam energy was adjusted from 190 MeV to 208 MeV. This corresponds to $\pm 5\%$ energy tuning. Since our modulator has only 10 periods, the observed tuning range is well within our expectation.

Taking advantage of the large tuning range of the HGHG modulator, we moved the electron beam energy to 197 MeV to demonstrate ESASE [7-8]. The resonance wavelength of the HGHG radiator at 197 MeV is about 210 nm, which is beyond the seed laser bandwidth. We successfully observed first lasing of a laser enhanced SASE FEL at the 210 nm (Fig. 6) using the same HGHG arrangement. The intensity of the ESASE is a couple orders of magnitude stronger than SASE without the seed laser.

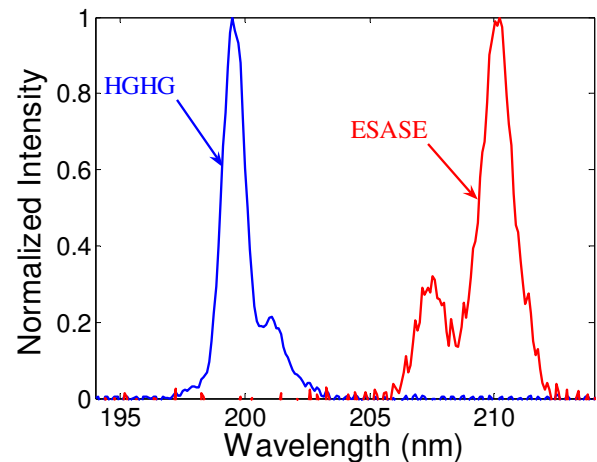


Figure 6: ESASE Spectrum vs. 4th harmonic HGHG.

SUMMARY AND ACKNOWLEDGMENT

We present the new lasing of a SASE FEL at 193 nm, and the first ever lasing of the 4th harmonic HGHG and ESASE. We have experimentally investigated the spectral instability and broadening of the HGHG FEL; the bandwidth of the seed laser is one of the major sources of the HGHG spectral instability. This observation could have important implications for a future X-ray FEL based on a cascaded HGHG concept, where a short broad band seed laser will be employed. By taking advantage of the large tuning range of the HGHG modulator we have successfully demonstrated the first lasing of the so called ESASE. Our experiment shows that ESASE not only will open a new avenue to improve the performance of a SASE FEL, but will also greatly expand the HGHG tunability. More detailed analysis and simulation of the experiments presented here will publish in the future.

We are grateful for support from the NSLS and its staff, and this work is partially supported by the Office of Naval Research (ONR) and U.S. Department of Energy under contract No. DE-AC02-98CH1-886.

REFERENCES

- [1] S. Milton et al., *Science* **292**, 2037 (2001).
- [2] A. Tremaine et al., *Phys. Rev. Lett.* **88**, 204801-1 (2002).
- [3] V. Ayvazyan, et al., *Phys. Rev. Lett.* **88**, 104802-1(2002).
- [4] L.H. Yu, et al, *Phys. Rev. Lett.* **91**, 074801-1 (2003).
- [5] E. Schneidmiller, et al, "Lasing of FLASH at 13 nm", this proceedings.
- [6] T. Shintake, "First Lasing at SCSS", this proceedings.
- [7] Y. Liu et al, *Phys. Rev. Lett.* **80**, 4418 (1998).
- [8] A.A. Zholents, *Phys. Rev. ST Accel. Beams* **8**, 040701 (2005).
- [9] X. J. Wang et al, *Proceeding of the 2004 FEL conf.*, Trieste, Italy, 209-211 (2004).
- [10] W. Fawley, "Output Bandwidth Effects in Seeded Harmonic Cascaded FELs", this proceedings.

STATUS OF THE LINAC COHERENT LIGHT SOURCE

D. Dowell, SLAC, Menlo Park, California

Abstract

The world's first x-ray free electron laser, the Linac Coherent Light Source (LCLS), is currently under construction at the Stanford Linear Accelerator Center (SLAC). This facility uses the last kilometer of the SLAC 3 km Linac to produce 1.5 to 15 angstrom photons in a 100 meter long undulator with up to 15 GeV electrons. The production of the high-brightness electron beam requires the construction of a new RF photocathode gun and a 135 MeV injector at the 2/3 point of the SLAC Linac. In addition, two stages of chicane compressors will be installed for compressing the electrons to a 22 micron bunch length, boosting the peak current to 3.5 kiloamperes. The bright, dense electron bunches then radiate via the SASE process in the long undulator. The coherent x-ray beam propagates through a gas attenuator and various diagnostics, before delivery to the experimental stations in the Far Hall. The design features and status of this novel facility will be presented.

**PAPER NOT
AVAILABLE**

RESULTS AND LESSONS FROM FLASH

B. Faatz, DESY, Hamburg

Abstract

Since first lasing beginning of 2005, we have continuously extended the wavelength range and improve the performance of FLASH. With regular blocks of accelerator and FEL studies and user beam time, we have now covered a wavelength range between 13 and 45 nm, at power levels between 5 and 50 μJ . Depending on user demands, we have delivered single bunch or multiply bunches at repetition rates of 1 MHz or 250 kHz. The latest results of the machine performance will be shown. In addition, the specific problems that have been encountered and our solutions during the past 18 months will be discussed. Finally, future plans for FLASH will be presented.

**PAPER NOT
AVAILABLE**

THE EUROPEAN XFEL PROJECT

R. Brinkmann, Deutsches Elektronen-Synchrotron (DESY), D-22607 Hamburg, Germany
for the XFEL Team

Abstract

The European X-ray Free Electron Laser XFEL is a 4th generation synchrotron radiation facility based on the SASE FEL concept and the superconducting TESLA technology for the linear accelerator. This multi-user facility will provide photon beams in a wavelength regime from 0.1nm to 5nm in three FEL beam lines and hard X-rays in two spontaneous radiation beam lines, serving in total 10 experimental stations in the first stage. The project is in an advanced planning and technical preparation stage and its construction as a European/International facility near DESY in Hamburg will start in 2007. This talk gives an overview of the overall layout and parameters of the facility, with emphasis on the accelerator design, technology and physics.

INTRODUCTION

The XFEL was originally proposed as part of the TESLA facility, first in a version integrated with the linear collider using the same linac [1,2], in a later version with its own separate linac [3]. In February 2003 the German Government announced the decision that the XFEL should be realized as a European project, with 60% of the funding provided by Germany (Bund and Länder Hamburg and Schleswig-Holstein) and 40% requested from partner countries. In mid-2003 an XFEL project group was established at DESY which, together with partner institutes, pushed forward the preparation work necessary to achieve the status of readiness for start of construction by 2006. Besides the optimization of the overall design, main objectives in this phase are preparations for the site and civil construction (including the legal procedure for construction permission), industrialization of major technical components and detailed studies of beam physics and the FEL process. The XFEL has a strong link to the FLASH (VUV-FEL) facility at DESY [4 – 6], which is in nearly all respects (accelerator technology, FEL operation, photon beam lines and user experiments) truly a pilot facility for the future project.

The project organization at the international level is supervised by a steering committee (ISC) with members from all countries interested in participating in the project. Up to date, 13 countries (Figure 1) have signed the XFEL Memorandum of Understanding for the preparation phase.

The ISC is supported by two working groups: STI for scientific and funding issues and AFI for administrative and funding issues. In 2005 ISC nominated a European Project Team (EPT), with the main charge to deliver the technical and administrative documents required for the

process of negotiations and decisions at the political level towards achieving the final go-ahead for the project.



CH CN DE DK ES FR GB GR HU IT PL RU S

Figure 1: Signature countries of the European XFEL MoU as of August 2006.

In July 2006, an updated Technical Design Report (TDR) was completed [7] and delivered to ISC. The report had previously been reviewed and endorsed by STI and additional experts from the international scientific community. In addition, the administrative documents have been essentially completed and reviewed by AFI.

LAYOUT AND PARAMETERS

The main components of the XFEL Facility are the injector, the linear accelerator, the beam distribution system, the undulators, the photon beam lines, and the instruments in the Experiments Hall (see Figure 2).

These components are distributed along an essentially linear geometry, 3.4 km long, starting on the DESY campus in the northwest part of the city of Hamburg, and ending in the neighbouring Federal State of Schleswig-Holstein, south of the city of Schenefeld, where the Experimental Hall is located. Permission for construction and operation on this site was recently (July 2006) obtained (concluding a so-called Plan Approval Procedure) and publicly announced by the authority in charge (*LBEG Clausthal-Zellerfeld*).

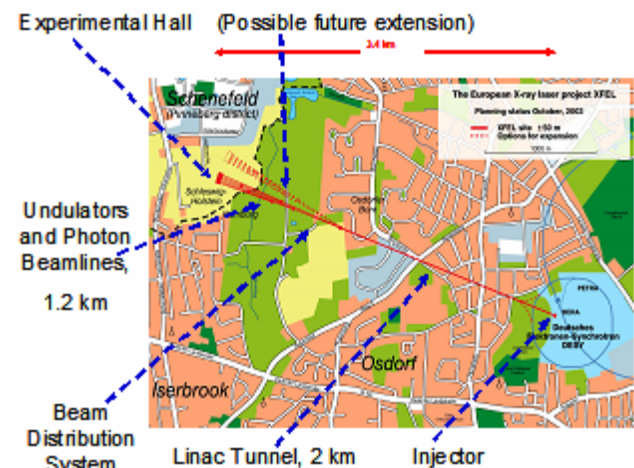


Figure 2: Site and schematic layout of the European XFEL Facility.

The basic functions of the main components are schematically described in the following: In the injector, electron bunches are extracted from a solid cathode by a laser beam, accelerated by an electron RF gun and directed towards the linear accelerator, consisting of a 1.6 km long sequence of superconducting accelerating modules, magnets for beam steering and focusing, and diagnostic equipment, the electrons are accelerated to energies of up to 20 GeV (17.5 GeV is the energy foreseen for the standard mode of operation of the XFEL facility at 0.1nm FEL wavelength). Along the accelerator, two stages of bunch compression are located, to produce the short and very dense electron bunches required to achieve saturation in the SASE process. At the end of the linac follows a beam transport section with collimation, stabilization feedback and diagnostics systems, after which the individual electron bunches are fed into one or the other of two electron beam lines by the beam distribution system. The linac and beam transport line are housed in a 2.1 km long underground tunnel (Figure 3).

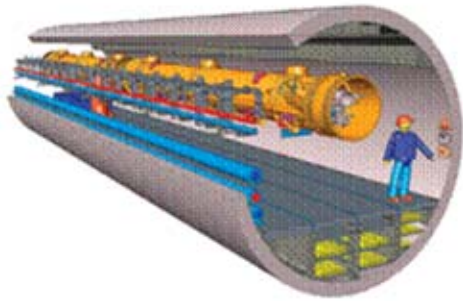


Figure 3: Layout of the 5.2 m diameter linac tunnel.

In the initial configuration the user facility has 3 SASE-FEL and two spontaneous radiation undulator beam lines (Figure 4) with in total 10 experimental stations. The site layout permits a later extension of the facility by another 5 beam lines. Independent wavelength tuning by undulator gap variation is foreseen and, together with electron beam energy variation, a total wavelength range of 0.1 – 5 nm (FEL) and 0.014 – 0.2 nm (spontaneous radiation) can be covered. The peak brilliance of FEL radiation (Figure 5) is in the range $10^{32} - 5 \cdot 10^{33}$ photons/0.1%bw/s/mm²/mrad². The baseline operating point for 0.1nm wavelength (SASE1) at 17.5 GeV electron energy has been chosen on the basis of extensive studies of the FEL process with a relatively conservative assumption on the minimum undulator gap (10mm). At the design electron beam emittance ($\epsilon_N = 1.4$ mrad·mm, see below) very good transverse coherence of the FEL radiation is predicted [8]. The magnetic lengths of the undulators (105 – 210 m) include a safety margin of at least 20% w.r.t. the calculated saturation lengths.

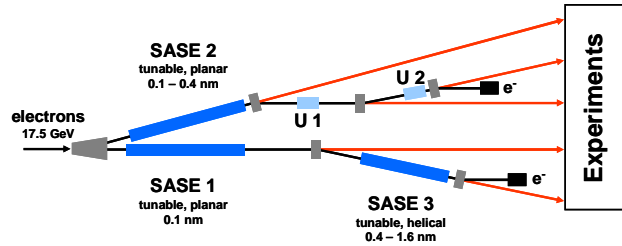


Figure 4: Schematic layout of the beam lines in the user facility.

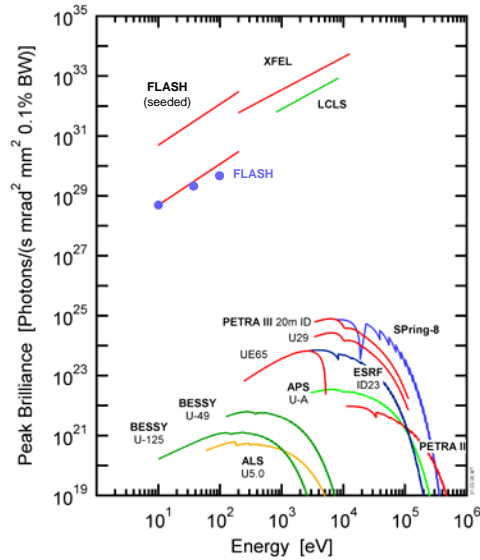


Figure 5: Peak brilliance of X-ray FELs versus 3rd generation SR light sources. Blue spots show experimental performance of the FLASH facility.

ACCELERATOR COMPLEX

The layout of the accelerator is schematically shown in Figure 6 and its main parameters are summarized in Table 1. The beam energy required for 0.1 nm photon wavelength in the SASE1 and SASE2 beam lines is 17.5 GeV. The linac design energy of 20 GeV thus already includes the potential to reach a lower wavelength of about 0.08 nm. The required peak power per RF station is well below the limit of the 10 MW multibeam klystrons. This de-rated mode is beneficial for highly reliable operation on one hand and for an upgrade potential regarding beam energy or duty cycle on the other. Likewise, the cryogenic system is laid out with an overhead of 50% with similar operational benefits.

The electron beam is generated in a laser-driven photocathode RF gun and pre-accelerated in a single superconducting accelerator module. The injector is housed in an underground enclosure separate from the linac tunnel, so that it can be commissioned at an early stage, well before installation work in the linac tunnel is

completed. Furthermore, there is space foreseen for a completely separate and radiation-shielded second injector, which can be constructed, commissioned and maintained independently from the operation of the first injector.

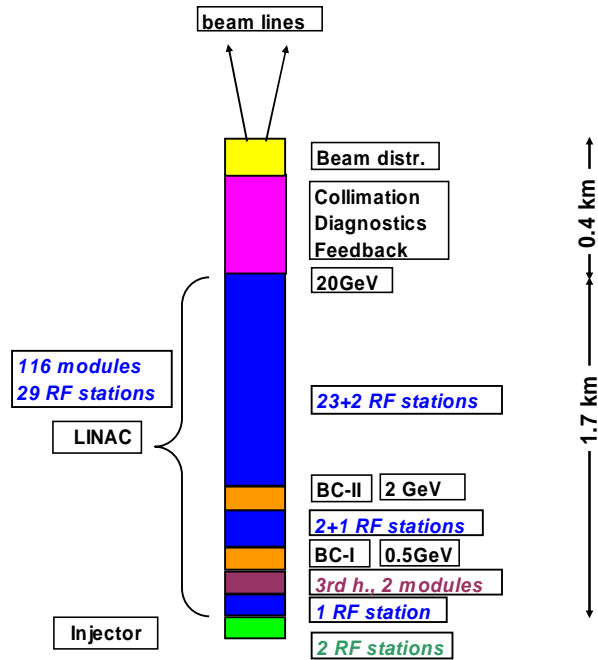


Figure 6: Schematic layout of the accelerator.

Table 1: Main parameters of the XFEL accelerator.

Energy for 0.1 nm wavelength	17.5 GeV
(max. design energy)	(20 GeV)
# of installed accelerator modules	116
# of cavities	928
Acc. Gradient (104 act. mod.) at 20 GeV	23.6 MV/m
# of installed RF stations	29
Klystron peak power (26 active stations)	5.2 MW
Loaded quality factor Q_{ext}	4.6×10^6
RF pulse length	1.4 ms
Beam pulse length	0.65ms
Repetition rate	10 Hz
Max. average Beam power	600 kW
Unloaded cavity quality factor Q_0	10^{10}
2K cryo load (incl. transfer line losses)	1.7 kW
Max. # of bunches per pulse (at 20 GeV)	3,250 (3,000)
Min. bunch spacing	200 ns
Bunch charge	1 nC
Bunch peak current	5 kA
Emittance (slice) at undulator	1.4 mm×mrad
Energy spread (slice) at undulator	1 MeV

The results from simulation studies of the RF gun show that a normalized beam emittance below 1mrad·mm at the design RF field of 60MV/m on the cathode is achievable, even if the thermal emittance is somewhat larger than

originally expected, as measurements performed at the PITZ facility (DESY-Zeuthen) indicated [9]. A high priority of the future program [10] at PITZ will be on the verification of the XFEL gun design parameters, with improvements expected from higher cathode field and optimized laser profile.

After transfer to the main accelerator tunnel (see the layout sketched in Figure 7), the beam is further accelerated by one linac unit (4 accelerator modules with 8 cavities each, driven by one RF station) to an energy of 0.5 GeV before entering the first bunch compression stage. A third harmonic (3.9 GHz) RF system is foreseen to optimize the longitudinal phase space properties. After acceleration to 2 GeV with three linac units the beam enters the second (final) compression stage, after which the 1nC bunch peak current has increased to 5 kA ($\sigma_z = 23\mu\text{m}$ for a 1nC bunch), a factor of 100 higher than the initial peak current from the RF gun. Considerable attention has been paid to foresee beam diagnostics stations in order to assess the beam phase space properties after the compression process in great detail [11]. Beam simulation studies of the compression system (see [12] for a recent overview of simulation code developments) show that the slice emittance growth due to space charge and CSR effects can be kept at a low level and there is room for further parameter optimization beyond the nominal design bunch parameters [13].

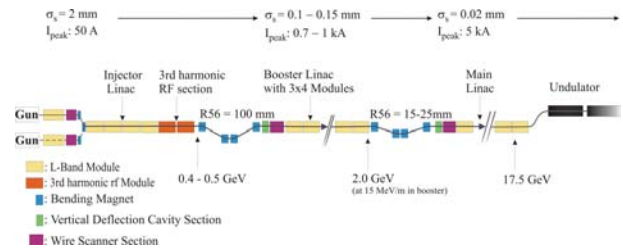


Figure 7: Layout of the XFEL bunch compression system.

The large compression factor and resulting short bunches (70fs rms) require timing, synchronization and diagnostics devices at the fs level. A considerable R&D program is ongoing in this field, see e.g. [14 – 16] for recent developments. Furthermore, extremely accurate RF control is required in the low-energy part of the accelerator [17].

Final acceleration to a nominal maximum beam energy of 20 GeV takes place in the main part of the linac, consisting of 25 RF stations and 100 accelerator modules in total. Downstream from the linac follows a conventional beam line for installation of the beam collimation and trajectory feedback systems, as well as providing distribution of the beam into the different undulator beam lines, including the connection to a future upgrade of the user facility with more beam lines. A combination of slow and fast switching devices permits to generate bunch trains of different time patterns for

different experiments without having to generate and accelerate bunch trains with strongly varying transient beam loading. A fraction of each bunch train will be used to accurately stabilize the following bunches in position and energy by means of a fast feedback system [18]. After having passed through the undulators, the “spent” beam is stopped in radiation shielded solid absorbers. An additional beam dump is installed in the beam distribution shaft XS1, just upstream from the undulator beam lines. It allows to commission or to operate the accelerator while installation or maintenance work is ongoing in the undulator tunnels.

The layout of the linac includes precautions for energy management in case of RF component failure. The section between the two bunch compression stages consists of three RF units with four accelerator modules each, out of which only two have to be active to accelerate the beam to 2 GeV at the design gradient. Likewise, the main section of the linac (from 2 to 20 GeV) has an overhead of two RF stations. This guarantees that in case of an RF unit failure there is sufficient energy reserve to maintain both the beam energy at the second bunch compressor stage as well as at the end of the linac. Tunnel access for repair of RF stations during scheduled operation time can thus be safely avoided. In practice, the reserve stations will not be left idle when not needed. Instead, all available stations will be operated with reduced gradient and in case a station fails the gradient will be increased in the other sections such as to keep the beam energy constant.

Operational Flexibility

The single set of basic reference parameters in Table 1 does not cover the full range of operational flexibility of the linac. There is, within certain limits, a considerable flexibility regarding operation parameters, based on built-in performance reserves of its technical components. Operation at lower beam energy, thus extending the photon wavelength range to softer X-rays, is an obvious possibility. On the other hand, based on the experience gained with the superconducting TESLA cavities, it can be realistically expected that the linac can be operated at an accelerating gradient somewhat above the specified design value of 23.6 MV/m at 20 GeV. An increase of the gradient to about 28 MV/m would permit a maximum beam energy of 24 GeV, thus significantly extending the photon wavelength range to harder X-rays, provided that simultaneously also an improved injector beam quality becomes available to be able to maintain saturation of the SASE FEL process. In addition to the possibility of higher beam energies, the available reserve in the RF and cryogenic systems can also be used for increasing the linac repetition rate and thus the duty cycle of the pulsed linac. At sufficiently low beam energy, a 100% duty cycle, i.e. continuous wave (CW), mode of operation is conceivable, an option which is only possible with a superconducting linac. This option is viewed as not being part of the first stage of the XFEL facility but is considered as a future option. A preliminary set of

possible parameters for CW operation is shown in Table 2.

Table 2: Sketch of possible parameters for a future option of operating the linac in CW mode.

Beam energy	7 GeV
Accelerating Gradient	7.5 MV/m
# of CW RF stations	116
RF power per accelerator module	≈20 kW
Beam current	0.18 mA
Loaded quality factor Q_{ext}	2×10^7
Bunch frequency	180 kHz
Unloaded quality factor Q_0	$2 \cdot 10^{10}$
2K cryogenic load	≈3.5 kW

PROJECT COST AND SCHEDULE

An in-depth re-evaluation of project construction costs has been performed as part of the project preparation work (see the TDR [7] for more details). In year 2005 prices, the construction costs are 986 M€ out of which 736 M€ are capital investment and 250 M€ personnel costs (including overhead). A breakdown of the construction costs is shown in Figure 8 and the budget time profile in Figure 9.

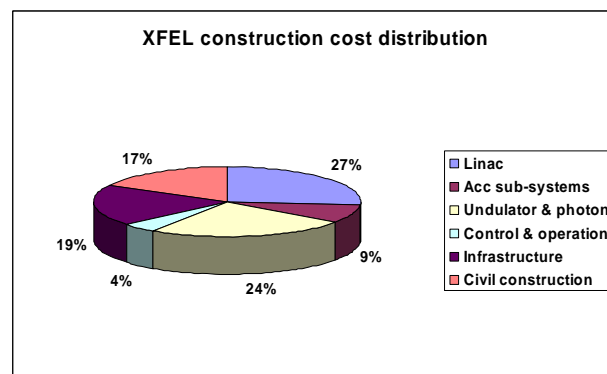


Figure 8: XFEL construction cost distribution.

The project schedule assumed for the profile of Figure 9 is based on an expected project go-ahead decision in the beginning of 2007. After a construction period of 6.5 years, beam through the linac and the first beam line (SASE1) is scheduled for 2013 and first user operation for 2014. There will be a transition phase until end of 2015, during which operation of beam lines takes place in parallel with completion of construction and commissioning of others. By 2016 the entire facility will be operational. The yearly operation budget (in 2005 prices) has been estimated at 83 M€, including administrative overhead and user support.

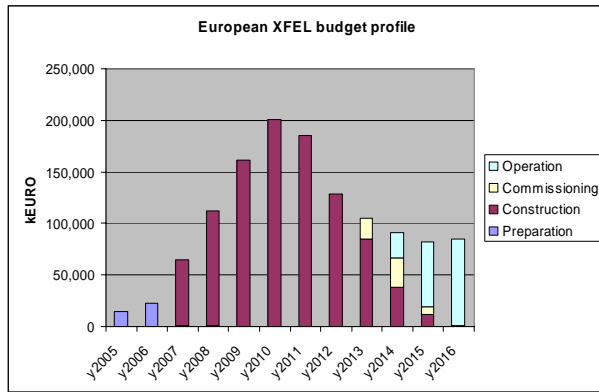


Figure 9: XFEL budget profile, including preparation phase and transition from construction to operation.

ACKNOWLEDGEMENT

The paper presented here is based on the recently published XFEL Technical Design Report. The author would like to express his thanks to the co-editors and co-authors of the TDR, who contributed and shaped a vast amount of material for that comprehensive report, of which this paper can be viewed as a short summary.

REFERENCES

- [1] R. Brinkmann, et al., "An X-Ray FEL Laboratory as Part of a Linear Collider Design", Nucl. Instr. Meth A393, (1997) 86-92.
- [2] R. Brinkmann et al. (eds.), "TESLA Technical Design Report", DESY-2001-011, March 2001.
- [3] R. Brinkmann et al. (eds.), "TESLA XFEL Technical Design report – Supplement", DESY-2002-167, Oct. 2002.
- [4] J. Roßbach, "Results from the VUV-FEL", Proc. EPAC, Edinburgh 2006.
- [5] H. Weise, "The TTF/VUV-FEL (FLASH) as the Prototype for the European XFEL Project", Int. Linac conf., Knoxville 2006.
- [6] B. Faatz, "Results and Lessons from FLASH", This conference MOBAU02.
- [7] "XFEL Technical Design Report", DESY 2006-097, <http://xfel.desy.de>.
- [8] E. Saldin et al., "Transverse and Longitudinal Coherence Properties of the Radiation from X-ray SASE FELs", this conference MOPPH069 .
- [9] J. H. Han et al., "Emission Mechanisms in a Photocathode RF Gun", Proc. PAC, Knoxville 2005.
- [10] A. Oppelt et al., "Upgrade of the PITZ Facility and First Beam Measurements", this conference THPPH022 .
- [11] C. Gerth, "Layout of the Diagnostic Sections for Emittance and Energy Spread Measurements at the European XFEL", this conference THPPH010.

- [12] M. Dohlus, "Modeling of Space Charge and CSR Effects in Bunch Compressor Systems". Proc. EPAC, Edinburgh 2006.
- [13] T. Limberg et al., "Optimized Bunch Compression System for the European XFEL", Proc. PAC, Knoxville 2005.
- [14] A. Winter et al., "High Precision Master Oscillator for Optical Timing Distribution Systems". Proc. EPAC, Edinburgh 2006.
- [15] J.-W. Kim, "Femtosecond Synchronization and Stabilization Techniques", this conference TUBAU02.
- [16] B. Schmidt, "Overview on Diagnostics for X- and VUV-FELs", this conference THCAU01.
- [17] F. Ludwig et al., "Phase Stability of the Next Generation RF Field Control for VUV- and X-ray Free Electron Lasers", Proc. EPAC, Edinburgh 2006.
- [18] V. Schlott et al., "An Intra Bunch Train Feedback System for the European XFEL", Proc. EPAC, Edinburgh 2006.

OPTICAL KLYSTRON ENHANCEMENT TO SASE X-RAY FELS

Yuantao Ding*, Paul Emma, Zhirong Huang†, SLAC, Menlo Park, CA 94025, USA
 Vinit Kumar‡, ANL, Argonne, IL 60439, USA.

Abstract

The optical klystron enhancement to self-amplified spontaneous emission (SASE) free electron lasers (FELs) is studied in theory and in simulations. In contrast to a seeded FEL, the optical klystron gain in a SASE FEL is not sensitive to any phase mismatch between the radiation and the microbunched electron beam. The FEL performance with the addition of four optical klystrons located at the undulator long breaks in the Linac Coherent Light Source (LCLS) shows significant improvement if the uncorrelated energy spread at the undulator entrance can be controlled to a very small level. In addition, FEL saturation at shorter x-ray wavelengths (around 1.0 Å) within the LCLS undulator length becomes possible. We also discuss the application of the optical klystron in a compact x-ray FEL design that employs relatively low electron beam energy together with a shorter-period undulator.

INTRODUCTION

An x-ray free electron laser (FEL) operated in the self-amplified spontaneous emission (SASE) mode is the primary candidate for the next-generation light source and is under active development around the world [1, 2, 3]. In such a device, based on the achievable electron beam qualities such as peak current and transverse emittances, the total length of the undulator required to reach the x-ray intensity saturation usually exceeds 100 m. The electron beam energy spread is typically too small to affect the SASE performance.

To enhance the FEL gain, the optical klystron concept has been invented by Vinokurov and Skrinsky [4] and has been successfully implemented in many FEL oscillator facilities such as the Duke FEL [5]. An optical klystron consists of two undulators, separated by a dispersive section (a magnetic chicane). The dispersive section converts beam energy modulation into density modulation and hence speeds up the gain process. Theoretical studies of the optical klystron in high gain FEL amplifiers show that its performance depends critically on the electron beam energy spread [6, 7, 8]. More recently, Neil and Freund [9] have studied a distributed optical klystron configuration using the LCLS parameters. Based on the FEL amplifier simulations that start with a coherent seed, they point out that the performance of the optical klystron for short-wavelength FELs is very sensitive to the exact slippage of

the electron beam relative to the radiation in the dispersive section. Thus, the magnetic fields of the chicane must be carefully designed and controlled to very high precision.

Motivated by the very small uncorrelated energy spread of the electron beam that has been measured in a photocathode RF gun [10], we study the possible optical klystron enhancement to SASE x-ray FELs. We show that a SASE optical klystron is not sensitive to the relative phase of the electron beam to the radiation as long as the electron slippage length in the dispersive section is much longer than the coherence length of the radiation. Based on extensive SASE simulations, we illustrate the gain enhancement of the optical klystron to the LCLS and a compact x-ray FEL scheme.

ONE-DIMENSIONAL ANALYSIS

In this section, we analyze an optical klystron configuration with a magnetic chicane between two high-gain FEL undulators and extend the previous theoretical treatments [6, 7, 8] to the high-gain SASE operating mode. A detailed description may be found in [11].

A magnetic chicane introduces an energy-dependent longitudinal delay of the electron relative to the radiation, which can be expressed as a change of the radiation phase “seen” by the electron:

$$\Delta\theta = -\frac{k_r R_{56}}{2} + k_r R_{56} \delta \quad (1)$$

Here $\lambda_r = 2\pi/k_r = 2\pi c/\omega_r$ is the FEL resonant wavelength, R_{56} is the momentum compaction of the chicane, and $\delta = (\gamma - \gamma_0)/\gamma_0$ is the relative energy deviation. The first term in Eq. (1) describes the overall phase slippage between the FEL radiation and the reference electron having the energy $\gamma_0 m c^2$, and the second term describes the relative phase change for an electron with a slightly different energy. Following the one-dimensional (1D) theory of Kim [8] but keep the overall phase slippage, we write down the optical klystron (OK) enhancement factor to the radiation field E_ν at the scaled frequency $\nu = \omega/\omega_r$:

$$R(\nu) \equiv \frac{E_\nu^{\text{OK}}}{E_\nu^{\text{no OK}}} = \frac{1 - \int d\xi \frac{dV(\xi)/(d\xi)}{(\mu - \xi)^2} e^{-i\rho k_r \nu R_{56} \xi} e^{i k_r \nu R_{56} / 2}}{1 + 2 \int d\xi \frac{V(\xi)}{(\mu - \xi)^3}} \quad (2)$$

where $\xi = \delta/\rho$ is the normalized energy variable, ρ is the FEL Pierce parameter [12], μ is the complex growth rate of the radiation field in each undulator, $\mu = (-1 + i\sqrt{3})/2$ for a beam with a vanishing energy spread, and $V(\xi)$ is the

* Electronic address: ding@slac.stanford.edu. On leave from IHIP, Peking University, Beijing, China.

† Electronic address: zrh@slac.stanford.edu.

‡ Current address: G-20, ADL Building, Raja Ramanna Centre for Advanced Technology, Indore-452013, INDIA.

energy distribution of the electron beam with the normalization $\int V(\xi)d\xi = 1$.

The first term in the numerator of Eq.(2) represents the contribution from the radiation in the first undulator, while the second term in the numerator represents the contribution of the microbunched electron beam. For a seeded FEL with $\nu = 1$, $k_r R_{56}/2 = 2\pi n$ ($n = 1, 2, 3, \dots$) yields a nearly matched phase (i.e., constructive interference between two terms). The optical klystron is then optimized for a matched phase. However, in the hard x-ray wavelength range, changing R_{56} of the chicane by a fraction of 1 Angstrom can result in a complete phase mismatch. Thus, there can be large fluctuations in the radiation power due to small fluctuations in the magnetic fields as observed in Ref. [9]. Even when the magnetic fields are held constant, a small energy jitter (on the order of 10^{-4}) can also mismatch the phase.

Nevertheless, SASE FELs start from shot noise and have a relatively wide bandwidth. For a given value of R_{56} , the phase may be mismatched for one particular wavelength but may be properly matched for another wavelength within the SASE bandwidth. Thus, we should integrate over the SASE spectrum $S(\nu)$ to obtain the optical klystron power gain factor as:

$$G = \int d\nu |R(\nu)|^2 S(\nu) \quad (3)$$

For an electron beam with a Gaussian energy distribution of rms width $\sigma_\delta \ll \rho$ (i.e., $\sigma_\xi \ll 1$), we can integrate Eq. (1) over energy and Eq. (3) over frequency (assuming a Gaussian average SASE spectrum) to obtain

$$G = \frac{1}{9} \left[5 + D^2 \exp(-D^2 \sigma_\xi^2) + 2\sqrt{3} D \exp\left(-\frac{D^2 \sigma_\xi^2}{2}\right) + \left(4 + \sqrt{3} D \exp\left(-\frac{D^2 \sigma_\xi^2}{2}\right) \cos\left(\frac{D}{2\rho}\right) - D \exp\left(-\frac{D^2 \sigma_\xi^2}{2}\right) \sin\left(\frac{D}{2\rho}\right) \right) \exp\left(-\frac{D^2 \sigma_\nu^2}{8\rho^2}\right) \right] \quad (4)$$

where $D = k_r R_{56} \rho$. The power gain factor G as a function of the chicane strength R_{56} is shown in Fig. 1 for two typical values of the rms energy spread σ_δ , assuming a typical rms SASE bandwidth $\sigma_\nu = \rho$.

When R_{56} is very small, the optical klystron operates as a phase shifter, and the FEL power is oscillatory depending on the relative phase between the radiation and the electron beam. As $k_r R_{56} \sigma_\delta \rightarrow 1$, the optical klystron gain peaks and starts to decay exponentially due to the smearing effect of the intrinsic energy spread. Thus, the phase matching is no longer important when the optical klystron is near its peak performance.

A simple physical picture emerges in the time domain. The path length difference between the SASE radiation and the electron beam passing the dispersive section is about $R_{56}/2 \approx 1/(2k_r \sigma_\delta) = \lambda_r/(4\pi \sigma_\delta)$ at the optimal chicane

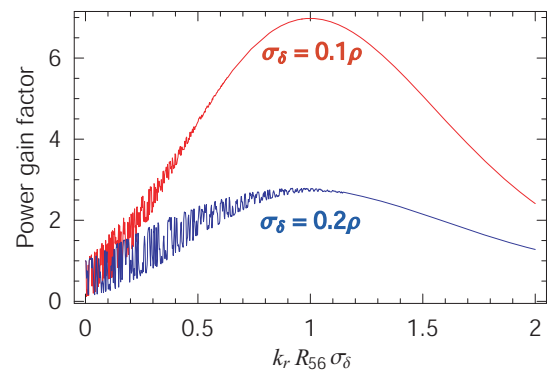


Figure 1: (color) 1D power gain factor with relative energy spread $\sigma_\delta = 0.1\rho$ (red line) and $\sigma_\delta = 0.2\rho$ (blue line)

setting. Since the typical SASE coherence length is on the order of $\lambda_r/(4\pi\rho)$ [13, 14], it is much smaller than the path length difference introduced by the chicane when the beam energy spread $\sigma_\delta \ll \rho$ (a necessary condition for the operation of the high-gain optical klystron). Therefore, there is no place for the electron beam to match the radiation phase after the beam is slipped from the SASE radiation more than a few temporal spikes. The radiation power averaged over many statistically independent spikes is then not sensitive to the exact slippage introduced by the chicane.

UNCORRELATED ENERGY SPREAD

Since the uncorrelated energy spread plays a crucial role for the gain enhancement of the optical klystron, we analyze here two main sources of energy spread. One is from the gun and the linac, which forms the initial energy spread at the entrance of the FEL undulator; while the other is the quantum diffusion due to spontaneous radiation along the undulator, which leads to an increase of energy spread after the electron beam is injected into the undulator. The uncorrelated energy spread of electron beams generated from a photocathode rf gun can be extremely small, at an rms value of 3 to 4 keV from both measurements [10] and simulations. Nevertheless, a microbunching instability driven by longitudinal space charge and coherent synchrotron radiation in the accelerator system may be large enough to significantly degrade the beam qualities including the energy spread [15, 16]. This microbunching instability occurs at much longer wavelengths than the FEL microbunching and requires much larger R_{56} (from bunch compressor chicane) than the optical klystron chicane. To maintain a relatively small energy spread after compression and acceleration, a laser heater [15, 16] will be used in the LCLS injector to increase the rms energy spread from 3 to 40 keV. After a total compression factor of about 30, the slice rms energy spread at the undulator entrance can be controlled to 1×10^{-4} at 14 GeV, which is tolerable for the SASE FEL at 1.5 Å. However, considering the gain enhancement of the optical klystron (see Fig.1), a smaller energy spread (e.g., 5×10^{-5} or 0.1ρ) is desirable. This may be achiev-

able by dropping the heater-induced energy spread to 20 keV at the expense of the increased microbunching instability gain. For a smooth enough photocathode drive laser profile, this higher instability gain may still be tolerable after acceleration and bunch compression. Thus, the final slice energy spread at the undulator entrance may be kept at 5×10^{-5} for the LCLS.

The energy diffusion due to spontaneous radiation along the undulator was discussed by Saldin et al [17]. This energy diffusion rate increases with γ^4 and K^3 for $K^2 \gg 1$. For the LCLS at $\lambda_r = 1.5 \text{ \AA}$ and $K = 3.5$, the rms energy spread increases from initial value of 5×10^{-5} to 1×10^{-4} at the undulator position of 40 m due to the spontaneous radiation. We will include this effect in the FEL simulations to be discussed below.

THREE DIMENSIONAL SIMULATIONS

Three-dimensional (3D) simulation code Genesis 1.3 [18] is used to explore the LCLS gain enhancement with a distributed optical klystron configuration for two different radiation wavelengths of 1.5 \AA and 1.0 \AA and a very compact x-ray FEL at 1.5 \AA .

We place four 4-dipole chicanes in the first four long breaks between LCLS undulator sections (at 12, 24, 36, and 48 m) to form a distributed optical klystron configuration. For each chicane, the optimal gain enhancement is obtained by scanning the chicane dipole magnetic field strength. Two initial rms energy spread values of 1×10^{-5} and 5×10^{-5} at the entrance of the undulator are used in the 3D simulations. While we consider the energy spread of 5×10^{-5} may be achievable in the LCLS with a reasonably smooth drive-laser profile or with the low-charge option [19], the energy spread of 1×10^{-5} requires to switch off the laser heater completely and is probably not allowed by the microbunching instability in the linac. It is still included in the simulations in order to study the best possible optical klystron performance and the influence of spontaneous energy diffusion in the undulator.

Fig. 2 shows the FEL power gain along the undulator with and without optical klystrons at the resonant wavelength of 1.5 \AA for $K = 3.5$ (the current LCLS design parameters), with an electron peak current of 3.4kA and normalized rms emittance of $1.2 \mu\text{m}$. The saturation length is shortened by 13 m using these optical klystrons with an initial energy spread of 5×10^{-5} and R_{56} of the chicanes at around $0.25 \mu\text{m}$ (with a small variation for each chicane). Note that a 10% variation of the chicane R_{56} values does not make a visible difference for the FEL output power.

To allow for the LCLS to reach 1.0 \AA without increasing the beam energy, the undulator gap may be increased by 2 mm to reduce the undulator parameter to $K = 2.7$. The 3D simulation results are presented in Fig. 3, using a peak current of 3.4kA and normalized rms emittance of $1.2 \mu\text{m}$. Without any optical klystron, the nominal LCLS beam cannot reach SASE saturation at this wavelength. With the addition of four optical klystrons as described here, the sat-

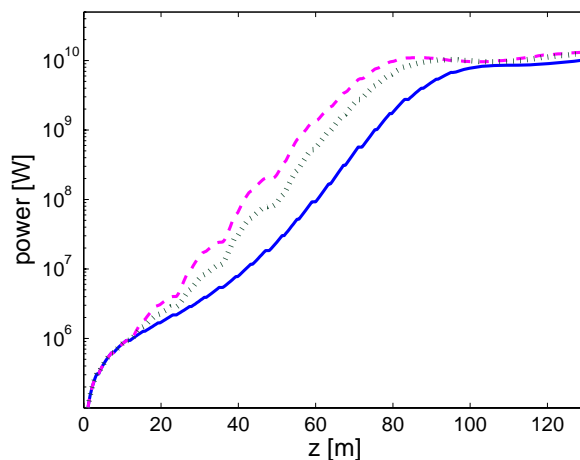


Figure 2: (color) SASE FEL power along the undulator without any optical klystron (blue solid curve), and with 4 optical klystrons for the initial rms energy spread of 1×10^{-5} (magenta dashed curve) and 5×10^{-5} (green dotted curve). The FEL wavelength is 1.5 \AA , and the undulator parameter $K = 3.5$.

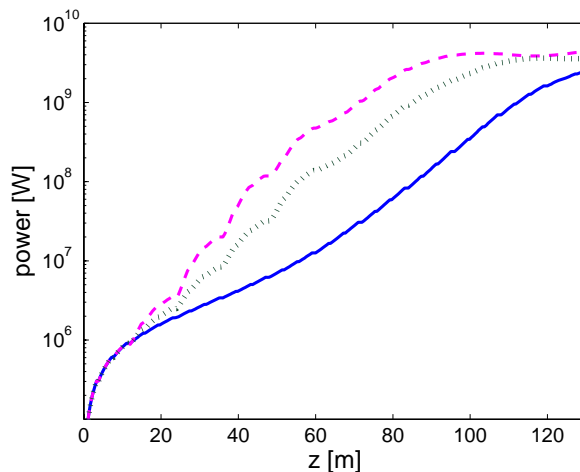


Figure 3: (color) SASE FEL power along the undulator without any optical klystron (blue solid curve), and with 4 optical klystrons for the rms energy spread of 1×10^{-5} (magenta dashed curve) and 5×10^{-5} (green dotted curve). The FEL wavelength is 1.0 \AA , and the undulator parameter $K = 2.7$.

uration distance is shortened by about 26 m and is well within the LCLS total undulator length. At this K value and using a lower beam energy (11.0 GeV), simulations also show the FEL at 1.5 \AA approximately save 25 m of saturation length compared to that without any optical klystron.

It is clear from these numerical examples that a simultaneous reduction in beam energy and undulator parameter for the same radiation wavelength is beneficial for the optical klystron enhancement, where the energy diffusion due

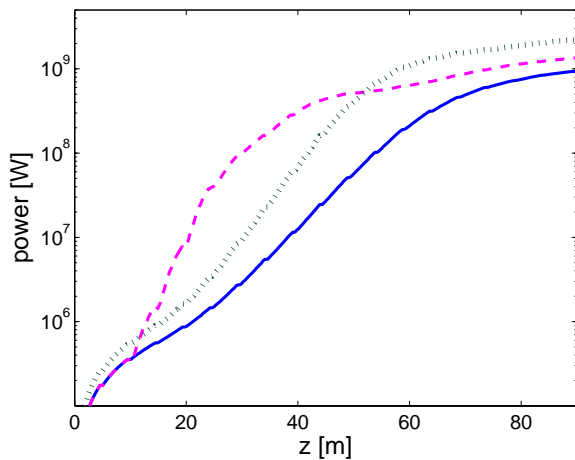


Figure 4: (color) SASE FEL power along the undulator at a peak current of 2kA without any optical klystron (blue solid curve) and with 4 optical klystrons (magenta dashed curve), and at peak current of 3kA without any optical klystron (green dotted curve). The FEL wavelength is 1.5 \AA and the undulator parameter $K = 1.3$.

to spontaneous radiation in the undulator is much reduced. Inspired by the Spring-8 Compact SASE Source (SCSS) design [3], we study the possibility of using a relatively low energy electron beam together with a short-period undulator to drive a compact x-ray FEL with the aid of the distributed optical klystrons. A 1.5-cm period in-vacuum undulator with $K = 1.3$ is used according to the design parameters in SCSS. To produce 1.5-\AA FEL radiation, the necessary electron energy is about 5 GeV. Rather than a standard peak current of 3 kA as described in Ref. [3], we assume a lower peak current of 2 kA and an rms energy spread of 100 keV (or 2×10^{-5}) at the undulator entrance. A smaller peak current allows for a smaller energy spread and may also help reduce the microbunching instability gain in the accelerator, as well as any wakefield effect in the small gap, in-vacuum undulator. Fig. 4 shows the simulation results for the SASE mode without any optical klystron (for both 3-kA and 2-kA bunches) and with four optical klystrons (for a 2-kA bunch). The latter saturates at around 50 m of the undulator distance, which is still about 10 m shorter than the higher-current case without any optical klystron.

SUMMARY

The small, experimentally measured uncorrelated energy spread from RF guns offers the opportunity to consider applications of optical klystrons in x-ray FELs. In contrast to a seeded FEL, our study shows that the optical klystron gain is not sensitive to the relative phase between the SASE radiation and the electron beam, and that the radiation power is very stable with a relatively large tuning range of optical klystrons. 3D simulations of the LCLS with a

distributed optical klystron configuration show significant gain enhancement if the slice energy spread at the undulator entrance can be controlled to a very small level. The improved performance can be used to obtain the FEL saturation at shorter x-ray wavelengths for a fixed undulator length or to relax the stringent requirement on the beam emittance. The exploration of optical klystrons in a very compact x-ray FEL also indicates promising results. Therefore, we think that the optical klystron configuration can be an easy "add-on" to SASE x-ray FELs provided that electron beams with very small energy spreads are obtainable at the final beam energy.

We thank J. Wu and S. Reiche for useful discussions, J. Galayda and R. Ruth for their encouragement on this work. This work was supported by Department of Energy Contracts No. DE-AC02-76SF00515.

REFERENCES

- [1] Linac Coherent Light Source (LCLS) Conceptual Design Report, SLAC Report No. SLAC-R-593, 2002.
- [2] Technical Design Report, DESY TESLA-FEL Report, 2002.
- [3] SCSS X-FEL conceptual design report, RIKEN, 2002.
- [4] N.A. Vinokurov and A.N. Skrinsky, Preprint of INP 77-59, Novosibirsk, (1977).
- [5] Y. K. Wu *et al.*, Phys. Rev. Lett. 96, 224801 (2006).
- [6] R. Bonifacio, R. Corsini, and P. Pierini, Phys. Rev. A 45, 4091 (1992).
- [7] N.A. Vinokurov, Nucl. Instrum. Methods Phys. Res. A 375, 264 (1996).
- [8] K.J. Kim, Nucl. Instrum. Methods Phys. Res. A 407, 126 (1998).
- [9] G.R. Neil and H.P. Freund, Nucl. Instrum. Methods Phys. Res. Sec. A 475, 381 (2001).
- [10] M. Huning and H. Schlarb, in Proceedings of the 2003 Particle Accelerator Conference, Portland, 2074 (2003).
- [11] Y. Ding, P. Emma, Z. Huang, V. Kummer, Phys. Rev. ST Accel. Beams 9, 070702 (2006).
- [12] R. Bonifacio, C. Pellegrini, and L.M. Narducci, Opt. Commun. 50, 373 (1984).
- [13] R. Bonifacio, L. De Salvo, P. Pierini, N. Piovella, and C. Pellegrini, Phys. Rev. Lett. 73, 70 (1994).
- [14] E.L. Saldin, E.A. Schneidmiller, and M.V. Yurkov, Opt. Commun. 148, 383 (1998).
- [15] E. Saldin, E. Schneidmiller, and M. Yurkov, TESLA-FEL-2003-02, DESY (2003).
- [16] Z. Huang *et al.*, Phys. Rev. ST Accel. Beams 7, 074401 (2004).
- [17] E.L. Saldin, E.A. Schneidmiller, and M.V. Yurkov, Nucl. Instrum. Methods Phys. Res. A 381, 545 (1996).
- [18] S. Reiche, Nucl. Instrum. Methods Phys. Res. A 429, 243 (1999).
- [19] P. Emma *et al.*, the Proceedings of 2005 Particle Accelerator Conference, Tennessee, 344, (2005).

STATUS OF JAPANESE XFEL PROJECT AND SCSS TEST ACCELERATOR

Tsumoru Shintake[#] and SCSS Team
RIKEN/JASRI/SPring-8, Hyogo 679-5148 Japan.

Abstract

On 20 June, the first lasing has been observed at 49 nm in SCSS test accelerator, which is prototype machine for Japanese XFEL project. A challenging approach is employed in injector system: a low density electron beam is generated from 500 kV gun using thermionic cathode, followed by velocity bunch compression by factor of a few 100 times, and magnetic chicane bunch compression. The injector created high quality and high density electron bunch, whose measured emittance was $3 \pi \cdot \text{mm} \cdot \text{mrad}$ normalized with 800 A peak current and 1 psec pulse width or less. When we firstly closed the gap in one undulator in 15th June, we observed the SASE signal at 49 nm. Using two undulators, the signal amplification gain reached 10^5 , which is close to the saturation level. The average radiation energy is 1 micro-J/pulse at moment, we need more beam tuning.

The XFEL project aiming at generating 1 Å coherent intense X-ray laser based on SASE using 8 GeV normal-conducting accelerator has been funded. The construction is scheduled 2006-2010, and beam operation will start in 2011.

INTRODUCTION

SCSS project has started in 2001 [1]. Unique combination of three key technologies: the in-vacuum short period undulator, the C-band high gradient accelerator and low emittance injector using thermionic electron source make possible to realize SASE-FEL at 1 Å within available site length at SPring-8 less than 800 m as shown in Fig. 1. It was named as SCSS: SPring-8 Compact SASE Source because of this reason. From year

of 2001, we have been carrying out R&D for key components: the electron gun, injector, C-band klystron modulator with oil-filled compact design, high resolution beam position monitor, digital rf signal processing system, etc [2]. In order to check performance of developed hardware components and verify system performance, especially the low emittance electron injector, we constructed prototype accelerator for XFEL in 2004-2005 as shown in Fig. 2. The tunnel length is 60 m long, the maximum electron beam energy is 250 MeV, the shortest lasing wavelength is around 50 nm. From May 2006, we started dedicated beam tuning to demonstrate first lasing.

In 2006, the Japanese MEXT: Ministry of Education, Culture, Sports, Science and Technology has decided construction of XFEL at SPring-8 site. The project is aiming at generating 1 Å coherent intense X-ray laser, which is based on SASE using 8 GeV normal-conducting accelerator. Figure 2 shows the computer image of the facility, the XFEL will be constructed right next to the 1 km beam line. The construction is scheduled 2006-2010.

One big benefit to have XFEL at SPring-8 site is to share human resources and sample preparation facilities in the existing 8 GeV synchrotron light source.

CHOICE OF ACCELERATOR TECHNOLOGY

We have decided to use normal conducting linear accelerator technology at C-band frequency (5712 MHz). It is “warm” technology, not super conducting “cold” technology. The reason why we chose this technology is

- (1) Since C-band accelerator can generate high



Fig. 1: The XFEL will be build at SPring-8 site.



Fig. 2: Tunnel view in SCSS test accelerator.

[#]shintake@spring8.or.jp

gradient, as high as 35 MV/m, with reasonable cost. Technology is available right now.

- (2) Pulse repetition frequency of C-band accelerator is limited to 60 pps maximum, and average flux becomes quite lower (about 1/100 times) than the case of super conducting machine. The special feature of XFEL radiation is extremely high peak power (~ 2 GW) and short pulse duration (~ 30 femto-sec), and most of all scientific case to make use these features does not request high average flux. The existing SPring-8 3rd generation light source provides high average flux, thus XFEL and SPring-8 are complementary facilities in the same site.

CHOICE OF ELECTRON SOURCE

The SASE-FEL at 1 Å wavelength region requires high quality electron beam of extreme parameter: peak current > 2 kA, low slice emittance $\sim 1 \pi$.mm.mrad, and low slice energy spread $< 10^{-4}$. Additionally, it requires fairly long undulator line, near 100 m long, where the beam trajectory has to be guided in a straight line within small error $< 10 \mu\text{m}$. In this alignment, we use high resolution e-beam position monitors, and relay on beam-based-alignment. To perform this alignment, the electron beam has to be very stable, and also the beam hallow component and dark-current must be negligibly small (clean beam).

The transverse electron beam size at the undulator section is order of $30 \mu\text{m}$, from this beam the X-ray is radiated with diffraction limited condition, thus the X-ray beam spot is also quite small, which is order of $100 \mu\text{m}$ at the sample located 30 m or 100 m downstream from the undulator. Pointing of the radiated X-ray beam follows e-beam trajectory, therefore, e-beam trajectory angle has to be fairly stable, such as, $3 \mu\text{rad}$, and otherwise X-ray does not hit small samples.

In order to make such a stable and clean beam, first of all, the initial condition of electron beam trajectory, or the emission condition of the electron from the source has to be very stable. One candidate to meet this requirement is the thermionic cathode.

The LaB₆ or CeB₆ have been widely used in the scanning electron microscope, because of its high brightness and superior performance of quick recovery from contaminations [3]. Since they operate at high temperature near 1800 K, no any residual gases can condensed on the cathode surface. Additionally, there is constant rate of cathode material evaporation from the surface, which provides continuous activation, and also self-cleaning process. If we use a high quality single crystal, a very flat surface is formed in a single atomic layer after evaporation, which provides very uniform emission density and ensures no emittance break associated with rough cathode surface or non-uniform emission density sometimes observed in Ba-oxide cathode materials.

It should be noted that the pin-shaped cathode is commonly used in electron micro scope, since it provides extremely high brightness, i.e., small emission area provides small emittance while high current density, which meets imaging optics in microscope. However, it can emit fairly low current beam, typically less than $1 \mu\text{A}$. In contrast, the SASE-FEL requires a few Ampere beam from the cathode, thus we use a flat surface. We chose CeB₆ rather than LaB₆, because of longer life time. At 1700 K operation temperature, expected lifetime is 20,000 hours for $100 \mu\text{m}$ material loss due to evaporation.

We use rod shape CeB₆ of 3 mm in diameter as shown in Fig. 3. We extract 1 A beam via 10 MV/m acceleration field in the gun (500 kV/5cm), which is in the temperature limited condition. The theoretical normalized emittance due to thermal motion at the cathode is 0.4π .mm.mrad. The emittance was carefully measured at the gun using double slits, it was 1.1π .mm.mrad including tail component for 1 A beam current. Eliminating tail components from the data, we estimated the net emittance of core beam as 0.6π .mm.mrad [3].



Fig. 3: CeB₆ single crystal thermionic cathode for low emittance electron source.

BUNCH COMPRESSION

In the X-ray FEL for 1 Å wavelength, very high peak current is required for e-beam to obtain high SASE-FEL gain. Nominal beam current value of 3 kA is required in our design. We can not generate such beam from any kind of electron sources, therefore we compress the bunch length in longitudinal direction by means of velocity bunching in injector and magnetic chicane bunch compressor. We designed the compression factor as 20, 18, 8 in velocity bunching at injector, the first and second bunch compression system, respectively. Big question is how we maintain low emittance value from the gun to undulator through these compressions.

In the injector and bunch compressors, if the following conditions are satisfied, the slice emittance can be conserved.

- (1) Radiation damping or excitation through synchrotron radiation is small.

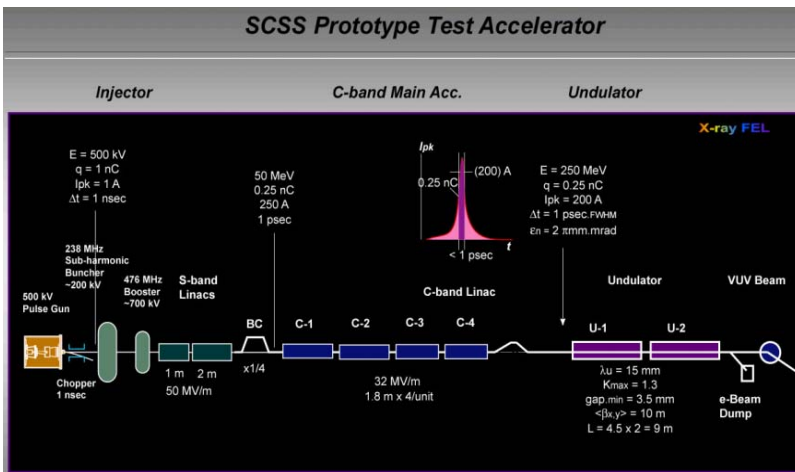


Fig. 4: SCSS prototype accelerator, two undulators of 15 mm pitch, 250 MeV e-beam, generates VUV-radiation.

- (2) There is no highly nonlinear optics, which mix particle in radial direction, resulting in non laminar flow.
- (3) There is no over-bunching process, which mixes and overlaps two or more slice components from different z-positions.

To satisfy above condition, we designed the injector system based on “adiabatic compression” scheme: the gun with beam chopper generate 1 A x 1 nsec x 500 kV beam, then velocity modulation by 238 MHz sub-harmonic buncher cavity, followed by velocity bunching along a drift section, then the space charge effect becomes severe as raising peak current, then 476 MHz booster cavity accelerates beam energy to 1 MeV, relativistic effect lowers the space charge effect, followed by velocity bunching, and inject into the S-band standing wave accelerator, and capture single bunch.

In order to test this challenging scheme, and check all hardware components developed in our R&D [4], we constructed prototype accelerator in 2004-2005 as shown in Fig. 2. Beam line layout is shown in Fig. 4. We use four C-band accelerating structures, 1.8 m long each, energy gain 32 MV/m maximum. With maximum beam energy of 250 MeV, the shortest wavelength of VUV-radiation at 50 nm can be obtained.

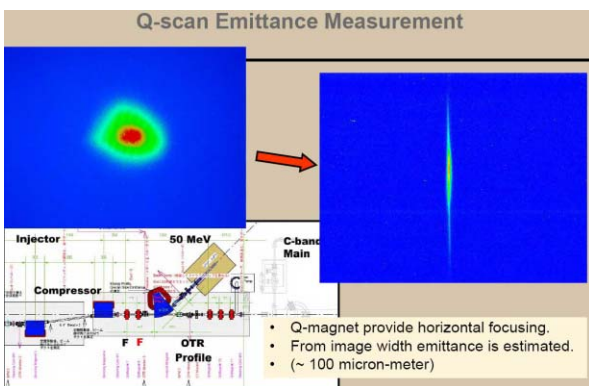


Fig. 5: Beam profile during Q-scan emittance measurement. Transition radiation from Au coating of optical mirror was monitored by CCD camera.

EMITTANCE MEASUREMENT

At the injector end, the velocity bunching and chicane bunch compression complete, where the beam energy reaches to 50 MeV, bunch charge is 0.25 nC and the bunch length is 1 psec or less, which depending on operation condition, specifically phase & amplitude tuning of 238 MHz and 476 MHz cavities.

We measured projected emittance right before the C-band accelerators, using Q-scan method. By reversing polarity of one of the Q-magnets to provided strong focusing in X- and Y-direction, and measured the minimum beam width. By varying focusing power, the beam width response was measured

as Fig. 5 and 6. We found the normalized projected emittance of around $3 \pi \cdot \text{mm} \cdot \text{mrad}$ for both X- and Y-directions. The slice emittance was also measured at 50 MeV beam dump, it was $2 \pi \cdot \text{mm} \cdot \text{mrad}$, where the measurement was limited by spatial available resolution of profile monitor.

We repeated many measurements in this kind, always observed emittance around $3 \sim 4 \pi \cdot \text{mm} \cdot \text{mrad}$. This experimental data indicates that the velocity bunching in our system does not largely deteriorate the projected emittance for compression ratio exceeding 100 times. For more detail, refer the report by H. Tanaka [6].

FIRST LASING EVENT

Two in-vacuum undulators were installed, whose undulator period is 15 mm, minimum gap is 3.5 mm, nominal K value is 1.3 and one undulator length is 4.5 m. In the beam tuning, we firstly opened the gap to 20 mm and passed the e-beam through gap and transported into the beam dump. We tuned the beam optics upstream of the undulator. We setup the optics, in coming beta-matching and focusing Q-magnet in between two undulators.

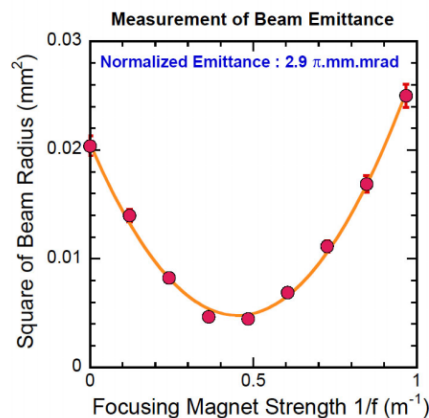


Fig. 6: Beam width as a function of focusing power. At beam energy 50 MeV, charge 0.25 nC, length <math>< 1 \text{ psec}</math>.

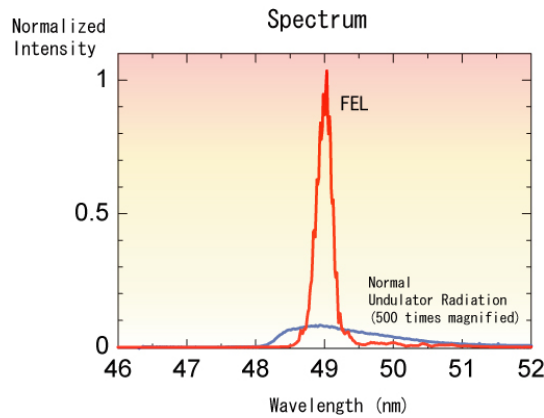


Fig. 7: Radiation spectrum at the lasing condition, 0.25 nC per bunch and 250 MeV. Peak at 49 nm is the coherently amplified signal (6000 times) from the spontaneous undulator radiation (blue line).

On 15th June evening, we firstly closed the gap in the upstream undulator, and measured radiation spectrum, where the spectrum width was already quite narrow, peaked at 49 nm, and totally different from the natural spontaneous radiation, as shown in Fig. 7. The spectrum width is around 1% FWHM, which is much narrower than the spontaneous undulator radiation, while it is dominated by e-beam energy fluctuation, at moment.

As shown in Fig. 8, when we varied the bunch charge, the lasing power drastically changed. This threshold phenomenon indicates high FEL gain. The power has not yet reached the saturation.

By varying K-value of undulator, response of the power gain was measured. Comparing to numerical simulation we determined the electron beam brightness as $270 \sim 310 \text{ A}/(\pi.\text{mm.mrad})^2$ in the undulator.

FROM TEST ACCELERATOR TO XFEL

To obtain enough FEL-gain at 1 \AA , we need ten times higher brightness than the test accelerator case, i.e., 3 kA at $1 \pi.\text{mm.mrad}$. This will be easily obtained by the second stage bunch compressor at high energy (designed compression factor is $\times 8$, at 1.8 GeV).

On the other hand, about the X-ray energy, we need improvement. The lasing pulse energy in the test accelerator is 1 micro-J/pulse average, which is about ten times lower than theoretically predicted value for 0.25 nC charge. This is partly due to the fact that the second undulator field is not perfectly matched with requirement, and may be also due to non-uniform charge distribution in electron bunch [6]. While we do not have enough data to determine amount of charge contributed to lasing, it may be 10% or less.

In XFEL machine, to raise fraction of charge for lasing and increase total charge, we improve injector design as follows.

- (1) Run the electron gun at 2 A beam current (twice higher than test accelerator case). The cathode and gun handle this beam without losing cathode lifetime and breaking emittance.

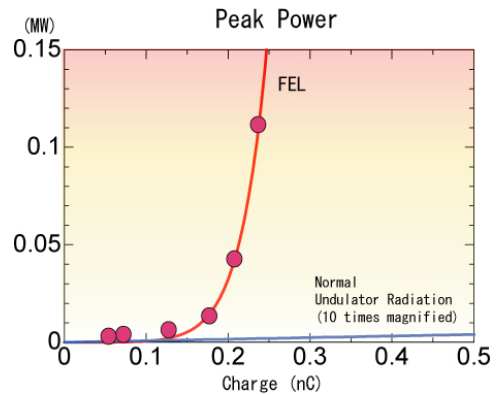


Fig. 8: Peak output power v.s. bunch charge. Using photo diode, peak height was detected from averaged pulses.

- (2) Use L-band accelerator instead of S-band at the buncher cavity, which makes beam acceptance 8-times larger. In the test accelerator, acceptance is limited upstream end of the S-band standing-wave buncher. Lowering frequency twice, all structure dimensions will scale twice larger, resulting in larger acceptance in x, y, z-directions.
- (3) Flat-topping cavities will be used in the injector. Since we use rf-field to compress bunch, the non-linear curve associated with cosine-function creates non-uniform charge distribution after bunching. Applying higher harmonic cavity, we can obtain a linear response function. This technique is well known as “flat-topping cavity” in traditional cyclotrons.

With this improvement, we will be able to generate bunch to drive FEL with 1 nC charge, with emittance $1 \pi.\text{mm.mrad}$ and with uniform charge distribution.

CONCLUSION & SCHEDULE

We measured the e-beam emittance and observed first lasing in the SCSS prototype accelerator. From this experiment, superior performance of the thermionic gun and injector system has been demonstrated.

Analysing the experimental data carefully, we refine hardware design, and start XFEL construction this year.

REFERENCES

- [1] T. Shintake *et al.*, "SPRING-8 Compact SASE Source", SPIE2001, San Diego, USA, June 2001.
- [2] <http://www-xfel.spring8.or.jp>
- [3] <http://www.feibeamtech.com>
- [4] K. Togawa *et al.*, "Emittance Measurement on the CeB6 Electron Gun for the SPRING-8 Compact SASE Source", FEL2004, Trieste Italy, August 2004.
- [5] T. Shintake, Status of SCSS Project, 3rd Asian Particle Accelerator Conference, APAC2004, Gyeongju, Korea, March 2004.
- [6] H. Tanaka *et al.*, "Low Emittance Injector at SCSS", FEL2006 conference, Berlin, August, 2006.

COHERENT HARMONIC GENERATION EXPERIMENT ON UVSOR-II STORAGE RING

M. Labat, CEA, Saclay, France
 G. Lambert, CEA, Saclay, France, RIKEN SPring-8 Harima, Hyogo, Japan
 M.E. Couprie, Synchrotron Soleil, Saint-Aubin, France
 D. Nutarelli, LAC, Orsay, France
 M. Hosaka, A. Mochihashi, J. Yamazaki, M. Shimada, M. Katoh, IMS, Okazaki, Japan
 Y. Takashima, Nagoya University, Nagoya, Japan
 T. Hara, RIKEN SPring-8 Harima, Hyogo, Japan.

Abstract

In the Coherent Harmonic Generation Free Electron Laser configuration, an external seed signal, a commercial laser source, is focused inside the first undulator. The interaction between the electron beam and this seed leads to a more coherent light emission. Such devices are very promising for short wavelength operation with a rather compact facility. Experiments have been performed on the UVSOR-II Storage Ring (Okazaki, Japan) with electrons stored at 600 MeV, and using a 2.5 mJ Ti:Sa laser at 800 nm wavelength, 1 kHz repetition rate, and 150 fs up to 2 ps pulse duration, allowing emission at 266 nm. This third harmonic has been characterised versus various parameters. Optimizations have been realized on the electron beam and laser synchronisation. The dependency of the harmonic signal on the gain (undulator gap, magnetic functions) has also been studied. Theory is compared to experiment using analytical model. These encouraging results make UVSOR-II storage ring an active test facility for Coherent Harmonic Generation scheme, as well as a potential VUV source for users experiments.

INTRODUCTION

Recent Free Electron Lasers aim at reducing the radiated wavelength to the X-ray domain, the time duration to the femto-second domain, and at improving the coherence of the source. FELs based on linear accelerators are mainly experimenting SASE [1], HGHG, and seeded configurations. Coherent Harmonic Generation (CHG) is a seeded FEL configuration based on storage ring [2, 3]. The seed can be either the own spontaneous emission of the electrons as demonstrated on DUKE [4] and ELETTRA [5] storage rings, or an external source [6] such as a commercial laser. This paper presents the successful generation of the third coherent harmonic of a Ti:Sa laser in USOR-II.

In the Coherent Harmonic Generation configuration, the laser is focused in the modulator [7], and synchronized with the circulating electron bunch. The electron beam is micro bunched at fundamental and sub harmonic wavelengths of the seeded laser. The light emission of the electrons is then enhanced in the radiator at the third harmonic of the seed, i.e. 266 nm. Figure 1 presents the general scheme of the

experiment.

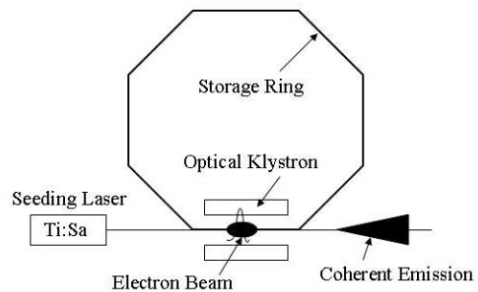


Figure 1: Coherent Harmonic Generation scheme on a storage ring

The seeding laser used for the CHG experiment was initially optimized for Slicing and Coherent Synchrotron Radiation experiments (CSR) [8], requiring high repetition rate (1 kHz) and short pulse duration (150 fs), and therefore not perfectly adapted for generation of the third harmonic. UVSOR-II facility can now provide coherent, short duration and intense light in the far infra red (using CSR) and in the VUV range (using CHG) simultaneously, using one single high power laser. Figure 2 illustrates a burst of CSR emission observed in CHG operation.

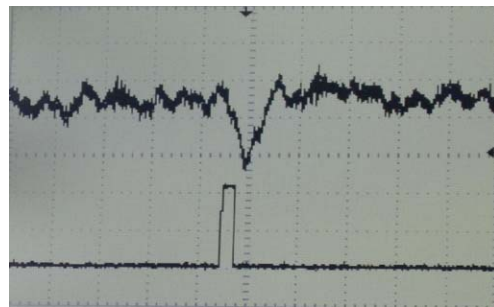


Figure 2: Oscilloscope trace of CSR signal detected by a bolometer observed in CHG operation.

Throughout this paper, an analytical model for CHG will be reminded, followed by a description of the components of the experiment. The first results and optimisation on the third harmonic are finally presented.

ANALYTICAL MODEL FOR CHG

In 1982, R. Coisson and F. De Martini [9] proposed an analytical model to describe the Coherent Harmonic Generation process in an optical klystron. The intensity of the light emitted by a relativistic electron bunch in an optical klystron can be expressed as the sum of an incoherent and a coherent term. The coherent term equals zero for randomly distributed electronic phases. In the case of CHG process, and assuming that the energy modulation only occurs in the first undulator, the interaction between the electric field E_L and the electrons induces an additional energy spread given by:

$$\Delta\gamma = \frac{eKN E_L \lambda_0}{2\gamma^2 m c^2} (J_0(\xi) - J_1(\xi)), \quad (1)$$

where J are Bessel functions, depending of $\xi = \frac{K^2}{4(1+K^2/2)}$. K is the undulator deflexion parameter, λ_0 the spatial period, N the number of periods, c the velocity of light, e the electrons charge, m their mass, and γ their normalized energy. This energy spread results into an additional phase difference at the exit of the dispersive section, equal at its maximum to: $\Delta\alpha = 4\pi(N + N_d)\Delta\gamma$. N_d is the number of equivalent periods of the dispersive section. The intensity of the coherent emission no longer averages to zero, and is given by the following expression:

$$\frac{\delta W_{coh}}{\delta\omega\delta\Omega} = \frac{n^2 e^2 N_e^2 f_n^2 J_n^2(n\Delta\alpha)}{16\pi\epsilon_0 c \lambda_L^2} \left(\frac{KN\lambda_0}{\gamma}\right)^2 A_n^2. \quad (2)$$

n is the harmonic number, N_e the number of electrons in the bunch, f_n the modulation rate, λ_L the seeded laser wavelength, and:

$$A_n = 1/2(J_{n+1}(n\xi) - J_{n-1}(n\xi)). \quad (3)$$

The intensity of the incoherent emission is given by:

$$\frac{\delta W_{incoh}}{\delta\omega\delta\Omega} = \frac{n^2 e^2 N_e}{16\pi\epsilon_0 c \lambda_L^2} (1 + f_n) \left(\frac{KN\lambda_0}{\gamma}\right)^2 A_n^2. \quad (4)$$

This model, already used for ACO [2] and Super-ACO [3] storage rings configurations, allows apprehending Coherent Harmonic Generation process and its dependency to electron beam and seeded laser parameters. In addition, calculations performed before the experimental sessions provided with reasonable expectations on the generation of the third coherent harmonic with UVSOR-II storage ring, and its laser parameters.

CHARACTERISTICS OF THE EXPERIMENTAL COMPONENTS

Electron Beam

For CHG experiment, UVSOR-II [10] facility (see Figure 3) was used in single bunch mode. The characteristics of the electron beam delivered are given in Table 1. Experiments have been performed with beam current up to 40 mA, since no beam instability occurs below this value.

The modulator and radiator of UVSOR-II's optical klystron [11] are identical and made up of 9 periods of 11 cm, separated by a 33 cm long dispersive section.



Figure 3: UVSOR-II storage ring

Table 1: Characteristics of the electron beam on UVSOR-II Storage Ring for CHG operation.

Parameter (Unit)	Symbol	Value
Energy (MeV)	E	600
Circumference of the Ring (m)	C	53.2
Cavity voltage (kV)	V_{RF}	100
RF Frequency (MHz)	f_{RF}	90.1
Harmonic number	n_H	16
Number of bunches stored	n_b	1
Period of revolution (ns)	T_0	178
Momentum compaction	α	0.028
Synchrotron frequency (kHz)	f_S	19.4
Current (mA)	I	0 - 40
Natural Energy spread	σ_γ	0.00034

Beam diagnostics

Four different diagnostics have been used to characterize the output radiation of the radiator (which includes electron beam radiations, and IR laser), and therefore the coherent emission. For spectral selection, the light is sent to an interferometric filter (CVI-F25-265), centered at 266 nm with 25 nm bandwidth. The detection of the UV light is then performed using a solar blind PhotoMultiplier (PM, Hamamatsu, R759). In order to observe the coherent emission at 1 kHz, among incoherent emission at 5.6 MHz, the PM signal is observed on an oscilloscope, triggered by the laser timing system. A streak camera (Hamamatsu, C5680) has also been used. It allows to follow the longitudinal distribution of the electron bunch, and to measure relative position in the time domain between laser pulse and electron bunch. The light was spectrally characterised using a spectrometer for spontaneous emission, and a monochromator followed by the photomultiplier for the coherent emission.

Seeding Laser

The characteristics of the seeding laser system used are given in Table 2. This system includes a mode-locked titanium-sapphire (Ti:Sa) laser oscillator (Coherent, Mira 900-F) and a regenerative amplifier (Coherent, Legend HE) driven by a Q switched pump laser, which delivers high intense femto-second pulses. Those elements are shown in Figure 4.

Table 2: Seeded Laser characteristics

Parameter	Value	Unit
Wavelength	800	nm
Spectral width	12	nm
Repetition rate	1	kHz
Pulse duration (Δt)	0.15 to 2	ps
Average Power (P_L)	1.8	W
Diameter	11.5	mm
Gaussian quality factor	1.25	
Polarization	Horizontal	



Figure 4: Photograph of the laser system used for CHG experiment.

Synchronisation

The overlap in the modulator for the micro bunching of the electronic distribution, requires a precise synchronisation of the laser pulse and the electron bunch, and therefore a specific timing system for UVSOR-II facility [12] organized as following. The mode-locked Ti:Sa laser is synchronised with the RF signal (f_{RF}) of the storage ring. In addition, the repetition frequency f_Q of the Q switched laser is based on the sub-harmonics of the revolution frequency of the bunches $f_{rev}=f_{RF}/n_H=5.6$ MHz, leading to $f_Q=f_{rev}/5632=1$ kHz. To select and fix the electron bunch with the laser pulse cuts, an RF bucket selector is used for making the Q switching trigger signal. The timing of the laser pulse within the bunch spacing time is adjusted using a phase shifter modifying the phase of the RF signal. The condition of synchronisation is observed using in first stage a photodiode, receiving both laser pulses and synchrotron radiation (SR). More accurate tuning is further performed using the streak camera, which temporal resolution reaches 10 ps.

Alignment

Spatial overlap is an other key step in Coherent Harmonic Generation. An accurate alignment of the IR laser on the electrons trajectory has to be performed in the modulator. The electronic orbit of the FEL oscillator at 800 nm has been selected for this trajectory. Auto collimation was then used to mark the seeded laser path from the laser hutch through out the FEL cavity. Three periscopes made of two flat mirrors at 45° incidence allowed the transport of the IR and a 5 m long focal lens its focusing inside the modulator. This allows to optimize the overlapping with the e-beam and to increase the local energy. Both beams have horizontal polarization. Figure 5 illustrates the experimental setup for transport and alignment of the seeding laser.

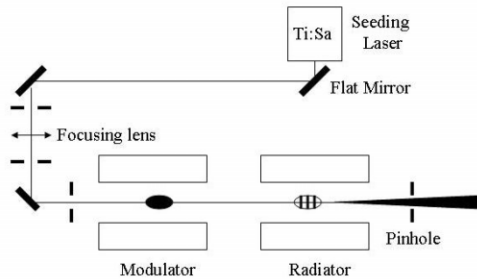


Figure 5: Setup of the laser transport to the FEL cavity.

OBSERVATION OF THE THIRD COHERENT HARMONIC

A picture of the oscilloscope screen is presented in Figure 6, illustrating the output radiation of the undulators. Central peak corresponds to the radiation of the laser heated electron bunch. The intensity at 266 nm is dramatically enhanced thanks to the coherent emission at the third harmonic of the seeding laser.

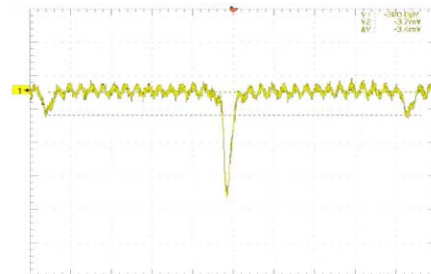


Figure 6: Oscilloscope trace of of the optical klystron output radiation. Central peak corresponds to the laser heated bunch emission, and edged peaks to unheated bunch emission. $P_L=1.78$ W, $\Delta t= 1.12$ ps, $I=4.29$ mA. Time scale: 40 ns/division.

Figure 7 shows the streak camera image of CHG signal. This diagnostic confirms the enhancement of the intensity at 266 nm radiated by the heated electron bunches (see

bright blue spots). In addition, the vertical axis of the image allows to evaluate the duration of the heated bunch radiation: it is much shorter than unheated one's, and measurement of the pulse duration is limited by the streak camera resolution. The temporal coherence achieved with Coherent Harmonic Generation allows to expect pulse durations below 2 ps.

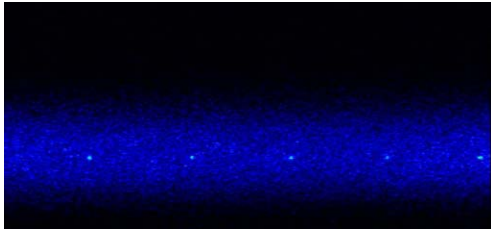


Figure 7: Photograph of the streak camera image. The bright spots correspond to laser heated bunch emission (coherent emission). Full scales are 85 ms for the horizontal and 700 ps for the vertical axis.

Once the Coherent Harmonic Generation systematic and reproducible, the harmonic radiation was studied as a function of various parameters.

According to the analytical model previously mentioned, the number of coherent photons produced is proportional to the square of the number of electrons heated by the laser, linearly related to the peak current, assuming that the electron bunch duration is much wider than the laser pulse duration (by two orders of magnitude). First results seem to confirm the expected quadratic behaviour.

The third harmonic has then been studied versus synchronisation. Using a 3 mA beam current, the laser pulse position in time was shifted back and forth by 200 ps from its initial position: where maximum UV intensity is recorded. Coherent emission could be detected over 360 ps, with total disappearing for delays longer than 200 ps, giving an rms width of 70 ps. This result is in good agreement with the rms bunch length measured at this current: 85 ps. Indeed, since the coherent emission is linked to the electronic density, maximum emission is obtained when the seeding laser heats the centre of the bunch, and a scan with the laser pulse in the time domain gives back the longitudinal distribution of the bunch.

The undulator gap has also been studied as a varying parameter. CHG process is based on the amplification by the radiator of the sub harmonics of the seeding laser wavelength. To be properly amplified, this sub harmonic wavelength must correspond to a resonant wavelength of the optical klystron, defined by the undulator parameter K , and therefore by its gap. Consequently, a detuning of this parameter might kill the radiation at 266 nm. Indeed, CHG emission is maximum for an undulator gap of 40.8 mm and the signal vanishes for gaps of 39.7 and 42.5 mm.

CONCLUSION

Using a 1 kHz Ti:Sa laser, a Coherent Harmonic Generation FEL configuration has been successfully set up at UVSOR-II facility. Short (below 2 ps), UV (266 nm), coherent laser pulses are delivered. In addition, both CHG and CSR can be operated in parallel, using the same laser system and experimental setup: an important step in the development of the fourth generation light sources.

More Coherent Harmonic Generation experiments on UVSOR-II are to be performed in order to study the influence of the seeding laser characteristics: energy, diameter, pulse duration, as well as shaping inside the modulator. Observation of the fifth harmonic is also foreseen.

ACKNOWLEDGMENTS

We would like to thank all the UVSOR-II staff for its help during experimental sessions. This work was supported by International Collaboration program of IMS.

REFERENCES

- [1] F. Ciocci et al., IEEE Jour. Quant. Elec. 31 (1995) 1242.
- [2] R. Prazeres, J.M. Ortega, C. Bazin, M. Bergher, M. Billardon, M.E. Couprie, M. Velgue and Y. Petroff, Nucl. Inst. Meth. A 272 (1988) 68-72.
- [3] R. Prazeres, P. Guyot-Sionnest, J. M. Ortega, D. Jaroszynski, M. Billardon, M. E. Couprie, M. Velghe and Y. Petroff, Nucl. Inst. Meth. A 304 (1991) 72-76.
- [4] V. Litvinenko, Nucl. Inst. Meth. A 507, 265 (2003).
- [5] G. De Ninno, M. B. Danailov, B. Diviacco, M. Ferianis and M. Trovo, FEL'04, August 2004, p. 237-240.
- [6] P.L. Csonka, Part.acele. 8, 225 (1978).
- [7] N.A. Vinokurov and A.N. Skrinsky, Preprint 77-59, Nuclear Physics Institute of Novosibirsk (1977).
- [8] M. Katoh, M. Hosaka, S. Kimura, A. Mochihashi, M. Shimada, T. Takahashi, Y. Takashima and T. Hara, to be published in the Proceedings of EPAC'06, THPLS041.
- [9] R. Coisson, F. De Martini, Phys. of Quant. Electron., 9, p. 939, Addison-Wesley (1982).
- [10] M. Katoh, M. Hosaka, A. Mochihashi, J. Yamazaki, K. Hayashi, Y. Hori, T. Honda, K. Haga, Y. Takashima, T. Koseki, S. Koda, H. Kitamura, T. Hara, T. Tanaka, AIP'04, 2004, (708) p. 49-52.
- [11] H. Hama, K. Kimura, M. Hosaka, J. Yamazaki and T. Kinshita, Nucl. Instr. and Meth. A393 (1997) 23.
- [12] A. Mochihashi, M. Hosaka, M. Katoh and Y. Takashima, UVSOR ACTIVITY REPORT 2005 (2006).

GENERATION REGIMES OF FEL WITH VOLUME DISTRIBUTED FEEDBACK*

K. Batrakov[†], S. Sytova[‡], INP BSU, Minsk, Belarus.

Abstract

This paper discusses different generation regimes of Volume Free Electron Lasers (VFELs) which utilize Volume distributed feedback (VDFB). Dependence of VFEL operation on VDFB parameters is studied.

INTRODUCTION

VDFB significantly extends operation possibilities of Free Electron Lasers (FELs). It was shown in [1] that properly parameters choice of VDFB geometry lowered down the threshold current magnitude of generation. VDFB can solve the problem of mode discrimination at great electromagnetic power generation in oversized systems. The beam cross section in such systems significantly exceeds wavelength. Large sizes of electron beam cross section allow to distribute power and to lower local load of system elements. However, standard oversized system suffers from excitation of great number of parasitic undesired modes. As a result, the destructive interference takes place, the coherence of radiation degrades and the generation efficiency significantly reduces. So, analysis of electron beam dynamics dependence on VDFB parameters is of great importance. Partly, threshold parameters of electron beam instability in VFEL can be investigated by using linear theory. For example, the first threshold point j_1 corresponds to beginning of the electron beam instability. At this point the first radiating mode appears. Instability stage corresponding to regenerative amplification is in the range of parameters $j_1 < j < j_2$ when generating mode is already appeared, but the radiation gain of this mode is less than radiation losses of the coupled feedback mode. Such system can amplify incident wave. Parameters at which radiation gain becomes equal to absorption correspond to the second threshold point. When magnitude of beam current exceeds the second threshold value, generation process occurs without incident wave. For current density j in the range $j_2 < j < j_3$ the beam instability in short period of time changes into the stationary nonlinear saturation regime. If current exceeds the third threshold value $j > j_3$, the nonlinear stage becomes non-stationary. The threshold currents mentioned above depend on parameters of VDFB. So, variation of VDFB can change the type of generation. For providing VFEL experiments and their interpretation it is necessary to have theoretical description and numerical simulation of effects considered. Here some such theoretical results are presented.

* Work supported by Belarus Foundation for Fundamental Research, Grant F06R-101.

[†] batrakov@inp.minsk.by

[‡] sytova@inp.minsk.by

ENERGY TRANSFER IN VDFB SYSTEMS

Let's study energy exchange between electron beam and radiation in the system with VDFB. Electromagnetic field in this case can be expressed as

$$\mathbf{E} = \sum_{\alpha} a_{\alpha} \exp \{i\mathbf{k}_{\alpha}\mathbf{r} - i\omega t\} \{\mathbf{e} + \dots + \mathbf{e}_i s_i \exp [i\tau_i \mathbf{r}] + \dots\}, \quad (1)$$

where τ_i are the set of reciprocal vectors, \mathbf{e}_i are unit polarization vectors, s_i are coupling coefficients between waves, a_{α} are mode amplitudes which are determined from initial and boundary conditions. Using the equation of electron motion in the electromagnetic field and averaging over initial electron phases the following expression for mean electron energy can be obtained

$$\Delta\gamma = -\frac{e^2(\mathbf{ue})^2}{2m^2u^3c^2\gamma} \left(\frac{k^2}{\omega} - \frac{\mathbf{ku}}{c^2} \right) L_*^3 F, \quad (2)$$

where L_* is the length of interaction region,

$$F = \text{Im} \left[\sum_{\alpha\beta} a_{\alpha} a_{\beta}^* \left(\frac{\exp \{i(\nu_{\beta} - \nu_{\alpha})\} - 1}{(\nu_{\beta} - \nu_{\alpha}) \nu_{\beta}^2} + \frac{\exp [-i\nu_{\alpha}] - 1}{\nu_{\alpha} \nu_{\beta}^2} + \frac{\exp [-i\nu_{\alpha}] (i\nu_{\alpha} + 1) - 1}{i\nu_{\alpha}^2 \nu_{\beta}} \right) \right],$$

$\nu_i = (\omega - \mathbf{k}_i \mathbf{u}) L_* / u$ are parameters of detuning from synchronism.

Control of Emission Line Shape by VDFB

Generally in the case of n -wave VDFB the energy transfer (2) between electron and electromagnetic field depends on n detuning parameters. This gives additional possibilities to regulate the shape of emission line in comparison with one-wave synchronism case.

Shapes of one-wave and different two-wave synchronism lines is illustrated in Fig. 1. It is seen that corresponding selection of parameter $a = \nu_1 - \nu_2$ increases the width of amplification region by two times (compare the curves "one-wave" and "a=7"). Due to this fact, electron beam will be synchronous with electromagnetic wave for a longer time. So, more energy is transferred to electromagnetic wave that raises the laser efficiency. On the other hand emission line can be narrowed by properly choice of detuning parameters.

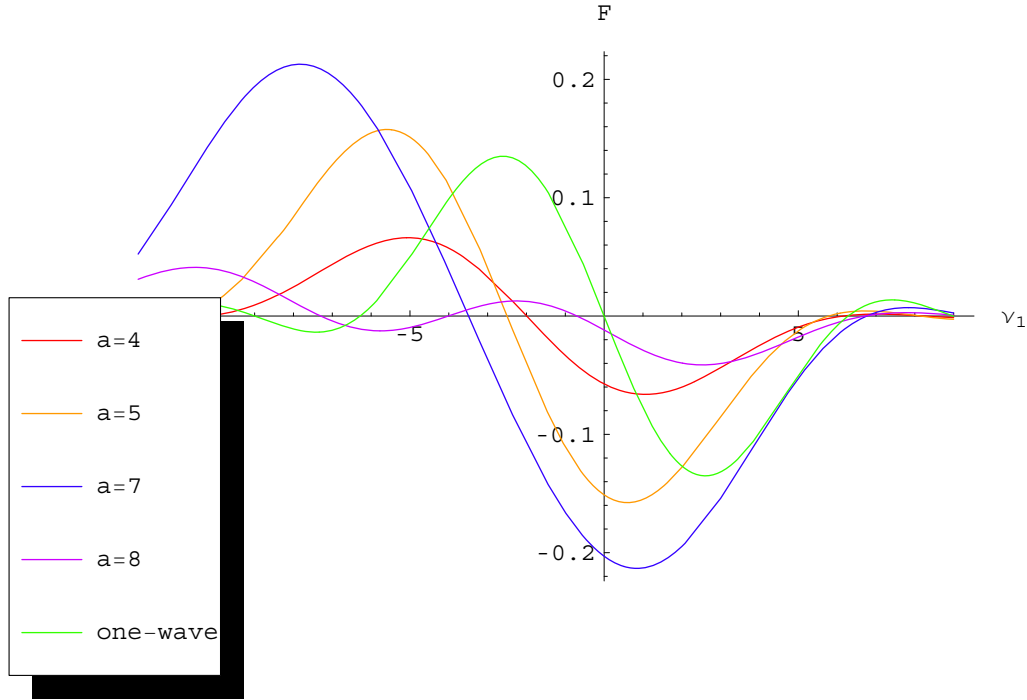


Figure 1: Emission line dependence on the relation between detuning parameters $a = \nu_1 - \nu_2$ for one and two-wave synchronism.

REGENERATIVE AMPLIFICATION (LINEAR STAGE)

Eigenmodes for two-wave VDFB are obtained from the dispersion equation [1]

$$(\omega - \mathbf{k}\mathbf{u})^2 \{ (k_\tau^2 c^2 - \omega^2 \varepsilon_0) (k_\tau^2 c^2 - \omega^2 \varepsilon_0) - \omega^4 r \} = - \frac{\omega_L^2 (\mathbf{u}\mathbf{e})^2}{\gamma} (k^2 c^2 - \omega^2) (k_\tau^2 c^2 - \omega^2 \varepsilon_0). \quad (3)$$

Here $\mathbf{k}_\tau = \mathbf{k} + \tau$, $\varepsilon_0 = 1 + \chi_0$, $r = \chi_\tau \chi_{-\tau}$, χ_0 and χ_τ are polarizabilities of periodical structure with VDFB which appear in the expansion of permeability:

$$\varepsilon(r, \omega) = 1 + \sum_{\tau} \chi_\tau \exp \{ -i\tau r \}. \quad (4)$$

Representing solutions of (3) as $\mathbf{k} = \mathbf{k}_0 + \mathbf{n}\delta\omega/c$, where \mathbf{k}_0 satisfies to the condition $\omega - \mathbf{k}_0\mathbf{u} = 0$ the following boundary conditions for mode amplitudes a_i can be written:

$$\begin{aligned} \sum_i a_i &= a, & \sum_i s_i a_i \exp \{ ik_i \delta_i L \} &= b, \\ \sum_i \frac{a_i}{\delta_i} &= 0, & \sum_i \frac{a_i}{\delta_i^2} &= 0. \end{aligned} \quad (5)$$

The first and the second equalities in (5) correspond to the continuity of electromagnetic field at the input ($z = 0$) and the output ($z = L$) of VDFB structure, a and b are amplitudes of incident waves. The third and the fourth equations

correspond to the density and current density continuity of unperturbed at the input electron beam. Solving system (5) one can obtain the following expression for intensity of output electromagnetic waves:

$$\begin{aligned} \frac{I}{I_0} &= \frac{\gamma_0 |\mathbf{E}_0|^2 + \gamma_1 |\mathbf{E}_\tau|^2}{\gamma_0 |a|^2 + \gamma_1 |b|^2} = \\ &= \left(\frac{\gamma_0 c}{\mathbf{n}\mathbf{u}} \right)^3 \frac{16\pi^2 n^2}{-\beta (k\chi_\tau L_*)^2 (\Gamma_{th} - \Gamma)}, \end{aligned} \quad (6)$$

where

$$\Gamma_{th} = \frac{\left(\frac{\gamma_0 c}{\mathbf{n}\mathbf{u}} \right)^3 16\pi^2 n^2}{-\beta (k\chi_\tau L_*)^2 k L_*} + \text{Im}\chi_0 \left(1 - \beta \pm \frac{\text{Im}r}{\chi_\tau \text{Im}\chi_0} \right)$$

$$\begin{aligned} \Gamma &= \frac{\pi^2 n^2}{4\gamma} \left(\frac{\omega_L}{\omega} \right)^2 k^2 L_*^2 (\chi_0 \pm \sqrt{-\beta} |\chi_\tau| - \gamma^{-2}) \cdot \\ &\quad \cdot (\chi_0 \pm \sqrt{-\beta} |\chi_\tau|) f(y), \end{aligned}$$

$$f(y) = \sin y \frac{(2y + \pi n) \sin y - y(y + \pi n) \cos y}{y^3 (y + \pi n)^3}.$$

$I_0 = \gamma_0 |\mathbf{E}_0|^2 + \gamma_1 |\mathbf{E}_\tau|^2$ is the intensity of incident waves. $y = \nu_1/2$, β is diffraction asymmetry factor, γ_0 and γ_1 are diffraction cosines. Expression (6) is derived in the low gain approximation.

It follows from (6) that $I/I_0 > 1$ when $\Gamma > \text{Im}\chi_0 (1 - \beta \pm \text{Im}r / (\chi_\tau \text{Im}\chi_0))$ ($j > j_1$ is the first threshold point) and the amplification process starts. Fig. 2

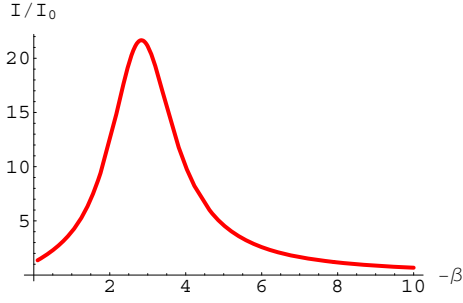


Figure 2: Dependence of regenerative amplification coefficient on asymmetry factor β of VDFB.

demonstrates amplification dependence on VDFB geometry factor β . So, VDFB can control amplification process. When current reaches some critical value $j > j_2$ the oscillation regime develops. Dependence of the second threshold current on VDFB asymmetry is illustrated in Fig. 3. It is seen that VDFB allows to control the second thresh-

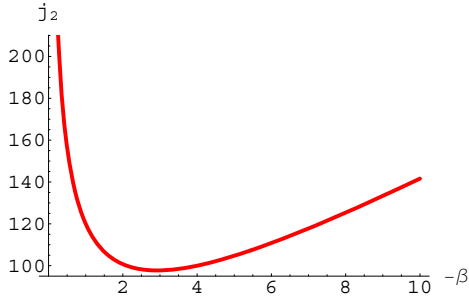


Figure 3: Dependence of the second threshold current j_2 on asymmetry factor β of VDFB.

old current too. Regenerative amplification ($j_1 < j < j_2$) is stationary and can occur in linear or nonlinear regime depending on magnitudes of I (nonlinear regime will be discussed below). In contrary, oscillation regime has the non-stationary character and the linear stage rapidly transfers to the nonlinear one. To study nonlinear regime the numerical simulation of VFELs must be carried out.

NUMERICAL SIMULATION OF THE SYSTEM WITH VDFB

For n -wave VDFB from Maxwell equations in the approximation of slow varied amplitudes the system of n equations for n strong coupled waves can be obtained. Here we restrict ourselves by considering three-wave VDFB. The system for n -wave VDFB can be written by evident generalization. So, using the field representation in the form $\mathbf{E} = \sum_{\tau_i} \mathbf{e}_i E_i \exp\{i\mathbf{k}_{\tau_i} \mathbf{r} - \omega t\}$, $i = 0, 1, 2$ we obtain the following nonlinear equations:

$$\begin{aligned} & \frac{\partial E_0}{\partial(\omega t)} + \gamma_0 \frac{\partial E_0}{\partial(kz)} + \frac{1}{2} l E_0 - \frac{1}{2} \chi_1 E_1 - \frac{1}{2} \chi_2 E_2 \\ & = 2\pi j \Phi / \omega \int_0^{2\pi} \frac{2\pi-p}{8\pi^2} (\exp(-i\Theta(t, z, p) + \\ & \exp(-i\Theta(t, z, -p))) dp, \\ & \frac{\partial E_1}{\partial(\omega t)} + \gamma_1 \frac{\partial E_1}{\partial(kz)} - \frac{1}{2} \chi_{-1} E_0 + \frac{1}{2} l_1 E_1 - \\ & \frac{1}{2} \chi_{2-1} E_2 = 0, \\ & \frac{\partial E_2}{\partial(\omega t)} + \gamma_2 \frac{\partial E_2}{\partial(kz)} - \frac{1}{2} \chi_{-2} E_0 - \frac{1}{2} \chi_{1-2} E_1 \\ & + \frac{1}{2} l_2 E_2 = 0. \end{aligned} \quad (7)$$

Here $l_i = (k_{\tau_i}^2 c^2 - \omega^2 \varepsilon_0) / \omega^2$. $\gamma_0, \gamma_1, \gamma_2$ are three VDFB cosines.

System (7) must be supplemented with equations for the phase dynamics:

$$\begin{aligned} & \frac{d^2 \Theta(t, z, p)}{dz^2} = \frac{e\Phi}{m\gamma^3 \omega^2} \left(k_z - \frac{d\Theta(t, z, p)}{dz} \right)^3 \cdot \\ & \cdot \text{Re}(E_0 \exp(i\Theta(t, z, p))), \\ & \frac{d\Theta(t, 0, p)}{dz} = k_z - \omega/u, \quad \Theta(t, 0, p) = p. \end{aligned} \quad (8)$$

In (8) it was proposed that the electron beam is synchronous with the wave \mathbf{E}_0 only. The integral form of beam current in the right hand side of (7) is obtained by averaging over the following initial phases of electrons in the beam: entrance time of electron in interaction zone ωt_0 and transverse coordinate of entrance point in interaction zone $\mathbf{k}_{\perp} \mathbf{r}_{\perp}$.

Equation (8) depends on these two initial phases only in combination $\mathbf{k}_{\perp} \mathbf{r}_{\perp} - \omega t_0$ (that appears in initial condition for phase at $z = 0$). Therefore, in the mean field approximation double integration over two initial phases can be reduced to the single integration. As the result, the averaged current in right hand side of the first equation of (7) differs from expressions frequently used in literature (in which the current is used in the form $\int_0^{2\pi} d\Theta_0 \exp\{-i\Theta\}$).

Regimes of VFEL Generation (Nonlinear Stage)

VFEL dynamics simulated on the basis of the system (7) and (8) is illustrated in Fig. 4 - 7. In the Fig. 4 the regimes of regenerative amplification and stationary generation are presented. It follows from this Fig., that the region of regenerative amplification is rather narrow. This region $j_1 < j < j_2$ is marked by two dotted lines. Therefore, the idea to control amplification by regulating VDFB parameter β (and other VDFB parameters) seems to be very useful. Let's note, that the region of regenerative amplification by corresponding choice of VDFB parameters can be

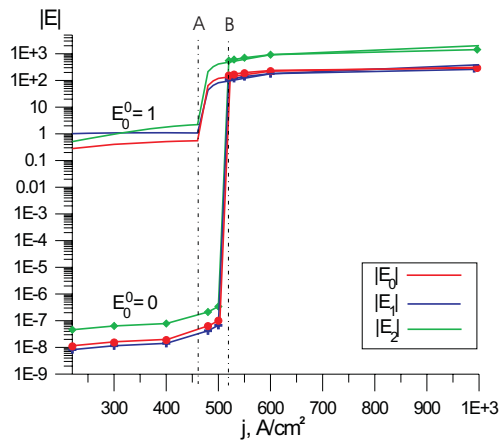


Figure 4: Amplification and oscillation regimes for three-wave VDFB. Vertical dotted lines (*A* and *B*) shows positions of the first and the second threshold currents.

increased for three-wave VDFB in comparison with two-wave VDFB ([2]).

When electron beam current increases, generation remains stationary up to the third threshold current j_3 . Then at $j > j_3$ non-stationary periodic regime of generation starts. Fig. 5 demonstrates temporal dynamics of generation in this region ($j > j_3$).

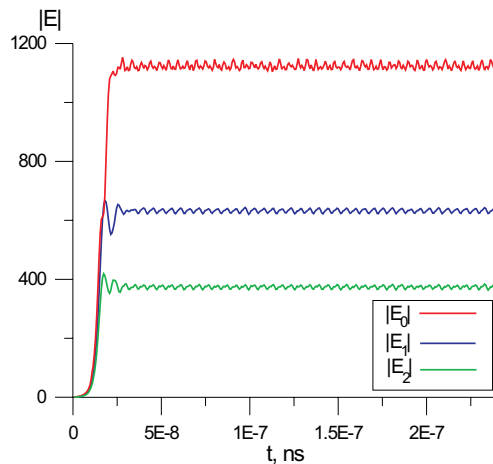


Figure 5: Current exceeds third threshold value ($j > j_3$). Periodic regime of oscillation for three-wave VDFB.

Oscillations appear at discrete number of frequencies at further current increase.

At some current value dynamics becomes chaotic and the regions with continuous frequency spectrum appears (Fig. 6 and Fig. 7).

CONCLUSION

In the paper presented it was shown that VDFB allows to regulate the generation regime. Changing VDFB parameters at given current value can transfer generation process

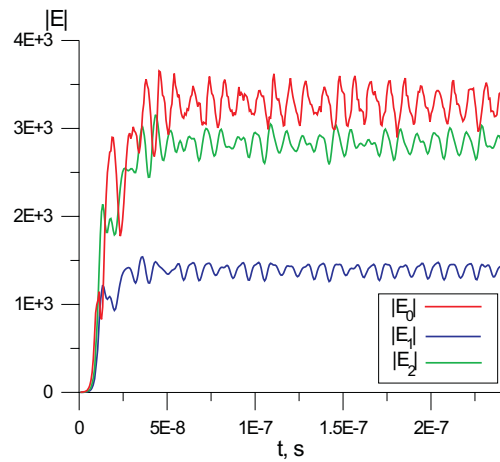


Figure 6: Chaotic oscillation regime.

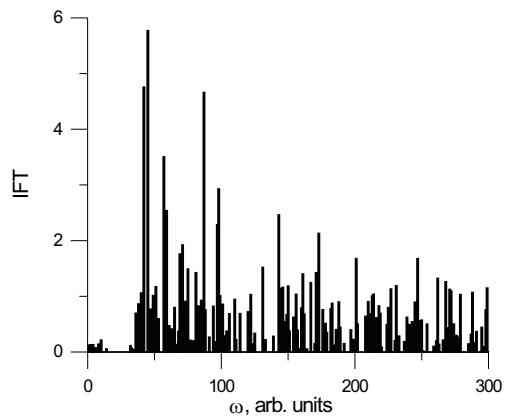


Figure 7: Fourier transform of E_0 corresponding to chaotic generation in Fig. 6.

between different regimes. In addition n -wave VDFB allows to discriminate parasitic modes at generation of great power in large volume. First experiments with VFEL generation was presented in [3, 4] and the following papers. So, VFEL has great future prospect.

REFERENCES

- [1] V. Baryshevsky, K. Batrakov, I. Dubovskaya, J. Phys. D. 24 (1991) 1250.
- [2] K. Batrakov, S. Sytova, Nonlinear Phenomena in Complex Systems, 8 (2005) 359.
- [3] V. Baryshevsky, K. Batrakov, A. Gurinovich et al., NIM 483A (2002) 21.
- [4] V. Baryshevsky, K. Batrakov, N. Belous et al., LANL archive, physics/0409125 (2004), <http://arxiv.org/pdf/physics/0409125>, 3 p.

EXTRACTING INFORMATION FROM SMITH-PURCELL FEL SIMULATIONS

J.T. Donohue, Centre d'Etudes Nucléaires de Bordeaux-Gradignan, BP 120, 33175 Gradignan,
France

J. Gardelle, CEA CESTA, BP 2, F-33114 Le Barp, France

Abstract

Simulations of coherent Smith-Purcell radiation using 2D particle-in-cell codes have provided insight into the nature of the process, and have generally provided support to the viewpoint of the Vanderbilt University FEL group. However, if one is interested in terahertz frequencies, the need for small meshes and short time intervals makes the calculations exceedingly long. In particular, the S-P correlation between frequency and angle is only valid at distances large compared to the grating size, and may not be apparent if the simulation area is too small. With the help of the multipole expansion, we show how simulation data obtained with a small area may be extended to an area of arbitrary size. This enables us to confirm the presence of coherent higher order S-P peaks at the appropriate angles. We also isolate the forward and backward surface Floquet waves. Evidence for the presence of unsuspected components is presented.

INTRODUCTION

In attempting to simulate Smith-Purcell (S-P) radiation at terahertz frequencies with a 2D particle-in-cell code, one is confronted with problems of time and memory, at least if the simulation is performed on a PC. The reasons are easy to understand. Typical wavelengths are hundreds of μm , which means that mesh sizes must be tens of μm . The time step is tied to the mesh size Δ through stability conditions, and is, typically Δ/c , where c denotes the speed of light. Finally, the overall size of the simulation area is determined by the experimental circumstances. For example, the Dartmouth College experiment[1] using a low energy continuous electron beam has a grating about 12.7 mm long, and we perform our simulation in an area of approximately $20\text{ mm} \times 5\text{ mm}$, with $\Delta = 10\ \mu\text{m}$. To follow the system through one ns takes about 10 hours of calculation with the commercially available code we use, MAGIC[2]. In contrast the MIT experiment using a 15 MeV pre-bunched beam[3](at 17.1 GHz) had a grating 10 cm long, which means that our simulation area must be considerably larger than for the Dartmouth set-up. However, two ns are all that is needed to get a satisfactory simulation, since the beam is already bunched. At FEL 2005,[4] we reported our first attempts to simulate coherent S-P radiation in these two experiments. While we did find some interesting results, we used an unrealistically large current in the Dartmouth case, which led to copious emission of radiation from the ends of the grating at a

frequency less than any allowed S-P frequency. This corresponded to the evanescent surface wave predicted by the theory of Andrews and Brau (AB)[5] but it obscured the true S-P signal that we sought. In the MIT simulation, we found that there remained a substantial emission of radiation even when we removed the grating. Furthermore, although we observed up to 20 harmonics of the bunching frequency, we didn't see the usual S-P relation between wavelength and angle. This is given by $\lambda = L(1/\beta - \cos\phi)/n$, where λ is the wavelength, L the grating period, β the relative velocity (in a plane parallel to the grating and perpendicular to the direction of the grooves), ϕ the angle of emission (with respect to the beam direction), and the integer n denotes the order. While this relation is true, it only holds precisely when the radiation is observed at distances large compared to both the wavelength and the grating size. Given the constraints of small mesh size, it is impractical to simulate in an area large enough to see the wavelength-angle correlation.

Another problem we encountered was the presence on the grating surface of two distinct surface waves. One of these, according to the AB theory, is in resonance with the electron beam, while the other, of the same frequency but propagating in the opposite direction, is generated by reflection at the grating ends. It is of some interest to isolate these two Floquet waves, in order to obtain a direct verification of the AB theory, and to determine the reflection coefficient when such a wave reaches the grating end. This coefficient may be used in a refinement of the AB theory proposed by Andrew, Boulware, Brau and Jarvis[6] in order to estimate the start current needed to produce coherent S-P radiation in the Dartmouth experiment. In reference 6 an estimate of 50 A/m was made, while Kumar and Kwang-Je Kim[7] obtained a slightly smaller value of 36.5 A/m.

In this paper we describe two methods we have developed to address these problems. The first method we call the Small Box \rightarrow Big Box transformation, since it allows us to simulate in a small area and extrapolate to a much larger area, so as to see the S-P wavelength-angle correlation. While the near-to-far-field transformation is the subject of a chapter of Taflove's monograph[8], our simple method uses Finite Fourier Transforms (FFT) and fitting procedures readily available in such high-level programs as *Mathematica* and MAPLE, and thus involves relatively little effort on the part of the user. The second

method has been developed to extract from a simulation the two oppositely moving Floquet evanescent waves, which are important only in the neighborhood of the grating. Again, the FFT and fitting capacities of *Mathematica* or *MAPLE* may be used to execute the task.

In Section II we describe the Small Box→Big Box transformation as applied to a MIT simulation. In Section III we show how to separate the Floquet components from a simulation of the Dartmouth set-up. The anomalies observed in our fitting procedure reveal an unsuspected presence of higher temporal harmonics in the field, as well as incipient coherent S-P radiation. Our conclusions are given in Section IV.

SMALL BOX→BIG BOX TRANSFORMATION

In a source-free half-plane region extending to infinity, the magnetic field in the z -direction may be written as

$$B_z(\rho, \phi, t) = \Re \int_0^\infty d\omega e^{-i\omega t} \sum_{m=1}^{\infty} \sin(m\phi) H_m^1 \left(\frac{\omega \rho}{c} \right) b_m(\omega),$$

where the standard Hankel functions H_m^1 are used and the complex quantities $b_m(\omega)$ are the coefficients of the multipole field. They may be written as

$$b_m(\omega) = \frac{2}{\pi^2 H_m^1 \left(\frac{\omega \rho_0}{c} \right)} \int_{-\infty}^{\infty} dt e^{i\omega t} \int_0^\pi d\phi \sin(m\phi) B_z(\rho_0, \phi, t).$$

The azimuthal component of the electric field (cgs units) may then be written as

$$E_\phi(\rho, \phi, t) = -\Re \int_0^\infty d\omega e^{-i\omega t} \sum_{m=1}^{\infty} i \sin(m\phi) H_m^1 \left(\frac{\omega \rho}{c} \right) b_m(\omega)$$

The total energy/cm radiated across a semicircle of radius ρ is then

$$\frac{dW}{dz} = \left(\frac{c\rho}{4\pi} \right) \int_{-\infty}^{\infty} dt E_\phi(\rho, \phi, t) B_z(\rho, \phi, t)$$

which reduces, after some manipulations involving the Wronskian, to

$$\frac{dW}{dz} = \frac{c^2}{4} \int_0^\infty d\omega \sum_{m=1}^{\infty} \frac{|b_m(\omega)|^2}{\omega},$$

which is independent of the radius.

In the context of our simulation, we calculate $B_z(\rho_0, \phi_k, t_r)$, with $\phi_k = (2k-1)\pi/180$, $1 \leq k \leq 90$ and $t_r = t_1 + (r-1)T/N$, $1 \leq r \leq N$, where the time step T/N is chosen by *MAGIC*. Accordingly, we use FFT rather than continuous Fourier transforms, and we perform a FFT at each of the 90 angles, obtaining

$\tilde{b}(s, \phi_k) = \text{FFT}(B_z(\rho_0, \phi_k, t_r))$, where $\omega \rightarrow 2\pi(s-1)/T$. Then at fixed s , we write

$$\tilde{b}(s, \phi_k) = \sum_{m=1}^{85} \tilde{b}_m(s) \sin(m\phi_k)$$

and we apply a fitting procedure to determine the $\tilde{b}_m(s)$ for $1 \leq m \leq 85$. Finally we introduce the normalized multipole coefficients $\hat{b}_m(s)$,

$$\hat{b}_m(s) = \tilde{b}_m(s) / H_m^1(2\pi(s-1)\rho_0 / cT).$$

We may now calculate the magnetic field and the azimuthal component of the electric field at any point in the source-free region by taking the Inverse FFT of the sequence of sums

$$B_z(\rho, \phi, t) = \text{IFFT} \left\{ \sum_{m=1}^{85} \hat{b}_m(s) \sin(m\phi) H_m^1(2\pi(s-1)\rho / cT) \right\}$$

$$E_\phi(\rho, \phi, t) = \text{IFFT} \left\{ \sum_{m=1}^{85} -i \hat{b}_m(s) \sin(m\phi) H_m^1(2\pi(s-1)\rho / cT) \right\}$$

It is often desirable to examine the fields in a given frequency range, and this may be accomplished by introducing a filter in the Inverse FFT. We should point out that since the FFT assumes a periodic function, the time behavior we obtain at an arbitrary point may violate causality. However, an *ad hoc* translation in time allows one to find the true pulse shape at the new radius.

The energy radiated during the interval of time T is given by (ergs/cm if $\hat{b}_m(s)$ is in Gauss)

$$\frac{dW}{dz} = \left(\frac{c^2 T^2}{4\pi^2 N} \right) \sum_{s=2}^N \left(\sum_{m=1}^{85} |\hat{b}_m(s)|^2 \right) / (s-1).$$

To illustrate this procedure, we plot in Figure (1) our simulated $B_z(t)$ (for the MIT set-up) vs. t at a distance 5.5 cm from the center of the grating, and at angle 89° , with its FFT.

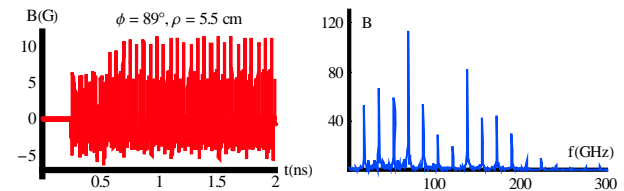


Figure 1. $B_z(t)$ vs. t and its FFT, $\phi = 89^\circ$, $\rho = 5.5$ cm.

After performing the operations indicated above, we obtain the extrapolated function $B_z(t)$ vs. t at a distance 50 cm from the center, again with its FFT, which are shown in Figure (2).

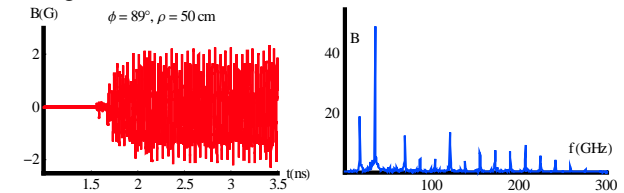


Figure 2. $B_z(t)$ vs. t and its FFT, $\phi = 89^\circ$, $\rho = 50$ cm.

The reconstructed signal is smaller than the original, as expected, since the fields decrease asymptotically as $\rho^{-1/2}$. Even taking into account the overall reduction in size, the reconstructed FFT is quite different from that at small radius. This must be attributed to the fact that for the

second harmonic, there is a broad S-P first order peak at 82° , close enough to our angle of 89° to favor the frequency near 34 GHz.

To indicate how the small box \rightarrow big box transformation affects the angular distribution of energy, we show in Figure (3) the energy radiated during our 2 ns pulse as a function of angle for a band of frequencies centered around the sixth harmonic, near 103 GHz.

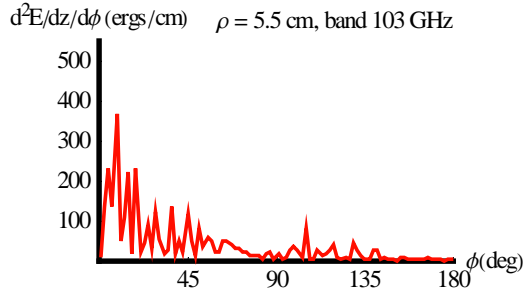


Figure 3. The angular distribution of energy at 5.5 cm in a frequency band centered at 103 GHz.

For comparison we show in Figure (4) the reconstructed distribution of energy as predicted by our small box \rightarrow big box transformation with $\rho = 50$ cm. The angles at which coherent S-P radiation is expected in the MIT experiment at this frequency are indicated. For both distributions we find the same total energy radiated

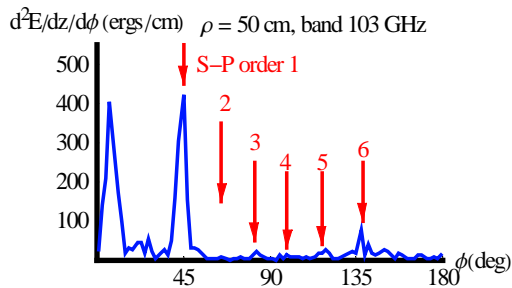


Figure 4. The reconstructed angular distribution of energy at 50 cm in a frequency band centered at 103 GHz.

119.3 ergs/cm, calculated by numerical integration. This is in good agreement with the direct formula for the energy radiated in that band. Results similar to these were obtained for the first 20 harmonics. The prominent peak at small angles (8° here) is not S-P radiation but is associated with the appearance and disappearance of short current pulses, even in the absence of a grating.

ISOLATING FLOQUET WAVES

In the AB approach the electron beam interacts with a component of an evanescent Floquet wave. In the Dartmouth configuration, the wave has a negative group velocity, and the mechanism is that of a Backward Wave Oscillator. Upon reaching the end of the grating, the wave is partly reflected, and some of its energy is emitted

as free radiation. The magnetic field in the neighborhood of the grating is then a sum of two Floquet evanescent waves propagating in opposite directions, and one may write,

$$B_z(x, y, t) = \Re \sum_{p=-\infty}^{\infty} e^{-\alpha_p y} \{ B_p e^{i((k_F + pK)x - \omega t)} + B'_p e^{i((-k_F - pK)x - \omega t)} \}$$

where $\alpha_p = \sqrt{(k_F + pK)^2 + (\omega/c)^2}$.

The reflected wave is not in resonance with the beam, and essentially traverses the grating without change, until it is also reflected at the other end, again emitting radiation. To better understand this, we have developed a simple method for isolating the Floquet waves. We use the “range” command of MAGIC, which measures a component of the electromagnetic field along some straight line in space (along the x -direction here), at a fixed time. An example is shown in Figure (5).

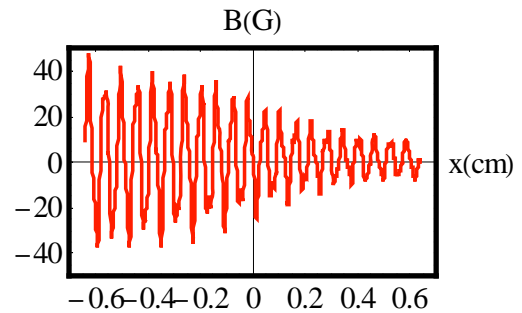


Figure 5. B_z vs. x at fixed t and y . Dartmouth Grating.

By performing three ranges separated by short time intervals, obtaining the spatial FFTs and fitting the three complex amplitudes for each wave number k to an assumed form $\alpha_k e^{-i\omega x} + \beta_k e^{i\omega x}$, we can empirically determine the coefficients α_k and β_k . An FFT is shown in

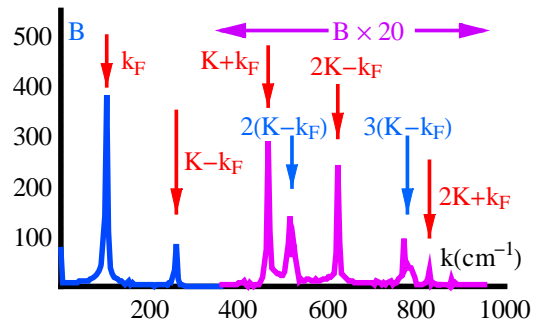


Figure 6. FFT of signal in Figure 5.

Figure (6). The prominent peaks are indicated by red arrows, and the right-hand side of the figure has been multiplied by 20 to make details visible. The blue arrows indicate second and third harmonics of $K-k_F$, the component resonant with the beam. Here the frequency ω is known ($2\pi f$, with $f = 432$ GHz). By comparing with the general expression for B_z , we see that the components of the Forward Floquet wave have peaks at $k_F + pK$, while the Backward Floquet wave has support at $pK - k_F$. If we multiply the α_k by a filter that includes only the peaks at $k_F + pK$, and perform the Inverse FFT, we obtain the

Forward Floquet waves at each of the three instants. Similarly, by filtering around $pK-k_F$, we find the backward wave, and both are shown in Figure (7).

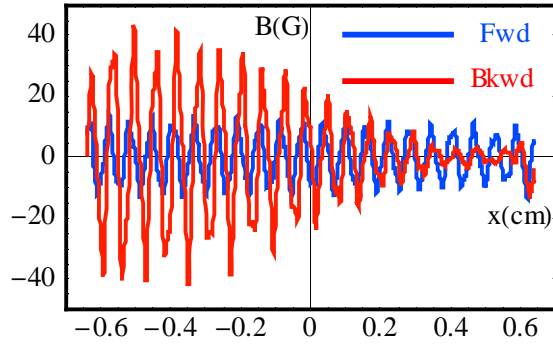


Figure 7. Forward (blue) and backward (red) Floquet waves extracted from signal in Figure 5.

It is clear from this figure that the forward Floquet wave shows little or no growth across the grating, while the backward wave shows considerable growth, indicating an imaginary part of k of order 4 cm^{-1} . We note also that at both ends of the grating the ratio of the incident to the reflected wave is approximately 3:1.

As a check on our empirical method, which uses a least-square method to fit all the FFT components, we attempted to see whether the fit is adequate. This led to a somewhat serendipitous discovery that we now discuss. If we define

$$\Delta B_k(t) = \text{FFT}_k(t) - \alpha_k e^{-i\alpha} - \beta_k e^{i\alpha},$$

the complex number that is a measure of the validity of our fit, we may plot its absolute value as a function of wave number. The results are shown in Figure (8). The

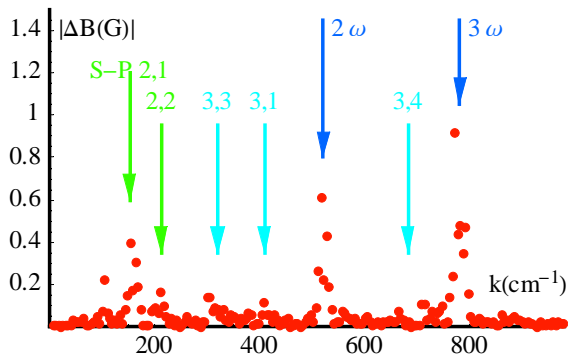


Figure 8. Discrepancy ΔB vs. wave number k .

major anomalies occur at 520 and 780 cm^{-1} , which are just the second and third harmonics, respectively, of the resonant wave number, 260 cm^{-1} . They appear also in Figure (6). Upon examining the data, we found that these anomalies disappear if we fit using 2ω and 3ω instead of ω in our fitting procedure. That means that there are components of the form $e^{im((K-k_F)x-\alpha)}$, with $m = 2, 3$, etc. Such components are readily found in the FFT analysis of the current, and they follow from the non-linear nature of the bunching phenomenon. By an argument based on Ampère's law, modulation of the current must appear as

modulation in the magnetic field, and that is what we see. Aside from these two major anomalies, there appear to be several smaller ones. We attribute these to the presence, in small amounts, of the coherent S-P signal corresponding to various harmonics and orders. From the S-P relation and the fact that all coherent radiation will occur at a multiple of the frequency of the evanescent wave, one may derive the following expression,

$$k = m\omega/\beta c - 2\pi n/L,$$

where n denotes the order, m the harmonic, the period L is $173 \text{ } \mu\text{m}$, and $\omega = 2\pi \times 4.32 \times 10^{11} \text{ s}^{-1}$. Using it we have drawn arrows to indicate the wave numbers associated with some pairs m, n . It must be noted that our FFT is symmetric, and peaks that should occur for negative k values are shown at positive values.

CONCLUSIONS

We have presented results concerning our attempts to extract information from simulations of coherent Smith-Purcell Radiation, using a 2-D PIC code. Two distinct methods have been discussed. One permits results obtained in a small area to be extended to a larger area. In doing so, we see more clearly the coherent S-P radiation produced in the MIT experiment with a high-energy pre-bunched beam. The second method involves fitting the FFT data at three closely spaced times, in order to separate the forward and backward Floquet surface waves postulated in the approach of Andrews and Brau. As a by-product, the presence of second and third harmonics of the fundamental bunching component were demonstrated, and evidence for tiny amounts of coherent S-P radiation was provided.

REFERENCES

- [1] A. Bakhtyari, J. E. Walsh, and J. H. Brownell, Phys. Rev. E **65**, 066503 (2002).
- [2] MAGIC, Mission Research Corporation.
- [3] S.E. Corbly, A. S. Kesar, J. R. Sirigiri, and R. J. Temkin, Phys. Rev. Lett. **94**, 054803 (2005).
- [4] J.T. Donohue and J. Gardelle, *Proceedings of the 2005 FEL Conference, Stanford, California USA* p. 262 (<http://www.JACoW.org>).
- [5] H.L. Andrews and C.A. Brau, Phys. Rev. ST Accel. Beams **7**, 070701 (2004).
- [6] H.L. Andrews, C. H. Boulware, C. A. Brau and J. D. Jarvis, Phys. Rev. ST Accel. Beams **8**, 050703 (2005).
- [7] Vinit Kumar and Kwang-Je Kim, Phys. Rev. E **73**, 026501 (2006).
- [8] A. Taflov, *Computational Electrodynamics*, (Artech House, Boston, 1995), p. 203.

SIMULATION OF SMITH-PURCELL FELS AT TERAHERTZ FREQUENCIES

J.T. Donohue, Centre d'Etudes Nucléaires de Bordeaux-Gradignan, BP 120, 33175 Gradignan,
France

J. Gardelle, CEA CESTA, BP 2, 33114 Le Barp, France

Abstract

Our previous work on the 2D simulation of a coherent Smith-Purcell FEL operating in the terahertz domain is extended to a systematic study of the dependence on various parameters. The important question of the starting current required to produce coherent radiation is addressed, and our new results are presented. As in our previous work we concentrate on two configurations, one similar to the Dartmouth S-P FEL, with a low energy continuous beam, and the other similar to the MIT experiment that used a pre-bunched 15 MeV beam.

INTRODUCTION

At FEL 2005[1] we reported on simulations of coherent Smith-Purcell (S-P) radiation at terahertz (THz) frequencies using a two-dimensional (2D) particle-in-cell code, MAGIC. Two quite different experimental set-ups were considered; one similar to the long-running Dartmouth College experiments initiated by Walsh[2], while the other was similar to the MIT experiment that used a pre-bunched 15 MeV electron beam[3]. The results we presented were rather preliminary and a fuller account has recently appeared[4]. We remind the reader of the S-P relation, $\lambda = L(1/\beta - \cos\phi)/n$, where λ is the wavelength, L the grating period, β the relative velocity (in a plane parallel to the grating and perpendicular to the direction of the grooves), ϕ the angle of emission (with respect to the beam direction), and the integer n denotes the order. One of our aims was to verify the analytical model proposed by Andrews and Brau[5](AB) and subsequently extended by Andrews, Boulware, Brau and Jarvis[6] to explain coherent Smith-Purcell radiation. Our results did indeed support the viewpoint of Brau and co-workers, that the mechanism for coherent radiation is the bunching of the initially continuous beam by an evanescent wave that is significant only in the vicinity of the grating. The frequency of this wave is always less than the minimum allowed S-P frequency. The process is unstable in the sense that the wave bunches the beam, the beam drives the wave and growth occurs, both in time and along the grating. Our simulation of the Dartmouth set-up found that this is indeed what happens. In particular, the frequency and axial wave number (in the first Brillouin zone) of the simulated grating wave were very close to what the model predicts. Since the bunching is inherently non-linear, once it becomes significant the current is modulated at harmonics of the fundamental frequency, and these may correspond to allowed S-P frequencies.

The radiation emitted then shows both intrabunch (since the bunches are small compared to a wavelength) and interbunch (since the fields of all bunches over the grating add up) coherence. Consequently, the coherent radiation occurs only at integer multiples of the fundamental, and only at the corresponding S-P angles. However, the simulation also revealed a major unexpected effect, namely the copious emission of radiation at the fundamental frequency. Indeed, this unforeseen radiation made the direct observation of the S-P radiation quite difficult. Our simulated grating has a finite length. When the evanescent wave reaches the end of the grating, part of its energy is emitted as free radiation of the same frequency, and part of it is reflected back in the opposite direction. The result is that there are two evanescent waves on the grating, which propagate with equal and opposite wave numbers. Only one of these waves is resonant with the electron beam, and since the beam-wave instability is absolute in the Dartmouth configuration, it displays growth both in space and time. The other Floquet wave grows in time only (through reflections), but not in space. In a companion paper we show how both of these Floquet waves may be extracted from the simulation data.

For the MIT experiment, since the beam was already bunched, the bunching mechanism referred to played no role, and the simulation was expected to be straightforward. However, the simulation failed to display unambiguous S-P radiation. In fact, there were two distinct problems, first the emission of considerable radiation even when no grating was present, and secondly, the expected frequency-angle correlation was not apparent. The former has been understood to be a consequence of standard electrodynamics. It is associated with the appearance and disappearance of a relativistic short bunch of electrons. The latter was caused by the fact that the S-P relation is valid only at distances large compared to the grating size. Since the MIT grating was 10 cm long, S-P radiation can be seen clearly only at distances of order 40 cm or more from the center of the grating. Since we are dealing with radiation whose wavelength is a few hundred μm , the mesh size in the simulation must be kept on the order of tens of μm . Under such circumstances, the computing time and memory needed become unreasonable, at least for a PC-based simulation. In the companion paper we outline a simple method we call the Small Box \rightarrow Big Box transformation, which enables us to circumvent this difficulty. While techniques for passing from the near

zone fields to the far zone based on Green's theorem are well known[7], our method appears to work quite well. It makes use of Finite Fourier Transforms (FFT) and fitting tools available with symbolic manipulation programs such as *Mathematica* or MAPLE. Once this transformation is performed, we see clearly the expected coherent S-P radiation at a large number of angles and frequencies.

Since the last FEL conference, other work on coherent S-P radiation has appeared, notably by Dashi Li and collaborators[8], who also use MAGIC for simulations, and by Kumar and Kwang-Je Kim[9]. In their simulations Li and co-workers studied the effects both of a single short bunch and a periodic train of such bunches passing over a grating of the Dartmouth type. The former showed intrabunch coherent S-P radiation, followed by the emptying of the evanescent wave from the grating after the passage of the bunch. The latter illustrated interbunch coherence, since the second harmonic of the imposed bunch frequency was S-P allowed and indeed emerged at the expected angle. The extensive analysis of Kumar and Kim, based on the traditional approach of diffraction by the grating of the incident electron's field, yielded a dispersion relation quite similar to that obtained by Andrews and Brau. The analysis included a treatment of coherent S-P radiation similar to that of a Backward Wave Oscillator (BWO), for which a start current is known to exist. Using both numerical and analytical methods, they estimated a start current (minimum current needed to produce the instability) of 36.5 A/m for a sheet beam 10 μm above the grating. This is similar to the estimate of 50 A/m found in reference 6.

Our attempt to find the start current for the Dartmouth configuration is discussed in the second Section, and some results on our simulation of the MIT set-up are presented in the third Section. Simulation parameters are shown in the Table 1.

Table 1. Parameters of the Simulations

Parameters	Dartmouth	MIT
beam energy	35 keV	15 MeV
Current (peak for MIT)	variable	25 kA/m
Beam thickness	$\delta = 10 \mu\text{m}$	1 mm
Beam-grating distance	$e = 10 \mu\text{m}$	0.7 mm
Grating period	$L = 173 \mu\text{m}$	1 cm
Max. wave number	$K = 363 \text{ cm}^{-1}$	$2\pi \text{ cm}^{-1}$
Grating groove depth	$H = 100 \mu\text{m}$	echelette
Grating groove width	$A = 62 \mu\text{m}$	
Number of periods	$N = 74$	10
External magnetic field	$B_x = 2 \text{ T}$	0
Mesh size	$8.65 \times 8 \mu\text{m}^2$	$(100 \mu\text{m})^2$

START CURRENT FOR DARTMOUTH

In Figure (1) we show a contour map of the magnetic field B_z in the area of our MAGIC simulation. The beam appears as a red line, and one sees cylindrical waves of wavelength $\approx 700 \mu\text{m}$ radiating from the grating ends. This is the evanescent wave, predicted by AB.

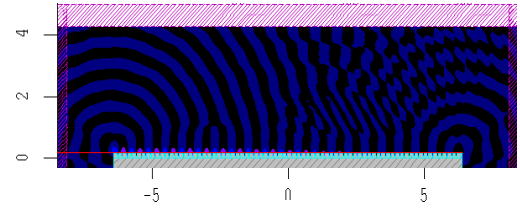


Figure 1. Contour map of B_z .

In contrast to our earlier simulations, we have raised the grating slightly. This is more consistent with the physical situation, where the grating is not flush with a ground plane. Upon doing so, we found that the height of the grating plays a significant role in the reflection at the ends of the grating. In the Dartmouth set-up the system behaves like a BWO, with two Floquet waves proceeding in opposite directions. The backward wave has a component in resonance with the beam, and it displays an absolute instability, with growth both in time and in space. The forward wave shows no growth in space, but since it is fed by reflection at the upstream end, it does grow in time. We found this to be the case in our earliest simulations, with a very large current. In fact, more sophisticated analyses, such as those of references 6 and 9 point out that the boundary conditions at the grating ends play an important role in determining the start current. In our companion paper[10], we separate the two Floquet waves, and we see that the forward wave is essentially constant across the grating, while the backward wave grows strongly in the negative x -direction. However, this was for a current of 175 A/m, which reached saturation in about 1 ns. In order for the BWO mechanism to work, the gain must be sufficient to allow the ratio of the backward wave to forward wave be small at the downstream end and large at the upstream end. The greater the reflection the less is the gain needed to close the loop, and in principle the smaller the starting current.

In order to estimate the start current, we monitor the variation with time of the current at the middle of the grating. We filter the signal, and then estimate the gain by fitting a logarithmic plot of the summits. We also note the time required to reach saturation, t_{sat} , defined by the first maximum of the bunched current. Finally we note the ratio of the peak current at saturation to the direct current, I_{sat}/I . Once the details of the simulation have been fixed, such as mesh size, beam width, beam height above grating, kinetic energy, we then repeat the simulations for various currents. To our surprise, we obtained the curves shown below.

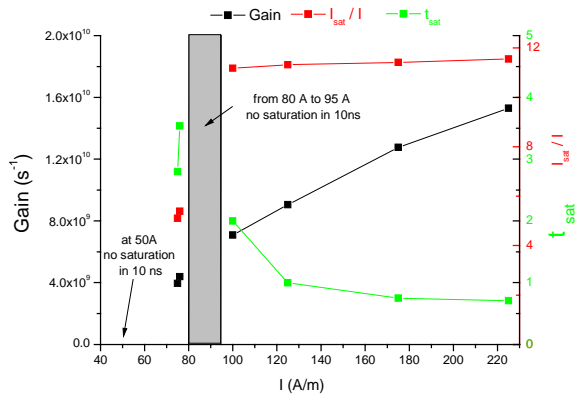


Figure 2. Gain, t_{sat} and I_{sat}/I vs. current I .

In the shaded region running from 80 to 95 A/m, and including three runs at 80, 90 and 95 A/m, no instability was observed, even for times of 10 ns. In contrast for currents > 100 A/m, the system always saturated in just a few ns. More astonishingly, at 75 and 76 A/m, the system reached saturation. However, at 50 A/m, it again failed. We are unable to understand these results, but clearly more work is needed. As additional evidence, we show the MAGIC phase space densities (kinetic energy-x) for the 76, 95 and 100 A/m runs.

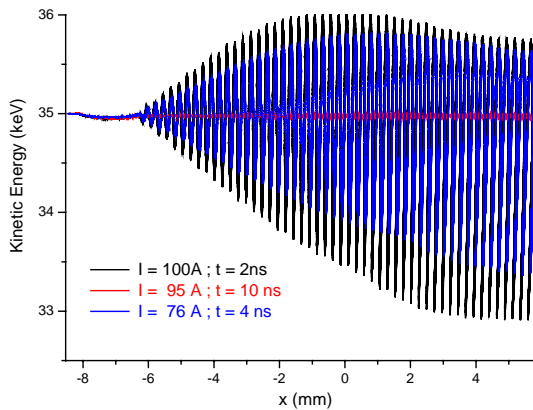


Figure 3. Phase space density plots in the Kinetic Energy-x plane, for 76 (blue), 95 red and 100 (black) A/m.

The oscillations correspond to an axial wave number of 260 cm^{-1} , which is what the AB theory suggests. For the 76 and 100 A/m runs, the average energy losses are roughly 0.5 and 0.8 keV, respectively, while the red curve shows neither oscillation nor energy loss. Again, we can only express our surprise at this result.

MIT SIMULATION

In our first simulation of the MIT experiment, we encountered a major difficulty in trying to identify the coherent S-P radiation that was produced. The beam consisted of short pulses (1 ps) produced by a linear accelerator functioning at 17.14 GHz. Consequently, the only frequencies allowed are integer multiples of that frequency. Since the beam energy was 15 MeV, and the grating period was 1 cm, it is straightforward to compute the frequencies predicted by the standard S-P relation. If we keep only the first six orders, and concentrate on angles in the forward direction, we find the curves shown in Figure (4). The harmonics are shown as horizontal lines, and each intersection of any of them with any of the curves marked “order” corresponds to coherent S-P radiation at the angle shown. Clearly there are a great number of possibilities, and for some angles like 49, 65 and 82 degrees, several frequencies may occur. The problem of observing S-P radiation is thus quite complex.

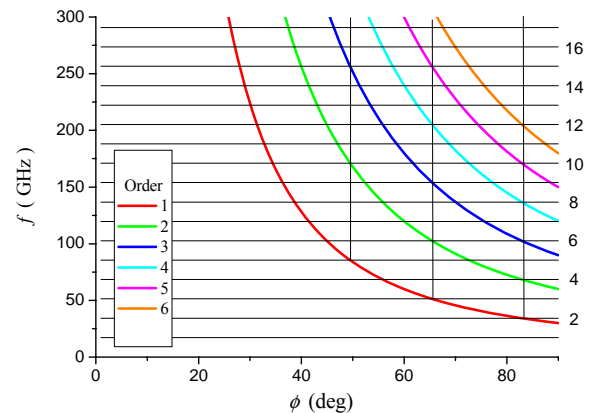


Figure 4. Intersections of the harmonics of 17.14 GHz with the first six S-P orders.

The situation was complicated further when we found that even if we removed the grating, we still observed substantial radiation. This was clearly not S-P radiation but it was present in our simulation. As we indicated in reference 4, the radiation we observed without grating may be calculated exactly using classical electrodynamics, at least for a sheet beam of infinitesimal width. We show in Figure (5) the results of such a calculation. The contour map of B_z in a $120 \text{ mm} \times 100 \text{ mm}$ region of the x-y plane bears a strong resemblance to the results of our simulation without grating. A «plume» in which the magnetic field is mainly concentrated accompanies each bunch. The tiny red dots visible beneath each bunch indicate a large positive magnetic field between the beam and the ground plane. This component is an important contribution even when a grating is present, and no attempt to understand our simulation can avoid taking it into account.

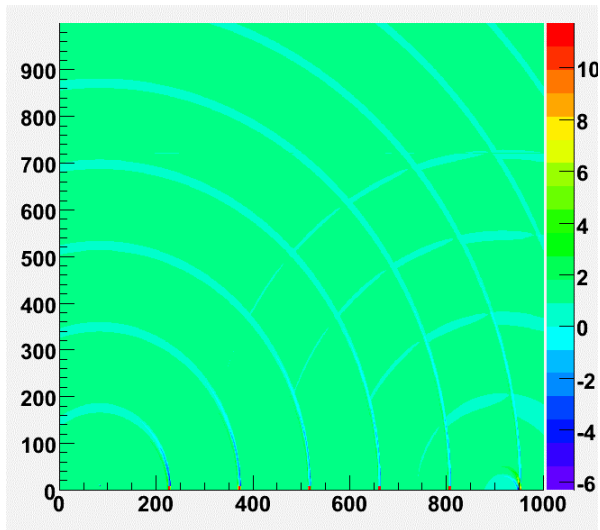


Figure 5. Contour map of B_z following the predictions of classical electrodynamics. The area shown corresponds to 12 cm in x , and 10 cm in the y direction.

In order to illustrate the difficulty of interpreting the simulation directly, we show in Figure (6) the Finite Fourier Transform (FFT) of $B_z(t)$ as observed directly in our simulation, which was made in a relatively small area, $12 \times 6 \text{ cm}^2$. The observation point is at 5.5 cm from the center of the grating, and placed at 65° . The most prominent lines in the spectrum are the fourth, sixth and eighth harmonics, but only the sixth is an S-P frequency at this angle.

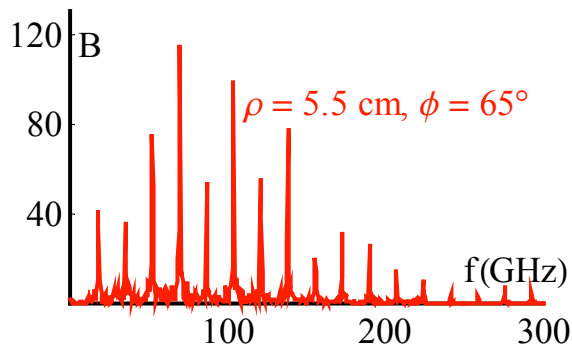


Figure 6. FFT of B_z at position indicated.

As outlined in reference 10, we have developed a procedure for extrapolating the results of our simulation to larger distances from the grating. Shown in Figure 7 is the result of applying our procedure to the data obtained in the small area simulation, after extrapolation to a larger distance from the center, but at the same angle.

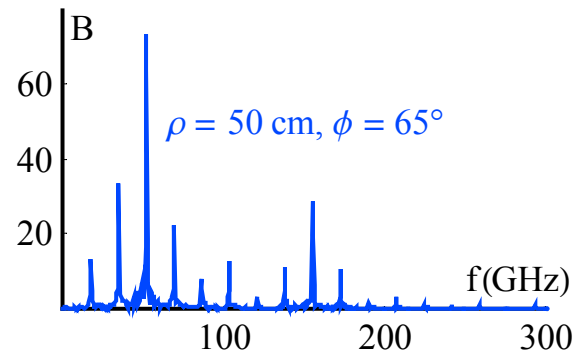


Figure 7. FFT of B_z following extrapolation. Third, sixth and ninth harmonics are more apparent.

It is clear that the relative importance of the third, sixth, ninth and twelfth harmonics, all of which are S-P allowed at this angle, has increased.

REFERENCES

- [1] J.T. Donohue and J. Gardelle, *Proceedings of the 2005 FEL Conference, Stanford, California USA*, p. 262 (<http://www.JACoW.org>).
- [2] A. Bakhtyari, J.E. Walsh, and J. H. Brownell, *Phys. Rev. E* **65**, 066503 (2002).
- [3] S.E. Corbly, A. S. Kesar, J. R. Sirigiri, and R. J. Temkin, *Phys. Rev. Lett.* **94**, 054803 (2005).
- [4] J.T. Donohue and J. Gardelle, *Phys. Rev. ST Accel. Beams* **9**, 060701 (2006).
- [5] H.L. Andrews and C. A. Brau, *Phys. Rev. ST Accel. Beams* **7**, 070701 (2004).
- [6] H.L. Andrews, C. H. Boulware, C. A. Brau and J. D. Jarvis, *Phys. Rev. ST Accel. Beams* **8**, 050703 (2005).
- [7] A. Taflove, *Computational Electrodynamics*, (Artech House, Boston, 1995), p. 203.
- [8] Dashi Li, Z. Yang, K. Imasaki and Gun-sik Park, *Phys. Rev. ST Accel. Beams* **9**, 040701 (2006).
- [9] Vinit Kumar and Kwang-Je Kim, *Phys. Rev. E* **73**, 026501 (2006).
- [10] J. T. Donohue and J. Gardelle, these Proceedings.

A BEAM SHAPER FOR THE OPTICAL BEAMLINE OF RF PHOTOINJECTORS

G. Klemz[#], I. Will, Max-Born-Institute, D-12489 Berlin, Germany.

Abstract

The paper reports on first results on beam shaper for the generation of a flat-top beam profile in the ultraviolet (UV). The shaper can be integrated into the optical beamline of the PITZ facility [1]. This will improve the efficiency of the optical beamline significantly.

INTRODUCTION

A high performance of SASE FELs requires a low emittance of the electron bunches that emerge from the photoinjector. This in turn can be favoured by irradiating the cathode by a laser beam with a spatial and temporal flat-top profile [2]. A simple way to illuminate the photocathode with a uniform beam profile is to strongly expand the laser beam with a telescope and select the very central region of the magnified beam by means of a small "beam shaping aperture". This method which is presently implemented at PITZ, inherently gives rise to a large loss of the incident UV-laser power. At PITZ the transmission amounts to approximately 20%, and 80% of the UV laser radiation are lost at the beam shaping aperture.

Thus, a more efficient technique for optical beam-shaping is desirable.

BEAM SHAPING TECHNIQUES

Conceivable technical solutions can be associated with one of the following methods:

Field mapping: The input beam is transformed into the desired output beam by refraction at appropriately designed aspherical surfaces in a prescribed manner. This technique works well for diffraction-limited beams and can be nearly lossless. A plane wavefront, i.e. a collimated beam can be generated at the output of the shaper by adding a second aspherical lens. Both, the temporal shape of the pulse and the coherence of the laser beam are maintained, which is particularly important for the optical beamline of photoinjectors. Field mapping permits to

precisely control the final intensity profile. For these reasons it is the method of choice for our beam shaper compared to the alternatives outlined below.

We suggest the setup of Fig. 1 for integration of the beam shaper into the optical beamline. Two magnifying telescopes are used to match the beam diameter to the requirements of the individual components. The former beamshaping aperture remains in place. It is needed to increase the edge steepness in the wings of the flat-top.

Another alternative are **beam integrators** which split the input beam by a lens array into a large number of facets. Subsequently, the energy within each facet is dispersed over the cross section of the desired output beam. The output profile is the sum of the diffraction patterns of each individual aperture of the lens array. That's why the output beam exhibits strong, small-scale intensity modulations (speckles) and the beam integrators work satisfactory only for multimode beams. They are lossless as well.

However, due to their principle of operation they destroy the spatial coherence of the laser beam. There is also no condition of constant optical path, so some temporal broadening of the pulse duration results.

A third method is the **radial intensity filter** (RIF) [3]. This filter can be realized based on birefringent crystals with a curved surface that provides a radial variation of polarization retardation. One or more such radial birefringent elements in combination with polarizers form a RIF. They are lossy due to the absorption of light in the polarizers. As a further disadvantage, flattening of the nearly Gaussian infrared (IR) laser beam can only approximately be obtained due to limited degrees of freedom in its design parameters.

Beam shaping elements based on **internal conical refraction** are commercially available [4]. These systems require depolarized or circular polarized monochromatic radiation and contain a biaxial/trigonal crystal. The crystal

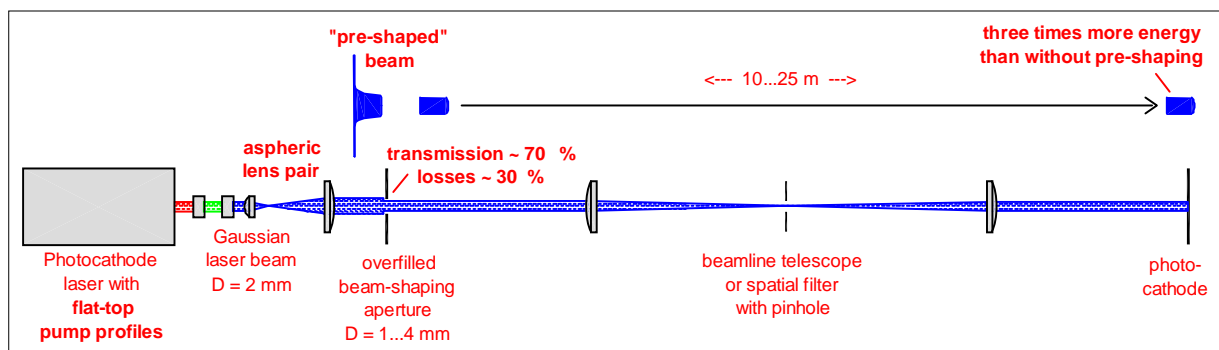


Figure 1: Proposed scheme of an optical beamline for the rf-photoinjector at PITZ that integrates a refractive beam shaper.

[#]klemz@mbi-berlin.de

length has to be adapted to wavelength and diameter of the input beam. Since no polarizers are needed, this system can be highly transmissive. Unfortunately, there are no suitable biaxial birefringent crystals available for the UV at present. That's why the technique cannot be used in the UV beamline of a photocathode laser.

EXPERIMENT

We have designed a beam shaper that consists of a Galilean telescope made of two refractive aspherical lenses. Fig. 2 shows how the input rays from the laser system are redirected into a uniform distribution within a Galilean telescope. The Fig. 3 shows our measured beam profiles at the input, in the middle and the exit of the lens pair when using a HeNe-laser. The absence of a focus between the aspheres is important for application at the PITZ beamline, since this excludes possible optical breakthrough due to high UV peak powers.

Our beam shaper is presently designed for 4 mm diameter (FWHM) of the flat-top and 2.8 mm ($1/e^2$) diameter of the Gaussian input. The aspheres are 100 mm apart. These diameters were chosen for a nominal power transmission of 99.9%. Following [5], a smooth Fermi-dirac profile instead of a step function was chosen to represent the flat-top profile, since this reduces diffraction effects along the propagation path of the output profile.

Sensitivity against beam size fluctuations

For application of the shaper in a beamline of a photocathode laser, the beam profile at the cathode should be stable as far as possible, even if the diameter of the input beam varies slightly. That's why we have carefully examined the sensitivity of the output beam against a 10% fluctuation of the input beam diameter for our spherical lens pair. The results are depicted in Fig. 4.

The amount of the deviations on the edge of the flat-top depends approximately linear on the dimensionless shape parameter β of the Fermi-dirac profile. β represents the ratio of the radius of the flat-top and the total width of the soft transition region where the intensity returns to zero [5]. With increasing β the profile becomes gradually flat and square, approaching a step function as $\beta \rightarrow \infty$. In the example shown in Fig. 4 the overshoot amounts to 15%.

We conclude from our experience with the current beam shaper that a design tolerant against fluctuation of the input beam diameter is more important than an almost perfectly flattened output profile with steep edges. This means that β should be reduced considerably, a future value of $\beta = 6$ seems to be suitable for our application.

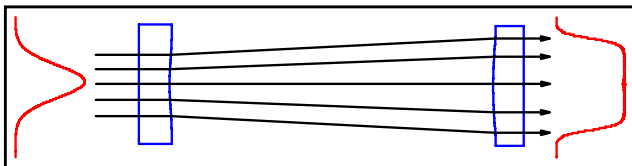


Figure 2: Basic scheme of the refractive field mapping beamshaper (Galilean design)

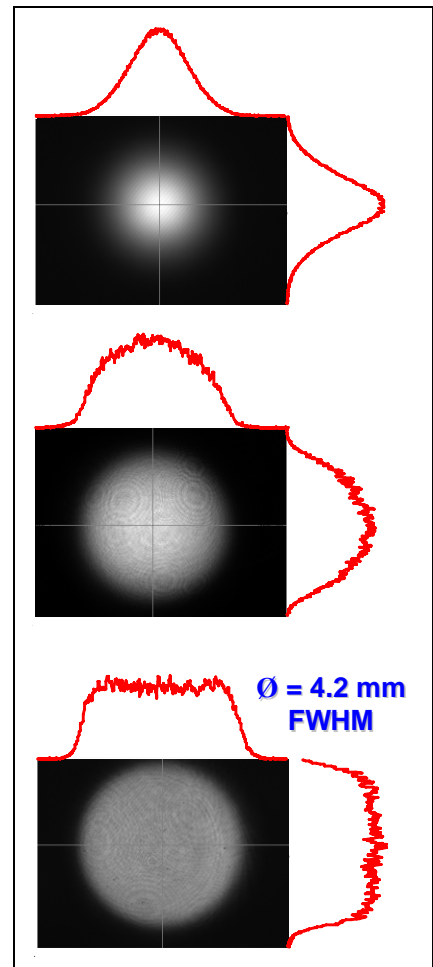


Figure 3: Measured beam profiles at the entrance, midway and at the exit of the beam shaper

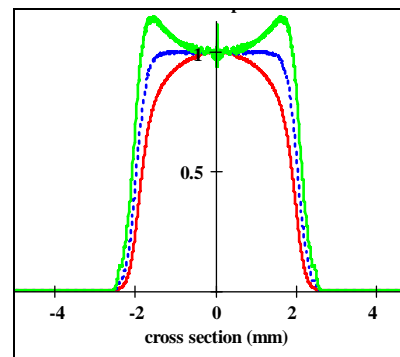


Figure 4: Output profile for varying beam radius w at the input (shape parameter $\beta = 16$): $w = 0.9 \cdot w_0$ (red), $w = w_0$ (blue), $w = 1.1 \cdot w_0$ (green), design value: $w_0 = 1.422$ mm ($1/e^2$)

With the additional option of a spatial light modulator that might precede the aspherical lens pair the remaining error at the edges as well as some remaining radial variation of the intensity might be corrected.

Propagation of the UV beam

Fig. 5 shows the beam profile produced by the refractive beam shaper in a matched UV beam (left). The present realization of the nonlinear frequency conversion produces a slight elliptical beam in the UV. Its horizontal cross section is slightly larger than in the vertical direction. This is responsible for the observed overshoot in the horizontal cross section at the output plane of the aspherical lens pair. The beam profile was reasonable preserved by relay imaging over a distance of about 1 m, see Fig. 5 (right).

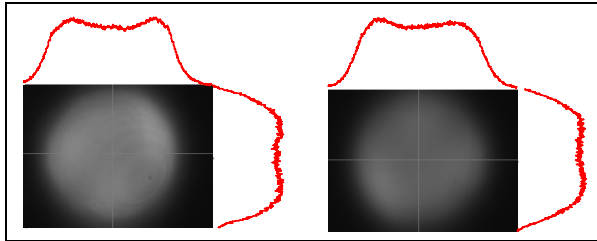


Figure 5: Output beam profile of the aspherical lens pair at 262 nm wavelength (left) and its relay image in a distance of approx. 1 m with (right).

CONCLUSION AND OUTLOOK

The suggested integration of a refractive beam-shaper into the optical beamline of the PITZ photothode laser has the potential to form a flat-top beam profile and simultaneously improve the energy efficiency of the complete beam-line. Consequently, the application of an appropriately designed beam shaping system can lead to a

significant reduction of the overall costs of the laser due to its reduced power requirements.

ACKNOWLEDGEMENT

This work is in part supported by the European Community, Sixth Framework Programme, Research Infrastructure Actions EUROFEL Design Study, contract number 011935. Further support comes from the German ministry of Education and Research (BMBF), contract number 05ES4 BR1/8.

REFERENCES

- [1] J. Bähr et al., "Upgrades of the laser Beam-Line at PITZ", Proc. FEL2005, JaCoW/eConf C0508213, p.110-113.
- [2] M.Krasilnikov, "Experimental Characterization and Numerical Simulation of the Electron Source at PITZ", ICAP2004, St. Petersburg.
- [3] M. Yun et al., "Transformation of Gaussian to uniform or annular beams by radial birefringent filters", Proc. of SPIE 5525 (2004), p.182-187.
- [4] "Laser beam shaping with only one element", OLE (October 2004), p. 18, <http://www.vct-ag.de>.
- [5] J.A. Hoffnagle and C.M. Jefferson, "Design and performance of a refractive optical system that converts a Gaussian to a flattop beam", Appl. Opt. 39 (2000), p.5488-5499.

Beam Dynamics Experiments and Analysis on CSR Effects at FLASH

Bolko Beutner, Winfried Decking, Martin Dohlus, Torsten Limberg
and Michael Röhrs,

Deutsches Elektronen-Synchrotron DESY, D-22603 Hamburg, Germany.

Abstract

The Free Electron Laser in Hamburg (FLASH) is a linac driven SASE-FEL in the vacuum-ultra-violet (VUV) wavelength range [1]. High peak currents are produced using magnetic bunch compressor chicanes. In these magnetic chicanes, the energy distribution along an electron bunch is changed by the emission of Coherent Synchrotron Radiation (CSR). Energy changes in dispersive sections lead to transverse displacements along the bunch. Measurements of CSR induced transverse displacements are presented and compared with simulations.

INTRODUCTION

The peak current of an electron bunch emitted by an rf gun is about 50-100 A. For SASE operation at FLASH, the necessary peak currents of 1-3 kA are reached using longitudinal bunch compression. A two stage bunch compression system with the magnetic chicanes BC2 and BC3 is employed (see Fig.1).

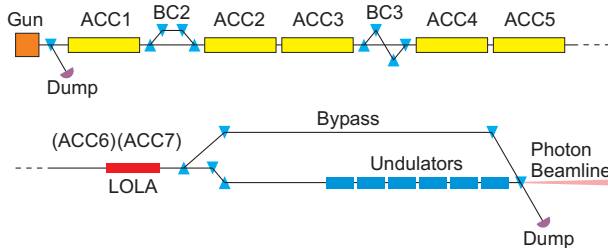


Figure 1: Sketch of FLASH. The blue triangles indicate dipole magnets, the yellow boxes TESLA acceleration modules.

A transverse deflecting rf-structure (LOLA) [2] is used to take "top view" pictures of the bunch - the projection into the longitudinal-horizontal plane. Thus, centroid shifts along the bunch, for instance caused by CSR fields, can be observed.

However, other forces like space charge cause transverse shifts of beam centroids as well. For an undisturbed measurement of CSR effects, space charge effects have to be reduced. To that purpose, we over-compress the bunch. The longitudinal energy correlation (chirp) introduced in the module ACC1 is chosen to reach minimum bunch length and a peak current beyond 2 kA towards the end of the second magnet in the BC2 chicane. The bunch will exit the chicane roughly with its incoming length of about 2 mm,

corresponding to about 50 A peak current. The integrated effect of space charge from the exit of BC2 to LOLA is then small compared to the centroid offsets caused by CSR.

MEASUREMENTS AND ANALYSIS

For our measurements, we vary the ACC1 phase and keep ACC2/3 on crest. The expected CSR effects are created during over-compression in BC2. Downstream, the transverse deflecting rf structure is passed at the zero-crossing phase. The particles are kicked transversely with a strength proportional to their longitudinal offset to the bunch center. The bunch is thus tilted and its longitudinal-transverse projection is observed on a screen.

Fig.2 shows a LOLA measurement. The red curve shows the longitudinal beam profile, the white dashed lines indicate the fwhm points.

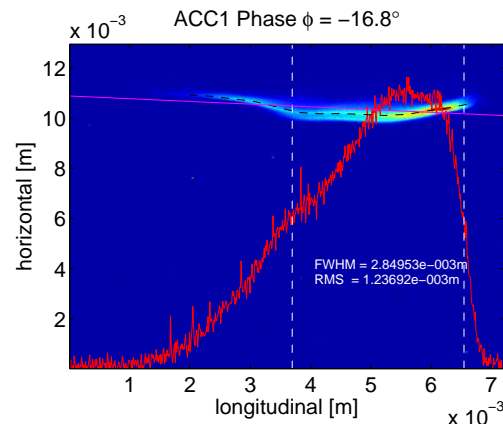


Figure 2: An example of a LOLA measurement. Longitudinal charge profile (red line), fwhm and rms bunch length are shown.

Fig.3 shows measured bunch length at LOLA as a function of the ACC1 phase as well as simulation results. The measured bunch length agrees well with the simulation downstream of BC3, as it should. The calculated bunch length downstream of BC2 (green line) is, for small phase offsets, longer, since the bunch is further compressed in BC3. At about 12 degrees, the bunch is fully compressed in BC2. Above 12 degrees, the bunch is over-compressed, the chirp changes its sign and the BC2 bunch length is shorter.

Fig.4 shows measured longitudinal-horizontal projections of the bunch for different compression scenarios. In the uppermost picture, the ACC1 phase is on crest, no com-

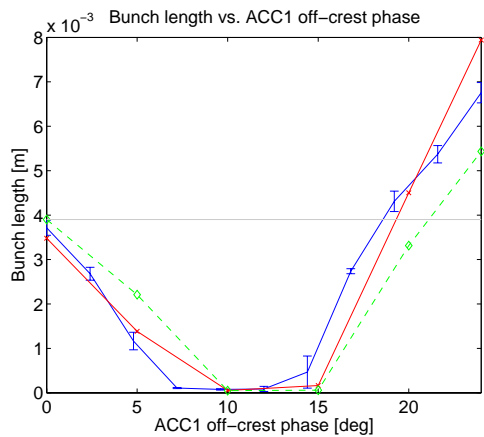


Figure 3: Measured fwhm bunch length at LOLA (blue line) are compared with simulations. Red line: calculated bunch length at LOLA. Green line: calculated bunch length after BC2.

pression occurs and the horizontal centroid positions line up straight. Close to full compression (middle picture), the beam is heavily distorted by CSR and space charge effects. This is understood and simulated [3], but would be very challenging as a starting point for quantitative CSR studies.

The bottom picture shows the over-compressed case, where the space charge effects are negligible and strong CSR occurs only in BC2. The beam centroids are still on a smooth line. Its shape and sag will be compared with simulations in the next paragraph.

Fig.5 reflects the bunch shape changes described above in plotting the peak to peak bunch centroid shift as a function of ACC1 phase offset.

Comparison with Simulations

Tracking calculations were done to simulate longitudinal-horizontal beam projections at LOLA. Beam transport through ACC1 was calculated with the space charge tracking code ASTRA [4]. After ACC1, wake fields are applied as a discrete effective kick [5]. The tracking code CSRTrack [6] is used to simulate CSR effects in BC2. The 1D projected model is used [7]. The long bunch length after BC2 in the over-compression case allows the simulation of the beam transport to LOLA by a first order matrix.

To compare the simulated longitudinal slice centroid positions with the measurements these data have to be extracted from the measured distributions. In a first step each distribution is divided into slices along the longitudinal axis. The horizontal charge profiles of these slices are then calculated. Gaussian fits are used to determine the center of each profile. An example for the resulting centroid curve is the dashed black line in Fig.2.

At big ACC1 phase offsets, the bunches start to be tilted

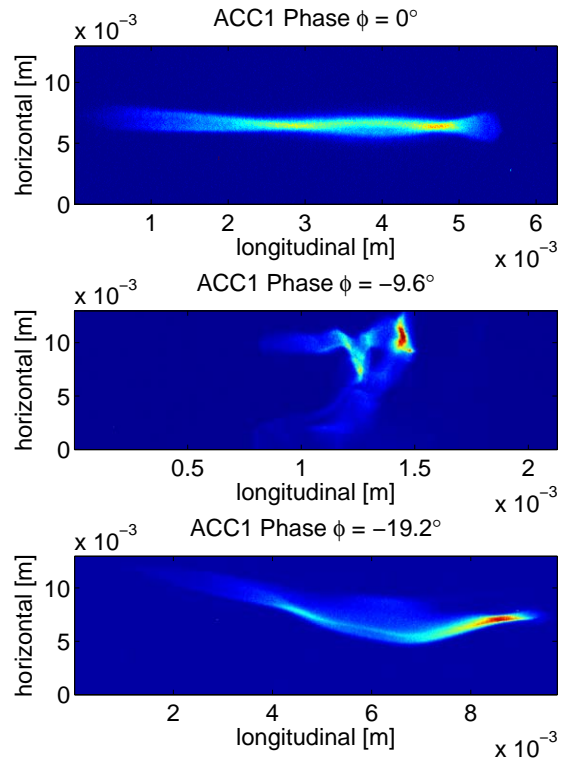


Figure 4: Measured top view for different ACC1 phase off-sets. Top: no compression. Middle: near full compression. Bottom: over-compression.

on the screen. The cause of this is under investigation. The linear correlation as indicated by the magenta line in Fig.2 is subtracted from the centroid curve.

For error analysis, a series of pictures is taken for each ACC1 phase setting. The different centroid curves are

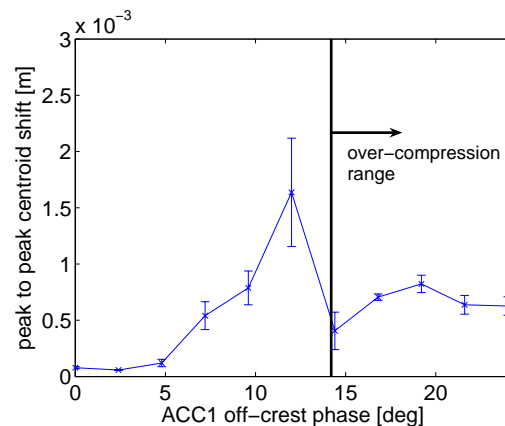


Figure 5: The peak to peak centroid shift along the bunch is plotted vs. the phase offset in ACC1. Phase range used for the experiment: 14 to 24 degrees.

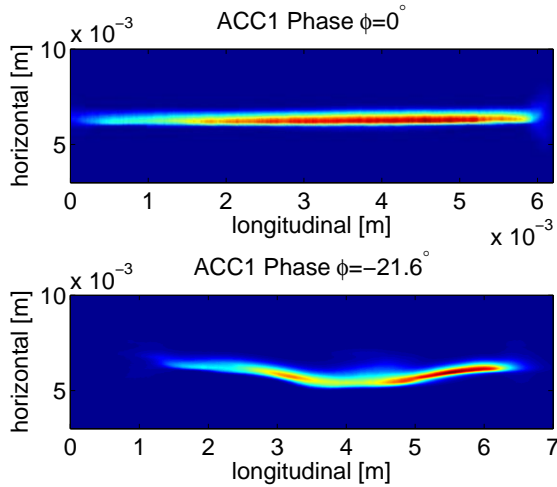


Figure 6: Simulated top view after BC2 for different ACC1 phase offsets. Top: no compression. Bottom: over-compression.

aligned to their individual centre of mass. The curves are then fitted with a polynomial and their mean value and rms spread are calculated for different longitudinal positions. In Fig. 7, these results are compared with the tracking calculations.

CONCLUSION AND OUTLOOK

CSR effects in the first bunch compressor chicane in FLASH were observed using the transverse deflecting rf-structure LOLA.

The offsets of the centers of the longitudinal bunch slices for different over-compression scenarios were measured and compared with simulation calculations.

Next steps in the experimental program are studies of slice emittance growth due to CSR effects and dependences on bunch charge and beam optics in the chicanes [8].

The observed beam tilt will be investigated to improve both SASE operation and CSR measurements.

REFERENCES

- [1] E. Schneidmiller and M. Yurkov: "Lasing at 13 nm of the SASE FEL at FLASH", this conference.
- [2] M. Röhrs et. al.: "Investigations of the Longitudinal Electron Bunch Structure at the FLASH Linac with a Transverse Deflecting RF-Waveguide", this conference.
- [3] M. Dohlus: "CSR Calculation for TTF-II", 2005, http://www.desy.de/xfel-beam/talks_a.html#dohlus.
- [4] K. Flöttmann: "ASTRA user manual", http://www.desy.de/mpyflo/Astra_dokumentation.
- [5] I. Zagorodnov: private communication.
- [6] M. Dohlus, T. Limberg: "CSRtrack: Faster Calculation of 3D CSR effects", FEL 2004, 2004.

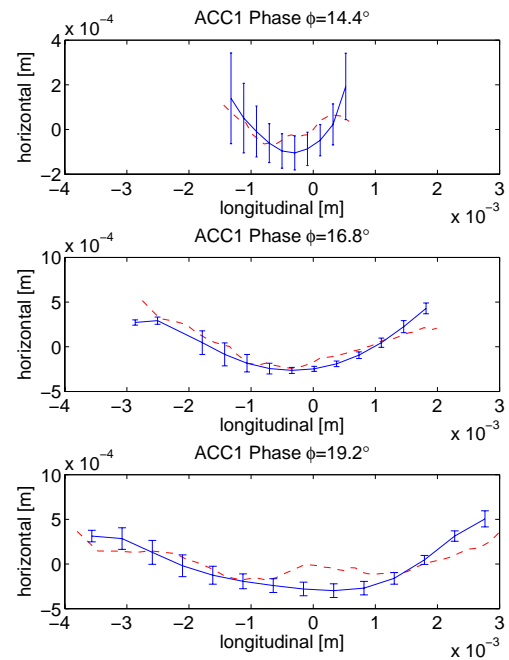


Figure 7: Experimental centroid curves are compared with simulated data. The blue lines represent the data taken with LOLA and the dashed red curves represent the results of simulations. Linear correlations are subtracted.

- [7] M. Dohlus: "Two Methods for the calculation of CSR Fields", TESLA-FEL-2003-05.
- [8] M. Dohlus, T. Limberg: "Impact of Optics on CSR-related Emittance Growth in Bunch Compressor Chicanes", PAC 2005, 2005.

FELO: A ONE-DIMENSIONAL TIME-DEPENDENT FEL OSCILLATOR CODE

B.W.J. McNeil, G.R.M. Robb, SUPA, Department of Physics, University of Strathclyde, Glasgow, UK
 D. Dunning and N.R. Thompson, ASTeC, CCLRC Daresbury Laboratory, UK.

Abstract

A one-dimensional, SDDS compliant time-dependent FEL oscillator code has been developed in Fortran 90. The code, FELO, solves universally-scaled FEL equations to simulate oscillator FELs operating from the low to high gain regime. The code can simulate start-up from shot noise, different electron pulse current distributions, the effects of cavity length detuning and temporal jitter between electron bunches. Cavity detuning curves for both the low-gain IR-FEL and the regenerative amplifier VUV-FEL of the 4th Generation Light Source (4GLS) proposal at Daresbury Laboratory are modelled. The code predictions for the VUV-FEL output are compared with simulations performed with the parallel implementation of Genesis 1.3 and are found to be in good agreement.

INTRODUCTION

Several computational codes are available to the FEL community to aid with the simulation and design of FEL amplifiers e.g. Genesis 1.3 [1]. The authors have developed a simulation package containing FEL simulation code and pre and post-processors that models a FEL with cavity feedback. The code, called FELO, solves a one-dimensional spatio-temporal set of equations which are able to model much of the physics relevant to such FELs. The design of two of the UK 4GLS project FELs were aided by FELO and examples from the 4GLS Conceptual Design Report [2] are presented.

THEORETICAL MODEL

The 1D equations governing the spatio-temporal evolution of the pulsed FEL interaction are well known and in the the universal scaling of [3, 4] may be written:

$$\frac{d\theta_j}{d\bar{z}} = p_j \quad (1)$$

$$\frac{dp_j}{d\bar{z}} = -(A(\bar{z}, \bar{z}_1) \exp(i\theta_j) + c.c.) \quad (2)$$

$$\left(\frac{\partial}{\partial \bar{z}} + \frac{\partial}{\partial \bar{z}_1} \right) A(\bar{z}, \bar{z}_1) = \chi(\bar{z}_1) b(\bar{z}, \bar{z}_1) \quad (3)$$

where $\theta_j = (k + k_u)z - \omega t_j$ is the phase of the j th electron with respect to the particular ponderomotive potential well in which it evolves and $p_j = (\gamma_j - \gamma_r) / \rho \gamma_r$ is its scaled energy, $b(\bar{z}, \bar{z}_1) \equiv \langle e^{-i\theta(\bar{z})} \rangle|_{\bar{z}_1}$ is the bunching factor and is the average over the electrons contained within the ponderomotive well centred at \bar{z}_1 at distance through

the interaction region \bar{z} . The weight factor $\chi(\bar{z}_1) = I(\bar{z} = 0, \bar{z}_1) / I_{pk}$ where $I(\bar{z} = 0, \bar{z}_1)$ describes the electron pulse current distribution of peak value I_{pk} at the entrance to the FEL interaction region and $A(\bar{z}, \bar{z}_1)$ is the scaled complex radiation field envelope with magnitude defined by the radiation and electron beam powers as $|A|^2 = P_{rad} / \rho P_{beam}$.

The scaled independent variables may be written [4]:

$$\bar{z} = \frac{z}{l_g} = 2\rho k_u z \quad (4)$$

$$\bar{z}_1 = \frac{z - c\bar{\beta}_z t}{l_g(1 - \bar{\beta}_z)} \quad (5)$$

where $l_g = \lambda_u / 4\pi\rho$ is the nominal gain length of the FEL interaction, the initial z-component of the mean electron velocity within the interaction region is $c\bar{\beta}_z = \langle v_{z0} \rangle$ and ρ is the fundamental FEL, or Pierce, parameter [3]. The latter may be written in practical units for a planar undulator as $\rho \approx 5.7 \times 10^{-3} \gamma_r^{-1} (I \bar{a}_u^2 \lambda_u^2 f_B^2 / \sigma_b^2)^{1/3}$ where f_B is the usual difference of Bessel function factor associated with planar undulators and σ_b is the RMS electron beam radius which for an electron beam of normalised emittance ϵ_n in a focussing channel of beta-function β is given by $\sigma_b = \sqrt{\epsilon_n \beta} / \gamma_r$.

For the case of small gain FELs typical to those encountered in high-Q cavity FELs, previous studies [5] have shown that the effects of emittance and energy spread, electron/radiation pulse slippage effects and the relative transverse overlap between electron beam and cavity modes may be accounted for in correction factors to the expressions for the FEL gain. A small signal gain coefficient was defined which in the universal scaling of the above equations may be written:

$$g_0 = \frac{\bar{z}^3}{\pi} \quad (6)$$

The maximum single pass gain is then approximated by the fitting formula:

$$G_{max} = g_0 F (0.85 + g_0 F (0.19 + 4.12 \times 10^{-3} g_0 F))$$

where the factor $F = F_{inh} F_f F_c$ is a product of correction factors that that respectively account for the effects of inhomogeneous broadening due to emittance and energy spread; a filling factor for the transverse overlap; and the effects of relative slippage between the radiation and electron pulses. The inhomogeneous broadening factor is given by:

$$F_{inh} = \frac{1}{(1 + 1.7\mu_z^2)(1 + \mu_\epsilon^2)} \quad (7)$$

where $\mu_\gamma = 4N_u\sigma_\gamma/\gamma$ and $\mu_\epsilon = 2N_u\epsilon_n\bar{a}_u/\lambda_u(1 + \bar{a}_u^2)$. The filling factor is given by:

$$F_f = \frac{1}{1 + \bar{w}^2/4\sigma_b^2} \quad (8)$$

where \bar{w} is the mean optical mode size, defined by the radius at which the intensity drops to $1/e^2$ of its on-axis value, averaged over the length of the undulator.

Noting from (4 & 6) that $g_0 \propto \rho^3$ and that the expression for G_{max} contains only factors g_0F allows the inhomogeneous fitting factor F_{inh} and that for the filling factor F_f to be incorporated into the definition of an effective FEL parameter

$$\rho_{eff} \equiv (F_{inh}F_f)^{1/3} \rho \quad (9)$$

to replace that of ρ in the definitions and working equations of (2..5). Note that the factor that accounts for slippage effects, F_c , is not used in the definition of ρ_{eff} as slippage is directly modelled by the partial derivatives of the wave equation (3). It is interesting to note that from the definitions of g_0 and the filling factor F_f that the product g_0F_f , can be expressed as

$$g_0F_f \propto \frac{1}{\sigma_b^2 + \bar{w}^2/4}.$$

Hence, if the electron beam radius $\sigma_b \ll \bar{w}$, as for example in a long wavelength FEL, the gain is independent of the electron beam radius.

When used with the ρ_{eff} scaling the above equations (2..3) will then estimate the effects of inhomogeneous broadening due to electron energy spread and emittance, and also the effects of transverse electron-radiation coupling, without the need for increased number of computational particles required in 2-D and 3-D models. The FELO code which uses these equations is therefore significantly faster to run than these codes and yet, as will be shown in the following work, gives results which are in good agreement with 3-D simulations.

COMPUTATIONAL MODEL

The working equations (2..3) are solved using the method of characteristics as described in [6] using a code written in Fortran-90. The method of characteristic allows the resultant equations to be integrated via a 4th order Runge-Kutte method with slippage effects between electrons and radiation modelled using simple array shifts. Because the effects of electron energy spread, emittance and transverse coupling are simply accounted for in the modified FEL parameter ρ_{eff} , no electron macroparticle distribution in the scaled energy parameter p is required and $p_j = 0 \forall j$ to describe a resonant FEL interaction. Thus, only a relatively small number of macroparticles are required per ponderomotive well (typically ~ 100) distributed uniformly in θ . The option to include shot-noise effects is included using the method of [7]. Although other shot-noise models more correctly describe the physics [8],

the method of [7] is sufficient here. The FEL cavity length can be varied to allow investigation of cavity detuning effects and the effects of a random temporal jitter in the electron arrival into the cavity can be simulated by introducing a small random variation about the mean cavity length [9].

The FELO source code is written in Fortran-90 and is freely available [10]. The code has been tested using the open-source g95 compiler [11]. A parameter spreadsheet is available to assist the user in preparing the relatively simple input file for the code. Output from the code is written into SDDS formatted files [12]. Post-processing and plotting routines are provided using both SDDS toolkit functions in Tcl script files and MATLAB and are described in more detail in the user-manual provided for the code.

EXAMPLE SIMULATIONS

The FELO code has been used in the design of two of the three FELs of the UK 4GLS project [2]. Both the IR-FEL and the VUV-FEL are cavity FELs. The IR-FEL is designed to operate in the wavelength range 2.5-200 μm . It has a relatively low gain and needs a relatively high Q cavity to lase. The VUV-FEL is designed to generate photon energies of 3-10 eV and will operate in the intermediate gain regime ($\bar{z} \sim 4$) where the FEL interaction evolves exponentially but cannot achieve saturation without seeding in a single pass. Saturation is made possible by introducing a small amount of feedback via a low Q cavity [13]. This also has the advantage of cleaning up the spectral quality of the output over that of SASE [14]. FELO simulations for both of these designs are presented and, in the case of the VUV-FEL, comparison is made with the results of the 3-D code Genesis 1.3 [1]. No such comparison is available for the IR-FEL due to the large number of cavity round-trips required to achieve saturation and the prohibitively long simulation time this would require.

4GLS IR-FEL

The IR-FEL simulations presented are for 2.5 μm operation of the IR-FEL. From the detailed specifications of [2], with an electron energy of 60 MeV, charge 200 pC and RMS duration of 2 ps the IR-FEL operates at 2.5 μm . The undulator has 50 periods, so that the approximate efficiency $\eta \approx 1/4N_u$ gives a peak power output at saturation of $P_{pk} \approx 12$ MW. A more detailed estimate of the efficiency that accounts for passive cavity losses due to mirror reflectivity and all diffraction losses has been derived and reduces the efficiency from that above [2]. Including these effects gives the optimised power estimate for operation of the IR-FEL from 2.5-25 μm as shown in Fig. 1. A FELO simulation at 2.5 μm operation with cavity length detuning of $\delta_c = 9 \mu\text{m}$, so that the output pulse width is close to its maximum, gives good agreement with these estimates as shown in Fig. 2. (Note that positive values of δ_c correspond to a shortened cavity length.) Fig. 3 plots the results of FELO simulations for both the peak power and FWHM

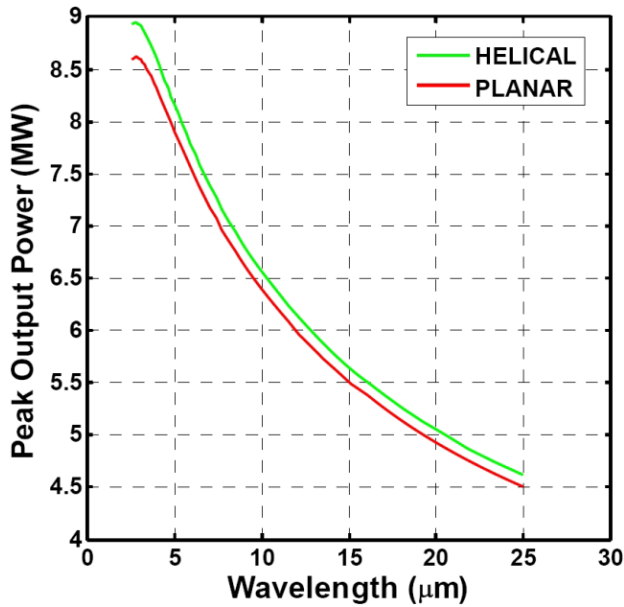


Figure 1: The peak output power for the 4GLS IR-FEL, assuming 2 ps RMS electron pulses and an outcoupling fraction optimised for every wavelength to give the maximum output power. Calculations for helical and planar mode are shown in green and red respectively.

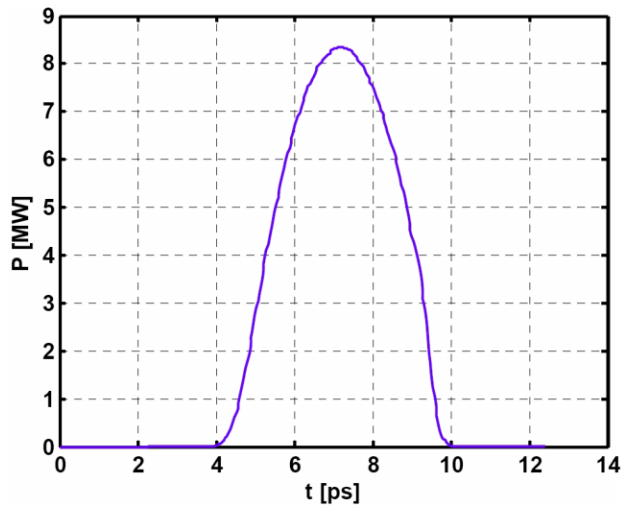


Figure 2: 4GLS IR-FEL pulse power as a function of time for 2.5 μm operation with a cavity length detuning of 9 μm.

pulse width for 2.5 μm operation as a function of cavity detuning δ_c . As cavity resonance is approached at $\delta_c = 0$ it is seen that the peak output power increases and pulse width decreases, typical of superradiant behaviour in an FEL cavity [15].

4GLS VUV-FEL

FELO simulations have also been used in the conceptual design of the 4GLS VUV-FEL. This FEL operates with an intermediate gain of $\bar{z} \sim 4$ and uses a low Q cavity.

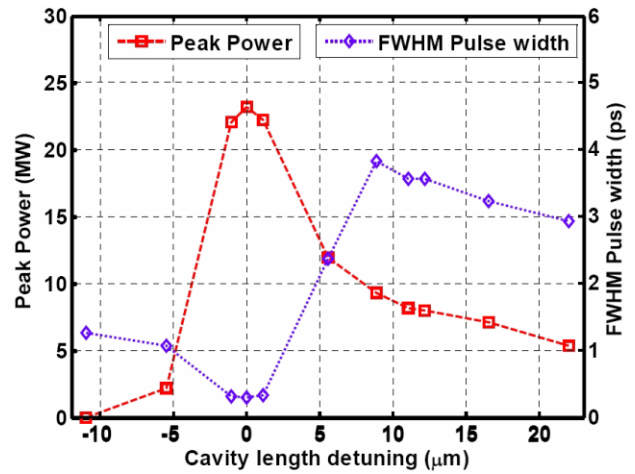


Figure 3: Peak power and FWHM pulse width as a function of cavity length detuning, for the 4GLS IR-FEL at 2.5 μm with 2 ps electron bunches.

Saturation then occurs after only a few cavity passes, typically ~ 10 , which allows multi-pass simulation to saturation using the 3-D code Genesis. For 10 eV operation in a planar undulator, the VUV-FEL conceptual design uses a 600 MeV, 300A peak current electron beam and gives an FEL parameter of $\rho \approx 1.5 \times 10^{-3}$. Although utilising cavity feedback, the VUV-FEL still saturates as a high-gain FEL [13] so that the efficiency is $\eta \approx \rho$. Hence, the saturated power can be approximated as $P_{sat} \approx \rho P_{beam} \approx 270$ MW. Fig. 4 plots the results of FELO simulations for both the peak power and FWHM pulse width for 10 eV photon energy operation as a function of cavity detuning δ_c . There are clear similarities with the IR-FEL cavity detuning curve of Fig. 3. As with the IR-FEL, assuming the greatest pulse width approximates most closely to the steady-state, the saturated power for cavity length detuning of $\delta_c \approx 18 \mu\text{m}$ agrees well with the saturated power estimate of ≈ 270 MW of above. The plot of Fig. 5 shows a comparison of the pulse power as the VUV-FEL pulse energy saturates for the case of a FELO (blue) and Genesis (red) simulation for a cavity detuning of 12 μm. The number of cavity passes for the Genesis simulation was 8 while that for the FELO was 30. Although the FELO simulation approached pulse energy saturation after 8 cavity passes, the shape of the pulse power underwent a transition from a narrower, higher peak power pulse to that shown. This accounts for the higher peak power and narrower pulse width of Fig. 4 where $\tau_{FWHM} \approx 65$ fs $\Rightarrow s \approx 20 \mu\text{m}$ in the units of Fig. 5. This effect of higher peak power and narrower pulse width of the FELO simulation appears to be a transitory superradiant phase. It is not thought that the Genesis simulations show this behaviour, although this will need to be investigated further. As cavity resonance is approached, the radiation pulse width shortens to approximately an order of magnitude less than the electron pulse width of 250 fs FWHM (75 μm). Also, pulse

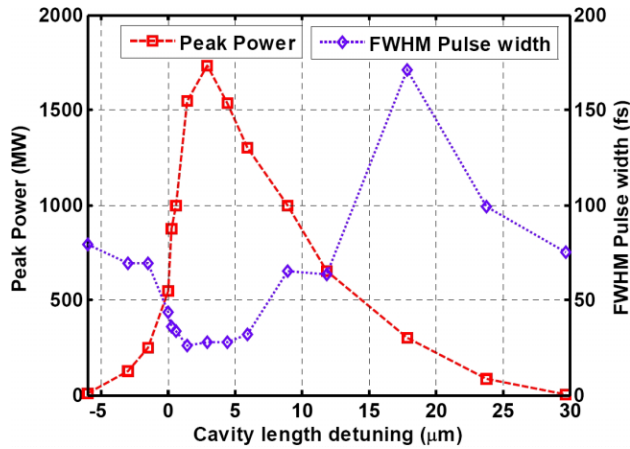


Figure 4: Peak power (red) and FWHM pulse width (blue) as a function of VUV-FEL cavity detuning. The parameters are for 10 eV photon output.

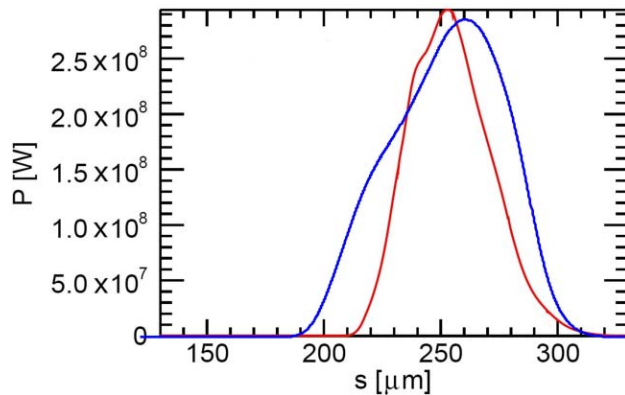


Figure 5: Comparison between FELO radiation power output pulse (blue) with that of a Genesis simulation (red) approaching saturation of the output energy. The parameters are for 10 eV photon output.

peak powers are significantly greater than the predicted by the steady-state simulations [2]. A plot of the shape of the pulse output close to cavity resonance is shown in Fig. 6. This pulse shape is typical of superradiant radiation with a narrow, high peak power spike followed by secondary pulses or ringing [15].

CONCLUSIONS

The FELO code package has been developed to allow reasonably quick and accurate simulations of cavity FELs operating from the low to high gain. The package has been used successfully in the development of the design of two cavity FELs for the UK 4GLS project. Some of these simulation results were presented. The code including manual is freely available for general use [10].

REFERENCES

- [1] S. Reiche, Nucl. Inst. and Meth. A **429**, 243 (1999)

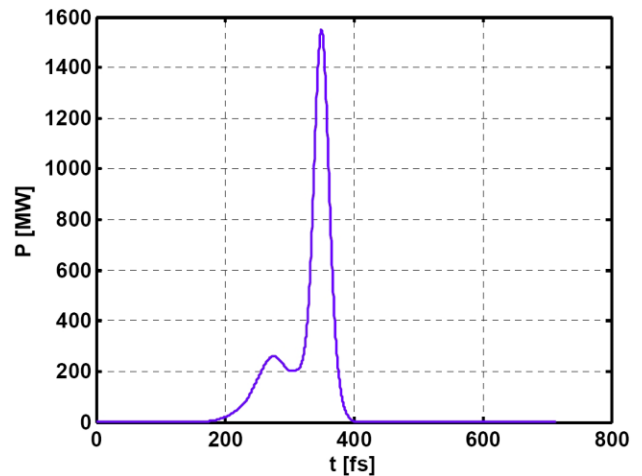


Figure 6: FELO simulation showing the 10 eV radiation power at saturation as a function of time for near-zero cavity detuning. The pulse shape demonstrates a spiking behaviour typical to FEL superradiance.

- [2] *4GLS Conceptual Design Report*, Council for the Central Laboratory of the Research Councils, UK, <http://www.4gls.ac.uk/documents.htm#CDR> (2006)
- [3] R. Bonifacio, C. Pellegrini and L.M. Narducci, *Opt. Commun.* **50**, 373 (1984)
- [4] R. Bonifacio and B.W.J. M^cNeil, *Nucl. Instrum. Methods A* **272**, 280 (1988)
- [5] F. Ciocci, A. Torre, G. Dattoli and A. Renieri, *Insertion Devices for Synchrotron Radiation and Free Electron Lasers*, World Scientific Publishing, Singapore (2000)
- [6] R. Bonifacio, B.W.J. M^cNeil and P. Pierini, *Phys. Rev. A* **40**, 4467 (1989)
- [7] C. Penman and B.W. J. M^cNeil, *Opt. Commun.* **90**, 82 (1992)
- [8] B.W.J. M^cNeil, M.W. Poole, and G.R.M. Robb, *Phys. Rev. ST Accel. Beams* **6**, 070701 (2003)
- [9] D. Dunning et al., *First Tolerance Studies for the 4GLS FEL Sources*, *ibid.*
- [10] Currently available from http://www.astec.ac.uk/id_mag/ID-Mag_Software.htm
- [11] Currently available from <http://www.g95.org/>
- [12] M. Borland, L. Emery, H. Shang and R. Soliday, *Proceedings of the IEEE 2003 Particle Accelerator Conference 2003*, Portland, Oregon
- [13] B.W.J. M^cNeil, *IEEE Journal of Quantum Electronics* **26**, 1124 (1990)
- [14] N.R. Thompson, B.W.J. M^cNeil and M.W. Poole, *A VUV-FEL for 4GLS: Design Concept and Simulation Results*, *Proceedings of the 27th International Free Electron Laser Conference*, Stanford (2005)
- [15] D.A. Jaroszynski et al., *Phys. Rev. Lett.* **78**, 1699 (1997)

THE CONCEPTUAL DESIGN OF THE 4GLS XUV-FEL

B.W.J. McNeil, SUPA, Department of Physics, University of Strathclyde, Glasgow, UK

N.R. Thompson, ASTeC, CCLRC Daresbury Laboratory, UK

B. Sheehy, Sheehy Scientific Consulting, New York, USA.

Abstract

The Conceptual Design Report for the 4th Generation Light Source (4GLS) at Daresbury Laboratory in the UK was published in Spring 2006 [1]. A key component of the proposal is an XUV-FEL amplifier directly seeded by a High Harmonic source and operating in the photon energy range 8-100eV. Numerical modelling shows the FEL may generate 50fs (FWHM) pulses of variably-polarised, temporally-coherent radiation with peak powers in the range 2-8 GW.

INTRODUCTION

Synchronised free-electron laser (FEL) sources which operate in the XUV, VUV and IR regions of the spectrum are fundamental components of the 4GLS design. These sources will deliver ultra-short pulses of temporally coherent photons with peak brightness at least 10^8 greater than that available from the best 3rd-generation light sources. 4GLS is intended to be a beyond state-of-the-art facility that must operate over extended periods, generating stable, synchronous and reproducible radiation pulses over the wide spectral range to end-user stations. In the conceptual design of 4GLS, therefore, the aim has been to create a robust design that does not overly stretch the specification of its individual components. This mildly cautious approach should minimise the risk in proceeding to the future design phase and enable further, more advanced, designs to be incorporated as technological progress permits. Here details mainly relating to the choice of undulator and electron focussing specifications and their relation to the FEL output are presented for the conceptual design of the XUV-FEL covering the 8-10eV photon energy range of the spectrum. The effects of FEL seeding by High Harmonic pulses are discussed in [2, 3] and the temporal seed/electron pulse offset due to jitter is discussed in [4].

GENERAL SPECIFICATION

The XUV-FEL baseline design will generate short, tunable, high-brightness pulses of 8-100 eV photons from an undulator system directly seeded by an external laser source. The radiation output will have good temporal and transverse coherence and also have variable polarisation. These specifications are expected to satisfy a wide range of current user requirements and also open up many new areas of science for exploration. It is also possible to utilise the exhaust electrons of the XUV-FEL in a spontaneous-spent-beam undulator source, before the electron beam is

dumped. The radiation from this source is then guaranteed to be synchronous with the XUV-FEL output for pump-probe type experiments. A schematic of the conceptual design for the 4GLS XUV-FEL is given in [3] of these conference proceedings.

Photon energy tuning in the XUV-FEL will be achieved by a combination of both undulator gap tuning and energy tuning of the electron bunches between 750 and 950 MeV. The electron bunches are assumed to have a rep-rate of 1-10 kHz, to be Gaussian of width $\sigma_t = 266$ fs and total charge of 1 nC giving a peak current of 1.5 kA, and with normalised emittance $\epsilon_n = 2$ mm mrad and fractional RMS energy spread of 0.1%. The FEL undulator will consist of a lattice of individual undulator modules allowing electron beam focusing elements and diagnostics to be placed in between. The final undulator modules of the FEL will be of APPLE-II design that will enable the generation of variable elliptically polarised radiation. Existing HHG laser systems can provide seed energies of 10 - 100 nJ with pulse widths of 30 fs FWHM over the photon energy range [2, 3]. The quality of XUV-FEL output can be expected to be similar to that of the input seed pulse which has a high degree of both spatial and temporal coherence [5]. The amplified pulse widths will also be only slightly longer than the seed pulse.

UNDULATOR AND FOCUSSING LATTICE

The design for the XUV-FEL undulator consists of a lattice of undulator modules containing both planar and variable polarisation undulator modules. For the planar undulators a relatively simple pure permanent magnet (PPM) was chosen and an APPLE-II design was chosen for the variable polarisation undulators. Each type of module will have a fixed period and a variable magnetic gap, g , that allows tuning of the RMS undulator parameter \bar{a}_u via the undulator magnetic field. A minimum undulator magnetic gap is assumed for the design of both planar and variable undulators. Note that the gap between the vacuum vessel walls will be $(g - 3)$ mm, the 3 mm reduction from the magnetic gap being the estimated thickness of the vacuum vessel walls and the clearance between magnets and vacuum vessel. A schematic giving further detail of the undulator lattice and incorporating BPMs, phase matching devices and the focussing quadrupoles is shown in Fig. 1. The variable polarisation undulator sections, VU1..VU5, ensure that variably polarised photons may be generated across the full design spectrum. In practice, operation at higher photon energies will require a longer undulator

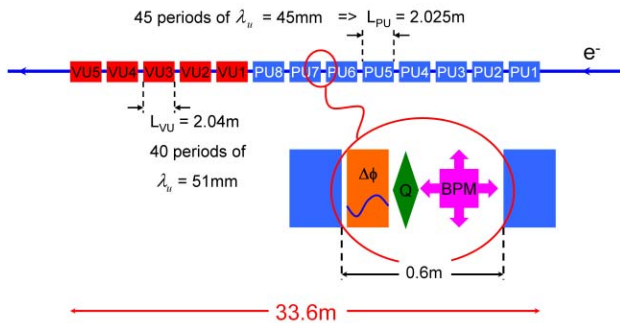


Figure 1: Schematic of the modular undulator system of the XUV-FEL. Undulator modules PU1..8 (blue) are planar undulators; VU1..5 (red) are variable polarisation undulators. The gap between undulator sections may contain a beam position monitor, quadrupole and radiation/electron phase matching unit.

length to achieve saturation. The effective undulator length may be varied by opening the magnetic gaps of individual undulator modules to their maximum. Those modules that have maximum magnetic gap generate only small on-axis magnetic fields and are effectively switched off for the purpose of the FEL interaction. For example, when operating for 100eV photon energy generation all undulator modules PU1..VU5 would be functional to achieve saturation, whereas for 50 eV operation only modules PU5..VU5 would need to be functional to achieve saturation, with PU1..PU4 gaps fully opened. This method of operation should allow a tapered vacuum vessel to be used along the undulator modules which will assist with reducing diffraction effects of HHG seed injection at lower photon energies [1, 3]. The minimum undulator parameter due to undulator gap tuning is taken to be $\bar{a}_u \approx 1$ to ensure sufficient FEL coupling. With this constraint then for a beam energy of 950 MeV the maximum planar undulator period that can achieve 100 eV FEL resonance is $\lambda_u \approx 45$ mm with a gap of $g \approx 28$ mm. At the lower beam energy of 750 MeV and for $\lambda_u \approx 45$ mm, the resonant photon energy is ≈ 10 eV for the minimum magnetic gap of $g \approx 10$ mm. The period of $\lambda_u \approx 45$ mm is then the optimum for the beam energy, magnetic gap and photon tuning range. A similar analysis for the variable polarisation APPLE-II undulators gives them an optimum period $\lambda_u \approx 51$ mm

A FODO focussing lattice has been chosen for the conceptual design. Other systems based upon quadrupole doublet and triplet focussing were investigated [5] and rejected. Although these latter designs allow longer, and therefore fewer, undulator modules of up to 4-5 m in length to be used, the quadrupole field strengths must be significantly greater by a factor of 3-4 than those required for a FODO lattice distributed between more modules. Tighter quadrupole alignment tolerances would therefore be required for the doublet and triplet positioning [6]. Monitoring of the electron beam transverse position, critical to the FEL interaction, would also be limited as would the

ability to step-vary the full undulator length by opening the individual module gaps. For these reasons a simpler FODO focussing lattice of module length ≈ 2 m is the chosen design option.

In order to investigate the effect of β -function variation due to the discrete focussing quadrupoles of the FODO lattice, the 3-D code Genesis 1.3 [7] was used to determine both the saturation length L_{sat} and power P_{sat} as a function of average β -function. This was carried out for a planar undulator system of module length ≈ 2 m. The respective results are shown in Fig. 2. It is seen that $\beta \approx 3.5$

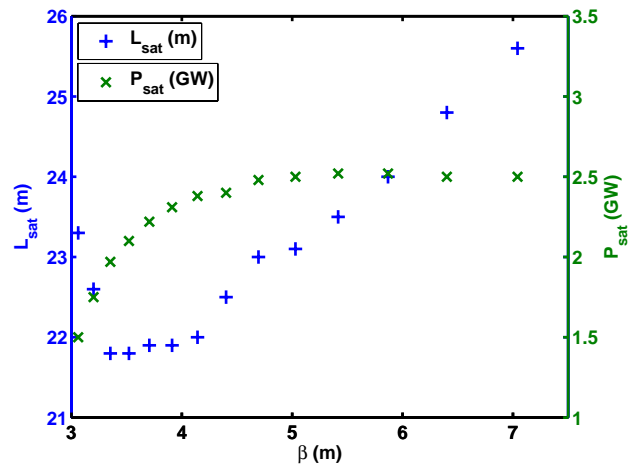


Figure 2: Genesis simulation of the saturation length, L_{sat} , and power, P_{sat} , as a function of the β -function in a FODO lattice for 100 eV operation.

m minimises the saturation length whereas $\beta \approx 5.5$ m maximises the output power. The nominal value of the β -function is chosen to be that which gives the maximum output power: $\beta = 5.5$ m. This is motivated by the fact that the planar modules PU1-PU8 produce a seed pulse (and pre-bunched beam) which will be amplified to saturation in the APPLE-II modules VU1-VU5, so maximising the power of the seed into the VU modules reduces the required length of the more technologically challenging APPLE-II modules. For the parameters used here a β -function of 5.5 m is satisfied by quadrupoles of magnetic length 0.09 m and of strength =13 T/m. The RMS electron beam radius may be calculated as $\sigma_b = \sqrt{\epsilon_n \beta / \gamma} = 77 \mu\text{m}$ for beam energy 950 MeV and the design normalised emittance $\epsilon_n = 2$ mm mrad.

UNDULATOR MODULE & GAP LENGTH

The modular construction of the combined undulator and FODO focussing lattice requires choice of the length of each undulator module, L_{PU} for planar and L_{VU} for variable undulators, and L_{gap} the spacing between modules. The FEL performance has a functional dependence on these parameters so optimisation is needed. The energy dispersion induced into the electron beam by the FEL interaction, and the natural homogeneous energy spread, are trans-

formed into a spatial dispersion in proportion to the gap between undulator sections, L_{gap} which may disrupt the FEL bunching process. Furthermore, it is seen from Fig. 1 that the undulator module length and gap define the FODO focussing lattice period, $\lambda_{FODO} = 2(L_{PU} + L_{gap})$. In a FODO lattice, the β -function varies about its mean value by $\pm\lambda_{FODO}/2$ so affecting the electron beam radius via the relation above for σ_b . Thus if λ_{FODO} is too large (as determined principally by the module length) the electron beam radius variation may also adversely affect the FEL coupling. Alignment of the electron beam through the undulators is of critical importance to maintain the electron-radiation coupling. This requires both beam alignment between undulator modules and careful construction of the undulators to ensure that the beam wander due to magnetic field errors and pole alignment are minimised. Ideally, beam wander off the optical axis should be no greater than 20% of the electron/radiation beam radius.

Genesis 3-D simulations were carried out to simulate the FEL operating at 100 eV. Only the planar undulator modules were used with the nominal design parameters. Fig. 3 plots the results of Genesis steady-state simulations for the saturation power, P_{sat} , as a function of the gap between undulator modules, L_{gap} , for three different module lengths, L_{PU} . It is seen that the saturation power is nearly independent

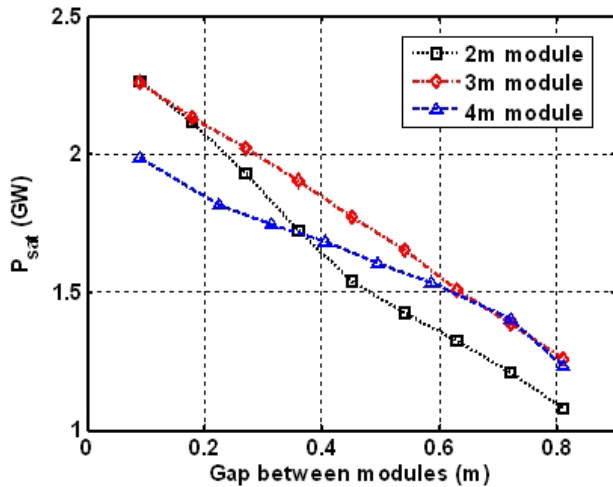


Figure 3: Simulation of the saturation power, P_{sat} , for XUV-FEL planar undulator operation at 100 eV as a function of the gap between undulator modules. The results are plotted for three module lengths: $L_{PU}=2, 3$ and 4 m.

of the undulator module length and decreases almost linearly with the undulator gap. A gap of $L_{gap} = 0.6$ m is chosen for the design specification. This is the estimated minimum length into which the quadrupoles, BPMs and phase matching units can fit.

Simulations of the saturation length L_{sat} of a seeded amplifier interaction, starting from a seed power of 30 kW at 100 eV, are shown in Fig. 4. For each length of undulator module L_{sat} is seen to increase with the module gap. However, there is a significant difference between each un-

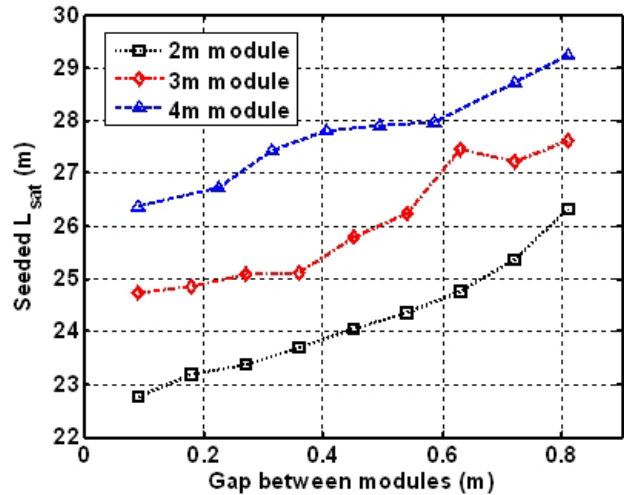


Figure 4: Simulation of the saturation length L_{sat} for XUV-FEL planar undulator operation at 100 eV as a function of the undulator module gap, L_{gap} for three module lengths: $L_{PU}=2, 3$ and 4 m. (The saturation length is the undulator length only: gaps between modules are not included.

dulator module length, with the 4 m module having a saturation length longer than that of the 2 m module. This is attributed to the greater variation in the β -function for the longer module as discussed above. For this reason, and the greater opportunities for beam monitoring and control afforded by the greater number of undulator modules, the module lengths for the design specification are chosen to be $L_{VU} \approx L_{PU} \approx 2$ m. Hence, for the baseline design for 8 - 100 eV operation, each planar PPM undulator will have 45 periods of 45 mm giving a module length $L_{PU} = 2.025$ m and each variable undulator APPLE-II undulator will have 40 periods of 51 mm giving a length $L_{VU} = 2.04$ m.

3D STEADY-STATE SIMULATIONS

The design choices and optimisations discussed may be summarised by plotting both the saturation powers and lengths across the operating spectrum of the XUV-FEL. It has been assumed that the XUV-FEL is operating in an amplifier mode with a seed power equal to 10% of the peak power currently available from seed pulses as described in [2, 3]. The reduction in seed power by a factor of approximately ten conservatively estimates the power available following transmission and focussing losses from the seed laser into the undulator. The seed is focussed to the centre of the first in-use undulator module with Rayleigh length equal to half the module length. For seed pulses of 30 fs FWHM and of energy 3 nJ for 10 to 40 eV photons and 1 nJ for 40 to 100 eV give corresponding approximate peak powers of 100 kW and 30 kW. The saturation power over the operational spectral range as calculated by both Genesis (in steady state mode) and Xie formulae [8] are shown

in Fig. 5. Both planar and helical mode results are shown.

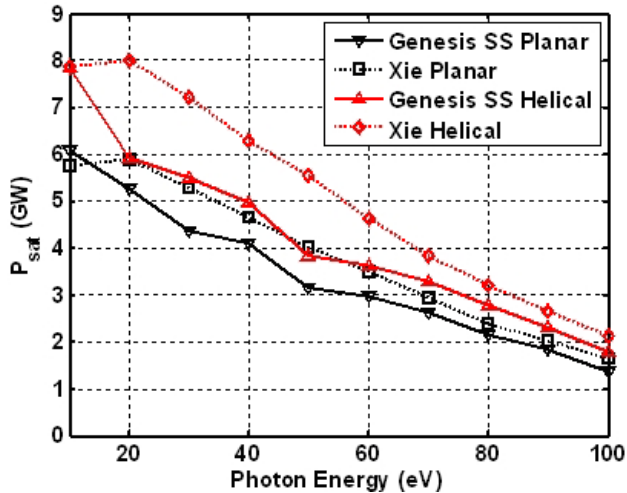


Figure 5: Summary of saturation power estimates for the XUV-FEL across its spectral operating range. 3-D Genesis steady-state (SS) simulations and the Xie formulae are in excellent agreement.

Note that the Xie design formulae cannot take into account mixed planar/helical undulators, so the 'Xie Helical' estimates assume a helical-only undulator for the equivalent length of the planar-helical combination. The Xie estimates also do not include the effects of gaps between undulator modules. These differences account for the small discrepancy of the 'Xie Helical' estimates from the other simulations, in the slightly higher saturation power estimation. Notwithstanding this, the 3-D numerical and Xie estimates are in excellent agreement. In Fig. 6, the length of undulator required for saturation is plotted as a function of photon energy. Note that the gaps between undulator modules are not included in this length and must be added on to obtain the total length of the combined undulator-focussing lattice.

CONCLUSIONS

A robust conceptual design for the XUV-FEL has been developed. Established FEL theory and state-of-the-art simulation codes predict this free-electron laser will generate 8-100 eV photon energies at giga-watt power levels and, as shown elsewhere [3], in pulses of duration 40-60 fs FWHM. The pulses will have very good temporal and spatial coherence with time-bandwidth products close to the Fourier transform limit for a Gaussian pulse [3, 5]. Unlike the SASE mode of operation, which effectively self-starts from intrinsic noise, the FEL interaction here is truly acting as a simple, bandwidth limited amplifier. So long as the radiation input seed pulses have sufficient spectral purity, the output radiation is very nearly a simple amplified version of the input. Recent advances in the High Harmonic seed sources of choice ensure that the seed requirements for the XUV-FEL already exist [2, 3]. Research in the next de-

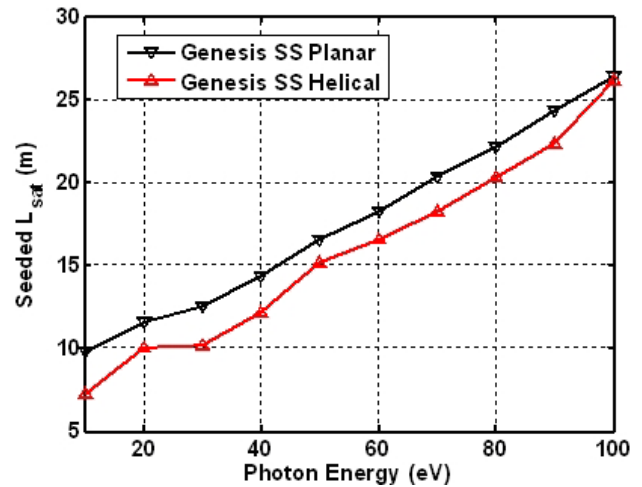


Figure 6: Summary of steady-state 3-D Genesis simulation estimates for the XUV-FEL undulator saturation length across the spectral operating range.

sign phase will require full start-to-end simulations from the electron gun through to the end of the undulator. This will allow the modelling of the FEL interaction with more realistic electron pulses than that used here which assume a Gaussian variation of most variables. Investigation of tolerances, for example in quadrupole position and undulator field errors, will also be required, as will a more detailed study of the effects of relative electron-seed pulse jitter than the initial results presented at this conference [4]. Extension of the operational range down to 6eV photons may be possible and will be investigated further in the next design phase.

REFERENCES

- [1] *4GLS Conceptual Design Report*, Council for the Central Laboratory of the Research Councils, UK, <http://www.4gls.ac.uk/documents.htm#CDR> (2006)
- [2] B. Sheehy *et al.*, *High harmonic seeding and the 4GLS XUV-FEL*, 37th ICFA Advanced Beam Dynamics Workshop on Future Light Sources, Hamburg, Germany (2006)
- [3] B.W.J. McNeil, *The Use of HHG at 4GLS*, (*ibid.*) (2006)
- [4] D. Dunning, *First Tolerance Studies for the 4GLS FEL Sources*, (*ibid.*) (2006)
- [5] B.W.J. McNeil *et al.*, *Design considerations for the 4GLS XUV-FEL*, Proceedings of the 27th International Free Electron Laser Conference, Stanford, USA (2005)
- [6] B. Faatz and J. Pflger, *Nucl. Inst. Meth. Phys. Res. A*, **475**, 603 (2001)
- [7] S. Reiche, *Nucl. Inst. Meth. Phys. Res. A*, **429**, 243, (1999)
- [8] Ming Xie, *Proc. Of 1995 Part. Accel. Conf.*, 183 (1996)

OPTIMIZATION OF PARAMETERS OF SMITH-PURCELL BWO *

Vinit Kumar[†], RRCAT, Indore, M.P. 452013, INDIA
 Kwang-Je Kim, ANL, Argonne, IL 60439, USA.

Abstract

We study the dependence of start current in Smith-Purcell backward wave oscillator (SP-BWO) on grating parameters and electron beam parameters. The attenuation due to finite conductivity of the grating material is taken into account and three-dimensional effects are included in an approximate way in the analysis. We find that the start current can be significantly reduced by optimizing the grating parameters.

INTRODUCTION

The Smith-Purcell free-electron laser (FEL) is a backward wave oscillator (BWO) for low energy electron beam [1,2]. In a BWO, like any oscillator system, the electron beam current needs to be higher than a threshold value, known as the start current, in order to produce coherent electromagnetic oscillation. In a recent paper [2], we have performed a calculation of start current for the case of sheet electron beam skimming over the grating surface in a SP-BWO. The attenuation of the backward wave due to finite conductivity of the grating was not taken into account in this calculation. The issue of attenuation becomes important while optimizing the parameters of SP-BWO. Recently, Andrews et al. [3] have discussed the calculation of attenuation coefficient for the backward wave supported by the grating. They have also studied the dependence of gain and attenuation in SP-BWO as a function of group velocity as the energy of the co-propagating electron beam is varied, keeping the grating parameter fixed. In this way, they have calculated the net gain. However, gain does not have a straightforward meaning in a BWO. In this paper, we therefore present a calculation of start current taking into account the effect due to attenuation. We use this calculation to study the dependence of start current on grating parameters as well as electron beam parameters.

START CURRENT CALCULATION

In a SP-BWO, the electron beam interacts with the co-propagating surface electromagnetic mode supported by the grating. The co-propagating surface mode has a group velocity in the direction opposite to the electron beam. We consider a sheet electron beam in the (y, z) plane propagating at a height b from the grating top surface along the z -axis. The grating grooves are in the y -direction and perpendicular to the grating is in the x -direction. Due to the

finite conductivity of the material of the grating, the surface electromagnetic mode suffers attenuation. The attenuation coefficient can be calculated as per the prescription given by Andrews et al. in Ref. 3. Attenuation occurs in the direction in which the energy is flowing. Here, the phase velocity of the resonant surface mode is along the positive z -axis and the group velocity v_g is along the negative z -axis. Let the longitudinal component of the the electric field of the backward wave be given by $E(z, t) \exp(ik_0z - i\omega t)$. Including attenuation in the analysis, the equation for the evolution of the amplitude $E(z, t)$ of the backward wave described in Ref. 2 gets modified to

$$\frac{\partial E}{\partial z} - \frac{1}{v_g} \frac{\partial E}{\partial t} = \frac{IZ_0\chi}{2\beta\gamma\Delta y} e^{-2\Gamma_0 b} \langle e^{-i\psi} \rangle + \alpha E, \quad (1)$$

where α is the complex attenuation coefficient having positive real part. Note that we are here closely following the notations and derivations given in Ref. 2. Here, I is the electron beam current, Δy is the beam width in the y -direction assumed to be so large that two-dimensional approximation is valid, β is the electron velocity in the unit of speed of light c , γ is the electron energy in unit of rest energy, $Z_0 = 377 \Omega$ is the characteristic impedance of free space, $\Gamma_0 = k_0/\gamma$, ψ is the electron phase and χ is the residue of the singularity associated with the surface mode as defined in Ref. 2. Converting to dimensionless variables, this equation can be transformed to the following form

$$\frac{\partial \mathcal{E}}{\partial \tau} - \frac{\partial \mathcal{E}}{\partial \zeta} = -\mathcal{J} \langle e^{-i\psi} \rangle - \alpha L \mathcal{E}, \quad (2)$$

where L is the length of the grating, \mathcal{E} is the dimensionless electric field, \mathcal{J} is the dimensionless beam current, τ is the dimensionless time and $\zeta = z/L$ is the normalised distance along the grating [2]. The second term in the right hand side of the above equation is the contribution due to attenuation. The above equation for the evolution of surface mode electric field will be coupled to equations for the electron beam dynamics as discussed in Ref. 2. We then linearise the equations and look for the solution for the electric field growing as $e^{\nu\tau}$. For a given value of \mathcal{J} and αL , we can obtain the complex growth rate ν by simultaneously solving the following set of two equations

$$\kappa^3 - (\nu + \alpha L)\kappa^2 + i\mathcal{J} = 0. \quad (3)$$

$$\begin{aligned} \kappa_1^2(\kappa_2 - \kappa_3)e^{\kappa_1} + \kappa_2^2(\kappa_3 - \kappa_1)e^{\kappa_2} \\ + \kappa_3^2(\kappa_1 - \kappa_2)e^{\kappa_3} = 0. \end{aligned} \quad (4)$$

Note that we have ignored the space charge parameter Q defined in Ref. 2, and assumed $Q = 0$. Here, κ_1 , κ_2 and κ_3 are three solutions for κ in Eq. (3). For a particular

* Work supported by U.S. Department of Energy, Office of Basic Energy Sciences, under Contract No. W-31-109-ENG-38.

[†] vinit@cat.ernet.in

value of αL , by solving these equations numerically, we can find out the minimum value of \mathcal{J} for which the real part of ν is positive. Let us call this as dimensionless start current denoted by \mathcal{J}_s , which is a function of αL . For the case when there is no attenuation ($\alpha L = 0$), we had earlier obtained that $\mathcal{J}_s = 7.68$ [2]. Here, by numerically solving Eqs. (3) and (4), we obtain the dependence of \mathcal{J}_s on αL . This is shown in Fig. 1. Note that \mathcal{J}_s depends only on the real part of αL .

The expression for the start current density dI_s/dy is given by

$$\frac{dI_s}{dy} = \mathcal{J}_s(\alpha L) \frac{I_A}{2\pi\chi} \frac{\beta^4 \gamma^4}{kL^3} e^{2\Gamma_0 b}, \quad (5)$$

where $I_A = 17$ kA is the Alfvén current. Here, $k = \omega/c = 2\pi/\lambda$ and λ is the free space wavelength of the surface mode. In the next section, we use the above formula to calculate and optimize the start current.

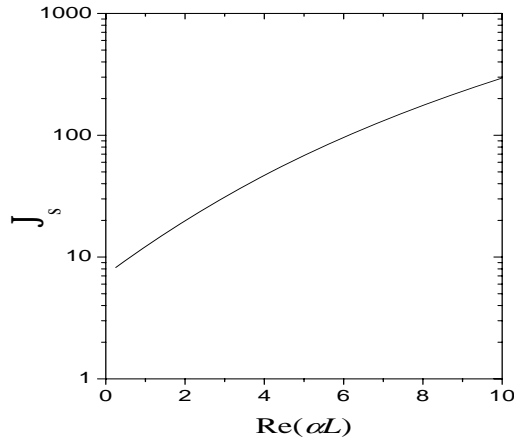


Figure 1: Plot of threshold dimensionless current \mathcal{J}_s as a function of the real part of the attenuation coefficient αL .

OPTIMIZATION OF GRATING PARAMETERS

In the past, many authors [1-5] have used the parameters corresponding to the Dartmouth experiment [6] for studying the performance of SP-BWO. For the Dartmouth experiment, the grating parameters and the electron beam parameters are given in Table 1. Note that we interpret the electron beam radius in Table 1 as the parameter b in our model. Using the formula derived in the previous section, we optimize the grating parameters for this case to minimize the start current.

Table 1: Parameters for the Dartmouth experiment

Groove width (w)	62 μm
Groove depth (d)	100 μm
Period (λ_g)	173 μm
Grating length (L)	12.7 mm
Electron beam radius (b)	10 μm
Electron beam energy	35 keV

First, we calculate the attenuation coefficient for different values of groove depth d and groove width w . For $w = 62$ μm , we vary the groove depth d and find out the attenuation coefficient α for each groove depth. This is shown in Fig. 2(a). Note that for the calculation of the attenua-

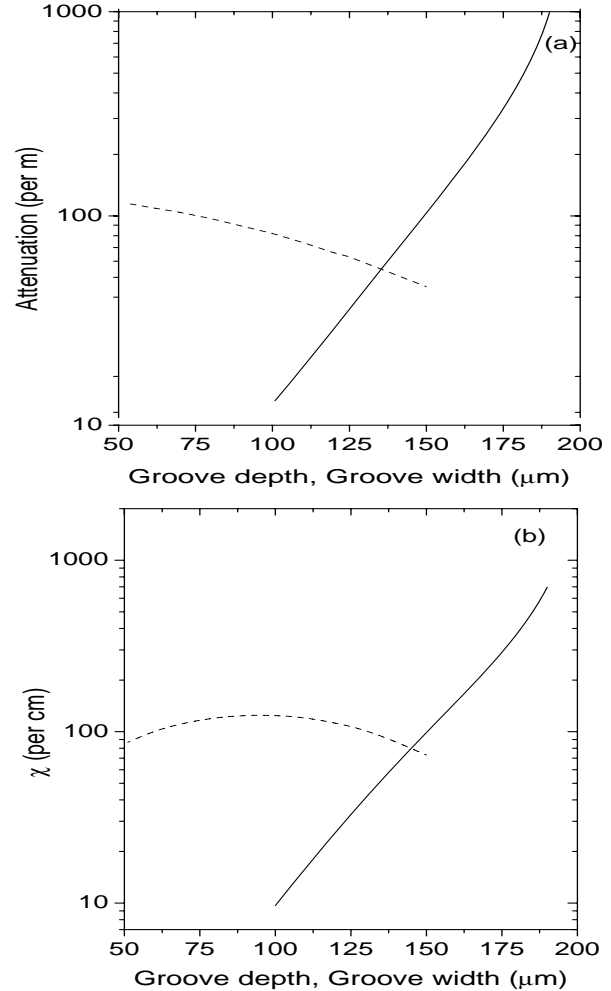


Figure 2: Plot of the real part of attenuation coefficient α (a), and the χ parameter (b) as a function of groove depth (solid curves) for groove width = 62 μm , and as a function of groove width (dashed curves) for groove depth = 150 μm .

tion coefficient, we have chosen Aluminum as the material of the grating and used the prescription given by Andrews et al. in Ref. 3. Then, keeping $w = 62$ μm , we calculate χ for different values of d as shown in Fig. 2(b). For the calculation of χ , we have used the prescription given in our earlier paper [2]. Next, knowing the value of α and χ , we use Eq. (5) to obtain the start current density as a function of groove depth for $w = 62$ μm . As the groove depth increases from 100 μm , the χ parameter increases, which means that the start current density decreases. However, as the groove depth is increased beyond 100 μm , the attenuation also increases, which tends to reduce the start current

density. Consequently, there is an optimum groove depth at which dI_s/dy is minimum. As we find in Fig. 3, the start current density is minimum for $d = 150 \mu\text{m}$. The value of dI_s/dy reduces from 40 mA/mm to 7.7 mA/mm when the groove depth is changed from $100 \mu\text{m}$ to $150 \mu\text{m}$.

After optimizing the groove depth, we next optimize the groove width. Keeping $d = 150 \mu\text{m}$, we vary w from $50 \mu\text{m}$ to $150 \mu\text{m}$ and obtain the attenuation coefficient and the χ -parameter as shown in Fig. 2. Then, using Eq. (5), we obtain the value of dI_s/dy for different values of groove width, keeping groove depth fixed at $150 \mu\text{m}$. This is shown in by the dotted curve in Fig. 3. We find that the optimum value of groove width is $110 \mu\text{m}$ for which the start current density is 5.6 mA/mm.

Hence, we find that the parameters for the Dartmouth experiment are not optimized for the minimum value of the start current. The optimized value of the groove depth and the groove width are $150 \mu\text{m}$ and $110 \mu\text{m}$ respectively. For these parameters, the start current density is 5.6 mA/mm, which is a substantial reduction compared to start current density of 40 mA/mm corresponding to the parameters given in Table 1.

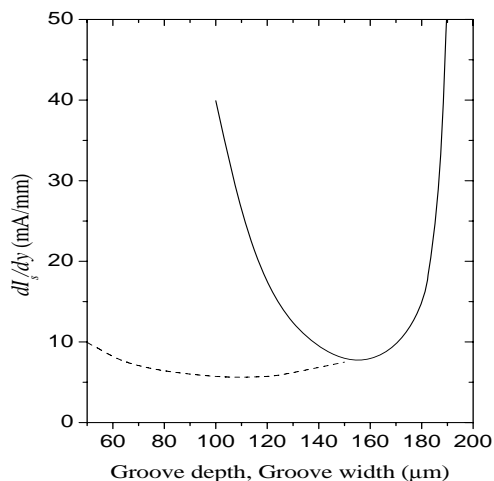


Figure 3: Plot of the start current density dI_s/dy with groove depth (solid line) as well as groove width (dashed line). For the solid line, we have kept groove width fixed at $62 \mu\text{m}$. For the dashed line, the groove depth is fixed at $150 \mu\text{m}$.

In the above calculations, when we change the groove width and the groove depth, the resonant wavelength λ of the surface mode also changes. The value of λ can be obtained by finding out the location of the singularity of the reflection matrix associated with the surface mode, as discussed in Ref. 2. Fig. 4 shows the variation of the resonant wavelength. We find that for $w = 110 \mu\text{m}$ and $d = 150 \mu\text{m}$, for which the start current is minimum, the resonant wavelength is $819 \mu\text{m}$. Note that for the calculation of dI_s/dy , one needs to put the value of the free-space resonant wavelength λ of the surface mode in Eq. (5), which has been taken from Fig. 4.

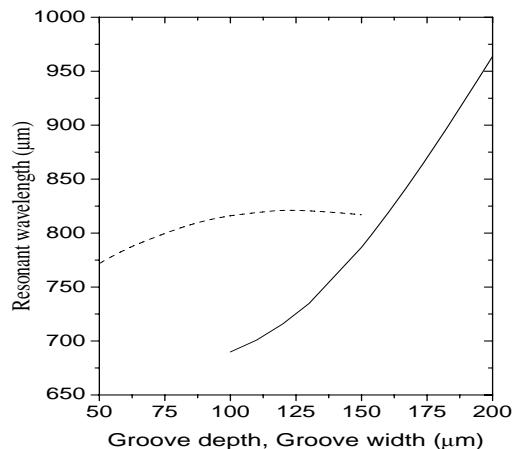


Figure 4: Plot of the free-space resonant wavelength λ with groove depth (solid line) as well as groove width (dashed line). For the solid line, we have kept groove width = $62 \mu\text{m}$. For the dashed line, groove depth = $150 \mu\text{m}$.

DISCUSSIONS

We would now like to discuss the dependence of the start current on the length of the grating. It is important to include three-dimensional effects for such an analysis [7]. A fully three-dimensional analysis of SP-BWO does not exist yet. However, we will attempt an approximate analysis here. The surface mode in the (y, z) plane is expected to diffract freely as an optical packet of wavelength $\beta\lambda$ since the grating is open in y -direction. The minimum average rms beam size of the optical beam over the length L due to diffraction effects is given by $\sqrt{\beta\lambda L/4\pi}$. In order to maximize the overlap between the electron beam and the optical beam, the rms electron beam size σ_y in the y -direction should be chosen equal to this. Putting the electron beam size in the y -direction in Eq. (5), we obtain that the start current I_s should be proportional to $\mathcal{J}_s(\alpha L)/L^{5/2}$. As we increase the length, the start current increases due to increase in \mathcal{J}_s . This is however counterbalanced by the $L^{5/2}$ factor in the denominator. For $\alpha L < 1$, \mathcal{J}_s can be assumed to be slowly varying. Hence, the start current should decrease as $1/L^{5/2}$. For the larger values of αL , the attenuation effects will be dominating since \mathcal{J}_s becomes exponential as shown in Fig. 1. In this case, the start current increases with grating length.

One of the important requirements for the operation of SP-BWO is that the electron beam should be sufficiently close to the grating surface. As the electron beam size in the x -direction increases, the start current increases exponentially due to the $\exp(2\Gamma_0 b)$ factor in Eq. (5). Hence, the rms electron beam size σ_x in the x -direction should be around $1/4\Gamma_0$. In order that the electron beam size in the

x -direction is maintained around this value over a length L , we need that the normalised electron beam emittance ϵ_x is less than $\beta\gamma/L(4\Gamma_0)^2$. We therefore notice that although the start current reduces by increasing the grating length, the requirement on electron beam emittance in the x -direction becomes more stringent.

One should also confirm that the space charge effect does not blow up the emittance. For this to be valid, the space charge term in the envelope equation should be less than the emittance term. This leads to the following condition in the x -direction [7]

$$\frac{4}{\beta\gamma} \frac{I}{I_A} \frac{\sigma_x^3}{(\sigma_x + \sigma_y)\epsilon_x^2} < 1. \quad (6)$$

It is important to point out here that for the Dartmouth parameters given in Table 1, the above inequality is not satisfied. After optimizing the grating parameters, the start current is reduced and then the above inequality is satisfied.

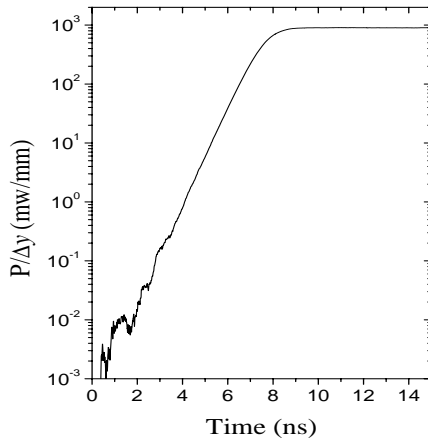


Figure 5: Plot of power per unit beam width in the surface mode as a function of time at the entrance of the grating for the optimized grating parameters.

We would like to point out that for the optimized grating parameters that we discussed, although the start current is reduced significantly compared to the grating parameters in Table 1, the attenuation is increased as seen in Fig. 2. This means that the heat loss in the grating will be more for the optimized parameters, which implies that the power conversion efficiency of SP-BWO will be reduced. For example, for the optimized grating parameters that we discussed, $I_s/\Delta y = 5.6$ mA/mm. For this case, if we take $I/\Delta y = 7$ mA/mm, we obtain $P/\Delta y = 900$ mW/mm at saturation as shown in Fig. 5. This translates to a power conversion efficiency of 0.37%. Note that this calculation is performed by numerically solving the coupled Maxwell-Lorentz equations as discussed in Ref. 8. On the other hand, for the Dartmouth parameters, we have $I_s/\Delta y = 40$ mA/mm. For this case, if we take $I/\Delta y = 50$ mA/mm, we

obtain $P/\Delta y = 14.3$ W/mm at saturation. This translates to a power conversion efficiency of 0.56%.

CONCLUSIONS

We have derived a simple formula for the start current density in a SP-BWO taking the attenuation due to finite conductivity of the grating material into account. This formula has been used to optimize the parameters of the grating. We find that for the parameters corresponding to the Dartmouth experiment, the start current can be reduced by six times by optimizing the grating parameters.

ACKNOWLEDGMENTS

It is a pleasure to thank Charlie Brau for many helpful discussions.

REFERENCES

- [1] H. L. Andrews and C. A. Brau, Phys. Rev. ST Accel. Beams, 7 (2004) 070701.
- [2] V. Kumar and K.-J. Kim, Phys. Rev. E 73 (2006) 026501.
- [3] H. L. Andrews et al., Phys. Rev. ST Accel. Beams, 8 (2005) 050703.
- [4] J. T. Donohue and J. Gardelle, Phys. Rev. ST Accel. Beams, 9 (2005) 060701.
- [5] D. Li et al., Phys. Rev. ST Accel. Beams, 9 (2005) 040701.
- [6] J. Urata et al., Phys. Rev. Lett. 80 (1998) 516.
- [7] K.-J. Kim and V. Kumar, under preparation.
- [8] V. Kumar and K.-J. Kim, these proceedings.

ANALYSIS OF SMITH-PURCELL BWO WITH END REFLECTIONS *

Vinit Kumar[†], RRCAT, Indore, M.P. 452013, INDIA
 Kwang-Je Kim, ANL, Argonne, IL 60439, USA.

Abstract

We present a one-dimensional time-dependent analysis and simulation of Smith-Purcell (SP) backward wave oscillator (BWO) taking end reflections and attenuation into account. In the linear regime, we obtain an analytic solution and calculate the start current. The dependence of start current on end reflections is studied taking the attenuation due to finite conductivity into account.

INTRODUCTION

The Smith-Purcell (SP) free-electron laser in the terahertz (THz) regime using a low energy electron beam is a backward wave oscillator (BWO) [1,2]. Previous analyses of SP-BWO [1-3] have ignored the reflection at the ends of the grating. However, there will in general be some reflection at the end of the grating due to discontinuity in the medium. One can, if desired, also add external mirrors to enhance reflection. In the presence of reflection, the start current, which is defined as the minimum value of the electron beam current needed to produce coherent electromagnetic oscillations, can be reduced. In this paper, we present a self consistent nonlinear analysis of SP-BWO including end reflections and attenuation. We set up Maxwell-Lorentz equations and develop a computer code to solve these equations. We present the results of numerical simulation and discuss the evolution of power. In the linear regime, we solve the coupled Maxwell-Lorentz equations analytically and calculate the start current taking end reflection and attenuation into account.

MAXWELL-LORENTZ EQUATIONS

In a SP-BWO, the electron beam interacts with the backward surface wave co-propagating with the electron beam. We assume that the electron beam is in the form of a thin sheet moving along the z -axis above a metal grating with rectangular grooves, the direction of the grooves is along the y -axis and the outward normal to the grating surface is along the x -axis. The plane of the sheet electron beam is at $x = 0$, and the top surface of the grating is at $x = -b$. We have earlier studied the interaction between the electron beam and the backward surface mode using Maxwell-Lorentz equations where we ignored the reflection at the end of the grating [2]. The backward surface mode supported by the grating is a linear combination of infinite number of Floquet-Bloch harmonics hav-

ing the z -component of propagation vectors differing from each other by an integral multiple of k_g , where $k_g = 2\pi/\lambda_g$ and λ_g is the period of the grating. The y -component H_y of the magnetic field of the backward surface mode can be written as $\sum A_n \exp(ik_0z + ink_gz - \Gamma_n x - i\omega t)$, where the summation is implied over all n from $-\infty$ to $+\infty$ [2]. Here, ω is the frequency, k_0 is the propagation vector of the backward surface mode, $\Gamma_n = \sqrt{(k_0 + nk_g)^2 - \omega^2/c^2}$ and c is the speed of light. The zeroth-order component of this mode has the longitudinal electric field given by $E_-(z, t) \exp(ik_0z - i\omega t)$ at $x = 0$. The amplitude of all other components of the backward surface mode have to maintain a fixed ratio with the amplitude of the zeroth-order component such that the electromagnetic field satisfies the required boundary conditions. Hence, as the zeroth-order component of the surface mode evolves due to interaction with co-propagating electron beam, the amplitude of all other components also evolve proportionately. One can calculate the group velocity, which is $d\omega/dk$, from the dispersion relation of the backward surface mode. For low energy electron beam, the group velocity of the co-propagating surface mode having $\omega/k_0 = \beta c$ is along the negative z -axis [1,2]. Let us denote the magnitude of the group velocity by v_g . Here, βc is the velocity of electrons.

For a grating with rectangular grooves considered here, a wave going along the positive z -axis will see the same boundary as the wave going along the negative z -axis. Hence, if we construct a mode having H_y given by $\sum A_n \exp(-ik_0z - ink_gz - \Gamma_n x - i\omega t)$, it will satisfy the Maxwell equations and the required boundary condition for the reflection grating. This is actually the forward surface mode supported by the grating. This has the propagation vector $-k_0$ and the group velocity v_g along the positive z -axis. Hence, the grating supports forward as well as backward surface mode. However, none of the components of the forward surface mode co-propagate with the electron beam. Consequently, the forward surface mode does not interact with the electron beam. It however arises due to reflection of the backward wave at the end of the grating. As the backward surface mode extracts energy from the electron beam and grows, it gets reflected at the end to the forward surface mode and consequently the forward surface mode also grows. Let us denote the zeroth-order component of the forward surface mode as $E_+(z, t) \exp(-ik_0z - i\omega t)$ at the location of sheet electron beam.

In our previous work [2], we had set up Maxwell equation for the backward wave, which is coupled to Lorentz equations for the beam dynamics. We will now add the Maxwell equation for the forward wave to this set of equa-

* Work supported by U.S. Department of Energy, Office of Basic Energy Sciences, under Contract No. W-31-109-ENG-38.

[†] vinit@cat.ernet.in

tions. We will be following notations used in Ref. 2. The energy flows along the negative z -axis for the backward wave and hence, it gets attenuated along the negative z -axis. Similarly, for the forward wave, the energy flows along the positive z -axis and it gets attenuated along the positive z -axis. The complex attenuation coefficient α for the backward wave supported by a rectangular reflection grating can be obtained as per the prescription given in Ref. 3. For the forward wave, the complex attenuation coefficient will be simply $-\alpha$. Taking the attenuation into account, the equation for the evolution of the amplitude E_+ of the forward wave becomes

$$\frac{\partial E_+}{\partial z} + \frac{1}{v_g} \frac{\partial E_+}{\partial t} = -\alpha E_+. \quad (1)$$

The equation for the evolution of the amplitude E_- of the backward wave as derived earlier is given by [2,4]

$$\frac{\partial E_-}{\partial z} - \frac{1}{v_g} \frac{\partial E_-}{\partial t} = \frac{IZ_0\chi}{2\beta\gamma\Delta y} e^{-2\Gamma_0 b} \langle e^{-i\psi} \rangle + \alpha E_-, \quad (2)$$

where I is the electron beam current, $Z_0 = 377 \Omega$ is the characteristic impedance of free space, χ is the residue of the singularity associated with the surface mode as defined in Ref. 2, γ is the energy of the electron beam in unit of rest energy, ψ is the electron phase and Δy is the width of the sheet electron beam in the y -direction. Both these equations are coupled through boundary condition at the end of the grating. Let ρ_0 and ρ_L be the complex reflection coefficient at the entrance and exit end of the grating. The boundary conditions will then given by $E_+(z=0) = \rho_0 E_-(z=0)$, and $E_-(z=L) = \rho_L E_+(z=L) e^{ik_0 L}$, where L is the length of the grating. The entrance and the exit of the grating are at $z=0$ and $z=L$ respectively.

In order to further simplify the analysis, we define a new amplitude of the forward wave given by $E_+ = -\rho_0 \tilde{E}_+$. The boundary conditions, in term of this definition can then be written as $\tilde{E}_+(z=0) = -E_-(z=0)$ and $E_-(z=L) = \mathcal{R} e^{-i2k_0 L} \tilde{E}_+(z=L)$, where $\mathcal{R} = -\rho_0 \rho_L$. As discussed in Ref. 2, we can define dimensionless variables and make a transformation from (z, t) to (ζ, τ) to simplify the analysis. Here, $\zeta = z/L$ is the normalised length and τ is the dimensionless time defined in Ref. 2. We define dimensionless amplitude of the forward and the backward wave denoted by \mathcal{E}_+ and \mathcal{E}_- respectively as

$$\mathcal{E}_\pm = \frac{4\pi}{I_A Z_0} \frac{k_0 L^2}{\beta^2 \gamma^3} \tilde{E}_\pm, \quad (3)$$

where $I_A = 17$ kA is the Alfvén current and $\tilde{E}_- = E_-$. After making these transformations, the equation for evolution of \mathcal{E}_+ and \mathcal{E}_- are given by

$$\frac{\partial \mathcal{E}_-}{\partial \tau} - \frac{\partial \mathcal{E}_-}{\partial \zeta} = -\mathcal{J} \langle e^{-i\psi} \rangle - \alpha L \mathcal{E}_-, \quad (4)$$

$$\frac{\partial \mathcal{E}_+}{\partial \tau} + d_1 \frac{\partial \mathcal{E}_+}{\partial \zeta} = -d_1 \alpha L \mathcal{E}_+, \quad (5)$$

where $d_1 = (v_p + v_g)/(v_p - v_g)$. The boundary conditions now become $\mathcal{E}_+(\zeta=0) = -\mathcal{E}_-(\zeta=0)$ and $\mathcal{E}_-(\zeta=1) = \mathcal{R} e^{-i2k_0 L} \mathcal{E}_+(\zeta=1)$. These equations are coupled to the electron beam dynamics equations

$$\frac{\partial \eta_i}{\partial \zeta} = (\mathcal{E}_- + \mathcal{E}_{sc}) e^{i\psi_i} + c.c., \quad (6)$$

$$\frac{\partial \psi_i}{\partial \zeta} = \eta_i, \quad (7)$$

where the \mathcal{E}_{sc} is the dimensionless longitudinal electric field due to space charge given by $\mathcal{E}_{sc} = iQ \langle e^{-i\psi} \rangle$, and $Q = (\mathcal{J}/\chi L)(\chi_1 - e^{2\Gamma_0 b})$. The χ_1 -parameter appears in the analysis of singularity associated with the surface mode and can be calculated as per prescription discussed in Ref. 2. Here the subscript i stands for i^{th} electron and $\eta_i = (\gamma_i - \gamma)/\gamma$ is the relative energy deviation of the i^{th} electron. Eqs. (4-7) along with the boundary conditions form the complete set of differential equations needed to describe the one-dimensional time-dependent behavior of SP-BWO with end reflections and attenuation. In the next section, we discuss the analytic solution of these equations in the linear regime.

LINEAR ANALYSIS

We can linearize Eqs. (4-7) around an equilibrium solution and perform a stability analysis to find out the parameter regime in which the instability for exchange of energy from electron beam to electromagnetic oscillation can be excited. For simplicity, let us assume that the injected beam is monoenergetic, and $\eta_i = 0$ for all the electrons at $\zeta = 0$. Further, we assume that the injected beam is unbunched, i.e., $\langle e^{-i\psi_0} \rangle = 0$, where $\psi_{0,i}$ is the phase of the i^{th} particle at $\zeta = 0$. An equilibrium solution of the system of Eqs. (4-7) is obviously $\mathcal{E}_- = 0$, $\mathcal{E}_+ = 0$, $\eta_i = 0$, and $\psi_i = \psi_{0,i}$. Let us define the perturbative solution by $\mathcal{E}_- = \tilde{\mathcal{E}}_-$, $\mathcal{E}_+ = \tilde{\mathcal{E}}_+$, $\eta_i = \delta\eta_i$, and $\psi_i = \psi_{0,i} + \delta\psi_i$. We introduce the following collective variables as done by Bonifacio et al. [5] for conventional FELs:

$$\tilde{x} = \langle \delta\psi e^{-i\psi_0} \rangle, \quad \tilde{y} = \langle \delta\eta e^{-i\psi_0} \rangle. \quad (8)$$

In terms of these variables, Eqs. (4-7) can be linearized and written as

$$\frac{\partial \tilde{\mathcal{E}}_-}{\partial \tau} - \frac{\partial \tilde{\mathcal{E}}_-}{\partial \zeta} = i\mathcal{J}\tilde{x} - \alpha L \tilde{\mathcal{E}}_-, \quad (9)$$

$$\frac{\partial \tilde{\mathcal{E}}_+}{\partial \tau} + d_1 \frac{\partial \tilde{\mathcal{E}}_+}{\partial \zeta} = -d_1 \alpha L \tilde{\mathcal{E}}_+, \quad (10)$$

$$\frac{\partial \tilde{x}}{\partial \zeta} = \tilde{y}, \quad (11)$$

$$\frac{\partial \tilde{y}}{\partial \zeta} = \tilde{\mathcal{E}}_- + Q\tilde{x}. \quad (12)$$

The boundary conditions for these equations are: (1) $\tilde{x} = 0$ at $\zeta = 0$ at all τ since the injected beam has no phase modulation, i.e., it is injected unbunched. (2) $\tilde{y} = 0$ at $\zeta =$

0 at all τ since the injected beam has no energy modulation, i.e., it is injected monoenergetically. (3) $\tilde{\epsilon}_+ = -\tilde{\epsilon}_-$ at $\zeta = 0$ for all τ , and $\tilde{\epsilon}_- = \mathcal{R}e^{-i2k_0L}\tilde{\epsilon}_+$ at $\zeta = 1$ for all τ . Assuming a solution of the type $e^{\nu\tau}$, we can find out the growth rate ν for the above linearised equations with the boundary conditions. In order to find out the growth rate ν , one has to first solve the following cubic equation

$$\kappa^3 - (\nu + \alpha L)\kappa^2 - Q\kappa + \nu Q + i\mathcal{J} = 0. \quad (13)$$

Then, the three roots of the above cubic equation κ_1, κ_2 and κ_3 should satisfy the following transcendental equation

$$\begin{aligned} & \mathcal{R}e^{-\alpha L}e^{-i(2k_0L - i\frac{\nu}{\alpha})}[(\kappa_1^2 - Q)(\kappa_2 - \kappa_3) \\ & + (\kappa_2^2 - Q)(\kappa_3 - \kappa_1) + (\kappa_3^2 - Q)(\kappa_1 - \kappa_2)] \\ & + (\kappa_1^2 - Q)(\kappa_2 - \kappa_3)e^{\kappa_1} + (\kappa_2^2 - Q)(\kappa_3 - \kappa_1)e^{\kappa_2} \\ & + (\kappa_3^2 - Q)(\kappa_1 - \kappa_2)e^{\kappa_3} = 0. \end{aligned} \quad (14)$$

By solving the above two equations, we can find out the minimum value of \mathcal{J} , called the dimensionless start current \mathcal{J}_s for a given Q, \mathcal{R}, α and L , for which the real part of the complex growth rate ν is positive.

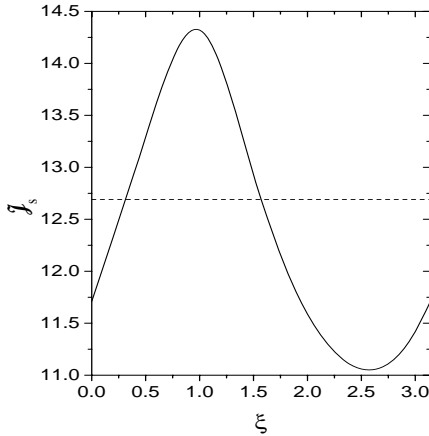


Figure 1: Variation in the dimensionless start current with ξ for $\mathcal{R} = 0.8$ (solid curve) and $\mathcal{R} = 0$ (dashed curve).

Next, we use Eqs. (13-14) for the calculation of start current. In a companion paper [4], we have optimized the parameters corresponding to Dartmouth experiment [6] taking attenuation into account, but excluding end reflection. We use those parameters for calculation of start current here. For the grating, we use groove depth $d = 150 \mu\text{m}$, groove width $w = 110 \mu\text{m}$, period $\lambda_g = 173 \mu\text{m}$ and length $L = 12.7 \text{ mm}$. For the 35 keV sheet electron beam, we use $b = 10 \mu\text{m}$. From our calculation [2], for these parameters, we obtain the free-space wavelength $\lambda = 819 \mu\text{m}$, $\chi = 120$ per cm, $\chi_1 = 3.9$, $\alpha L = 0.94(1 - i)$ and $v_g/c = 0.0925$. Note that in Eq. (14), for a given grating length, when we change the electron beam energy, the value of k_0 will change, which will change the phase factor term e^{-2ik_0L} . Let us define $\xi = \text{mod}(k_0L, \pi)$. Hence, for a

given set of parameters, if we make a slight change in the electron beam energy, the value of ξ changes accordingly and affects the value of start current. For our parameters, Q is very small, and we take $Q = 0$. Figure 1 shows the variation of dimensionless start current \mathcal{J}_s with ξ for $\mathcal{R} = 0.8$. We find that the value of \mathcal{J}_s oscillates between 11.1 and 14.2. Note that the start current density corresponding to $\mathcal{J} = 11.1$ is 4.7 mA/mm. The value of \mathcal{J}_s is 12.7, when we neglect end reflection. When the attenuation is smaller, the effect of end reflection is more pronounced.

NUMERICAL SIMULATION

For numerically solving Eqs. (4-7), we use the approach used by Ginzburg et al. [7] and later also by Levush et al. [8] for BWO. The electron dynamics equations for a given field distribution along the interaction region are solved by the predictor-corrector method. Then, knowing the modified electron distribution in phase space, the field distribution at the next time step is obtained by solving the partial differential equations (Eqs. 4-5) by the finite difference method. The method is stable for $\Delta\tau < \Delta\zeta$ for the backward wave and for $\Delta\tau < (1/d_1)\Delta\zeta$ for the forward wave. Here, $\Delta\tau$ and $\Delta\zeta$ are the step sizes in τ and ζ respectively, used in the finite difference method.

For initializing the electron beam in phase space, we simulate the shot noise using the algorithm given by Penman and McNeil [9], which is commonly used in FEL codes.

We performed a couple of tests on the code we developed. We first checked for the convergence of the solution by increasing the number of particles and also by reducing the step size. Based on this convergence test, we chose the number of particles to be used in the simulation as 1024 and the step sizes as $\Delta\tau = 0.01$ and $\Delta\zeta = 0.02$. We also confirmed that the energy conservation equation along with the damping term due to attenuation is satisfied in the code at each integration step.

Figure 2 shows the evolution of power in the backward wave at the entrance of the grating for $\mathcal{J} = 11.6$ and $\mathcal{J} = 10.6$. The parameters used in the calculation are same as mentioned in the last section. We have chosen $\xi = 2.5$ for which \mathcal{J}_s is minimum as shown in Fig. 1. For these parameters, $\mathcal{J}_s = 11.1$ and hence for the case $\mathcal{J} = 10.6$, there is no build-up of power, whereas for the case $\mathcal{J} = 11.6$, we find that the power grows exponentially and saturates. Note that $I/\Delta y = 4.9 \text{ mA/mm}$ for $\mathcal{J} = 11.6$. After saturation, the variation of the amplitude of electric field for the forward as well as the backward wave along the length of the grating is shown in Fig. 3.

Let us now discuss the calculation of outcoupled power. Power in the backward and the forward surface mode denoted by P_- and P_+ respectively can be obtained by the following expression

$$\frac{P}{\Delta y} = 2 \frac{\beta\gamma}{Z_0\chi} \left(\frac{mc^2\beta^3\gamma^3}{ek_0L^2} \right)^2 e^{2\Gamma_0 b} |\mathcal{E}|^2, \quad (15)$$

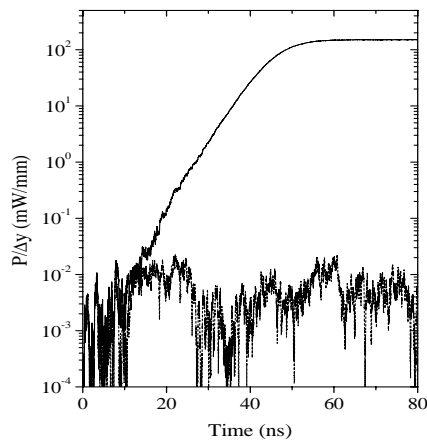


Figure 2: Evolution of power in the backward wave at the entrance of the undulator for $\mathcal{J} = 11.6$ (solid curve), and $\mathcal{J} = 10.6$ (dashed curve). We have used $\mathcal{R} = 0.8$ and $\xi = 2.5$ in the calculation.

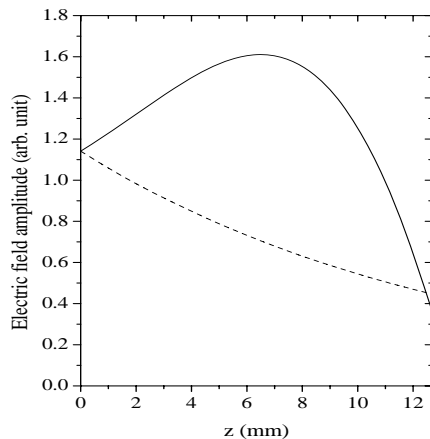


Figure 3: Variation of the amplitude $|\mathcal{E}_-|$ of the backward wave (solid curve) and the amplitude $|\mathcal{E}_+|$ of the forward wave (dashed curve) along the length of the grating for $\mathcal{J} = 11.6$. Other parameters are same as those used in Fig. 2.

where $P = P_-$ for $\mathcal{E} = \mathcal{E}_-$ and $P = P_+$ for $\mathcal{E} = \rho_0 \mathcal{E}_+$. The outcoupled power P_0 at the entrance of the grating is given by $P_-(z = 0) - P_+(z = 0)$ and at the exit, the outcoupled power P_1 is given by $P_+(z = L) - P_-(z = L)$. If we assume $\rho_L = 1$, the power will be outcoupled only at the entrance of the grating. For the case of Fig. 3, the outcoupled power is calculated to be 54 mW for $\Delta y = 1$ mm. The total power in the electron beam for this case is 171.5 W for 35 keV, 4.9 mA electron beam current. Hence, the overall efficiency is only 0.03%. Such a low efficiency is there because we have chosen the electron beam current very close to the start current and also the heat loss occurring in the grating due to attenuation deteriorates the efficiency. We have checked that the efficiency is improved

at higher value of beam current. Our emphasis here is to show that including reflection, it is possible to reduce the start current surface density to as low as 4.7 mA/mm.

In our calculation, we have not calculated the value of reflectivity, instead we have assumed a value for reflectivity. In a realistic situation, there will be some reflectivity at the end of the grating due to change of boundary, which needs to be calculated. However, we can put an external mirror and the reflectivity \mathcal{R} can be adjusted to a desired value. By introducing a reflectivity, the start current is reduced, but the outcoupled power may not be optimized. Using our calculation in the saturation regime, one can optimize the parameters to obtain optimum combination of start current and outcoupled power.

CONCLUSIONS

In this paper, we have set up Maxwell-Lorentz equations for the one-dimensional time-dependent analysis of SP-BWO including end reflection and attenuation due to finite conductivity. We have obtained a solution in the linear regime and extended the analysis to the nonlinear regime by solving the Maxwell-Lorentz equations numerically. Our analysis can be used for detailed optimization of outcoupled power and start current in SP-BWO taking end reflection and attenuation into account.

REFERENCES

- [1] H. L. Andrews and C. A. Brau, Phys. Rev. ST Accel. Beams, 7 (2004) 070701.
- [2] V. Kumar and K.-J. Kim, Phys. Rev. E 73 (2006) 026501.
- [3] H. L. Andrews et al., Phys. Rev. ST Accel. Beams, 8 (2005) 050703.
- [4] V. Kumar and K.-J. Kim, these proceedings
- [5] R. Bonifacio, C. Pellegrini, and L. M. Narducci, Opt. Commun. **40** 373 (1984).
- [6] J. Urata et al., Phys. Rev. Lett. 80 (1998) 516.
- [7] N. S. Gingburg, S. P. Kuznetov, and T. N. Fedoseeva, Sov. Radiophys. Electron., 21 (1979) 728.
- [8] B. Levush et al., IEEE Trans. Plasma Sci. 20, (1992) 263.
- [9] C. Penman and B. W. J. McNeil, Opt. Commun. 90 (1992) 82.

MODE COUPLINGS IN A RAMAN FREE-ELECTRON LASER WITH ION-CHANNEL GUIDING

B. Maraghechi^{a,b,*}, T. Mohsenpour^a

^aDepartment of Physics, Amirkabir University of Technology, Tehran, Iran

^bInstitute for Studies in Theoretical Physics and Mathematics (IPM),

P.O. Box 19395-5531, Tehran, Iran.

Abstract

The free-electron laser (FEL) theory in the collective or Raman regime relies on the unstable coupling between the radiation and the negative-energy space-charge wave. Due to the high density and low energy of electron beam a focusing mechanism like an axial magnetic field is usually required to guide the beam. It is found that the wiggler has direct effect on the right and left waves and the wiggler effect on their dispersion relations are of the second order in the wiggler amplitude. Due to the fully relativistic treatment the dispersion relation is to fourth order in wiggler amplitude and it can be used to study new couplings between the negative and positive-energy space-charge waves as well as between the right and left circularly polarized electromagnetic waves.

INTRODUCTION

Relativistic electron beam injected into an ionized plasma channel ejects plasma electrons leaving a positive ion core which attracts and confines the beam electron. There are important applications in this subject such as advanced accelerators [1] and free-electron lasers (FELs) [2,3]. Ion-channel guiding as an alternative to the conventional axial magnetic-field guiding, was first proposed for use in FELs by Takayama and Hiramatsu [4]. Experimental results of a FEL with ion-channel guiding have been reported by Ozaki et al. [5] Also, Yu et al. [6] have reported that the combination of ion focusing and beam conditioning would lead to high gain FEL operation in the soft x-ray regime. Jha and Wurtele [7] developed a three-dimensional code for FEL simulation that allows for the effects of an ion channel. The theoretical studies of this problem with a helical wiggler are carried out in the low-gain [8] and high-gain [9,10] regimes. In Ref 10, the relativistic Raman backscattering theory is used to find the FEL dispersion relation with ion-channel guiding, in the beam frame of electrons, with the left circularly polarized backscattered wave neglected. This DR was used to find the growth rate of the FEL resonance due to the coupling of radiation with the slow space-charge wave.

The purpose of the present investigation is to obtain the dispersion relation (DR) for the interaction of all possible waves in a relativistic electron beam that passes through a one-dimensional helical wiggler magnetic field with ion-channel guiding. The motion of a relativistic electron

through the wiggler is analyzed. Three coupled equations are derived and a formula for the general DR is obtained.

ELECTRON MOTION

Consider a relativistic electron moving along the z axis of an idealized helical wiggler magnetic field described by

$$\mathbf{B} = B_w (\hat{\mathbf{x}} \cos k_w z + \hat{\mathbf{y}} \sin k_w z), \quad (1)$$

where B_w denotes the wiggler amplitude, and $k_w (= 2\pi/\lambda_w)$ is wiggler wave number. In the presence of an ion channel, with its axis coincident with the wiggler axis, the following transverse electrostatic field is acted on the electron beam

$$\mathbf{E}_i = 2\pi e n_i (x \hat{\mathbf{x}} + y \hat{\mathbf{y}}), \quad (2)$$

where n_i is the number density of positive ions with charge e . The steady-state motion of an electron in the above field consists of an axis centred helical motion, with radius $R_0 = v_w/k_w v_{\parallel}$, given by Eq. (16) with [8,11]

$$v_w = \frac{\Omega_w k_w v_{\parallel}^2}{\omega_i^2 - k_w^2 v_{\parallel}^2}, \quad (3)$$

where $\Omega_w \equiv e B_w / \gamma m c$, $\omega_i^2 = 2\pi n_i e^2 / \gamma m$, m is the electron rest mass, e is the magnitude of the charge of an electron, and c is the speed of light in vacuum. This velocity is related to the axial velocity v_{\parallel} through

$$\gamma_0^{-2} = 1 - \frac{v_w^2}{c^2} - \frac{v_{\parallel}^2}{c^2}. \quad (4)$$

Equation (4) is cubic in v_{\parallel}^2/c^2 and describes two classes of trajectories propagating along the positive z axis of the FEL.

DISPERSION RELATION

An analysis of the propagation of electromagnetic/electrostatic waves in the electron beam may be based on the continuity equation,

$$\frac{\partial n}{\partial t} + \nabla \cdot (n \mathbf{v}) = 0, \quad (5)$$

the relativistic momentum equation

$$\frac{d \mathbf{v}}{d t} = - \frac{e}{\gamma m_0} \left(\mathbf{E} - \frac{1}{c^2} \mathbf{v} \mathbf{v} \cdot \mathbf{E} + \frac{1}{c} \mathbf{v} \times \mathbf{B} \right), \quad (6)$$

* Electronic mail: behrouz@aut.ac.ir

and the wave equation

$$\nabla \times (\nabla \times \mathbf{E}) + \frac{1}{c^2} \frac{\partial^2 \mathbf{E}}{\partial t^2} = \frac{\partial}{\partial t} \frac{4\pi e n \mathbf{v}}{c^2}. \quad (7)$$

Here n is the electron density, \mathbf{v} is the electron velocity, γ is the Lorentz factor corresponding to \mathbf{v} , \mathbf{E} is the electric field, and \mathbf{B} is the magnetic field. With the unperturbed electron density n_0 taken to be independent of position and time and the self-fields of the unperturbed state neglected, the electron and field variables may be expressed in the form

$$n = n_0 + \delta n, \quad (8)$$

$$\mathbf{v} = \mathbf{v}_0 + \delta \mathbf{v}, \quad (9)$$

$$\mathbf{E} = \mathbf{E}_i + \delta \mathbf{E}, \quad (10)$$

$$\mathbf{B} = \mathbf{B}_w + \delta \mathbf{B}, \quad (11)$$

$$\mathbf{R} = \mathbf{R}_0 + \delta \mathbf{R} \quad (12)$$

The linearized equations for the continuity equation, the relativistic momentum equation, and the wave equation may be derived as

$$\frac{\partial \delta n}{\partial t} + n_0 \nabla \cdot \delta \mathbf{v} + \mathbf{v}_0 \cdot \nabla \delta n = 0, \quad (13)$$

$$\begin{aligned} \frac{\partial \delta \mathbf{v}}{\partial t} + \mathbf{v}_0 \cdot \nabla \delta \mathbf{v} + \delta \mathbf{v} \cdot \nabla \mathbf{v}_0 = & -\frac{e}{\gamma_0 m_0} \left[\delta \mathbf{E} - \frac{1}{c^2} \mathbf{v}_0 \mathbf{v}_0 \cdot \delta \mathbf{E} \right. \\ & - \frac{1}{c^2} \mathbf{v}_0 \delta \mathbf{v} \cdot \mathbf{E}_i - \frac{1}{c^2} \delta \mathbf{v} \mathbf{v}_0 \cdot \mathbf{E}_i + \frac{1}{c} \delta \mathbf{v} \times \mathbf{B}_w + \frac{1}{c} \mathbf{v}_0 \times \delta \mathbf{B} \\ & \left. - \frac{\gamma_0^2}{c^2} \left(\mathbf{E}_i + \frac{1}{c} \mathbf{v}_0 \times \mathbf{B}_w - \frac{1}{c^2} \mathbf{v}_0 \mathbf{v}_0 \cdot \mathbf{E}_i \right) (\mathbf{v}_0 \cdot \delta \mathbf{v}) \right], \quad (14) \end{aligned}$$

$$\nabla \times (\nabla \times \delta \mathbf{E}) + \frac{1}{c^2} \frac{\partial^2 \delta \mathbf{E}}{\partial t^2} = \frac{\partial}{\partial t} \frac{4\pi e}{c^2} (\delta n \mathbf{v}_0 + n_0 \delta \mathbf{v}). \quad (15)$$

By introducing a new set of basis vectors $\hat{\mathbf{e}} = (\hat{\mathbf{x}} + i\hat{\mathbf{y}})/\sqrt{2}$, $\hat{\mathbf{e}}^* = (\hat{\mathbf{x}} - i\hat{\mathbf{y}})/\sqrt{2}$, and $\hat{\mathbf{e}} = \hat{\mathbf{z}}$, the unperturbed magnetic field, electron density, and transverse electrostatic field can be written as

$$\mathbf{B}_w = (B_w/\sqrt{2}) \exp(-ik_w z) \hat{\mathbf{e}} + (B_w/\sqrt{2}) \exp(ik_w z) \hat{\mathbf{e}}^*, \quad (16)$$

$$\mathbf{v}_0 = (v_w/\sqrt{2}) \exp(-ik_w z) \hat{\mathbf{e}} + (v_w/\sqrt{2}) \exp(ik_w z) \hat{\mathbf{e}}^* + v_{\parallel} \hat{\mathbf{e}}_z, \quad (17)$$

$$\mathbf{E}_i = i\sqrt{2} \pi e n_i R_0 \left(\exp(-ik_w z) \hat{\mathbf{e}} + \exp(ik_w z) \hat{\mathbf{e}}^* \right), \quad (18)$$

The perturbed state is assumed to consist of a longitudinal space-charge wave and right and left circularly polarized electromagnetic waves, referred here as radiation, with all perturbed waves propagating in the positive z direction. Accordingly, solution of the system of equations (13)-(15) may be assumed as

$$\delta \mathbf{v} = \delta v_R \hat{\mathbf{e}} + \delta v_L \hat{\mathbf{e}}^* + \delta v_z \hat{\mathbf{e}}_z, \quad (19)$$

$$\delta \mathbf{E} = (2\pi e n_i \delta R_R + \delta E_R) \hat{\mathbf{e}} + (2\pi e n_i \delta R_L + \delta E_L) \hat{\mathbf{e}}^* + \delta E_z \hat{\mathbf{e}}_z, \quad (20)$$

$$\delta \mathbf{B} = \delta B_R \hat{\mathbf{e}} + \delta B_L \hat{\mathbf{e}}^*, \quad (21)$$

$$\delta \mathbf{R} = \delta R_R \hat{\mathbf{e}} + \delta R_L \hat{\mathbf{e}}^* \quad (22)$$

$$\delta n = \tilde{n} \exp[i(kz - \omega t)], \quad (23)$$

$$\delta v_R = \tilde{v}_R \exp[i(k_R z - \omega t)], \quad (24)$$

$$\delta v_L = \tilde{v}_L \exp[i(k_L z - \omega t)], \quad (25)$$

δv_z and δE_z are analogous to δn ; δE_R , δR_R , and δB_R are analogous to δv_R ; δE_L , δR_L , and δB_L are analogous to δv_L ; the wave numbers are related to by

$$k_R = k - k_w, \quad (26)$$

$$k_L = k + k_w. \quad (27)$$

The linearized wave equation yield

$$(k_R^2 c^2 - \omega^2) \tilde{E}_R = -4\pi i e \omega \left(\tilde{n} \frac{v_w}{\sqrt{2}} + n_0 \tilde{v}_R \right), \quad (28)$$

$$(k_L^2 c^2 - \omega^2) \tilde{E}_L = -4\pi i e \omega \left(\tilde{n} \frac{v_w}{\sqrt{2}} + n_0 \tilde{v}_L \right), \quad (29)$$

$$-\omega^2 \tilde{E}_z = -4\pi i e \omega (\tilde{n} v_{\parallel} + n_0 \tilde{v}_z). \quad (30)$$

Similarly, the linearized continuity and momentum equations yield

$$\tilde{n} (\omega - k v_{\parallel}) = n_0 k \tilde{v}_z, \quad (31)$$

$$\begin{aligned} \left[\omega - k_R v_{\parallel} - \frac{\omega_i^2}{\omega - k_R v_{\parallel}} \left(1 - \frac{v_w^2}{2c^2} \right) - \frac{\omega_i^2}{k_w v_{\parallel}} \frac{v_w^2}{2c^2} + A_1 \right] \tilde{v}_R \\ + \left[\frac{\omega_i^2}{k_w v_{\parallel}} \frac{v_w^2}{2c^2} + \frac{\omega_i^2}{\omega - k_L v_{\parallel}} \frac{v_w^2}{2c^2} + A_1 \right] \tilde{v}_L + \frac{i e}{\gamma_0 m_0} \left[\left(1 - \frac{v_w^2}{2c^2} \right) - \frac{k_R v_{\parallel}}{\omega} \right] \tilde{E}_R - \frac{i e}{\gamma_0 m_0} \frac{v_w^2}{2c^2} \tilde{E}_L - \frac{i e}{\gamma_0 m_0} \frac{v_w v_{\parallel}}{\sqrt{2} c^2} \tilde{E}_z \\ + A_2 \tilde{v}_z = 0, \quad (32) \end{aligned}$$

$$\begin{aligned} \left[\omega - k_L v_{\parallel} - \frac{\omega_i^2}{\omega - k_L v_{\parallel}} \left(1 - \frac{v_w^2}{2c^2} \right) + \frac{\omega_i^2}{k_w v_{\parallel}} \frac{v_w^2}{2c^2} - A_1 \right] \tilde{v}_L \\ + \left[-\frac{\omega_i^2}{k_w v_{\parallel}} \frac{v_w^2}{2c^2} + \frac{\omega_i^2}{\omega - k_R v_{\parallel}} \frac{v_w^2}{2c^2} - A_1 \right] \tilde{v}_R + \frac{i e}{\gamma_0 m_0} \left[\left(1 - \frac{v_w^2}{2c^2} \right) - \frac{k_L v_{\parallel}}{\omega} \right] \tilde{E}_L - \frac{i e}{\gamma_0 m_0} \frac{v_w^2}{2c^2} \tilde{E}_R - \frac{i e}{\gamma_0 m_0} \frac{v_w v_{\parallel}}{\sqrt{2} c^2} \tilde{E}_z \\ - A_2 \tilde{v}_z = 0, \quad (33) \end{aligned}$$

$$\begin{aligned} -i(\omega - k v_{\parallel}) \tilde{v}_z + \frac{e}{\gamma_0 m_0} \left(1 - \frac{v_{\parallel}^2}{c^2} \right) \tilde{E}_z + \frac{e}{\gamma_0 m_0} \left[-\frac{v_w v_{\parallel}}{\sqrt{2} c^2} \right. \\ \left. + \frac{k_R c}{\omega} \frac{v_w}{\sqrt{2} c} \right] \tilde{E}_R + \frac{e}{\gamma_0 m_0} \left[-\frac{v_w v_{\parallel}}{\sqrt{2} c^2} + \frac{k_L c}{\omega} \frac{v_w}{\sqrt{2} c} \right] \tilde{E}_L \\ + i \left[\left(\frac{\omega_i^2}{k_w v_{\parallel}} - \frac{\omega_i^2}{\omega - k_R v_{\parallel}} \right) \frac{v_w v_{\parallel}}{\sqrt{2} c^2} - \frac{\Omega_w}{\sqrt{2}} \right] \tilde{v}_R \\ + i \left[\left(-\frac{\omega_i^2}{k_w v_{\parallel}} - \frac{\omega_i^2}{\omega - k_L v_{\parallel}} \right) \frac{v_w v_{\parallel}}{\sqrt{2} c^2} + \frac{\Omega_w}{\sqrt{2}} \right] \tilde{v}_L = 0, \quad (34) \end{aligned}$$

where

$$\gamma_{\parallel}^{-2} = 1 - \frac{v_{\parallel}^2}{c^2}, \quad (35)$$

$$A_L = k_L^2 c^2 - \omega^2, \quad (36)$$

$$A_R = k_R^2 c^2 - \omega^2, \quad (37)$$

$$A_1 = \left(\frac{1}{2} \right) \gamma_0^2 \frac{v_w}{c} \left(\frac{v_w}{c} \frac{\omega_i^2}{k_w v_{\parallel}} - \frac{v_{\parallel}}{c} \Omega_w \right), \quad (38)$$

$$A_2 = \left(\frac{1}{\sqrt{2}} \right) (k_w v_w + \Omega_w) + \left(\frac{1}{\sqrt{2}} \right) \gamma_0^2 \frac{v_{\parallel}}{c} \left(\frac{v_w}{c} \frac{\omega_i^2}{k_w v_{\parallel}} - \frac{v_{\parallel}}{c} \Omega_w \right). \quad (39)$$

The electron density \tilde{n} may be eliminated in (30) by use of (29) to obtain

$$\tilde{v}_z = -i \frac{\omega - k v_{\parallel}}{4\pi e n_0} \tilde{E}_z. \quad (40)$$

with the use of Eqs. (28)-(31) and (40), \tilde{v}_R , \tilde{v}_L and \tilde{v}_z may be eliminated in the three components of the momentum equation (32)-(34) to obtain

$$\left[D_R^0 + \psi_R^+ v_w^2 / c^2 \right] \tilde{E}_R + \left[\psi_L^- v_w^2 / c^2 \right] \tilde{E}_L + \left[\xi_{R1} v_w / c + M^+ v_w^3 / c^3 \right] \tilde{E}_z = 0, \quad (41)$$

$$\psi_R^- (v_w^2 / c^2) \tilde{E}_R + \left[D_L^0 + \psi_L^+ v_w^2 / c^2 \right] \tilde{E}_L + \left[\xi_{L1} v_w / c + M^- v_w^3 / c^3 \right] \tilde{E}_z = 0, \quad (42)$$

$$\xi_{R2} \left(\frac{v_w}{c} \right) \tilde{E}_R + \xi_{L2} \left(\frac{v_w}{c} \right) \tilde{E}_L - \omega \left[\varepsilon^0 + k v_{\parallel} \left(\frac{\omega_i^2}{\omega - k_L v_{\parallel}} + \frac{\omega_i^2}{\omega - k_R v_{\parallel}} \right) \frac{v_w^2}{2c^2} \right] \tilde{E}_z = 0, \quad (43)$$

where D_R^0 , D_L^0 , ψ_R^{\pm} , ψ_L^{\pm} , M^{\pm} , ξ_{R1} , ξ_{R2} , ξ_{L1} , ξ_{L2} , ε^0 are defined in the appendix. Here, D_R^0 , D_L^0 , and ε^0 are the uncoupled dispersion relations, i.e., in the absence of the wiggler, for the right and left circularly polarized electromagnetic waves, and the space-charge wave, respectively. Equations (41) and (42) show that the DR for the right and left waves, alone, in the absence of the other two waves, are

$$D_R = D_R^0 + \psi_R^+ (v_w^2 / c^2) = 0, \quad (44)$$

$$D_L = D_L^0 + \psi_L^+ (v_w^2 / c^2) = 0, \quad (45)$$

which indicate that the wiggler has direct effect on the right and left waves and the wiggler effect on their DRs are of the second order in the wiggler amplitude. On the other hand, Eq. (43) Shows that the DR for the space-charge wave in the absence of the right and left wave is $\varepsilon^0 = 0$, which indicates that the wiggler has no direct effect on the space-charge wave. The reason is that the transverse helical motion of electrons, due to the wiggler, has no effect on the longitudinal oscillations of the space-charge wave. Therefore, if the electromagnetic waves are removed the wiggler effect on the space-charge wave will

also be removed and the space-charge wave will be unaffected by the wiggler in the absence of the transverse electromagnetic waves.

The necessary and sufficient condition for a nontrivial solution consists of the determinant of coefficients in Eqs. (41)-(43) equated to zero. Imposing this condition yields the dispersion relation

$$\omega \left[\varepsilon^0 + \omega k v_{\parallel} \left(\frac{\omega_i^2}{\omega - k_L v_{\parallel}} + \frac{\omega_i^2}{\omega - k_R v_{\parallel}} \right) \right] D_R D_L = - \left[D_R \xi_{L2} \left(\xi_{L1} + M^- \frac{v_w^2}{c^2} \right) + D_L \xi_{R2} \left(\xi_{R1} + M^+ \frac{v_w^2}{c^2} \right) \right] \frac{v_w^2}{c^2} + \left[\psi_L^- \xi_{R2} \left(\xi_{L1} + M^- \frac{v_w^2}{c^2} \right) + \psi_R^- \xi_{L2} \left(\xi_{R1} + M^+ \frac{v_w^2}{c^2} \right) + \omega \varepsilon^0 \psi_L^- \psi_R^- \right. \\ \left. + \psi_L^- \psi_R^- \omega k v_{\parallel} \left(\frac{\omega_i^2}{\omega - k_L v_{\parallel}} + \frac{\omega_i^2}{\omega - k_R v_{\parallel}} \right) \right] \frac{v_w^4}{c^4}. \quad (46)$$

Equation (46) is the DR for coupled electrostatic and electromagnetic waves propagating along a relativistic electron beam in the presence of a wiggler magnetic field and an axial guide magnetic field. A numerical analysis of the general dispersion relation can be used to study interactions among all possible waves. In group II orbits, with relatively large wiggler induced velocities, new couplings between the negative and positive-energy space-charge waves as well as between the right and left circularly polarized electromagnetic waves are expected to be found. These instabilities are distinct from the usual FEL resonance.

APPENDIX: DEFINITION OF QUANTITIES

The following quantities are used in equations (41)-(43)

$$D_R^0 = \left(\omega - k_R v_{\parallel} - \frac{\omega_i^2}{\omega - k_R v_{\parallel}} \right) A_R + \omega_p^2 (\omega - k_R v_{\parallel}),$$

$$D_L^0 = \left(\omega - k_L v_{\parallel} - \frac{\omega_i^2}{\omega - k_L v_{\parallel}} \right) A_L + \omega_p^2 (\omega - k_L v_{\parallel}),$$

$$\psi_R^{\pm} = \left(\frac{1}{2} \right) \left[\left(\frac{\omega_i^2}{\omega - k_R v_{\parallel}} - \frac{\omega_i^2}{k_w v_{\parallel}} \pm \gamma_0^2 k_w v_{\parallel} \right) A_R - \omega \omega_p^2 \right],$$

$$\psi_L^{\pm} = \left(\frac{1}{2} \right) \left[\left(\frac{\omega_i^2}{\omega - k_L v_{\parallel}} + \frac{\omega_i^2}{k_w v_{\parallel}} \frac{\omega_i^2}{\omega - k_L v_{\parallel}} \mp \gamma_0^2 k_w v_{\parallel} \right) A_L - \omega \omega_p^2 \right]$$

$$M^{\pm} = \left(\frac{\omega k c}{2\sqrt{2}} \right) \left(\frac{\omega_i^2}{\omega - k_R v_{\parallel}} + \frac{\omega_i^2}{\omega - k_L v_{\parallel}} \pm 2\gamma_0^2 k_w v_{\parallel} \right),$$

$$\xi_{R1} = \left(\frac{\omega}{\sqrt{2}} \right) \left[k c \left(\omega - k_R v_{\parallel} - \frac{\omega_i^2}{\omega - k_R v_{\parallel}} \right) - \omega_p^2 \frac{v_{\parallel}}{c} \right]$$

$$\begin{aligned}
& - \left[\frac{\omega_i^2 c}{k_w v_{\parallel}^2} + \frac{\gamma_0^2 k_w v_{\parallel}}{c} \right] (\omega - k v_{\parallel}) \Big], \\
\xi_{L1} &= \left(\frac{\omega}{\sqrt{2}} \right) \left[k c \left(\omega - k_L v_{\parallel} - \frac{\omega_i^2}{\omega - k_L v_{\parallel}} \right) - \omega_p^2 \frac{v_{\parallel}}{c} \right. \\
& \quad \left. + \left(\frac{\omega_i^2 c}{k_w v_{\parallel}^2} + \frac{\gamma_0^2 k_w v_{\parallel}}{c} \right) (\omega - k v_{\parallel}) \right], \\
\xi_{R2} &= \left(\frac{1}{\sqrt{2}} \right) \left[-A_R \left(\frac{\omega_i^2}{k_w c} - \frac{\omega_i^2 c}{k_w v_{\parallel}^2} + k_w c - \frac{\omega_i^2}{\omega - k_R v_{\parallel}} \right) \right. \\
& \quad \left. + \omega_p^2 (k_R c - \omega v_{\parallel} / c) \right], \\
\xi_{L2} &= \left(\frac{1}{2} \right) \left[-A_L \left(-\frac{\omega_i^2}{k_w c} + \frac{\omega_i^2 c}{k_w v_{\parallel}^2} - k_w c - \frac{\omega_i^2}{\omega - k_L v_{\parallel}} \right) \right. \\
& \quad \left. + \omega_p^2 (k_L c - \omega v_{\parallel} / c) \right], \\
\varepsilon^0 &= (\omega - k v_{\parallel})^2 - \omega_p^2 / \gamma_{\parallel}^2.
\end{aligned}$$

REFERENCES

- [1] E. Esarey, P. sprangle, J. Krall, and A. Ting, IEEE Trans. Plasma Sci. **24** (1996) 252.
- [2] D.H. Whittum, A.M. Sessler, and J.M. Dawson, Phys. Rev. Lett. **64** (1990) 2511.
- [3] S. Wang, C.E. Clayton, B.E. Blue *et al.*, Phys. Rev. Lett. **88** (2002) 135004.
- [4] K. Takayama and S. Hiramatsu, Phys. Rev. A **37** (1988) 173.
- [5] T. Ozaki, K. Ebihara, S. Hiramatsu, Y. Kimura, J. Kishuro, T. Monaka, K. Takayama, and D.H. Whittum, Nucl. Instrum. Methods Phys. Res. A **318** (1992) 101.
- [6] L.H. Yu, A.M. Sessler, and D.H. Whittum, Nucl. Instrum. Methods Phys. Res. A **318** (1992) 721.
- [7] P. Jha and J.S. Wurtele, Nucl. Instrum. Methods Phys. Res. A **331** (1993) 477.
- [8] P. Jha and P. Kumar, IEEE Trans. Plasma Sci. **24** (1996) 1359.
- [9] P. Jha and P. Kumar, Phys. Rev. E **57** (1998) 2256.
- [10] A.A. Kordbacheh, B. Maraghechi, B. Farokhi, and J.E. Willett, Phys. Plasmas **12** (2005) 113106.
- [11] S. Mirzanejhad, P. Maraghechi, and B. Maraghechi, Phys. Plasmas **11** (2004) 3047.

ENHANCEMENT OF A COHERENT (SUPER-RADIANT) EMISSION IN FEL BY MEANS OF ENERGY MODULATION OF AN EMITTING SHORT ELECTRON BUNCH

Yu. Lurie* and Y. Pinhasi, The College of Judea and Samaria, Ariel, Israel
 A. Gover, Tel-Aviv University, Tel-Aviv, Israel

Abstract

Super-radiant emission from a wiggling short electron bunch, is strongly suppressed at high frequencies in comparison with radiation, obtained in a FEL if an ultra-short e -beam pulse of the same total charge is available. However, radiation intensity of a wiggling short electron bunch can be greatly enhanced by means of energy modulation. In this way, a super-radiant FEL source driven by short electron bunches and operating in the Tera-Hertz regime can be realized. Analytical evaluations and numerical simulations utilizing a space-frequency 3D model show, that a linear energy modulation enables one to increase the power of super-radiant emission by few orders of magnitude. Possible limitations in application of this method are also discussed, as well as a spectral purity of enhanced radiation.

INTRODUCTION

Development of experimental set-ups utilizing mechanism of short bunching of relativistic electron beams enables construction of high-power free-electron lasers (FELs) operated by a single short pulse or by a train of such pulses. Optimal efficiency of such radiation sources may be achieved with ultra-short beam pulses, when a super-radiant (SR) emission occurs (see [1, 2] and references therein).

Unfortunately, a beam pulse duration obtained in practice is still relatively long, leading to a dramatic reduction in SR emission at high frequencies. For example, in a case of Gaussian electron pulse, the super-radiant to spontaneous emission ratio at a synchronism frequency f_s is decreases with the beam duration as fast as the Gauss function [1]:

$$\text{SNR} \equiv \frac{dP_q^{sr}(z)/df}{dP_q^{sp}(z)/df} = \bar{k} \cdot e^{-(2\pi f_s T)^2} \quad (1)$$

(here \bar{k} is a number of electrons in the bunch and T is the standard deviation of the electron Gauss distribution, which corresponds to the bunch duration $\Delta T \approx 2T$). It means that to provide an intense high frequency SR emission, ultra-short electron bunches of time duration $\Delta T \ll 1/f_s$ have only to be applied. For example, with ultra-short femtoseconds bunches, intense SR emission may be obtained at radiation frequencies up to approximately 100 THz only.

* e-mail: ylurie@yosh.ac.il

It was suggested that emission of a short electron bunch of some finite duration may be greatly enhanced by means of its proper energy modulation [3]. In this work, the effect of energy modulation on SR emission of a wiggling short electron bunch is analyzed in a space-frequency 3D approach and demonstrated by numerical simulations carried out using WB3D code [4].

ANALYTICAL EVALUATIONS

The total electromagnetic field emitted by a wiggling electron bunch may be found in the frequency domain in terms of expansion over transverse eigenmodes of the medium (free-space or waveguide) in which the radiation is excited and propagates [5]:

$$\vec{E}(\vec{r}, t) = \sum_q \Re \left\{ \int_0^\infty \tilde{C}_q(z, f) \tilde{\mathcal{E}}_q(x, y) e^{+jk_{zq}(f)z} df \right\} \quad (2)$$

where $\tilde{\mathcal{E}}_q(x, y)$ is the transverse profile (Hermitte-Gaussian free-space mode or waveguide mode) of the mode q and $k_{zq}(f)$ is its wavenumber. (Although the form of mode presentation given in Eq. (2) is not valid in the far-field free-space propagation, it is still applicable to most electron devices in which the interaction takes place within a Rayleigh length of the Hermitte-Gaussian modes, where the diffraction is small). $\tilde{C}_q(z, f)$ is the propagating mode amplitude, which may be found from the excitation equation (see [4, 5] for details).

Neglecting the influence of the emitted electromagnetic field on the emitting electrons, the mode expansion coefficients $\tilde{C}_q(z, f)$ of electromagnetic field emitted by a *single wiggling electron* may be found in the following simple analytical form:

$$\tilde{C}_q(L_w, f) = \mathcal{A}_q \text{sinc} \left(\frac{1}{2} \theta_q L_w \right) e^{j(2\pi f t_0 + \frac{1}{2} \theta_q L_w)} \quad (3)$$

where \mathcal{A}_q is some normalization coefficient, $\text{sinc}(\alpha) \equiv \sin(\alpha)/\alpha$, t_0 is the time that the electron enters into the interaction region, L_w is the length of the interaction region, and

$$\theta_q \equiv \frac{2\pi f}{v_z} - (k_{zq} + k_w) \quad (4)$$

is the detuning parameter (k_w is the wiggler wave number and v_z is the electron longitudinal velocity in z -direction).

In the low-gain regime, electromagnetic field emitted by a bunch of N electrons may be given in the terms of a summation of (3) over all the electrons in the bunch:

$$\tilde{C}_q(L_w, f) = \mathcal{A}_q \sum_{p=1}^N \text{sinc}\left(\frac{1}{2}\theta_{q_p} L_w\right) e^{j(2\pi f t_{0_p} + \frac{1}{2}\theta_{q_p} L_w)} \quad (5)$$

here the coefficient \mathcal{A}_q is supposed to be approximately a constant for all the electrons in the bunch. At some synchronism frequency f_s , a coherent summation in (5) may only be obtained when $\text{sinc}\left(\frac{1}{2}\theta_{q_p} L_w\right) \approx 1$ (or $\theta_{q_p} \approx 0$, what defines the synchronism frequency f_s), and the phase matching condition $2\pi f t_{0_p} + \frac{1}{2}\theta_{q_p} L_w \approx 0$ is satisfied. A SR emission from a single ultra-short ($\Delta T \ll 1/f_s$) bunch takes place in this situation, when the radiated field is simply proportional to a number of the electrons in the bunch (to the total charge of the driving bunch): $\tilde{C}_q \approx \mathcal{A}_q \cdot N$, and energy flux spectral density of the emitted radiation may be given as

$$\frac{dW}{df} \sim |\tilde{C}_q|^2 \sim \mathcal{A}_q^2 \cdot N^2$$

As mentioned above, this energy flux is drastically reduced if the driving bunch duration is increasing compared with period $1/f_s$ of the emitted radiation. But also in this case of "finite-duration" beam bunches, the summation in (5) may still remain a partly coherent in the vicinity of synchronism frequency f_s , if the previous conditions are fulfilled in a bit modified form:

- The most part of sinc-functions in (5) save their sign: $\text{sinc}\left(\frac{1}{2}\theta_{q_p} L_w\right) > 0$, to prevent the terms compensation in the summation; and
- The phase shifts $2\pi f_s t_{0_p} + \frac{1}{2}\theta_{q_p} L_w$ remains constant.

The first condition means, that:

$$\left| \frac{2\pi f_s}{v_{z_p}} - (k_{z_q} + k_w) \right| \lesssim \frac{2\pi}{L_w}$$

Introducing

$$k_{z_q} + k_w \equiv \frac{2\pi f_s}{\beta_z c} \quad (6)$$

where $\beta_z c$ is some bunch mean longitudinal velocity in z -direction, the previous equation may be rewritten as:

$$\left| \frac{1}{\beta_{z_p}} - \frac{1}{\beta_z} \right| < \frac{\lambda_s}{L_w} \quad (7)$$

here λ_s is the radiation wave length and $\beta_{z_p} = v_{z_p}/c$. The phase-matching condition may only be satisfied, if the driving electron bunch is *pre-modulated* so that the longitudinal velocities of the electrons are distributed as follows:

$$\beta_z(t) = \beta_z \frac{L_w}{L_w - 2\beta_z c t} \quad (8)$$

where we assume that $\beta_z(t=0) = \beta_z$. Substitution of (8) into (7) provides the following limitation on the maximal bunch duration:

$$|t| < \frac{1}{2f_s} \quad (9)$$

Therefore the considered enhancement of SR emission may be obtained with as long as $\Delta T \approx 1/f_s$ beam bunches.

Condition (8) actually requires an *energy modulation* of the driving electron bunch as follows:

$$E_k(t) = m_e c^2 \left\{ \sqrt{\frac{1+a_w^2}{1-\beta_z^2/(1-2\beta_z c t/L_w)^2}} - 1 \right\} \quad (10)$$

here $a_w = eB_w/(k_w m_e c)$ is the wiggler parameter. Because

$$\left(\frac{2\beta_z c}{L_w} \right) |t| < \left(\frac{2\beta_z c}{L_w} \right) \frac{1}{2f_s} = \beta_z \frac{\lambda_s}{L_w} \ll 1$$

the distribution (10) may be linearized:

$$E_k(t) \approx E_k(t=0) + \left(\frac{dE_k}{dt} \right) \Big|_{t=0} \cdot t \quad (11)$$

where

$$E_k(t=0) \equiv m_e c^2 \left\{ \sqrt{\frac{1+a_w^2}{1-\beta_z^2}} - 1 \right\} \quad (12)$$

and the modulation rate is

$$\left(\frac{dE_k}{dt} \right) \Big|_{t=0} \approx m_e c^2 \left(\frac{2\bar{\gamma}\beta_z^3}{1-\beta_z^2} \right) \frac{c}{L_w} \quad (13)$$

here

$$\bar{\gamma} = \frac{m_e c^2 + E_k(t=0)}{m_e c^2} = \sqrt{1 - \frac{1+a_w^2}{\beta_z^2}} \quad (14)$$

So, energy modulation of a wiggling electron bunch according (10) or (11) may considerably enhance its SR emission, even if the driving bunch is as long as $\Delta T \approx 1/f_s$.

Obviously, energy modulation of the beam reduces the spectral purity of the emitted radiation in comparison with that of SR emission, emitted by an unmodulated ultra-short electron bunch. The reason is that the synchronism frequencies of radiation emitted by individual electrons are different due to difference in their kinetic energies. Therefore a bandwidth of radiation, emitted by energy modulated bunch is supposed to be more wide by a factor of $\Delta f \approx |f_s(+T) - f_s(-T)|$, so that the radiation band width may be evaluated by

$$BW \approx \frac{f_s}{N_w} + \underbrace{\frac{df_s}{dE_k} \left(\frac{dE_k}{dt} \right) \Delta T}_{\Delta f} \quad (15)$$

revealing a linear growth with the energy chirp rate dE_k/dt .

NUMERICAL SIMULATIONS

To demonstrate the effect, a number of numerical simulations with the code WB3D [4] were carried out for a THz-regime free-electron laser with operational parameters given in the table 1. Simulations demonstrate, that extremely short electron bunches ($f_s \Delta T \lesssim 2\%$) have to be applied in order to produce a strong super-radiant emission. With such ultrashort bunches, the total energy flux of super-radiant emission may be as large as $W_{SR} = 22.5$ nJ. With a longer unmodulated bunches, the total energy flux of emitted radiation is drastically reduced and it is just about $W = 4.9$ pJ when $\Delta T \approx 1.0$ pSec unmodulated bunches are applied. In accordance with analytical evaluations, a linear energy modulation (11) of the electron bunch enables one to enhance this radiation by more than a three orders of magnitude, as demonstrated in the figure 1. It is evident, that the energy modulation causes the emitted total energy flux to increase rapidly, saturating at the energy chirp rate dE_k/dt of about 0.12 MeV/pSec (resulting in the energy flux of $W_{SR} \approx 9$ nJ) and slowly reducing for a higher values of the energy chirp rates. Note, that equation (13) provides the value of $dE_k/dt \approx 0.17$ MeV/pSec. With a longer bunches ($\Delta T \approx 2.0$ pSec, $f_s T \approx 1.0$), the obtained effect is even more strong (circle symbols at the picture).

Energy spectrums of the radiation emitted by energy modulated $\Delta T=1.0$ pSec bunches are given in the figure 2, comparing to that emitted by an unmodulated ultrashort bunch (solid line) and by unmodulated $\Delta T=1.0$ pSec bunch. A spectral purity of the emitted radiation is obviously reduced if the driving electron bunch is energy modulated. At high energy chirp rates, the radiation band width grows linearly with dE_k/dt , as demonstrated at the figure 3, in accordance with above evaluation (15). It's interesting to note some non-linear dependence near the "optimal" value of the energy chirp rate $dE_k/dt=0.12$ MeV/pSec, when a high-power radiation is emitted.

To explain the effect, a microscopic analysis of trajectories of emitting electrons was carried out (see figure 4). As easily seen from the picture, a non-modulated bunch propagates through the undulator saving its initial temporal duration. Initial energy modulation of the driving bunch

Table 1: Operational parameters for THz FEL.

Accelerator

Electron beam energy: $E_k=2.8$ MeV
 Total charge: $Q = I_0 \cdot \Delta T = 10$ pC

Wiggler

Magnetic induction: $B_w=3$ kGauss ($a_w \approx 0.56$)
 Period: $\lambda_w=20$ mm
 Number of periods: $N_w=20$

Waveguide

Rectangular waveguide: 5×5 mm

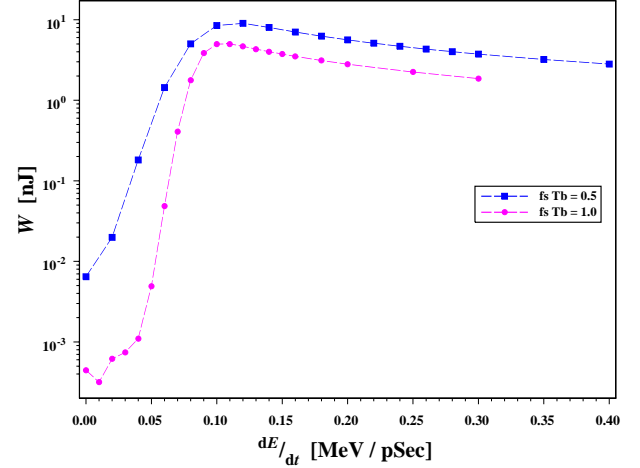


Figure 1: Total energy flux emitted by $\Delta T = 1.0$ pSec (box symbols) and $\Delta T = 2.0$ pSec (circle symbols) bunches as a function of the energy chirp rate dE_k/dt .

develops while propagating in the wiggler to a density compression and the e -beam pulse becomes an ultra-short one, generating a strong super-radiant emission. At this moment, the most intensive radiation is emitted, as may be seen from the time-domain dependence of electric component of the emitted field given in figure 5.

CONCLUSIONS

In a practical case of FEL driven by a single short bunch or by a train of such bunches, a super-radiant emission is strongly suppressed at high frequencies. It was shown that it can be greatly enhanced by means of a proper energy modulation of the driving beam. The effect is studied in the framework of space-frequency model and is explained in a

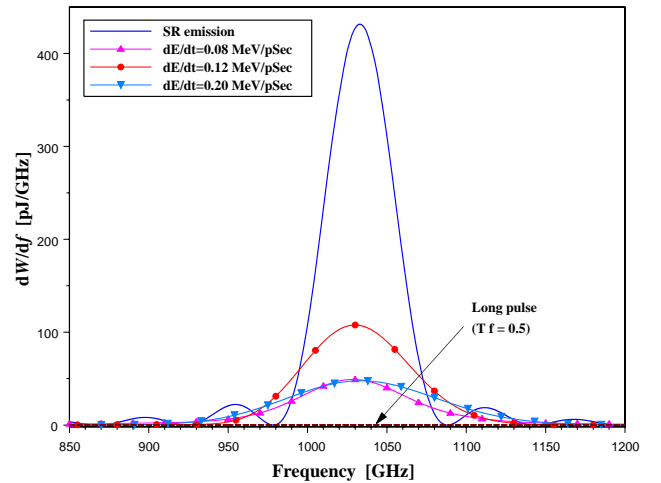


Figure 2: Total energy flux emitted by $\Delta T = 1.0$ pSec bunch as a function of the energy chirp rate dE_k/dt .

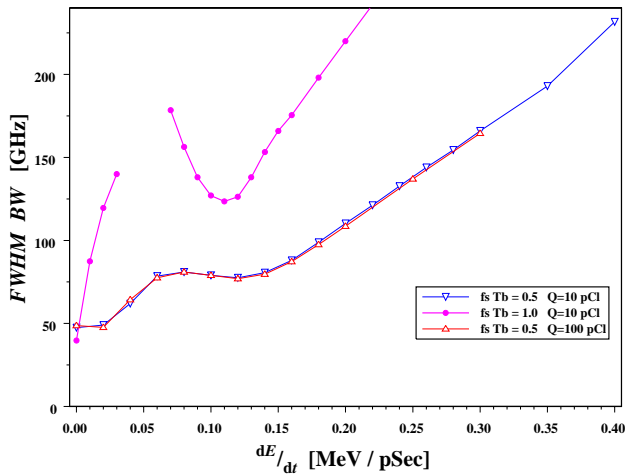


Figure 3: Full-width half-maximum radiation bandwidth as function of the energy chirp rate dE_k/dt .

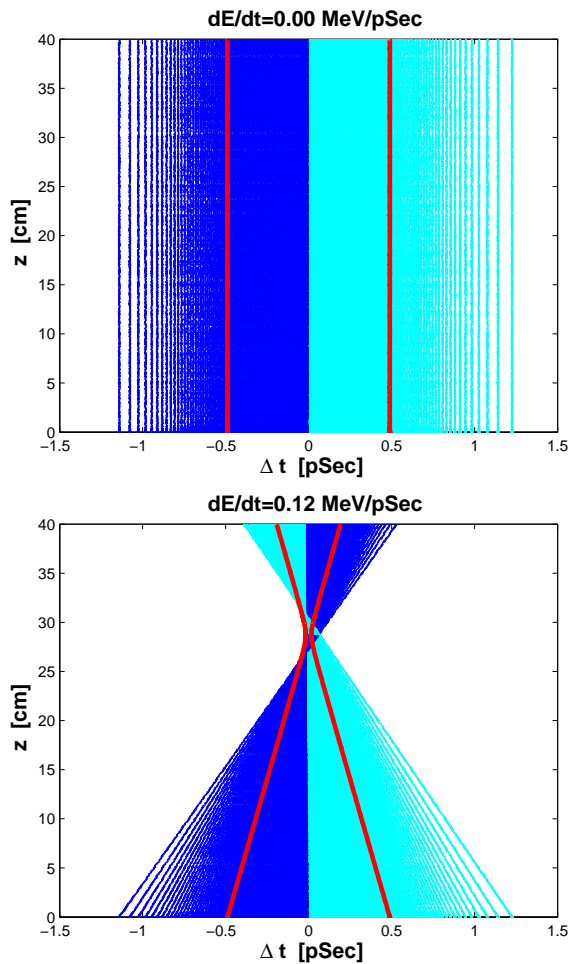


Figure 4: Trajectories of the emitting electrons in unmodulated (top) and energy modulated with $dE_k/dt=0.12$ MeV/pSec (bottom) bunches.

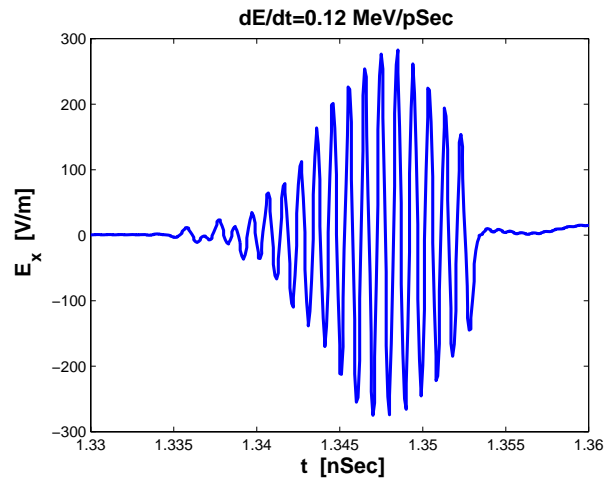
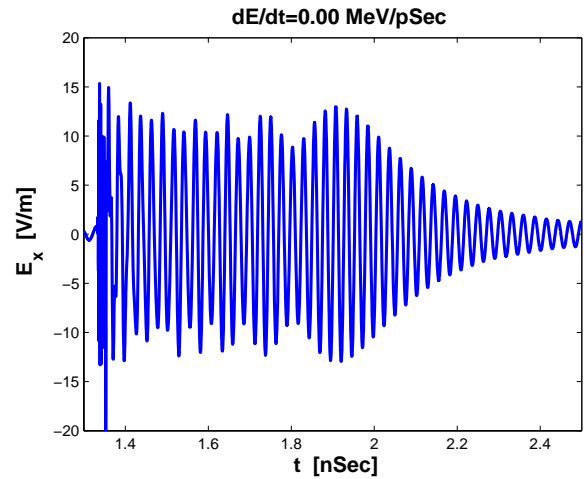


Figure 5: Time-domain electromagnetic field, emitted by unmodulated (top) and by energy modulated ($dE_k/dt=0.12$ MeV/pSec, bottom) bunches.

simple analytical approach as well as by numerical simulations with WB3D code. The considered principal scheme may be realized in a construction of a pulsed FEL, which enables to provide intensive high-frequency radiation with a reasonable spectral quality.

REFERENCES

- [1] Y. Pinhasi, and Yu. Lurie, Phys. Rev. E **65**, 026501 (2002).
- [2] A. Gover, Phys. Rev. ST Accel. Beams. **8**, 030701 (2005).
- [3] A. Doria et al., PRL **80**, 2841 (1998).
- [4] Y. Pinhasi, Yu. Lurie and A. Yahalom, Nucl. Instr. and Meth. in Phys. Res. A, **475**, 147 (2001).
- [5] Y. Pinhasi and A. Gover, Phys. Rev. E **51**, 2472 (1995).

CONTROL OF THE INTENSITY OF A WAVE INTERACTING WITH CHARGED PARTICLES

R. Bachelard, C. Chandre, X. Leoncini, M. Vittot
 CNRS Luminy, Case 907, F-13288 Marseille Cedex 9, France
 A. Antoniazzi, D. Fanelli*

Dipartimento di Energetica and CSDC, Università di Firenze, INFN, Italy

Abstract

The interaction of a wave with a beam of particles is of paramount importance in a great number of physical applications. We here focus on the case of a Free Electron Laser and review two control strategies aimed at re-shaping the inner topology of the single-particle phase-space to stabilize the oscillations of the laser intensity in the deep saturated regime.

INTRODUCTION

The interaction between a wave and a bunch of charged particles plays a central role in many branches of applied physics ranging from particle accelerators to laser physics. Generically, this self-consistent interaction leads to an exponential increase of the intensity of the wave, followed by an oscillating saturation. Oscillations are generated by the rotations in phase space of a clustered bunch of particles.

The wave-particle interaction can be cast in a Hamiltonian form with $N+M$ degrees of freedom, where N and M are respectively the number of charged particles and electromagnetic waves. Examples include the so called electron beam-plasma instability, a phenomenon of paramount importance in the wide realm of kinetic plasma turbulence, and single-pass high-gain Free Electron Lasers (FELs). In the following we shall refer to the latter case, focusing in particular on seeding schemes where a small laser signal is injected at the entrance of the undulator and guides the subsequent amplification process [1]. Basic features of the system dynamics are successfully captured within a simplified one-dimensional framework discussed in the pioneering work by Bonifacio and collaborators [2]. The Hamiltonian reads:

$$H = \sum_{j=1}^N \frac{p_j^2}{2} - \delta I + 2\sqrt{\frac{I}{N}} \sum_{j=1}^N \sin(\theta_j - \varphi), \quad (1)$$

where I and φ stands respectively for the intensity and phase of the wave, while the N conjugated pairs (p_j, θ_j) refer to the electrons. The detuning parameter δ measures the average relative deviation from the resonance condition.

As previously anticipated, the theory predicts a linear exponential instability and a late oscillating saturation for the

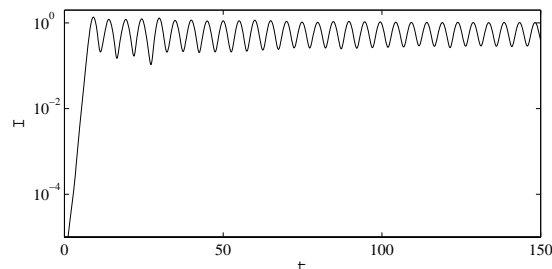


Figure 1: Normalized intensity calculated from the dynamics of Hamiltonian (1).

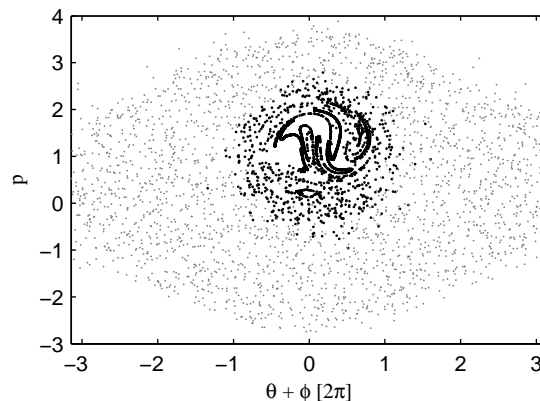


Figure 2: Snapshot of the N particles at $t = 1000$, with $N = 10^4$. The grey points correspond to the chaotic particles, the dark ones refer to the macro-particle

amplitude of the radiation field, Fig. 1. Inspection of the asymptotic phase-space, see Fig 2, suggests that a bunch of particles gets trapped in the resonance and forms a clump that evolves as a single macro-particle localized in space. The remaining particles are almost uniformly distributed between two oscillating boundaries, and populate the so called *chaotic sea* [3].

The macro-particle rotates around a well defined fixed point and this *microscopic* dynamics is shown to be responsible for the *macroscopic* oscillations observed at the intensity level. Qualitatively similar observations have been reported for the case of a Travelling Wave Tube (TWT)[4], a specially designed apparatus that mimics the plasma in-

* duccio.fanelli@ki.se

stability and enables to accurately investigate the non linear regime of the self-consistent wave-particles interaction. Given the above, it is an interesting problem to define dedicated strategies aiming at regularizing the saturated dynamics that could eventually contribute to improve the performance of the aforementioned devices.

The goal of this paper is to show that it is indeed possible to influence by an external perturbation the dynamics of the particles and enhance the stability of the system. To this end we shall consider a mean field type of approach which constitutes the natural reduction of the original N -body formulation (1). According to this simplified picture, the conjugated variables (ϕ, I) are replaced by two functions of time $\phi(t)$ and $I(t)$, the latter being obtained from direct simulations of the self-consistent dynamics. This in turn amounts to formally neglecting the action of the electrons on the field, an assumption that holds true in the late saturated regime.

The N -body Hamiltonian (1) can therefore be reduced to

$$\tilde{H}_N = \sum_{i=1}^N H_{1p}(\theta_i, p_i, t), \quad (2)$$

where

$$H_{1p}(\theta, p, t) = \frac{p^2}{2} - 2\sqrt{\frac{I(t)}{N}} \cos(\theta + \phi(t)). \quad (3)$$

In conclusion, the dynamics of a FEL can be addressed by monitoring the evolution of a *test particle*, obeying the Hamiltonian (3) where the functions $I(t)$ and $\phi(t)$ act as external fields and are here imposed by assuming their simplified asymptotic behaviour as obtained by a frequency analysis [5] :

$$2\sqrt{\frac{I(t)}{N}} e^{i\phi(t)} \approx F - \epsilon \sum_{k=1}^K W_k e^{i\omega_k t}, \quad (4)$$

in the reference frame of the wave.

TOWARD STABILIZATION: TWO ALTERNATIVE APPROACHES

Two different control strategies are here shortly discussed and shown to produce beneficial effects on stability of the system at saturation. For a detailed account on the techniques and an extensive report of the main findings, the interested reader may refer to [6] and [7].

Hamiltonian control of a test particle

First let us consider a Hamiltonian control technique. The method is based on the introduction of a small and apt modification of the potential that enables to recreate (alternatively destroy) invariant (KAM) tori in phase space. The Hamiltonian control addresses systems which are close to integrable, i.e. whose Hamiltonian can be written as $H = H_0 + V$, where H_0 is integrable and V a perturbation of order ϵ (compared to H_0). The results we use

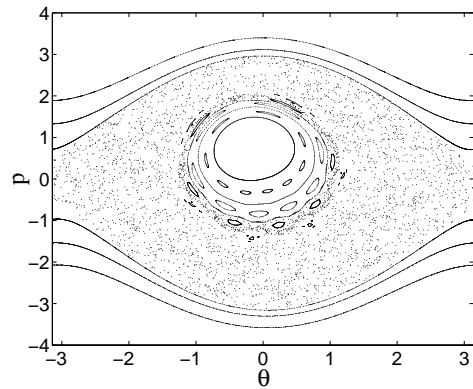


Figure 3: Poincaré sections of a test-particle of Hamiltonian $H_{1p}(\theta, p, t)$.

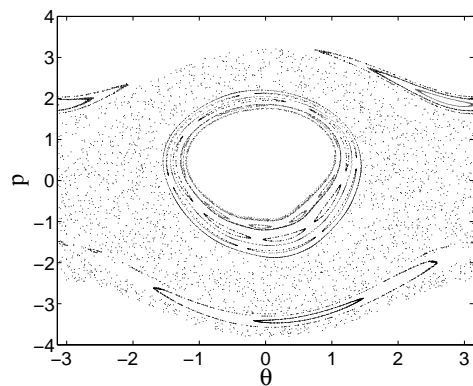


Figure 4: Poincaré sections of a *controlled* test-particle of Hamiltonian $H_{1p}(\theta, p, t) + f(\theta, p, t)$ (right).

here have been proven rigorously [8, 9]. In practice, it can be shown that a suitable *control term* f of order ϵ^2 exists such that $H_0 + V + f$ has an invariant torus at a given frequency ω_0 . In the present case, and focusing on the late saturated regime, the perturbation term is associated with the oscillating part of the intensity.

The calculation of the control term [6] is carried on into action-angle variables (φ, J) and the derivation is not explicitly reported here due to space limitations¹. Instead, we shall present results of numerical experiments which clearly demonstrate (see Figs.3 and 4), that, in (θ, p) variables the analytical control term derived in [6] is successful in reconstructing some invariant tori around the macro-particle. In other words, it enlarges the macro-particle which in turn corresponds to enhancing the bunching factor, a quantity of paramount importance in FEL context. Finally, it is worth emphasising that according to this approach the form of the control term is derived and not imposed a priori.

¹As a side remark, note that the exact change of variables from (φ, J) to (θ, p) presents a singularity at the pendulum separatrices. In order to implement our control on the whole space, a simplified, but regular, change of variables is used which mimics the exact one in the region of the invariant torus predicted by the control

The residue method

An alternative strategy can be elaborated that enables to modifying the intrinsic characteristics of the macro-particle. Contrary to the above technique, a (generic) parametrized perturbation is here a priori introduced, which allows to modify the topology of phase-space, by tuning appropriately the parameters. The residue method [10, 11, 12, 13] is used to predict the resulting local bifurcations, by an analysis of linear stability of periodic orbits. Information on the nature of these orbits (elliptic, hyperbolic or parabolic) is provided using e.g. an indicator like Greene's residue [10, 14], to monitor local changes of stability in a system subjected to an external perturbation [11, 12, 13, 15]. As we shall see, this approach enables one to tune the size, gyration radius and internal structure of the macro-particle, thus resulting in an effective tool for the stabilization of the intensity.

Consider an autonomous Hamiltonian flow with two degrees of freedom which depends on a set of parameters² $\lambda \in \mathbb{R}^m$:

$$\dot{z} = \mathbb{J} \nabla H(z; \lambda),$$

where $z = (p, E, \theta, t) \in \mathbb{R}^4$ and $\mathbb{J} = \begin{pmatrix} 0 & -\mathbb{I}_2 \\ \mathbb{I}_2 & 0 \end{pmatrix}$, and \mathbb{I}_2 being the two-dimensional identity matrix. In order to analyze the linear stability properties of the associated periodic orbits, we also consider the tangent flow written as

$$\frac{d}{dt} J^t(z) = \mathbb{J} \nabla^2 H(z; \lambda) J^t,$$

where $J^0 = \mathbb{I}_4$ and $\nabla^2 H$ is the Hessian matrix (composed of second derivatives of H with respect to its canonical variables). For a given periodic orbit with period T , the linear stability properties are given by the spectrum of the monodromy matrix J^T . These properties can be synthetically enclosed in the definition of Greene's residue :

$$R = \frac{4 - \text{tr} J^T}{4}.$$

In particular, if $R \in]0, 1[$, the periodic orbit is elliptic; if $R < 0$ or $R > 1$ it is hyperbolic; and if $R = 0$ and $R = 1$, it is parabolic.

Since the periodic orbit and its stability depend on the set of parameters λ , the features of the dynamics will change under opposite variations of such parameters. Generically, stability of periodic orbits is robust to small changes of parameters, except at specific values when bifurcations occur. The residue method [11, 12, 13] detects these rare events thus allowing one to calculate the appropriate values of the parameters leading to the prescribed behaviour in the dynamics. This method yield reduction as well as enhancement of chaos.

To illustrate the potentiality of method we shall introduce a parametrized perturbation, in the form [7]:

²At this level λ represents any generic family of parameters that influence the dynamics of the system

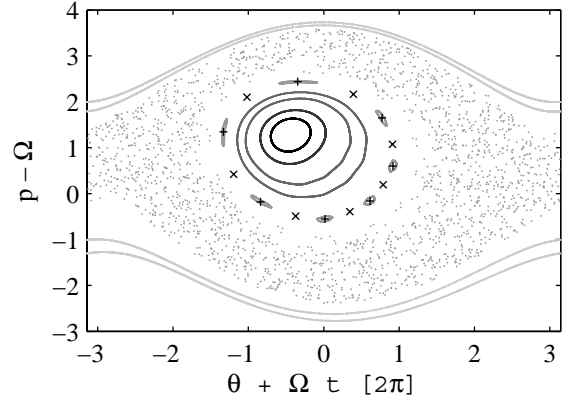


Figure 5: Poincaré section of a test-particle, described by Hamiltonian (3). The periodic orbits with r.n. 7 are marked by plus (elliptic orbit) and crosses (hyperbolic orbit). Ω stands for the wave velocity.

$$H_{1p}^c(\theta, p, t; \lambda) = H_{1p}(\theta, p, t) - 2\lambda \sqrt{\frac{I(t)}{N}} \cos(2\theta + \phi(t)). \quad (5)$$

Here λ controls the amplitude of the injected wave. Focus then on $\lambda = 0$, which corresponds to the original Hamiltonian H_{1p} , and consider two coupled Birkhoff periodic orbits, i.e. orbits having the same action but different angles in the integrable case and having the same rotation number (r.n.) on the Poincaré section, one elliptic \mathcal{O}_e and one hyperbolic \mathcal{O}_h (see Fig. 5)³.

Call R_e and R_h the residues of these orbits: We have $R_e(0) > 0$ and $R_h(0) < 0$. We then modify the parameter λ until the following condition is matched :

$$R_e(\lambda_c) = R_h(\lambda_c) = 0, \quad (6)$$

at $\lambda_c = -0.0370$ [7]. Bifurcation (6) is associated with the creation of an invariant torus [13]. This diagnostic is confirmed by the Poincaré section (see Fig.6) of the *controlled* Hamiltonian (5), at $\lambda = \lambda_c$: The elliptic islands with r.n. 7 have been replaced by a set of invariant tori, leading to an enlargement of the macro-particle. Note that elliptic islands with r.n. 6 are now present around the regular core.

The associated couple of elliptic/hyperbolic orbits can be treated similarly as those of r.n. 7, in order to gain further enlargement of the macro-particle (not reported here).

The control is naturally introduced in the self-consistent dynamics as :

$$H_N^c(I, \phi, p_i, \theta_i, \lambda) = H_N(I, \phi, p_i, \theta_i) - 2\lambda \sqrt{\frac{I}{N}} \sum_i \cos(2\theta_i + \phi) \quad (7)$$

³Let us recall that the rotation number (or winding number) of a periodic orbit is the number of times it crosses the Poincaré section before closing back on itself

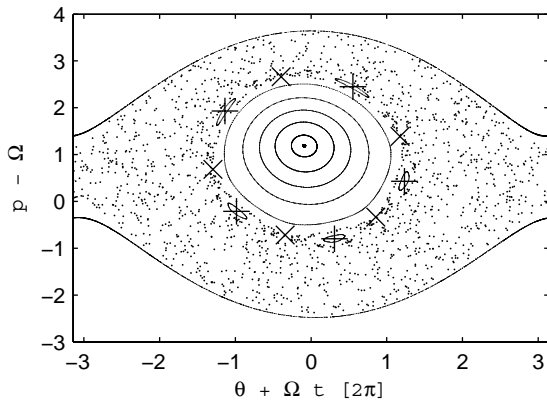


Figure 6: Poincaré section of a controlled test-particle of Hamiltonian (5), with $\lambda = \lambda_c \approx -0.0370$. The periodic orbits with r.n. 6 are marked by plus (elliptic orbit) and crosses (hyperbolic orbit). Ω stands for the wave velocity.

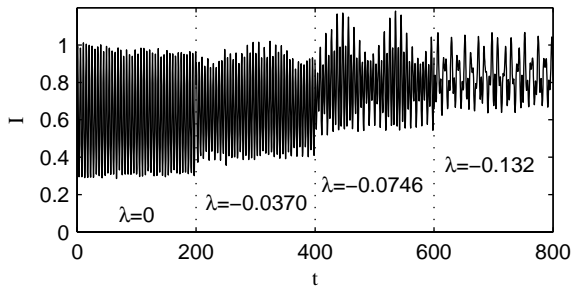


Figure 7: Intensity of the wave at saturation, in the four regimes : $\lambda = 0, -0.037, -0.0746$ and -0.1321 . Further improvements over this condition are discussed in [7]

where H_N is given by Eq. 1. The behaviour of the system is investigated in correspondence of the critical values ($\lambda_c, \lambda'_c, \lambda''_c$) which have been calculated in the framework of the test-particle model, and identifying successive corrections as outlined in the preceeding discussion. Importantly, the macro-particle is shown to increase also when operating within the relevant self-consistent context. As concerns the wave, the control results in a stabilization of its intensity (see Fig.7) [7].

CONCLUSIONS

In this paper, we focus on the physics of the wave-particle interaction and consider in particular the case of a FEL. Control techniques are developed in the framework of a simplified mean-field description aiming at stabilizing the laser behavior at saturation. In both cases, the size of the macro-particle is shown to be increased by adding a small pertubation to the system. These procedures result in a low-cost correction in term of energy⁴. Both ap-

proaches are utterly general and could be eventually considered to define innovative strategies aimed at adjusting the size of the macro-particle, and consequently enhancing the bunching factor. In this respect, it is worth stressing that an experimental test of the Hamiltonian control method on a modified Travelling Wave Tube has been performed [16] in absence of self-consistency. Exploring the possibility of experimentally implementing the above control terms in both FEL and TWT contexts will be addressed in future research.

REFERENCES

- [1] L.H. Yu et al., *Science* **292**, 2037 (2003).
- [2] R. Bonifacio, *et al.*, *Rivista del Nuovo Cimento* **3**, 1 (1990).
- [3] A. Antoniazzi, Y. Elskens, D. Fanelli and S. Ruffo, *Europ. Phys. J. B*, *in press* (2006).
- [4] Y. Elskens, D. Escande, *Microscopic Dynamics of Plasmas and Chaos* IoP Publishing, Bristol (2003).
- [5] J. Laskar, *Proc. of NATO ASI Hamiltonian Systems with Three or More Degrees of Freedom*, (C. Simò Ed, Kluwer) 134 (1999).
- [6] R. Bachelard, A. Antoniazzi, C. Chandre, D. Fanelli, M. Vittot, *Comm. in Nonlinear Sci. and Num. Simu. in press* (2006).
- [7] R. Bachelard, A. Antoniazzi, C. Chandre, D. Fanelli, X. Leoncini, M. Vittot, preprint nlin/0609030 (2006).
- [8] Vittot, M. (2004). Perturbation theory and control in classical or quantum mechanics by an inversion formula. *J. Phys. A: Math. Gen.*, **37**, pp. 6337-6357.
- [9] Chandre C., M. Vittot, G. Ciraolo, Ph. Ghendrih, R. Lima (2006). Control of stochasticity in magnetic field lines. *Nuclear Fusion*, **46**, pp. 33-45.
- [10] J.M. Greene, *J. Math. Phys.* **20**, 1183 (1979).
- [11] J. Cary, J.D. Hanson, *Phys. Fluids* **29**(8), 2464 (1986).
- [12] J.D. Hanson, J. Cary, *Phys. Fluids* **27**(4) 767 (1984).
- [13] R. Bachelard, C. Chandre, X. Leoncini, *Chaos* **16** 023104 (2006).
- [14] R.S. MacKay, *Nonlinearity* **5** 161 (1992).
- [15] J.E. Howard, R.S. MacKay, *J. Math. Phys.* **28** 1036 (1987).
- [16] Chandre, C., G. Ciraolo, F. Doveil, R. Lima, A. Macor and M. Vittot (2005). Channeling chaos by building barriers. *Phys. Rev. Lett.*, **74**, 074101.

⁴As concerns the method of residues, the fact that the applied corrections are indeed small is confirmed by the values of λ that are calculated for the various setting considered above.

FREE ELECTRON LASER AS A PARADIGMATIC EXAMPLE OF SYSTEMS WITH LONG-RANGE INTERACTIONS

A. Antoniazzi, D. Fanelli, S. Ruffo

Dipartimento di Energetica and CSDC, Università di Firenze, INFN, Italy

J. Barré, T. Dauxois, ENS, Lyon, France

G. De Ninno, Sincrotrone Trieste, Trieste, Italy

Abstract

We here shortly review the field of long-range interactions and presents selected issues of fundamental interest for statistical mechanics and dynamical systems theory. Applications to the case of a Single-Pass Free Electron Laser are discussed.

INTRODUCTION

Physical systems are constituted by interacting elements, point particles or atoms. In presence of short-range couplings, every element is solely sensitive to the adjacent environment, being therefore uniquely subjected to the interaction with local neighbors. Conversely, when long-range forces are to be considered, the direct coupling of each element to every other element in the system must be taken into account (the system is dominated by *mean-field* effects). This crucial distinction is responsible for the enhanced degree of complexity in the treatment of long-range systems when compared to short-range ones.

Moreover, basic concepts in physics, notably in the framework of equilibrium statistical mechanics, have been developed only for short range interactions. The potential interest of such tools is however very broad since for all fundamental interactions in nature (with the exception of gravity), screening mechanisms manifest, resulting in effective short-range couplings. For this reason, it has essentially only been in the context of astrophysics and cosmology that the very specific and difficult features of long-range interactions have been tackled. Recently, however, a growing number of physical laboratory systems have emerged in which the interactions are truly long-range, e.g. unscreened Coulomb interactions, vortices in two-dimensional fluid mechanics, wave-particle systems relevant to plasma physics and Free-Electron Lasers (FELs). These developments gave new impetus [1] to attempts aiming at describing the peculiar behaviour of long-range interacting systems, in a context where, in contrast to astrophysics, laboratory experiments are possible. Moreover, a number of “toy models” have been proposed that provide the ideal ground for theoretical investigations. Among others, the Hamiltonian Mean Field (HMF) model [2] is nowadays widely analyzed for pedagogical reasons, because of its intrinsic simplicity.

In presence of long-range interactions, physics is in fact very peculiar and a wide range of striking and curious phe-

nomena appears. Importantly, energy is non additive, hence the system under scrutiny cannot be divided into independent macroscopic parts, as it is usually the case for short-range interactions. This fact leads to unexpected consequences when performing the analysis in terms of statistical mechanics.

Single-pass FELs constitute an example of systems with long-range interactions, where the interplay between collective (wave) and individual (particles) degrees of freedom is well known to be central. This interplay being essentially non dissipative, its prototype is described by a self-consistent Hamiltonian [3], which provides a clear and intuitive picture of the basic mechanisms that drive the process of light amplification and saturation. In this respect, FELs provides a very general experimental ground to investigate the universal features that characterize systems with long range interactions.

In this paper we shall present a short review of recent progress in this field of research by focusing in particular on the relevant case of a Single Pass FEL. A wider overview on long range systems can be found in Ref. [1].

DEFINITION OF LONG-RANGE SYSTEMS

Let us consider the potential energy U of a given particle positioned in the center of a sphere of radius R . Assume that the matter is homogeneously distributed with density ρ and introduce a lower cut-off $\varepsilon \ll R$, as depicted in Fig. 1. Focusing on the case where the interaction potential decays at large distances with a power-law with exponent α , one gets:

$$\begin{aligned} U &= \int_{\varepsilon}^R \rho \left[\frac{1}{r^{\alpha}} \right] 4\pi r^2 dr = \\ &= 4\pi\rho \int_{\varepsilon}^R r^{2-\alpha} dr \propto [r^{3-\alpha}]_{\varepsilon}^R \sim R^{3-\alpha}, \end{aligned}$$

Clearly, the above energy diverges with R if the exponent α is smaller than 3, which in turn corresponds to the dimension of the physical space where the interaction is embedded.

This argument holds true in any dimension d , implying that similar divergences are found when $\alpha \leq d$. We hence define the interaction to be *long-range* if $\alpha \leq 3$ (resp. $\alpha \leq d$). Equivalently, it can be said that the contribution to the

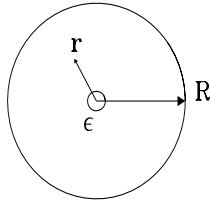


Figure 1: The energy in a sphere of radius R diverges as $R^{3-\alpha}$ if the interaction is long-range and $\alpha \leq 3$.

energy due to the surface of the sphere with respect to the bulk can be safely neglected *only if* $\alpha > 3$. In the latter case, the interaction is of the *short-range* type.

As anticipated in the preceding discussion, long-range forces arise in many different contexts. Few physical examples of broad relevance are listed below:

- **Gravity:** $\alpha = 1, d = 3$. In addition to the long range nature of the interaction, the system displays a singularity at the origin that needs to be carefully tackled by involving dedicated regularization schemes.
- **Coulomb interactions:** $\alpha = 1, d = 3$.
- **Dipolar interactions:** $\alpha = 3, d = 3$. The shape-dependence phenomenon is found, which makes the energy dependent on the form of the sample.
- **Onsager's 2D vortex systems or 2D Coulomb systems.** Here $\alpha = 0$, because the interaction decays logarithmically, and $d = 2$.
- **Mean-Field:** $\alpha = 0$, due to the infinite-range interaction, and any d . This latter category does not reflect a pure physical example, but rather a useful (and common) approximation to which one resorts when treating complex problems. In fact, it provides the ideal setting to gain insight into a number of different physical problems and eventually enables to perform analytical calculations. As we shall see, Single Pass FELs can be effectively described by resorting to a mean-field type of approach.

THE PROBLEM OF ADDITIVITY

The long range nature of the interaction reflects in a number of peculiar phenomena which will be shortly reviewed in the forthcoming sections. Such curious behaviours are intrinsically connected to the *non additivity* of the system, a crucial concept that one can illustrate with reference to a specific case, namely the Curie-Weiss model of magnetism. Consider the following Hamiltonian:

$$H = -\frac{J}{2N} \sum_{i,j} S_i S_j, \quad (1)$$

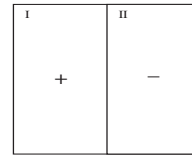


Figure 2: A microscopic configuration with total zero magnetization, illustrating the lack of additivity in the Curie-Weiss model.

where $S_i = \pm 1$ labels a spin variable, J is the ferromagnetic coupling and the sum extends over all pairs spins, N being their total number. Note that Hamiltonian (1) is *extensive*, since $H \propto N$, but, as we shall see, *not additive*.

Refer, in fact, to the situation schematized in Fig. 2 where all the spins in the left portion of the space are equal to 1, whereas the ones in the right are assumed to be -1 . Under this conditions the energy of the two regions reads $E_I = E_{II} = -(J/8)N \neq 0$. Conversely, when computing the total energy, one finds $E = -J/(2N)(N/2 - N - 2)^2 = 0$. The relation $E = E_I + E_{II}$ does not hold, and consequently the system is not additive. The underlying reason is that the above Hamiltonian is long range, since every spin interacts with all the others. This in turn implies that the energy at the interface cannot be neglected, the latter being of the same order of the energies in the two bulks. As a side remark, we shall note that the lack of additivity affects dramatically the usual construction of the canonical ensemble, and therefore peculiar behaviours are to be expected for a long-range system in contact with a thermal reservoir. Next paragraph is devoted to a short account on this topic.

THERMODYNAMICS PECULARITIES

As previously pointed out, the non-additivity issue is responsible for a number of important and non trivial consequences. As soon as first order phase transitions are present, “convex intruders” in the microcanonical entropy appear [4, 5]. A typical situation is displayed in Fig 3. Only if interactions are short-range and, hence, the additivity property holds, the states in the convex entropy region $\epsilon_1 < \epsilon < \epsilon_2$ of Fig 3a are unstable, when compared to those obtained by combining, in appropriate portions, the two limiting states with energies ϵ_1 and ϵ_2 . This is not the case if long-range interactions are to be considered and additivity is violated. The presence of stable, non-concave, entropy regions implies the appearance of *negative specific heat* in the microcanonical ensemble. As an immediate consequence *statistical ensembles are not equivalent*, since the specific heat is always positive in the canonical ensemble. Note that, *large deviation techniques* allow one to solve, both in the microcanonical and in the canonical ensemble, a large class of mean-field models and constitute therefore a powerful tool to detect possible discrepancies.

Another intriguing effect is related to temperature jumps, as depicted in Fig. 3b. In this case, two branches of the

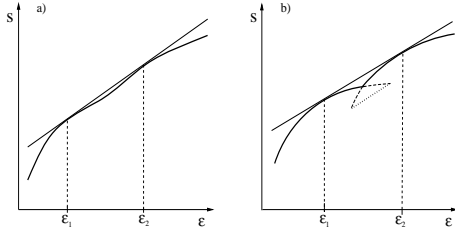


Figure 3: (a) Entropy $s(\epsilon)$ can be non-concave in the microcanonical ensemble, giving rise to negative specific heat. (b) In the non-concave region, entropy can develop kinks in the slope, creating temperature jumps.

entropy exist, respectively a high and a low energy ones. When crossing each other, they generically form an angle: this sets the origin of the temperature jumps, the derivative of the entropy with respect to energy being different on the two sides of the intersection point.

NON-LINEAR DYNAMICAL ASPECTS

In this Section we shall shortly report about a selection of peculiar dynamical features, which are generically encountered when dealing with long-range interacting systems. First, the existence of *quasi-stationary states* has been often discussed in the literature with reference to various test models. Particularly important is the case of the so called Hamiltonian Mean Field (HMF) model [2], which describes the motion of N coupled rotators and is characterized by the following Hamiltonian

$$H = \frac{1}{2} \sum_{j=1}^N p_j^2 + \frac{1}{2N} \sum_{i,j=1}^N [1 - \cos(\theta_j - \theta_i)] \quad (2)$$

where θ_j represents the orientation of the j -th rotor and p_j is its conjugate momentum. Note that the HMF model corresponds to the XY model with $J = 1, K = 0$. To monitor the evolution of the system, it is customary to introduce the magnetization, a global order parameter defined as $M = |\mathbf{M}| = |\sum \mathbf{m}_i|/N$, where $\mathbf{m}_i = (\cos \theta_i, \sin \theta_i)$ is the local magnetization vector. A second order phase transition is found at $\epsilon_c = E_c/N = 0.25$ ($T_c = 0.5$). For energy close to the transition value, the finite N system can remain trapped in *quasi-stationary states* whose life-time increases with a power of N . An example of the evolution of magnetization from an initial homogeneous (non-magnetized) water-bag state to the final maximum entropy state is displayed in Fig. 4. As N is increased the lifetime of the non-equilibrium quasi-stationary state increases: curves with growing N go from left to right. Importantly, in this intermediate regime, the magnetization is lower than predicted by the Boltzmann–Gibbs equilibrium and the system apparently displays non Gaussian velocity distributions. The above phenomena can be successfully interpreted in the framework of the statistical theory of the Vlasov equation [6], a wide general approach originally in-

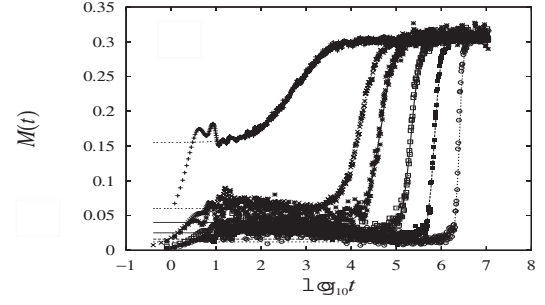


Figure 4: Temporal evolution of the magnetization $M(t)$ for different particles numbers: $N = 10^2(10^3), 10^3(10^2), 2.10^3(8), 5.10^3(8), 10^4(8)$ and $2.10^4(4)$ from left to right (the number between brackets corresponding to the number of samples).

roduced in the astrophysical and 2D Euler turbulence contexts [7, 8].

Finally, let us mention that recently [9], in analyzing a Ising model with both short and long-range interactions on a ring, it has been realized that the accessible region of extensive parameters (energy, magnetization, etc.) may be non convex. This implies that *broken ergodicity* can appear, due to the fact that the accessible magnetization states at a given energy can be disconnected.

THE CASE OF A SINGLE-PASS FEL

For Single-Pass FEL amplifiers, the Colson-Bonifacio [3] model applies:

$$\frac{d\theta_j}{d\bar{z}} = p_j \quad (3)$$

$$\frac{dp_j}{d\bar{z}} = -\mathbf{A}e^{i\theta_j} - \mathbf{A}^*e^{-i\theta_j} \quad (4)$$

$$\frac{d\mathbf{A}}{d\bar{z}} = i\delta\mathbf{A} + \frac{1}{N} \sum_j e^{-i\theta_j} \quad (5)$$

The complex field amplitude \mathbf{A} is the degree of freedom associated to the wave, while θ_i, p_i are the conjugate variables related to the electron position and “momentum”. \bar{z} is the (rescaled) longitudinal position along the undulator, N is the number of electrons and δ stands for the so-called detuning parameter. The above model can be derived from the *mean-field* Hamiltonian

$$H_N = \sum_{j=1}^N \frac{p_j^2}{2} - N\delta I^2 + 2I \sum_{j=1}^N \sin(\theta_j - \varphi), \quad (6)$$

where $\mathbf{A} = I \exp(-i\varphi)$. In this respect, FELs fall naturally in the realm of systems with long-range interactions.

The microcanonical equilibrium entropy of this model can be obtained using large deviation techniques [10]. Ensembles are equivalent, no negative specific heat or temperature jump appears. However, the evolution towards the maximum entropy equilibrium state is highly non trivial, as shown in Fig. 5, and shares many similarities with

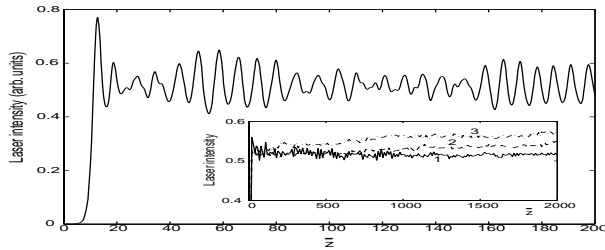


Figure 5: Typical evolution of the radiation intensity using Hamiltonian (6). The detuning δ is set to 0, the energy per electron $H/N = 0.2$ and $N = 10^4$ electrons are simulated. The inset presents averaged simulations on longer times for different values of N : $5 \cdot 10^3$ (curve 1), 400 (curve 2) and 100 (curve 3).

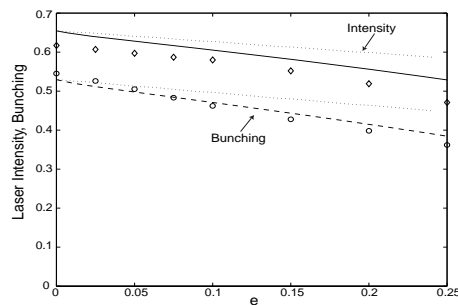


Figure 6: Comparison between theory (solid and long-dashed lines) and simulations (symbols) for a non monoenergetic beam when the energy (e) characterizing the initial velocity dispersion of the initial electron beam, is varied. The dotted lines represent the intensity and bunching ($b = |\sum_j e^{i\theta_j}|/N$) predicted by the full (Boltzmann-Gibbs) statistical equilibrium, not very appropriate here, whereas the solid line and long-dashed lines refer to the Vlasov equilibrium [10]. The discrepancy between theory and numerical experiments is small over the whole range of explored energies.

the case of the HMF. After the initial exponential growth, the system converges to a *quasi-stationary state* that gets more pronounced when increasing the number of simulated electrons N . Finally it relaxes to the Boltzmann-Gibbs equilibrium, driven by granularity. The intermediate quasi-stationary state is indeed the only experimentally relevant regime, due to the finite extension of the undulators. As already pointed out, the latter state, is a *Vlasov equilibrium*, sufficiently well described by Lynden-Bell's Fermi-like distribution arising from "violent relaxation" (constrained maximum entropy principle) [7, 8, 10, 11]. Results reported in Fig. 6 provide a clear support to this conclusion.

CONCLUSIONS

In this paper, we discussed the concept of long-range interactions and shortly reviewed the fundamental properties of such systems. In particular, microcanonical and canonical ensembles disagree for long range interactions at canonical first order transitions. Negative specific heat and temperature jumps are typical signatures of this ensemble inequivalence. Dynamical non equilibrium features arise, and more specifically, *quasi-stationary* states, where the system gets trapped for long times. Their life-time increases in fact with the system size N . Moreover, as an indirect signature of non-additivity, broken ergodicity manifests as a generic feature of systems with long-range interactions.

Further we focused on a simple model of the Free Electron Laser dynamics, which shares many similarities with the so called Hamiltonian Mean Field model, a paradigmatic toy-model often referred to for theoretical applications. For the case of the FEL, we have shown that collective phenomena for wave-particle interactions can be successfully interpreted through a constrained maximum entropy principles of the associate Vlasov system. Given the above, it is here anticipated that FELs will constitute a promising experimental set up to investigate the universal peculiarities that characterize systems with long range interactions.

REFERENCES

- [1] T. Dauxois, S. Ruffo, E. Arimondo and M. Wilkens (eds), *Dynamics and thermodynamics of systems with long-range interactions*, Lecture Notes in Physics 602 (Springer, Berlin, 2002).
- [2] M. Antoni and S. Ruffo, *Phys. Rev. E* **52** (1995) 2361.
- [3] W. B. Colson, *Phys. Lett. A* **59**, 187 (1976); R. Bonifacio et al., *Opt. Comm* **50**, 373 (1984).
- [4] J. Barré, D. Mukamel and S. Ruffo, *Phys. Rev. Lett.* **87** (2001) 030601.
- [5] D. H. E. Gross, *Microcanonical Thermodynamics: Phase Transitions in Small Systems*, Lecture Note in Physics, **66**, World Scientific, Singapore (2001).
- [6] A. Antoniazzi, D. Fanelli, J. Barré, P.H. Chavanis, T. Dauxois, S. Ruffo, submitted to *Phys. Rev. Lett.*, cond-mat/0603813 (2006)
- [7] D. Lynden-Bell, *Monthly Notices of the Royal Astronomical Society* **136**, 101 (1967).
- [8] P.H. Chavanis, J. Sommeria, R. Robert, *Astrophys. J.*, **471**, 385 (1996).
- [9] D. Mukamel, S. Ruffo and N. Schreiber, *Phys. Rev. Lett.* **95**, 240604 (2005)
- [10] J. Barré, T. Dauxois, G. De Ninno, D. Fanelli, S. Ruffo, *Phys. Rev. E, Rapid Comm.* **69** (2004) 045501.
- [11] F. Curbis, A. Antoniazzi, G. De Ninno, D. Fanelli, submitted to *Phys. Rev. E* (2006)

OVERVIEW OF PERSEO, A SYSTEM FOR SIMULATING FEL DYNAMICS IN MATHCAD

L. Giannessi, ENEA C. R. Frascati, Via E. Fermi 45, 00044 Frascati (Rome) Italy.

Abstract

Perseo is a library of functions devoted to the simulation of FEL dynamics in the *Mathcad* environment. Functions for the generation of phase space variables, for the solution of the pendulum-like equation and for manipulating the phase space in a number of devices are available. These function can be combined in order to model more complicated situations as time dependent simulations, 3D simulations, oscillator FEL configurations, optical klystron, cascaded FELs ...

INTRODUCTION

Mathematical computer aided scratchpads which integrate standard mathematical notation, text, graphs and programming capabilities in worksheets as *Mathcad* or *Mathematica* and *Matlab*, are widespread tools in the scientific community. Nowadays computers are fast enough to execute interactively from start-up to saturation an FEL simulation involving a few thousands macro-particles. This suggested to develop a set of basic functions which can be called from within the *Mathcad* environment, devoted to solve FEL dynamics related problems. The result is *Perseo*[1], a flexible tool that can be simply programmed to set up FEL simulations in a wide variety of configurations.

THE FEL MODEL IN PERSEO

The core of the library consists of a routine solving the pendulum-like FEL equations coupled with the field equations which govern the FEL longitudinal dynamics [2,3]. This routine includes self consistently the field variables for the higher order harmonics. In this picture the field is the superposition of slowly varying complex amplitudes $a_n = |a_n| e^{i\varphi_n}$ for each harmonic n , $E(z, t) = \sum_n \tilde{E}_n |a_n| e^{i(k_n z - \omega_n t + \varphi_n)}$. The parameters \tilde{E}_n link the dimensionless field amplitude a_n to the field at the harmonic n . They may be defined in terms of the saturation intensity [4] as $\tilde{E}_n = \sqrt{z_0 I_s(n) / 4\pi}$ where z_0 is the vacuum impedance. In a linear undulator the n^{th} harmonic saturation intensity is defined as $I_s(n) = 1 / (4\pi) (m_0 c^3 / r_0) (\gamma / N)^4 (\lambda_u K f_b(n, \xi))^{-2}$ where γ is the beam energy in $m_0 c^2$ units, λ_u is the undulator period, N is the number of undulator periods, K is the undulator parameter. The function $f_b(n, \xi) = J_{(n-1)/2}(\xi) - J_{(n+1)/2}(\xi)$ where $\xi = K^2 / 4(1 + K^2/2)$, is the Bessel factor arising from the average over the longitudinal fast motion typical

of linear undulators. The evolution of the amplitudes a_n is governed by the equations:

$$\begin{aligned} \frac{\partial \text{Re}(a_n(\tau))}{\partial \tau} &= -2\pi g_n \langle \cos(in\vartheta_i(\tau)) \rangle_i \\ \frac{\partial \text{Im}(a_n(\tau))}{\partial \tau} &= 2\pi g_n \langle \sin(in\vartheta_i(\tau)) \rangle_i \end{aligned} \quad (1)$$

where the variable $\tau = \beta_z c t / L_u$ is a dimensionless interaction time, $L_u = N\lambda_u$ is the undulator length and $c\beta_z$ is the longitudinal beam velocity. The phase $\vartheta_i = (k_L + k_u)z_i - \omega_L t$ is the electron phase in the ponderomotive bucket corresponding to the first harmonic field ($n=1$, $k_L = \omega_L/c = k_1 = 2\pi/\lambda_1$ is the wave-vector corresponding to the first harmonic and $k_u = 2\pi/\lambda_u$ is the wave-vector associated to the undulator period). The coupling coefficients at the odd harmonics g_n are given by [3]

$$g_n = 2\pi \left(\frac{N}{\gamma} \right)^3 [\lambda_u K f_b(n, \xi)]^2 \frac{I_{peak}}{I_A \Sigma_b} \quad (2)$$

where I_{peak}/Σ_b is the electron current density and I_A is the Alfvén current. The i^{th} particle motion is governed by pendulum-like equations:

$$\begin{aligned} \frac{d\vartheta_i}{d\tau} &= \nu_i \\ \frac{d\nu_i}{d\tau} &= \sum_n \cos(n\vartheta_i) \text{Re}(a_n) - \sin(n\vartheta_i) \text{Im}(a_n) \end{aligned} \quad (3)$$

where $\nu_i = 2\pi N (\omega_i - \omega_L) / \omega_i$ represents the frequency shift of the i^{th} particle resonance $\omega_i/c = 2\gamma_i^2 k_u / (1 + K^2/2)$ from the reference frequency ω_L . Note that the above choice for the coefficients (\tilde{E}_n, g_n) leads to the expression (3) for the particles dynamics, where all the harmonics in the expression of $d\nu_i/d\tau$ have the same weight factor. Analogous expressions for the helical undulator are easily obtained by substituting $f_b(n=1, \xi) = 1$, $K \rightarrow K_{helical} = \sqrt{2}K$ in (2) and in the definition of $I_s(n)$, and neglecting the higher order harmonic coupling ($f_b(n \neq 1, \xi) = 0$) in (2).

In the following we will analyze the subset of functions that are necessary for setting up a simple FEL simulation

in the *Mathcad* environment. Some knowledge of the basic *Mathcad* language is assumed [5].

The function FELPendulum_h

In *Perseo* the coupled equations (2) and (3) are solved by calling the function:

$$PHSP_{new} := FELPendulum_h(PHSP_{old}, g, \tau_0, \tau_1, tol) \quad (4)$$

This function integrates the coupled system of equations (2) and (3) with the coupling coefficients g (g is indeed an array with number of components equal to the number of simulated harmonics) advancing the system from τ_0 to τ_1 with tolerance tol . The variables $PHSP_{new}$ and $PHSP_{old}$ represent the status of the system before and after the integration and are defined as:

$$PHSP = \begin{pmatrix} n_h & \text{not used} \\ \text{Re}(a_1) & \text{Im}(a_1) \\ \vdots & \vdots \\ \text{Re}(a_{n_h}) & \text{Im}(a_{n_h}) \\ v_1 & \vartheta_1 \\ \vdots & \vdots \\ v_{n_p} & \vartheta_{n_p} \end{pmatrix} \quad (5)$$

The first line contains the number of harmonics n_h , then n_h lines contain the real and imaginary part of the field at each harmonic, followed by the coordinates (v, ϑ) of an arbitrary number of simulated particles n_p .

The function FELquietstart_h

The variable $PHSP$ may be prepared by filling the matrix with the desired field values and particles coordinates, but a more convenient way is that of using the function

$$PHSP := FELquietstart_h(v_0, \sigma_v, n_v, \vartheta_0, \vartheta_1, n_\vartheta, a) \quad (6)$$

that fills the variable $PHSP$ with $n_p = n_v \cdot n_\vartheta$ particles, n_v particles in the v space, over a Gaussian centred in v_0 with r.m.s. σ_v , and n_ϑ particles distributed uniformly in the interval $(\vartheta_0, \vartheta_1)$.

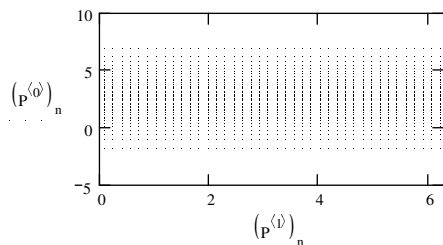


Figure 1: Phase space distribution obtained by calling the function *FELquietstart_h* with $v_0=2.6$, $\sigma_v=2$, $n_v=40$, $\vartheta_0=0$, $\vartheta_1=2\pi$, $n_\vartheta=40$.

A quiet start distribution is obtained by setting $\vartheta_1 = \vartheta_0 + 2n\pi$ with n integer (normally $\vartheta_0, \vartheta_1 = 0, 2\pi$).

An example of the phase space distribution as returned by *FELquietstart_h* is shown in Fig. 1.

A simple simulation

A simple simulation is realized by the *Mathcad* sequence in Fig. 2

```

v_0 := 2.6  sigma_v := 2  n_v := 40
n_theta := 40  theta_0 := 0  theta_1 := 2*pi  a := (1 + 3i)
P := FELquietstart_h(v_0, sigma_v, n_v, theta_0, theta_1, n_theta, a)
g_0 := (10)
      (0)
      (0)
P := FELpendulum_h(P, g_0, 0, 1, TOL)
    
```

Figure 2: *Mathcad* sequence integrating the pendulum-like equation coupled to the field equations with coupling coefficient $g=10$ on the first harmonic and 0 on the higher harmonics.

The phase space in P is integrated over the undulator length with the coupling coefficient $g=10$ on the first harmonic and 0 on the higher harmonics. The resulting phase space is plotted in Fig. 3.

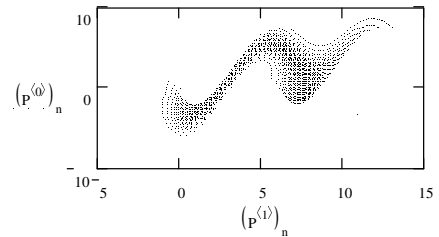


Figure 3: Phase space distribution at the end of the simulation with the parameters listed in Fig. 2.

After the FEL interaction the phase space is distributed in an interval longer than $(0, 2\pi)$. The periodicity in ϑ of the system of equations (2) and (3) can be imposed to the phase space variables with the function $P := FELBox_h(P, \vartheta_0, \vartheta_1)$. By calling this function with $(\vartheta_0, \vartheta_1) = (0, 2\pi)$ we obtain the phase space distribution of Fig. 4.

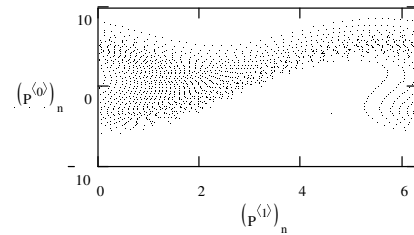


Figure 4: Phase space distribution after imposing a periodicity condition in the interval $(0, 2\pi)$.

Start-up from e-beam shot noise

Startup from shot noise may be simulated by using the function *FELquasiquietstart_h*($v_0, \sigma_v, n_v, v_0, v_1, n_\vartheta, \phi_{ns}$, a) which is analogous to the function *FELquietstart_h* except for the additional argument ϕ_n which is used to displace the particles according to the function

$$v_i = \arg(\phi_{ns}) + (1 - |\phi_{ns}|) \left[\left(\frac{v_1 - v_0}{n_\vartheta} \right) \left(i - \frac{n_\vartheta - 1}{2} \right) \right] \quad (7)$$

In the limit of small perturbation ($|\phi_{ns}| \rightarrow 0$) and sufficiently large number of particles n_ϑ the distribution has Fourier coefficients $b_n \equiv \phi_{ns}$ (bunching coefficients at the harmonic n) almost independent from n (see ref. [1]). The coefficient b_1 can be estimated in a steady state simulation using the procedure of ref.[6].

Inhomogeneous broadenings and three dimensional effects

The variable $v_i = 2\pi N (\omega_i - \omega_L) / \omega_i$ represents the relative shift of the resonance of the i^{th} particle from a given reference frequency ω_L . According to the definition of the resonant frequency of the i^{th} particle $\omega_i = 2\gamma_i^2 ck_u / (1 + K(x_i, y_i)^2 / 2 + \gamma_i^2 (\theta_{x,i}^2 + \theta_{y,i}^2))$, where we have included the dependence on the angle between the average particle trajectory and the undulator axis $\theta_{xy,i} = \beta_{xy} / \beta_z$ (we use the notation $\theta_{xy,i} = \theta_{x,i}, \theta_{y,i}$) and the dependence of the undulator K parameter on the transverse coordinates, the particles distribution in energy and transverse phase space may be converted in a distribution in the detuning parameter space v . At the lowest order in x_i, y_i and $\theta_{xy,i}$ we have [7]

$$\begin{aligned} \sigma_{x,y} &= \sqrt{2\pi} N h_{x,y} \frac{2\gamma^2}{1 + K^2/2} \left(\frac{\pi K}{\gamma \lambda_u} \right)^2 \left(\frac{\beta_{x,y} \varepsilon_{n,xy}}{\gamma} \right) \\ \sigma'_{x,y} &= \sqrt{2\pi} N \frac{2\gamma^2}{1 + K^2/2} \left(\frac{\pi K}{\gamma \lambda_u} \right)^2 \left(\frac{\varepsilon_{n,xy}}{\beta_{x,y} \gamma} \right) \\ \sigma_e &= 4\pi N \frac{\sigma_\gamma}{\gamma} \end{aligned} \quad (8)$$

where $h_{x,y}$ are the undulator focusing parameters (with $h_x + h_y = 2$), $\varepsilon_{n,xy}$ and $\beta_{x,y}$ are the normalized emittances and the β Twiss coefficients in the x and y planes respectively. An approximated expression for standard deviation in the v space is obtained by combining quadratically the standard deviations (8)

$$\sigma_v \equiv \sqrt{\sigma_x^2 + \sigma_y^2 + \sigma_x'^2 + \sigma_y'^2 + \sigma_e^2} \quad (9)$$

In an oscillator FEL or in a seeded FEL and in general, when the transverse properties of the radiation may be considered as a constraint of the problem, the coupling coefficients (2) have to be corrected by a proper filling factor. In general when the radiation size is the result of the balance between diffraction and focusing induced by the gain, as in a single pass FEL, a filling factor coefficient may be derived from the Xie scaling laws [8] by calculating the ratio between the Xie factor with and without diffraction effects. In a similar way a coefficient correcting the coupling factor g may be derived from the semi-analytical model in [9].

TIME DEPENDENT SIMULATIONS

Mathcad programming may be used to set up FEL simulations in a wide variety of conditions. As an example we analyse the case of 1D FEL simulations including pulse propagation effects. The field is governed by the evolution equation

$$\left(\frac{\partial}{\partial \tau} + \Delta \frac{\partial}{\partial \zeta} \right) a_n(\tau, \zeta) = -2\pi g_n I(\zeta) \langle \exp(in\vartheta(\tau, \zeta)) \rangle_\zeta \quad (10)$$

where $\Delta = N\lambda_i$ is the slippage length, ζ is the longitudinal coordinate in the frame moving with the electron bunch and $I(\zeta)$ is the normalized current shape. The average on the r.h.s. of (10) is intended in a region λ_i at the position ζ . The solution of this equation is obtained by defining an array of variables of the type of *PHSP* in (5), representing the sampling of both the field and the beam phase space variables along the coordinate ζ at the positions $\boldsymbol{\zeta} = \zeta_0, \zeta_1, \dots, \zeta_{nb-1}$. The phase space beamlets are defined as

$$\mathbf{P} = (P_0, P_1, \dots, P_{nb-1}) \quad (11)$$

The undulator is divided in time steps such that the step length $\Delta\tau$ is related to the spatial sampling $\Delta\zeta$ by the condition $\Delta\zeta = \Delta/\Delta\tau$. With such a choice, at each time step the field variables at the i^{th} position in the \mathbf{P} array have to slip to the next position: $i^{\text{th}} \Rightarrow i^{\text{th}}+1$. For this purpose the function in Fig. 5 is defined.

$$\boxed{\begin{array}{l} \text{FELSlipField}(P1, P2) := \text{for } n \in 1..P1_{0,0} \\ \left| \begin{array}{l} P1_{n,0} \leftarrow P2_{n,0} \\ P1_{n,1} \leftarrow P2_{n,1} \end{array} \right. \\ P1 \end{array}}$$

Figure 5: Function *FELSlipField* loading the field data from beamlet $P2$ to $P1$. Fields in $P2$ are overwritten.

The simulation of a single pass FEL in time dependent mode is then simply obtained with the function shown in Fig. 6. The first loop over the nb beamlets loads the initial phase space array \mathbf{P} , generating each beamlet with a

different shot noise coefficient $\phi_{n,i}$. The initial field amplitude a_0 is multiplied by a modulating coefficient se_i which can be defined in order to simulate the ζ dependence of an input seed. The second loop over the variable n_τ takes care of the integration of the phase space beamlets P along the undulator. At each time step of length $\Delta\tau$ the array of beamlets P is stored in the matrix OUT , particles and fields are advanced by the *FELpendulum_h* and the slippage is applied by the *FELSlipField* procedure defined in Fig. 5. Each column of the matrix OUT contains the array P at time $\Delta\tau n_\tau$. As an example of a simulation obtained with the routine in Fig. 6, we have considered the case of a SASE FEL with the resonance at 200 nm, a FEL parameter $\rho \approx 4 \times 10^{-3}$ and gain length of about 0.3 m. In Fig. 7 the longitudinal phase space at saturation is shown. The beamlets at the same time frame have been joined together in the same plot. The horizontal axis represents the beamlets position along ζ . The phase space variable ϑ in each beamlet is expanded by the factor $\Delta\zeta/2\pi$ in order to give the impression of a continuous beam. The ζ window is large

enough to contain two spikes, the red line represents indeed the separatrix of the motion and is proportional to the root of the field.

```

FELTimeDep :=
  for i ∈ 0..nb - 1
    Pi ← FELquasiquietstart_h (v0, σv, nv, 0.0, 2·π, nθ, φn,i, a0·sei)
  τ ← 0
  for nτ ∈ 0..nT
    for i ∈ 0..nb - 1
      OUTnτ,i ← Pi
      Pi ← FELpendulum_h (Pi, g1, l1, τ, τ + Δτ, TOL)
    for n ∈ nb - 1..0
      PT ← FELSlipField (Pi, Pif(i=0,nb-1,i-1))
      Pi ← FELbox_h (PT, 0, 2·π)
    τ ← τ + Δτ
  OUT

```

Figure 6: Function simulating the longitudinal dynamics of a single pass FEL in time dependent mode. The result returned by the matrix OUT contains the beamlets phase spaces composing the beam at the n_T time steps.

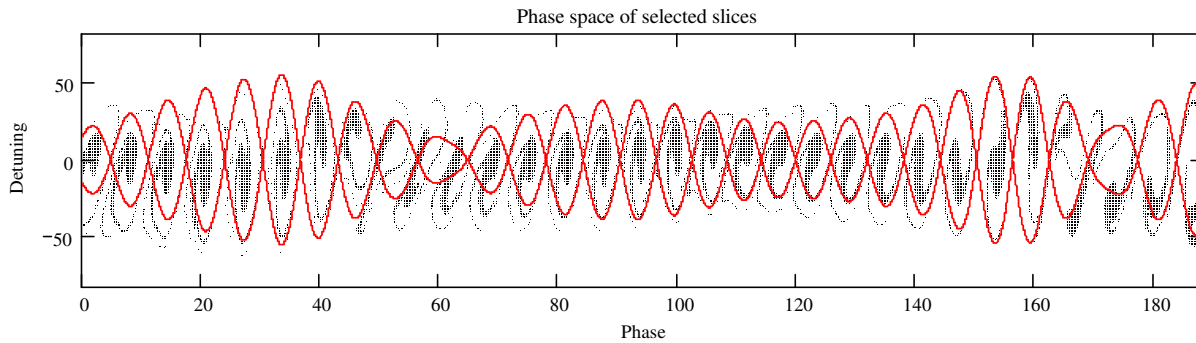


Figure 7: The beamlets resulting after a SASEFEL simulation at saturation have been joined together in the same plot. The horizontal axis represents the beamlets position along ζ . The phase space variable ϑ in each beamlet is expanded by the factor $\Delta\zeta/2\pi$ in order to give the impression of a continuous beam. The red line represent the separatrix of the motion and is proportional to the root of the field.

CONCLUSIONS

We have provided a brief overview of the physical model implemented in *Perseo*. The main functions required for setting up a simple simulation have been analysed and the algorithm for implementing time dependent simulation has been explained. With a similar procedure fully 3D simulations can be implemented but the cpu and memory requirements becomes excessive for an interactive execution.

For additional information and further insight in *Perseo* capabilities the reader is addressed to the web page [1] and to the *Perseo* Electronic Handbook included in the installation package.

REFERENCES

[1] See www.perseo.enea.it

- [2] W. B. Colson, Laser Handbook vol 6, *Classical Free Electron Laser Theory*, 301 North-Holland, Amsterdam, 1990.
- [3] W. B. Colson, G. Dattoli, F. Ciocci, Phys. Rev. A 31, 828, 1985.
- [4] G. Dattoli, S. Cabrini, L. Giannessi, Phys. Rev. A 44, 8433, 1991.
- [5] Mathcad Help files – see also www.mathsoft.com
- [6] L. Giannessi, in Proc. of the 26th FEL conference, Trieste 2004, p. 37.
- [7] G. Dattoli, A. Renieri, Laser Handbook vol. 4 ed. by M.L.Stich and M.S. Bass, North Holland Amsterdam 1985.
- [8] M. Xie, in Proceedings of the 1995 Particle Accelerator Conference, Dallas, Texas, 1–5 May 1995, IEEE, Piscataway, NJ, 1996, p. 183.
- [9] G. Dattoli et al., Journal of Appl. Phys. 95, 3206 2004.

FUTURE SEEDING EXPERIMENTS AT SPARC

L. Poletto, G. Tondello, Università di Padova, Padova, Italy
 S. De Silvestri, M. Nisoli, G. Sansone, S. Stagira, Politecnico di Milano, Milano, Italy
 P. Musumeci, M. Petrarca, M. Mattioli, INFN Sez. Roma I, Rome, Italy
 M. Labat, O. Tcherbakoff, M. Bougeard, B. Carré, D. Garzella, G. Lambert, H. Merdji, P. Salières,
 Service des Photons Atomes et Molécules, CEA Saclay, DSM/DRECAM, France.
 M. E. Couprie, SOLEIL, Sant-Aubin, Gif-sur-Yvette CEDEX, France
 D. Alesini, M. Biagini, R. Boni, M. Castellano, A. Clozza, A. Drago, M. Ferrario, V. Fusco, A.
 Gallo, A. Ghigo, M. Migliorati, L. Palumbo, C. Sanelli, F. Sgamma, B. Spataro, S. Tomassini, C.
 Vaccarezza, C. Vicario, INFN-LNF, Frascati, Italy
 L. Serafini, INFN, Milano, Italy
 S. Ambrogio, F. Ciocci, G. Dattoli, A. Doria, G. P. Gallerano, L. Giannessi, E. Giovenale, I.
 Spassovsky, M. Quattromini, A. Renieri, C. Ronsivalle, ENEA C. R. Frascati, Rome, Italy
 P.L. Ottaviani, S. Pagnutti, M. Rosetti, ENEA C.R. Bologna, Italy
 A. Dipace, E. Sabia, ENEA C. R. Portici, Napoli, Italy.

Abstract

This communication describes the research work plan that is under implementation at the SPARC FEL facility in the framework of the DS4 EUROFEL programme. The main goal of the collaboration is to study and test the amplification and the FEL harmonic generation process of an input seed signal obtained as higher order harmonics generated both in crystals (400 nm and 266 nm) and in gases (266 nm, 160 nm, 114 nm). The SPARC FEL can be configured to test several cascaded FEL layouts that will be briefly analysed.

INTRODUCTION

The SPARC FEL experiment is based on two main components, a high brightness photoinjector that is expected to provide a high quality beam at energies between 150 and 200 MeV (see Tab.I and ref.[1]) and a single pass FEL, whose undulator beam-line is composed by six undulator sections of 77 periods each, with a period length of 2.8 cm and a gap ranging from 6 to 25 mm[2].

The FEL will operate in self amplified spontaneous emission (SASE) mode at a wavelength of about 500 nm with an expected saturation length of about 10-12 m, according to the beam parameters listed in table 1. The flexibility offered by the variable gap configuration of the SPARC undulator and the natural synchronization of the electron beam with the laser driving the photoinjector, makes the SPARC layout particularly suited for a number of experiments where the FEL amplifier is seeded by an external laser source. The seed laser is driven by the same oscillator initiating the laser cascade which is used to run the photocathode and consists in a regenerative amplifier delivering 2.5mJ at 800 nm with a pulse duration shorter than 120 fs.

Table 1. List of the main SPARC beam parameters

Beam energy	155-200 MeV
Bunch Charge	1.1 nC
Rep. Rate	1 – 10 Hz
Peak current (>50% bunch)	100 A
Norm. emittances (integrated)	2 mm-mrad
Norm. emitt. (slice len. 300µm)	< 1 mm-mrad
Total correlated energy spread	0.2 %
Total uncorrelated energy spread	0.06 %
e-bunch duration (rms)	~ 4 ps

Different schemes of non-linear harmonic generation are then implemented to generate the shorter wavelength radiation for seeding the FEL. Second and third harmonic generation in LBO crystals will provide the powerful pulses required to reach saturation and study the non-linear pulse propagation in FELs and FEL cascades in superradiant regime, at 400nm and 266nm [3], [4]. The other method considered for the frequency up-conversion of the Ti:Sa fundamental wavelength, is based on the non-linear higher order harmonics generation of the Ti:Sa laser in a gas-jet or in a gas-cell [5]. While at SPARC we plan to seed the FEL with the harmonics up to the 9th of the Ti:Sa [6], the harmonic generation in gas allows to extend the seed source spectral range down to the EUV region of the spectrum and represents a promising technique to seed FEL amplifiers at shorter wavelengths.

In the following we will review some of the planned experiments with the two different seed sources.

SEEDING WITH HIGH HARMONICS GENERATED IN GAS

The experiment of seeding high harmonics generated in gas at SPARC is based on the installation of a gas jet interaction chamber and an in vacuum optical system which matches the transverse optical mode of the harmonic to that of the e-beam in the first undulator section [6]. The UV pulse is injected into the SPARC undulator by means of a periscope and a magnetic chicane deflecting the e-beam from the straight path. High-order odd harmonics of the Ti:Sa laser may be generated at the wavelengths 266nm, 160nm, and 114nm. The undulator resonance condition is tuned at these wavelengths by varying the beam energy and undulator strength K according to the plot shown in Fig. 1.

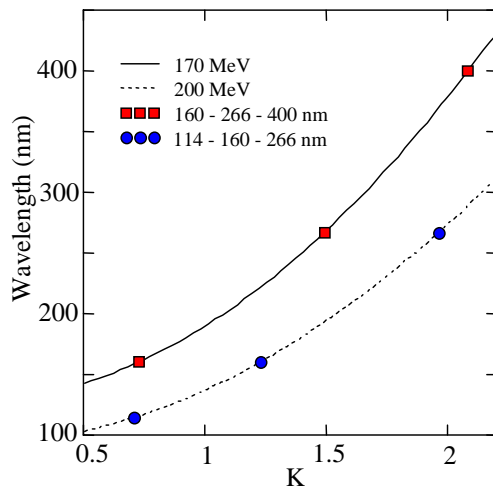


Figure 1: Seeded SPARC FEL operation wavelengths.

The high order harmonics result from the strong non-linear polarisation induced on the rare gases atoms, such as *Ar*, *Xe*, *Ne* and *He*, by the focused intense electromagnetic field of the "pump" laser. The emitted pulse is composed by a sequence of short bursts separated by one half of the fundamental laser period (400nm) and the spectrum contains the odd harmonics of the original laser. A simulation of the amplification of a pulse at 160nm with the typical time structure of harmonics generated in gas has been done with *Perseo*[7]. The laser pulse shape vs. the longitudinal coordinate is shown in Fig. 2 at different positions along the undulator. The radiation spectrum is also shown in Fig.2 and the effect of the spectral "cleaning" associated with the limited FEL bandwidth (FEL parameter $\rho \approx 4 \cdot 10^{-3}$) is evident. An analogous behaviour is observed at the third harmonic generated by the non-linear FEL dynamics. More detailed simulations based on an accurate model of the seed fields distribution and including transverse effects are under study.

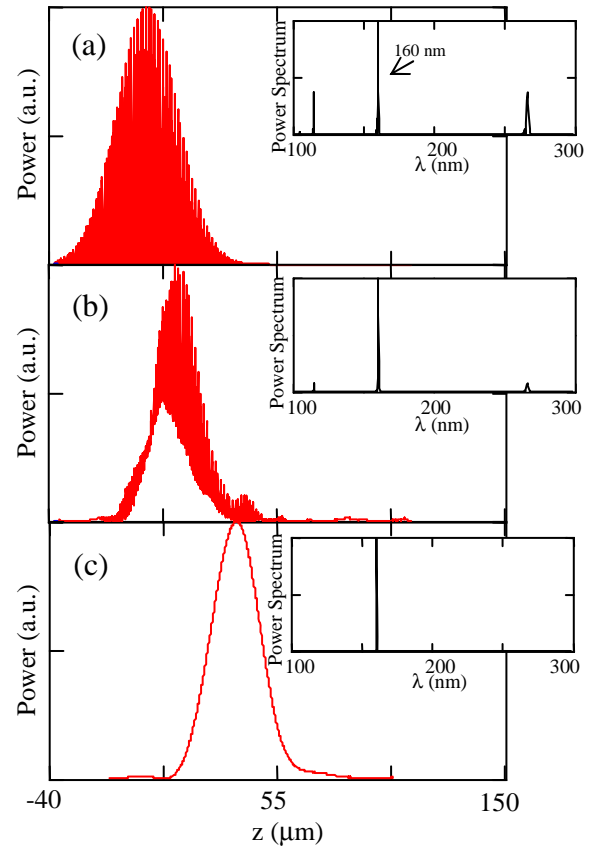


Figure 2 Power and spectrum of the radiation at different positions in the undulator for the SPARC FEL seeded at 160nm. Seed signal (a), after the first undulator section (b), at the end of the undulator (c). Beam energy 200 MeV, $K=1.226$, the other beam parameters as in Table 1.

SEEDING WITH 2ND AND 3RD HARMONICS OF TI:SA GENERATED IN CRYSTAL

The six SPARC undulators may be configured in order to set up a single stage cascaded FEL based on a modulator – radiator configuration, similar to the one tested at BNL [8]. The layout of this configuration is shown in Fig.3.

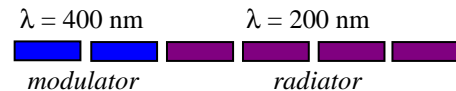


Figure 3 Single stage cascaded FEL layout.

The number of sections of the modulator and of the radiator may be tuned depending on the intensity of the laser seed. The availability of intense short pulses from the seed laser allows to test the superradiant cascade concept [4]. The seed laser power is indeed sufficient to bring at saturation a modulator made by a single undulator segment tuned at 400 nm. The pulse generated in these conditions propagates with the typical signature of superradiance in the following radiator composed by the re-

maining five sections. The feasibility of this experiment was studied in[9].

A second interesting configuration consists in the experimental test of the fresh-bunch injection technique [10]. The layout is shown in Fig.4. In this case the first two undulators (A and B) represent the modulator and radiator sections of single stage cascade, the following two undulators (C and D) are tuned off resonance with the seed wavelength and its higher order harmonics. These undulators play the role of the dispersive section where the radiation exiting the first radiator at 200 nm (B) is longitudinally separated from the electron beam part where the high quality beam has been heated in the previous sections, by the FEL interaction with the seed.

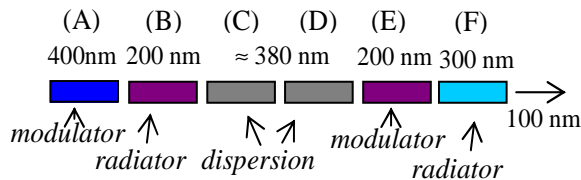


Figure 4 Fresh bunch injection technique layout.

Section (E) is the modulator of the second stage cascade and section (F) is the radiator that is tuned in order to match the resonance of its third harmonic with the second harmonic of the radiator (E). This is necessary since the K parameter excursion of the undulator is not sufficient to span the 1st to 3rd harmonic range and coupling on the higher order odd harmonics in a linear undulator based FEL has been considered [11].

The last configuration considered in this overview consists in the harmonic FEL cascade [12]. As in the last stage of the previous configuration, the two undulators are tuned at different, not-harmonic fundamental frequencies, but have instead one of their higher order harmonics in common. According to the SPARC FEL undulator properties, this scheme may be tested in configurations where the fourth or the sixth harmonic of the 266nm signal used as seed of the first section, are amplified as the third or fifth harmonics in the second section. This configuration has been analysed with numerical simulations in time dependent mode. Both the codes *Perseo* and a modified version of the code *Genesis 1.3* [13-14] which includes the self consistent dynamics of the higher order harmonics have been used. In the example considered in Fig. 5, we show the result obtained with *Perseo*. The cascade is driven by a seed of 2 MW peak power at a wavelength corresponding to the third harmonic of the Ti:Sa drive laser. The first undulator has the fundamental resonance at 266nm and the second section is tuned at 222nm. The two undulators have a common resonance at 44nm, corresponding to the 6th harmonic of the first section and the 5th of the second.



Figure 5 FEL Harmonic cascade FEL configuration.

The energy of the radiation pulse at the wavelength of 44nm vs the longitudinal coordinate in the radiator is shown in Fig. 6.

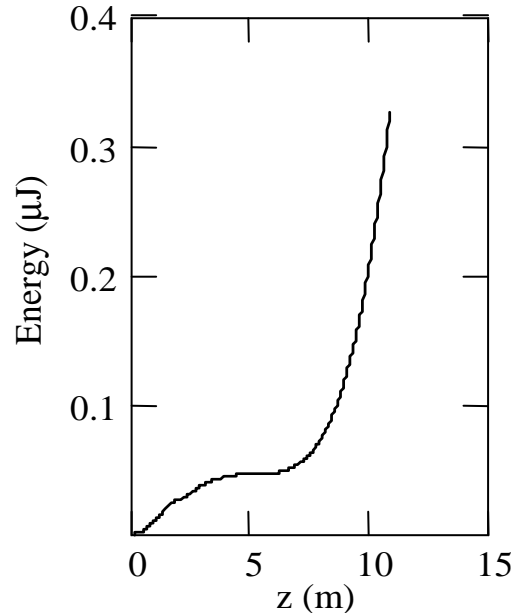


Fig. 6 Pulse energy vs. the longitudinal coordinate in the radiator.

A transition to superradiance where the pulse energy grows as $z^{3/2}$ occurs after about five meters of the radiator section.

The pulse shape is shown in Fig. 7 and the relevant spectrum is shown in Fig. 8.

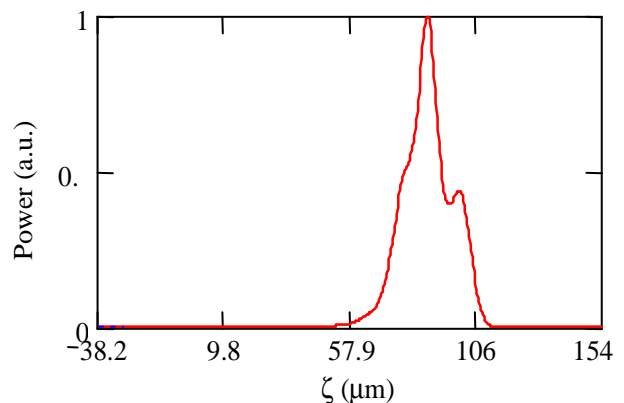


Fig. 7. Longitudinal profile of the radiation power at the end of the second undulator.

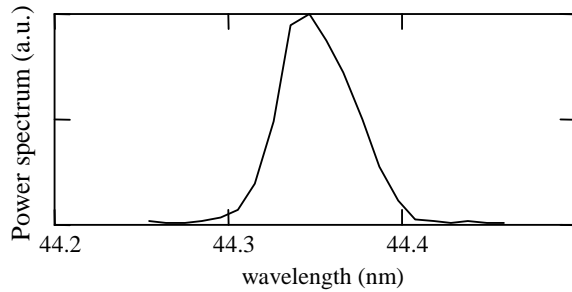


Fig. 8 Power spectrum of the radiation pulse as shown in Fig. 7.

CONCLUSIONS

We have given a brief overview of some of the experiments that will be implemented at SPARC thanks to the flexibility of the SPARC configuration and of the variable gap undulator. Seeding the FEL with harmonics generated in gas and testing schemes as the fresh bunch injection technique and the harmonic FEL cascade are among the capabilities of the SPARC hardware. The harmonic cascaded FEL scheme is in particular a promising scheme to extend to the short wavelength the operation range of a Free Electron Laser. A wavelength of 44nm was obtained in simulations with a beam energy of only 200 MeV.

The opportunities provided by the SPARC experiment of a deeper understanding of the amplification process and of experimentally testing and of the FEL dynamics through a whole cascade, may affect in the future the design of the foreseen FEL facilities aiming at the generation of radiation in the VUV-EUV region of the spectrum.

ACKNOWLEDGMENTS

Work partially supported by the EU Commission in the sixth framework programme, contract no. 011935 – EU-ROFEL.

REFERENCES

- [1] SPARC Collaboration, Nucl. Instr. & Meth. A507 (2003) 345-349, see also <http://www.sparc.it> and these proceedings.
- [2] A. Renieri et al. Status report on SPARC project, in Proc. of the 26th FEL conference, Trieste 2004 JACoW (Joint Accelerator Conference Website) at <http://www.JACoW.org>, p. 163 (2004).
- [3] R. Bonifacio, L.De Salvo Souza, P.Pierini, and N. Piovela, Nucl.Instrum. & Meth. A 296, 358 (1990)
- [4] L. Giannessi, P. Musumeci, S. Spampinati, J. Appl. Phys. 98, 043110 (2005).
- [5] T. Brabec, F. Krausz, Rev. Mod. Phys. 72, 545 (2000).
- [6] M. Labat et al., Seeding SPARC Facility with Harmonic Generation in Gases, MOPPH047 these proceedings.
- [7] L. Giannessi, *Perseo* see <http://www.perseo.enea.it>
- [8] L. H. Yu et al. Phys. Rev. Lett. 91, 074801 (2003).

- [9] L. Giannessi, P. Musumeci, in Proc. of the 27th FEL conference, JACoW (Joint Accelerator Conference Website) at <http://www.JACoW.org>, p. 210 (2005).
- [10] I. Ben-Zvi, K.M. Yang, L. H. Yu, Nucl. Instrum. & Meth. A 318, 726 (1992).
- [11] W. B.Colson, G. Dattoli and F. Ciocci, Phys. Rev. A 31, 828 (1985).
- [12] L. Giannessi and P. Musumeci, in proc. of 46th workshop on the Physics and applications of high brightness electron beams, Erice (Tr), 9 - 14 October 2005.
- [13] S. Reiche, Nuclear Instrum. & Meth. A429, 243 (1999).
- [14] L. Giannessi and P. Musumeci, "The Free Electron Laser Harmonic Cascade" submitted to New Journal of Physics, June 2006.

X-RAYS GENERATION WITH A FEL BASED ON AN OPTICAL WIGGLER

A. Bacci, C. Maroli, L. Serafini, *INFN-Sezione di Milano*, 20133 Milano (Italy)

V. Petrillo, Dipartimento di Fisica dell'Università di Milano-INFN Sezione di Milano, 20133 Milano (Italy)

M.Ferrario, INFN-LNF, 00044 Frascati, Roma, Italy.

Abstract

The interaction between high-brilliance electron beams and counter-propagating laser pulses produces X rays via Thomson back-scattering. If the laser source is long and intense enough, the electrons of the beam can bunch and a regime of collective effects can be established. In the case of dominating collective effects, the FEL instability can develop and the system behaves like a free-electron laser based on an optical undulator. Coherent X-rays can be irradiated, with a bandwidth very much thinner than that of the corresponding incoherent emission. The main quantities that limit the brilliance of the X-rays are emittance, mean radius, current and energy spread of the electron beam, and the distribution and intensity of the laser beam. In this work we discuss first some ideal examples. Secondly we present the preparation of the electron beam by means of the use of a genetic code that optimizes the output of the code ASTRA. The electron beam obtained is analysed in slices and the best one is used in the 3-D radiation code.

INTRODUCTION

A Thomson back-scattering set-up can be considered in principle as a source of intense X-ray pulses which is at the same time easily tunable and highly monochromatic. Due to recent technological developments in the production of high brilliance electron beams and high power CPA laser pulses, it is now even conceivable to make steps toward their practical realisation.

The radiation generated in the Thomson back-scattering is usually considered incoherent and calculated by summing at the collector the intensities of the fields produced in single processes by each electron. If the laser pulse is long enough, however, collective effects can establish and become dominant. The system in this range of parameters behaves therefore like a free-electron laser, where the static wiggler is substituted by the optical laser pulse.

From the point of view of the theoretical description of the process, it is convenient to start with the same set of one-dimensional equations that are used in the theory of high-gain free-electron laser amplifier [1,2]. To take into account the many aspects of the process connected with the finite transverse geometry of the electron beam and of the laser and radiation pulses it is necessary to consider 3D equations [3].

A set of numerical results based on ideal electron beams is first presented. Secondly we present a genetic code that permits the optimization of the outputs of the beam dynamics code ASTRA, in order to obtain an electron

beam with suitable characteristics. The electron beam obtained is analysed in slices and the best slice is used in the computation of the X-ray radiation under the effect of the laser. A short discussion of the importance of the data will be given at the end of the paper.

MODEL EQUATIONS AND IDEAL EXAMPLES

We start from the Maxwell-Lorentz equations that describe both laser and collective electromagnetic fields and from the relativistic equations of motion for the electrons of the beam. The laser and collective fields are given in terms of the corresponding scalar and vector potentials in the Coulomb gauge.

We assume that the laser is circularly polarised with the following form of the vector potential \mathbf{A}_L (the laser pulse propagates along the z-axis in the negative direction):

$$\mathbf{A}_L(\mathbf{r}, t) = \frac{a_{L0}}{\sqrt{2}} (g(\mathbf{r}, t) e^{-i(k_L z + \omega_L t)} \hat{\mathbf{e}} + cc) + O\left(\frac{\lambda_L}{w_0}\right) \quad (1)$$

where $\lambda_L = 2\pi/k_L$ is the laser wavelength, w_0 the laser spot size, $\omega_L = ck_L$ the angular frequency and $\hat{\mathbf{e}} = (\mathbf{e}_x + i\mathbf{e}_y) / \sqrt{2}$. The envelope $g(\mathbf{r}, t)$ is considered to be a slowly varying function of all variables xyz and t and is defined as a complex number with $|g(\mathbf{r}, t)| \leq 1$. In the case of a laser pulse with a Gaussian transverse shape, the envelope has the form

$$g(r, t) = \Phi(z + ct) \frac{1 + i \frac{z}{z_0}}{1 + \frac{z^2}{z_0^2}} \exp \left[-4 \frac{x^2 + y^2}{w_0^2 (1 + \frac{z^2}{z_0^2})} - 4i \frac{x^2 + y^2}{w_0^2 (\frac{z}{z_0} + \frac{z_0}{z})} \right] \quad (2)$$

where $z_0 = \pi w_0^2 / 4\lambda_L$ is the Rayleigh length and the form of the (real) function Φ (with $0 \leq \Phi(z) \leq 1$) depends on the shape of the pulse along the z-axis. In the case of a guided laser pulse the quantity $g(\mathbf{r}, t)$ is a step function. We suppose that $\varphi(\mathbf{r}, t)$ and $\mathbf{A}(\mathbf{r}, t)$ have a slow dependence on x and y , i.e., that they vary on a transverse scale L_T much greater than the radiation wavelength $\lambda = 2\pi/k$ and write, accordingly to the single-mode hypothesis frequently used in 1D treatments

$$\begin{aligned} \mathbf{A}(\mathbf{r}, t) &= M(\mathbf{r}, t) \hat{\mathbf{e}} + cc + O(\lambda / L_T) \\ &= A(\mathbf{r}, t) e^{i(kz - \omega t)} \hat{\mathbf{e}} + cc + O(\lambda / L_T) \end{aligned} \quad (3)$$

where $M(\mathbf{r}, t) = A(\mathbf{r}, t) e^{i(kz - \omega t)}$ and $\omega = ck$ is the radiation angular frequency. In the three-dimensional equation of

the model derived in details in Ref [3] a critical role is played by the FEL parameter $\rho = \frac{1}{\gamma_0} \left(\frac{\omega_b^2 a_{L0}^2}{16\omega_L^2} \right)^{\frac{1}{3}}$.

The resonant frequency is at $\omega \approx \frac{4\gamma_0^2 \omega_L}{1+a_{L0}^2}$. The fact that the quantum effects are negligible is guaranteed by taking the quantum parameter $q = \frac{\hbar k}{p_{mc} \langle \gamma \rangle} < 1$.

First, we have solved our model equations in the following case: the laser has a wavelength $\lambda_L = 10$ micron and the parameter $a_{L0} = 0.3$. The diameter of the laser focal spot w_0 has been assumed 50 μm , the length of the pulse 70-100 psec, for a total power of 40-100 GW and a total energy of 4-10 J. The bunch of electrons has been chosen with an average value of γ , $\langle \gamma \rangle = 60$, corresponding to an energy of 30 MeV. This value of $\langle \gamma \rangle$ leads to a resonant wavelength $\lambda = 7.56$ Angstrom. The quantum parameter $q = 0.2$ and the classical model is expected to be fully valid. The collective effects appear and saturate after 7 gain lengths which in our case correspond to times of the order of 60-70 ps (each gain length corresponds to $L_g = 1$ mm), i.e., of the same order of the duration of the laser pulse.

The electron beam has a mean radius $\sigma_0 = 25$ micron, a total charge of 1-5 nC and a length $L_b = 1$ mm, so that the Pierce parameter is $\rho = 2.8 \cdot 10^{-4}$. Its energy spread $\Delta\gamma/\gamma$ ranges from 0 to $1.5 \cdot 10^{-4}$ and the initial normalized transverse emittance ϵ_n has been varied up to 1.

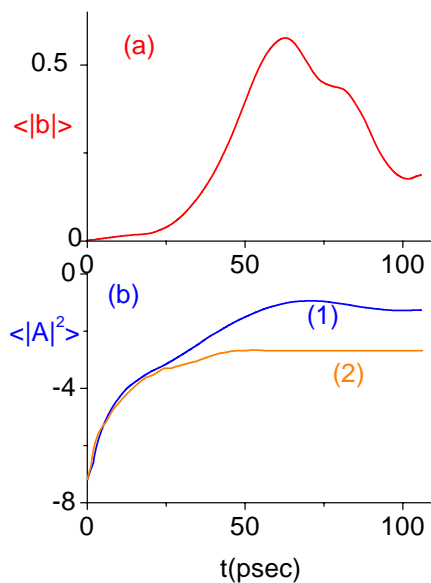


Figure 1 (a) $\langle |b| \rangle$ averaged on the transverse section vs t in psec and (b), (1) coherent value of $\langle |A|^2(z_m) \rangle$ (b), (2) incoherent value for $w_0 = 50 \mu\text{m}$, $\epsilon_n = 0.6$ mm mrad

Fig 1 shows the typical growth of the bunching factor in time (a), as well as the collective potential (b) curve 1 and the incoherent potential (b) curve 2. The amplitude of the vector potential $|A|^2$ has been calculated in the middle of

the electron bunch at the position $z_m = \langle z \rangle$ and averaged on the transverse plane. The peak number of X coherent photons is $2.5 \cdot 10^{10}$, while the incoherent process provides $2 \cdot 10^8$ photons.

In this case $w_0 = 50$ micron, $\epsilon_n = 0.6$ mm mrad, $Q = 3$ nC, $I = 0.9$ KA and the signal saturates at $t = 70$ psec.

Figure 2 gives the first peak value of $\langle |A|^2 \rangle$ versus $\Delta\omega/(\omega\rho)$, representing the spectrum of the signal. As can be seen the width of the spectrum is few times ρ . In Fig 3 the peak value of $\langle |A|^2 \rangle$ is given as function of the transverse emittance, showing a depletion of the emission for emittances larger than 0.6-0.7 mm mrad.

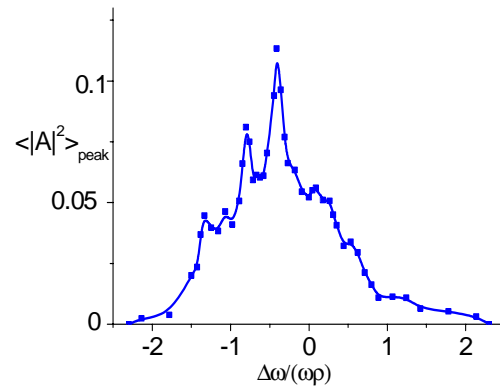


Figure 2: First peak value of $\langle |A|^2 \rangle$ versus $\Delta\omega/(\omega\rho)$ for the same parameters as Fig 1

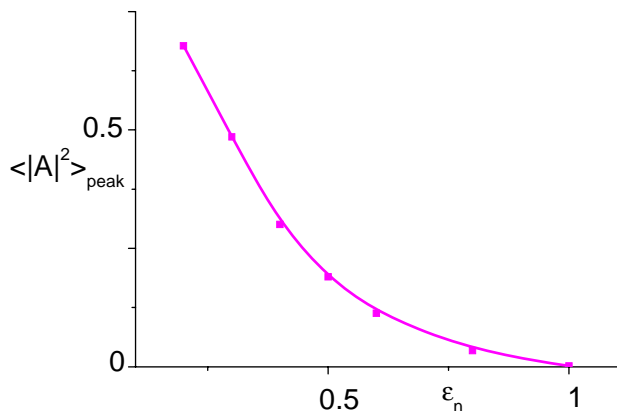


Figure 3: $\langle |A|^2 \rangle_{\text{peak}}$ versus ϵ_n evaluated in micron for the same case of Fig 1 and with $\Delta\omega/\omega = -10^{-4}$, $w_0 = 50$ micron, $a_{L0} = 0.3$, $\Delta\gamma/\gamma = 10^{-4}$.

In Figures 4,5,6,7 a different case is shown. The laser wavelength in this case is 0.8 μm . The electron beam has $\langle \gamma \rangle = 30$, for a Pierce parameter $\rho = 4.38 \cdot 10^{-4}$. Other parameters of the beam are: a mean radius $\sigma_0 = 10$ micron, a total charge of 1 nC, a length $L_b = 200$ micron, corresponding to a beam current of $I = 1.5$ KA.

In Fig 4 the bunching (a) and the collective (b) (1) and

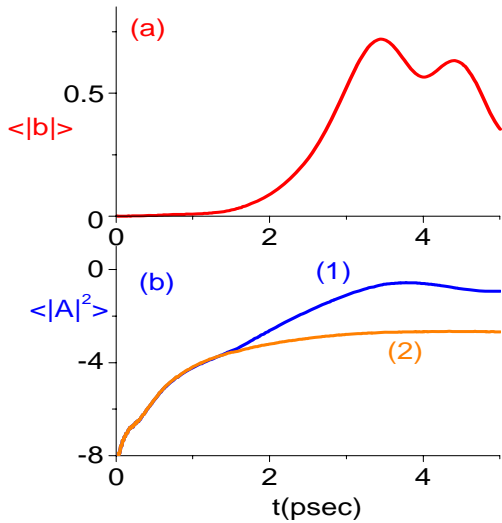


Figure 4: Bunching (a) and log of the radiation intensity (b) vs t in the coherent (1) and incoherent (2) case for: $\lambda_L=0.8 \mu\text{m}$, $a_{L0}=0.8$, $\Delta\gamma/\gamma=10^{-4}$, $\Delta\omega/\omega=-2 \cdot 10^{-4}$, $\epsilon_n=0.88$.

incoherent (b) (2) potential amplitude are shown versus time. Furthermore, we have assumed a focal spot of radius w_0 of about $50 \mu\text{m}$ with a laser parameter of $a_{L0}=0.8$ so that the radiation turns out to have $\lambda=3,64$ Angstrom. With these values the gain length corresponds to about 145 micron, the appearance and the saturation of the collective effects (taking place in 7-12 gain lengths) being contained in 5 picoseconds, a time of the same order of the duration of the laser pulse. The quantum parameter q is 0.5.

The energy spread $\Delta\gamma/\gamma$ of the electron beam has been chosen $1 \cdot 10^{-4}$ and the initial normalized transverse emittance has been varied from 0 up to 2.

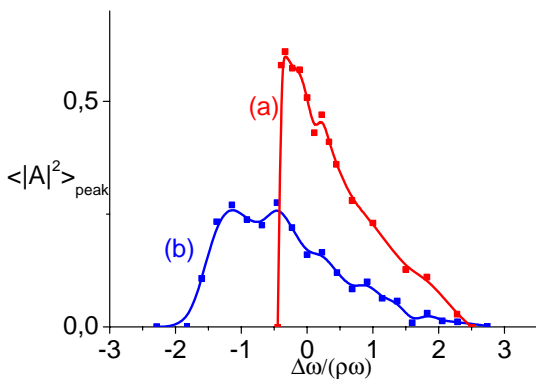


Figure 5: $\langle |A|^2 \rangle_{\text{peak}}$ versus $\Delta\omega/(\omega\rho)$ for the case of fig 5 and (a) $\epsilon_n=0,44 \mu\text{m}$ and (b) $\epsilon_n=0,88 \mu\text{m}$.

The saturation level of the radiation is reached at $t=4$ psec at $\langle |A|^2 \rangle_{\text{peak}}=0,275$, with a total number of photons of $1,86 \cdot 10^{10}$, against the $2 \cdot 10^8$ provided by the incoherent process.

In Fig. 5 the spectrum of the radiation is presented, while in Fig. 6 the dependence of the maximum of $\langle |A|^2 \rangle$ on the transverse normalized emittance is shown. Curve (a) is relevant to the situation of flat laser pulse with $w_0=50$ micron, while curve (b) shows the more critical situation where a Gaussian profile for the laser has been assumed. In this case the quantity σ_L has been taken equal to $106 \mu\text{m}$ with $a_{L0}=0.8$, increasing consequently the laser power. We must note that we have considerable emission also in violation of the Pellegrini criterion for a static wiggler. In fact, the emittances considered exceed largely the value $\gamma\lambda/4\pi$, which in this case is $9 \cdot 10^{-4} \mu\text{m}$. On the other hand, on the fact that $Z_R/Lg=1.2 \cdot 10^4$, the criterion of Pellegrini can be rewritten in a generalized form for both static and optical undulators as $\epsilon_n \leq \alpha \sqrt{Z_R/Lg} \lambda_R \gamma/4\pi$ [5] where $\alpha = \sqrt{d\omega/(\omega\rho)} \approx 2$, giving the more relaxed limit $\epsilon_n < 0,3\mu$.

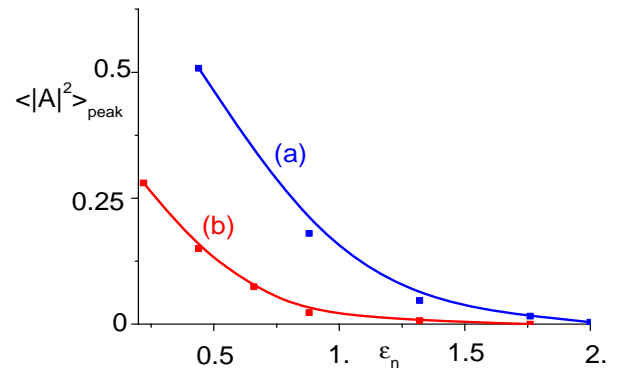


Figure 6: $\langle |A|^2 \rangle_{\text{peak}}$ vs ϵ_n , with $\Delta\omega/\omega=0$. and: (a) flat laser profile with $w_0=50 \mu\text{m}$ and $a_{L0}=0.8$ and (b) Gaussian laser profile with $a_{L0}=0.8$ and $\sigma_L=106 \mu\text{m}$.

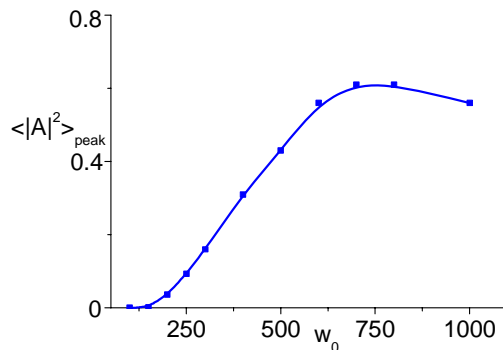


Figure 7 $\langle |A|^2 \rangle_{\text{peak}}$ vs w_0 for a Gaussian laser for $\epsilon_n=0,44 \mu\text{m}$, $\Delta\omega/\omega=-1 \cdot 10^{-4}$, $a_{L0}=0.8$.

Fig 7 shows the dependence of the growth of the signal on the transverse energy distribution of the laser in the case of a Gaussian pulse for $\epsilon_n=0,44 \mu\text{m}$, $\Delta\omega/\omega=-1 \cdot 10^{-4}$, $a_{L0}=0.8$. In fact, in this case, a spot size with a radius smaller than 75 micron does not permit the instauration of the instability. The collective signal in this condition, therefore, does not grow.

REALISTIC EXAMPLE OBTAINED BY MEANS OF A GENETIC ALGORITHM

A realistic electron beam has been generated using the beam dynamic code ASTRA. The sequence of the accelerating and focalization elements in the beam line is shown in Fig 8, where the RF section works in the velocity bunching configuration.

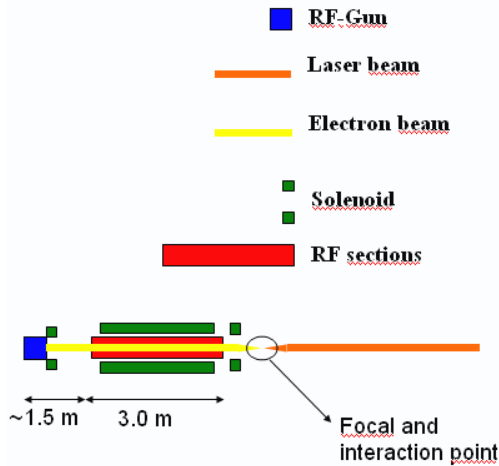


Figure 8: Beam line lay-out.

However, the optimization of the output is very difficult due to the high number of parameters which have to be fixed and to the non linear correlations existing between them. To circumvent this difficulty we have developed a genetic code that manages to fix the values of the parameters. The optimization is made by maximizing the following fitness function:

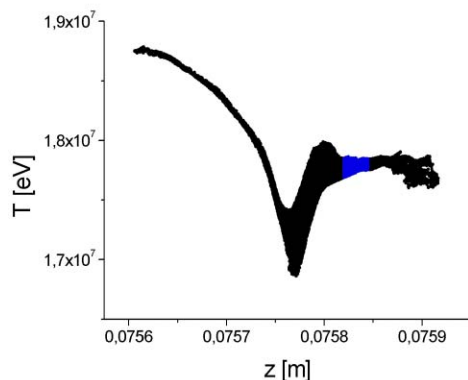


Figure 9: Bunch phase space and slice used (in blue).

$$F_{fitness} = \frac{I^{3.5}}{\varepsilon_{n-x,y} \cdot \sigma_{x,y} \cdot \sqrt{\left(\frac{\Delta\gamma}{\gamma}\right)}}$$

as function of the following genes defining the beam line: 1) Phase of the gun radiofrequency ϕ_{rf} . 2) Acceleration gradient in the bunching structure g_a . 3)

Injection phase in the bunching structure ϕ_b . 4) Position of the bunching structure l_b . 5) Intensity of the first solenoid field B_1 , used to control the envelope in the emittance compensation layout. 6) Intensity of the second solenoid field B_2 , used to control the envelope. 7) Position of the second solenoid l_{s2} .

The convergence is reached in 500 generations on an electron beam configuration whose best slice has an emittance of 0,56 mm mrad, a radius of 15 micron, a length of 15 micron with a charge $Q=0.05$ nC. The genis values for the final configuration are: $\phi_{rf} = 9.77^\circ$, $g_a = 17.68$ MV/m, $\phi_b = -91.57^\circ$, $l_b = 1.3868$ m, $B_1 = 0.256$ T, $B_2 = 0.0532$ T, $l_{s2} = 1.3685$ m. The energy spread of the slice $\Delta\gamma/\gamma$ is 0.15 %. The growth of the signal is shown in fig 10, while the spectrum is in Fig 11. The saturation occurs in 6 psec, the focal spot size is $w_0 = 30$ μm , $a_{L0} = 0.8$, for a total laser power of $W = 9.77$ TW.

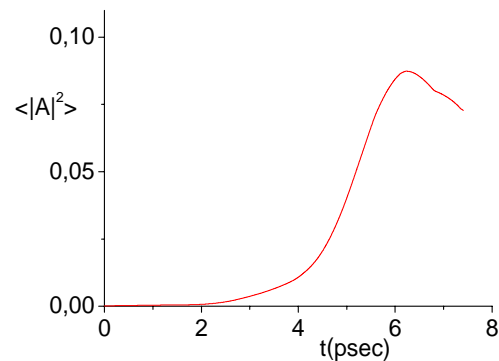


Figure 10: Growth of the signal.

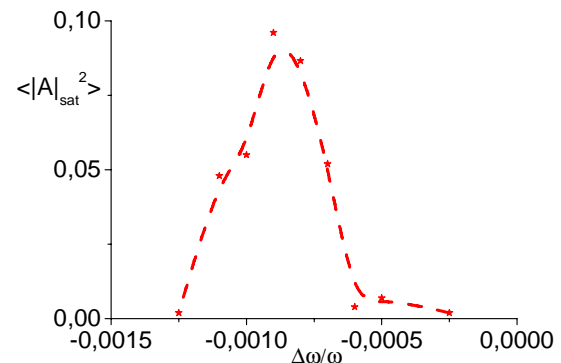


Figure 11: Spectrum of the signal.

REFERENCES

- [1] W.B. Colson, Phys.Lett. 59A,187,(1976). R. Bonifacio, C. Pellegrini, L. Narducci Opt. Commun. 50 (1984) 313
- [2] A.Bacci, C.Maroli, V.Petrillo, L.Serafini: "Collective effects in the Thomson back-scattering between a laser pulse and a relativistic electron beam" EPJAP (in print)
- [3] A.Bacci, M.Ferrario, C. Maroli, V. Petrillo, L. Serafini PRST-AB 9 (2006) 060704

THE SATURATED REGIME OF A SEEDED SINGLE-PASS FREE ELECTRON LASER: A THEORETICAL INVESTIGATION THROUGH THE STATISTICAL MECHANICS OF THE VLASOV EQUATION

F. Curbis*, University of Trieste & Elettra, Basovizza, Trieste, Italy,
 A. Antoniazzi, Dipartimento di Energetica, Università di Firenze, Italy
 G. De Ninno, Elettra, Basovizza, Trieste, Italy,
 D. Fanelli, Dipartimento di Energetica, Università di Firenze, Italy.

Abstract

The quasi-stationary state characterizing the saturation of a single-pass free-electron laser is governed by the Vlasov equation obtained by performing the continuum limit of the Colson-Bonifacio model. By means of a statistical treatment, this approach allows to predict analytically the saturated laser intensity as well as the final electron-beam energy distribution. In this paper we consider the case of coherent harmonic generation obtained from a seeded free-electron laser and present predictions for the first stage of the project FERMI@Elettra project at Sincrotrone Trieste.

INTRODUCTION

In a single-pass FEL, the physical mechanism responsible for the light emission and amplification is the interaction between a relativistic electron beam, a magnetostatic periodic field generated by an undulator and an optical wave co-propagating with electrons. Two different schemes can be distinguished, depending on the origin of the optical wave which is used to initiate the process. In the SASE configuration, the initial seed is provided by the spontaneous emission of the electron beam which is forced by the undulator field to follow a curved trajectory. The seed is then amplified all along the undulator until the laser effect is reached. The SASE radiation produces tunable signal at short (x-ray) wavelengths with several GW peak power and excellent spatial mode. An alternate approach to SASE is Coherent Harmonic Generation (CHG) [1], which is capable of producing temporally coherent pulses. A schematic layout of CHG is shown in Figure 1.

In this case, the initial seed is produced by an external light source, e.g. a laser. The light-electron interaction in a short undulator, called modulator, imposes an energy modulation on the electron beam. The modulator is tuned to the seed wavelength λ . The energy modulation is then converted into a spatial density modulation as the electron beam transverses a magnetic dispersion. Figure 2 shows the evolution of the electron-beam phase space (i.e. energy vs. electrons' phase in the undulator plus radiator field) from the entrance of the modulator to the exit of the dis-

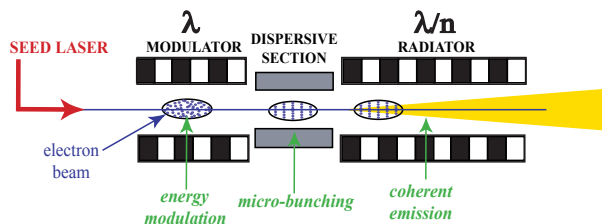


Figure 1: Schematic layout of the CHG scheme.

persive section. Finally, in a second undulator, called radiator and tuned at the n-th harmonic of the seed frequency, the micro-bunched electron beam emits coherent radiation at the harmonic wavelength λ/n . Such a radiation is then amplified until saturation is reached.

Importantly, it shall be noticed that Single-pass FELs represent an example of systems with long-range interactions [2]. When long-range forces are to be considered, a global network of connections between individual constituting elements is active, and *mean-field* effects are dominant. Surprisingly, within the realm of long range interacting systems, a wide number of striking phenomena appear including ensemble inequivalence, negative specific heat and emergence of Quasi-Stationary States (QSS), i.e., long-living states where the system gets eventually trapped before relaxing to its final statistical equilibrium. This latter remarkable non equilibrium feature is also reported for

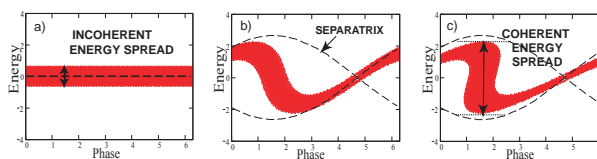


Figure 2: Electron-beam phase space at the entrance a) and at the exit b) of the modulator; c) phase space at the exit of the dispersive section. In a), the thickness of the distribution corresponds to the (initial) incoherent energy spread of the electron beam. In c) the gap between the boundaries of the separatrix corresponds to the energy modulation induced by the seed-electron interaction (see Figure 1).

* francesca.curbis@elettra.trieste.it

FELs, where it plays a central role, being the only state experimentally accessible in real devices. In this respect, FELs provide a general experimental ground to investigate the universal characteristics of systems with long range interactions.

Motivated by this analogy, we shall apply a maximum entropy principle, inspired to Lynden-Bell's theory of "violent relaxation" [3]–[6] for the Vlasov equation and analytically predict the characteristics of the laser signal at saturation. More specifically, the above theoretical interpretative framework will enable us to estimate the expected intensity for the case of FERMI@Elettra [7], a future user-facility based on CHG, without resorting to direct numerical simulations. Our results will be shown to correlate well with Genesis-based [8] estimates.

FROM THE MEAN-FIELD MODEL TO THE LYNDEN-BELL PREDICTION

In this section we will introduce the model that is customarily employed to investigate the time evolution of a single-pass FEL, both in SASE and CHG configurations. By putting forward the hypothesis of one-dimensional (longitudinal) motion and monochromatic radiation, the steady-state dynamics of a single-pass FEL is described by the following set of equations:

$$\frac{d\theta_j}{d\bar{z}} = p_j \quad , \quad (1)$$

$$\frac{dp_j}{d\bar{z}} = -Ae^{i\theta_j} - A^*e^{-i\theta_j} \quad , \quad (2)$$

$$\frac{dA}{d\bar{z}} = i\delta A + \frac{1}{N} \sum_j e^{-i\theta_j} \quad , \quad (3)$$

where $\bar{z} = 2k_u \rho z \gamma_r^2 / \langle \gamma_0 \rangle^2$ is the re-scaled longitudinal coordinate, which plays the role of time. Here, $\rho = (a_w \omega_p / 4ck_u)^{2/3} / \gamma_r$ is the so-called Pierce parameter, γ_r the resonant energy, $\langle \gamma_0 \rangle$ the mean energy of the electrons at the undulator's entrance, k_u the wave vector of the undulator, $\omega_p = (e^2 \bar{n} / m \epsilon_0)^{1/2}$ the plasma frequency, \bar{n} being the electron number density, c the speed of light, e and m respectively the charge and mass of one electron. Further, $a_w = eB_w / (k_u m c^2)$, where B_w is the rms undulator field. Introducing the wavenumber k of the FEL radiation, the phase θ is defined by $\theta = (k + k_u)z - 2\delta \rho k_u z \gamma_r^2 / \langle \gamma_0 \rangle^2$; its conjugate momentum reads $p = (\gamma - \langle \gamma_0 \rangle) / (\rho \langle \gamma_0 \rangle)$. The complex amplitude $A = A_x + iA_y$ represents the scaled field, transversal to z . Finally, the detuning parameter is given by $\delta = (\langle \gamma_0 \rangle^2 - \gamma_r^2) / (2\rho \gamma_r^2)$, and measures the average relative deviation from the resonance condition. The above system of equations (N being the number of electrons) can be deduced by the Hamiltonian:

$$H = \sum_{j=1}^N \frac{p_j^2}{2} - \delta I + 2\sqrt{\frac{I}{N}} \sum_{j=1}^N \sin(\theta_j - \varphi), \quad (4)$$

where the intensity I and the phase φ of the wave are defined by $A = \sqrt{I/N} \exp(-i\varphi)$. Here, the canonically conjugated variables are (p_j, θ_j) for $1 \leq j \leq N$ and (I, φ) . Besides the "energy" H , the total momentum $P = \sum_j p_j + I$ is also a conserved quantity. Let us finally define the bunching parameter as $b(t) = \sum \exp(i\theta_i(t)) / N := \langle \exp(i\theta(t)) \rangle$. The latter provides a quantitative measure of the degree of spatial compactness of the particles distribution.

Numerical simulations based on the above system of equations show that the amplification of the wave occurs in several subsequent steps. First, an initial exponential growth takes place, which is successfully captured by a linear analysis. Then, as previously anticipated, the system attains a QSS, where the wave intensity displays oscillations around a well-defined plateau. As predicted by the Boltzmann-Gibbs statistics, for longer times a slow evolution toward the final equilibrium is found. The process is driven by granularity and the relaxation time diverges with the system size N . Hence, due to the constraint imposed by the typical length of an undulator, the QSS is the only regime experimentally accessible in the case of single-pass FELs.

When performing the thermodynamics limit, i.e., $N \rightarrow \infty$, one gets to the following Vlasov-wave picture:

$$\frac{\partial f}{\partial \bar{z}} = -p \frac{\partial f}{\partial \theta} + 2(A_x \cos \theta - A_y \sin \theta) \frac{\partial f}{\partial p} \quad , \quad (5)$$

$$\frac{dA_x}{d\bar{z}} = -\delta A_y + \int f \cos \theta \, d\theta \, dp \quad , \quad (6)$$

$$\frac{dA_y}{d\bar{z}} = \delta A_x - \int f \sin \theta \, d\theta \, dp \quad . \quad (7)$$

which can be shown to govern the initial growth and relaxation towards the QSS. The latter conserves the pseudo-energy per particle

$$h(f, A) = \int \frac{p^2}{2} f(\theta, p) \, d\theta \, dp - \delta(A_x^2 + A_y^2) + \int (A_x \sin \theta + A_y \cos \theta) f(\theta, p) \, d\theta \, dp \quad (8)$$

and the momentum per particle

$$\sigma(f, A) = \int p f(\theta, p) \, d\theta \, dp + (A_x^2 + A_y^2). \quad (9)$$

In ref. [4] it was shown that the average statistical parameters of the laser (intensity and the bunching in the QSS) are accurately predicted by a statistical mechanics treatment of the Vlasov equation, according to prescriptions of the seminal work by Lynden-Bell [5]. The analysis developed in [4] was limited to the case of spatially homogeneous initial conditions (i.e., initial zero bunching). In [9], we extended the analysis by including initially bunched distributions. In the remaining part of this section we will review the foundation of the analytical method and presented select numerical results.

The basic idea of Lynden–Bell “violent relaxation” theory [4, 6] is to coarse-grain the microscopic single-particle distribution function $f(\theta, p, t)$, which is filamented and stirred by the dynamics. An entropy is then associated to the coarse-grained function \bar{f} , which essentially counts the number of microscopic configurations giving rise to it.

Starting with an initial centered water-bag distribution, which corresponds to a rectangle uniformly occupied in the phase space (θ, p) with $-p_0 < p < p_0$ and $-\theta_0 < \theta < \theta_0$, the normalization condition reads $f_0 = 1/(4\theta_0 p_0)$.

The entropy can be expressed as [5, 6]:

$$s(\bar{f}) = - \int \left[\frac{\bar{f}}{f_0} \ln \frac{\bar{f}}{f_0} + \left(1 - \frac{\bar{f}}{f_0} \right) \ln \left(1 - \frac{\bar{f}}{f_0} \right) \right] d\theta dp. \quad (10)$$

The equilibrium is computed by maximizing this entropy:

$$\max_{\bar{f}, A_x, A_y} (s(\bar{f})), \quad (11)$$

while imposing the dynamical constraints:

$$h(\bar{f}, A_x, A_y) = h_0, \quad (12)$$

$$\sigma(\bar{f}, A_x, A_y) = \sigma_0, \quad (13)$$

$$\int f(\theta, p) d\theta dp = 1, \quad (14)$$

where h_0 and σ_0 stand, respectively, for the energy and momentum (per particle) of the system. Performing the analytical calculation and introducing the rescaled Lagrange multipliers for the energy, momentum and normalization constraints (β/f_0 , λ/f_0 and μ/f_0) one obtains the typical Fermi-Dirac distribution:

$$\bar{f} = f_0 \frac{e^{-\beta(p^2/2 + 2A \sin \theta) - \lambda p - \mu}}{1 + e^{-\beta(p^2/2 + 2A \sin \theta) - \lambda p - \mu}} \quad (15)$$

$$A = \sqrt{A_x^2 + A_y^2} = \frac{\beta}{\beta\delta - \lambda} \int \sin(\theta) \bar{f}(\theta, p) d\theta dp.$$

The three constraints (12)–(14) are then imposed by making use of the above expression for $f(\theta, p)$ and A , and the obtained equations numerically solved to provide an estimate of the multipliers as functions of energy h_0 and momentum σ_0 of the system. Once β , γ , μ are calculated, one can in turn estimate the value of the intensity I and the bunching parameter b of the QSS.

To validate our findings, we performed numerical simulation for a water-bag initial distribution as specified above, where $\theta_0 < \pi$. Further, label with $|b_0|$ the initial bunching, i.e., the positive quantity given by $|b_0| = |\langle \exp(i\theta(0)) \rangle|$. Numerical calculations are performed based on the discrete system (1–3). In Figure 3 the average intensity at saturation is reported as function of $|b_0|$, for different values of the initial kinetic energy. Results are compared with the analytical estimate obtained above. Analogous plots for the average value of the bunching parameter at saturation are

reported in Figure 4. A direct inspection of the figures confirms the adequacy of the proposed theoretical framework: predictions based on the Vlasov theory correlate well with numerical curves. In the next section, starting from these results, we will elaborate a strategy to gain insight into the non-linear evolution of a CGH scheme without resorting to direct numerical investigations. In particular, we will focus on the case of the FERMI@Elettra project.

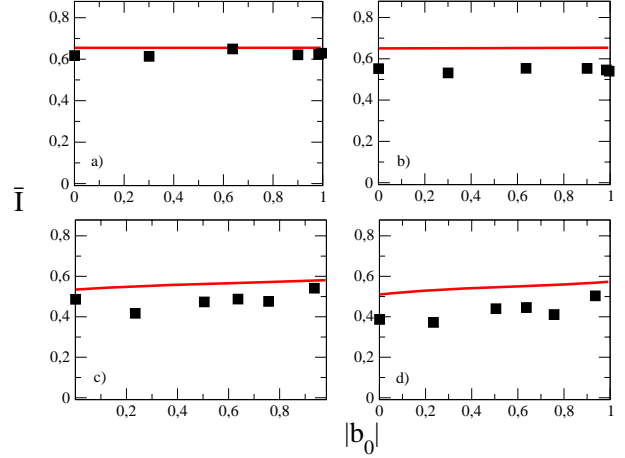


Figure 3: Average intensity \bar{I} at undulator exit as function of the initial bunching $|b_0|$ for different values of the initial average kinetic energy, respectively a) $h_0 = 0.01$ b) $h_0 = 0.16$ c) $h_0 = 0.21$ d) $h_0 = 0.315$. The continuous lines correspond to the Lynden–Bell theoretical prediction, while symbols represent numerical results obtained averaging intensity fluctuations in the saturated regime over ten different realizations of the initial conditions resting on the same values of θ_0 and p_0 .

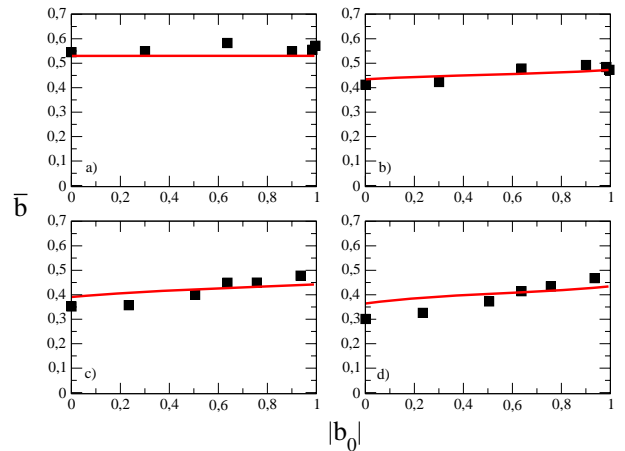


Figure 4: Average values of the bunching parameter $|\bar{b}_0|$ at the undulator exit as function of $|b_0|$. Same choice of parameters as in Figure 3.

CHARACTERIZING THE SATURATION OF CHG FELS

The seed-electron interaction in the first undulator of a CHG scheme induces a coherent modulation, $\Delta\gamma$, of the electron-beam energy, which superimposes to the initial incoherent energy spread σ_γ . Inside the dispersive section, the energy modulation is converted into a spatial density modulation. Performing a Fourier analysis of the spatial beam distribution at the end of the dispersive section one finds the following bunching parameters:

$$|b_0| \simeq J_n(n)/\exp(1/2), \quad (16)$$

where J_n stands for the n -th order Bessel function ¹.

On the other hand, the total energy spread $\sigma_{\gamma,tot}$ at the entrance of the second undulator reads:

$$\sigma_{\gamma,tot} = \sqrt{\sigma_\gamma^2 + \frac{(\Delta\gamma)^2}{2}} \simeq \sigma_\gamma \sqrt{1 + \frac{n^2}{2}}, \quad (17)$$

where n is the harmonic number. Moreover, in term of the rescaled variables used in the formulation of the above one-dimensional model, the associated energy profile can be ideally schematized as a water-bag distribution, where

$$p_0 = \frac{\sigma_{\gamma,tot}}{\gamma\rho}. \quad (18)$$

Taking full advantage of the above theoretical analysis, we are therefore in a position to quantify the saturated (QSS) behaviour of a CHG device. In particular, we shall focus on the case of the project FERMI@Elettra [7] and assume the experimental setting relative to the output wavelength 100 nm. In this case, $n = 3$ (i.e., the initial seed wavelength is 100 nm), $\gamma = 2348$, $\sigma_\gamma = 150$ KeV and $\rho = 3 \cdot 10^{-3}$. Direct numerical simulations are performed using GENESIS [8], a three dimensional code that explicitly accounts for the coupling between the transverse and longitudinal dimensions. Assuming a radiator length of 16 m, a horizontal and vertical (normalized) beam emittance of $1.5 \mu\text{m}$ and on optical waist of $w \simeq 300 \mu\text{m}$, simulations give an output power of about 3 GW.

Independently, one can calculate the value of $|b_0|$ and p_0 by inserting the nominal values of the relevant parameters in equations 18-16. Then, Lynden-Bell theory enables us to predict the QSS value for the intensity which are shown to correlate extremely well with Genesis based calculation, the disagreement being quantified in at most 10 % [9].

CONCLUSIONS

The theoretical approach outlined in this paper constitutes a novel strategy to predict the intensity at saturation

for a CHG setting, provided the value of the incoherent energy spread is assigned and without involving to direct numerical investigations.

The short recipe goes as follows: by knowing σ_γ one can calculate $\sigma_{\gamma,tot}$ by means of eq.(17) and consequently estimate both $|b_0|$ and p_0 , based on eqs.(16)–(18). The spatial width, θ_0 , of the initial water-bag distribution (here assumed to mimic the more natural Gaussian profile) is eventually obtained upon inversion of relation $|b_0| = \sin(\theta_0)/\theta_0$. Once the values of θ_0 and p_0 are given, the theory of the violent relaxation allows to quantitatively predict the saturated state of the system.

Finally let us stress that the applicability of the method we have developed is currently limited to situations in which transverse effects are neglected. This in turn entails the possibility of assuming the electron-beam geometrical emittance smaller than the radiation wavelength, the beam relative energy spread smaller than ρ and the Rayleigh length of emitted radiation much longer than the radiator length. These conditions apply for instance to the case of the whole spectral range that is to be covered by the FERMI@Elettra FEL (100-10 nm).

REFERENCES

- [1] L. H. Yu, *Phys. Rev. A* **44** 5178 (1991).
- [2] T. Dauxois, S. Ruffo, E. Arimondo, M. Wilkens (Eds), *Lecture Notes in Physics 602, Springer Dynamics and Thermodynamics of Systems with Long Range Interactions* (2002).
- [3] A. Antoniazzi, D. Fanelli, J. Barré, P. H. Chavanis, T. Dauxois, S. Ruffo, submitted to *Phys. Rev. Lett.* (2006).
- [4] J. Barré *et al.*, *Phys. Rev. E* **69** 045501 (2004).
- [5] D. Lynden-Bell, *Mon. Not. R. Astron. Soc.* **136**, 101 (1967).
- [6] P. H. Chavanis, J. Sommeria, R. Robert, *Astrophys. J.* **471**, 385 (1996).
- [7] See <http://www.elettra.trieste.it/FERMI/>.
- [8] <http://pbpl.physics.ucla.edu/reiche/>.
- [9] F. Curbis, A. Antoniazzi, G. De Ninno, D. Fanelli, preprint submitted to *Phys. Rev. E* (2006).

¹Note that in deriving equation (16) an optimization scheme for the bunching parameter has been put forward according to the standard experimental procedure. A detailed account on the approximations involved is presented in [9] starting from the usual expression given in [1]

ANALYSIS OF FEL OSCILLATIONS IN A PERFECTLY SYNCHRONIZED OPTICAL CAVITY

N. Nishimori*, JAEA, Ibaraki, Japan.

Abstract

We analyze free-electron-laser (FEL) oscillations in a perfectly synchronized optical cavity by solving the one-dimensional FEL equations. The radiation stored in the cavity can finally evolve into an intense few-cycle optical pulse in the high-gain and low-loss regime. The evolution of the leading slope of the optical pulse, which is defined from the front edge toward the primary peak, is found to play an important role in generating the intense few-cycle pulse. The phase space evolution of electrons on the second pass which interact with the leading slope of a SASE output pulse is obtained in a perturbation method similar to that used in our previous study for a SASE FEL. The resulting analytical solution of the leading slope in the second pass is shown to be approximated by that of a SASE FEL with FEL parameter greater than ρ . The same perturbation method can thus be used to the subsequent passes.

INTRODUCTION

The FEL dynamics is affected by the slippage that is caused by the velocity difference between the electron bunch and the optical pulse inside an undulator. The group velocity of the optical pulse becomes slightly slower than the vacuum speed of light, since the trailing slope of the optical pulse is mainly amplified due to the slippage. This phenomenon, called the laser lethargy (see Ref. [1] and references therein), can be compensated in oscillators by slightly shortening the optical cavity length from the perfect synchronism ($\delta L = 0$), where the cavity length exactly matches with the injection period of the electron bunches. The FEL dynamics of the oscillators with shorter cavity length ($\delta L < 0$) has been studied extensively [2, 3]. At $\delta L = 0$, the optical pulse centroid continues to be retarded on successive passes through the undulator, and the optical pulse finally dissipates, as shown in theoretical studies [4, 5, 6].

An experiment of a high-power FEL driven by a superconducting linac in the Japan Atomic Energy Research Institute (JAERI) FEL facility has however showed that an intense, ultrashort optical pulse is generated at $\delta L = 0.0 \pm 0.1 \mu\text{m}$ despite the lethargy [7, 8]. The optical power curve measured with respect to δL is well reproduced by the time-dependent simulation code based on one-dimensional (1D) FEL equations [9], if shot-noise effect is included in every fresh electron bunch. A few theoretical studies have attempted to explain the FEL oscillations at $\delta L = 0$, proposing that sideband instability [10] or superradiance in short-pulse FELs [11] is the fundamental physics responsi-

ble for the lasing at $\delta L = 0$. Nevertheless, the underlying physics responsible for the FEL oscillations at $\delta L = 0$ has not been clearly explained yet.

In this paper, we investigate the FEL evolution at $\delta L = 0$ by analytically solving the 1D FEL equations. A set of nondimensional parameters and the 1D FEL equations used in Ref. [12] are employed for the present study. The optical pulse on the first pass, which is equivalent to the output of a self-amplified spontaneous-emission (SASE) FEL and represented by the solution of the cubic equation [14, 15, 16], is reflected back into the undulator for subsequent amplifications in FEL oscillators. The phase space evolution of electrons on the second pass which interact with the leading slope of the FEL pulse, which is defined from the front edge toward the primary peak amplitude in the present paper, is obtained in a perturbation method similar to that used in our previous work for the phase space evolution of electrons in a SASE FEL [12]. Consequently, an analytical solution for the optical growth of the leading slope during the second pass is derived. The leading slope of the output pulse is shown to be approximated by that of a SASE FEL with FEL parameter greater than ρ . The same process can thus be applied to pass numbers greater than $n = 2$ and the evolution of the leading slope with respect to n is obtained analytically. The output field similar to that of a SASE FEL accounts for the exponential increase of the field amplitude in the leading slope from the front edge toward the primary peak, and the amplitude gradient with respect to the longitudinal position is shown to increase with n . With the increasing gradient, the field gain per pass decreases down to the level of optical cavity loss α , and a self-similar radiation pulse is generated at saturation. The evolution of the leading slope leads to sustained FEL oscillations at $\delta L = 0$ and thus disappearance of the lethargy effect. More details are described in Ref. [13].

1D FEL EQUATIONS

The dimensionless 1D FEL equations of Colson are used in the present study under the slowly varying envelope approximation [17], while the variables used here are similar to Bonifacio's variables [16]. The simplest situation is considered in the present study. The electron beam energy is given by $\gamma_0 mc^2$ with small energy spread. The initial electron bunch has a rectangular shape with density of n_e and a uniform distribution in phase. The fundamental FEL parameter in MKSA units is given by

$$\rho = \frac{1}{\gamma_0} [e a_w F \sqrt{n_e / (\epsilon_0 m)} / (4ck_w)]^{2/3}. \quad (1)$$

Here $\lambda_w = 2\pi/k_w$ is the period of the undulator, a_w is the undulator parameter, and F is unity for a helical undulator

* nishimori.nobuyuki@jaea.go.jp

or Bessel function $[J J]$ for a planar undulator [16]. The dimensionless time is defined by $\tau = 4\pi\rho ct/\lambda_w$, so that $\delta\tau = 1$ corresponds to the transit time of light through one gain length of $\lambda_w/(4\pi\rho)$. The longitudinal position of the i th electron is defined by $\zeta_i(\tau) = 4\pi\rho[z_i(t) - ct]/\lambda_r$, so that $\delta\zeta = 1$ corresponds to the cooperation length defined by $L_c = \lambda_r/(4\pi\rho)$. Here $\lambda_r = \lambda_w(1 + a_w^2)/(2\gamma_0^2)$ is the resonant wavelength. The dimensionless field envelope is defined by

$$a(\zeta, \tau) = \frac{2\pi e a_w \lambda_w F}{(4\pi\rho)^2 \gamma_0^2 m c^2} E(\zeta, \tau) \exp[i\phi(\zeta, \tau)], \quad (2)$$

with phase $\phi(\zeta, \tau)$, which is equivalent to Bonifacio's envelope [16]. Here $E(\zeta, \tau)$ is the rms optical field strength. The dimensionless energy and phase of the i th electron are respectively defined by $\mu_i(\tau) = [\gamma_i(t) - \gamma_0]/(\rho\gamma_0)$ and $\psi_i(\tau) = (k_w + k_r)z_i(t) - \omega_r t$, where $k_r = 2\pi/\lambda_r$ is the wave number of the resonant wavelength λ_r . The dimensionless energy $\mu_i(\tau)$ also means the dimensionless energy change at τ from $\tau = 0$, since the energy spread of the initial electron beam is assumed to be small, i.e., $\mu_i(0) = 0$.

In the present definition, the evolutions of the field envelope $a(\zeta, \tau)$, the energy $\mu_i(\tau)$ and phase $\psi_i(\tau)$ of the i th electron during FEL interaction are respectively given by [5]

$$\frac{d\mu_i(\tau)}{d\tau} = a[\zeta_i(\tau), \tau] \exp[i\psi_i(\tau)] + \text{c.c.}, \quad (3)$$

$$\frac{d\psi_i(\tau)}{d\tau} = \mu_i(\tau), \quad (4)$$

$$\frac{\partial a(\zeta, \tau)}{\partial \tau} = -\langle \exp[-i\psi_i(\tau)] \rangle_{\zeta_i(\tau)=\zeta}. \quad (5)$$

The angular bracket indicates the average of all the electrons in the volume V around ζ .

EVOLUTION OF SASE FEL PULSE

The optical field and electron phase space evolutions on the first pass, which are equivalent to those in a SASE FEL, are presented in our previous work [12]. The startup process known as spectrum narrowing [18] or as longitudinal phase mixing [19] leads to a uniform field in time and space. The phase of the field $\phi(0)$ is almost uniform over the length $N\lambda_r$ along the propagation direction when the incident electron beam passes through N undulator periods [5, 19]. In the present study, the initial uniform field is assumed to be given by $|a(0)|e^{i\phi(0)}$ for simplicity. The initial field evolves through electric interaction with undulating electrons as it passes through the undulator. The incident electron beam is assumed to be uniformly distributed in phase $\psi_i(0)$ with resonant energy $\mu_i(0) = 0$ and interacts with the SASE FEL field in the steady-state region due to the slippage [16]. The evolution of the uniform field as a function of time is derived from Eqs. (3), (4), and (5), as described by Colson *et al.* in Ref. [15].

The electron phase can be expressed as $\psi_i(\tau) = \psi_i(0) + \Delta\psi_i(\tau)$ where $\Delta\psi_i(\tau)$ is the first-order perturbation in

$a(\tau)$. The field at time τ for the steady-state region where $\zeta < -\tau$ is given by

$$a(\tau) = a(0) + i \int_0^\tau \langle e^{-i\psi_i(0)} \Delta\psi_i(\tau') \rangle_{\zeta_i(\tau)=\zeta} d\tau'. \quad (6)$$

The i th electron interacts with the field in the steady-state region due to the slippage, and the energy modulation at τ' during $\delta\tau'$ is given from Eq. (3) by $\delta\mu_i(\tau') = [a(\tau')e^{i\psi_i(0)} + \text{c.c.}]\delta\tau'$. The energy change of the i th electron at time τ , $\mu_i(\tau)$, is given by the sum of those modulations during τ :

$$\mu_i(\tau) = \int_0^\tau \{a(\tau')e^{i\psi_i(0)} + \text{c.c.}\} d\tau'. \quad (7)$$

The electron phase perturbation is given from Eq. (4) by

$$\Delta\psi_i(\tau) = \int_0^\tau \mu_i(\tau') d\tau' \quad (8)$$

$$= \int_0^\tau d\tau' \int_0^{\tau'} \{a(\tau'') \exp[i\psi_i(0)] + \text{c.c.}\} d\tau'' \quad (9)$$

Substitution of Eq. (9) into Eq. (6) leads to

$$a(\tau) = a(0) + i \int_0^\tau d\tau' \int_0^{\tau'} d\tau'' \int_0^{\tau''} a(\tau''') d\tau'''. \quad (10)$$

The integral equation (10) can be written in a differential form by taking successive derivatives. The solution is expressed in the form $a(\tau) = \sum_{n=1}^3 a_n \exp(\alpha_n \tau)$ where the α_n are three complex roots of the cubic equation $\alpha^3 = i$ [14, 15, 16]. When the initial conditions $\dot{a}(0) = \ddot{a}(0) = 0$, the field at time τ for the steady-state region where $\zeta < -\tau$ is given by

$$a(\tau) = \frac{|a(0)|e^{i\phi(0)}}{3} \left(e^{\tau} e^{i\pi/6} + e^{-\tau} e^{-i\pi/6} + e^{\tau} e^{-i\pi/2} \right). \quad (11)$$

Equation (11) is valid in the linear regime before saturation when the incident electron beam is resonant.

EVOLUTION OF OSCILLATOR FEL PULSE

We first study the optical field and electron phase space evolutions on the second pass ($n = 2$) in an analytical way and then show that the analytical method can be applied to the n th pass with reasonable approximations. At first the notation n is thus used for $n = 2$.

FEL evolution on the second pass

The input field for the second pass, $a_n(\zeta) = a_n(\zeta, 0)$, is the same as the output of a SASE FEL with FEL parameter ρ except for a decrease of the amplitude due to the cavity loss α . The leading slope of the input field for the second pass is therefore given as a function of ζ by

$$a_n(\zeta) = (|a_n(0)|e^{i\phi_n(0)}/3) \left(e^{-\rho_n \zeta} e^{i\pi/6} + e^{\rho_n \zeta} e^{-i\pi/6} + e^{-\rho_n \zeta} e^{-i\pi/2} \right), \quad (12)$$

where $\rho_2 = 1$ and $|a_2(0)| \approx (1 - \alpha/2)|a(0)|$. Equation (12) can be used where $|\zeta| < L_s$ and $|\zeta| < L_b$ before the field reaches saturation. Here L_b is the incident electron bunch length in units of L_c and $L_s = 4\pi\rho N_w$ is the slippage distance. The phase space evolution of electrons during interaction with the leading slope given by Eq. (12) is quite similar to that of a SASE FEL. The perturbation method used in Ref. [12] can be applied to a study of the optical growth during the second pass, as long as the growth is small and the field $a_n(\zeta)$ remains almost unchanged during the FEL interaction. The electron phase can be expressed as $\psi_i(\tau) = \psi_i(0) + \Delta\psi_i(\tau)$ where $\Delta\psi_i(\tau)$ is the first-order perturbation in $a_n[\zeta_i(\tau)]/\rho_n^2$, since the field in the leading slope divided by ρ_n^2 is weak even after saturation except for a narrow range near ζ_p . When the i th electron is modulated in energy by interacting with the leading slope, the energy modulation at τ' during $\delta\tau'$ is expressed from Eq. (3) by $\delta\mu_i(\tau') = \{a_n[\zeta_i(\tau')]e^{i\psi_i(0)} + \text{c.c.}\}\delta\tau'$. The energy change of the i th electron at time τ , $\mu_i(\tau)$, is given by the sum of those modulations during τ :

$$\mu_i(\tau) = \int_0^\tau \{a_n[\zeta_i(\tau')] \exp[i\psi_i(0)] + \text{c.c.}\} d\tau'. \quad (13)$$

The integration of Eq. (13) after substitution of Eq. (12) yields

$$\begin{aligned} \mu_i(\tau) = & [2|a_n(0)|/3\rho_n] \times \\ & \{e^{-\sqrt{3}\rho_n\zeta_i(\tau)/2} \cos[\psi_i(0) + \phi_n(0) - \rho_n\zeta_i(\tau)/2 - \pi/6] \\ & - e^{-\sqrt{3}\rho_n\zeta_i(0)/2} \cos[\psi_i(0) + \phi_n(0) - \rho_n\zeta_i(0)/2 - \pi/6] \\ & - e^{\sqrt{3}\rho_n\zeta_i(\tau)/2} \cos[\psi_i(0) + \phi_n(0) - \rho_n\zeta_i(\tau)/2 + \pi/6] \\ & + e^{\sqrt{3}\rho_n\zeta_i(0)/2} \cos[\psi_i(0) + \phi_n(0) - \rho_n\zeta_i(0)/2 + \pi/6] \\ & + \cos[\psi_i(0) + \phi_n(0) + \rho_n\zeta_i(\tau) + \pi/2] \\ & - \cos[\psi_i(0) + \phi_n(0) + \rho_n\zeta_i(0) + \pi/2]\}. \end{aligned} \quad (14)$$

The integration of Eq. (8) after substitution of Eq. (14) yields

$$\begin{aligned} \Delta\psi_i(\tau) = & [2|a_n(0)|/3\rho_n^2] \times \\ & \{e^{-\sqrt{3}\rho_n\zeta_i(\tau)/2} \cos[\psi_i(0) + \phi_n(0) - \rho_n\zeta_i(\tau)/2 - \pi/3] \\ & - e^{-\sqrt{3}\rho_n\zeta_i(0)/2} \cos[\psi_i(0) + \phi_n(0) - \rho_n\zeta_i(0)/2 - \pi/3] \\ & - \rho_n\tau e^{-\sqrt{3}\rho_n\zeta_i(0)/2} \cos[\psi_i(0) + \phi_n(0) - \rho_n\zeta_i(0)/2 - \pi/6] \\ & + e^{\sqrt{3}\rho_n\zeta_i(\tau)/2} \cos[\psi_i(0) + \phi_n(0) - \rho_n\zeta_i(\tau)/2 + \pi/3] \\ & - e^{\sqrt{3}\rho_n\zeta_i(0)/2} \cos[\psi_i(0) + \phi_n(0) - \rho_n\zeta_i(0)/2 + \pi/3] \\ & + \rho_n\tau e^{\sqrt{3}\rho_n\zeta_i(0)/2} \cos[\psi_i(0) + \phi_n(0) - \rho_n\zeta_i(0)/2 + \pi/6] \\ & - \cos[\psi_i(0) + \phi_n(0) + \rho_n\zeta_i(\tau)] \\ & + \cos[\psi_i(0) + \phi_n(0) + \rho_n\zeta_i(0)] \\ & - \rho_n\tau \cos[\psi_i(0) + \phi_n(0) + \rho_n\zeta_i(0) + \pi/2]\}, \end{aligned} \quad (15)$$

where $\zeta_i(\tau) = \zeta_i(0) - \tau$ is used, which is valid as long as the electron energy change $\mu_i(\tau)$ is small and $d\zeta_i(\tau)/d\tau = -1$ holds. Equations (14) and (15) represent the phase space evolution of the i th electron during the second pass.

The field gain $da_n(\zeta)/d\tau$ caused by the electron microbunch in units of λ_r whose initial position is $\zeta_i(0) = \zeta + \tau$ is derived from substitution of $\psi_i(\tau) = \psi_i(0) + \Delta\psi_i(\tau)$ into Eq. (5) as follows:

$$\begin{aligned} da_n(\zeta)/d\tau = & (|a_n(0)|e^{i\phi_n(0)}/3\rho_n^2) \\ & \times \{e^{(-\rho_n\zeta e^{i\pi/6} + i\pi/6)} [1 - e^{-\rho_n\tau e^{i\pi/6}} (1 + \rho_n\tau e^{i\pi/6})] \\ & - e^{(\rho_n\zeta e^{-i\pi/6} - i\pi/6)} [1 - e^{\rho_n\tau e^{-i\pi/6}} (1 - \rho_n\tau e^{-i\pi/6})] \\ & + e^{(-\rho_n\zeta e^{-i\pi/2} - i\pi/2)} [1 - e^{-\rho_n\tau e^{-i\pi/2}} (1 + \rho_n\tau e^{-i\pi/2})]\}, \end{aligned} \quad (16)$$

when $|\Delta\psi_i(\tau)| \ll 1$.

The field $a_n(\zeta)$ is sequentially amplified from $\tau = 0$ to $\tau = -\zeta$ by the electron microbunches whose initial position are $\zeta_i(0) = \zeta + \tau$ as it passes through the undulator. The field gain per pass is given by

$$\begin{aligned} da_n(\zeta)/dn = & [|a_n(0)|e^{i\phi_n(0)}/3\rho_n^3] \\ & \times \{-\rho_n\zeta [e^{(-\rho_n\zeta e^{i\pi/6} + i\pi/6)} - e^{(\rho_n\zeta e^{-i\pi/6} - i\pi/6)} \\ & + e^{(-\rho_n\zeta e^{-i\pi/2} - i\pi/2)}] - 2[e^{(-\rho_n\zeta e^{i\pi/6})} + e^{(\rho_n\zeta e^{-i\pi/6})} \\ & + e^{(-\rho_n\zeta e^{-i\pi/2})}] + 6\}. \end{aligned} \quad (17)$$

The leading slope of the output field for the second pass is thus given by

$$\begin{aligned} a_n(\zeta) + da_n(\zeta)/dn = & [|a_n(0)|e^{i\phi_n(0)}/3\rho_n^3] \\ & \times \{-\rho_n\zeta [e^{(-\rho_n\zeta e^{i\pi/6} + i\pi/6)} - e^{(\rho_n\zeta e^{-i\pi/6} - i\pi/6)} \\ & + e^{(-\rho_n\zeta e^{-i\pi/2} - i\pi/2)}] + (\rho_n^3 - 2)[e^{(-\rho_n\zeta e^{i\pi/6})} \\ & + e^{(\rho_n\zeta e^{-i\pi/6})} + e^{(-\rho_n\zeta e^{-i\pi/2})}] + 6\}. \end{aligned} \quad (18)$$

The amplitude and phase of the output field given by Eq. (18) are plotted as solid circles in Figs. 1(a) and 1(b), respectively, as a function of ζ . The solid line shows the output field of the second pass obtained in a time-dependent numerical calculation, which solves Eqs. (3)–(5) with an input field given by Eq. (12) with $\rho_n = 1$ and represented by the dotted line. In the calculation, the shot-noise effect is neglected. One can see that the field given by Eq. (18) agrees well with the numerical calculation where $|\zeta| < 3.5$ but the phase gradually deviates from the calculation where $|\zeta| \geq 3.5$. This is because the assumption that the field remains almost unchanged during the passage through an undulator does no longer hold where $|\zeta| \geq 3.5$ for the second pass.

FEL evolution on pass numbers greater than 2

The output field of the second pass is equivalent to the input field for the third pass except for amplitude decrease due to the optical cavity loss α . If the input field for the third pass is found to be approximated by Eq. (12), the same procedure described in the previous subsection can be used for a study of the optical growth during the third pass. The dash-dotted line in Fig. 1 shows the field given by Eq. (12) with $\rho_n = 1.28$. The amplitude of this field is different from that obtained in a numerical calculation

(solid line) by only 10% to -20% where $|\zeta| < 5$, and the phase is different from the numerical calculation by only ± 0.17 rad. These results suggest that the input field for the third pass can be approximated by Eq. (12) with $\rho_3 = 1.28$. In a similar way, one can obtain ρ_n of the input field for pass numbers greater than $n = 3$ as well. For example $\rho_4 = 1.52$, $\rho_5 = 1.73$, $\rho_6 = 1.90$, and $\rho_7 = 2.05$.

As ρ_n increases, $\rho_n^3 - 2 \sim \rho_n^3$ and Eq. (18) asymptotically approaches

$$a_n(\zeta) + da_n(\zeta)/dn \sim a_n(\zeta) + [|a_n(0)|e^{i\phi_n(0)}/3\rho_n^3] \times \{-\rho_n\zeta[e^{(-\rho_n\zeta e^{i\pi/6} + i\pi/6)} - e^{(\rho_n\zeta e^{-i\pi/6} - i\pi/6)}] + e^{(-\rho_n\zeta e^{-i\pi/2} - i\pi/2)}\}, \quad (19)$$

The field evolution per pass can also be obtained by differentiation of Eq. (12) with respect to the pass number n under the assumption that ρ_n is independent of ζ as follows:

$$da_n(\zeta)/dn = (|a_n(0)|e^{i\phi_n(0)}/3)(d\rho_n/dn) \times \{-\zeta[e^{(-\rho_n\zeta e^{i\pi/6} + i\pi/6)} - e^{(\rho_n\zeta e^{-i\pi/6} - i\pi/6)}] + e^{(-\rho_n\zeta e^{-i\pi/2} - i\pi/2)}\}. \quad (20)$$

Equation (20) should be equal to Eq. (19) subtracted by $a_n(\zeta)$ as long as the gain is much higher than the optical cavity loss and ρ_n is large enough for Eq. (19) to hold. This yields

$$d\rho_n/dn = 1/\rho_n^2. \quad (21)$$

When we assume that Eq. (19) holds when $\rho_n > 2$, Eq. (21) gives

$$\rho_n \approx (3n - 12)^{1/3} \quad (22)$$

for $n \geq 7$. Substitution of Eq. (22) into Eq. (20) yields

$$(1/|a_n(\zeta)|)(d|a_n(\zeta)|/dn) \approx -(\sqrt{3}/2)\zeta(3n - 12)^{-2/3}, \quad (23)$$

when $\exp(-\sqrt{3}\rho_n\zeta/2) \gg 1$. Equation (23) shows that the gain per pass decreases with increasing pass number n . Please see Ref. [13] for further discussions.

ACKNOWLEDGEMENTS

The author would like to acknowledge valuable discussions with T. Shizuma at JAERI, S. Hiramatsu at KEK, and H. Hama at Tohoku University.

REFERENCES

- [1] G. Dattoli and A. Renieri, in *Laser Handbook*, edited by M.L. Stitch and M. Bass (North Holland, Amsterdam, 1985), Vol.4, p.75.
- [2] N. Piovella et al., PRE **52**, 5470 (1995); P. Chaix et al., PRE **59**, 1136 (1999).
- [3] G. Dattoli and A. Renieri, Nuovo Cimento B **59**, 1 (1980); G. Dattoli et al., Opt. Comm. **35**, 407 (1980).
- [4] H. Al-Abawi et al., Opt. Comm. **30**, 235 (1979); J. G. Kuper et al., Opt. Comm. **34**, 117 (1980).

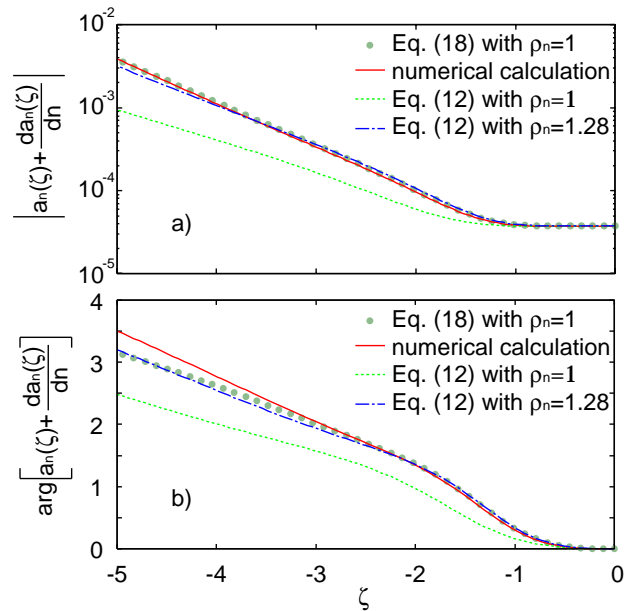


Figure 1: The amplitude (a) and phase (b) of the output field $a_n(\zeta) + \frac{da_n(\zeta)}{dn}$ as a function of ζ . The solid circles stand for the output field of the second pass given by Eq. (18) with $\rho_n = 1$, and the solid line is that obtained from a numerical calculation where Eq. (12) with $\rho_n = 1$, which is represented by the dotted line, is used as an input field envelope. The dash-dotted line expresses an approximated output field of the second pass given by Eq. (12) with $\rho_n = 1.28$. The amplitude of the front edge $|a_n(0)| = 3.7 \times 10^{-5}$ is used.

- [5] W.B. Colson, in *Laser Handbook*, edited by W.B. Colson, C. Pellegrini, and A. Renieri (North Holland, Amsterdam, 1990), Vol.6, pp. 115–193.
- [6] Nicola Piovella, PRE **51**, 5147 (1995).
- [7] N. Nishimori et al., PRL **86**, 5707 (2001); NIM A **483**, 134 (2002).
- [8] R. Nagai et al., NIM A **483**, 129 (2002).
- [9] R. Hajima et al., NIM A **475**, 270 (2001); *ibid.* **483**, 113 (2002).
- [10] Z.-W. Dong et al., NIM A **483**, 553 (2002).
- [11] Ryoichi Hajima and Ryoji Nagai, PRL **91**, 024801 (2003).
- [12] Nobuyuki Nishimori, PRST AB **8**, 100701 (2005).
- [13] Nobuyuki Nishimori, accepted for publication in PRE.
- [14] Norman M. Kroll and Wayne A. McMullin, PRA **17**, 300 (1978).
- [15] W. B. Colson et al., PRA **34**, 4875 (1986).
- [16] R. Bonifacio et al., Riv. Nuovo Cimento **13**, 9 (1990).
- [17] W.B. Colson and S.K. Ride, Phys. Lett. **76A**, 379 (1980).
- [18] Kwang-Je Kim, PRL **57**, 1871 (1986); NIM A **250**, 396 (1986).
- [19] N. Nishimori, R. Hajima, R. Nagai and E.J. Minehara, NIM A **507**, 79 (2003).

TWO-STREAM SMITH-PURCELL FREE-ELECTRON LASER USING A DUAL-GRATING: LINEAR ANALYSIS*

Wenxin Liu^{1#}, Zheng Liang¹, Ziqiang Yang¹, D. Li², K. Imasaki²

¹Institute of High Energy Electronics, University of Electronic Science and Technology of China, Sichuan Chengdu, 610054, P. R. China

²Institute for Laser Technology, 2-6 Yamada-oka, Suita, Osaka 565-0871, Japan

Abstract

A linear theory of two-stream Smith-Purcell Free-Electron Laser (SP-FEL) using a dual-grating has been given in this paper. A rectangular dual-grating is considered to be driven by two admixed electron beams with velocity separation. The linear dispersion equations for even and odd modes are derived with the help of fluid theory and the beam-wave interaction is analyzed through the numerical solutions. The considerable enhancement of growth rate is demonstrated due to the presence of two-stream instability. An example of THz-band two-stream SP-FEL is discussed.

INTRODUCTION

It is well known that Smith-Purcell (SP) radiation is emitted when an electron passes near the surface of grating [1]. At present, an intense interest has been raised in SP radiation since J. Urata *et al* observed the superradiance in the THz regime from the experiment at Dartmouth college [2,3]. The superradiance is regarded as the result of periodic electron bunching, which is produced by the interaction between the electron beam and the fields above the grating. Some theories [4,5] have been proposed to understand the physical mechanism of beam-wave interaction. Recently, D. Li and Z. Yang [6,7], J. T. Donohue and J. Gardelle [8] have performed the simulations of SP-FEL in the THz regime with PIC code.

The THz sources, a currently flourish research area, are of importance in varieties of applications in far-infrared spectroscopy, imaging, ranging and biomedical [9]. In order to improve the performance of such kind of device, it is necessary to find an efficient mechanism for the beam-wave interaction. The two-stream instability is an important physical mechanism, which has been successfully applied to some high power microwave sources [10-12].

In this paper, we present a two-stream Smith-Purcell Free-Electron Laser using a dual-grating, as shown in Fig.1. The two admixed electron beams are symmetric about z axial and guided by an infinite magnetic field. For simplicity, we assume that the system is uniform in the y direction which is parallel to the slots of grating.

DISPERSION EQUATION

The system of beam-wave interaction is illustrated in Fig.1. Two admixed beams with thickness $2b$ are located

above the rectangular grating, which drift in the z direction at a constant velocity v_1 and v_2 , respectively. The quantities D , H , d , a denote the rectangular grating period, groove depth, slot width, the distance between z axial and grating surface, respectively. For convenience, the operation area is divided into five regions: $-a \leq x < -b$ is region I, $b < x \leq a$ is region II, $-b \leq x \leq b$ is region III, Region IV and V is the lower groove $-a-h \leq x < -a$ and upper groove $a < x \leq a+h$. In the following analyses, we focus on the TM waves.

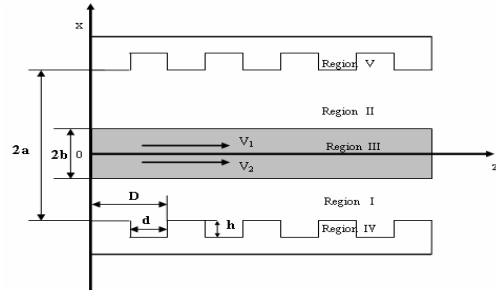


Fig.1 Schematic illustration of two admixed beams propagating over the dual-grating

We assume that (i) the externally applied magnetic field is so strong that perturbed electron motions are restricted in the z direction; (ii) the effect of beams self static fields are negligible; and (iii) the perturbations are uniform along the y direction. Maxwell's equations and relativistic hydrodynamic equations for two cold electron beams are employed to describe this system as follows:

$$\nabla \times \vec{E} + \frac{1}{c} \frac{\partial \vec{B}}{\partial t} = 0 \quad (1)$$

$$\nabla \times \vec{B} + \frac{1}{c} \frac{\partial \vec{E}}{\partial t} = \frac{4\pi}{c} \sum_{i=1}^2 J_i \quad (2)$$

$$\left(\frac{\partial}{\partial t} + v_{i0} \frac{\partial}{\partial z} \right) \delta v_{i1} = -\frac{e}{\gamma_i^3 m_0} E_z \quad (3)$$

$$\left(\frac{\partial}{\partial t} + v_{i0} \frac{\partial}{\partial z} \right) \delta n_{i1} = -n_{i0} \frac{\partial}{\partial z} \delta v_{i1} \quad (4)$$

Here, subscript $i=1,2$ represents the first and second electron beam, respectively. \vec{E} and \vec{B} are the electric and

*Work supported by National Nature Science Foundation of P. R. China (60571020), #liuwenxin76@163.com

magnetic field vectors. $\gamma_i = 1 + eV_i/m_0c^2$ is the relativistic mass factor, c is the speed of light, V_i is the i th beam voltage, the voltage ratio of two electron beams is $v_r = V_2/V_1$, and $v_{i0} = c \cdot [(\gamma_i^2 - 1)^2 / \gamma_i^2]^{1/2}$ is the unperturbed velocity of i th beam. $-e$, m_0 , n_{i0} , δn_{i1} , δv_{i1} are the electron charge, the electron rest mass, the unperturbed density, perturbed density and perturbed velocity of i th beam, respectively. $J_i = -e(n_{i0}\delta v_{i1} + \delta n_{i1}v_{i0})$ is perturbed current density. The relative density factor α is n_{20}/n_{10} . To obtain the dispersion equation, we expand $n_i = n_{i0} + \delta n_{i1}$, $v_i = v_{i0} + \delta v_{i1}$, $\vec{E} = \vec{\delta E}_z$, $\vec{B} = \vec{\delta B}_y$ and solve for the perturbed variables. Using Floquet's theorem, all the fields and beam parameters can be written as a sum of space harmonics which have the periodicity of the grating [13],

$$f(x, z) = \sum_{n=-\infty}^{\infty} f_n(x) \exp(jk_n z - j\omega t) \quad (5)$$

where $k_n = k_0 + 2\pi n/D$, k_0 is wave number, ω is the angular frequency, n is an integer.

From Eqs.1, 2, 3, 4 and expression (5), the wave equation for the n th space harmonic of axial electric field is given and the transverse components of electric and magnetic fields can be expressed in terms of the axial electric field as follows[14]:

$$\left[\frac{\partial^2}{\partial x^2} + \epsilon_{l,n} \left(\frac{\omega^2}{c^2} - k_n^2 \right) \right] \delta \hat{E}_{z,n,l}(x) = 0, \quad l=1,2,3 \quad (6)$$

$$\delta \hat{E}_{x,n,l} = \frac{jk_n}{\kappa_n^2} \frac{\partial}{\partial x} \delta \hat{E}_{z,n,l} \quad (7)$$

$$\delta \hat{B}_{y,n,l} = \frac{j\omega}{c\kappa_n^2} \frac{\partial}{\partial x} \delta \hat{E}_{z,n,l} \quad (8)$$

$$\epsilon_{3,n} = 1 - \sum_{i=1}^2 \frac{\omega_{pi}^2}{\gamma_i^3 (\omega - k_n v_i)^2}, \quad \epsilon_{1,n} = \epsilon_{2,n} = 1 \quad (9)$$

where $\omega_{pi} = (e^2 n_{i0} / m_0 \epsilon_0)^{1/2}$ is the beam-plasma angular frequency, $\epsilon_{l,n}$ is the dielectric function, $\kappa_n = [(\omega/c)^2 - k_n^2]^{1/2}$ is the transverse wave number. $l = 1, 2, 3$ represents the region I, II, III, respectively.

Components of electromagnetic fields in each region [13]

Employed the wave Eq.6 and expressions (7) and (8), the components of electromagnetic fields in the three regions can be treated as follows:

The fields in Region I $-a \leq x < -b$ and II $b < x \leq a$ can be expressed in terms of two coefficients, respectively:

$$\delta \hat{E}_{z,n,l_0} = A_n^{l_0} \sin \kappa_n x + B_n^{l_0} \cos \kappa_n x \quad (10)$$

$$\delta \hat{E}_{x,n,l_0} = \frac{jk_n}{\kappa_n} (A_n^{l_0} \cos \kappa_n x - B_n^{l_0} \sin \kappa_n x) \quad (11)$$

$$\delta \hat{B}_{y,n,l_0} = \frac{j\omega}{c\kappa_n} (A_n^{l_0} \cos \kappa_n x - B_n^{l_0} \sin \kappa_n x) \quad (12)$$

where superscript $l_0 = 1, 2$ respects the region I and region II, respectively.

Region III ($-b \leq x \leq b$)

$$\delta \hat{E}_{z,n,3} = C_n \sin \beta_n x + D_n \cos \beta_n x \quad (13)$$

$$\delta \hat{B}_{y,n,3} = \frac{j\omega\beta_n}{c\kappa_n^2} (C_n \cos \beta_n x - D_n \sin \beta_n x) \quad (14)$$

where $\beta_n = \sqrt{\epsilon_{3,n}} \kappa_n$.

Region IV and V is the lower groove $-a-h \leq x < -a$ and upper groove $a < x \leq a+h$, respectively. As the grating period is less than the free-space wavelength, we represent the fields inside the 1th groove using the form of TEM standing wave modes as follows:

$$\delta \hat{E}_z = S_{\pm a} \sin \left[\frac{\omega}{c} (x \mp (a+h)) \right] \exp(ik_0 D) \quad (15)$$

$$\delta \hat{B}_y = jS_{\pm a} \cos \left[\frac{\omega}{c} (x \mp (a+h)) \right] \exp(ik_0 D) \quad (16)$$

where the “ \mp ” denotes the upper interface $x=a$ and the lower face $x=-a$, respectively. The $A_n^{l_0}$, $B_n^{l_0}$, C_n , D_n , $S_{\pm a}$ mean unknown coefficients, which are depended on the boundary conditions.

Dispersion equation

Applying the boundary conditions at the grating surfaces $x = \pm a$, the beam surfaces $x = \pm b$, solving simultaneously Eqs.10-16 and then eliminating the coefficients of $A_n^{l_0}$, $B_n^{l_0}$, C_n , D_n , $S_{\pm a}$, the odd mode and even modes dispersion equation is obtained as follows, respectively.

$$\frac{D}{d} \cot\left(\frac{\omega h}{c}\right) + \sum_{n=-\infty}^{\infty} \frac{\omega}{cK_n} \operatorname{sinc}^2\left(\frac{k_n d}{2}\right) \frac{Q_n - R_n / \epsilon_{3,n}^{1/2}}{\epsilon_{3,n}^{1/2} + T_n} = 0 \quad (17)$$

is the dispersion equation for the odd modes, and

$$\frac{D}{d} \cot\left(\frac{\omega h}{c}\right) - \sum_{n=-\infty}^{\infty} \frac{\omega}{cK_n} \operatorname{sinc}^2\left(\frac{k_n d}{2}\right) \frac{1 + T_n \epsilon_{3,n}^{1/2}}{Q_n / \epsilon_{3,n}^{1/2} - R_n} = 0 \quad (18)$$

is the dispersion equation of the even modes, where

$$Q_n = \epsilon_{3,n}^{1/2} \cot[\kappa_n(a-b)], \quad R_n = \epsilon_{3,n}^{1/2} \cdot \tan \beta_n b,$$

$T_n = \tan \beta_n b \cdot \cot[\kappa_n(a-b)]$. The Eqs.17 and 18 is similar to Ref.[13] when the voltages of two electron beams are the same. In the absence of beams, the dispersion equations of odd modes and even modes can be reduced to:

$$\frac{D}{d} \cot\left(\frac{\omega h}{c}\right) + \sum_{n=-\infty}^{\infty} \frac{\omega}{cK_n} \operatorname{sinc}^2\left(\frac{k_n d}{2}\right) \cot \kappa_n a = 0 \quad (19)$$

is the dispersion equation for the odd modes, and

$$\frac{D}{d} \cot\left(\frac{\omega h}{c}\right) - \sum_{n=-\infty}^{\infty} \frac{\omega}{cK_n} \operatorname{sinc}^2\left(\frac{k_n d}{2}\right) \tan \kappa_n a = 0 \quad (20)$$

is the dispersion equation for the even modes.

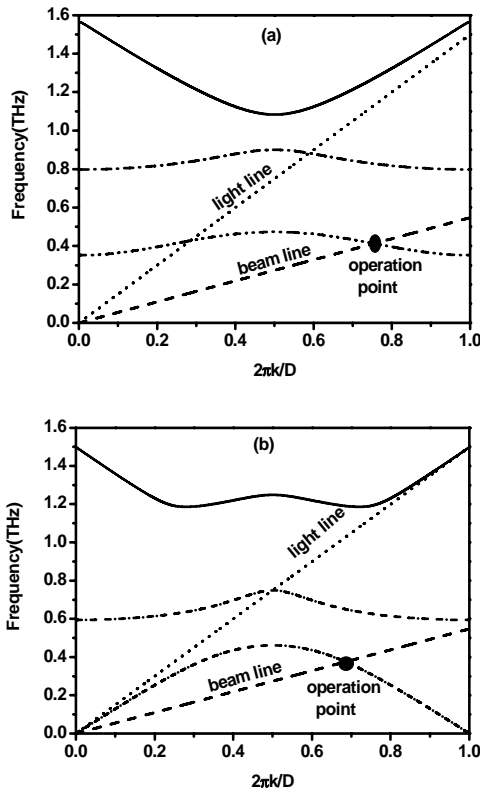


Fig2. Dispersion curves of (a) even mode and (b) odd mode. The parameters are period $D=0.2\text{mm}$, slot width $d=0.1\text{mm}$, slot depth $h=0.1\text{mm}$ and the distance of two-gratings $2a=0.3\text{mm}$

NUMERICAL SOLUTIONS

In this section, we focus on the characteristics of dispersion equation through the numerical solutions.

The dispersion curves without beams for the even modes are found by the solutions of Eq.20, which are shown in Fig.2 (a). The beam line with voltage 40kv is plotted for reference. It is observed that the lowest order mode has a cutoff frequency of 0.345THz and has a maximum frequency 0.475THz. There is a stop band between the two lowest order modes extending from 0.475THz to 0.8THz.

Similarly, the dispersion curves without beams for the odd modes are obtained by the solutions of Eq.19, which are shown in Fig.2 (b). The band gap is evident extending from 0.46THz to 0.6THz. Obviously, the band gap of even modes and the frequency of operation point (solid dot) which is the intersection point of beam-wave are greater than that of the lowest odd mode.

The two admixed beams are turned into a single beam when the beam voltages are the same. The dispersion curves of single beam for the even mode found by the solution of Eq.18 are shown in Fig.3, where the left

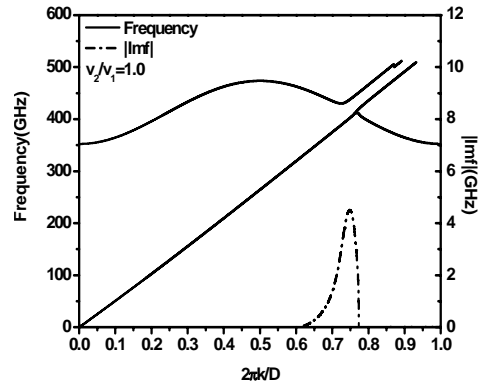


Fig3. Dispersion curves showing the real and imaginary components of the frequency for the lowest-order even mode, the parameters of grating are the same as that of in Fig.2. The beam voltage is 40kv, electron beam density is $n_0=5.97 \times 10^{18} \text{m}^{-3}$

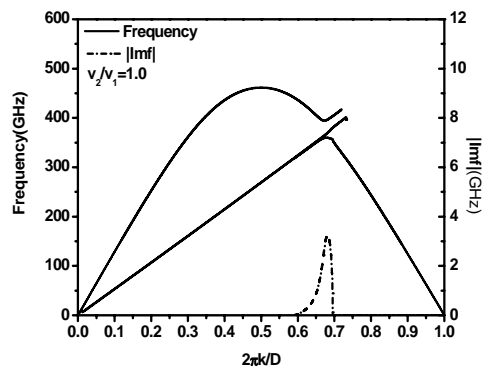


Fig4. Dispersion curves showing the real and imaginary components of frequency for the lowest-order odd mode, the parameters are the same as in Fig.3

axis is the real component of frequency and the right axis is the growth rate. Seen from Fig.3, the growth rate is found at the vicinity where the slow-wave and electron beam are synchronous, which occurs at a frequency near 0.41 THz. The peak growth about 4.5GHz is found at a frequency of 0.403THz. Similarly, the dispersion curves of single beam for the odd modes are shown in Fig.4. The peak growth rate about 3.24GHz is found at the normalized wave number of 0.68, which occurs at a frequency of 0.371THz. Obviously, the peak growth rate of the lowest order even mode are greater than that of odd mode.

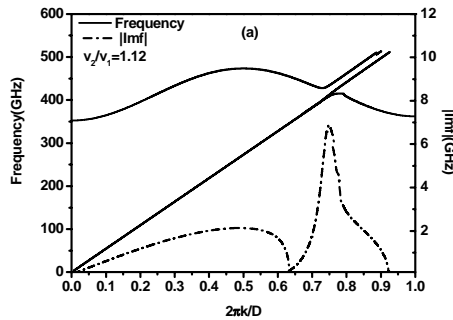


Fig5. Dispersion curves showing the real and imaginary components of the frequency for the lowest-order even mode, the parameters of grating are the same as that of in Fig.2. The beam voltage is 40kv, electron beam density is $n_0=5.97 \times 10^{18} \text{ m}^{-3}$, the voltage ratio is $v_r=1.12$

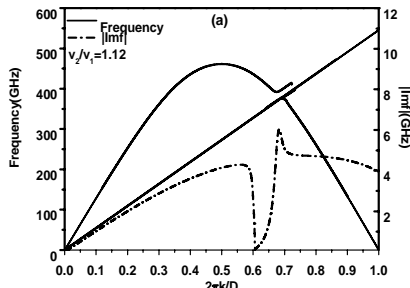


Fig6. Dispersion curves showing the real and imaginary components of the frequency for the lowest-order odd mode. The parameters of grating are the same as that of in Fig.2. The beam voltage is 40kv, electron beam density is $n_0=5.97 \times 10^{18} \text{ m}^{-3}$, and the voltage ratio is $v_r=1.12$

The dispersion curves of two-stream for the lowest-order even mode obtained by the solution of Eq.18 are shown in Fig.5. Obviously, the growth rate is remarkably different from that of single beam, the cambered growth rate is produced by the TSI, and the growth rate is remarkably enhanced when the TSI wave is synchronous with the slow-wave. The peak growth rate about 6.91GHz is found at the frequency of 0.412THz, which is enhanced by a factor of 2 than that of single beam. Outside the synchronous range of TSI and electro-magnetic wave, the growth rate is still existed, which is thought to be yielded by the TSI

Similarly, the dispersion curves of two-stream for the lowest-order odd mode solved the Eq.29 are shown in Fig.6. The peak growth rate about 6.04GHz is found at the frequency of 0.375THz, which is enhanced by a factor 2. We may note from Figs.3, 4, 5 and 6 that the even mode

could be an operation mode for which the growth rate is greater than that of odd mode. To obtain the higher operation frequency, we should make the even mode as an operation mode.

CONCLUSIONS

In this paper, we have studied the two-stream Smith-Purcell Free-Electron Laser with a dual-grating. The linear dispersion equations for the even modes and odd modes are derived by making use of fluid theory, and those of characteristics are analyzed through the numerical solutions. We find that the peak growth rate is enhanced by a factor of 2 than that of single beam when the TSI wave is synchronous with the electromagnetic wave. The nonlinear effect is under consideration, which will be reported in the future.

ACKNOWLEDGEMENT

This work is supported by National Natural Science Foundation of P. R. China (60571020, 60178011).

REFERENCES

- [1]S.J.Smith, E.M.Purcell, "Visual light from localized surface charges moving across a grating", *Phys. Rev.* **92**,1069,1953
- [2]J.Urata,M.Goldstein,M.F.Kimmitt,A.Naumov,C.Platt. and J.E.Walsh,"Superradiant Smith-Purcell Radiation", *Phys.Rev.Lett.*80,(1998)516
- [3]A.Bakhtyari,J.E.Walsh,and J.H.Brownell,"Amplified-spontaneous-emission power oscillation in a beam-wave interaction" *Phys.Rev.E.*65,066503(2002)
- [4]K.J.Kim, and S.B.Song, "Self-amplified spontaneous in Smith-Purcell free electron lasers", *Nucl. Instrum.,Methods Phys. Res., Sect. A* **475**,158 (2001)
- [5]H.L.Andrews and C.A.Brau. "Gain of a Smith-Purcell free-electron laser", *PRSTAB* **7**, 070701 (2004)
- [6]D.Li, K. Imasaki, Z.Yang and Gun-Sik Park, "Three-dimensional simulation of super-radiant Smith-Purcell radiation", *Appl.Phys.Lett.* **88** (201501), 2006
- [7]D.Li and Z.Yang, K. Imasaki, and Gun-Sik Park "Particle-in-cell simulation of coherent and super-radiant Smith-Purcell radiation", *Phys Rev. ST. Accel. Beams*, **9**, (2006)040701,
- [8]J.T.Donohue and J.Gardelle "Simulation of Smith-Purcell terahertz radiation using a particle-in-cell code" *Phys Rev.ST.Accel.Beams*,**9**,060701,2006
- [9]P.H Siegel, "Terahertz technology", *IEEE Trans, Microwave and Tech.*, **50**, (2002)910,
- [10]J. R. Pierce, *et al* "A new type of high frequency amplifier," *Bell Syst.Tech.J.***28**. (1949) 33
- [11]V.V. Kulish, A.V. Lysenko, V.I. Savchenko. Two-stream free electron lasers. General properties. *Int. J. Infrared Millim. Waves*, vol. **24**, (2003)129
- [12]H.P. Freund, *et al.*, "Multiple-beam free-electron laser", *Nucl. Inst. Method A***507**, (2003)373
- [13]H.P. Freund and T.M.Abu-Elfadl., "Linearized Field Theory of a Smith-Purcell Traveling Wave Tube", *IEEE, Plasma Science* **32**,1015,2004
- [14]K. Mehrany and B. Rshidaian, "Dispersion and Gain Investigation of a Cerenkov Grating Amplifier", *IEEE Trans. On Electron Devices*, **50**,1562, 2003.

PRODUCTION OF ‘GIANT’ PULSES OF SCATTERED RADIATION FROM PUMP WAVE SPOT RUNNING OVER THE ELECTRON BEAM*

V. Baryshev, N. Ginzburg[#], A. Sergeev, I. Zotova IAP RAS, Nizhny Novgorod, Russia.

Abstract

To generate ultrashort electromagnetic pulses it is suggested to scan a spot formed by pump wave along an electron beam. When pump spot velocity is equal to the group velocity of scattered radiation the short ‘giant’ pulse of scattered radiation with amplitude increasing proportional to interaction distance will be produced. The running spot of pump wave can be realized after reflection of frequency chirped laser beam from echelette grating.

INTRODUCTION

In [1] the generation of millimetre wave superradiance (SR) pulses have been observed in the process of stimulated backscattering of relatively long pump wave pulse by extended electron bunch with the length restricted by cooperative length (the distance of the scattered wave propagation during the time of instability growth up). Under such conditions the scattered radiation represented a single pulse with peak power strongly exceeding the level of spontaneous emission.

In this paper we study the alternative method of generation superradiance type pulses in the process of stimulated scattering when the relatively short spot illuminated by pump wave runs over the quasi-continuous electron beam. Obviously scattering and beam modulation take place only in area illuminated by pump wave. In the

case when the pump spot moves with group velocity of scattered radiation the pulse of scattered radiation propagating along electron beam will be amplified continually by fresh (unmodulated) electrons due to difference between signal wave group velocity c and electron translational velocity $v_{||}$. As a result the peak amplitude of scattered pulse increases proportionally to shifting distance. The running spot of pump wave can be realized after passing (reflection) of frequency chirped laser pulse from frequency depended refraction system like prism or echelette grating (see Fig. 1). It should be noted that the shifting direction and velocity of the pump wave spot are not correlated with the phase and group velocities of this wave. For our purpose to obtain the large frequency conversion the direction of spot shifting should be approximately opposite to the group velocity vector.

In the case of scattering of laser radiation by a moderately relativistic electron beam with energy $\sim 1-3$ MeV above process can be used to produce intense SR pulses either at UV band (up frequency conversion), at terahertz band (down frequency conversion) or bands depending on direction of scattered wave propagation with respect to electron beam. Correspondingly at the first case illuminated spot should run together with scattered wave in the direction of electron motion while in the second case this spot together with scattered wave should run at opposite direction.

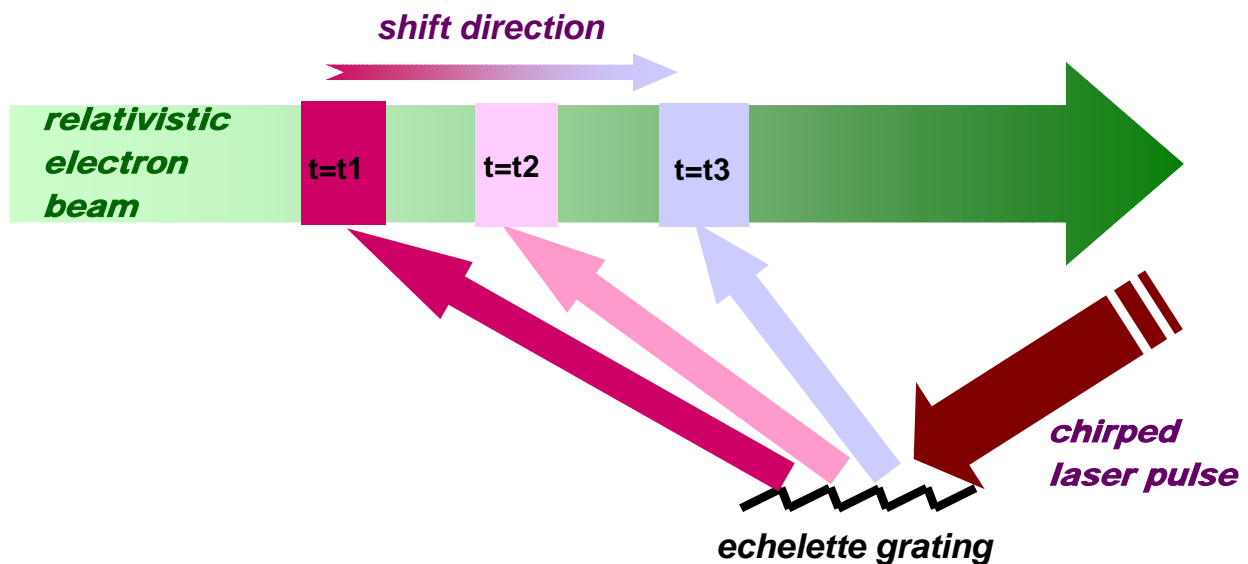


Figure 1: Echelette scheme of scanning of pump field spot using frequency chirped laser pulse.

*Work supported by ... Russian Fund for Fundamental Researches, grant 05-02-17553

[#]ginzburg@appl.sci-nnov.ru

MODEL AND BASIC EQUATIONS

Let us consider the process of stimulated scattering in situation when the spot illuminated by a pump wave runs along electron beam with velocity u in the direction of electron motion. In this case due to the Doppler effect the frequency of scattered radiation ω_s essentially exceeds the frequency of pump wave ω_i . Neglecting pump wave exhaustion the generation of pulses of scattered radiation in the above process can be described by the system of equations including the nonstationary equation for scattering signal amplitude and the averaged electron motion equations [2]:

$$\begin{aligned} \left(\frac{\partial}{\partial z} + \frac{1}{c} \frac{\partial}{\partial t} \right) a_s &= i \chi(t - z/u) k_c a_i I \frac{1}{\pi} \int_0^{2\pi} e^{-i\theta} d\theta_0 \\ \left(\frac{\partial}{\partial z} + \frac{1}{v_{||}} \frac{\partial}{\partial t} \right)^2 \theta &= \mu k_c^2 \chi(t - z/u) \text{Im} \{ a_s a_i^* e^{i\theta} \} \end{aligned} \quad (1)$$

Here $a_{i,s} = eA_{i,s}/m_0\gamma_0 c^2$ is the dimensionless amplitude of scattered and pump waves, $\theta = \omega_c t - k_c z$ is the

electron phase respect to the combination wave, $\omega_c = \omega_s - \omega_i$, $k_c = \omega_c/c - \omega_i/c$, $\mu = \gamma_0^{-2} \beta_{||}^{-3}$, I is the dimensionless parameter which is proportional to the beam current. Function $\chi(t - z/u)$ describes the profile of the spot illuminated by pump field. Introducing the new independent variables

$$Z = C \frac{\omega_c}{c} z, \quad \tau = C \frac{\omega_c c (t - z/v_{||})}{1/c - 1/v_{||}} \quad (2)$$

and assuming that the velocity of pump spot is equal to the group velocity of scattered signal ($u=c$) Eqs. (2) can be presented in the form

$$\begin{aligned} \frac{\partial a}{\partial Z} + \frac{\partial a}{\partial \tau} &= -\frac{i}{\pi} \chi(\tau - Z) \int_0^{2\pi} e^{-i\theta} d\theta_0 \\ \frac{\partial^2 \theta}{\partial Z^2} &= \chi(\tau - Z) \text{Im} \{ a e^{-i\theta} \} \end{aligned} \quad (4)$$

where $a = \mu a_s a_i^* C^{-2}$, $C = (\omega_p^2 |a_i|^2)^{1/3}$ is the gain (Pierce) parameter. Under assumption that the development of instability starts from the small perturbation of electron beam density the initial and boundary conditions can be

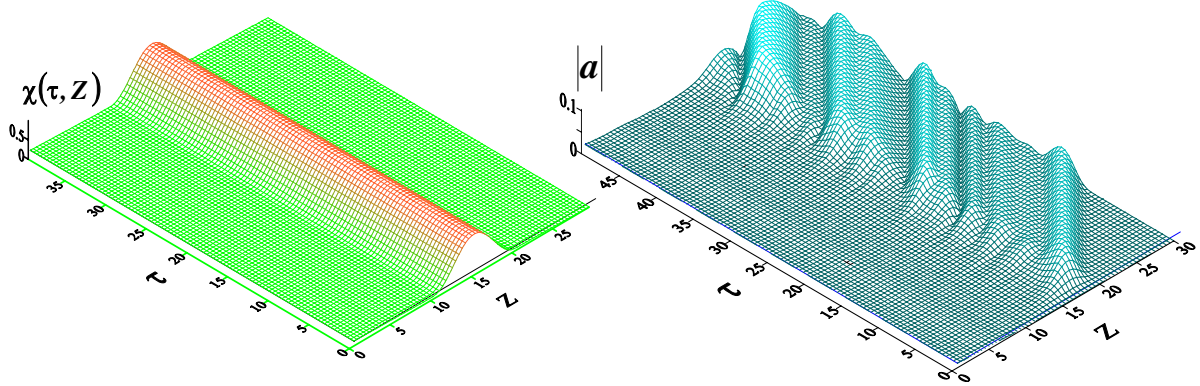


Figure 2: Production of the SASE signal in the case of standing pump field spot.

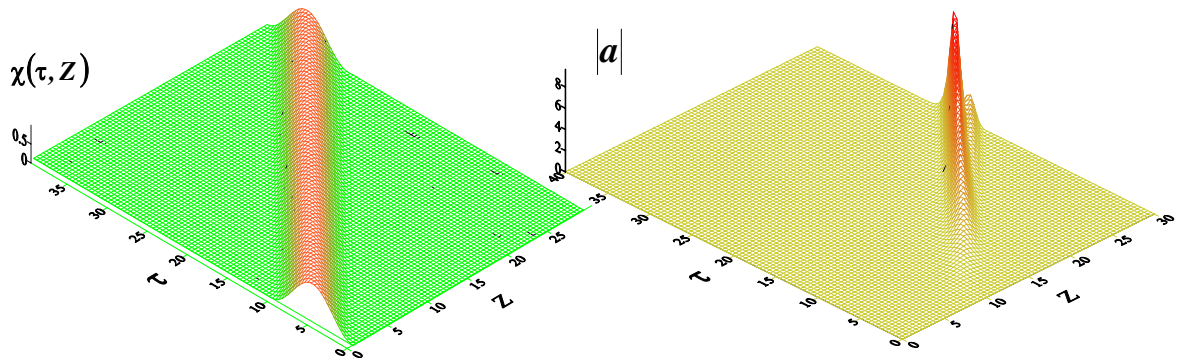


Figure 3: Production of 'giant' single pulse in the case of moving pump field spot.

written in the form

$$\theta|_{Z=0} = \theta_0 + r \cos(\theta_0 + \varphi(\tau)), \quad \theta_0 \in [0, 2\pi], \quad r \ll 1$$

$$\left. \frac{\partial \theta}{\partial Z} \right|_{Z=0} = 0, \quad a|_{Z=0} = 0 \tag{5}$$

where $\varphi(\tau)$ is the random function.

SIMULATION RESULTS

Let's consider at first the traditional situation with the unmovable $u = 0$ bell-shaped pump spot: (see Fig. 2a). In this case, due to the slippage, radiation escapes from pump spot. As a result the well-known multi-spikes regime of SASE [3,4] is realized (Fig. 2b) when different parts of beam radiate practically independently.

The totally different situation takes place when the pump spot moves along the electron beam together with scattered signal: $u = c$ (Fig. 3a). But because electron velocity $v_{||}$ is slightly less than c , the interaction (scattering) spot slips along beam and the pulse of scattered radiation formed at initially stage of interaction propagates through the unmodulated electrons being effectively amplified (see Fig. 3b). As a result the scattered radiation represents the single short pulse with amplitude essentially exceeding the amplitude of spikes in the SASE regime (compare with Fig. 2b). In the ideal situation the amplitude of above 'giant' pulse grows proportionally to the interaction distance L (see Fig. 4).

It is important to note that due to short lifetime of individual electrons in the interaction spot above process is less sensitive to the spread of beam parameters in comparison with traditional steady state regime (see Fig. 5).

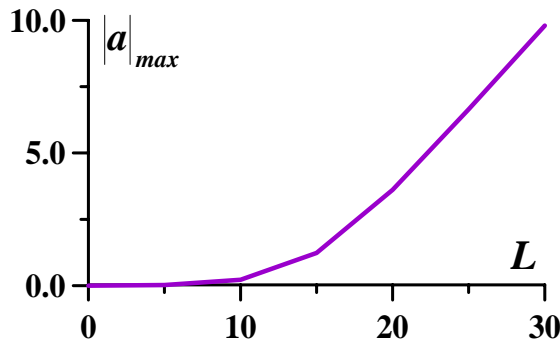


Figure 4: Dependence of pulse peak amplitude on the shifting distance.

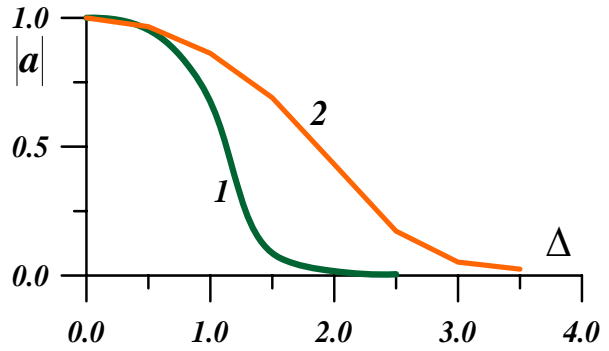


Figure 5: Dependence of radiation peak amplitude on electron velocity spread Δ for steady state regime (1) and 'giant' pulse regime (2).

CONCLUSION

In conclusion lets make preliminary estimations of possible experiments on backscattering of 10μ CO_2 laser radiation by high current () relativistic electron beam. For electron energy 3 MeV scattered wavelength ~ 200 nm will belong to UV bands. For laser pump pulse with duration 1 ns the shift of pump spot will be about 30 cm. For power density of pump wave $\sim 150 \text{ GW/cm}^2$ and current density 30 kA/cm^2 the gain parameter is $C \approx 6.3 \cdot 10^{-5}$. As a result for initial perturbation $r = 0.001$ the maximal power density of scattered radiation can achieved $\sim 1 \text{ GW/cm}$.

REFERENCES

- [1] A. Reutova, M. Ulmaskulov, A. Sharypov, V. Shpak, S. Shunailov, M. Yalandin, V. Belousov, G. Denisov, N. Ginzburg, A. Sergeev and I. Zotova JETP Lett. 82(5) 295.
- [2] V. Bratman, N. Ginzburg, M. Petelin JETP 76(3) (1979) 930.
- [3] R.H. Bonifacio, N. Piovella and B.W.J. McNeil, Phys. Rev. A, 44, (1991) 3441.
- [4] C. Pelegrini "High power femtosecond pulses from an X-ray SASE-FEL", FEL'1999, Hamburg, Germany August 1999, p.124.

INFLUENCE OF LINER FLUCTUATIONS ON LOW- AND HIGH-GAIN CHERENKOV FELS

I. de la Fuente*, P.J.M. van der Slot, K.-J. Boller
Laser Physics and Non-Linear Optics Group, University of Twente
PO Box 217, 7500 AE Enschede, The Netherlands.

Abstract

Imperfections in the dielectric liner of a Cherenkov Free-Electron Laser (CFEL) result in fluctuations in the phase velocity of a radiation wave when it propagates through the lined waveguide. Random fluctuations in the phase velocity reduce the bunching of the electrons and consequently lower the gain of CFELs. Here we theoretically investigate the influence of these liner-induced phase fluctuations in the radiation field on the saturated power of low to high gain CFELs. To obtain different gain regimes, we keep the electron beam radius constant and vary the current density. As an example, we study a 50 GHz CFEL and quantify the reduction in the single-pass saturated power for different rms liner fluctuations when the CFEL is driven by an electron beam with current densities varying from 1 A/cm² (average gain of 0.43 dB/cm) to 25 A/cm² (average gain of 1.39 dB/cm).

INTRODUCTION

The increasing number of microwave applications in both research and industry [1, 2] has increased the interest in tuneable high-power microwave sources. The Cherenkov Free-Electron Laser (CFEL) is a promising candidate as a compact high-power microwave source for various applications. CFELs have been operated at 100 kW peak power level at 1 mm wavelengths, at 200 MW peak power level at 8 cm wavelengths and at wavelengths as short as in the far infrared [3]. The simplicity of its construction, the high efficiency and an affordable compact design have made the CFEL attractive for applications where high microwave frequencies and high powers are needed. However, simple imperfections in either the electron beam or the lined waveguide section, that are used to generate the laser gain, can seriously degrade the performance of the device [4].

In a CFEL, accelerated electrons are injected through a wave-guiding structure that slows the phase velocity of the electromagnetic wave to a sub-luminous value. An example is a metallic, cylindrical tube lined with a dielectric material, e.g., quartz. By choosing appropriate dimensions for the waveguide, i.e., the inner diameter for the tube, the thickness and dielectric constant of the liner, the phase velocity of EM waves can be matched to the velocity of the injected electron beam for a desired wave frequency [5]. A transversely magnetic (*TM*) wave can decelerate or accelerate co-propagating electrons. A net deceleration of elec-

trons in the pump beam and, correspondingly, a net amplification of the wave, occurs only if the electrons are forming bunches, if these bunches travel with the phase velocity of the radiation wave, and if the bunches are located within a certain phase range of the radiation wave (when seen from the frame of that wave). A fluctuating phase velocity of the wave in the waveguide would appear as a fluctuating relative phase of the bunches; it could bring bunches out of the optimum driving phase, and this would reduce the amplification. Likewise, a spread in longitudinal electron velocities results in a spread in relative phases between wave and the electrons. This results in a reduced bunching within the electron beam and consequently in a lower amplification of the wave [3].

Although the variations in the phase velocity can have different origins, we will model only one type of imperfection, namely, fluctuations in the inner radius of the liner. Other types of fluctuations, such as a spatial inhomogeneity of the liner's dielectric constant, are not treated separately because we expect widely analogous results. In a previous study we have shown that in a low current CFEL, a typical manufacturing tolerance in the inner radius of the liner of 5 % can reduce the saturated power by a factor of 2 [4]. In this paper, we investigate the sensitivity of the CFEL to small random liner imperfections for different gain regimes. We therefore consider a 50 GHz CFEL with a fixed liner geometry, electron beam energy, and electron beam radius. The different gain regimes are obtained by varying the electron beam current density from 1 A/cm² to 25 A/cm².

In the remainder of this paper we first present a summary of the theoretical model that describes the dynamics of the CFEL in the presence of radii fluctuations. Next, we will show the numerical results for a CFEL system operating in different gain regimes. We end with a discussion and conclusions.

THEORETICAL MODEL

The theoretical model describing the dynamics of a CFEL in the presence of small and random fluctuations of the liner inner radius is presented in previous work [4] and here we present a summary.

The standard CFEL dynamical model [3, 6] assumes that the electromagnetic wave co-propagating with the electron beam can be described by a superposition of empty (i.e., without the electron beam) waveguide eigenmodes with amplitudes that vary slowly with longitudinal distance z . Using the power orthogonality property of the eigenmodes,

* i.delafuentevalentin@utwente.nl

and applying the slowly varying amplitude and phase approximation to Maxwell's equations, the dynamical equation for the mode amplitudes are derived. The system is closed by the Newton-Lorentz equations, that describe the motion of the electrons under influence of the electromagnetic wave.

The effect of a small random fluctuation in the inner radius $r_d(z)$ of the liner that varies slowly along its length is twofold. First, it varies the phase velocity of the wave. Second, it modifies, in principle, the transverse mode profile. However, our analysis shows that the liner fluctuations mainly affect the phase velocity of the wave and that the transverse mode profile remains approximately unchanged [4]. In our model, we allow the wave number to vary slowly along the length of the liner, and write for the longitudinal component of the electric field $E_{z,n}$ for mode TM_{0n} :

$$E_{z,n}(r, z, t) = a_{0n}(z) \frac{f_n(r)}{\sqrt{k_n(z)}} \exp\left(i \int_0^z k_n(z') dz' - \omega t\right), \quad (1)$$

where $f_n(r)$ is the transverse mode profile of an empty lined waveguide [7], $a_{0n}(z)$ the slowly varying mode amplitude, and the slowly varying longitudinal wave number $k_n(z)$ is given by:

$$k_n(z) = k_{0n} + \int_0^z \frac{dk_n}{dz'} dz' \approx k_{0n} + \left. \frac{\partial k_n}{\partial r_d} \right|_{r_{d0}} \int_0^z \frac{dr_d}{dz'} dz', \quad (2)$$

where, for convenience, the inner radius of the liner at $z = 0$ is taken equal to the mean radius r_{d0} and k_{0n} is the wave number corresponding to a homogeneous waveguide with $r_d = r_{d0}$. The evolution of the normalized field amplitude $a'_{0n}(z) = \frac{e}{mc} a_{0n}(z)$ for the TM_{0n} modes is:

$$2\sqrt{k_n(z)} \left(1 - \frac{\kappa_n^2}{k_{0n}^2}\right) \frac{\partial a'_{0n}}{\partial z} = -4 \frac{\omega_p^2}{c_0^2} \frac{\beta_{z0}}{A_n r_{d0}^2} \times \int_0^{r_{d0}} dr r \left[i I_1(\kappa_n r) \left\langle \frac{\beta_r}{|\beta_z|} e^{i\alpha_n} \right\rangle + \frac{\kappa_n}{k_{0n}} I_0(\kappa_n r) \langle e^{-i\alpha_n} \rangle \right] \quad (3)$$

Here A_n is a normalization constant, ω_p is the plasma frequency, β is the electrons velocity normalized to the speed of light in vacuum, I_0 and I_1 are the Bessel functions of second kind, and κ_n is the transverse wave number. The symbol $\langle \dots \rangle$ represents an average over all electrons within one radiation wavelength. Undefined symbols are described in [4].

DESCRIPTION OF THE CFEL

This model has been applied to a particular design for a Cherenkov free-electron laser that can be operated with both low and high electron beam currents. In this analysis we choose Al_2O_3 with a dielectric constant of $\epsilon=9.8$ as the liner material, and keep the geometry constant. Likewise, the outer radius of the cylindrically shaped electron

beam is fixed at $r_b=5$ mm. However, to vary the single-pass gain and saturated power of this device, we consider different total beam currents I_b ranging from 0.8 A to 20 A. The remaining geometrical parameters are: an average inner liner radius of $r_{d0}=5.5$ mm and an average liner thickness of $d=0.57$ mm. This system requires an electron beam energy of 84.2 keV to operate at 50 GHz. We integrate the dynamic CFEL equation (eq. 3) up to the point where the laser saturates. Using a constant inner radius equal to r_{d0} and an initial seed power of 10 mW, these electron currents produce a saturated power P_0 of about 200 W at a distance z_0 of 100 cm and 20.8 kW at a distance of 45 cm for $I_b=0.8$ A and 20 A, respectively. The corresponding average gain is 0.43 dB/cm and 1.39 dB/cm, respectively.

The variation in the inner liner radius is modeled using a random fluctuation superimposed on the average radius r_{d0} . A spatial low-pass filter with cut-off distance z_c is used to remove fast fluctuations from the random distribution. Further, the fluctuations are scaled to obtain a certain standard deviation σ_{rd} of the distribution. For each particular realization of a fluctuating liner radius we numerically calculate the saturated power P_{sat} and the position z_{sat} at which this power is obtained. To obtain also statistical information on the output as a function of the experimental parameters, we generate 100 different realizations of liner fluctuations for each combination of the rms amplitude σ_{rd} and cut-off distance z_c . For each combination we determine the ensemble average $\overline{P_{sat}}$ and standard variation σ_p and corresponding values for the distance to saturation z_{sat} .

RESULTS AND DISCUSSION

First, we numerically study the sensitivity of this particular CFEL to an increasing amplitude of the random fluctuations in the liner inner radius while the spatial filter is kept constant at $z_c=10$ cm, corresponding to approximately 16 times the free-space wavelength. The ensemble average of the saturated power, $\overline{P_{sat}}$, normalized to the saturated power in absence of fluctuations, P_0 , is shown in Figs. 1a and 1b as a function of the standard deviation of the fluctuations in the inner liner radius, σ_{rd} , for the two beam currents of 0.8 A and 20 A, respectively. Corresponding values for the distance to saturation z_{sat} are shown in Fig. 2. Fig. 1 shows that for this particular CFEL and a beam current of 0.8 A, a small rms liner fluctuation of $2.5 \mu\text{m}$ ($=0.05\%$ of r_{d0}) is sufficient to reduce the saturated power by a factor of 2 on average. The rms liner fluctuation increases to $25 \mu\text{m}$ ($=0.5\%$ of r_{d0}) to obtain a similar reduction when the CFEL is driven by a beam current of 20 A. At the same time we observe that the relative spread $\sigma_p/\overline{P_{sat}}$ is much larger for the 0.8 A beam current compared to the 20 A beam current. The variation of the distance to saturation with the rms liner amplitude (see Fig. 2) shows a different behavior for the two beam currents. For the 0.8 A current, the distance increase quickly from 100 cm to close to 150 cm and then remains approximately constant. The ob-

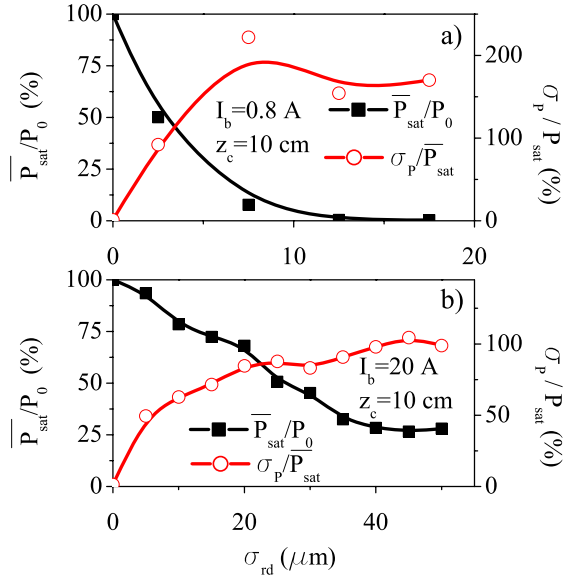


Figure 1: Normalized saturated power ($\overline{P_{sat}}/P_0$) and normalized standard deviation ($\sigma_p/\overline{P_{sat}}$) as a function of the standard deviation of the liner fluctuations σ_{rd} for a current of 0.8 A (a) and 20 A (b).

served spread in z_{sat} remains approximately constant. On the other hand, for the 20 A current the distance to saturation increases approximately linearly with σ_{rd} , while the relative spread is slightly reduced.

These findings indicate that this particular CFEL is far more sensitive to fluctuations in the inner liner radius than the system studied in our previous study [4]. In that study we also considered a CFEL operating at 50 GHz. However, that system used a 0.8 A electron beam with a 1 mm radius (25 A/cm² current density) to drive the CFEL. We found that an rms fluctuation of about 5 % was required to reduce the saturated power by a factor of 2. For the device of this work, this is 0.5 % and 0.05 % for the same current density and total beam current respectively. To allow the CFEL of this work to be driven by a higher total current, we have increased the beam radius. As a consequence, the transverse dimensions of the CFEL have increased and we have chosen a different liner material. This leads to a larger variation of k_n with inner liner radius r_d (see eq. 2): $\partial k_n/\partial r_d$ is $-4.6 \cdot 10^6 \text{ m}^{-2}$ for the device in this work, while it equals $-0.46 \cdot 10^6 \text{ m}^{-2}$ for the device in our previous study. It is therefore not surprising that the current system is more sensitive to liner imperfections than the system considered in our previous study.

Second, we have investigated the influence of spatial distribution of the liner imperfections by varying the cut-off distance z_c of the low pass filter applied to the randomly generated liner fluctuations. The normalized ensemble average $\overline{P_{sat}}/P_0$ and the normalized spread $\sigma_p/\overline{P_{sat}}$ are shown in Fig. 3 for $I_b = 0.8$ A and 20 A, and the corre-

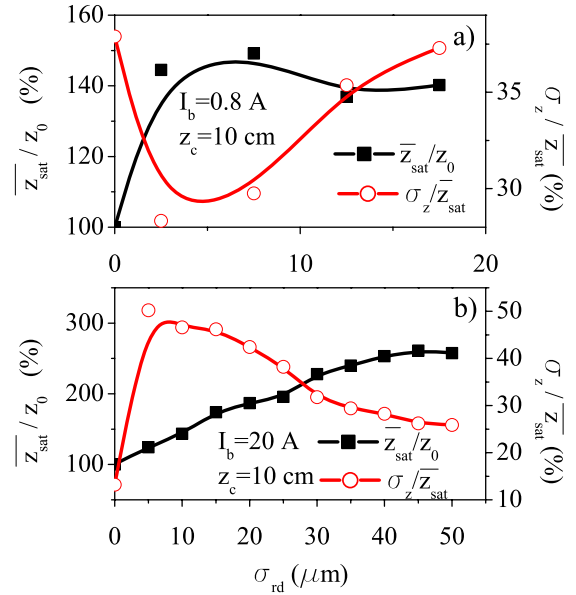


Figure 2: Normalized distance to saturation ($\overline{z_{sat}}/z_0$) and normalized standard deviation of z_{sat} ($\sigma_z/\overline{z_{sat}}$) as a function of the standard deviation of the liner fluctuations σ_{rd} for a current of 0.8 A (a) and 20 A (b).

sponding values for z_{sat} are shown in Fig. 4. These figures show that both the saturated power P_{sat} and the distance to saturation z_{sat} vary only weakly with increasing z_c if z_c is sufficiently large ($z_c \gg \lambda = c/f$). Note, that the latter condition is anyhow implicit in the approximations used in deriving the dynamical CFEL equation (eq. 3).

Last, we compare the sensitivity of this system to liner imperfections as a function of the total beam current I_b for a fixed $\sigma_{rd} = 15 \mu\text{m}$ and a fixed cut-off distance $z_c = 10$ cm. Fig. 5a shows the normalized ensemble average $\overline{P_{sat}}/P_0$ and spread $\sigma_p/\overline{P_{sat}}$ as a function of I_b and Fig. 5b shows the corresponding values for z_{sat} . These figures show that I_b must be larger than 30 A to keep the reduction in $\overline{P_{sat}}$ to less than 15 %. We also observe that the relative spread $\sigma_p/\overline{P_{sat}}$ reduces with increasing beam current, while the spread $\sigma_z/\overline{z_{sat}}$ shows a slight increase.

CONCLUSION

We have studied the sensitivity to imperfections in the liner of a particular CFEL operating at 50 GHz as a function of total beam current. The system studied in this work is based on a previously studied system with increased transverse dimensions and a different liner. The increased dimensions allow a larger total current to pass through the lined waveguide and study the system in different gain regimes. As a consequence, the variation of longitudinal wave number with inner radius increased by a factor of 10 compared to the system we used in a previous study, that also operated at 50 GHz. Taking this difference into ac-

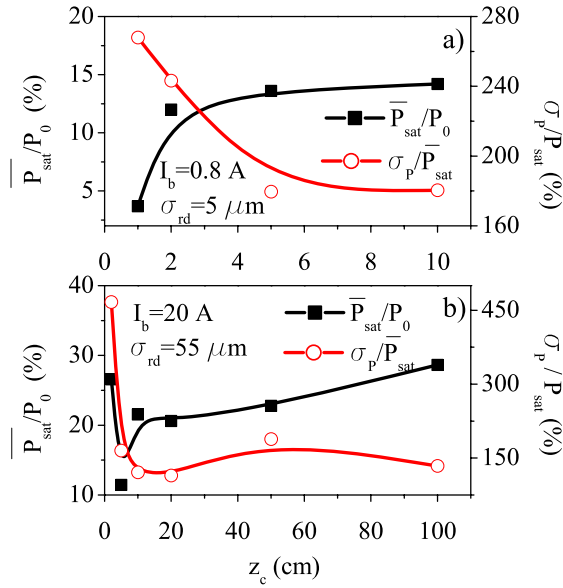


Figure 3: Normalized saturated power ($\overline{P_{sat}}/P_0$) and normalized standard deviation ($\sigma_p/\overline{P_{sat}}$) as a function of the cut-off distance z_c for a current of 0.8 A (a) and 20 A (b).

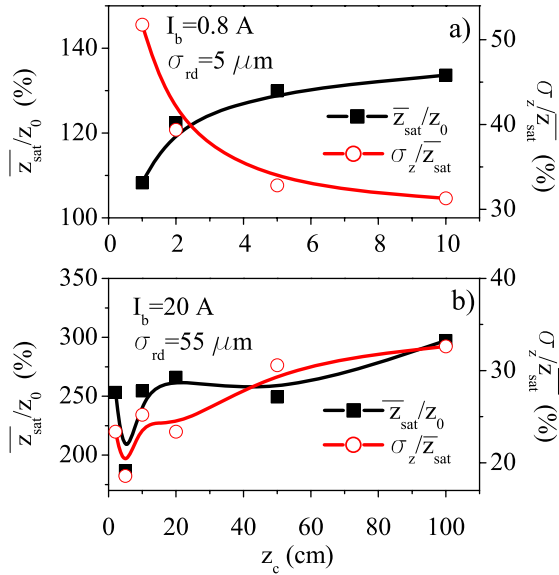


Figure 4: Normalized distance to saturation ($\overline{z_{sat}}/z_0$) and normalized standard deviation of z_{sat} ($\sigma_z/\overline{z_{sat}}$) as a function of the cut-off distance z_c for a current of 0.8 A (a) and 20 A (b).

count, we find that both systems show similar sensitivity to liner imperfections when the CFELs are driven by electron beams having the same current density of 25 A/cm². For the current system we find that a total current of at least 30 A is required to keep the reduction in ensemble average $\overline{P_{sat}}$ to less than ~ 15 % of P_0 (for $\sigma_{rd} = 15$ μm). The same

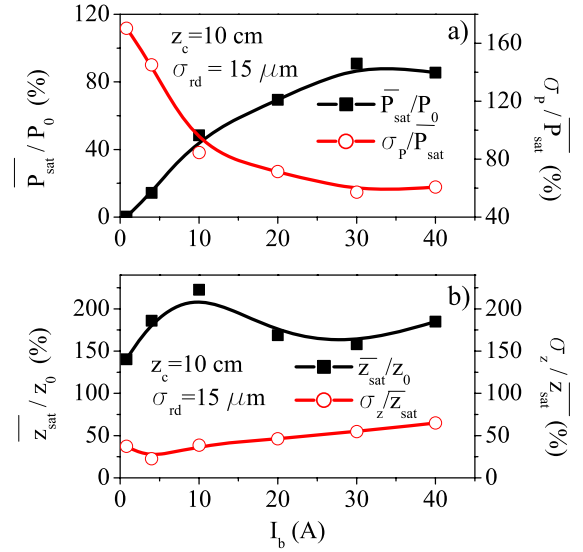


Figure 5: Normalized saturated power ($\overline{P_{sat}}/P_0$) and normalized standard deviation ($\sigma_p/\overline{P_{sat}}$) (a) and corresponding values for z_{sat} (b) as a function of the electron beam current for $\sigma_{rd} = 15$ μm and $z_c = 10$ cm.

rms liner fluctuation reduces $\overline{P_{sat}}$ to less than 20 % of P_0 for $I_b < 5$ A. A high gain also reduces the relative spread in P_{sat} for an ensemble of similar imperfections, while at the same time the relative spread in z_{sat} increases slightly. These findings show that systems with high gain are less sensitive to liner imperfections compared to systems with low gain. However, the actual allowable rms fluctuation depends both on the gain and on the particular geometry of the lined waveguide of the Cherenkov FEL.

REFERENCES

- [1] W.K. Gwarek, M. Celuch-Marcysiak, A review of microwave power applications in industry and research, 15th International Conference on Microwaves, Radar and Wireless Communications, MIKON, p 843-848 (2004).
- [2] D.A. Jones, T.P. Lelyveld, S.D. Mavrofidis, S.W. Kingman and N.J. Miles, Microwave heating applications in environmental engineering—a review, Resources, Conservation and Recycling, **34**, 2, 75-90 (2002).
- [3] H.P. Freund, 'Nonlinear Analysis of High-Power Cherenkov Masers', *Phys. Rev. Lett.*, **65**, p.2993 (1990).
- [4] I. de la Fuente, P.J.M. van der Slot, and K.-J. Boller, 'Phase velocity fluctuations and gain in Cherenkov free-electron lasers', *J. Appl. Phys.* (accepted for publication).
- [5] J.E. Walsh and J.B. Murphy, Tunable Cerenkov Lasers, *IEEE J. Quant. Electr.*, **QE-18**, 1259 (1982).
- [6] H.P. Freund and A.K. Ganguly, Nonlinear analysis of the Cherenkov maser, *Phys. Fluids*, **B2**, 2506 (1990).
- [7] R.A. Waldron, Theory of guided electromagnetic waves, Van Nostrand Reinhold Company, London (1970).

THEORY OF RADIATION OF ELECTRONS IN THE FIELD OF A LINEAR POLARIZED STATIONARY ELECTROMAGNETIC WAVE

Drebot I.V., Grigoryev Y.N., Zelinsky A.Y., NSC KPTI, Kharkov, Ukraine

Abstract

In the paper the results of exact integration of Lorentz equation for a free electron in the field of a linear polarized standing electro-magnetic wave are presented. Standing wave is considered as a sum of two running in opposite directions linear polarized waves. Projections of equations on coordinate axes can be integrated once. It allows us to reduce the task to solution of nonlinear equation of the second order for electron coordinate. The axis of projection coincides with a wave line. For approximate integration of the second order equation the expansion on two small parameters are used. Velocity and coordinate of electron in parametric form are presented in the paper. It is shown that under interaction of a relativistic electron with stationary wave there is a motion, which has of beating character. The amplitude and period of the beating were calculated.

INTRODUCTION

The theory of the electron interaction with a standing light wave originates in description of the Kapiza-Dirac effect [1]. The physical sense of the effect is stipulated radiation of electrons in the field of a stationary wave. After that sufficiently large amount of papers were devoted to the theoretical investigations of electron radiation in the field of a light wave.

The interest to the subject has been revived lately due to huge progress in intense laser technique. The latest works use both quantum and classical electrodynamics approach.

The main difficulty in using of classical electrodynamics approach is determination of solution of equations of electron motions in the form which will be convenient for analytical calculations of the radiation spectrum and for estimations of the electron velocity and coordinate evolutions. For example, in basic works [2,3] the solving of motion equations is reduced to the solving of the equation system of the two first order equations. But in this case one can find only approximate solution and the solution can be formulate as a function of intrinsic time of the electron. Such approach makes calculations of the radiation spectrum and other characteristics quite difficult. In the paper [4] an electron trajectory in the field of a standing linear polarized electromagnetic wave was reduced to the solving of nonlinear differential equation system with time dependent coefficients. After linearization of the system the Hill equations has to be solved.

In the presented paper, the approximate solutions of the Lorentz equation for an electron in the field of linear polarized standing wave are presented. The standing wave

is considered as a sum of two running in opposite directions waves with the same polarizations.

Two projections of the Lorentz equation can be integrated once [4]. It allows to reduce the task to the solving of a second order nonlinear equation. For the approximate solution the expanding on two small parameters was used.

In the work the expressions for velocity and coordinates of an electron were derived in a form of parametrical functions of time. Using [5] and with the help of derived formulas one can calculate radiation spectrum of an electron in the field of standing linear polarized electromagnetic wave.

As one can see from the derived solutions, the electron motion in the standing wave has beating character and can lead to electron grouping in the propagation direction. The period and amplitude of the beatings were calculated.

MOTION EQUATIONS

An electron motion in the field of standing wave can be described with Lorentz equation:

$$\frac{d}{dt} \frac{m_0 \vec{v}}{(1 - \beta^2)^{1/2}} = c \vec{E} + \frac{e}{c} [\vec{v} \vec{H}], \quad (1)$$

where, $\beta = v/c$, m_0 the rest mass of the electron, c is the velocity of light, e is the electron charge, $\vec{v} = \frac{\partial \vec{r}}{\partial t}$ is the vector of an electron velocity, $\vec{r} = \vec{i}x + \vec{j}y + \vec{k}z$, t is time, \vec{E}, \vec{H} are vectors electrical and magnetic field.

We will consider the standing wave as a sum of two linear polarized running in opposite direction waves:

$$\vec{E} = \vec{E}_1 + \vec{E}_2; \quad \vec{E}_1 = \vec{k}E_{1z}; \quad \vec{E}_2 = \vec{k}E_{2z};$$

$$E_{1x} = 0, \quad E_{1y} = 0, \quad E_{2x} = 0, \quad E_{2y} = 0, \quad (2)$$

$$\vec{H} = \vec{H}_1 + \vec{H}_2; \quad \vec{H}_1 = [\vec{i}; \vec{E}_1] = -\vec{j}E_{1z};$$

$$\vec{H}_2 = [-\vec{i}; \vec{E}_2] = \vec{j}E_{2z}; \quad (3)$$

$$H_{1z} = 0, \quad H_{1x} = 0, \quad H_{2z} = 0, \quad H_{2x} = 0,$$

$$\vec{E}_1 = \vec{k}E_{01} \cos \left[2\pi\nu_1 \left(t - \frac{x}{c} \right) + \delta_1 \right];$$

$$\vec{E}_2 = \vec{k}E_{02} \cos \left[2\pi\nu_2 \left(t + \frac{x}{c} \right) + \delta_2 \right]; \quad (4)$$

Substituting (4) in (2) and (3) one can get:

$$\vec{E} = \vec{k} \left(E_{01} \cos \left[2\pi\nu_1 \left(t - \frac{x}{c} \right) + \delta_1 \right] + E_{02} \cos \left[2\pi\nu_2 \left(t + \frac{x}{c} \right) + \delta_2 \right] \right); \quad (5)$$

$$\vec{H} = -\vec{j} \left(E_{01} \cos \left[2\pi\nu_1 \left(t - \frac{x}{c} \right) + \delta_1 \right] - E_{02} \cos \left[2\pi\nu_2 \left(t + \frac{x}{c} \right) + \delta_2 \right] \right); \quad (6)$$

Using expression: $mc/(1-\beta^2)^{1/2} = \xi$ (where ξ - is electron energy), and expressions (5),(6) we project equation (1) on coordinate axes:

$$\frac{1}{c} \frac{d}{dt} (\xi \beta_z) = e(1-\beta_x) E_{01} \cos \left[2\pi\nu_1 \left(t - \frac{x}{c} \right) + \delta_1 \right] + e(1+\beta_x) E_{02} \cos \left[2\pi\nu_2 \left(t + \frac{x}{c} \right) + \delta_2 \right] \quad (7)$$

$$\frac{1}{c} \frac{d}{dt} (\xi \beta_y) = 0 \quad (8)$$

$$\frac{1}{c} \frac{d}{dt} (\xi \beta_x) = e\beta_z \left(E_{01} \cos \left[2\pi\nu_1 \left(t - \frac{x}{c} \right) + \delta_1 \right] - E_{02} \cos \left[2\pi\nu_2 \left(t + \frac{x}{c} \right) + \delta_2 \right] \right) \quad (9)$$

where $\beta_x = \frac{1}{c} \frac{dx}{dt}$, $\beta_z = \frac{1}{c} \frac{dz}{dt}$, $\beta_y = \frac{1}{c} \frac{dy}{dt}$.

Equations (7,8) can be integrated once. As a results the following expressions can be derived:

$$\beta_z / \sqrt{1-\beta^2} = \psi \quad (10)$$

$$\beta_y / \sqrt{1-\beta^2} = A \quad (11)$$

where $\psi = PF + \xi_z$ (12)

$$F = \left(\text{Sin} \left[2\pi\nu_1 \left(t - \frac{x}{c} \right) + \delta_1 \right] + \text{Sin} \left[2\pi\nu_2 \left(t + \frac{x}{c} \right) + \delta_2 \right] \right) - \quad (13)$$

$$\left(\text{Sin} \left[2\pi\nu_1 \left(t_0 - \frac{x(t_0)}{c} \right) + \delta_1 \right] + \text{Sin} \left[2\pi\nu_2 \left(t_0 + \frac{x(t_0)}{c} \right) + \delta_2 \right] \right);$$

$$P = \frac{eE_0}{mc(2\pi\nu)}; \quad \xi_z = \gamma(t_0)\beta_z(t_0); \quad A = \gamma(t_0)\beta_y(t_0) \quad (14)$$

t_0 is initial time; $\vec{E}_0 = \vec{E}_{01} = \vec{E}_{02}$.

With use of two integrals (10) and (11) one can express, β_z, β_y, ξ through β_x, ψ, A

$$\beta_z^2 = \psi^2 (1 - \beta_x^2) / (1 + \psi^2 + A^2) \quad (14)$$

$$\beta_y^2 = A^2 (1 - \beta_x^2) / (1 + \psi^2 + A^2) \quad (15)$$

$$\xi = m_0 c^2 (1 + \psi^2 + A^2)^{1/2} / (1 - \beta_x^2)^{1/2} \quad (16)$$

Substituting (14-16) to (9) and using expression:

$$\frac{d\xi}{dt} = e(\vec{v}\vec{E}), \quad (17)$$

one can derive the second order equation for electron coordinate X .

$$\frac{\dot{\beta}_x}{1-\beta_x^2} = \frac{eE_0}{m_0c} \frac{\psi}{(1+\psi^2+A^2)} (1-\beta_x) \text{Cos} \left[2\pi\nu_1 \left(t - \frac{x}{c} \right) + \delta_1 \right] - (1-\beta_x) \text{Cos} \left[2\pi\nu_1 \left(t - \frac{x}{c} \right) + \delta_1 \right] - (1+\beta_x) \text{Cos} \left[2\pi\nu_2 \left(t + \frac{x}{c} \right) + \delta_2 \right] \quad (18)$$

where $\dot{\beta}_x = \frac{d}{dt} \beta_x = \frac{1}{c} \frac{d^2x}{dt^2}$.

Integrating (18), we derive:

$$\ln \frac{1+\beta_x}{1-\beta_x} = \frac{2eE_0}{m_0c} \int_{t_0}^t \frac{\psi}{(1+\psi^2+A^2)} \left\{ (1-\beta_x) \text{Cos}[\varphi_-] - (1+\beta_x) \text{Cos}[\varphi_+] \right\} dt + C_2 \quad (19)$$

$$C_2 = \ln \frac{1+\beta_x(t_0)}{1-\beta_x(t_0)}.$$

For standing wave we can set:

$$\vec{E}_0 = \vec{E}_0 = \vec{E}_{02}; \quad \delta_1 = \delta_2 = 0; \quad \nu_1 = \nu_2 = \nu.$$

Than $\varphi_- = 2\pi\nu \left(t - \frac{x}{c} \right)$; $\varphi_+ = 2\pi\nu \left(t + \frac{x}{c} \right)$.

As it follows from (19):

$$\frac{1+\beta_x}{1-\beta_x} = \frac{1+\beta_x(t_0)}{1-\beta_x(t_0)} e^{\Phi(t)} \quad (20)$$

where

$$\Phi(t) = \frac{2eE_0}{m_0c} \int_{t_0}^t \frac{\psi}{(1+\psi^2+A^2)} \left\{ (1-\beta_x) \text{Cos}[\varphi_-] - (1+\beta_x) \text{Cos}[\varphi_+] \right\} dt$$

APPROXIMATE SOLUTION

Assuming $P \ll 1$, $\xi_z \ll 1$, $\Phi(t) \ll 1$ and

$$e^{-\Phi(t)} \approx 1 - \Phi(t) + O\left(\frac{\Phi(t)^2}{2}\right)$$

one can get from (20):

$$\beta_x(t) \approx \beta_x(t_0) + \frac{1}{2} (1 - \beta_x^2(t_0)) \Phi(t) \quad (21)$$

$$\Phi(t) \approx P^2 \Phi_1 + P \xi_z \Phi_2 + P^2 \xi_z^2 \Phi_3 \quad (22)$$

where

$$\Phi_1 \approx \Gamma^{-2} \left\{ \left(-\frac{1}{2} \right) (\text{Cos}[2\varphi_-] - \text{Cos}[2\varphi_+]) - 2(\text{Sin}[\varphi_-(t_0)] + \text{Sin}[\varphi_+(t_0)])(\text{Sin}[\varphi_-] - \text{Sin}[\varphi_+]) \right. \\ \left. - \frac{1}{2} (\text{Cos}[2\varphi_-(t_0)] - \text{Cos}[2\varphi_+(t_0)]) \right\} \quad (23)$$

$$\Phi_2 \approx 2\Gamma^{-2} \{ (\text{Sin}[\varphi_-] - \text{Sin}[\varphi_+]) - (\text{Sin}[\varphi_-(t_0)] + \text{Sin}[\varphi_+(t_0)]) \} \quad (24)$$

$$\Phi_3 = 2(2\pi\nu)\Gamma^{-2} \left\{ \int_{t_0}^t \text{Sin} \left[4\pi\nu \frac{x}{c} \right] dt - \int_{t_0}^t \beta_x(t) \text{Sin}[4\pi\nu t] dt \right\} \quad (25)$$

$$\text{and } \Gamma^{-2} = 1 + \gamma^2(t_0)(\beta^2(t_0) - \beta_x^2(t_0)).$$

The approximate solution of (21) we will find in the form:

$$\frac{x}{c} = \beta_x(t_0)(t - t_0) + \alpha_1^m(\alpha_1 x_1 + \alpha_2 x_2) \quad (26)$$

$$\beta_x = \beta_x(t_0) + \alpha_1^m(\alpha_1 \dot{x}_1 + \alpha_2 \dot{x}_2) \quad (26)$$

$$\dot{x}_1 = \frac{dx_1}{dt}; \quad \dot{x}_2 = \frac{dx_2}{dt}; \quad \alpha_1 \ll 1; \quad \alpha_2 \ll 1;$$

Substituting (26,27) to (21) one can get $m=1$; $\alpha_1 = P$; $\alpha_2 = \xi_z$;

$$\frac{\dot{x}_1}{c} \approx \frac{1}{2}(1 - \beta_x^2(t_0))(\tilde{\Phi}_1 - \tilde{\Phi}_3) \quad (28)$$

$$\frac{\dot{x}_2}{c} \approx \frac{1}{2}(1 - \beta_x^2(t_0))\tilde{\Phi}_2 \quad (29)$$

$$\beta_x = \beta_x(t_0) + P^2 \dot{x}_1 + P \xi_z \dot{x}_2;$$

$$\frac{x}{c} = \beta_x(t_0)(t - t_0) + P^2 x_1 + P \xi_z x_2 \quad (30)$$

Expressions for $\tilde{\Phi}_1, \tilde{\Phi}_2$ one can produce from the corresponding expressions for Φ_1, Φ_2 by substitution of φ_-, φ_+ , to $x = c\beta(t_0)(t - t_0)$, and change $\varphi_- \rightarrow \tilde{\varphi}_-, \varphi_+ \rightarrow \tilde{\varphi}_+$.

$$\tilde{\varphi}_- = 2\pi\nu(1 - \beta_x(t_0)) + \eta_0$$

$$\tilde{\varphi}_+ = 2\pi\nu(1 + \beta_x(t_0)) - \eta_0$$

$$\text{where } \eta_0 = 2\pi\nu\beta_x(t_0)t_0$$

$\tilde{\Phi}_3$ And after approximate integration (25) is equal to:

$$\tilde{\Phi}_3 = \Gamma^{-2} \left\{ \left(\frac{1}{\beta_x(t_0)} \right) (1 - \text{Cos}[2\pi\nu\beta_x(t)t - 2\eta_0]) + \right. \quad (31)$$

$$\left. + \beta_x(t_0)[\text{Cos}[2\pi\nu t] - \text{Cos}[2\pi\nu t_0]] \right\}$$

Integrating (28) and (29) one can get for x_1, x_2

$$\frac{x_1}{c} = \frac{1}{2}(1 - \beta_x^2(t_0))\Gamma^{-2} \frac{1}{2\pi\nu} \left\{ \left(-\frac{1}{4} \right) \left[\frac{\text{Sin}2\tilde{\varphi}_-}{(1 - \beta_x(t_0))} - \frac{\text{Sin}2\tilde{\varphi}_+}{(1 + \beta_x(t_0))} \right] \right. \quad (32)$$

$$\left. + 4\text{Sin}[2\pi\nu t_0] \left[\frac{\text{Cos}2\tilde{\varphi}_-}{(1 - \beta_x(t_0))} - \frac{\text{Cos}2\tilde{\varphi}_+}{(1 + \beta_x(t_0))} \right] - \frac{7}{2}\text{Sin}[4\pi\nu t_0] \right. \quad (32)$$

$$\left. + \left[\frac{1}{\beta_x(t_0)} - \beta_x(t_0)\text{Cos}[4\pi\nu t_0] \right] 2\pi\nu(t - t_0) - \frac{\beta_x(t_0)}{2}\text{Sin}[4\pi\nu t_0] \right. \quad (32)$$

$$\left. - \frac{1}{2} \frac{1}{\beta_x^2(t_0)} \text{Sin}[2\pi\nu\beta_x(t)t - 2\eta_0] + \frac{1}{2} \beta_x(t_0)\text{Sin}[2\pi\nu t] \right\}$$

$$\frac{x_2}{c} = (1 - \beta_x^2(t_0))\Gamma^{-2} \frac{1}{2\pi\nu} \left\{ \left[\frac{\text{Sin}\tilde{\varphi}_-}{(1 - \beta_x(t_0))} - \frac{\text{Sin}\tilde{\varphi}_+}{(1 + \beta_x(t_0))} \right] + \right. \quad (33)$$

$\left. + \frac{\beta_x(t_0)}{1 - \beta_x^2(t_0)} \text{Cos}[2\pi\nu t_0] \right\}$
As it is followed from expressions (2-3), at $\beta_x \approx 1$ running in the initial propagation direction wave exits electron oscillations with larger amplitude than the wave running in opposite direction.

Two last items in (32):

$$\frac{1}{2}(1 - \beta_x^2(t_0))\Gamma^{-2} \frac{1}{2\pi\nu} \left\{ -\frac{1}{2} \frac{1}{\beta_x^2(t_0)} \text{Sin}[2\pi\nu\beta_x t - 2\eta_0] + \right. \quad (33)$$

$$\left. + \frac{1}{2} \beta_x(t_0)\text{Sin}[2\pi\nu t] \right\}$$

At $\beta_x \approx 1$ an electron motion, which has beating character [7] with period T :

$$T = \frac{1}{2\pi\nu(1 - \beta_x(t_0))} \quad (34)$$

The A_{\max} maximum and A_{\min} minimum beating amplitude can be described with following expressions

$$A_{\min} = \frac{p^2 c (1 - \beta_x^2(t_0)) (1 - |\beta_x(t_0)|^3)}{8\pi\nu\Gamma^2 \beta_x^2(t_0)} \quad (35)$$

$$A_{\max} = \frac{p^2 c (1 - \beta_x^2(t_0)) (1 + |\beta_x(t_0)|^3)}{8\pi\nu\Gamma^2 \beta_x^2(t_0)} \quad (36)$$

Substituting expressions for β_x and x from (30) to (14) and keeping items of the second order on p and \mathcal{E}_z

one can derive approximate expression for β_z

$$\beta_z = \Gamma^{-1}(1 - \beta_x^2(t_0))^{1/2}(PF_0 + \xi_z) + 0P^3$$

where

$$F_0 = \text{Sin}[2\pi\nu(1 - \beta_x(t))t + \eta_0] + \text{Cos}[2\pi\nu(1 - \beta_x(t_0))t - \eta_0] + 2\text{Sin}[2\pi\nu t_0]$$

In the same way, substituting expressions for β_x and x from (30) to (15) and keeping items of the second order on p and \mathcal{E}_z we can produce approximate expression for β_y :

$$\beta_y = \frac{A}{\Gamma^2}(1 - \beta_x^2(t_0))^{1/2} \left[1 - P^2 \frac{\beta_x(t_0)}{1 - \beta_x^2(t_0)} \dot{x}_1 - \right. \quad (38)$$

$$\left. - P \xi_z \frac{\beta_x(t_0)}{1 - \beta_x^2(t_0)} \dot{x}_2 - \frac{P^2}{2\Gamma^2} F_0^2 - \frac{P \xi_z}{\Gamma^2} F_0^2 \right] + 0P^3$$

Integrating (37) and (38) we derive dependence coordinates z and y on time t

$$z = \sqrt{c}\Gamma^{-1}(1 - \beta_x^2(t_0))^{1/2} \left\{ \frac{P(-1)}{2\pi\nu} * \left[\frac{\text{Cos}[2\pi\nu(1 - \beta_x(t_0))t + \eta_0]}{(1 - \beta_x(t_0))} + \frac{\text{Cos}[2\pi\nu(1 - \beta_x(t_0))t - \eta_0]}{(1 + \beta_x(t_0))} \right] + \frac{P}{2\pi\nu} \frac{2\text{Cos}[2\pi\nu t_0]}{(1 - \beta_x^2(t_0))} + (\xi_z + 2\text{Sin}[2\pi\nu t_0])(t - t_0) \right\} + z_0(t_0) \quad (39)$$

$$y = \frac{A}{\Gamma^2} (1 - \beta_x^2(t_0))^{1/2} \left[(t - t_0) - P^2 \frac{\beta_x(t_0)}{1 - \beta_x^2(t_0)} x_1 - P \xi_z \frac{\beta_x(t_0)}{1 - \beta_x^2(t_0)} x_2 - \frac{P^2}{2\Gamma^2} \int_{t_0}^t F_0^2 dt - \frac{P \xi_z}{\Gamma^2} \int_{t_0}^t F_0^2 dt \right] + y_0(t_0) \quad (40)$$

CONCLUSION

The expressions derived above, describe the electron motion in the field of standing linear polarized light wave and allows to calculate spectrum of electron radiation with use of methods described in [5,6].

Today, it is supposed to use interaction of relativistic electron with intense laser beams accumulated in an optical cavity for generation of shirt wave radiation. The transversal sizes of the beams in the interaction point are equal of about several tens of micrometers. For this reason, the evaluation of transversal sizes of the electron

beam during interaction is very actual task. It necessary to note, that the largest increasing of the electron beam transversal size is produced with the wave running in the direction of electron beam propagation and not the wave which generates the shirt wave radiation.

REFERENCES

- [1] P.L. Kapitze and P.A.M. Dirac, Proc. Cambridge Phys. Sos, 29, 287 (1933).
- [2] V.I Ritus, «Quantum effects of interactions elementary particles with intense electro magnetic fields», Proceedings Physics Institute of Lebedev. 5-151 ct. (1979).
- [3] A. Ts. Amatuni, Yerevan 375036 Republic of Armenia. I.V. Pogorelsky, Brookhaven National Laboratory, 725 C, Upton, New York 11973, (034001-034001-8) pp, (1998)
- [4]. A. F. Kurin, Letters JTP, 2005, vol 31. issue 13
- [5] Landau & Lifshic, «Theoru of field»
- [6] A.N. Krilov, «Proceedings of academian A.N. Krilov», vol. 3, mathematics, part two, Publishers of Academy USSR, 481p. (1949)

TRANSVERSE COHERENCE PROPERTIES OF THE LCLS X-RAY BEAM*

S. Reiche[†], UCLA, Los Angeles, CA 90095, USA.

Abstract

Self-amplifying spontaneous radiation free-electron lasers, such as the LCLS or the European X-FEL, rely on the incoherent, spontaneous radiation as the seed for the amplifying process. Though this method overcomes the need for an external seed source one drawback is the incoherence of the effective seed signal. The FEL process allows for a natural growth of the coherence because the radiation phase information is spread out within the bunch due to slippage and diffraction of the radiation field. However, at short wavelengths this spreading is not sufficient to achieve complete coherence. In this presentation we report on the results of numerical simulations of the LCLS X-ray FEL. From the obtained radiation field distribution the coherence properties are extracted to help to characterize the FEL as a light source.

INTRODUCTION

Self-Amplified Spontaneous Emission Free-Electron Lasers (SASE FEL) [1] allow to overcome the restriction in wavelength imposed by existing seeding sources and to explore new wavelength regimes. A particular interest is in the Ångstrom wavelength regime which opens entire new classes of experiments such the 3D imaging of individual molecules or the analysis of chemical reaction on the femtosecond scale. Supported by the successful demonstration of SASE FELs at wavelength down to 14 nm [2], several X-ray FELs are currently under construction such as the Linac Coherent Light Source (LCLS) [3] or the European X-FEL [4].

The drawback of any SASE FEL is that it uses the spontaneous undulator radiation as its seed signal, which is intrinsically broadband and incoherent. Though the FEL process increases the longitudinal and transverse coherence by slippage and diffraction over the length of the undulator it never reaches the coherence level of a seeded FEL amplifier. In particular at short wavelength diffraction – the main method to the build-up transverse coherence – is ineffective and under certain circumstances the FEL can reach saturation before obtaining transverse coherence [5].

For the design of the optical transport line and diagnostic as well as proposed experiments it is of importance to characterize the radiation properties of the SASE FEL as a light source in advance. For that simulations were con-

Table 1: LCLS Design Parameters

Beam Energy	13.4 GeV
Beam Current	3.4 kV
Undulator Period	3 cm
Undulator Parameter	3.5
Undulator Length	130 m
Radiation Wavelength	1.5 Å

ducted and the results are presented here. The work was done in context of the LCLS (Tab.1 list the main parameters of LCLS). The main radiation properties have been presented elsewhere [6] and this presentation focusses solely on the fluctuation in the spot size at the detector locations (expressed by divergence and effective source location of the FEL beam) and the degree of coherence of the FEL signal.

RADIATION SIZE AND DIVERGENCE

Because a SASE FEL has no well-defined input to be amplified, the output is of stochastic nature and varies from shot to shot. For the purpose of designing the X-ray beamline the evolution of the FEL pulse along the optical beam line is of importance to know. In particular the divergence and beam size determine the design of apertures and target sizes.

The easiest quantities to extract from the results of FEL simulations are the rms sizes of the radiation pulse in the near and far field. To these values the envelope equation of a fundamental Gauss-Hermite mode [7]

$$w(z) = w_0 \sqrt{1 + \left(\frac{z - z_0}{z_r} \right)^2} \quad (1)$$

is matched. Although Eq. 1 has three unknown parameter – the waist size w_0 , the waist position z_0 and Rayleigh length z_r – the system is fully deterministic because w_0 and z_r are related to each other by the radiation wavelength, which is a fixed parameter for our calculation.

Higher mode content obscures the results because the mode number becomes an additional unknown parameter. Due to the similarity of the Gauss-Hermite modes to the solution of the two-dimensional harmonic oscillator in quantum mechanics [8] and the fact that the calculation of the rms size is equivalent to the energy eigenvalue of the harmonic oscillator the waist size w_0 has to be corrected to

* Work supported by the U.S. Department of Energy contract DE-AC02-76F00515

[†] reiche@ucla.edu

$w_0 \rightarrow w_0(1+n+m)$, where n and m are the mode numbers of the Gauss-Hermite mode. In the far field zone ($z \ll z_0$) it can be also viewed as a reduction in the Rayleigh length $z_r \rightarrow z_r/(1+n+m)$ for a given and fixed waist size w_0 .

The motivation for this work is to estimate the radiation size of the FEL pulse at any detector position in the far field zone. With that assumption we treat the entire higher-mode content as a single fundamental mode, defined by its Rayleigh length and waist position. This will yield wrong results at the source position by a mismatch in the actually waist size and the assumed one, however that information is irrelevant for the design process of the X-ray beam beam-line and diagnostics.

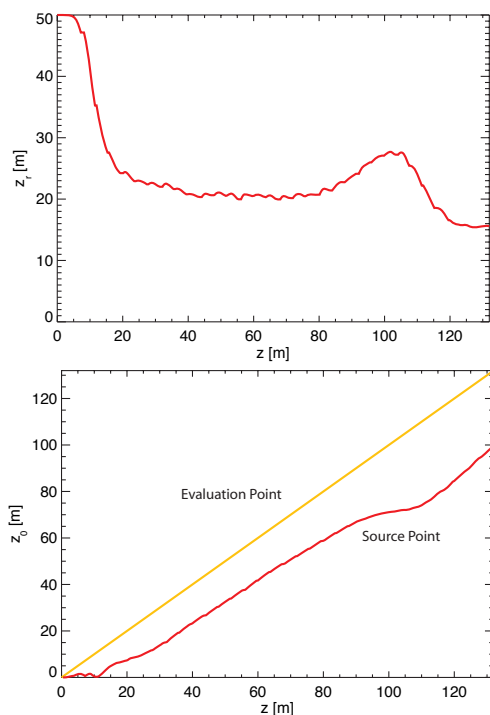


Figure 1: Effective Rayleigh length and waist position (top and bottom plot, respectively) along the undulator for an FEL amplifier.

As the initial step we analyze z_r and z_0 for the case of a seeded FEL with LCLS like parameters. The results are shown in Fig.1. The FEL is seeded with a radiation field ($z_r = 50$ m) larger than the electron beam size but after a few gain length the FEL-eigenmode is dominating. Because the mode size becomes smaller the Rayleigh length is reduced to about 20 m. In the lethargy regime of the FEL the radiation field remains almost unaffected and follows free-space diffraction as is seen by the almost constant waist position over the first 10 m. The FEL eigenmode has an intrinsic phase front curvature enhancing the diffraction and putting the source point behind the point where the field distribution is evaluated. At saturation gain-guiding vanishes and the phase front curvature straightens out as indicated by the growth in the Rayleigh length and a semi-

constant waist position. However in deep saturation electrons gain some energy back while the radiation field has spread out by diffraction. This causes a disruption in the phase front at the electron location, coupling higher mode to the field distribution. As a result the diffraction is enhanced and the Rayleigh length becomes shorter.

SASE Simulations, using the LCLS design parameters, yield a radiation pulse with about 200 spikes at the undulator exit. Each spike is analyzed and the effective source position and Rayleigh length are extracted. To avoid that the analysis is obscured by the incoherent part of the radiation pulse (namely the area between spikes) only spikes are considered which have a peak power of at least 20 % of the maximum power in the pulse. Also we assume that over a single spike the phase fronts are very similar and thus can be treated as a single sample point.

As it can be expected from the intrinsic stochastic nature of the SASE FEL process there is fluctuation in both waist position and Rayleigh length. The distributions are shown in Fig. 2. The effective waist position is in average 38 m within the undulator from the undulator exit and has a rms fluctuation of 4.8 m. The average Rayleigh length of 32 m is actually larger than the steady-state case. The rms variation is 4 m. The reason for a longer Rayleigh length is the deep saturation behavior of an SASE FEL, where the radiation further gains power in this super-radiant regime. The phase fronts are not as disrupted as in the seeded FEL case (see above). No significant correlation between Rayleigh length and waist position has been observed.

Start-end simulations yield a different electron distribution than specified in the design case. Most notable is that only the electron bunch as a whole is aligned and match to the undulator axis while each slice has a certain degree of mismatch and misalignment. In addition wakefields are included which alter the energy of the electron along the undulator and thus disrupt the FEL process. While the statistic of the waist position remains almost unchanged ($\langle z_0 \rangle = 37$ m with an rms fluctuation of 5.7 m) the Rayleigh length is significantly shorter with 7.8 m and a rms variation of 2 m. Though some asymmetry in the electron distribution and the mismatch of the beta-function yield a coupling of higher modes to the emission the main reason is the centroid motion of the electron slices. In the saturation regime most electron slices undergo a turning point of their betatron oscillation. The strong focusing lattice provides a rather sawtooth-like trajectory, typical for any alternating-gradient focusing system, and the electron beam slice emits predominantly in two directions. Instead of once central distribution in the far field there are two overlapping distributions, left and right of the axis. The resulting distribution is significantly broader than for the aligned case, which is reflected by the shorter Rayleigh length in the statistic.

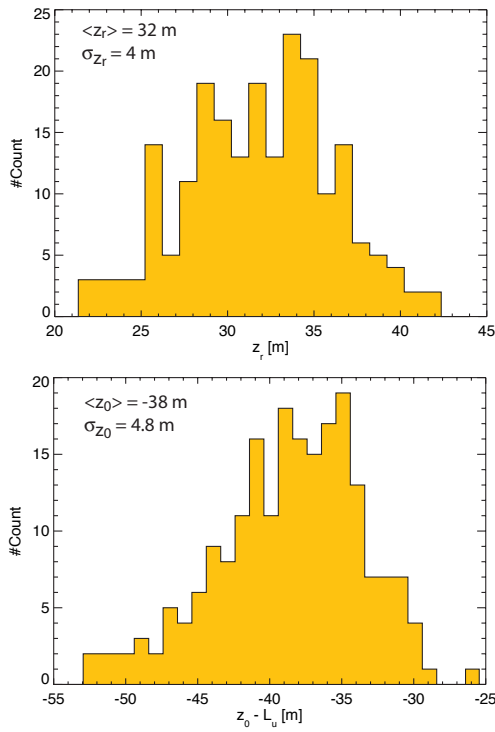


Figure 2: Histogram of Rayleigh length and waist position (top and bottom plot, respectively) for an SASE FEL pulse, evaluated at the undulator exit.

COHERENCE

In the previous section we expressed the quality of the SASE FEL radiation pulse by the fluctuation in the divergence and effected source position for all longitudinal modes (spikes in the radiation power profile). With the extracted Rayleigh length the size of a corresponding fundamental Gauss-Hermite can be calculated and be compared to the radiation size of the FEL mode as an indication for the higher mode content. However higher modes are not necessarily an indication for poor transverse coherence. In the case that the phase relation between all modes remains constant from shot to shot corresponds actually to a fully transverse coherent pulse.

Coherence is a statistical property of a radiation source and refers to how much you can extrapolate the radiation phase information in time and space for any given measurement. Mathematically it is expressed by the mutual coherence function [9]:

$$\Gamma_{12}(\tau) = \left\langle \vec{E}(\vec{r}_1, t) \vec{E}(\vec{r}_2, t + \tau) \right\rangle \quad (2)$$

While the temporal coherence function is easy to define ($\Gamma_{11}(\tau)$) any experiment which relies on spatial coherence (e.g. diffraction on a grating) will always include some temporal information due to the difference in the path length to the detector. For sake of simplicity we assume that the signal $\vec{E}(\vec{r}, t)$ is quasi-monochromatic so that the

time delay due to the path length difference from \vec{r}_1 and \vec{r}_2 falls within the temporal coherence of the signal and thus the time dependence in the mutual coherence function can be neglected. The mutual coherence function becomes then the mutual intensity $J_{12} \equiv \Gamma_{12}(0)$. In analogy to the temporal coherence function, the mutual intensity function is normalized as

$$\mu_{12} = \frac{J_{12}}{\sqrt{J_{11}J_{22}}} \quad (3)$$

to yield values between zero and one. It is referred to also as the complex coherence factor. A zero value refers to no correlation in phase between the observed field at the two positions \vec{r}_1 and \vec{r}_2 while a value of one means that the phase remains constant over time.

The complex coherence factor compares two fixed points in the transverse plane. If we allow both points to be free parameter μ_{12} would yield a four dimensional distribution. For sake of simplicity we restrict one point to be on the undulator axis. In analogy to the temporal coherence time [10] the coherence area is defined as

$$A_c = \int \mu_{12} dA \quad (4)$$

and reflects the size of a usable target area for experiments, relying on coherence, without the need to enforce coherence (e.g. with a pin hole). The optimum case would be when the coherence area is much larger than the actual spot size. Note that for a fully coherent signal the coherence area is infinite.

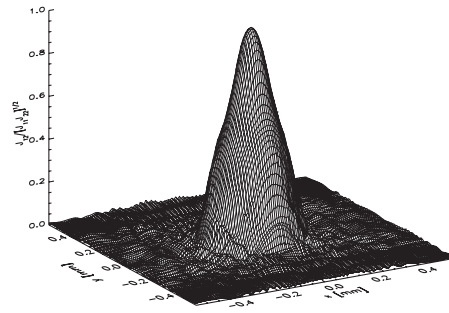


Figure 3: Complex coherence factor for LCLS design case at the undulator exit.

The entire field information of a time-dependent simulation for the LCLS design case was saved and used to evaluate the mutual intensity function and complex coherence factor. The resulting distribution for μ_{12} is shown in Fig. 3. The coherence area, as defined in Eq. 4, is 0.071 mm^2 , about five times larger than the spot size Σ . This indicates sufficient transverse coherence over the entire spot-size and that the FEL pulse can be used for diffraction experiments without the requirement to enhance coherence by a pin hole aperture. The growth in the transverse coherence can be seen in Fig. 4 which is a monotonically increasing function along the undulator. On the other hand

the radiation diffracts faster than the build up in the coherence area within the first tens of meter. However, at around 70 m gain guiding is dominant and the spotsize remains constant till saturation where the spot grows again due to diffraction. At around 60 m, the coherence area becomes larger than the spot size though it does not necessarily indicate good transverse coherence. For that the ratio between A_c and Σ must be much larger than one.

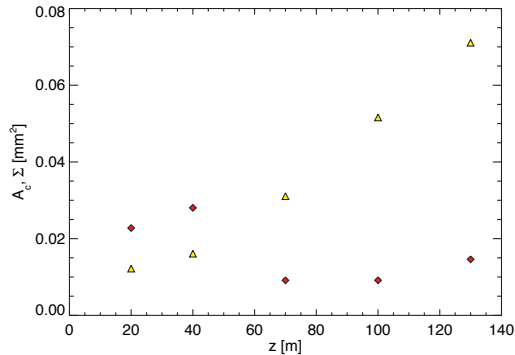


Figure 4: Evolution of the coherence area A_c and spotsize Σ (triangle and diamond shape, respectively) along the undulator.

For LCLS the FEL pulse has to propagate at least 115 m till it reaches the first user station. The coherence area is further increase and in the case of the LCLS design case the value becomes 0.32 mm² while the spot size is 0.044 mm². The reason is that noise consists typically of higher modes which diffracts stronger than the FEL pulse itself, clearing up the signal at the detector location. This becomes more apparent in the case of the start-end simulation where the electron beam slices are not aligned and matched to the focusing lattice (see previous section). The complex coherence factor is shown in Fig. 5 and the resulting coherence area is 0.27 mm² while the spotsize is 0.057 mm². The ratio indicates that the coherence is still sufficient.

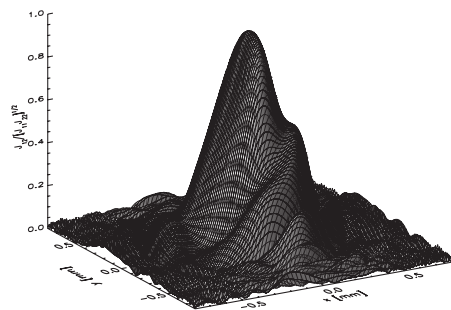


Figure 5: Complex coherence factor for LCLS for the start-end simulation, evaluated 115 m downstream of the undulator exit.

CONCLUSION

Simulations have been conducted to study the radiation properties of the LCLS pulse, namely the variation in the beam size at the detector location and the degree of coherence. A fundamental Gauss-Hermite has been matched to each spike in the radiation profile to describe the divergence by an effective Rayleigh length and source position. The average source position is about 35 m within the undulator before the undulator exit and fluctuate by about 5 m. The Rayleigh length depends strongly on the underlying model of the simulation and shows significantly smaller values for start-end simulation. It is caused by centroid misalignment of the individual electron slice of the LCLS electron bunch. The build-up of transverse coherence during the FEL amplification process is sufficient to spread throughout the entire bunch. For the LCLS case The effective coherence area, within which the field amplitude and phase have a significant correlation to each other, is about 5 times larger than the spot size when evaluated at the first experimental location 115 m downstream the undulator.

REFERENCES

- [1] R. Bonofacio *et al*, *Opt. Comm.* **50** (1984) 373.
- [2] A list can be found e.g. W.B. Colson, *Proc. of the FEL 2004 Conference* (2004) 706.
- [3] *LCLS CDR*, SLAC Report No. SLAC-R-593, 2002.
- [4] A.S. Schwarz, *Proc. of the FEL2004 Conference* (2004) 85.
- [5] E.L. Saldin, E.A. Schneidmiller and M.V. Yurkov, *Opt. Comm.* **97** (1993) 272.
- [6] S. Reiche *et al*, *Nucl. Inst. & Meth.* **A483** (2002) 70.
- [7] A.E. Siegman, *Lasers* (University Science Book, Mill Valley, CA, 1986).
- [8] S. Reiche, /it Numerical Studies for Single Pass HighGain Free-Electron Laser, Ph. D. Thesis, DESY report: DESY-Thesis-2000-012 (2000).
- [9] J. Goodman, *Statistical Optics* (John Wiley and Sons, New York, 1985).
- [10] E.L. Saldin, E.A. Schneidmiller and M.V. Yurkov, *Nucl. Inst. & Meth.* **A407** (1998) 291.

AN ANALYSIS OF SHOT NOISE PROPAGATION AND AMPLIFICATION IN HARMONIC CASCADE FELs

Zhirong Huang*

Stanford Linear Accelerator Center, Stanford, CA 94309, USA.

Abstract

The harmonic generation process in a harmonic cascade (HC) FEL is subject to noise degradation which is proportional to the square of the total harmonic order [1]. In this paper, we study the shot noise evolution in the first-stage modulator and radiator of a HC FEL that produces the dominant noise contributions. We derive the effective input noise for a modulator operating in the low-gain regime, and analyze the radiator noise for a density-modulated beam. The significance of these noise sources in different harmonic cascade designs is also discussed.

INTRODUCTION

Harmonic cascade (HC) FELs are envisioned to generate fully coherent x-ray pulses [2] and are currently under active development for several VUV and soft x-ray projects (see, e.g., Refs. [3, 4]). It was pointed out in Ref. [1] that electron shot noise can be amplified by at least the square of the total harmonic order in this process, much like a frequency multiplication chain in radar communications [5]. Thus, it is important to understand the shot noise contributions in the harmonic generation process which may be the limiting factors in determining the temporal coherence or the final wavelength reach of these seeded FELs.

In a self-amplified spontaneous emission (SASE) FEL, the one-dimensional (1D) shot noise power spectrum is $\rho\gamma mc^2/(2\pi)$ [6], where ρ is the FEL Pierce parameter [7] and γmc^2 is the electron energy. The shot noise power spectrum can be identified to be about the forward-direction spontaneous undulator radiation in the first two power gain lengths [8]. The three-dimensional (3D) correction to this simple 1D result including effects of energy spread and emittance is given in Refs. [9, 10]. If the first undulator of a HC FEL operates in the high-gain regime (i.e., much longer than the gain length), the SASE noise power (integrated over the gain bandwidth) may be used to estimate its noise contribution to a HC FEL. However, due to the availability of high-power seed laser, the typical design of the first undulator of a HC FEL is a short (energy) modulator that operates in the low-gain (or even no-gain) regime [3, 4, 11]. Thus, the shot noise content of this modulator can be different from a high-gain undulator. After the dispersion section, the density-modulated electron beam entering the radiator generates additional shot noise. In this paper, we analyze the shot noise evolution in the first-stage modulator and radiator of a HC FEL that produces the dominant noise contributions. We also dis-

cuss the significance of these noise sources in different harmonic cascade designs.

ANALYSIS

To illustrate this noise degradation process, we consider a seed signal at the fundamental wavelength $\lambda_1 = 2\pi/k_1 = 2\pi c/\omega_1$:

$$E_1 = (E_0 + \Delta E)e^{i\theta + i\Delta\theta} \approx (E_0 + \Delta E)e^{i\theta}(1 + i\Delta\theta). \quad (1)$$

Here E_0 and $\theta = -\omega_1 t$ are the amplitude and the phase of the signal, ΔE and $\Delta\theta$ represent any small amplitude and phase noises (such as caused by the electron shot noise and/or any noise carried by the seed laser). After a total of $N_h = h_1 h_2 \dots$ frequency multiplication, the electric field at the output harmonic is

$$\begin{aligned} E_{N_h} &= G(E_0 + \Delta E) \exp(iN_h\theta + iN_h\Delta\theta) \\ &\approx G(E_0 + \Delta E)e^{iN_h\theta} (1 + iN_h\Delta\theta), \end{aligned} \quad (2)$$

where we have assumed that $N_h\Delta\theta \ll 1$ (otherwise the effect is rather large), and G is an arbitrary function of the field amplitude (such as the Bessel function bunching factor). Thus, the noise-to-signal ratio at the final harmonic radiation is [1, 5]

$$\left(\frac{P_n}{P_s}\right)_{N_h} = N_h^2 \left(\frac{P_n}{P_s}\right)_1. \quad (3)$$

N_h can be a very large number (a few hundred to a few thousand when harmonic cascading a UV laser to an x-ray FEL). $(P_n)_1$ is the initial noise power which includes both the intrinsic laser noise and the electron shot noise. Suppose that the seed laser noise is controlled to a tolerable level, the shot noise fluctuations of the electron beam provide the essential contributions, which will be studied here.

We focus our analysis on the first-stage of a harmonic cascade that includes a modulator, a dispersion section and a radiator (tuned to the h^{th} harmonic of the seed wavelength) as shown in Fig. 1. This first stage has the largest total harmonic conversion factor and hence produces the dominate noise sources. The initial longitudinal phase space distribution function is

$$F(\theta_0, \eta_0) = \frac{k_1}{\chi} \sum_{j=1}^{N_e} \delta(\theta_0 - \theta_j) \delta(\eta_0 - \eta_j), \quad (4)$$

where $\theta_0 = -ck_1 t_0$ describes the electron phase relative to the EM wave (i.e., input laser field), η_0 describe the initial relative energy deviation, and $\chi = N_e/l_b$ is the line density of the electron bunch with N_e electrons and l_b bunch

* zrh@slac.stanford.edu

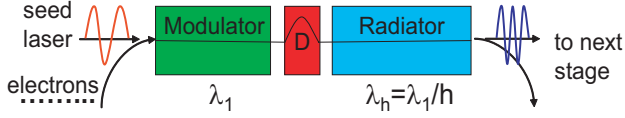


Figure 1: Schematic of the first-stage HC FEL.

length. The normalization in Eq. (4) is chosen so that the ensemble average

$$\left\langle \int F(\theta_0, \eta_0) d\eta_0 \right\rangle = 1 \quad (5)$$

for a constant current profile.

In typical HC FEL designs [3, 4, 11], the first undulator is relatively short and is mainly an energy modulator, then we have

$$\eta_1 = \eta_0 + \eta_s \sin \theta_0 + \eta_n(\theta_0), \quad (6)$$

where η_s is the energy modulation amplitude induced by the seed laser field, and η_n is the energy modulation induced by the noisy spontaneous undulator radiation.

A dispersion section immediately after the modulator can convert the beam energy modulation into a density modulation. This is accompanied by a magnetic chicane that changes the phase of the electron according to its energy deviation:

$$\theta_1 = \theta_0 + k_1 R_{56} \eta_1 = \theta_0 + D \eta_1. \quad (7)$$

Here R_{56} is the net momentum compaction of the chicane together with the first undulator (modulator), and $D = k_1 R_{56}$. The harmonic bunching near the h^{th} harmonic (when $\nu \sim h$) can be found as

$$\begin{aligned} b_\nu &= \int \frac{d\theta_1}{k_1 l_b} d\eta_1 e^{-i\nu\theta_1} F(\theta_1, \eta_1) \\ &= \int \frac{d\theta_0}{k_1 l_b} d\eta_0 e^{-i\nu[\theta_0 + D(\eta_0 + \eta_s \sin \theta_0 + \eta_n)]} F(\theta_0, \eta_0). \end{aligned} \quad (8)$$

Here we have assumed the laser pulse length is at least as long as the electron bunch length. If the laser pulse only overlaps a fraction of the electron bunch, l_b should be taken to be the laser pulse length instead of the electron pulse length, then N_e represents number of electrons within l_b . Let us also assume that the modulated part of the electron bunch is long compared to the laser wavelength (i.e., $k_1 l_b \gg 1$), and that the electron energy distribution is Gaussian with a slice rms energy spread σ_η , we expand Eq. (8) in Bessel series of η_s and to the first-order in η_n (as

$|hD\eta_n| \ll 1$) to obtain

$$\begin{aligned} b_\nu &= \int \frac{d\theta_0}{k_1 l_b} \int d\eta_0 \sum_{p=-\infty}^{\infty} J_p(-hD\eta_s) e^{i(p-\nu)\theta_0} e^{-i\nu D\eta_0} \\ &\quad \times (1 - ihD\eta_n) F(\theta_0, \eta_0) \\ &= \sum_{p=-\infty}^{\infty} J_p(-hD\eta_s) \left[\frac{1}{N_e} \sum_{j=1}^{N_e} e^{i(p-\nu)\theta_j} e^{-i\nu D\eta_j} \right. \\ &\quad \left. - ihD \exp\left(-\frac{h^2 D^2 \sigma_\eta^2}{2}\right) \int \frac{d\theta_0}{k_1 l_b} e^{i(p-\nu)\theta_0} \eta_n(\theta_0) \right], \end{aligned} \quad (9)$$

where we have applied the smooth distribution function in the second term of the bracket as η_n is treated as a small perturbation.

When $\nu = p = h$, the first term in the bracket produces the desired harmonic bunching signal as

$$\begin{aligned} b_h &= \frac{J_h(-hD\eta_s)}{N_e} \sum_{j=1}^{N_e} e^{-ihD\eta_j} \\ &= J_h(-hD\eta_s) \exp\left(-\frac{h^2 D^2 \sigma_\eta^2}{2}\right). \end{aligned} \quad (10)$$

When $\nu \neq h$, the first term produces the noise bunching in the radiator as the ensemble average

$$\langle |b_\nu^r|^2 \rangle = \frac{1}{N_e} \sum_{p=-\infty}^{\infty} J_p^2(-hD\eta_s) = \frac{1}{N_e}. \quad (11)$$

Thus, the modulated bunch generates the same amount of the shot noise bunching in the radiator as a fresh electron bunch.

The second term in the bracket of Eq. (9) is the noise bunching originated from the modulator. As η_n is nearly a sinusoidal function of θ_0 , it can be written as

$$\begin{aligned} b_\nu^m &= \exp\left(-\frac{h^2 D^2 \sigma_\eta^2}{2}\right) \left[-ihD J_{h+1}(-hD\eta_s) \eta_n^+(\Delta\nu) \right. \\ &\quad \left. - ihD J_{h-1}(-hD\eta_s) \eta_n^-(\Delta\nu) \right], \end{aligned} \quad (12)$$

where $\Delta\nu = \nu - h$ and

$$\eta_n^\pm(\Delta\nu) = \int \frac{d\theta_0}{k_1 l_b} e^{i(\pm 1 - \Delta\nu)\theta_0} \eta_n(\theta_0) \quad (13)$$

is the Fourier component of η_n near the first undulator (modulator) resonant frequency ck_1 .

If $x = hD\eta_s \ll 1$, we can expand $J_h(x) \sim (x/2)^h/h!$; If the dispersion strength is optimized to yield the maximum $|b_h|$ at $hD\eta_s \sim h$ or $D \sim 1/\eta_s$, then $J_h \sim J_{h\pm 1} \sim 0.3$. In either case, we can approximate the bunching ratio as

$$\left| \frac{b_\nu^m}{b_h} \right|^2 \approx 4h^2 \frac{|\eta_n^\pm(\Delta\nu)|^2}{\eta_s^2}. \quad (14)$$

The power spectrum $dP/d\omega$ in the radiator is proportional to $|b|^2$. Integrating over their respective bandwidths in the radiator, we obtain the modulator noise-to-signal power ratio as

$$\left(\frac{P_n^m}{P_s}\right)_h = 4h^2 \frac{\Delta\omega_m \langle |\eta_n^\pm(\Delta\nu)|^2 \rangle}{\Delta\omega_s \eta_s^2}, \quad (15)$$

where $\Delta\omega_s = 2\pi c/l_b$ is the Fourier transform limited bandwidth for the signal, and $\Delta\omega_m$ is the bandwidth of the modulator noise. For simplicity, we assume that the full modulator bandwidth is much smaller than the full radiator bandwidth centered around a much higher frequency (i.e., $\Delta\omega_m = \Delta\nu_m \omega_1 < \Delta\omega_r = \Delta\nu_r \omega_h$), then we have $\Delta\omega_n^m = \Delta\omega_m = \Delta\nu_m \omega_1$ without convoluting the bandwidths of the modulator and the radiator.

The laser-induced energy modulation amplitude can be estimated as

$$\eta_s^2 = K_1^2 [\text{JJ}]^2 \frac{L_{u1}^2 P_L}{\gamma^4 \sigma_L^2 P_0}, \quad (16)$$

where $P_0 = I_A mc^2/e \approx 8.7$ GW. Using the one-dimensional FEL theory, we find that the Fourier component of the shot-noise-induced energy modulation is

$$\begin{aligned} \eta_n^\pm(\Delta\nu) &= \frac{1}{8\gamma^3} \frac{I}{I_A} \left(\frac{\lambda_{u1} K_1 [\text{JJ}]}{\sigma_x} \right)^2 N_{u1}^2 f(\bar{\nu}) \\ &\times \frac{1}{N_e} \sum_{j=1}^{N_e} e^{i(\pm 1 + \Delta\nu)\theta_j}, \end{aligned} \quad (17)$$

where $\bar{\nu} = \pi \Delta\nu N_{u1}$ is the scaled detune in the first undulator with N_{u1} period, and

$$f(\bar{\nu}) = \left[\frac{e^{-i\bar{\nu}} \sin(\bar{\nu})/\bar{\nu} - 1}{i\bar{\nu}} \right] \quad (18)$$

describes the energy modulation bandwidth due to the shot noise with a relative bandwidth given by $\Delta\nu_m = 1/N_{u1}$ for $N_{u1} \gg 1$. Inserting Eq. (16) and (17) into Eq. (15), we obtain finally

$$\begin{aligned} \left(\frac{P_n^m}{P_s}\right)_h &= h^2 \frac{\lambda_{u1} N_{u1} r_e \sigma_L^2}{8\sigma_x^4} \frac{K_1^2 [\text{JJ}]^2}{1 + K_1^2/2} \frac{(mc^2/e) I}{P_L} \\ &= h^2 \left(\frac{P_n^m}{P_L}\right)_1. \end{aligned} \quad (19)$$

Thus, the effective modulator noise is

$$P_n^m = \frac{\lambda_u N_{u1} r_e \sigma_L^2}{8\sigma_x^4} \frac{K_1^2 [\text{JJ}]^2}{1 + K_1^2/2} \frac{mc^2}{e} I. \quad (20)$$

For efficient laser-beam interaction in the modulator, the laser spot size is usually chosen to be $\sigma_L = \sqrt{\lambda_1 \lambda_{u1} N_{u1}/8\pi}$ (i.e., the Rayleigh length is one half the undulator length with the laser waist located at the middle of the undulator). When the electron beam matches the

laser spot (i.e., $\sigma_x \approx \sigma_L$), we have

$$P_n^m \approx \frac{\lambda_{u1} N_{u1} r_e}{8\sigma_x^2} \frac{K_1^2 [\text{JJ}]^2}{1 + K_1^2/2} \frac{mc^2}{e} I \quad (21)$$

$$\approx \frac{\pi r_e mc^2}{\lambda_1 e} I. \quad (22)$$

Equation (21) can be shown to be the spontaneous undulator radiation in the forward direction (within a solid angle $\lambda_1^2/(2\pi\sigma_x^2)$ and a full bandwidth ω_1/N_{u1}). Equation (22) holds for $K_1^2 \gg 1$ and can be used for a quick estimation of modulator noise power. If the modulator length is much shorter than two power gain lengths, then the modulator noise power is much smaller than the usual SASE noise power as discussed in the introduction.

As shown in Eq. (11), the density-modulated beam generates the same shot noise bunching. The additional radiator noise-to-signal ratio can be estimated as

$$\left(\frac{P_n^r}{P_s}\right)_h = \frac{\Delta\omega_n^r \langle |b_\nu^r|^2 \rangle}{\Delta\omega_s b_h^2} = \frac{\Delta\omega_n^r/N_e}{\Delta\omega_s J_h^2 (hD\eta_s) e^{-h^2 D^2 \sigma_\eta^2}}, \quad (23)$$

where $\Delta\omega_n^r = \Delta\omega_r = \Delta\nu_r \omega_h$ is the noise bandwidth in the radiator. If the radiator is also a low-gain device, then $\Delta\nu_r \approx 1/N_{u2}$. If the radiator is a high-gain device, then $\Delta\nu_r \approx 2\rho$. In either case we can write

$$\left(\frac{P_n^r}{P_s}\right)_h = \frac{1/N_{lc}}{b_h^2} = \frac{1/N_{lc}}{J_h^2 (hD\eta_s) e^{-h^2 D^2 \sigma_\eta^2}}, \quad (24)$$

where $N_{lc} = N_e l_c/l_b$ is the number of electrons within the radiator coherence length $l_c = \lambda_h/(\Delta\nu_r)$. Note that the radiator noise-to-signal ratio is independent of the signal laser power P_L , but depends strongly on the harmonic bunching strength. This has implications on different designs of HC FELs to be discussed below.

NUMERICAL EXAMPLES AND DISCUSSIONS

Equations (20), (22), and (24) are the main results of this paper and may be used to estimate the shot-noise-to-signal ratio of a HC FEL using a high-power seed laser in a short modulator. Let us take some numerical examples to illustrate the significance of various noise contributions. Consider the BESSY HC FEL design at the final radiation wavelength $\lambda_f = 1.24$ nm [3]. For $I = 1.75$ kA and $\lambda_1 = 297.50$ nm, the modulator noise power according to Eq. (22) is 26 W. If the laser power is 100 MW, then the modulator noise-to-signal ratio at the final wavelength after the total harmonic number $N_h = 297.50/1.24 = 240$ is

$$\left(\frac{P_n^m}{P_s}\right)_{N_h} = N_h^2 \times \frac{26}{100 \times 10^6} \approx 1.5\%. \quad (25)$$

Thus, the modulator noise contribution is noticeable but still small. In passing, we note the bandwidth of the modu-

lator noise is about ω_1/N_{u1} , hence the final relative bandwidth of the first-stage modulator noise is

$$\frac{\Delta\omega_n^m}{\omega_f} = \frac{1}{N_h N_{u1}}. \quad (26)$$

This may still be a small relative bandwidth than a SASE FEL at 1 nm. For example, $N_h = 240$, $N_{u1} = 18$ in the BESSY FEL, and $\Delta\omega_n^m/\omega_f \sim 2 \times 10^{-4}$. Thus, even when the final noise level due to the first modulator is comparable to the signal strength, the temporal coherence of the HC FEL is still improved as any noisy structure within the slippage length $\lambda_1 N_{u1}$ of the first modulator is naturally smoothed. This noise filtering effect was observed in the LUX HC FEL simulations [11].

Let us now consider the radiator noise. First, we take $I = 1.75$ kA, $N_{u2} = 40$, and $\lambda_h = 297.50/5 = 59.50$ nm, then we have $N_{lc} = N_e N_{u2} \lambda_h / l_b \sim 10^8$ in Eq. (24). The BESSY FEL employs a fresh bunch approach that shifts the output radiation to a fresh part of the bunch for the next-stage interaction and hence allows for a large energy modulation to be induced in the part of the electron bunch that overlaps with a very short laser signal [12]. In this approach, the harmonic bunching is usually maximized by choosing $D \sim 1/\eta_s$. If $hD\sigma_\eta \ll 1$, we have $b_h^2 \sim 0.1$. The increase of the energy spread due to the large energy modulation is not an issue as the next stage interaction occurs at a fresh part of the bunch with the same initial energy spread. In this case, the radiator noise-to-signal ratio given by Eq. (24) is extremely small, at the 10^{-7} level. Even after another harmonic conversion factor of 48 (from the radiator wavelength $\lambda_h = 59.50$ nm to the final wavelength $\lambda_f = 1.24$ nm), the contribution from the radiator noise is still small.

Nevertheless, the fresh bunch technique requires a tight timing control between the short laser pulse and the electron bunch. In addition, experiments demanding most photons in a narrow bandwidth may benefit from using a laser pulse longer than the electron bunch length to seed the whole bunch. In this case, the induced energy modulation must be controlled to a small level in order not to degrade the beam energy spread (i.e., $\eta_s < \sigma_\eta$). In view of Eq. (10), the harmonic bunching cannot be maximized as $hD\eta_s < hD\sigma_\eta < 1$, then the radiator noise-to-signal ratio can increase dramatically. For example, in the whole-bunch seeding example described in Ref. [1], the second-harmonic bunching at the radiation wavelength 130 nm is only $b_2^2 \sim 0.25 \times 10^{-4}$ in order to avoid a significant increase in the energy spread. Thus, the radiator noise-to-signal ratio given by Eq. (24) can be much larger ($\sim 10^{-3}$). An additional harmonic conversion factor of 16 (to the final wavelength at 8 nm) will amplify this radiator noise-to-signal ratio to 25%. Therefore, the shot noise contribution, especially in the radiator section, may limit the temporal coherence of such a harmonic cascade.

ACKNOWLEDGMENTS

The author wishes to thank W. Fawley, W. Graves, K.-J. Kim, L.-H. Yu, and J. Wu for many useful discussions. This work was supported by the U.S. Department of Energy contract No. DE-AC02-76SF00515.

REFERENCES

- [1] E.L. Saldin, E.A. Schneidmiller, and M.Y. Yurkov, *Opt. Commun.* **202**, 169 (2002).
- [2] L.-H. Yu and J.H. Wu, *Nucl. Instrum. Methods Phys. Res., Sect. A* **483**, 493 (2002).
- [3] BESSY FEL Technical Design Report, http://www.bessy.de/publicRelations/publications/files/TDR_WEB.pdf.
- [4] C. J. Bocchetta et al, In *Proceedings of the 2005 Free Electron Laser Conference*, Stanford, CA, USA, 2005.
- [5] W. Robins, *Phase noise in signal sources*. Peter Peregrinus Ltd., London, 1982.
- [6] K.-J. Kim, *Phys. Rev. Lett.* **57**, 1871 (1986).
- [7] R. Bonifacio, C. Pellegrini, and L.M. Narducci, *Opt. Commun.* **50**, 373 (1984).
- [8] L.-H. Yu and S. Krinsky, *Nucl. Instrum. Methods Phys. Res., Sect. A* **285**, 119 (1989).
- [9] M. Xie, *Nucl. Instrum. Methods Phys. Res., Sect. A* **475**, 51 (2001).
- [10] Z. Huang and K.-J. Kim, *Nucl. Instrum. Methods Phys. Res., Sect. A* **475**, 59 (2001).
- [11] W. Fawley, W. Barletta, J. Corlett, and A. Zholents, In *2003 Particle Accelerator Conference*, Portland, OR, USA, 2003.
- [12] I. Ben-Zvi, K. Yang, and L.-H. Yu, *Nucl. Instrum. Methods Phys. Res. Sec. A* **318**, 726 (1992).

OPTICAL BEAM QUALITY IN FREE-ELECTRON LASERS*

P.A. Sprangle[#], Naval Research Laboratory, Washington, DC, 20375, U.S.A.

H.P. Freund, Science Applications International Corp., McLean, VA 22102, U.S.A.

J. Peñano, Naval Research Laboratory, Washington, DC, 20375, U.S.A.

B. Hafizi, Icarus Research Inc., P.O. Box 30780, Bethesda, MD 20824-0780, U.S.A.

Abstract

It is widely known that the mode quality of the output of free-electron lasers (FELs) is near the diffraction limit. In this paper, we analyze the optical mode quality in FELs using the M^2 parameter, which is an optical analogue of the emittance for particle beams and measures the divergence of the optical mode. For a perfect Gaussian beam $M^2 = 1$ and increases as the mode quality deteriorates (*i.e.*, the divergence angle and the higher order mode content increase). Thus, the optical mode is often described as M^2 times diffraction limited in the far field. We show how M^2 may be calculated in two ways: (1) by a direct integration over the transverse mode structure, and (2) by allowing the mode to expand beyond the wiggler and analyzing the divergence. We then simulate a forthcoming experiment at Brookhaven National Laboratory using the MEDUSA simulation code and show that M^2 , as expected, is near unity at saturation.

INTRODUCTION

It is widely known that the mode quality of the output of free-electron lasers (FEL) is near the diffraction limit [1-3]. The question of mode quality is relevant to atmospheric propagation of high power FELs [4,5]. Numerical analysis has shown that the mode content in oscillators is predominantly in the TEM₀₀ mode by solution of the paraxial wave equation for a fixed electron beam profile and the subsequent decomposition into Gaussian optical modes [1]. The optical mode quality was observed in the Los Alamos FEL oscillator [2,3] where the mode was shown to be near the diffraction limit. The mode quality in this experiment was characterized by a measurement of the Strehl ratio, which is defined as the ratio of the on-axis intensity at the mode waist to the intensity of a pure Gaussian mode (TEM₀₀) with the same spot size at the lens plane. However, the Strehl ratio is difficult to determine for optical modes that differ appreciably from a Gaussian. Higher order mode content is likely to be more important in single-pass FELs, such as Master Oscillator Power Amplifiers (MOPA) or Self-Amplified Spontaneous Emission (SASE) configurations that are operated past saturation. Hence, an alternate and less ambiguous measure of beam quality is desirable.

In this paper, we quantify beam quality by means of the M^2 parameter, which is an optical analog of the emittance for particle beams and provides a measure of the

divergence of the optical mode [6-8]. It is equal to unity for a perfect Gaussian beam (pure TEM₀₀) and increases as the mode quality deteriorates (*i.e.*, the divergence angle of the mode and the higher order mode content increase). Thus, the optical mode is often described as M^2 times diffraction limited in the far field. The M^2 parameter, as well as optical mode distortion due to mirror heating was measured in the FEL oscillator experiment at Thomas Jefferson National Accelerator Facility [9]. This experiment produced average powers in excess of 2 kW at a wavelength of 3.1 microns. Measurements indicated beam quality near the diffraction limit with $M^2 = 1.1$ at the output mirror for powers up to about 350 W. As the power increased beyond 350 W, M^2 increased and reached values of about 2 for powers of 500 W. However, much of the increase in M^2 that occurred at higher power increased was attributed to mirror distortions and not the wave-particle interaction in the FEL. As a result, the mode quality may be improved in high-power oscillators using mirrors that compensate for distortions. Note that the mode quality in high-power amplifiers is governed solely by the FEL interaction.

In this paper we determine M^2 in two ways: (1) by a direct integration over the transverse mode structure, and (2) by allowing the mode to expand beyond the wiggler and analyzing the mode divergence. This is discussed in Sec. II. In Sec. III we study M^2 in FEL amplifiers using the MEDUSA simulation code [10,11] and then simulate a forthcoming experiment at the Source Development Laboratory at Brookhaven National Laboratory. A summary and discussion is given in Sec. IV.

THE M^2 PARAMETER

A perfect Gaussian beam experiences parabolic expansion in which the spot size increases on either side of the waist via [12]

$$w^2(z) = w_0^2 + \frac{\lambda^2}{\pi^2 w_0^2} (z - z_0)^2, \quad (1)$$

where $w(z)$ is the spot size, w_0 is the minimum spot size (*i.e.*, at the waist), λ is the wavelength, and z_0 is the location of the waist. Note that the Rayleigh range is given by $z_R = \pi w_0^2 / \lambda$ so that $w^2(z_0 \pm z_R) = 2w_0^2$ and the optical mode area increases by a factor of two over the course of the Rayleigh range. The asymptotic diffraction angle is given by $\tan \theta_D = \lambda / \pi w_0 = w_0 / z_R$. Since the waist size is, typically, much less than the Rayleigh range, this means that $\theta_D \approx \lambda / \pi w_0$.

*Work supported by the JTO and ONR

[#]sprangle@ppd.nrl.navy.mil

A similar expression describing parabolic expansion also holds for a more general optical beam that includes higher order modes and can be written as [6-8]

$$W^2(z) = W_0^2 + M^4 \frac{\lambda^2}{\pi^2 W_0^2} (z - z_0)^2, \quad (2)$$

where the upper case W_0 corresponds to the average waist size for the overall optical beam, and

$$W^2(z) = 2 \frac{\iint dx dy r^2 I(x, y, z)}{\iint dx dy I(x, y, z)}, \quad (3)$$

denotes the spot size of the overall optical mode where $I(x, y, z)$ is the average (over a wave period) intensity. Observe that in the limit of a purely Gaussian optical beam, $W(z) = w(z)$ and $M^2 = 1$. As such M^2 (≥ 1) is a measure of the optical beam quality and is the optical analogue of the emittance for particle beams. Note also that this definition of M^2 can unambiguously deal with optical modes that differ markedly from a pure Gaussian, unlike the definition of the Strehl ratio. This asymptotic divergence angle θ_D is given by

$$\tan \theta_D = M^2 \frac{\lambda}{\pi W_0}, \quad (4)$$

so that $\theta_D \approx M^2 \lambda / \pi W_0$ for small divergence angles. This is shown schematically in Fig. 1.

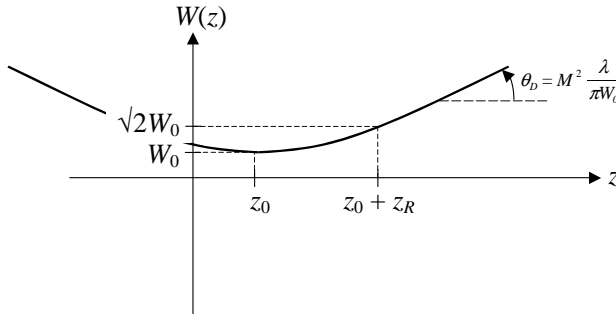


Figure 1: Schematic illustration of parabolic mode expansion

In general, the optical mode may be expressed as a superposition of Gauss-Hermite modes and we can write

$$\delta \mathbf{A}(\mathbf{x}, t) = \hat{\mathbf{e}}_x \sum_{l,n} e_{l,n}(x, y) [\delta A_{l,n}^{(1)} \cos \varphi(x, t) + \delta A_{l,n}^{(2)} \sin \varphi(x, t)], \quad (5)$$

where $e_{l,n}(x, y) = \exp[-r^2/w(z)^2] H_l[\sqrt{2}x/w(z)] H_n[\sqrt{2}y/w(z)]$, H_l is the Hermite polynomial of order l , $\varphi(\mathbf{x}, t) = k_0 z - \omega t + \alpha(z)r^2/w(z)^2$ for wavenumber k_0 ($= \omega/c$) and angular frequency ω and $\alpha(z)$ describes the curvature of the phase front. For propagation *in vacuo*, the amplitudes $\delta A^{(1,2)}$ are constant, φ is the overall phase, and the spot size and curvature vary as $w(z) = w_0 [1 + (z - z_0)^2/z_R^2]^{1/2}$ and $\alpha(z) = (z - z_0)/z_R$. However, the optical mode in an FEL is both amplified and guided by the interaction with the electron beam so that the amplitudes, spot size and curvature will vary in a more complex way along the length of the wiggler. Nevertheless, it may be shown that the overall spot size is given in terms of this representation by

$$W^2(z) = w^2(z) \frac{S_2}{S_1}. \quad (6)$$

where

$$S_1 = \sum_{l,n} 2^{l+n} l! n! \delta A_{l,n}^2, \quad (7)$$

$$S_2 = \sum_{l,n} 2^{l+n} l! n! [(l+n+1) \delta A_{l,n}^2 + 2(l+1)(l+2) (\delta A_{l,n}^{(1)} \delta A_{l+2,n}^{(1)} + \delta A_{l,n}^{(2)} \delta A_{l+2,n}^{(2)}) + 2(n+1)(n+2) (\delta A_{l,n}^{(1)} \delta A_{l,n+2}^{(1)} + \delta A_{l,n}^{(2)} \delta A_{l,n+2}^{(2)})], \quad (8)$$

and $\delta A_{l,n}^2 = \delta A_{l,n}^{(1)2} + \delta A_{l,n}^{(2)2}$. Observe that $S_1 = S_2$ for a pure Gaussian Mode (TEM₀₀) and we recover $W(z) = w(z)$.

We now discuss the calculation of the M^2 parameter. If we express the overall field in the form $\delta \mathbf{A}(\mathbf{x}, t) = A(\mathbf{x}) \hat{\mathbf{e}}_x \cos[k_0 z - \omega t + \theta(\mathbf{x})]$, then it may be shown that

$$M^2 = \left[\iint dx dy I \right]^{-1} \times \left\{ \left(\iint dx dy r^2 I \right) \left(\iint dx dy \left[\left(\frac{\partial I^{1/2}}{\partial r} \right)^2 + I \left(\frac{\partial \theta}{\partial r} \right)^2 \right] \right) - \left(\iint dx dy I \frac{\partial \theta}{\partial r} \right)^2 \right\}^{1/2}, \quad (9)$$

where the intensity is $I = (\omega k_0 / 8 \pi) A^2$. As a result, it can be shown that

$$M^2 = \frac{W^2(z)}{w^2(z)} \left[\frac{2w^2(z)}{W^2(z)} - 1 - \frac{S_3}{S_2^2} + \frac{S_4}{S_2} \right]^{1/2}, \quad (10)$$

where

$$S_3 = 2 \sum_{l,n} 2^{l+n} l! n! [(l+1)(l+2) (\delta A_{l,n}^{(2)} \delta A_{l+2,n}^{(1)} - \delta A_{l,n}^{(1)} \delta A_{l+2,n}^{(2)}) + (n+1)(n+2) (\delta A_{l,n+2}^{(2)} \delta A_{l,n}^{(1)} - \delta A_{l,n}^{(2)} \delta A_{l,n+2}^{(1)})], \quad (11)$$

$$S_4 = \sum_{l,l',n,n'} F_{l,l',n,n'} (\delta A_{l,n}^{(1)} \delta A_{l',n'}^{(1)} - \delta A_{l,n}^{(2)} \delta A_{l',n'}^{(2)}), \quad (12)$$

and

$$F_{l,l',n,n'} = \frac{1}{\pi} \int_0^{2\pi} d\theta \int_0^\infty d\rho \rho \exp(-\rho^2) \times [\cos \theta H_l'(\rho \cos \theta) H_n(\rho \sin \theta) + \sin \theta H_l(\rho \cos \theta) H_n'(\rho \sin \theta)] \times [\cos \theta H_{l'}'(\rho \cos \theta) H_{n'}(\rho \sin \theta) + \sin \theta H_{l'}(\rho \cos \theta) H_{n'}'(\rho \sin \theta)], \quad (13)$$

is a coefficient that depends only on the mode indices. In the limit of a purely Gaussian mode $S_1 = S_2$, $W(z) = w(z)$, and $S_3 = S_4 = 0$ so that Eq. (10) yields $M^2 = 1$ as expected.

In principle, if we know the modal decomposition at the exit from the wiggler in an FEL (including the mode amplitudes, the spot size w and the curvature α), then M^2 can be calculated for the output optical mode using the above method. However, if there is significant higher order mode content, then it can prove numerically arduous to evaluate the $F_{l,l',n,n'}$ coefficients. Therefore, it is useful to have an alternate technique for obtaining M^2 . One such technique makes use of the expansion of the optical mode. If the spot size is known at three different locations beyond the end of the wiggler, then the three equations $W_i^2 = W_0^2 + M^4 \theta_0^2 (z_i - z_0)^2$ for $i = 1-3$ can be solved for M^2 where $\theta_0 = \pi W_0 / \lambda$. Thus,

$$M^2 = \frac{\lambda}{\pi |z_i - z_0|} \sqrt{\frac{W_i^2}{W_0^2} - 1}, \quad (14)$$

for any choice of i , where

$$z_0 = \frac{z_3 + 2z_1 + z_2}{4} + \frac{z_3 - z_2}{4} \frac{(z_3 - z_1)(W_2^2 - W_1^2) + (z_2 - z_1)(W_3^2 - W_1^2)}{(z_3 - z_1)(W_2^2 - W_1^2) - (z_2 - z_1)(W_3^2 - W_1^2)}, \quad (15)$$

and

$$W_0 = \sqrt{W_1^2 + (z_1 - z_0)^2 \frac{(z_3 - z_1)(W_2^2 - W_1^2) - (z_2 - z_1)(W_3^2 - W_1^2)}{(z_3 - z_1)(z_3 - z_2)(z_2 - z_1)}} \quad (16)$$

This technique can be applied either in experiment or simulation. When used in simulation (experiment), the optical mode must be allowed to propagate into free space and the overall spot size [(3) or (6)] must be calculated (measured) at three such points.

NUMERICAL ANALYSIS

For simulation purposes, we use the 3-D FEL simulation code MEDUSA [10,11] which can model planar or helical wiggler geometry and treats the electromagnetic field as a superposition of Gaussian modes (Hermite or Laguerre) and uses an adaptive eigenmode algorithm called the Source-Dependent Expansion [13] to self-consistently describe the guiding of the optical mode through the wiggler and which reproduces free-space diffraction in the absence of the wiggler. The field equations are integrated simultaneously with the 3-D Lorentz force equations for an ensemble of electrons. No wiggler-average orbit approximation is used, and MEDUSA can propagate the electron beam through a complex wiggler/transport line including multiple wiggler sections, quadrupole and dipole corrector magnets, FODO lattices, and magnetic chicanes.

The example under consideration is that of a seeded amplifier experiment to be conducted at the Source Development Laboratory at Brookhaven National Laboratory [14] that will operate at a wavelength of 0.8 microns using the VISA wiggler [15]. The electron beam will have an energy of about 72.3 MeV and a peak current of 300 A. The emittance and rms energy spread are 2.0 mm-mrad and 0.01% respectively. The VISA wiggler is a Halbach design using NdFeB magnets and incorporates a FODO lattice for stronger beam focusing. The wiggler period is 1.8 cm and the maximum on-axis field strength is 7.5 kG with a field error of 0.4% and a gap of 6.0 mm. The FODO cells have a length of 24.75 cm and each quadrupole has a length of 9.0 cm and a focusing gradient of 33.3 T/m. Hence, the separation between quadrupoles is 12.375 cm. The VISA wiggler was built in segments, and the wiggler to be used in the experiment will have 110 periods of uniform field strength. The photo-cathode drive laser is also used to provide the seed for the

amplifier and can provide up to several tens of MW; however, this is larger than needed for the experiment that will use about 10-100 kW of seed power for saturation to be achieved within the length of the wiggler.

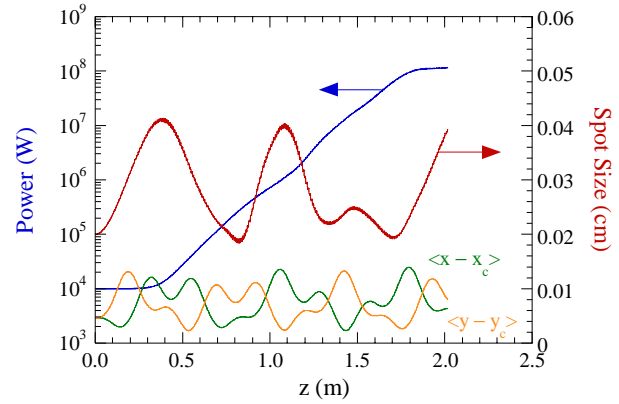


Figure 2: Evolution of the power, spot size and beam envelopes in the x - and y -directions.

The first case we consider makes use of 34 Gauss-Hermite modes and assumes a seed power of 10 kW. This yields saturation at the end of the wiggler at a power level of 115 MW. The evolution of the power, overall spot size of the optical mode, and the beam envelopes in the x - and y -directions is shown in Fig. 2. Observe that the beam is not perfectly matched into the wiggler/FODO lattice since the beam envelopes in the x - and y -directions vary in the FODO lattice and that the overall mode spot size expands and contracts with the beam envelope showing the optical guiding of the radiation; however, the guiding is not strong enough for the optical mode to follow all the variations in the beam envelope.

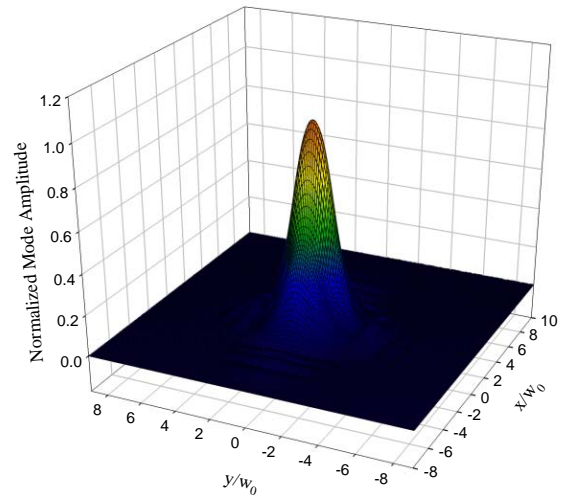


Figure 3: Transverse mode pattern at the wiggler exit for a seed power of 10 kW.

The use of 34 modes in the simulation means that very high order modes are included. Because of this the

method for calculating M^2 based on integration over the transverse mode profile is numerically arduous, and we choose rather to allow the mode to propagate beyond the end of the wiggler and use the three-point solution given in Eq. (14). This can be accomplished easily in simulation simply by terminating the wiggler, after which the Source-Dependent Expansion reproduces free-space propagation when the resonant wave-particle interaction ceases. The result of this calculation shows that $M^2 = 1.45$ for the optical mode at the wiggler exit. This is close to the diffraction limit as expected in FELs and corresponds to a near-Gaussian mode pattern as shown in a normalized transverse mode pattern in Fig. 3.

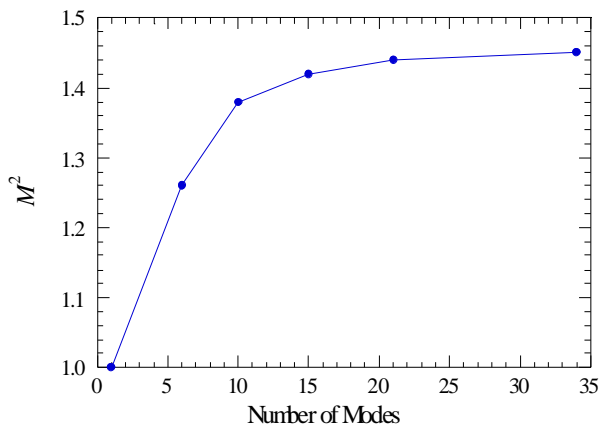


Figure 4: Variation in M^2 versus the number of modes included in the simulation showing convergence after about 20 modes.

An important issue in modeling the beam quality in FELs is the convergence of the simulation with respect to the number of modes in the superposition. The number of modes required to obtain reasonable values for the saturated power is generally smaller than that required to obtain an accurate determination of the optical mode quality as measured by M^2 . For example, simulation using 6 Gauss-Hermite modes also yields a saturated power of 115 MW but the exponentiation length is somewhat shorter and $M^2 = 1.26$. Hence, it is important to determine the number of modes required to reach convergence. This is shown in Fig. 4 for these parameters where we plot M^2 versus the number of Gauss-Hermite modes in the superposition. It is clear from the figure that convergence is achieved using about 20-25 modes for $M^2 = 1.45$. It is important to bear in mind, however, that the number of modes required for convergence will vary with the specific parameters of interest. In particular, for optical guiding to be effective the exponentiation length must be shorter than the Rayleigh range. In general, the smaller the ratio between the exponentiation length and the Rayleigh range, the fewer the number of modes that will be needed to achieve convergence.

SUMMARY AND DISCUSSION

In summary, we have discussed the determination of M^2 in FELs by two methods. One is a direct calculation based upon the mode decomposition at any point within the wiggler, and the other relies on a three-point fit to the optical mode spot size as it propagates beyond the end of the wiggler. These techniques have been applied to an example that corresponds to an amplifier experiment at Brookhaven National Laboratory. We found that the simulation required a relatively large number of higher order modes to achieve convergence in the determination of M^2 . While MEDUSA employs a Gaussian modal representation of the electromagnetic field, it is likely that this implies that alternate techniques using a transverse field solver will require a relatively fine mesh to achieve the same result. Further, the results indicate that the beam quality to be expected is near-diffraction limited when the wiggler length is comparable to the saturation length.

REFERENCES

- [1] D.C. Qiumby and J. Slater, IEEE J. Quantum Electron. QE-19 (1983) 800.
- [2] B.E. Newnam *et al.*, IEEE J. Quantum Electron. QE-21 (1985) 867.
- [3] B.E. Newnam *et al.*, Nucl. Instrum. Meth. A237 (1985) 187.
- [4] P.A. Sprangle, B. Hafizi, and J.R. Peñano, IEEE J. Quantum Electron. 40 (2004) 1739.
- [5] P.A. Sprangle, J.R. Peñano, and B. Hafizi, J. Directed Energy (to appear 2006).
- [6] A.E. Siegman, Proc. Soc. Photo-Opt. Instrum. Eng. 1224 (1990) 2.
- [7] T.F. Johnson, Jr., Laser Focus World 26 (1990) 173.
- [8] A.E. Siegman, IEEE J. Quantum Electron. 27 (1991) 1146.
- [9] S.V. Benson, J. Gubeli, and M. Shinn, Nucl. Instrum. Meth. A483 (2002) 434.
- [10] H.P. Freund *et al.*, IEEE J. Quantum Electron. 36 (2000) 275.
- [11] H.P. Freund, Phys. Rev. ST-AB 8 (2005) 110701.
- [12] A.E. Siegman, *Lasers* (University Science Books, Mill Valley, CA, 1986).
- [13] P.A. Sprangle, A. Ting, and C.M. Tang, Phys. Rev. A 36 (1987) 2773.
- [14] T. Watanabe *et al.*, "Design study of a compact megawatt class FEL amplifier based on the VISA undulator," presented at the 27th Int'l. Free Electron Laser Conference, Stanford, CA, 21-26 August 2005.
- [15] R. Carr *et al.*, Phys. Rev. ST-AB, 4 (2001) 122402.

SEEDING THE FEL OF THE SCSS PROTOTYPE ACCELERATOR WITH HARMONICS OF A TI: SA LASER PRODUCED IN GAS.

G. Lambert, M. Bougeard, W. Boutu, B. Carre, D. Garzella, M. Labat, CEA, Saclay, France
M.E. Couprie, O. Chubar, Synchrotron Soleil, Saint-Aubin, France

G. Lambert, T. Hara, H. Kitamura, T. Shintake SPring-8/RIKEN Harima Institute, Hyogo, Japan.

Abstract

A particular seeded configuration will be tested in 2006 on the SCSS prototype accelerator (SPring-8 Compact Sase Source, Japan). This facility is based on a thermionic cathode electron gun (1 nC), a C-band LINAC (5712 MHz, 35 MV/m) and an in-vacuum undulator (15 mm of period, 2 sections of 4.5 m length). The maximum electron beam energy is 250 MeV and the SASE emission from visible to 60 nm can be obtained. The external source, coming from the High order Harmonic Generation (HHG) process, can be tuned from the 3rd (266 nm) to the 13th harmonic (60 nm) of a Ti: Sa laser generated in a gas cell. The experiment contains a first chamber, dedicated to harmonic generation and a second one for harmonic beam diagnostics and adaptation of the harmonic waist in the first undulator section. The tests have been performed in Saclay (15 mJ, 10 Hz, 50 fs). An energy of 2 μ J with a high stability for the 3rd harmonic and a good transversal shape with an optimized energy level and a high stability for the 13th harmonic have been obtained at the first undulator center place. The performances using analytical formulas, GENESIS and SRW have been updated. The chambers will be installed on the SCSS prototype accelerator in the beginning of October for the seeding tests.

INTRODUCTION

These last years, most of the new FEL sources were dedicated to the so-called Self Amplified Spontaneous Emission (SASE) [1], which provides with a very high brightness photon beam at short wavelength but with limited temporal coherence. Consequently, a few FEL facilities, like ARC-EN-CIEL (Accelerator Radiation Complex for Enhanced Coherent Intense Extended Light) a French proposal for a 4th generation light source [2], have adopted a new configuration: a seeding configuration, in which High order Harmonics of a laser Generated in gas (HHG) are injected into a FEL, giving its full coherence property to the emitted radiation. It also reduces the saturation lengths allowing a more compact source [3]. In addition, other SASE projects have decided to implement it on their facility: SCSS prototype accelerator (SPring-8 Compact Sase Source) [4] and SPARC (Sorgente Pulsata e Amplificata di Radiazione Coerente) [5]. Recently such a seeding experiment with high harmonics produced in gases was performed in an X-ray laser [6]. It is proposed here to seed the FEL of the SCSS prototype accelerator at a 60 nm radiation, corresponding to the 13th harmonic of a Ti: Sa laser (H13) generated in a gas cell. June, the first lasing of

the SCSS prototype accelerator FEL [7] has been observed at 49 nm. The characteristics of the electron beam, undulators, laser and harmonics come from ref. [8] and the basic layout is given in Figure 1.

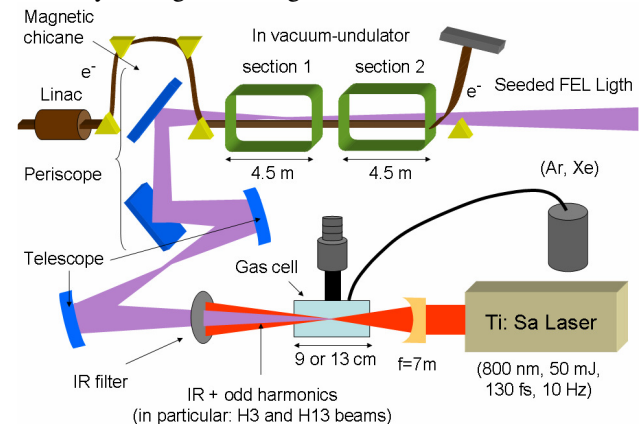


Figure 1: General layout of the seeding experiment with harmonics generated in a gas cell.

HHG SYSTEM

The harmonic generation in gas results from the strong non linear polarization induced on the rare gases atoms, such as Ar, Xe, Ne and He, by the focused intense electromagnetic field E_{Laser} of a "pump" laser [9]. In our case, a 7 m focal length lens focuses a Ti: Sa laser in a cell (Figure 2) filled with Xe or Ar gases, which are well-adapted for the generation of 60 nm radiation. The laser passes through the cell and is aligned by means of two pinholes of 1 mm of diameter, made on Tantalus plates, which create a constant leak of gas.

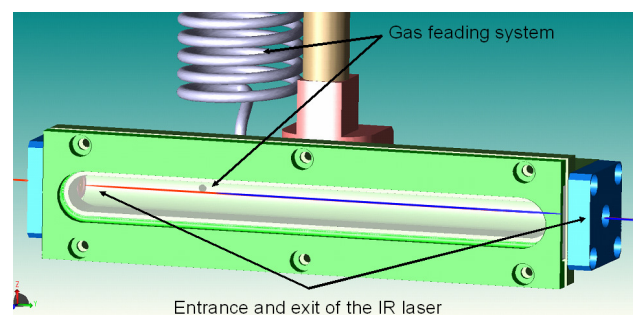


Figure 2: Gas cell system producing HHG light.

The general experiment is based on a system of two chambers (Figure 3).

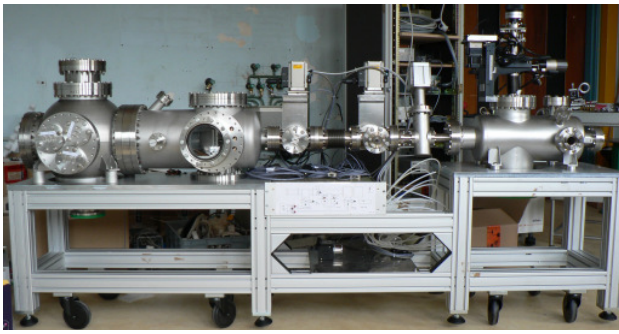


Figure 3: General layout of the HHG system.

The first one is dedicated to the HHG production (Figure 4). The cell position is motorized for accurate alignment of the IR laser and optimization of the harmonic production rate.

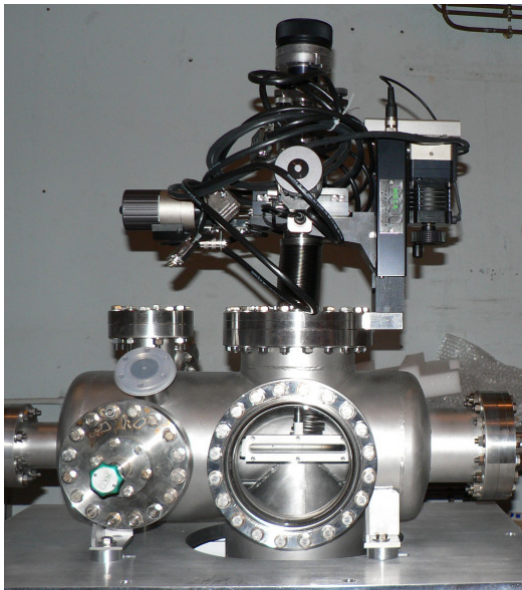


Figure 4: HHG chamber with gas cell and motorization system.

The second one (Figure 5) has been designed for adjusting the harmonic beam at the focusing point in the first undulator section by means of two SiC spherical mirrors. A periscope system is used to align the harmonic beam with the e-beam.

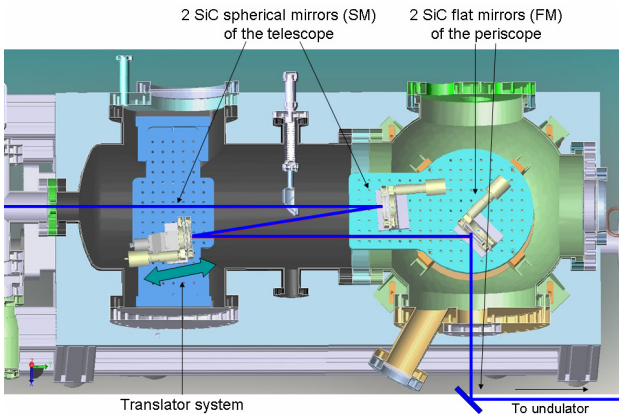


Figure 5: Refocusing system and periscope.

FIRST HHG TESTS IN SACLAY

The first tests have been performed in Saclay with the LUCA laser beam (1 to 15 mJ, 20 Hz, 50 fs, 5 m long of focal lens). In the starting phase of tests, the seeding wavelength was the 3rd harmonic (H₃, 266 nm), which is a more intense and easily useable source (can be propagated outside vacuum, and detected with a VUV photomultiplier). The behavior of the harmonics (Figure 6 for the 3rd harmonic) in operation is mainly optimized with the IR beam diameter (a), power, focusing position in the cell and the gas pressure (b). The respective optimal values, in the test configuration, are 20.8 mm, 115 mW, 4 cm before the cell center and 5 · 10⁻³ mbar in the first chamber.

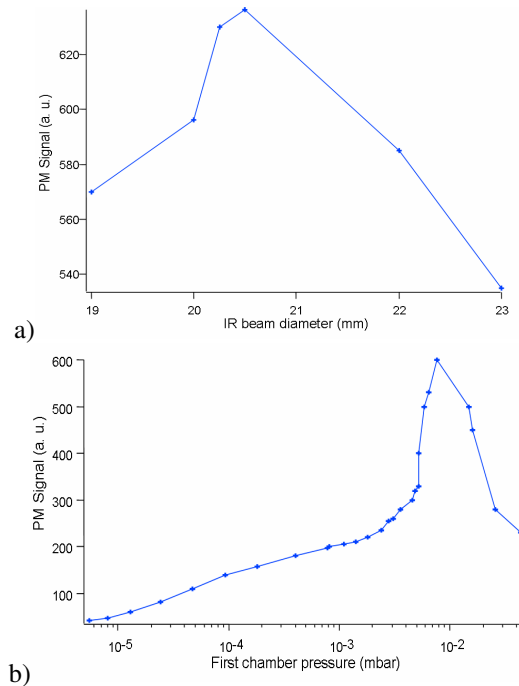


Figure 6: Optimization of the 3rd harmonic flux, generated in a 9 cm cell filled with Ar gas, with the Hamamatsu PM R759, as function of the IR beam diameter (a) and of the gas pressure in the first chamber (b).

The transverse profiles (Figure 7) of the 3rd harmonic, observed with a VUV CCD camera (COHU solid state camera) are quit similar to a Gaussian fit.

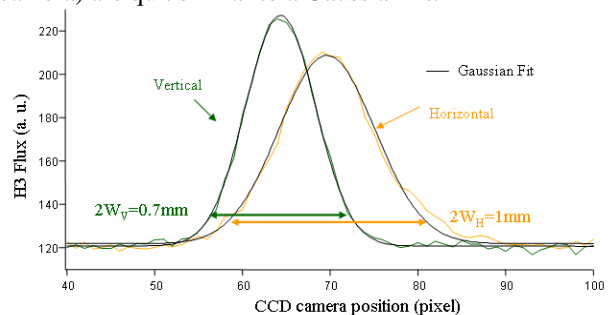


Figure 7: Horizontal and vertical profiles of the 3rd harmonic, at the theoretical focusing point in the first undulator section.

Figure 8 shows the influence of the gas pressure on the optimum of the flux on the two different harmonics.

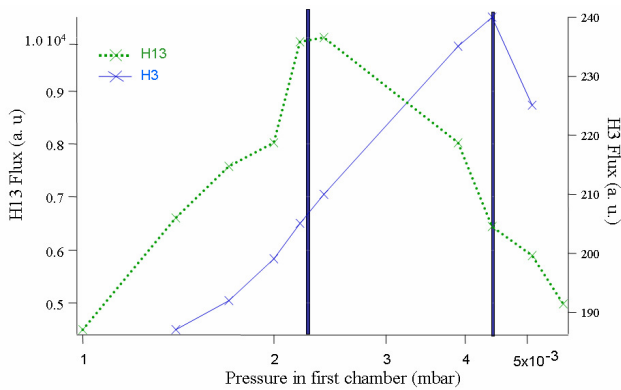
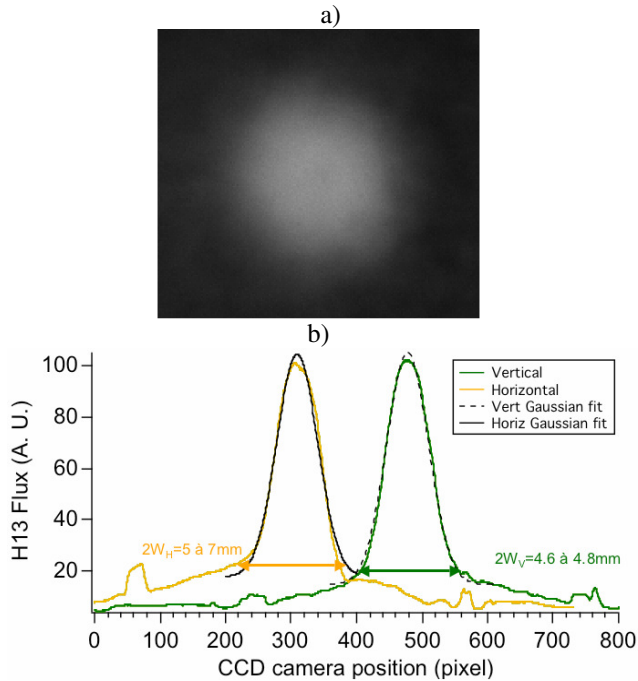


Figure 8: Comparison between optimization of 3rd and 13th harmonics (resp. H3 and H13) as function of the pressure inside the gas cell (proportional to the first chamber pressure)

The shape of the 13th harmonic can be observed (Figures 9 a and b), 3 m after the cell corresponding to 8 m before the theoretical focusing point in the first undulator section. A Micro-Channel Plate (MCP, Hamamatsu F2221) was used with a phosphor screen (P43) associated to a CCD camera and placed after a Sn filter (eliminating the IR laser and selecting especially the 13th harmonic). The beam section presents some light aberrations particularly visible in the horizontal profile. These latter must be really more important in the first undulator section, where the interaction occurs with the e-beam (the overlapping can be decreased of 15%), but can be compensated using a toroidal mirror.



Figures 9 a and b: Transverse section (a) and profiles (b) of the 13th harmonic, 3 m after the cell but 8 m before the theoretical focusing point in the first undulator.

IMPLANTATION ON THE SCSS PROTOTYPE ACCELERATOR

The harmonic generation experiment will be located in the SCSS prototype accelerator tunnel, together with the accelerator and the undulator sections, between the chicane and the shielding wall (Figure 10). The focusing of an intense IR laser comes from the laser hutch, on the opposite side of the shielding wall. The Ti: Sa laser is based on a Tsunami mode-locked oscillator, a Spitfire regenerative chirped-pulse amplifier and a Coherent multipass amplifier and delivers more than 50 mJ at 100 fs. On an optical table, the IR beam is adapted for harmonic generation optimization and synchronized with the e-beam.

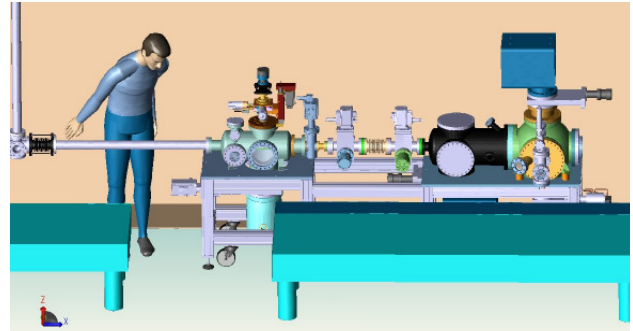
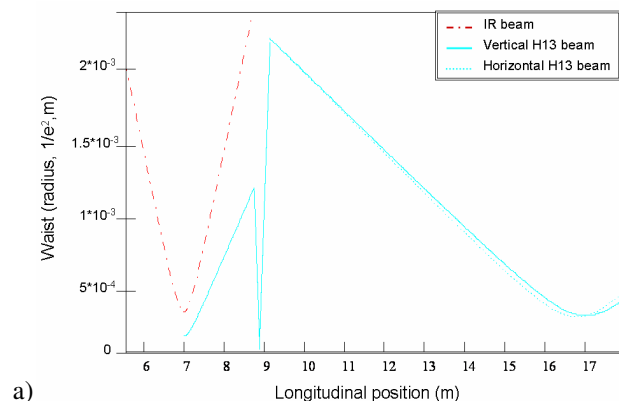
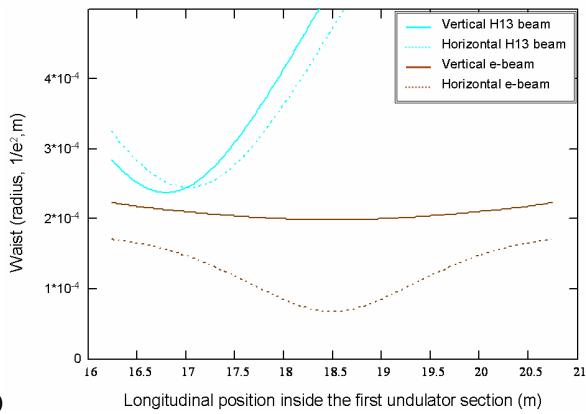


Figure 10: Location for the HHG experiment on the SCSS prototype accelerator.

The laser waist propagation in horizontal (x) and vertical (y) (W_{ox} and W_{oy}) has been calculated [10] to evaluate the geometrical aberrations caused by the two spherical mirrors at the theoretical focusing point in the first part of the first undulator section. Correlated to the e-beam transverse sections, the filling factor (measuring the overlapping of the two beams) can be calculated and is then implemented in our simulation codes (see next section). Figures 11 a and b present the focusing of the IR beam and the 13th harmonic vertical and horizontal propagations, which are quite similar until the focusing part, where the geometrical aberrations lead to a difference of 35 cm in the focusing position between the vertical and horizontal propagations. (b) is a zoom of (a) with the implementation of the e-beam dimensions [8].



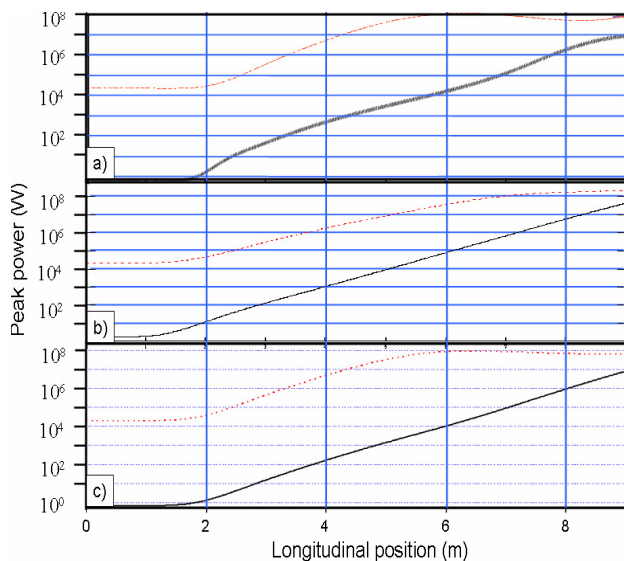
a)



b) Figure 11: a) propagation of focused IR laser and the 13th harmonic, b) focusing inside the first undulator section and overlapping with the e-beam.

SIMULATIONS

New calculations (with ref. [8] characteristics) with SRW [11], analytical expressions from G. Dattoli [12] and Genesis [13] (respectively Figures 12 a, b and c), have been performed for comparing the SASE and the seeding configuration, with 20 kW of seed (corresponding to a slightly pessimistic value of what can be expected). The different simulations converge very well to a similar evolution. First, the saturation peak power levels are very similar (10^8 W). Second, the saturation length for the SASE case is about 10.5 m (10^7 W at 9 m) for all the simulations but varies from 6m to 7.5 m in the seeding case.



Figures 12 a, b and c: Comparison between SASE (black plain line) and seeding configuration (red dash line) with a) SRW b) analytical expressions and c) Genesis.

CONCLUSIONS

Using state-of-the-art High Order Harmonics in gas for seeding a FEL appears very interesting, because the seed radiation is fully coherent and tunable in the VUV-XUV range. Moreover, it reduces the saturation lengths in a more compact source. From the HHG part, the experiment has been perfectly designed and optimized for producing harmonics and especially the 13th. New tests will be performed in situ (near SCSS area in September) with a more performing vacuum system, a more powerful laser system and with different optical characteristics, allowing to still increase the harmonic production and to completely test remote control system before installing it inside the accelerator tunnel for the seeding experiment (October).

REFERENCES

- [1] F. Ciocci et al, IEEE Jour. Quant. Elec. 31 (1995) 1242.
- [2] G. Lambert et al., Proceedings SPIE 2005, San Diego, USA, 31 July-4 August 2005.
- [3] G. Lambert et al., Proceedings FEL 2004, 155-158, Trieste, Italy, 29 August-3 September 2004.
- [4] <http://www-xfel.spring8.or.jp>
- [5] L. Giannessi et al., Proceedings EPAC 2006, 95-98, Edinburgh, 26-30 June 2006.
- [6] Ph. Zeitoun et al., Nature 431, 426-429 (23 Sep 2004). Letters to nature.
- [7] T. Shintake, Proceedings EPAC 2006, 2741-2743, Edinburgh, 26-30 June 2006.
- [8] G. Lambert et al., Proceedings EPAC 2006, 44-47, Edinburgh, 26-30 June 2006.
- [9] P. B. Corkum, Phys. Rev. Lett. 71 (1993) 1994.
- [10] G. Lambert et al., Proceedings FEL 2005, San Francisco, USA, 20 -26 August 2005.
- [11] O. Chubar and P. Elleaume, <http://www.esrf.fr/Accelerators/Groups/InsertionDevices/Software/SRW>
- [12] G. Dattoli, P. L. Ottaviani and S. Pagnutti, J. Appl. Phys. 97, 113102 (2005).
- [13] Sven Reiche, <http://pbpl.physics.ucla.edu/~reiche/>

SEEDING THE SPARC TEST FACILITY WITH HARMONIC GENERATION IN GASES: PRELIMINARY TESTS OF THE HARMONIC GENERATION IN GAS CHAMBER

O. Tcherbakoff, M. Labat, G. Lambert, D. Garzella, M. Bougeard, P. Breger, P. Monchicourt, H. Merdji, P. Salières, B. Carré, CEA, DSM/SPAM, 91191 Gif-sur-Yvette, France
M.E. Couprie, SOLEIL, 91192 Gif-sur-Yvette, France
A. Doria, L. Giannessi, ENEA C.R. Frascati, Italy.

Abstract

A coherent short wavelength source can be realised with a Free Electron Laser by using High Gain Harmonic Generation configuration. The injection of an external light source in the first part of an undulator results in a coherent light emission in its second part. The SPARC FEL (Frascati, Italy), delivering an electron beam at 200 MeV passing through an undulator of 6 sections, can be configured to test such schemes. We propose to use High order Harmonic Generation (HOHG) in gases process as the seed. HOHG produces a coherent XUV source by focusing an intense laser pulse into a gas medium. This beam, composed of odd harmonics of the fundamental laser, is then shaped using a telescope of two spherical mirrors, allowing the focusing at a given position, in the SPARC undulator. Appropriate tuning of the undulator gaps will amplify the 3rd and 5th harmonics seeded, and non-linear harmonics of those wavelengths, allowing the perspective of producing VUV coherent radiation. The chambers for harmonic generation and shaping have been realised and tested at the CEA (Saclay, France). We present these tests.

INTRODUCTION

Along the last few years, other Free Electron (FEL) schemes than the common Self Amplified Spontaneous Emission (SASE) [1] have been proposed to get intense and short pulse duration in XUV domain. In High Gain Harmonic Generation (HG) configuration an external seed, a laser source, induces energy modulation of the relativistic electrons in the modulator, leading to coherent emission of the microbunched electron beam by the radiator at the n^{th} harmonics of the laser fundamental wavelength. The harmonic radiated is selected through the undulator gap. The properties of the output radiation are determined by the seed laser and can thus inherit the degree of temporal coherence. Seeded FEL amplification in combination with harmonic generation has been demonstrated experimentally in midinfrared and VUV domain [4, 5].

A way to reach shorter wavelengths is to use a seed laser in VUV domain. Development in femtosecond laser technology have made possible to imagine new coherent short wavelength sources. One of these sources, called High Order Harmonics Generation (HOHG), is based on the inter-

action between the laser beam and a gas target [6, 7]. Microjoule energies can be obtained at wavelengths down to 50 nm [8, 9]. It has been proposed to use HOHG as seed to inject an undulator, either in the amplifier or in the HG configuration [10]. HOHG seems to be a very good candidate to seed FEL cascade, to extend the operating wavelength of FELs down to sub nm. The SPARC configuration will allow the study of the problems related to the injection of an external radiation seed in a single pass FEL and the analysis of the coupling efficiency of the electron-photon beams in terms of the input parameters [11].

EXPERIMENTAL SETUP FOR THE HARMONIC CHAMBERS

SPARC undulator is composed of 6 sections of 75 periods each. The e-beam energy may be varied up to 150-200 MeV. A Coherent femtosecond laser which delivers 120 fs, 2.5 mJ pulse with a central wavelength at 800 nm and a modified repetition rate of 10 Hz, generates HOHG in a gas jet. The VUV radiation is then injected into the undulator by means of a magnetic chicane. Electron and photon beams follow to test

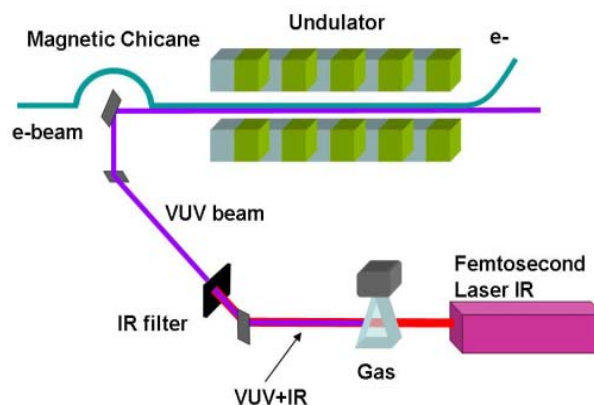


Figure 1: Experimental layout to seed harmonics generated in gas into FEL.

HIGH ORDER HARMONIC GENERATION

HOHG is obtained by focusing an intense laser pulse into a rare gas medium. The atoms of the gas medium are irradiated and ionized by the strong laser field, releasing free electrons with no kinetic energy. Those electrons are then accelerated by the laser electric field. When the electric field sign changes, the electrons can be driven back in the vicinity of the parent ions, and if a collision occurs, the extra-energy of the ion-electron recombination is released by emitting a photon. New frequencies are created and, after the gas medium, one can observe odd high order harmonics of the fundamental frequency co-propagating with the fundamental laser beam. This VUV radiation also exhibits an excellent spatial and temporal coherence [14, 15, 16]. The coherence properties of the harmonics are similar to those of the fundamental laser beam which make them suitable for seeding experiment.

The setup for the production of the harmonics in gas is mainly composed of two chambers. The laser is focussed by a plano-convex lens ($f=2$ m) and delivered through an antireflecting coated 790 nm window in the first chamber where HOHG occurs. Then, 1.5 meters downwards, the second chamber is used to adapt the waist, i.e. the harmonic beam mode in the middle of the first undulator for a correct overlap with the e-beam. This shaping is performed using two spherical mirrors reflecting nearly at normal incidence, both equipped with motorized mounts, and an additional translation stage under the second mirror, for the adaptation of the focusing point in the undulator. The distance between the gas jet and the middle of the first undulator is about 8 m. A scheme of the experimental setup is given in Figure 2.

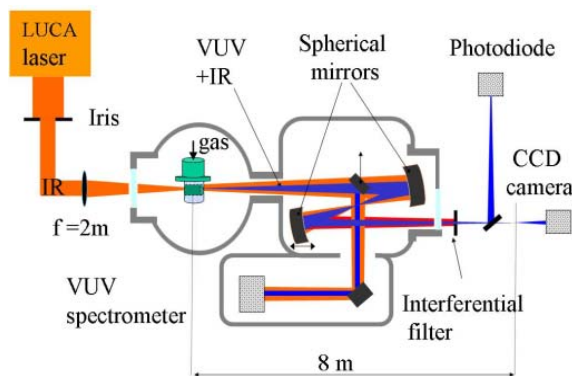


Figure 2: Experimental setup

CHARACTERISATION OF THE HHG PRODUCED IN CEA-SACLAY

In order to prepare the seeding experiment on SPARC facility, the chambers for harmonic generation have been tested during two months at the CEA-Saclay (see Figure 3). The radiation generated in the chambers passes through an interferometric filter centred at 266 nm (H3) eliminating

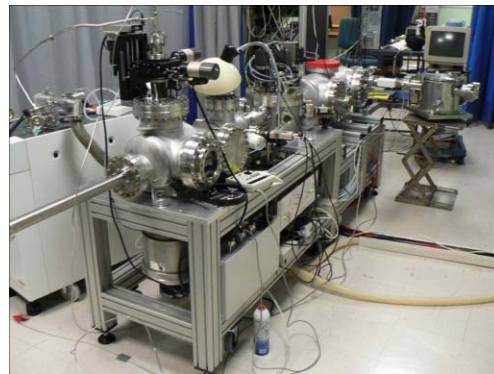


Figure 3: Picture of the chambers being tested at CEA-Saclay.

IR beam as well as other harmonics. The 266 nm radiation is then detected with a calibrated VUV photodiode blinded for diffused IR light.

The femtosecond laser system (LUCA) of the Saclay Laser-matter Interaction Center (SLIC) has been used as fundamental source for the tests. The characteristics of this laser based on 2 TW, 20 Hz CPA Titanium:Sapphire System [17] are given in Table . Both duration and energy of the laser pulse were tunable: several tests were performed using a 2.5 mJ - 120 fs laser pulse in order to work in similar conditions as the one expected on SPARC facility.

Table 1: Characteristics of the laser system LUCA used for the tests. The pulse duration was measured using autocorrelator, assuming a gaussian profile.

Laser characteristics	Value	Unit
Wavelength	800	nm
Spectral width	20	nm
Pulse duration	56.8	fs
Energy	50	mJ
Beam diameter	35	mm

The initial configuration foreseen for harmonic generation, a simple gas jet with an aperture of 0.5 mm and no additional nozzle, allowed a very small amount of UV photons to be produced. To reach a better conversion factor, the geometry was improved through out the testing of four different configurations: Jet and vertical guide, Jet and horizontal guide, Static Cell and finally Pulsed Cell. The increasing performances are summarized in Figure 4. In the Pulsed Cell configuration, the gas is injected in a 1 cm long-windowless cell by bursts of 1.3 μ s through an electromagnetic valve synchronized with the incoming laser pulses. A conversion factor of 10^{-3} was obtained as regularly achieved in recent experiments. A good stability was also reached, as well as a nearly perfectly gaussian harmonic beam.

The first step to optimize the harmonic yield was to con-

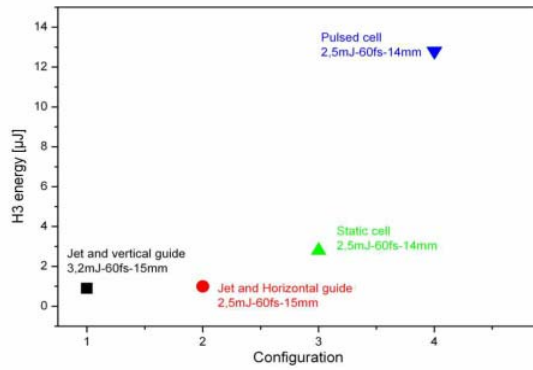


Figure 4: Energy obtained on the third harmonic using different interaction medium configurations.

control the laser aperture and the cell focus position [18, 19]. Closing an iris placed before the lens means decreasing the energy laser and increasing the focal spot size, therefore decreasing the focal intensity. As illustrated in Figure 5 with 2.5 mJ laser energy in Argon gas, a larger aperture is needed in case of a long pulse duration: 14 mm (resp. 18 mm) for 60 fs pulse (resp. 120 fs chirped laser pulse). The energy contained in each pulse remains unchanged, and fixed to 2.5 mJ. The optimum at 60 fs corresponds to a focal spot diameter of $340 \mu\text{m}$, and at 120 fs of $279 \mu\text{m}$; both leading to an intensity of $2 \times 10^{14} \text{ W/cm}^2$. The reduced spot diameter at 120 fs involves less medium in the laser-matter interaction, resulting into a lower energy emission (less photons are produced).

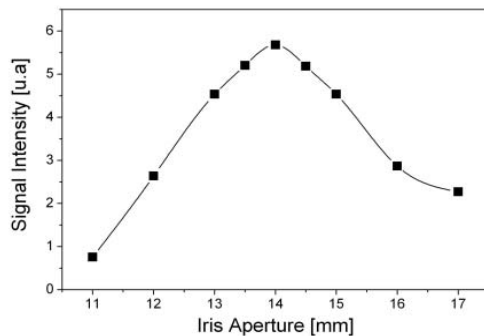


Figure 5: Aperture size dependence of H3 in Argon with 2.5 mJ laser energy for two pulse durations.

Figure 6 illustrates the third harmonic dependency in the cell position. The maximum efficiency has been reached when the focusing point of the laser beam was 1.5 cm after the cell.

Figure 7 illustrates the influence of the pressure on the 3rd harmonic signal. The amount of UV photons produced increases with the backing pressure. No optimum could be reached, since the electromagnetic valve was limiting the available pressure in the cell.

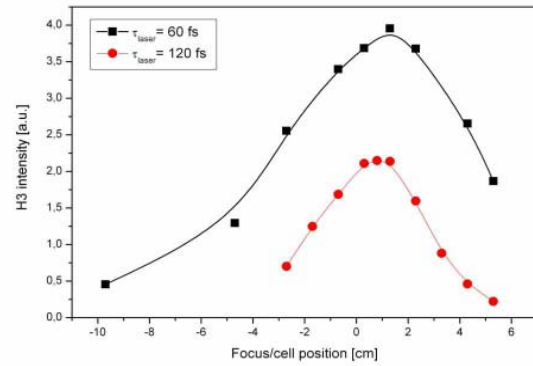


Figure 6: Cell position dependence of H3 in Argon with 2.5 mJ laser energy, for two pulse durations.

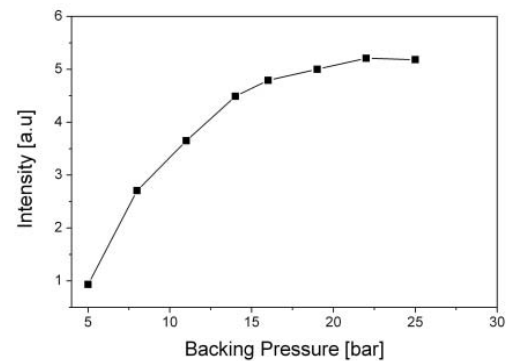


Figure 7: Pressure dependence of H3 in Argon.

The number of 3rd harmonic photons generated in the optimized conditions with 60 fs pulse is 1.3×10^{13} ($9.7 \mu\text{J}$) and the corresponding conversion efficiency reaches 4×10^{-3} . In the same conditions, when 3rd harmonic is generated by a chirped 120 fs pulse, the number of photons decreases by factor 4.

We used a VUV spectrometer composed of a LiF prism and a photomultiplier to measure H3 and H5 with an entrance pinhole of 5 mm. Scanning on the prism angle being manual, we only measured maximum signal at one position of the prism angle for H3 and H5 allowing the coarse comparison of the relative contribution of each harmonic, as illustrated in Figure 8.

The harmonic beam propagation has also been studied. It is crucial for evaluating the overlap between the light wave and the electron bunch in the undulator. The harmonic beam is shaped using two concave mirrors optimized for 266 nm wavelength with respectively a focal length of 200 mm and 150 mm. The distance between the two mirrors is about 38 cm. The incidence angle of 2° induces small geometric aberrations. The total transmission for 3rd harmonic is 90 %. The spatial profile of the 3rd harmonics has been measured using a CDD camera. Figure 9 shows the evolution of H3 from the exit of the chambers through out the undulator, and Figure 10 shows the transverse pro-

CONCLUSION

The results of the preliminary tests performed at CEA-Saclay on the chambers are encouraging. An efficient geometric configuration has been defined for the generating medium. According to those first measures, the laser system foreseen at SPARC (120 fs, 2.5 mJ) should be adapted for generation of both 3rd and 5th harmonics with HOHG. We expect more than $4\mu\text{J}$ on the 3rd harmonic in Argon. The telescope system focuses the 3rd harmonic beam, which is slightly astigmatic, at the estimated entrance of the first undulator with a focus waist size of $300\mu\text{m}$.

The peak power of this coherent VUV light was estimated to be 19 MW. Calculations with PERSEO and with GENESIS 1.3 code have shown that saturation can be reached with SPARC undulator, using a 266 and 160nm wavelength seed with only a few kW power [11].

The harmonic chambers should be transported to SPARC facility by the end of January 2007. After implementation on the linear accelerator modules, in spring 2007, first seeding experiments of SPARC FEL with this scheme should start.

ACKNOWLEDGMENTS

This work was supported by the EU Commission in the Sixth Framework Program, Contract No. 011935-EUROFEL.

REFERENCES

- [1] S.V. Milton *et al.*, Science **92**, 2037 (2001).
- [2] L.H. Yu, P.R.A. **44**, 5178 (1991).
- [3] I. Ben-Zvi *et al.*, Nucl. Instrum. Methods Phys. Res. Sect. A **304**, 181 (1991).
- [4] L.H. Yu, Science. **289**, 932 (2000).
- [5] L.H. Yu *et al.*, P.R.L. **91**, 074801 (2003).
- [6] M. Ferray *et al.*, J. Phys. B: At. Mol. Opt. Phys. **21**, L31 (1988).
- [7] A. McPherson *et al.*, J. Opt. Soc. Am. B **4**, 595 (1987).
- [8] J.F. Hergott *et al.*, Phys. Rev. A **66**, 21801 (2002).
- [9] E. Takahashi, N. Y., and M. K., Opt. Lett. **27**, 1920 (2002).
- [10] D. Garzella *et al.*, Nucl. Instrum. Methods Phys. Res. Sect. A **528**, 502 (2004).
- [11] L. Poletto *et al.*, FEL Conference, 63 (2005).
- [12] L. Giannessi *et al.*, www.sparc.it ref:SPARC-FEL-05/004.
- [13] L. Poletto *et al.*, proceedings EPAC 2006 (unpublished).
- [14] T. Ditmire *et al.*, Phys. Rev. Lett. **77**, 4756 (1996).
- [15] L. Le Déroff *et al.*, Phys. Rev. A **61**, 43802 (2000).
- [16] L. Bellini *et al.*, Phys. Rev. Lett. **81**, 297 (1998).
- [17] <http://www-femtodrecam.cea.fr/slic/luca/luca1.htm>.
- [18] P. Balcou *et al.*, J. Phys. B **25**, 4467 (1992).
- [19] T. Ditmire *et al.*, Phys. Rev. A **51**, R902 (1995).
- [20] A. E. Siegmann, "Lasers", University Science Books.

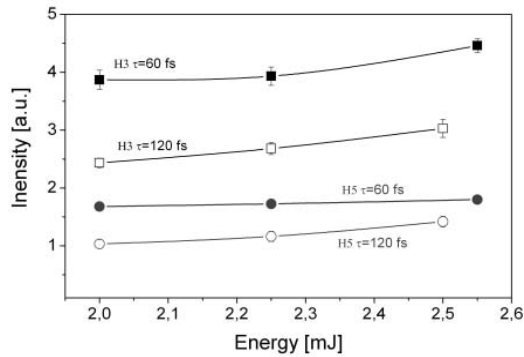


Figure 8: 3rd and 5th harmonics in argon as function of energy laser for two pulse widths.

file of the harmonic at focusing point. The focal spot size is about $940\mu\text{m}$. The theoretical fit with a quasi-gaussian beam [20] gives a M^2 value of 1.6 and a 3rd harmonic size of $220\mu\text{m}$ at generation point. With these measurements, we will be able to determine the filling factor which takes into account the interaction between electrons and photons.

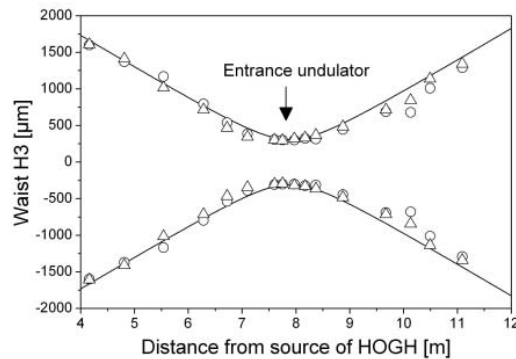


Figure 9: Longitudinal evolution of the beam waist of the 3rd harmonic in vertical (Δ) and horizontal (\circ) direction. In solid line indicate the quasi-gaussian beam fit.

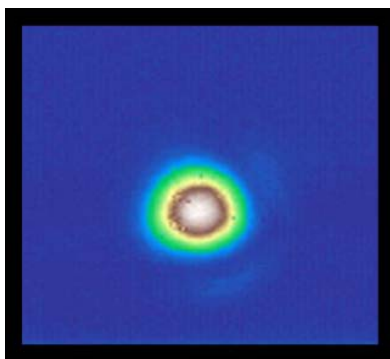


Figure 10: Transverse profile of the 3rd harmonic at focusing point

THE ARC-EN-CIEL FEL PROPOSAL

M. E. Couprie, C. Bruni, O. Chubar, J.M. Filhol, A. Loulergue, L. Nahon, Synchrotron SOLEIL, Saint-Aubin, France

B. Carré, D. Garzella, O. Gobert, P. Hollander, M. Labat, G. Lambert, P. Monot, O. Tcherbakoff, CEA-DSM-DRECAM Service de Photons, Atomes et Molécules, Gif-sur-Yvette, France

G. Petite, CEA-DSM-DRECAM Service des Solides Irradiés, Gif-sur-Yvette, France

P. Bosland, G. Devanz, M. Jablonka, M. Luong, F. Méot, A. Mosnier, B. Visentin, CEA-DSM-DAPNIA Service de Accélérateurs de la Cryogénie et du Magnétisme, Gif-sur-Yvette, France

J. R. Marquès, Lab. d'Utilisation des Lasers Intenses, École Polytechnique, Palaiseau, France

J. M. Ortega, H. Monard, Laboratoire de Chimie-Physique, Univ. Paris-Sud, Orsay, France

A. Rousse, Laboratoire d'Optique Appliquée, École Polytechnique, France.

Abstract

ARC-EN-CIEL (Accelerator-Radiation for Enhanced Coherent Intense Extended Light) aims at providing the user community with coherent femtosecond light pulses covering from UV to soft X ray in France. It is based on a CW 1.3 GHz superconducting linear accelerator delivering high charge, subpicosecond, low emittance electron bunches at high repetition rate. Phase 1 exploits the different sources of seeding with 220 MeV at 1 kHz, in particular High order Harmonic generation in Gas (HHG), to improve the longitudinal coherence and shorten the output radiation wavelength in a rather compact device. Phase 2 is based on a CW 10 KHz 1 GeV superconducting linear accelerator for HHG seeded High Gain Harmonic Generation (HGHG) extending to 1 nm. In phase 3, fs undulator sources in the IR, VUV and X ray and a FEL oscillator in the 10 nm range will be implemented on two ERL beam loops for beam current or energy enhancement.

INTRODUCTION

France is now equipped with a third generation synchrotron light source under commissioning [1] at Saint-Aubin, close to Paris. The Storage Ring consists in a 357 m circumference ring, with 16 cells and 24 straight sections, out of which up to 21 will house insertion devices (ID). High brilliance radiation, from the VUV up to the hard X ray domain will be provided to external users in 2007 with the low emittance (3.7 nm.rad) beam at the 2.75 GeV. Innovative ID's are under construction to provide the best possible performances in a wide energy range (5 eV to 50 keV) [2].

Prospects concerning the Fourth Generation Light Source in France are based on the ARC-EN-CIEL project [3], following a long tradition in FEL in France, in particular in storage ring based FELs (ACO [4], Super-ACO [5]) and on infra-red LINAC based FELs (CLIO [6], ELSA [7]). After considering the installation of an FEL in the VUV on SOLEIL in the oscillator or coherent harmonic generation configurations, it was decided to propose an independent LINAC based dedicated facility providing coherent radiation down to 1 nm, for easier access of the users. The possible implementation of the

first and potentially second phase of ARC-EN-CIEL in the former tunnel of the Accélérateur Linéaire de Saclay, at l'Orme des Merisiers, next to SOLEIL, would make a very attractive acclerator based light source complex.

From the beginning, the project aims at developing a strong synergy between the FEL and the laser communities, leading to couple the electron beam and lasers. The innovative choice of seeding the FEL with High order Harmonic produced in Gas, at a high repetition rate leads to a significant shortening of the wavelength of the seed, in addition to the advantages of seeding with respect to SASE (pulse to pulse intensity stability, reduction of jitter, compactness, enhanced longitudinal coherence). Indeed, more than 70% of the users intend to perform pump-probe experiments and a high stability is requested, confirming the choices of seeding and High Gain Harmonic Generation, as discussed in the frame of the user workshop "Applications of VUV X fs tunable sources combining accelerators and laser: "slicing" at SOLEIL and the ARC-EN-CIEL project" (Feb. 3-4 2004, Orsay). Besides, propositions of plasma acceleration and Thomson scattering emerged from the laser-electron beam combination.

The request of high repetition rate (1-10 kHz) in order to couple as efficiently as possible the electron beam with the high harmonics produced in gas led to the choice of a superconducting type of Linear Accelerator. Expertise exists in DAPNIA in CEA and in SOLEIL with the superconducting RF cavity. A high repetition rate of the photon source is also desirable for users. A 100 fs pulse corresponds to the typical demand.

ARC-EN-CIEL is planned into three phases: a first phase reaching an energy of 220 MeV for HGHG sources in the VUV, a phase 2 at 1 GeV with HGHG sources down to 1 nm using High Harmonics produced in gas, and a phase 3 including two recirculation loops, for Energy Recovery or energy enhancement where undulators (12 m long, period 30 and 20 mm) are installed, providing subpicosecond radiation in the VUV and X ray ranges ($5 \cdot 10^{12}$ phot/s/0.1%bw for 0.1 mA average current). In addition, a 0.1-1 kW average power, 0.1-1 % bandwidth FEL oscillator, installed in the first loop, could cover the 120-10 nm, thanks to recent development of multilayer

mirrors for lithography, and SiC mirrors in normal incidence. Harmonics can also be produced from the FEL oscillator, with 500 MW at 4.5 nm and 10 MW at 2.7 nm. The beam at 2 GeV from the loop will allow shortening further the radiation wavelength down to 0.4 nm with an additional undulator section. Expected radiation from ARC-EN-CIEL is illustrated in figure 1, comparing radiation of its three phases with respect to the insertion devices of SOLEIL. THz radiation will also be provided. The present work, part from the detailed analysis of the components of the project, is concentrating on the progress on several key elements.

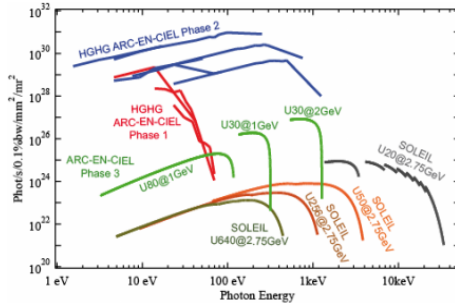


Figure 1 : Peak brilliance. Phase 1 : HHG radiation + seeding wavelength, $P_{\text{seed}} = 100$ kW for HHG harmonics $n^{\circ}7-9$, 600 kW for $n^{\circ}3-5$. 1 kA, $F = 0.1$. Phase 2 : HHG radiation 1.5 kA, 1.35π mm.mrad, 0.0004% slice energy spread, 200 fs, $\beta = 2$ m, $F = 0.088$. Phase 3 : spontaneous emission of undulators of period 30 and 80 mm calculated with SRW. Undulator period length in mm in ID name.

THE ACCELERATOR

The gun

The choice of the gun is not completely defined. It should provide 1 nC for 2π mm.mrad total emittance ϵ . At the beginning, we have considered a Zeuthen photo-injector [8], with a CsTe cathode, to be modified for operation at 1 KHz. This requires a coupler modification with respect to the present design. The active removal of the power can be performed via a phase inversion during falling time. A longer term system is based on a superconducting gun, as presently developed by Rossendorf [9], where emittance compensation and reliability can still be an issue. We also thought about the adaptation of the CeB6 thermo-ionic gun developed at RIKEN for the SCCS project, and the recent very spectacular results in terms of beam stability and emittance [10] bring us to go further in the analysis of this solution for ARC-EN-CIEL. Besides, R&D is going on the cathode materials in LSI (Polytechnique) with the use of Carbon nanotubes.

The cryomodules

ARC-EN-CIEL is based on TESLA type cavities at 1.3 GHz, to be operated in CW mode. The elliptical 9-cell cavities routinely provide 25 MV/m accelerating gradient, while recent advances in the cavity design and integration procedures indicate the possibility of pushing the gradient to 35 MV/m, which is a target parameter for the

International Linear Collider. The design of the cryomodule may be revisited for a better cryogenic efficiency accounting for the CW operation.

Studies concerning the compensation of the microphonics are presently under way at CEA-DAPNIA and BESSY [11]. The microphonics have been analysed with appropriate techniques and different compensation schemes are elaborated using active piezoelectric tuners. However, the large number of the transverse mechanical eigen-modes of the cavity represents a strong limitation for the compensation. A passive damping of these modes by a careful design and mounting of the cavity-tuner system in the cryomodule would alleviate the complexity of the active compensation scheme and improve its efficiency.

The electron beam dynamics

Calculations performed for ARC-EN-CIEL phase 1 accelerator consider an RF gun, a first cryomodule bringing the energy to 100 MeV, a third harmonic cavity compensating the non linearity of the longitudinal phase space, a S-chicane compressor, and a second cryomodule raising the energy to 220 MeV. 6 additional modules are included in phase 2. ASTRA [12] is used to simulate the RF gun and the cavity modules, and CSRTrack code [13] for the compression scheme, taking into account Coherent Synchrotron Radiation in the chicane.

Figure 2a presents the evolution of the different emittances along the bunch compressor. The total emittance is raised to 2.7π mm.mrad in the compression process through the chicane (from 2.1 to 0.1 mm/ 300 fs rms). With an adequate electron beam optics [14], the slice emittances along the bunch remain almost unchanged (ranging from 0.7 to 1.1) with a small mismatch from slice to slice. The compressor creates a correlated emittance that reaches 0.18π mm.mrad, betraying a spread of the slices in the transverse phase space. It is the main contribution to the total emittance increase by strong mismatching.

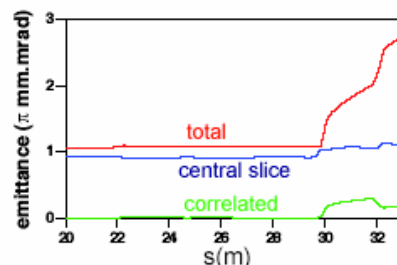


Figure 2 : Evolution of the emittance along the chicane. Chicane parameters: total length: 10 m, $R56 = 0.15$ m, dipole length : 0.3 m. First dipole at $s = 23$ m.

The influence of the laser pulse length on the optimization of the different emittances while keeping a constant space charge density was also investigated. A longer laser pulse is favorable in the compressor, for avoiding emittance degradation due to coherent synchrotron radiation, the longitudinal wake function being proportional to $\sigma_1^{-4/3}$, with σ_1 the beam length.

Although the output bunch is also compressed down to 300 fs, its mean length through the chicane is longer and the emittance is smaller. In order to avoid beam degradation due to non linear part of the R_{566} coefficient, the voltage of the harmonic cavity has to be increased to give an invert sign of the non linear component. For longer laser pulse and longer electron beam length before the chicane, the energy variation is more important and the deformation of phase space is larger (see fig. 3). Systematic simulations done for different pulse lengths (20-40 ps range) and harmonic cavity voltages (20-25 MV/m range), keeping the final bunch length constant at 0.1 mm bring to a minimum of the total emittance for $E_H=22$ MV/m. In Fig. 4, one finds at the end of the S-chicane, a minimum total emittance at 2.1π mm.mrad for the laser pulse length $\sigma_l=25$ ps. The total emittance globally increases with the laser pulse length apart for $\sigma_l=20$ ps, for which it is higher. The central slice emittance decreases with the laser pulse length (radial laser spot reduction). Further studies concern the pre-injection in the case of the thermo-ionic gun (SCSS type) will be studied, calculations for the phase 2, including the second bunch compressor and for phase 3 with ERL loops.

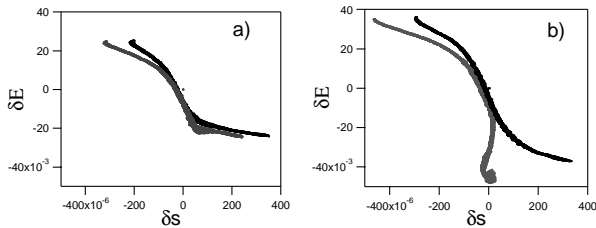


Figure 3 : Longitudinal phase space representation for a laser pulse length of a) 20ps, b) 40 ps for different voltages of the harmonic cavity. Black (resp. grey): $E_H=22$ (resp. 20)MV/m.

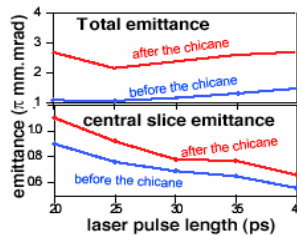


Figure 4 : Emittance evolution versus the laser pulse length.

THE LASER SYSTEM AND SYNCHRONISATION

The laser system

One passive mode locked Ti:Sa based oscillator is foreseen, delivering 1 W at 76 MHz repetition rate (around 13 nJ /pulse). This will feed three independent high power, multiple repetition rate, laser systems.

The first system, devoted to the photo-injector should provide ~ 50 -100 μ J pulse energy in the UV (266 nm), producing a 1 nC electron beam following interaction with a photocathode with 1 % quantum efficiency. Special attention will be paid to the laser beam transverse features

(dimensions and shape) for preventing the electron beam emittance increase [15]. A laser amplifier delivering at least 1 mJ in the IR (800 nm), followed by a regenerative amplifier and single pass preamplifier, both pumped by a 15 W Q-switched solid state laser can be adopted. Very highly efficient third harmonic generation will be performed with an ultra short pulse (~ 50 fs) on a sufficiently thin nonlinear crystal (BBO), in order to reduce pulse distortion. A prism or gratings based UV stretcher will bring the duration up to 20 ps.. Transverse and longitudinal measurement as well as shaping of the laser pulse call for a complete setup including a DAZZLER system [16] in the IR, spectral interferometric techniques (either self-referencing, like SPIDER [17] or not), a beam transverse filter and deformable mirror with high dynamics. Such approaches are under study on the CEA-SLIC servers LUCA (20 Hz) and PLFA (1 kHz) [18]. Recent promising developments by FASTLITE [19] of a Dazzler operating in the UV domain Dazzler, should allow a direct shaping of the laser beam issued by THG process. Otherwise, we intend to develop brand new solutions for a dedicated UV regenerative amplifier, based on the amplification and Kerr properties of crystals like $Ce^{3+}:\text{LiCaAlF}_6$ [20].

The second one, a broadband system, includes non linear processes like Optical Parametric Amplification, Third and Fourth Harmonic Generation (THG, FHG) and HHG, for two color pump-probe based experiments. It is based on Chirped Pulse Amplification (CPA) technique, on a basis of a 10 mJ, kHz or multi-kHz system, in which a 4-pass amplifier is injected with the beam issued a first regenerative amplifier. The first two systems will operate at a multi-kHz rate, while the third will be limited to few Hz (eventually few tens of Hz).

The third laser system will deliver high energy (1 J), short duration pulses and will be mainly devoted to plasma acceleration and Thomson scattering.

The synchronisation

The synchronisation of the RF and the master clock in respect to the femtosecond time scale taking into account the natural pulse-to-pulse jitter for a Ti:Sa oscillator of a few tens of fs lead to adopt a frequency-stabilized laser oscillator. Care will be devoted to minimize the intrinsic jitter encountered by the e- beam through its travel in the accelerator to the wiggler. The jitter between the different laser branches distributed on relatively long distance (~ 100 m) should also be reduced and environmental contributions such as slow thermal drift should be lowered. Moreover, unlike the accelerator benefiting of the vacuum technique, inherent jitter sources along the complex laser system (stretcher /compressor pair, regenerative /multipass amplifiers, thermal lensing...) is under study in CEA-SPAM. Measurement of the synchronisation between the laser pulse and the electron is a key issue, the development of the electro-optical measurement has been set-up on the ELYSE gun at LCI (Orsay). The first step of measurements leads to a resolution of 250 fs.

THE LIGHT SOURCES

The undulators

ARC-EN-CIEL phase 1 plans to use a 20 mm period in-vacuum hybrid undulator as a modulator (50 periods), and a 30 mm Apple-II undulator as a radiator (400 periods). Identical sections of modulator and radiator will be added for the second phase of ARC-EN-CIEL (4 to 8 m for the modulator, and 4 sections of 4 m for the radiator). Such undulators are currently developed for SOLEIL third generation facility.

The choice of such radiator type undulators follows estimations of magnetic performance of an Apple-II type undulator with a small period based on magnetostatic calculations performed using the Radia computer code [21]. The expected horizontal and vertical peak fields of an Apple-II at 30 mm period and 6 mm vertical gap are $B_x = B_z \approx 0.63$ T; corresponding to the effective deflection parameter $K \approx 2.5$ (see fig. 5).

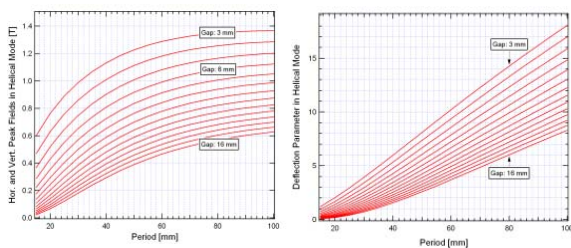


Figure 5. Peak magnetic fields (left) and deflection parameters (right) as functions of period of an Apple-II undulator in helical mode at different vertical gaps. Calculations done for NdFeB magnet blocks with remnant magnetization of 1.22 T and transverse dimensions 30 mm x 30 mm, horizontal gap between movable and fixed magnet arrays : 1 mm.

Seeding with High Harmonics generated in gas

Collaborations have been set up for demonstrating the feasibility to seed a LINAC based FEL with HHG on SCSS phase 1 in Japan [22] and on SPARC in Italy [23]. Tests of the chambers and of the optical transport have been performed this year with the Luca laser, and seeding will be performed at SCSS on fall 2006 and in summer 2007 on SPARC. This will provide an experimental demonstration of the concept for ARC-EN-CIEL. FEL radiation based on analogous systems for ARC-EN-CIEL is calculated using PERSEO 1D code [24] with a gain reduction due to the filling factor [25] and recently

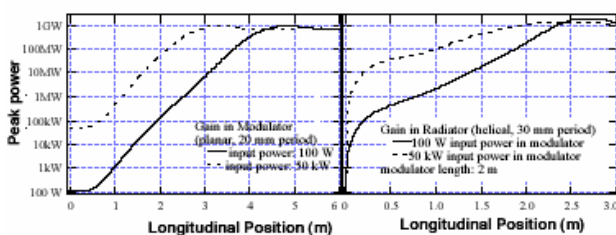


Figure 6: Steady-state GENESIS simulations for ArcEnCiel phase 1, 1 – 1 HHG scheme, 266 nm seed: a) gain in modulator, b) gain in radiator (30 mm period helical mode).

compared with GENESIS1.3 [26] integrated in a new test version of SRW [27] allowing the wavefront to be transported in the beamline to the user sample (see fig. 6).

ACKNOWLEDGMENTS

The support given by EUROFEL contract No 011935 is acknowledged, and to ANR. The authors thank L. Giannessi for fruitful discussions.

REFERENCES

- [1] J. M. Filhol et al, JACoW, EPAC'06, Edinburg, June 2006, p. 2723, <http://www.jacow.org>.
- [2] F. Briquez et al, JACoW, EPAC'06, Edinburg, June 2006, p. 3556.
- [3] M. E. Couprie et al, JACoW, FEL'05, Stanford, August 2005; M.E. Couprie et al, Proceed. SRI 06, Daegu, May 2006, M. E. Couprie et al, JACoW, EPAC'06, Glasgow, June 2006, p. 53, M.E. Couprie et al, EPAC 04, 55.
- [4] M. Billardon et al, Phys. Rev. Lett. 51, (1983) 1652.
- [5] M. E. Couprie et al., Phys. Rev. A . 44(2), (1991) 1301.
- [6] R.Prazeres et al Phys. Rev. Lett. 78(11), 2124-2127 (1997).
- [7] P. Guimbal et al, Nucl. Inst. Meth. A 341 (1994) 43.
- [8] D. Dwersteg et al , NIM. A393, 93 (1997).
- [9] R. Xiang et al, PAC 2005.
- [10] T. Shintake et al, EPAC'06, Edinburg, p 2741 ; Togawa et al, APAC2004, Gyeongju, Koera, March 2004.
- [11] M. Loung et al., JACoW, EPAC'06, Edinburg, June 2006, p. 3167, Kugeler et Neumann, EPAC06, p. 408, G. Devanz et al., EPAC'06, p. 378.
- [12] K. Flottman, "ASTRA, a space charge tracking algorithm", <http://www.desy.de/~mpyflo>
- [13] M. Dohlus, T. Limberg, "CSRtrack", <http://www.desy.de/xfel-beam/csrtrack/index.html>
- [14] M. Dohlus and T. Limberg., PAC 2005, p 1015.
- [15] C. Limborg and P. Bolton, NIMA 557 (2006), pp 106-116.
- [16] F. Verluise et al., JOSAB, n° 17 (2000), pp. 138-145).
- [17] C. Iaconis and I.A. Walmsley, IEEE Jour. Quant. Elec. 15 (4), April 1999 pp. 501-509.
- [18] D. Garzella et al., this conference.
- [19] N. Forget et al., "Direct Pulse shaping of ultraviolet pulses by an AOPDF", presented at CLEO/QELS 2006.
- [20] Liu et al., Opt. Lett, Vol.26 n°5 (2001), pp. 301-303.
- [21] P. Elleaume, O. Chubar, J. Chavanne, "Computing 3D Magnetic Field from Insertion Devices", PAC97 1997, 3509.
- [22] G. Lambert, this conference.
- [23] O. Tcherbakoff, this conference.
- [24] Luca Giannessi, PERSEO, www.perseo.enea.it
- [25] W. Colson P. Elleaume Appl. Phys. B 29, (1982)10.
- [26] GENESIS 1.3, <http://pbpl.physics.ucla.edu/~reiche/>
- [27] SRW, ESRF-SOLEIL collaboration <http://www-sources.synchrotron-soleil.fr:8002/mid.software>

THE PROPERTIES OF THE FEL OUTPUT FOR SELF SEEDING

J. Bahrtdt, BESSY, Berlin, Bart Faatz, Rolf Treusch, Deutsches Elektronen-Synchrotron (DESY), Hamburg, Velizar Miltchev, Hamburg University (Uni HH) Institut fuer Experimentalphysik, Ruben Reininger, ruben@sas-rr.com.

Abstract

Several seeding schemes, like self seeding for FLASH or seeded HGHG cascades for BESSY soft X-ray FEL, are proposed for existing or planned free electron laser facilities. The simulation of these schemes requires the detailed knowledge of the properties of the seeding radiation and the implementation of these properties in the codes. Time dependent simulations with the 3D code GENESIS calculate the electric field distribution in and at the end of the undulator. The physical optics code PHASE permits the propagation of wave fronts across grazing incidence optics. Using the combination GENESIS PHASE GENESIS, the properties of the FEL output for different seeding schemes can be obtained. For example, the radiation quality of a SASE FEL can be improved in a self seeding scheme. Here, the radiation is monochromatized after a first undulator section and seeded to the second undulator modules. We present simulation studies for the self seeding option of FLASH.

INTRODUCTION

Synchrotron radiation beamlines at 3rd generation storage rings are generally optimized with ray tracing codes which are based on geometrical optics. This is justified as long as the radiation is incoherent. Coherent radiation has to be propagated with physical optic codes which describe the coherent properties of the light. FELs, the 4th generation light sources, are built to produce transversally and longitudinally coherent radiation in the wavelength regime down to 1Å.

X-ray FEL facilities based on the SASE principle are under construction at various places [1-3]. Since the SASE is a random process the longitudinal distribution of the light pulse as well as the spectrum is spiky.

Using a coherent seed pulse the FEL output can hence significantly be improved. The cascaded HGHG FEL scheme uses the coherent properties of the seed laser and transforms these properties through several stages to the required wavelength regime where no seeding laser is available [4,5]. The radiation properties degrade with the number of stages involved. Therefore, it is advantageous to start with a rather short seeding wavelength which can be produced by high harmonic generation (HHG) [6] in order to reduce the number of stages.

Self seeding is another approach to improve the spectral properties of the FEL [7]. The SASE radiation is passed through a monochromator which filters out the central frequency. This radiation is used as a seed for the following undulators.

It has also been shown that the output power of a cascaded HGHG FEL can be enhanced if the radiation of the first stage is monochromatized before transportation to the next one [8].

These examples demonstrate that there is no strict separation between FEL undulators and monochromators. They have to be described in a closed form, instead. In this paper we demonstrate for the example of the self seeding option of FLASH the necessity for a three dimensional and time dependent description of the propagating coherent radiation within the undulators and the monochromators.

THE PHYSICAL OPTICS CODE PHASE

The propagation of wavefronts in free space is usually done using Fourier optics techniques [9]. Depending on the geometry one of three propagators can be applied:

- i) In the near field approximation the electric field distribution is expanded in plane waves, the plane waves are propagated by multiplication with a complex factor and the result is back transformed to real space.
- ii) In the far field approximation the image distribution is composed of the contributions from individual point sources.
- iii) In the very far field the field distribution equals the angle distribution in the source plane (apart from a constant factor).

Optical elements can be introduced into this formalism in the following way: The electric field is propagated to the center of the optical element with Fourier optics. Then, the wavefront is propagated over the optical element using a ray tracing technique which takes into account the phase differences. Then, the wavefront is further propagated with Fourier optics methods (ZEMAX, GLAD [10,11]).

The code PHASE, written at BESSY, is based on another technique, the stationary phase approximation [12] which will be briefly explained.

The following equation correlates the electric fields in the source and the image plane.

$$\vec{E}(\vec{a}) = \int h(\vec{a}', \vec{a}) \cdot \vec{E}(\vec{a}') \cdot d\vec{a}'$$

The integration is done over the source plane and the propagator \vec{h} has the form:

$$h(\vec{a}', \vec{a}) = \frac{1}{\lambda^2} \int_{Surface} \frac{\exp(ik(r+r'))}{rr'} \cdot b(w, l) \cdot \cos(\alpha) \cdot dw \cdot dl$$

r, r' are the distances between the source / image plane and the optical element, b is the obliquity factor

and the integration extends over the optical element surface. Each point in the image plane requires the evaluation of a four dimensional integral. Each additional optical element adds another two dimensions in the integral and it is obvious that the expressions can not be evaluated within reasonable time without certain assumptions. The stationary phase approximation uses the fact that the optical path length changes quadratically with the optical element coordinates in a region close to the principle rays (extremum of the optical path). The integration over the optical element coordinates can be done analytically if the beam is not scraped at that element and hence, the dimensions of the integral can be reduced from six to four.

All expressions (coordinates, path length, scaling factors etc.) are expanded up to fourth order in the coordinates and angles of the initial plane. Using these expansions the transformation of cross products of coordinates and angles can be derived as well. Using these cross terms the transformation over one element can be expressed via a 70x70 matrix. The combination of several optical elements is done simply by the multiplication of the individual matrices.

In principle the complete beamline can be described with one single matrix for each term as long as the photon beam does not hit an aperture. In case of a monochromator at least two runs are required: i) propagation from the initial plane to the exit slit and ii) propagation from the exit slit to the image plane.

Monochromatic light is assumed during the propagation. For time dependent simulations, the input data have to be Fourier transformed and the individual frequencies have to be propagated one after the other. The results are again Fourier transformed yielding the time dependent fields at the exit of the monochromator.

All equations have been derived with the algebraic code REDUCE [13] and the basic code has been produced automatically. For more details on the algorithm we refer to [12].

THE SELF SEEDING OPTION OF FLASH

The basic setup of the self seeding option is illustrated in Figure 1. It consists of two undulator stages separated by a magnetic chicane and a monochromator. The first undulator operates as a SASE FEL in the linear regime. After it the electrons are separated from the SASE radiation. The electron beam passes through the magnetic bypass that is used to remove the longitudinal charge density modulation (micro bunching). The radiation pulse is spectrally filtered in a high resolution grating monochromator and afterwards is superimposed with the electron beam at the entrance of the second undulator. Thus the monochromatic photon beam serves as a coherent radiation seed, which is amplified up to saturation in the second undulator. The self seeding technique increases the spectral brilliance significantly i.e. the output power of the seeded FEL is concentrated in a single line which is orders of magnitude narrower

than the spectrum of the conventional SASE FEL. The concept of the self seeding has the advantage that it is independent of any external radiation source and the seed is naturally synchronized with the electron bunch.

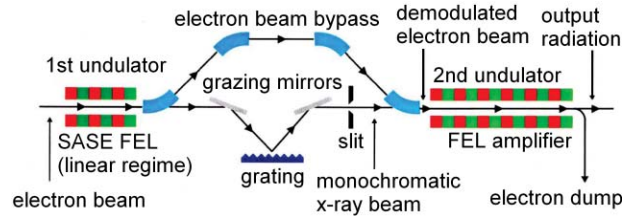


Figure 1: Schematic layout of the self seeding setup.

THE MONCHROMATOR

The seeding requirements for energy resolution, unity magnification, and only vertical deflections have been addressed [14] with a beamline (Figure 2) based on a spherical varied-line spacing grating (SVLSG).

The monochromator includes a plane mirror and three SVLSG (in the same spherical substrate) covering the energy range 6-64 nm. The plane mirror illuminates the grating at the correct angle of incidence such that the monochromator magnification is close to unity. In addition, each grating is designed to perfectly focus the beam along the dispersion (vertical) direction at the exit slit at two energies in its range, and to zero the coma aberration at one energy.

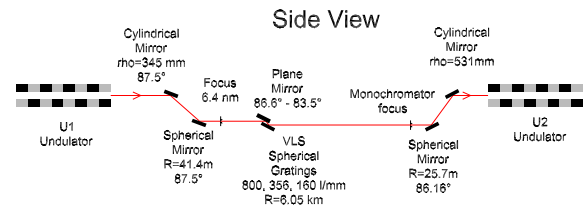


Figure 2: Seeding monochromator.

The pre and post focusing optics include four optical elements. The first and last optical components are two sagittally focusing cylinders that provide the unity magnification along the horizontal direction. The demagnification along the dispersion direction onto the entrance slit is performed with a spherical mirror. A spherical mirror after the exit slit magnifies the entrance slit width such that the size and divergence at the entrance of the second undulator overlaps with the electron beam for maximum amplification.

SIMULATIONS

Time dependent simulations for the first undulator at a carrier frequency of 60nm have been performed using GENESIS [15]. The standard FLASH undulator geometry has been assumed, where the electron beam is kicked in order to avoid saturation within the 15m undulator length which is required for shorter

wavelengths [16]. The total length over which the SASE interaction takes place is about 6.5 m, which is enough to reach a power level of about 0.2 GW. This value is well below saturation, but high enough to guarantee that after monochromatization the power is several orders of magnitude above shot noise. Electric fields for 560 slices (121x121 grid points) separated by 540nm provide the full information of the radiation pulse. The frequency resolution after Fourier transformation is determined by the length of the total pulse to be transformed. For a reasonable resolution the pulse length has been enlarged to 4096 slices by adding slices with no intensity.

After Fourier transformation the frequency slice for the central frequency (60nm) has been propagated upstream to find the beam waist. For this specific case the waist is located 1000mm upstream of the undulator exit.

The PHASE propagation has been limited to 40 frequencies. The other frequencies are diffracted by the grating to large angles such that they are blocked by the exit slit. The wavefronts corresponding to the 40 frequencies have been propagated to a plane close to the first element which is the initial plane for the subsequent PHASE propagation. The PHASE simulations have been done in two steps. First, the electric fields in the exit slit plane have been evaluated on a grid with 51x51 data points. The sizes of the slit aperture was chosen to be 2mm horizontally and 40 μ m, 200 μ m and 400 μ m vertically. These data have then been used in a second PHASE run from the exit plane to the center of the second undulator (2500mm downstream of the undulator entrance).

These 40 frequency slices plus the other 4096-40 frequency slices (the latter ones with no intensity) have been Fourier transformed to time space to be used in further GENESIS simulations through the second undulator. For this a modified version of GENESIS is used in order to include the full 6x6 matrix to describe the electron bypass that debunches the electron beam. The electric fields behind the monochromator have been scaled such that the intensity at the central frequency has dropped to 11 percent corresponding to the theoretical beamline transmission.

Figure 3 shows the temporal and spectral power of the initial pulse and the pulses behind the monochromator. Though the line width behind the monochromator shrinks with the slit width, the pulse duration does not increase.

The reason is the correlation between the wavelength and the spot location in the dispersion plane of the grating which is imaged to the center of the second undulator. The bandwidth at a certain grid point does not scale with the slit width because only a small frequency interval contributes to the intensity at that point.

For the simulation of the second undulator, the particle distribution of the first undulator is taken, which is debunched, using the full 6x6 matrix which has been simulated with ELEGANT. The field used as a seed is the one as calculated by PHASE. The total interaction

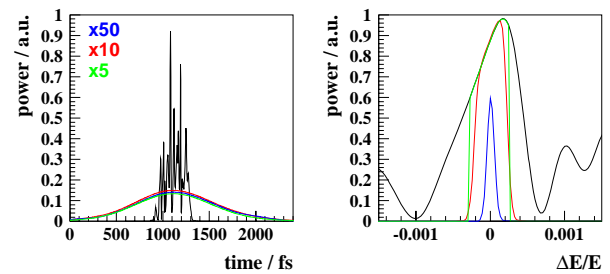


Figure 3: Relative power versus time (left) and frequency (right) for the initial pulse at the exit of the first undulator (black) and behind the monochromator for exit slits of 40 μ m (blue), 200 μ m (red) and 400 μ m (green). The monochromator transmission is not yet included.

length simulated is about 4.3 m, after which maximum peak brilliance has been reached.

RESULTS

The simulations for the three different slits show similar results. The main difference is that the seed power is different at the entrance of the second undulator. However, in all cases it is well above shotnoise and only influences the position at which saturation is achieved. In Figures 4 and 5, the results for a 400 μ m slit are shown.

Wider monochromator slits increase the total power which is, however, not completely passed to the electron beam because the transverse beam size acts as further slit. The spectral power increases by a factor of 2.5 going from 40 to 200 μ m slit width and does not increase further at 400 μ m.

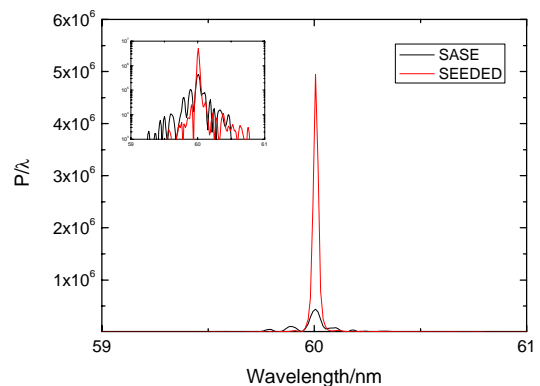


Figure 4: Comparison of the power spectrum for SASE (black curve) and a seeded pulse (red curve) for a slit of 400 μ m. The small graph in the top left corner shows the same spectrum on a logarithmic scale. Note that the central frequency of 60 nm for the seeded pulse is about an order of magnitude higher compared to SASE, whereas the other peaks are about a factor of 5 lower.

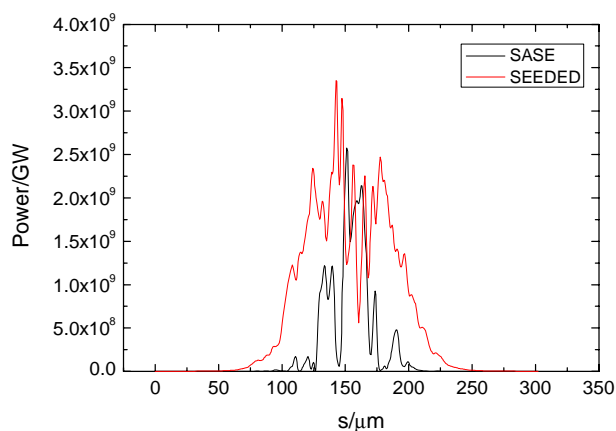


Figure 5: Power along the bunch for a SASE pulse (black curve) and the seeded pulse (red curve). Note that the seeded pulse is much smoother. The remaining spikes are at least partially due to the fact that the bunching is not fully suppressed in the simulation due to the limited number of particles used.

CONCLUSION

We presented for the first time combined time dependent FEL simulations and physical optics wavefront propagations using the codes GENESIS and PHASE. The wavefronts generated in a time dependent simulation of GENESIS have been propagated with the physical optics code PHASE and the result has been used as a seed for a further GENESIS run. It has been demonstrated that the self seeding scheme significantly improves the spectral performance of FLASH. The line width becomes narrower, the power increases and the temporal structure is smoother.

ACKNOWLEDGEMENT

We thank A. Meseck for adapting the code GENESIS and for many fruitful discussions.

REFERENCES

- [1] TESLA-Technical Design Report, TESLA X-FEL, Technical Design Report, 2002-9, 2002.
- [2] Linac Coherent Light Source (LCLS), Conceptual Design Report, SLAC-R-593, 2002.
- [3] T. Shintake, Nucl. Instr. and Meth., A507 (2003) 382-397.
- [4] L. H. Yu, NIM A, 483 (2002) pp493-498.
- [5] X. J. Wang et al., DUV, Proceedings of the 26th International FEL Conference, Trieste, Italy, 2004, pp 209-211.
C. Bochetta et al., FERMI, Proceedings of the 27th International FEL Conference, Stanford, CA, 2005, pp 632-685.
The BESSY Soft X-ray Free Electron Laser, Technical Design Report March 2004, eds.: D. Krämer, E. Jaeschke, W. Eberhardt, ISBN 3-9809534-08, BESSY, Berlin (2004).
- [6] M.-E. Cuprie et al., ARC-EN-CIEL, Proceedings of the 27th International FEL Conference, Stanford, CA, 2005, pp.55-58.
A. Andersson et al., MAX IV, Proceedings of the 26th International FEL Conference, Trieste, Italy, 2004, pp 190-192.
D. Wang et al., MIT, Proceedings of 2005 PAC, Knoxville, Tennessee, pp1961-1963.
J. Wu, Z. Huang, LCLS, Proceedings of the 27th International FEL Conference, Stanford, CA, 2005.
Gullens et al., LBNL, Proceedings of the EPAC 2006, Edinburgh, Scotland, pp 142-144.
J. Qi-ka et al., SDUV, Proceedings of the 26th International FEL Conference, Trieste, Italy, 2004, pp 494-497.
- [6] O. Tscherbakoff et al., Proceedings of the EPAC 2006, SPARC, Edinburgh, Scotland, pp 47-49.
G. Lambert et al., SCSS, Proceedings of the EPAC 2006, Edinburgh, Scotland, pp 44-46.
J. A. Clarke, 4GLS, Proceedings of the EPAC 2006, Edinburgh, Scotland, pp 181-183.
- [7] J. Feldhaus et.al., Opt. Commun., 140 (1997), 341.
- [8] K. Goldammer et al, Proceedings of the 27th International FEL Conference, Stanford, CA, 2005, pp.23-26.
M. Abo-Bakr et al., Proceedings of the 27th International FEL Conference, Stanford, CA, 2005, pp.19-22.
- [9] J. W. Goodman, "Introduction to Fourier Optics", McGraw-Hill Physical and Quantum Electronics Series, New York, 1968.
- [10] GLAD, Theory Manual, Applied Optics Research, 1087 Lewis River Road, 217 Woodland, WA, 2004.
- [11] ZEMAX, Optical Design Program, User's Manual, ZEMAX Development Corporation, November 2005.
- [12] J. Bahrtdt, Applied Optics, 34 (1995) 114-127.
J. Bahrtdt, Applied Optics, 36 (1997) 4367-4381.
J. Bahrtdt, Proceedings of the 27th International FEL Conference, Stanford, CA, 2005, pp694-701.
- [13] A. C. Hearn, "REDUCE 3.5, A General Purpose Algebra System" [RAND, Santa Monica, Calif. 90407-2138 (reduce@rand.org), 1993].
- [14] R. Reininger, J. Feldhaus, P. Gürtler, and J. Bahrtdt, Nucl. Instr. Methods A, **467**, 38-41, 2001
- [15] S. Reiche, GENESIS 1.3, Nucl. Instr. Meth. A 429 (1999) 243.
- [16] V. Miltchev, "Simulation studies on the self seeding option at FLASH", presented at this conference.

DEVELOPMENT AND APPLICATION OF FIGURES OF MERIT TO EVALUATE THE OUTPUT OF HGHG FEL CASCADES*

B. Kuske[†], R. Follath, A. Meseck, BESSY, Berlin, Germany

Abstract

In the design of Free Electron Lasers (FEL), parameters like the peak power and the spectral power were established as figures of merit to evaluate the FEL's output quality. However, spectra obtained with studies using bunches from start-to-end simulations including errors show that it is not sufficient to optimise these simple parameters. To establish a stable and reliable user facility, parameters like pulse reproducibility, stability of the source point or signal to background ratio have to be considered and optimised. This paper suggests different criteria and parameters to describe and compare the output of different FEL schemes with respect to a regular user operation. As these criteria are not readily available from common FEL codes a post processing IDL code has been written, that extracts the relevant information from a standard GENESIS output. The code is used to reevaluate start-to-end simulations for the BESSY low energy FEL [1].

INTRODUCTION

A growing number of proposals for FEL projects plan to use High Gain Harmonic Generation (HGHG) structures in order to exploit the advantages that arise from seeding the FEL process, at wavelengths much shorter than what is available today with conventional seed lasers [2]. As the efficiency in the generation of higher harmonics declines rapidly with the harmonic number, a multi step harmonic generation in cascaded structures can be used to extend the wavelength range of this concept down to a few nanometers. Cascaded structures require an overall bunch length of the electron beam in the order of some hundred femtoseconds, because for each stage an unspoiled part of the bunch must be used (fresh-bunch technique). These long bunches usually exhibit parameter profiles at the end of the linac that are far from being constant. For example, an energy chirp is needed for bunch compression, the current is not constant and the emittance and energy spread vary for different slices. As a result, the temporal and spectral power functions are not as smooth as known from theoretical studies. Fig. 1 shows the power spectra of three different simulations including errors of the BESSY low energy FEL. The spectra are not Gaussian anymore, and they vary considerably for each set of errors. Although the peak power varies by less than 20% the pulse energy differs significantly.

The result of start-to-end simulations including phase and amplitude errors in the gun and in the linac and charge

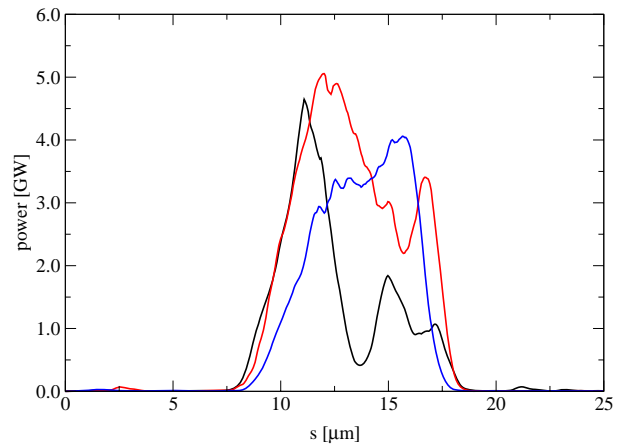


Figure 1: Power emitted by the final amplifier of the BESSY low energy FEL-line for three different sets of errors in the gun and the linac. The pulses are not Gaussian.

and timing errors of the photo cathode laser, for the two stage low energy FEL line have been published in [3]. Those 24 cases are reevaluated in the current paper incorporating aspects that are relevant for the users of the FEL radiation.

The BESSY soft X-ray FEL is designed as a user facility and hence the quality of the radiation will be judged at the position of the experiment. For the passage through the beam line, three radiation parameters are of major importance, namely the transverse and longitudinal position of the source point and its size. Vertical offsets give rise to energy fluctuations behind the monochromator. Horizontal offsets lead to intensity fluctuations behind horizontal slits. Both offsets should not exceed 20% of the radiation size. Variations in the size or the location of the source point degrade the energy resolution. Location fluctuations should not exceed one Rayleigh length. The signal to background ratio and the pulse energy within a selected bandwidth are further figures of great interest to the experimenters and beam line designers. Most of these criteria are indirectly supplied by FEL codes like GENESIS [5], but not easily accessible, especially when a larger number of runs are considered, as in tolerance studies. Therefore, a small evaluation program has been written using IDL [6] in combination with the original GENESIS output interpretation routines. The given figures of merit as well as the limits set for stability, result from discussions with the BESSY

* Funded by the Bundesministerium für Bildung und Forschung (BMBF), the State of Berlin and the Zukunftsfond Berlin

[†] Bettina.Kuske@bessy.de

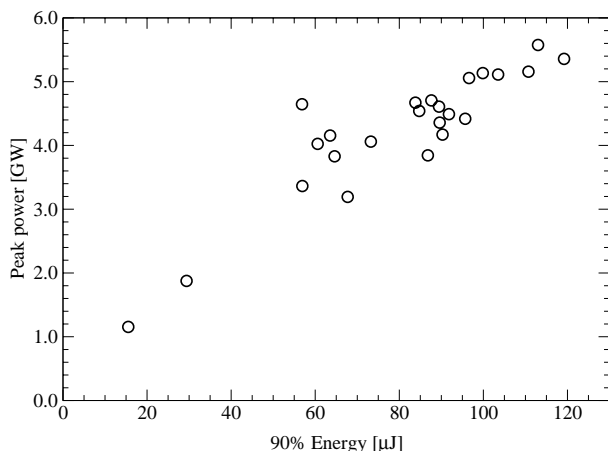


Figure 2: Peak power versus 90% energy for 24 pulses in the BESSY low energy FEL final amplifier. The spread in pulse energy can be considerable for similar peak power.

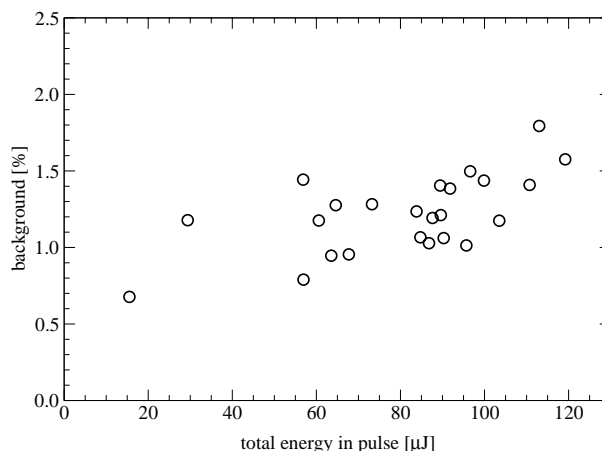


Figure 3: The background signal of the lasing part of the bunch in percent of the total pulse energy.

experimental group.

PULSE ENERGY AND BACKGROUND

In order to describe the FEL pulse, the FWHM of the pulse is determined as well as the width of the pulse at 10% of the peak power, called the 10%-width. For a Gaussian pulse, the ratio of the two is ≈ 1.8 . 75% of the 24 investigated cases have a ratio around 1.2, indicating a pulse shape with steep flanks, only one case showed a wide profile with a ratio bigger than three.

The integral of the power inside the 10%-width is called the 90% pulse energy. Fig. 2 shows the peak power versus the 90% energy for the 24 runs. Especially around peak powers of 4 GW, where most pulses lie, the spread in pulse energy, which is the figure of interest for the experiment is considerable, due to the different pulse shapes. Therefore the peak power is not well suited as a figure of merit.

Any power outside the 10%-width is considered to be background. The signal to background ratio is important for the quality of the experiments. The background is computed in percent of the total pulse energy, see Fig. 3. It is below 2% in all cases.

It must be mentioned, that in order to reduce the computation time only short parts of the complete 700 fs bunch are simulated in the studies. The calculation of the background at this point includes power emitted outside the 10%-width of the 100 fs long bunch part tracked through the final amplifier. Contributions of the two parts seeded in upstream stages will approximately double the shown background, while the contribution of unseeded parts is negligible.

SOURCE POINT CHARACTERISATION

In seeded devices, the determination of the radiation size is not straightforward. At the beginning, the radiation is

dominated by the seed. While the seeding radiation diverges, bunching builds up in the seeded part of the electron bunch and power is emitted, increasing exponentially. The radiation size calculated by FEL codes thus usually increases in the initial part of seeded FEL amplifiers due to the diverging seed and only later decreases due to the build up of coherent FEL radiation.

FEL codes usually calculate the radiation size for each slice of the bunch. For seeded devices though, averaging over all bunch slices will yield wrong results, as the radiation size at the location of the seed's interaction is much smaller than in the rest of the bunch, where the little power emitted is independent of the seeded process.

The radiation size and divergence of each slice provided by GENESIS has to be weighted with the power emitted by the slice. The result follows the behaviour described earlier. The radiation size has a maximum inside the final amplifier, where the divergence slightly decreases. In order to calculate the phase space volume, the radiation size and divergence at the end of the final amplifier are used. Note that from [7] it is known, that the beam waist, when calculated exactly by back tracking the radiation, lies a couple of meters upstream and is smaller than at the end of the device. Thus, the data plotted in Fig. 4 is an upper limit, and the phase space volume is expected to be up to 50% smaller. Still most points lie close to the line indicating twice the diffraction limit. As the waist location will jitter from shot to shot, this conservative estimate seems adequate.

SOURCE POINT STABILITY

Transverse Stability

As mentioned earlier, transverse jitter of the source point reduces the energy resolution of the beam line. It is desired to reduce the transverse fluctuations to less than 20% of the rms radiation size.

Rather than first locating the source point, and then com-

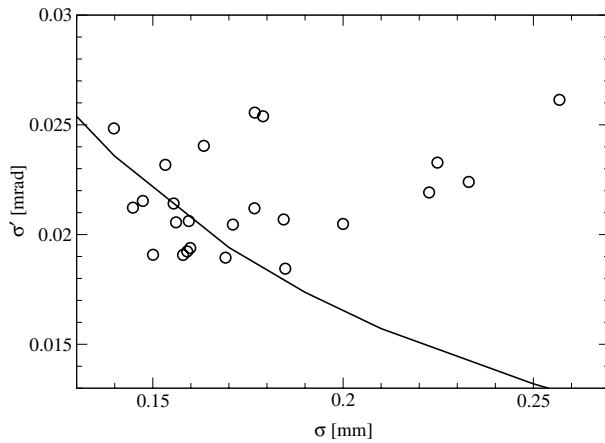


Figure 4: The size and divergence of the radiation field at the end of the final amplifier. The black line indicates twice the diffraction limit. The beam waist will in reality lie a few meters upstream the end of the undulator and will be up to 50% smaller, on the other hand jitter of the waist location has to be taken into account.

paring the beam offsets at this point to the radiation size, the ratio between the transverse offsets and the radiation size is computed at each point in final amplifier. The maximum of each of the resulting curves for the 24 runs is depicted in Fig. 5. These results only show shot-to-shot fluctuations, that are due to phase and amplitude errors in the gun and in the linac. The amplitudes at the beginning of the cascades amounted to $< 1\mu\text{m}$ rms in the horizontal and $< 0.5\mu\text{m}$ rms in the vertical plan.

The major source for beam steering, though, are quadrupole jitters, e.g. due to ground vibrations. All time independent beam offsets will be corrected by the steering magnets. Start-to-end calculations assuming a Gaussian rms quadrupole jitter of 300 nm, resulted in rms beam offsets at the beginning of the HGHG cascades as listed in Tab. 1.

Table 1: Transverse jitter (rms) at the end of the linac, due to random quadrupole vibrations with 300 nm offsets (rms).

	offset [μm]	angle [μrad]
horizontal	27.5	1.55
vertical	10.0	1.57

For an estimate of their effect, bunches were started on the phase space ellipse described in Tab. 1 and tracked through the final amplifier. The largest transverse offsets in the undulator were reached for large initial horizontal amplitudes, the maximum reached was $28\mu\text{m}$. The minimal radiation size of all investigated cases is $140\mu\text{m}$, Fig. 4, therefore the 20% criterion is fulfilled throughout the final amplifier for all runs. Alternative optics, taking the

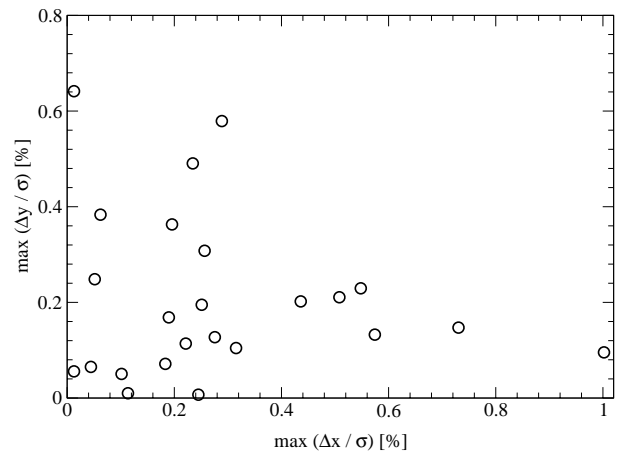


Figure 5: The maximum of the vertical and horizontal transverse offsets in the final amplifier in percent of the radiation size, when errors in the gun and the linac are included in the start-to-end calculations. To include effects of quadrupole offsets, the data can be linearly scaled.

larger horizontal trajectory jitter into account, could even improve on the results.

Longitudinal Stability

The longitudinal location of the source point is difficult to determine. It does not coincide with the saturation point. Furthermore, in start-to-end calculations including errors, each bunch is populated differently and is seeded at varying locations due to timing jitter, so that the source point moves from shot to shot.

In [7], an exact, but time consuming procedure is introduced to locate the position and size of the radiation waist. It is pointed out that the waist lies over 5m upstream of the end of the undulator for the investigated cases. Furthermore, the horizontal and vertical waist position do not necessarily coincide.

A shot-to-shot jitter in the location of the source point or a variation in its size, leads to a degradation of the energy resolution. The criterion for longitudinal stability has been set to fluctuations in the beam radius of less than a factor of $\sqrt{2}$, which for Gaussian beams corresponds to variations of the source point location of less than one Rayleigh length.

It can be extracted from [7] that the distance, in which the beam radius increases by $\sqrt{2}$ is $> 5\text{m}$ and thus much larger than the theoretical Rayleigh length. With a total length of the final amplifier of 7.5 m, the longitudinal stability criteria is fulfilled as long as the beam waist location lies well inside the final amplifier.

SPECTRUM

Due to the energy chirp on the electron bunch and the jitter between the arrival time of the bunch and the seeding laser, the average energy of the electrons interacting with

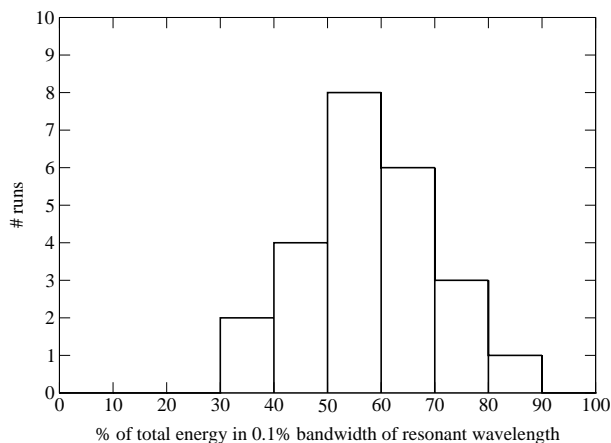


Figure 6: Histogram over the percent of total pulse energy in 0.1% bandwidth around the central frequency of each pulse. High temporal resolution experiments usually work without monochromator.

the seeding radiation varies, which results in a fluctuation of the central wavelength of the HGHG spectrum.

In order to evaluate spectral properties, the routines supplied by the post processing IDL-code XGENESIS are used on the Fairfield power on axis. The fraction of the energy in 0.1% bandwidth is calculated and compared to the total energy in the spectrum. The bandwidth can be either taken around a given frequency for all runs, or for the central frequency of the individual spectra.

Different experiments are interested in different spectral qualities. Experiments depending on high temporal resolution will usually work without monochromator and depend on the energy in a certain bandwidth around the resonant wavelength of each pulse. This case is depicted in Fig. 6, where 75% of the runs hold more than half and up to 90% of their power in 0.1% of the bandwidth of their resonant frequency, amounting to 50 μJ on average.

High energy resolution experiments need a large fraction of the total pulse energy close to the central frequency of the monochromator, Fig. 7. 70% of the runs would still deliver above 40% of their total pulse energy within the given bandwidth. These experiments usually average over many shots.

CONCLUSION

FEL codes deliver information about the development of the radiation inside the amplifying devices during the interaction between the electrons and the electro magnetic field. The quality of the produced radiation is judged much further down the beam line at the experimental station. Figures of merit have been proposed to evaluate the FEL output in view of the beam line and experimental demands. All quantities can be deduced from the output provided by, e.g. GENESIS. A post processing code for GENESIS has been

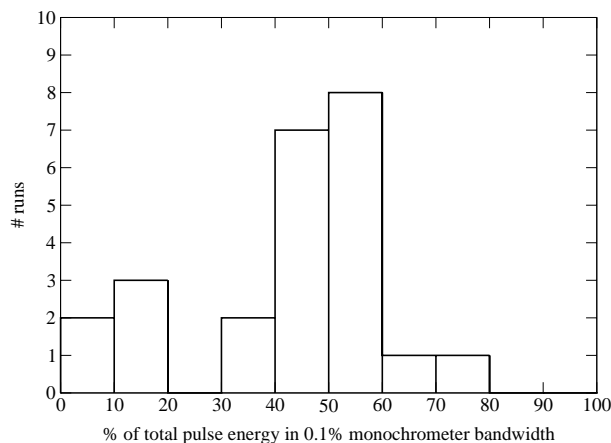


Figure 7: Histogram over the percent of total pulse energy in 0.1% bandwidth of a given (monochromator) frequency. The figure is important for high energy resolution experiments.

introduced. It has been used to evaluate the results of 24 complete start-to-end runs including errors in the gun and the linac of the BESSY low energy FEL line. The given criteria for the radiation quality could be met. Despite the immense computing effort it would be desirable to improve on the statistics.

ACKNOWLEDGEMENT

I would like to thank my colleges Johannes Bahrtdt and Michael Scheer of the BESSY experimental groups for the helpful discussions.

REFERENCES

- [1] "The BESSY Soft X-ray Free Electron Laser, Technical Design Report", March 2004, eds.: D. Krmer, E. Jaeschke, W. Eberhardt, ISBN 3-9809534-0-8, BESSY, BERLIN (2004)
- [2] "VUV/Soft X-ray FELs on the Horizon", Rene Bakker, http://leg.web.psi.ch/public/publications/TOAB001_Talk.pdf
- [3] "Start-To-End Simulations for the BESSY Low and Medium Energy FEL Line Including Errors", B. Kuske, M. Abo-Bakr, K. Goldammer, A. Meseck, BESSY, Berlin, Germany, FEL2005, proc.
- [4] "Impact of Realistic Bunch Profiles and Timing Jitter on the Output of the BESSY Low Energy FEL Line", B. Kuske, M. Abo-Bakr, A. Meseck, BESSY, Berlin, Germany, FEL2005, proc.
- [5] "GENESIS 1.3: A Full 3D Time Dependent FEL Simulation Code", S. Reiche, Nuclear Instruments and Methods A429 (1999) p. 243
- [6] Interactive Data Language, <http://www.itvis.com/idl/>
- [7] "Source Characterisation of the BESSY Soft X-Ray FEL" A. Meseck, M. Abo-Bakr, J. Bahrtdt, B. Kuske, BESSY, Berlin, Germany, FEL2005, proc.

STUDY OF A DEFLECTING DISPERSIVE CHICANE FOR THE BESSY SOFT X-RAY FEL*

A. Meseck[†], G. Wüstefeld[‡]

BESSY GmbH, Albert-Einstein-Str.15, Berlin, Germany.

Abstract

High power, short pulse length and full coherence are the main parameters of the second generation free electron lasers like the BESSY Soft X-ray FEL. To provide radiation with these properties, BESSY proposed a seeded FEL facility based on high-gain harmonic-generation (HGHG) scheme [1]. This scheme uses cascaded stages each consisting of undulator/dispersive chicane/undulator section to up-convert the seeding frequency.

The transverse separation of the seeding radiation and electron beam after the first undulator is desirable, as not only the output of the following undulators improves but also the seeding radiation itself can be used for diagnostics.

Based on an exact linear model, a dispersive chicane is designed for the BESSY FEL, which deflects the electron beam providing the separation without coupling and spoiling effects [2]. The linear model and the deflecting chicane will be presented and the properties of the chicane will be discussed by means of simulation results.

INTRODUCTION

The BESSY Soft X-Ray FEL is designed as a multi-user facility consisting of three independent FEL lines. Each line is seeded by a tunable laser covering the spectral range of 230 nm to 460 nm. The target wavelength ranges from 51 nm to 1.24 nm with peak powers up to a few GWs and pulse lengths less than 20 fs (rms). The polarization of the fully coherent radiation will be variable.

Cascades of two to four HGHG stages are planned to reduce the existing laser wavelength to the target range of the BESSY-FEL. In the first undulator of such an HGHG stage, the modulator, an energy modulation is imprinted on the electron beam by the seeding radiation. The following dispersive chicane converts this energy modulation to a spatial modulation which is optimized for a particular harmonic. The second undulator, the radiator, is resonant to this harmonic and generates radiation at the higher harmonic, which serves as seed for the next stage. The last HGHG-stage is followed by the so-called final amplifier. It is seeded at the desired wavelength and the amplification process is brought to saturation.

The quality of the FEL output radiation depends strongly on the quality of the frequency up-conversion procedure, which again depends on the quality of the spatial modulation (bunching) and on the quality of the seeding radiation.

Although in an HGHG stage, the radiator is resonant to a harmonic of the seeding radiation, short interactions between the seeding radiation and the electron beam are still possible. During such an interaction the phase correlation between the seeding radiation and the electron beam is good enough to permit an energy exchange. These interactions are short as the resonance condition is not fulfilled for the seeding radiation, but due to the high intensity of the radiation, the electron beam quality degrades, and thus the radiator output quality suffers. Separating the seeding radiation and the electron beam after the energy modulation would avoid these undesired interactions. In addition, the separation offers the possibility to use the radiation - seeding radiation as well as the spontaneous undulator radiation- for diagnostics.

In principle, the separation can take place before, inside or after the dispersive chicane, but it has not to affect the spatial modulation. Also other effects like residual dispersion, coupling or increased beam size have to be avoided. Each of the dispersive chicanes planned for the BESSY FEL consist of four dipoles providing a closed bump. Generally, the dispersion strength, which is necessary to convert the energy modulation to the spatial modulation, is not high. Hence the bump amplitudes are not large enough to install mirrors or other optical elements to deflect the radiation. A separation of the radiation and electrons can only take place by an additional bending of the electron beam. A simple bending, with an additional dipole or due to a mismatch of the four bump dipoles, causes residual dispersion, coupling between transverse and longitudinal motion and spoils the bunching. Thus it deteriorates the radiator output strongly.

However, an exact linear model offers the possibility to design an optimal dispersive section, which allows the separation of the electron beam and seeding radiation without any coupling and spoiling effect. In this paper we present the dispersive section which is designed based on this model. Comparisons of simulation results of an HGHG stage using the four dipole chicane and the deflecting dispersive section respectively, demonstrate that the new dispersive section meets all demands.

THE DEFLECTING DISPERSIVE CHICANE

The dispersive chicane, which converts the energy modulation of the bunch to a spatial density modulation is optimized for a particular harmonic of the seed. This spatial modulation results when the energy modulated beam passes through a dispersive chicane, which is described by

* Work funded by the Bundesministerium für Bildung und Forschung and the Land Berlin

[†] meseck@bessy.de

[‡] wuestefeld@bessy.de

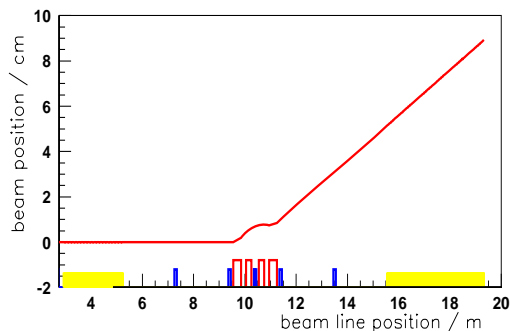


Figure 1: Horizontal trajectory of the electron beam as a function of beam line position. The red line shows the trajectory for the deflecting chicane (dipoles in red, quadrupoles in blue and undulators in yellow colours).

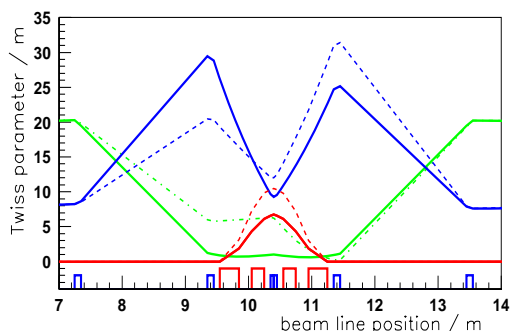


Figure 2: Horizontal (blue) and vertical (green) beta functions and dispersion (1000 times enhanced, red) of the deflecting chicane. The value of m_{56} is tuned to $6.5 \cdot 10^{-5}$ (solid line) and $26 \cdot 10^{-5}$ (dots), colours of magnets as described in fig. 1.

a properly chosen matrix element m_{56} . The energy modulated electrons must be shifted by $\lambda/4$ in the longitudinal position within the dispersion section for the optimal radiator output. For BESSY FEL seeding wavelength, this translates to a distance of 60 nm to 120 nm. Note, the factor two in the distance tuning-range is given by the spectral range of the seeding radiation.

The necessary density modulation is commonly achieved by a simple four dipole bump of zero integrated dipole field strength. By a scaled field strength change of the four dipoles, m_{56} can be varied.

Instead of the simple 2 m long bump, we propose a more elaborate optics, which deflects the beam by a fixed angle of 10 mrad, see Fig. 1 and 2. In addition, the value of m_{56} can be varied by a factor of four, twice as much as required.

This deflecting chicane consists of two dipole families and one quadrupole, tuned as an achromatic bend with variable m_{56} value. The integrated dipole fields are kept constant to define the deflection angle. One family is excited opposite to the other one, the difference between the integrated fields of both family yields the value of m_{56} . The quadrupole tunes the dispersion outside of the chicane to zero. At the entrance and exit side of the chicane an optical matching section is required, consisting of one quadrupole doublet on each side. For the full optical line $m_{56}=6.5 \cdot 10^{-5}$, the same tuning as for the simple bump. Different settings of the dipoles leads to different orbits inside the quadrupole, this steering has to be taken into account.

This optics is 10 m long and has the advantage of separating the electron and photon beams, and delivering the necessary m_{56} . In addition it avoids the coupling between different planes of the electron motion as described below. The separation can be used for easier diagnostics purposes and eliminates further unwanted interaction of the photon beam with the electrons.

The linear matrix theory can be used, to discuss the coupling of the horizontal (x, x') and longitudinal (z, z') particle oscillations [2]. Effects of the vertical plane have to be treated similarly, but are presently not discussed. A general transfer matrix m_{ij} describes the chicane plus matching sections. The longitudinal elements m_{51} and m_{52} are not independent. They are coupled to the horizontal plane, described by

$$m_{51} = m_{16}m_{21} - m_{11}m_{26}$$

and

$$m_{52} = m_{16}m_{22} - m_{12}m_{26}.$$

The coupling depends on the dispersive terms m_{16} and m_{26} . If dispersion is produced and m_{16} and m_{26} are nonzero, for example by a single dipole kick, one gets a dependency of the longitudinal position z on the horizontal plan (x, x'). Even a single dipole kick of 5 mrad generates dispersion and in turn coupling. Using the BESSY FEL parameters of a horizontal beam emittance of $0.9 \cdot 10^{-9}$ m rad one obtains a longitudinal spread of 280 nm as a result of the final beam diameter. This can not be tolerated for a proper seeding process. With the presented chicane, this coupling is cancelled, i.e. the matrix elements m_{51} and m_{52} are zero.

As the transverse beam amplitudes and the accumulated spread in chromatic phase errors stay sufficiently small, the layout of this section is done without any higher order correcting multi poles. The comparison between the simple dipole bump and this deflecting chicane shows very good agreement, as shown in the next section. For the comparison, the deflecting chicane has the same Twiss parameters β and α as the four bump chicane at the start and end points. Both sections have a m_{56} value of $6.5 \cdot 10^{-5}$. In this case the rms-beam dimensions are equal (within the numerical uncertainties due to limited number of macroparticle in the

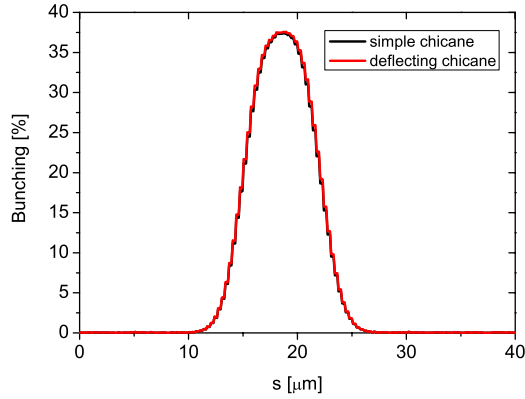


Figure 3: The bunching at the entrance of the first radiator of medium-energy FEL along the bunch for both dispersive sections. Both dispersive sections produces the optimal density modulation for the given energy modulation.

simulations) for both solutions, independent of the different phase advances obtained from the different approaches.

This chicane is similar to the optics of the NewSUB-ARU storage ring [3, 4]. It was recognized in this ring, that even a very small power supply ripple of the dipole families could limit the isochronous tuning of the optics [5]. However, this seems not to be a problem for our parameters. A deflection error of 10^{-3} in one of the dipole families leads to a two times larger error of m_{56} , which is negligible.

PERFORMANCE SIMULATION OF BOTH DISPERSIVE SECTIONS

In order to compare the performance of the new deflecting dispersive chicane with the simple four dipole chicane, the first stage of the medium-energy FEL-line of the BESSY FEL [1] was simulated for both cases. The simulations were carried out using a modified version of the simulation code GENESIS 1.3 [6] which includes a transfer matrix routine. This routine was used to model both dispersive sections at the entrance of the radiator.

The bunching at the entrance of the radiator is shown in Fig. 3 for both cases. For the given energy modulation, both dispersive sections produce the optimal spatial modulation. Fig. 4 displays the temporal power distribution at the exit of the first radiator. This radiation will be used as a seed for the next section. The difference in maximum power between both cases is negligible concerning the seeding.

The development of the horizontal and vertical electron beam size (rms) along the first radiator is shown in Fig. 5 and 6 for both dispersive sections. Because of the limited number of macroparticles that can be simulated, numerical deviations of the rms beam size of order 0.5% are expected. Therefore any deviation in beam sizes less than 0.5 % can be neglected. Obviously, there exist a small difference in

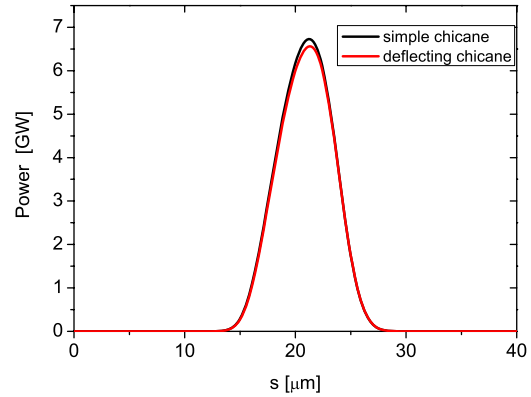


Figure 4: The radiator output power of the first stage of the medium-energy FEL for both dispersive sections. There exists a small difference between both cases, which is negligible concerning the seeding of the next section.

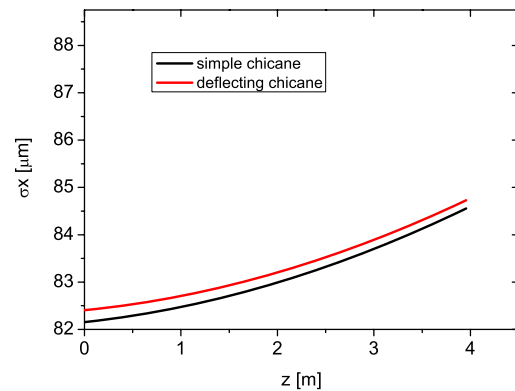


Figure 5: The development of the horizontal electron beam size (rms) along the first radiator for both dispersive sections. The difference between the beam sizes is less than 0.5 % and can be neglected.

vertical divergence for both cases of about 0.4μ rad. This difference might also indicate small tuning differences of the two chicanes.

The above simulations were done for constant average energy along the bunch. In order to exclude undesired effects due to the energy chirp of the electron beam needed for the bunch compression [7], the simulations of both dispersive sections were repeated with an energy chirped beam. The bunching and radiator output are almost the same for both dispersive sections. The spectral purity is conserved for both dispersive sections, see Fig. 7. Due to the energy chirp, there is a shift in the wavelength [7], which is independent of the choice of the dispersive section.

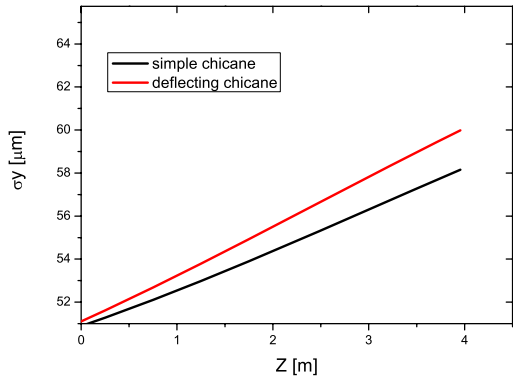


Figure 6: The development of the vertical electron beam size(rms) along the first radiator for both dispersive sections.

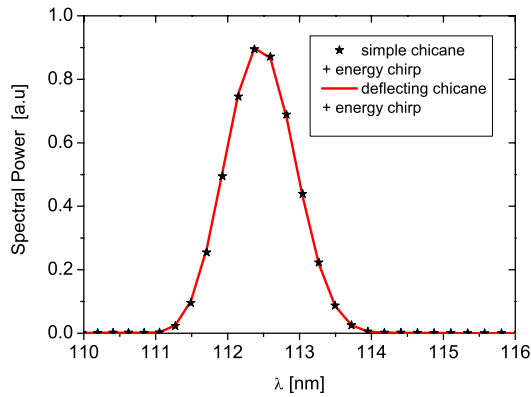


Figure 7: Spectrum of the output radiation for both dispersive sections. There is a shift in the wavelength due to the energy chirp. This is independent of the dispersive section.

CONCLUSION

Using an exact linear model an optimized dispersive section is designed for the medium-energy FEL-line, which allows the separation of the electron beam and seeding radiation without any coupling and spoiling effect. Based on the linear coupling matrix, a deflecting dispersive chicane is introduced. The comparison of the simulation results of an HGHG stage shows that the new dispersive section meets all demands.

REFERENCES

[1] The BESSY Soft X-ray Free Electron Laser, Technical Design Report March 2004, eds.: D.Krämer, E. Jaeschke, W. Eberhardt, ISBN 3-9809534-08, BESSY, Berlin (2004).
 [2] G. Wüstefeld, "Horizontal-longitudinal coupling in the FEL

beam line," BESSY (Berlin) Technical Report TB 227/05, 2005.

[3] A. Ando, S. Amano, S. Hashimoto, H. Kinoshita, S. Miyamoto, T. Mochizuki, M. Niibe, Y. Shoji, M. Terasawa, T. Watanabe and N. Kumagai, "Isochronous storage ring of the New SUBARU project," J. Synchrotron Rad. (1998). 5, 342-344.
 [4] A. Amiry, C. Pellegrini, E. Forest, D. Robin, "Study of magnetic lattice for a quasi-isochronous ring," Particle Accelerators, Vol. 44, Num. 2, p.65, 1994.
 [5] Y. Shoji, Y. Hisaoka, T. Matsubara, T. Mitsui, "Longitudinal Coherent Oscillation Induced in Quasi-isochronous Ring," proceedings EPAC 2006, Edinburgh (UK).
 [6] S. Reiche, GENESIS 1.3, Nucl. Instr. Meth. A 429 (1999) 243.
 [7] B. Kuske, M. Abo-Bakr, A. Meseck, "Impact of Realistic Bunch Profiles and Timing Jitter on the Output of the BESSY Low Energy FEL Line," proceedings FEL 2005, Stanford USA.

SIMULATION STUDIES ON THE SELF-SEEDING OPTION AT FLASH*

V. Miltchev[†], J. Rossbach, Hamburg University, 22761 Hamburg, Germany
B. Faatz, R. Treusch, DESY, 22603 Hamburg, Germany.

Abstract

In order to improve the temporal coherence of the radiation generated by the Free-electron LASer in Hamburg (FLASH), a two-stage seeding scheme [1] is presently under construction. It consists of two undulator stages separated by a magnetic chicane and a monochromator. In this contribution we investigate various configurations of the electron optics of the seeding set-up. The optimization of the lattice in the first (seeding) stage and the parameters of the magnetic chicane will be discussed. Simulation results for the performance of the second (seeded) stage of the FEL will be presented.

INTRODUCTION

The basic setup of the self-seeding option [1, 2] is illustrated in Fig. 1. It consists of two undulator stages separated by a magnetic chicane and a monochromator. The first undulator operates as a SASE FEL in the linear regime. After it, the electrons are separated from the SASE radiation. The

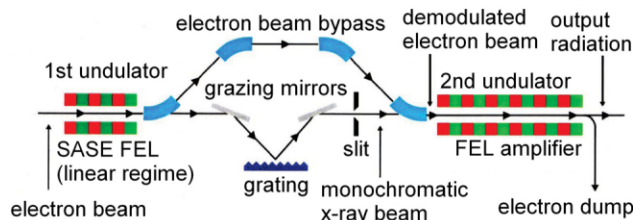


Figure 1: Schematic layout of the self-seeding setup.

electron beam passes through the magnetic bypass, that is used to remove the longitudinal charge density modulation (micro bunching). The radiation pulse is spectrally filtered in a high resolution grating monochromator [3] and afterwards is superimposed with the electron beam at the entrance of the second undulator. Thus the monochromatic photon beam serves as a coherent radiation seed, which is amplified up to saturation in the second undulator. The seeding increases the spectral brilliance by about a factor of 100, i.e. the output power of the seeded FEL is concentrated in a single line which is about a hundred times narrower than the spectrum of the conventional SASE FEL. The concept of the self-seeding has the advantage that it is independent of any external radiation source and the seed is naturally synchronized with the electron bunch. An additional advantage is that the seeding wavelength is continuously tunable. The monochromator optics, to be installed

at FLASH, is designed for operation in the 6-60 nm range [2]. It is important to note, that the gain in the first undulator section is essential for the effective operation of the self-seeded FEL. The output power level should be sufficiently low (about two-three orders of magnitude below saturation) in order to preserve the energy spread and the emittance of the electron beam. On the other hand the power of the seed, obtained from the first stage, should be much higher than the power of the shot noise in the second undulator.

ELECTRON OPTICS

Undulator stages

The undulator stages for the self-seeding option are subdivided into segments of about 4.5 m length. The first and the second undulator consist of three and six such segments respectively. A separated focusing system for the undulator stages is used at FLASH [4]. The focusing is accomplished by quadrupole doublets placed in-between two neighbouring undulator segments. The main feature of such focusing scheme, relevant to the implementation of the self-seeding, is the variable quadrupole strength. The total length of the first undulator (about 14.5 m) is optimized for operation at a wavelength in the order of 6 nm. The minimum average β -function for this case is about 4.5 m. As mentioned above, the power gain in the first undulator is crucial for the performance of the self-seeded FEL. Therefore, in order to compensate the scaling of the gain with the wavelength, one can vary the quadrupoles strength i.e. tune the average β -function accordingly.

Electron bypass

The bypass has to meet various requirements in order to ensure the proper operation of the self-seeding. The most essential of them are summarized in the following:

- Generation of an additional path length for the electrons, which is equal to the extra path length of the photons in the monochromator.
- Reduction of the micro bunching generated by the SASE process along the first undulator section. The micro bunching after the bypass is reduced by a factor of $\exp\left(-\frac{1}{2}\sigma_\delta^2 R_{56}^2 k_L^2\right)$ [5]. Here σ_δ is the fractional momentum spread, R_{56} is the momentum compaction factor of the bypass and k_L the radiation wavenumber.
- Adjustment of the electron optics to the optics of the two undulator sections for radiation wavelengths in the range 6-60 nm.

* This work has been partially supported by the EU Commission in the Sixth Framework Program, Contract No. 011935-EUROFEL

[†] velizar.miltchev@desy.de

- Correction of the first and second order dispersion, minimization of the degradation of beam quality due to coherent synchrotron radiation effects.

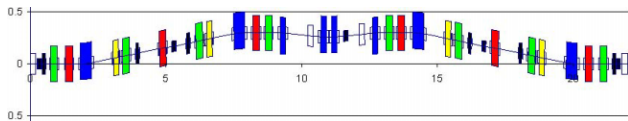


Figure 2: Final magnet layout of the electron bypass for the Seeding Option (side view). *black*: steerer, *blue*: dipole, *green*: quadrupole, vertical focusing, *red*: quadrupole, horizontal focusing, *yellow*: sextupole.

In contrast to the simplified scheme shown in Fig. 1, the final design of the electron bypass optics [2], as sketched in Fig. 2, consists of a total 37 magnets.

SIMULATION TECHNIQUES

The simulation studies presented in this paper divide into two groups: studies on the performance of the self-seeded FEL and investigations of the impact of the coherent synchrotron radiation (CSR), emitted in the electron bypass, on the output brilliance.

Performance of the self-seeded FEL

The performance of the self-seeded FEL has been simulated with the 3-D time dependent FEL-code GENESIS [6]. The simulation is split into two runs - the first undulator operating as a SASE FEL and then simulation of the electron bypass together with the second undulator. The complete particle distribution at the end of the first undulator is extracted and then is used in the next simulation step. The electron bypass is implemented in GENESIS by the means of a 6×6 transfer matrix. In the second step, the particle distribution extracted from the first part of the simulation is transformed with the help of the bypass matrix and then tracked through the second undulator section. A certain wavelength λ_{seed} and average power P_{seed} is assumed for the external seed, which should be obtained at the output of the monochromator beamline. In the presented studies the two extreme cases $\lambda_{seed} \approx 6$ nm and $\lambda_{seed} \approx 60$ nm are considered. It is helpful to remind that the seed power should fulfill the requirement $P_{seed} \gg P_{shot}$, where P_{shot} is the effective shot noise power. Since $P_{shot} \leq 100$ W, a seed of $P_{seed} \approx 10$ kW has been assumed in all cases. The code ELEGANT [7] has been used for the calculations of the electron optics, to find the electron beam matching conditions and for the calculation of the transfer matrix of the bypass. The electron beam parameters, which have been assumed in the simulations, are summarized in Table 1

Studies on CSR effects

These investigations follow a similar scheme as the one described above. However, in order to include CSR ef-

Table 1: Nominal electron beam parameters for operation at 6 nm

Energy, E_0	1000 MeV
Peak current, I_0	2500 A
rms energy spread	0.2 MeV
Normalized rms emittance, ϵ_n	2 mm mrad
rms bunch length, σ_z	50 μ m

fects in the numerical calculations, the bypass has been simulated together with the first undulator section with the ELEGANT code. The program incorporates 1-D CSR algorithm [8] for dipoles and drift spaces. The produced particle distribution file is afterwards analyzed and converted into averaged slice information, which is used by GENESIS to simulate the interaction between the electrons and the radiation field along the second undulator section. In order to quantify the influence of the emitted synchrotron radiation, the described procedure has been repeated twice. Once including the CSR effects and second time with the CSR algorithm switched off. The average spectral flux has been considered as a figure of merit to compare the radiation quality for the two cases.

SELF-SEEDING PERFORMANCE

As it is pointed out in [4], one of the main advantages of the separate focusing is that the number of quadrupoles in-between the undulator segments can be reduced, what

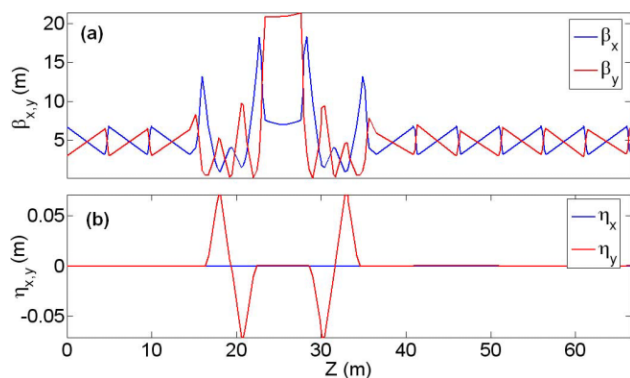


Figure 3: β -function (a) and dispersion (b) along the self-seeding electron beamline.

results however in an increase of the minimum average beta function $\langle \beta \rangle$. For the case of electron energy $E_0=1000$ MeV, corresponding to a wavelength $\lambda \approx 6$ nm, an average β -function of about 4.5 m is used. As shown in Fig.3, the design of the electron optics allows operation with the same $\langle \beta \rangle$ at the both sides of the magnetic chicane. For such setup the first stage works in the linear regime (see Fig. 4) with an average power of the output radiation of about 5 MW. Again in Fig. 4 it is shown the evolution of the micro bunching along the undulator. The kinks around $Z=10$ m and $Z=5$ m (less pronounced) are due

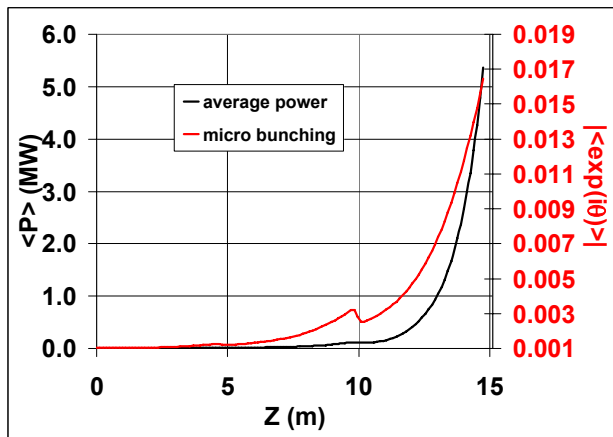


Figure 4: Average radiation power and micro bunching (right axis) along the first undulator.

to debunching taking place in the quadrupole doublet intersections [4]. Figure 5 shows the radiation power and

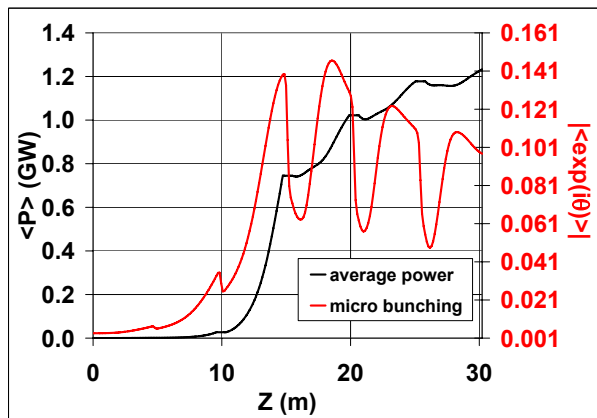


Figure 5: Radiation power and micro bunching (right axis) along the second undulator. Seeding wavelength $\lambda_{seed} \approx 6.31$ nm.

bunching as a function of the length of the second undulator. A comparison between the graphs in Fig.4 and Fig.5 demonstrates that the momentum compaction factor of the bypass $R_{56} \approx 0.73$ mm is sufficient for the reduction of the micro bunching induced in the first undulator.

For operation at electron beam energy of 325 MeV, corresponding to a resonant wavelength of about 60 nm, one has to consider modifications in the electron optics of the first undulator section and the chicane. These changes are necessary because of the scaling of the FEL gain with the wavelength. The electron optics designed for 6 nm, with $\langle \beta \rangle \approx 4.5$ m (see Fig.3), provides saturation length in the order of 20 m for SASE mode. For the 60 nm case, however, the saturation length is only about 9 m, which is significantly shorter than the first undulator (14.5 m) and therefore not acceptable from the point of view of the self-seeding option. One possible solution, as confirmed by

simulations, is to increase $\langle \beta \rangle$ in the first stage to a value in the order of 25 m, corresponding to the desired low gain of about three orders of magnitude below saturation.

Variation of the seeding wavelength

The monochromator design gives the possibility for variation of the wavelength of the seed across the full bandwidth of the FEL amplifier. Therefore it is interesting to investigate the influence of the seeding wavelength on the power and the spectrum of the output radiation. In Fig. 6 the spectral flux along the second undulator is presented for various seeding wavelengths. The simulations show a maximum at $Z \approx 15.5$ m for $\lambda_{seed} = 6.305$ nm. One has to

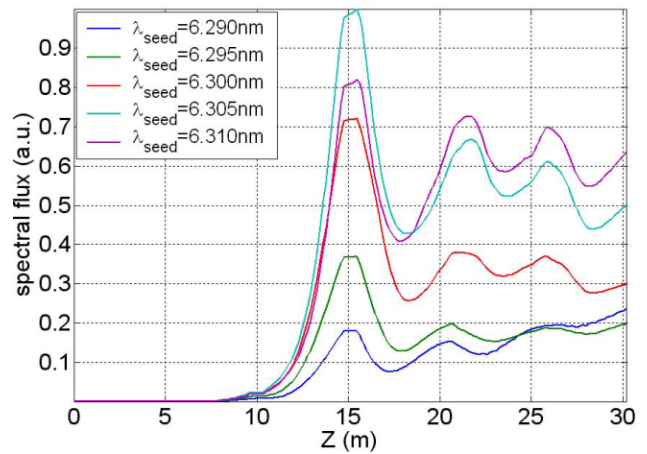


Figure 6: Spectral flux as a function of the undulator length for different λ_{seed} and constant seeding power.

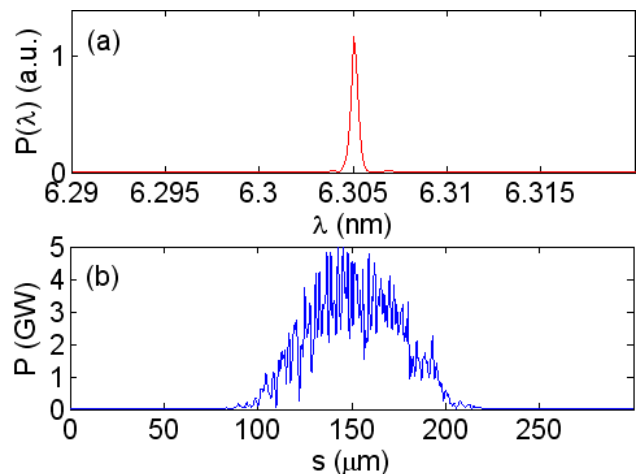


Figure 7: Spectrum (a) and power along the radiation pulse (b) in the second (seeded) section at $Z=15.5$ m.

mention that the position of the maximum of the spectral flux is related to the onset of the nonlinear regime (see Fig. 5). Further increase of the output power is coupled with a spectral broadening and in consequence with reduction of the spectral flux. As studied in [9], the length of the second

undulator can be optimized in order to compensate the large fluctuations of the seed intensity after the monochromator. The simulation results plotted in Fig. 7 demonstrate the effect of the self-seeding on the spectrum and the power of the output radiation. The two graphs in Fig. 7 correspond to the maximum of the spectral flux.

CSR effects

The electron bunches entering the magnetic chicane are of rms length $\sigma_z \approx 50 \mu\text{m}$ and high peak current $I_0 \approx 2.5 \text{ kA}$. Therefore, despite the small bending angle $\theta = 3^\circ$,

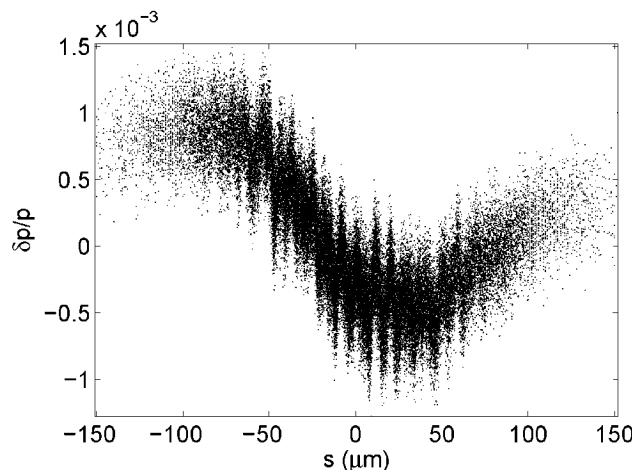


Figure 8: Distortion of the longitudinal phase space due to synchrotron radiation produced in the bypass dipoles.

the coherent component of synchrotron radiation, generated in the bypass dipoles, can be significant and might dilute the electron beam quality. Simulations of the CSR-induced emittance dilution have been made using the ELEGANT code, which result in a projected emittance growth in the order of a percent. The slice emittance is, however, almost unchanged. A much more significant impact on the longitudinal phase space is expected, as presented in Fig. 8. The total relative energy spread has increased from 2×10^{-4} up to about 5×10^{-4} . The growth of the energy spread is due to the correlation in the longitudinal phase space created by the synchrotron radiation, but on the other hand the slice energy spread is practically unaltered. The increased energy spread will drive more particles outside of the amplifier bandwidth and as a result one anticipates a reduction of the gain. Moreover the correlation in the phase space produces side bands in the spectrum or in other words spectral broadening. Fig. 9 shows that there is about a factor of two decrease in spectral flux due to CSR effects. It is important to note that we have considered the worst case scenario i.e. the bypass optics and electron beam parameters have not been tuned to mitigate the impact of CSR.

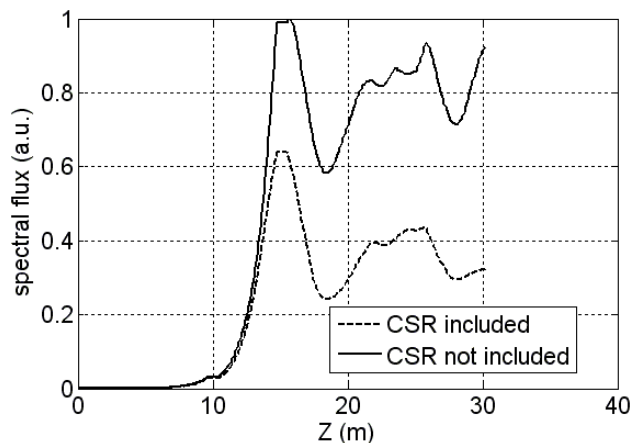


Figure 9: Demonstration of the impact of CSR effects - the spectral flux as a function of the undulator length.

CONCLUSIONS AND OUTLOOK

The operation of the two stage FEL has been studied, taking into account all the details in the design of the electron optics. Simulation results demonstrate a feasible operation in a wide range of electron energies and wavelengths. Investigated is also the possibility to fine tune the seeding wavelength, accomplished using the monochromator beamline settings. The impact of the coherent synchrotron radiation emitted in the bypass dipoles was studied. The simulations predict about a factor of two reduction of the spectral flux due to CSR. Further studies including wave front propagation through the monochromator beamline are ongoing [10]. As a next step the tolerances of the electron beam parameters, the accuracy of magnets alignment and the impact of the magnetic field errors will be analyzed.

ACKNOWLEDGEMENTS

We thank A. Meseck for the modifications of the code GENESIS and for many fruitful discussions.

REFERENCES

- [1] J. Feldhaus et. al., Opt. Commun., 140 (1997), 341.
- [2] R. Treusch et. al. "The Seeding Project for the FEL in TTF Phase II", HASYLAB Annual Report 2001.
- [3] R. Reininger et. al., Nucl. Instr. and Meth. A (2001) 467-468, 38.
- [4] B. Faatz et. al., Nucl. Instr. and Meth. A 475 (2001), 603.
- [5] E.L. Saldin et al., Nucl. Instr. and Meth. A 539 (2001), 499.
- [6] S. Reiche, Nucl. Instr. and Meth. A 429 (1999), 243.
- [7] M. Borland, "elegant: A Flexible SDDS-Compliant Code for Accelerator Simulation," Advanced Photon Source LS-287, September 2000.
- [8] M. Borland, Phys. Rev. ST Accel. Beams 4, 070701 (2001).
- [9] E.L. Saldin et al., Nucl. Instr. and Meth. A 445 (2000), 178.
- [10] Johannes Bahrtdt et.al., "The Properties of the FEL Output for Self Seeding", these proceedings.

FERMI@ELETTRA: A SEEDED FEL FACILITY FOR EUV AND SOFT X-RAYS

E. Allaria, C.J. Bocchetta, D. Bulfone, F. Cargnello, D. Cocco, M. Cornacchia, P. Craievich, G. D'Auria, M.B. Danailov, G. De Ninno, S. Di Mitri, B. Diviacco, M. Ferianis, A. Galimberti, A. Gambitta, M. Giannini, F. Iazzourene, E. Karantzoulis, M. Lonza, F. Mazzolini, F. Parmigiani, G. Penco, L. Rumiz, S. Spampinati, M. Stefanutti, G. Tromba, M. Trovo', A. Vascotto, M. Veronese, M. Zangrando, Sincrotrone Trieste, Trieste, Italy
 J.N. Corlett, L.R. Doolittle, W.M. Fawley, S.M. Lidia, G. Penn, I.V. Pogorelov, J. Qiang, A. Ratti, J.W. Staples, R.B. Wilcox, A. Zholents, LBNL, Berkeley, CA, USA
 P. Emma, Z. Huang, J. Wu, SLAC, Stanford, CA, USA
 W. Graves, F.X. Kaertner, D. Wang, MIT, Cambridge, MA, USA

Abstract

We describe the conceptual design and major performance parameters for the FERMI@Elettra Free Electron Laser (FEL) project funded for construction at Sincrotrone Trieste, Italy. This user facility complements the existing storage ring light source at Sincrotrone Trieste, and will be the first facility to be based on seeded harmonic cascade FELs. Seeded FELs provide high peak power pulses, with controlled temporal duration of the coherent output allowing tailored x-ray output for time domain explorations with short pulses of 100 fs or less, and high resolution with output bandwidths of the order of meV. The facility uses the existing 1.2 GeV S-band linac, driven by electron beam from a new high-brightness RF photocathode gun, and will provide tunable output over a range from ~100 nm to ~10 nm, and APPLE undulator radiators allow control of x-ray polarization. Initially, two FEL cascades are planned, a single-stage harmonic generation to operate over ~100 nm to ~40 nm, and a two-stage cascade operating from ~40 nm to ~10 nm or shorter wavelength, each with spatially and temporally coherent output, and peak power in the GW range.

INTRODUCTION

The single-pass seeded FEL project FERMI@Elettra will be a User facility providing quality photons in the EUV to soft X-ray range. Photon production will be based on harmonic generation. The concept design has been studied and optimised towards a detailed engineering phase [1]. All major parameters and systems have been studied and an overview is presented here. Comprehensive studies including collective effects from space charge, coherent synchrotron radiation and wakefields as well as nonlinear dynamics from RF waveforms and bunch compressors have been performed to determine the optimum electron beam parameters for the facility. The studies have included error tolerances and beam jitter sensitivities in start-to-end computations.

The project covers the lower energy region of the XUV-X ray spectrum. With a peak brightness of more than ten orders of magnitude greater than 3rd generation sources, full transverse coherence, transform limited

bandwidth, choice of pulse lengths of the order of a ps or less, variable polarization and energy tuneability, the FERMI source represents a powerful tool of scientific exploration in a large field of research. The coherence properties will provide single-shot imaging, allowing the study of chemical reactions as they happen. The high peak power will allow the study of non-linear multi-photon processes in a regime never explored before. The short time properties will allow the visualisation of ultra-short nuclear and electronic dynamics. The facility will enable the study of dilute samples of paramount importance in atmospheric, astrophysical and environmental physics, as well as in the characterization of nano-size materials. The applications extend from chemical reaction dynamics to biological systems, materials and surfaces, nano-structures and superconductors. The nature of harmonic generation schemes, with an external laser driving the FEL process, is particularly suitable for pump/probe synchronization at the ps time scale or less.

Figure 1 shows the layout of the facility. The accelerator and FEL complex is housed below ground and is composed of the following parts: (a) A photo-injector and two short linac sections, where a bright electron beam is generated and accelerated to ~100 MeV. (b) The main linear accelerator, where the electron beam is time-compressed and accelerated to a final energy of ~1.2 GeV. (c) A beam transport system to the undulators. (d) The undulator chains where the FEL radiation is generated. (e) The undulator to experimental area transport lines. (f) The experimental area. The new constructions include pushing back by ~ 80 m the linac tunnel and surface klystron gallery to make room for the photo-injector, accelerating sections and the first bunch compressor. At the downstream end, the klystron gallery is extended by ~30 m to power more accelerating sections. A FEL hall will be constructed below ground at the exit of the linac with transverse dimensions for the installation of up to four undulators side-by-side. Finally, an experimental hall, also below ground, will be constructed to house the FEL radiation transport optics and the experimental hutches. The facility will be provided with new support laboratories and office spaces.

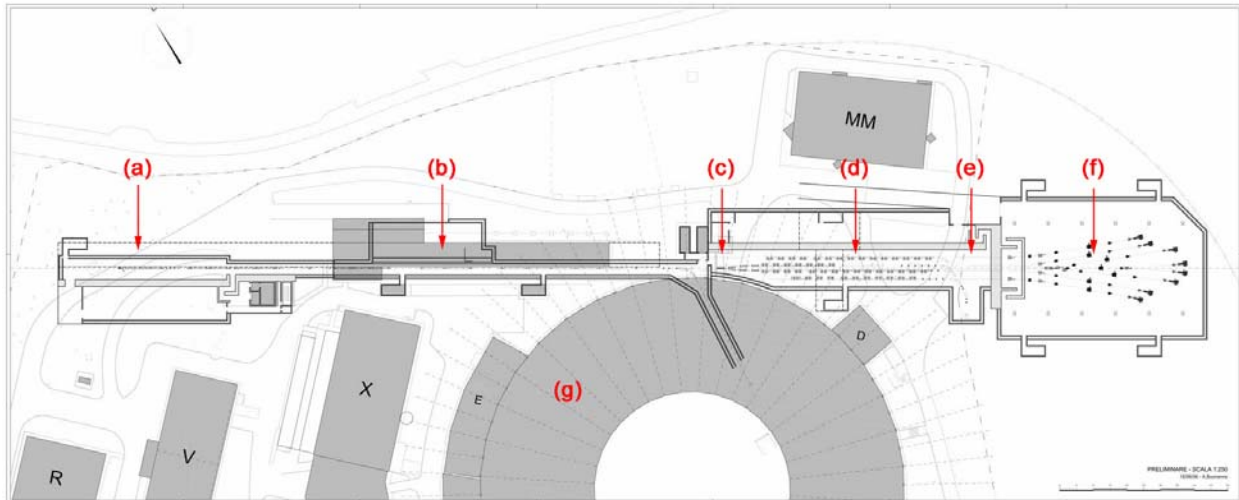


Figure 1: Schematic FERMI layout beside the ELETTRA storage ring building (g). See text for details.

THE PHOTO-INJECTOR

The photo-injector [2] is based on the proven 1.6 cell electron gun developed at BNL/SLAC/UCLA and adopted by the Linac Coherent Light Source (LCLS). The RF gun will provide a peak-accelerating gradient of 110 MV/m and an exit beam energy of around 5 MeV from a 10 MW peak input pulse (2.8 μ sec). The injector will produce a 10ps long pulse with 0.8-1 nC charge and a rms normalized transverse emittance of 1.2 mm-mrad at 100 MeV. The initial repetition rate of 10 Hz will later be increased to 50 Hz following a modified gun design. The design includes a solenoid for emittance compensation, an off-axis diagnostic line and acceleration to 100 MeV with two booster S-band rf sections. These sections, named S0A and S0B, are part of the present Elettra injection system. Their on-axis, iris coupled cells resonate at 2.998 GHz in the $2\pi/3$ mode, and provide peak accelerating gradients of ~ 18 MV/m, for a total energy gain of ~ 45 MeV (with operational 10% energy margin). The booster modules include solenoid magnets to provide transverse focusing, to assist with emittance compensation, and to match the optical functions at the input to the main linac.

A laser pulse provides temporal and spatial shaping of the electron bunch. To compensate wakefield effects in the main linac sections [3], the electron bunch should ideally have a linear ramped peak current distribution at the exit of the injector rather than a flat top [4]. Studies have showed that such a profile at the start of acceleration produces a more uniform energy and current profile at the entrance to the undulators. The FERMI photo-injector addresses this novel concept by using a laser profile that has a quadratic ramp. Space charge forces subsequently transform this distribution to a linear ramped current shape at the exit of the injector, i.e. a profile where the current in the bunch increases approximately linearly with time. The photo-injector laser system [5] includes two amplifier stages, a regenerative one followed by a multipass, and reaches pulse energy of 20 mJ in the IR.

Pulse shaping is done partially in the IR, by an acoustic optic dispersive filter (DAZZLER), and completed in UV in a transmission grating based stretcher or Fourier-system. Beam shaping is done either in the IR or in the UV by an aspheric shaper. A small part ~ 400 μ J of the IR beam is split away and transported for use by the laser heater.

Beam dynamics in the injector system have been extensively modelled from photocathode emission to the exit of the booster accelerator modules using 2D and 3D space-charge tracking codes (GPT and ASTRA). Simulations confirm that electron beam performance objectives for injection into the main linac at ~ 100 MeV are reachable. The timing and charge stability are both challenging, 0.5 ps and 1% respectively, but have been shown to be within present state of the art techniques.

ACCELERATION, COMPRESSION AND BEAM TRANSPORT

The accelerator is shown schematically in Figure 2 [6]. It consists of four linacs, two bunch compressors, a laser heater and a beam transport system (spreader) to the undulators. The function of this system is to accelerate the electron beam to the FEL energy of ~ 1.2 GeV and to compress the ~ 10 ps long pulse from the photo-injector to the final lengths and peak current. Two FEL layouts are envisaged. FEL-1 will provide photons with wavelengths in the range 100-40 nm. Depending on the experiments, electron bunch lengths of 200 fs and a peak current of 800 A or higher can be provided (in this case with shorter bunch lengths). For those experiment where small time jitter is important, and to account for a predicted jitter of up to 400 fs, an electron bunch of 600 fs ("medium bunch") has been designed. Including the inevitable inefficiency of the compression system, the obtainable peak current is ~ 800 A with 0.8 nC of charge from the photo-injector. FEL-2 will cover the wavelength range 40-10 nm and will make use of a ~ 1 ps long pulse to provide close to Fourier-transform-limited radiation and

or a ~ 200 fs high brightness FEL radiation using the fresh-bunch technique. In both cases a “long bunch” of 1.5 ps is required from the accelerator. With 1 nC charge from the injector, the attainable peak current is ~ 500 A.

For both FELs the final energy and charge distributions correlated with the distance along the electron bunch should be as flat as possible in order not to broaden the FEL bandwidth. The aim is to produce an energy variation no greater than $1-2 \times 10^{-4}$ along the useable part of the bunch and a peak current variation no greater than ~ 100 A. In transverse space, the horizontal and vertical normalized emittances at the end of the linac, 1.2 GeV, will not be greater than 1.5 mm-mrad in order to meet the desired photon throughput. This represents a $\sim 30\%$ increase from the photo-injector simulation results and includes a safety margin against emittance dilution effects. The emittance value of 1.5 mm-mrad is a condition of the shortest wavelength and accelerator performance is aimed at satisfying this most stringent requirement. This specification may be relaxed for longer photon wavelengths.

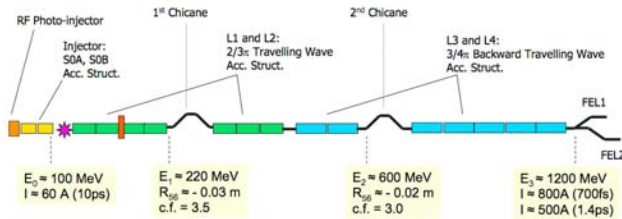


Figure 2: Schematic layout of the accelerator. The star indicates the position of the laser heater, while the red section the X-band accelerator.

At the exit of the photo-injector the electrons enter the L1 linac where they are accelerated to ~ 250 MeV. Acceleration occurs off-crest to provide correlated energy spread along the bunch that will compress it in the first compressor BC1. An RF structure tuned at the 4th harmonic of the main s-band sections, ie at X-band frequency, is placed half-way in L1. The function of the X-band linac is to provide the non-linear quadratic and, when operated off-crest, cubic corrections of the correlated momentum distribution along the bunch in the presence of the non-linearities of the photo-injector, the magnetic compressors and the non-linear effects of the longitudinal wakefields.

The linac structures L2 and L3 between the first and second bunch compressors accelerate the beam from ~ 250 MeV to ~ 650 MeV. They also provide the residual momentum chirp for the second compressor, BC2. After BC2 the beam is further accelerated to its final energy in the L4 structure. The phases of the linac after BC1 are chosen to provide the necessary momentum spread for compression and also to cancel the linear part of the longitudinal wakefields. The non-linear correlated momentum spread at the end of the linac is fine-tuned with the amplitude and phase of the X-band structure. The focusing structure of the linac is designed to minimize transverse emittance dilution due to transverse

wakefields, momentum dispersion and coherent synchrotron radiation in bending magnets. Exhaustive computations with codes LITRACK and “elegant” were performed to optimise beam parameters and to simulate expected jitter and parameter sensitivities. The computed electron distributions were further used in the FEL simulation studies.

The electron beam is transported from the end of the linac to the FELs by a FODO spreader channel. It is designed for diagnostics and parallel separation of the two FELs. The spreader has been designed to preserve electron beam emittance. This is done in two ways: by using a lattice with a small “curly- H ” function in the magnets and by employing a scheme of self emittance compensation. Quadrupoles in the deflecting arcs, located near the positive and negative peaks of the dispersion function, are separated by a unit transfer matrix and. This allows simultaneous change of their gradients and the production of a dispersion bump localized between the quadrupoles. Control of this bump regulates R56 within the spreader allowing it to be exactly zero or any other reasonable value. It is in fact kept slightly positive in some cases to disperse the electrons in the spikes of the peak current.

THE UNDULATORS AND THE FEL PROCESS

FEL configurations are based on harmonic generation schemes seeded by an external laser. FEL-1 will utilise one stage (modulator, dispersion section and radiator) while for FEL-2 two stages will be used in a fresh part of the bunch seeding scheme. A whole bunch seeding scheme was also studied for FEL-2 and requires a larger number of undulators and a higher quality electron beam.

FEL-1 and FEL-2 are required to have continuously tuneable output polarizations at all wavelengths, ranging from linear-horizontal to circular to linear-vertical. For this reason, the FEL-1 radiator and the final radiator in FEL-2 have been chosen to have APPLE-II configurations with pure permanent magnets. For the modulator a simple, linearly-polarized configuration, is optimal both due to its simplicity and because the input radiation seed can be linearly polarized. The tuning of the wavelength will be done by changing the gap of the undulator while keeping the electron beam energy constant. The magnetic lengths of the undulators segments are 2.34 m (containing 36 periods) for the FEL-1 and 1st FEL-2 radiators and 2.40 m (48 periods) for the 2nd FEL-2 radiator. FEL-1 and 2 consist of 6 and 10 segments respectively. The intra-segment spools contain electromagnetic quadrupoles, high quality beam position monitors and quadrupole movers to steer the electron trajectory.

Theoretical and computational studies led to a selection of the accelerator and FEL parameters. An exhaustive study through start-to-end simulations, that included the use of FEL codes GENESIS and GINGER, was performed [7]. The simulations took into account

perturbations in the accelerator and FEL parameters. In particular parameter sensitivity and time dependent jitter studies were carried out for both FELs. Studies of the variation of mean energy, energy spread, peak current, emittance and seed input power were done both for single and multi-parameter variations. Methods, such as undulator tapering, to reduce the sensitivity to variations, were also examined. Table 1 gives the expected performance parameters for the two FELs.

The seed laser will provide tuneable UV radiation in two pulse duration schemes: 100 fs and 1 ps. A dual pulse duration regenerative amplifier will be used. In the 100 fs case the amplifier directly pumps a travelling wave parametric amplifier (TOPAS) followed by harmonic conversion stages. In the 1 ps case this output is further amplified in a two pass stage to the 10 mJ level that then pumps a ps TOPAS. Timing and synchronization [8] of RF, laser and diagnostic systems will be guaranteed to sub 50 fs levels by an integrated system handling both

CW and pulsed transmission schemes. A central clock system generating stable timing signals for the whole facility will be used. The signals will be distributed over distances exceeding 300 m by optical fibres in a star configuration. Timing information is transmitted using either RF modulated CW light mainly for the RF systems or pulsed light mainly for the laser systems.

The consequence of orbit displacements from the ideal trajectory in the undulators were simulated. The FEL process at the shortest wavelength, 10 nm, requires the straightness of the electron orbit in the undulators to be within 10 μm (rms value over the undulators length). Although this is beyond state-of-the art mechanical alignment techniques, realistic simulations show that a combination of the latter and of beam-based-alignment (tested at the Stanford Linear Collider and proposed for the LCLS) will achieve the desired performance.

Table 1: Principal FEL output parameters

Parameter	FEL-1	FEL-2
Wavelength range [nm]	100 to 40	40 to 10
Output pulse length (rms) [fs]	< 100	> 200
Bandwidth (rms) [meV]	17 (at 40 nm)	5 (at 10 nm)
Polarization	variable	Variable
Repetition rate [Hz]	50	50
Peak power [GW]	1 to >5	0.5 to 1
Harmonic peak power (% of fundamental)	~2	~0.2 (at 10 nm)
Photons per pulse	10^{14} (at 40 nm)	10^{12} (at 10 nm)
Pulse-to-pulse stability	$\leq 30\%$	~50%
Pointing stability [μrad]	< 20	< 20
Virtual waist size [μm]	250 (at 40 nm)	120
Divergence (rms, intensity) [μrad]	50 (at 40 nm)	15 (at 10 nm)

PHOTON BEAM TRANSPORT AND EXPERIMENTAL AREAS

After leaving the undulators the electron beam, carrying an average power of 75 W (at 50 Hz) will be dumped into a shielding block by a sequence of bending magnets, while the FEL radiation will be transported to the experimental areas. The transport optics is designed to handle the high power density (up to 10 GW) in a very short temporal interval. In order to handle the high peak photon energy density, the beam line optics operate at low grazing incidence angles with low Z-materials and the radiation intensity can be controlled by a gas absorption cell. The vacuum system is windowless with differential pumping sections. Pulse length preservation, monochromatization, energy resolution, source shift compensation, focusing in the experimental chamber and beam splitting are all included in the design of the FEL radiation transport system.

REFERENCES

- [1] FERMI@Elettra Conceptual Design Report, 2006, to be published.

- [2] M. Trovo', et al., "Further Studies in the FERMI@Elettra Photoinjector Optimisation", this conference.
- [3] S. Di Mitri, "How to obtain high quality electron bunches in the presence of normal conducting wakefields", this conference.
- [4] G. Penco, et al., "Ramping longitudinal distribution studies for the FERMI@Elettra injector", this conference.
- [5] M. Danailov, et al., "Design of a two stage laser pulse shaping system for FEL photoinjectors", this conference.
- [6] G. D'Auria, "Linac design for the FERMI Project", LINAC conference, 2006, Knoxville, Tennessee, USA.
- [7] G. De Ninno, et al., "Design and optimisation of the FERMI@Elettra FEL" and "Start to end time-dependent study of FEL output sensitivity to electron beam jitters for the first stage of FERMI@Elettra project", this conference.
- [8] M. Ferianis, "Timing and Synchronization in Large-Scale Linear Accelerators", LINAC conference, 2006, Knoxville, Tennessee, USA.

COHERENT HARMONIC EMISSION OF THE ELETTRA STORAGE RING FREE ELECTRON LASER IN SINGLE PASS CONFIGURATION: A NUMERICAL STUDY FOR DIFFERENT UNDULATOR POLARIZATIONS

F. Curbis*, University of Trieste & Elettra, Basovizza, Trieste, Italy,
H.P. Freund, Science Applications International Corporation (SAIC),
G. De Ninno, Elettra, Basovizza, Trieste, Italy.

Abstract

The optical klystron installed on the Elettra storage-ring is normally used as interaction region for an oscillator free-electron laser, but, removing the optical cavity and using an external seed laser, one obtains an effective scheme for single-pass harmonic generation. In this configuration the high-power external laser is synchronized with the electron beam entering the first undulator of the optical klystron. The laser-electron beam interaction produces a spatial partition of electrons in micro-bunches separated by the seed wavelength. The micro-bunching is then exploited in the second undulator to produce coherent light at the harmonics of the seed wavelength. The Elettra radiator is an APPLE type undulator and this allows to explore different configurations of polarization. We present here numerical results obtained using the code Medusa for both planar and helical configurations. We also draw a comparison with predictions of the numerical code Genesis.

INTRODUCTION

Coherent Harmonic Generation (CHG) can be implemented in a storage ring using two undulators as a cascade. The first undulator (called modulator) is tuned at the wavelength of an external high-power laser and the second undulator (called radiator) at a higher harmonic of the seed. Between the undulators there is a region, i.e., dispersive section, with a strong magnetic field, which, in single-pass configuration, converts the energy modulation, occurred in the modulator, in spatial modulation (usually referred as “bunching”). The Elettra storage-ring FEL is presently operating in oscillator configuration [1, 2], but, with minor modification, the optical klystron will be used as interaction region for CHG in single-pass configuration. In the new configuration (see Figure 1) the optical cavity will be removed and a conventional laser will be focused into the modulator and synchronized with the electron beam. The main difference between conventional single-pass seeded FEL and storage-ring harmonic generation is that in the latter case the electron beam is re-circulated and not renewed each pass through the optical klystron. This peculiarity determines the maximum repetition rate for this configuration, because the electrons need few synchrotron damping times (order of ten of milliseconds) to cool down after each interaction with the seed laser. Preliminary sim-

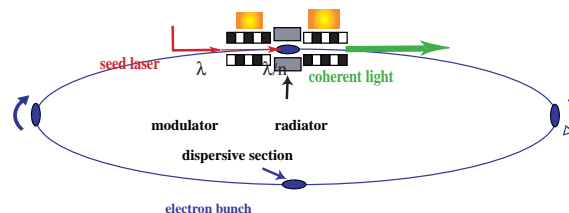


Figure 1: Layout of the Elettra storage-ring FEL after removing the optical cavity and using an external seed laser.

ulations [3] have been done using Genesis [4] for different working points, i.e. different machine (electron-beam energy, Twiss parameters, emittance, strength of the dispersive section) and the seed laser (power and duration) parameters. The work reported in this paper characterizes the emission of the Elettra APPLE-type undulator, operated in both linear and helical configurations. Numerical results are obtained using Medusa and Genesis. Medusa provides the possibility to calculate the harmonic power at the end of the radiator. This means that the radiator is tuned at the third harmonic of the seed laser (i.e. the fundamental in the modulator) and Medusa is able to calculate any desired harmonics besides the fundamental. This will allow to investigate if wavelengths shorter than the fundamental will be detectable. The external seed laser [5] is a titanium-sapphire (Ti:Sa) with a very high peak power (2.5 GW) and very short pulse duration (variable between 100 and 250 fs (RMS)). The repetition rate will be initially 10Hz. Using this frequency, the contribution from incoherent synchrotron emission, provided by electrons circulating in the storage ring but not interacting with the seed laser, may spoil the signal-to-noise ratio. Possible strategies will be explored in the aim of increasing the repetition rate, therefore improving the signal quality. The first undulator is tuned at the fundamental of the seed laser (240 nm), while the second undulator at the third harmonic (80 nm).

OPTIMIZATION FOR MEDUSA SIMULATIONS

In this section we report some studies performed in time-independent mode in order to optimize the parameters before the introduction of the slippage, e.g. time-dependent simulation. The main run parameters used in Medusa simulations are reported in Table 1 [5, 6]. With respect to the

* francesca.curbis@elettra.trieste.it

values used in Genesis simulations, there are some minor differences: the pulse shape of the electron bunch and the seed laser is parabolic instead of Gaussian, the seed duration is 250 fs FWHM instead of 140 fs and the number of periods for both undulators is 22 instead of 20, because Medusa needs one period more at the entrance and exit of the undulator to properly model the simulation. The vari-

Table 1: Run parameters used in Medusa simulations

Electron beam	
Energy	0.9 GeV
Peak current	77 A
x-Emittance	2.46 mm-mrad
y-Emittance	0.246 mm-mrad
Energy-spread	0.12%
Bunch length	27 ps
Bunch charge	1.38 nC
Bunch shape	parabolic
Twiss parameters	
$\alpha_x = 0.24$	$\beta_x = 8.986$
$\alpha_y = 0.89$	$\beta_y = 4.695$ m
Modulator	
Magnitude	5.62 kG
Period	10.0 cm
Length	22 periods
Radiator	
Magnitude	3.00 kG
Period	10.0 cm
Length	22 periods
Undulator-to-undulator gap	0.9 m
Seed laser	
Wavelength	240 nm
Seed power	2.5 GW
Seed duration	0.25 ps
Seed shape	parabolic

ation of the radiator output power versus the dipole field strength in the chicane is shown in Figure 2 for the case of a planar radiator. We have found from Genesis simulation that the energy spread induced by the seed laser is so high that the beam needs only a drift to transform the energy modulation in spatial modulation (bunching). In Medusa simulation instead, the power level when the chicane field vanishes is 1.06 MW (and this is very close to the time-dependent result), but a little more power (about 1.36 MW) could get using a chicane field of about 0.5 kG. However, in order to compare the results of these two codes, we have chosen to set to zero the chicane field also in this case. The same power optimization with respect to the magnetic field has been performed tuning the radiator at the third harmonic (see Figure 3). The output power at 80 nm is about 1.7 MW which is almost a factor two over the value found for the planar undulator. The second harmonic (40 nm) power is not very sensitive to the variation of the chicane

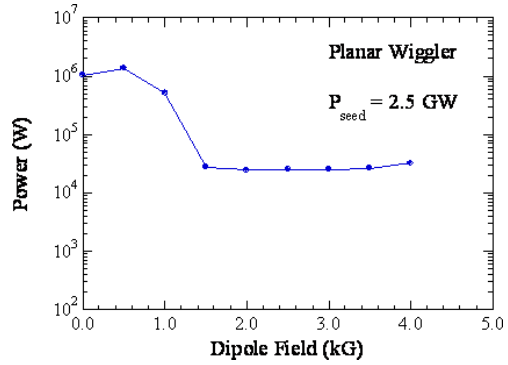


Figure 2: Output power versus dipole field strength at 80 nm for planar radiator.

field and is about 200 W when the chicane field is set to zero. These results have been confirmed by time dependent simulations. The same behavior has been found for a heli-

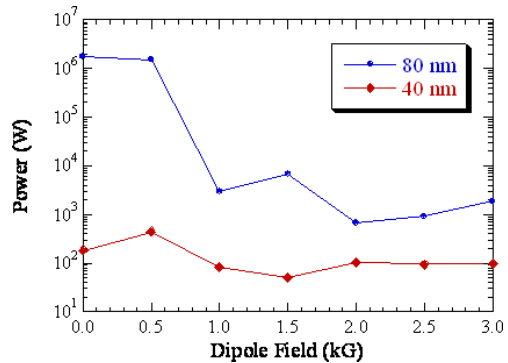


Figure 3: Output power versus dipole field strength for helical undulator tuned at 80 nm and second harmonic (40 nm) power.

cal undulator tuned at the second harmonic (120 nm) of the seed laser. The result, shown in Figure 4, looks similar to previous case: the highest power is found when the chicane field is set to zero and the power is about 4.7 MW at 120 nm and 5.7 kW at 60 nm. As before, while the power at the fundamental (120 nm) drops fast with increasing chicane field, the harmonic power (60 nm) doesn't drop so much. An other important issue to be considered when using numerical codes is the number of simulated particles which is needed in order to guarantee a correct modelization of the process. For the CHG in helical configuration, we found that a larger number of particles is needed with respect to planar configuration. The case for zero energy-spread is reported in Figure 5. We can argue from the results that to do this kind of simulation about 60000 particles per slice are needed without energy spread and, including the energy spread, an order of magnitude more particles is required. In the latter case, the power level will be of course smaller. To conclude, in order to treat the energy spread and the additional harmonics, the following runs used 1210104 particles.

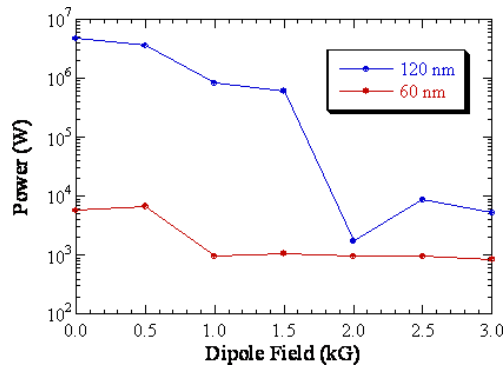


Figure 4: Output power versus dipole field strength for helical undulator tuned at 120 nm and second harmonic (60 nm) power.

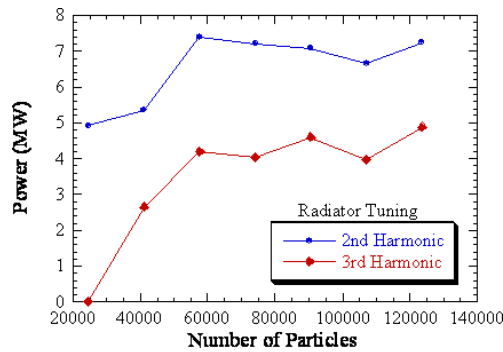


Figure 5: Output power versus number of simulated particles for helical undulator tuned at the second and the third harmonic of 240 nm.

MEDUSA PERFORMANCE

Planar undulator

In time-dependent mode, we firstly looked at the harmonics of the 80 nm wavelength, using 2.5 GW seed power and zero magnetic field inside the dispersive section. The evolution along the undulator of the fundamental (80 nm) and the first three harmonics of that wavelength are shown in Figure 6. The second harmonic (40 nm) reaches a power level of about 2 kW, the third harmonic (26.67 nm) a power level of about 500 W and the fourth harmonic (20 nm) a power of 2 W. While in the steady-state simulations we looked exclusively at the evolution of the power along the radiator, in time-dependent simulations the output temporal profile (see Figure 7) and the harmonic spectrum (see Figure 8) can be displayed. The electron bunch is two order of magnitude longer than the seed laser (27 ps versus 250 fs) and the total slippage, considering 80 nm wavelength and 44-periods undulator, is much smaller than the bunch-length, thus the differences between steady-state and time-dependent simulations are expected to be small. Indeed, the observed peak power is about 1 MW in both cases. The shortness of the laser pulse may lead to numerical problems because one should increase the number of slices

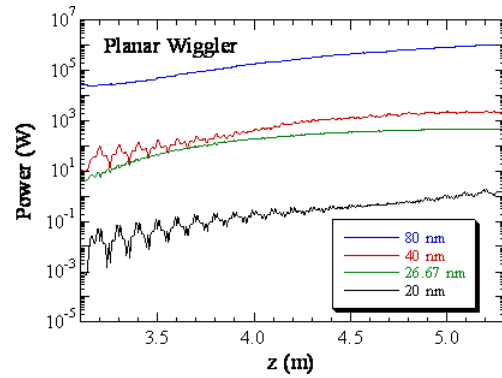


Figure 6: Evolution of the 80 nm radiation and its first three harmonics in planar configuration.

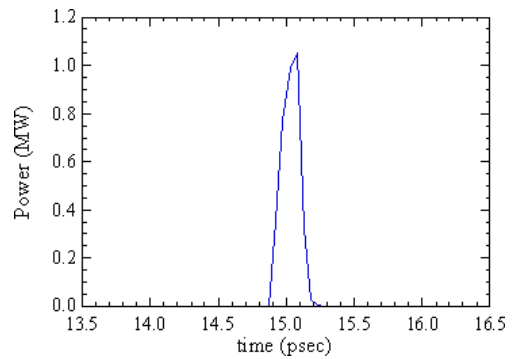


Figure 7: Power versus time of the 80 nm pulse at the end of the radiator in planar configuration.

in order to resolve the FEL pulse structure and an adequate number of particles must be holden in each slice. In our case, the simulation includes 600 slices, with 17496 particles per slice, but only about 10 slices across the seed pulse. This is the reason why the output spectrum in Figure 8 is not smooth and displays a spiky behavior. If one believes the problem is the lack of resolution, the envelope could be considered as the spectral shape. Considering the Fourier

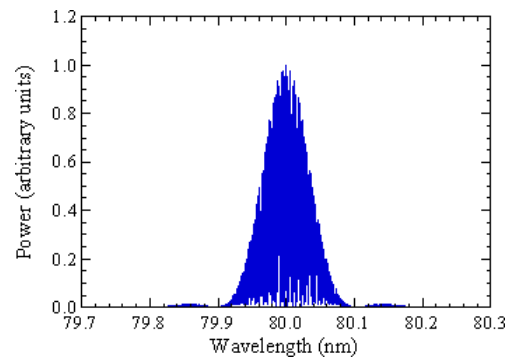


Figure 8: Fourier transform of the output spectrum at 80 nm (planar configuration).

limit, given by the equation:

$$c \cdot \frac{\Delta t [FWHM] \Delta \lambda [FWHM]}{\lambda^2} = 0.441 \quad (1)$$

where c is the speed of light, Δt is the $FWHM$ duration of the output pulse, $\Delta \lambda$ is the $FWHM$ of the output spectrum and λ is the emission wavelength, the results presented here give a quantity that is 1.7 times above the limit. This value indicates that the emitted light have an high level of coherence.

Helical undulator

As already reported before, the steady-state simulation could give enough information about the power level of the 80 nm signal and the first two harmonics of that. For this reason, the simulation of the helical configuration has been obtained in time-independent mode. In Figure 9 the evolution of the signal power along the radiator is displayed. One can observe that the 40 nm harmonic is still about 1 kW as in planar configuration, but the 26.67 nm harmonic has a much lower power than for the planar undulator.

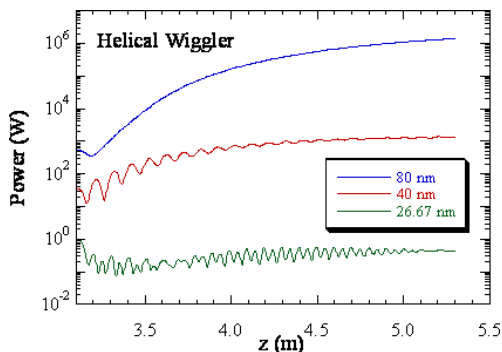


Figure 9: Evolution of the 80 nm radiation and its first two harmonics in helical configuration.

Comparison with Genesis simulation

The campaign of simulation has been completed exploring the helical polarization in Genesis. The power level founded at 80 nm for each configuration is very close between Genesis and Medusa and between planar and helical configuration the differences are lower than one order of magnitude. All Genesis simulation has been performed in time-dependent domain, but, to limit the computing time, just a portion of the electron bunch around the seed pulse has been simulated, with the implicit assumption that the slippage doesn't not affect too much the emission.

The evolution of the output power along the radiator is shown in Figure 10 for both planar and helical configuration. In comparison with Medusa, Genesis results don't exhibit a big difference between planar and helical power. The value found is about 1.1 MW in both cases, as shown also in Figure 11, where the power is plotted as a function of time at the end of the radiator.

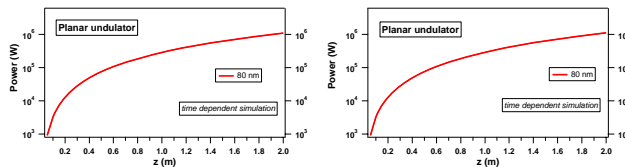


Figure 10: Harmonic power for planar undulator (at left) and helical undulator (at right) obtained tuning the radiator at 80 nm.

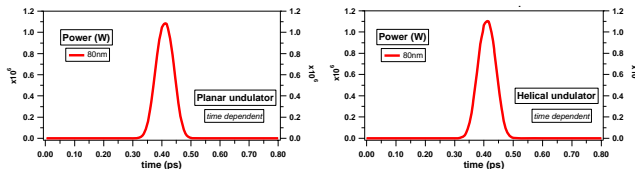


Figure 11: Temporal profile for planar undulator (at left) and helical undulator (at right) obtained tuning the radiator at 80 nm.

The Fourier transform of the output spectrum is reported in Figure 12. Using the Equation 1, we found a value that is 1.6 times above the limit. Also in this case, the radiation emitted shows an high degree of coherence.

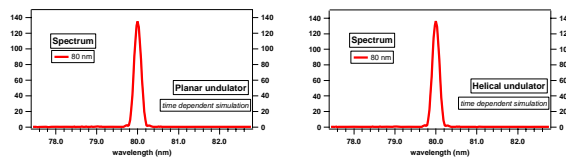


Figure 12: Harmonic spectrum for planar undulator (at left) and helical undulator (at right) obtained tuning the radiator at 80 nm.

CONCLUSION

The Medusa simulations confirmed in general the results already obtained by Genesis, with a good agreement in both planar and helical configuration. Some differences should be longer investigated, i.e., the higher power level found in planar configuration when the dispersive section is 0.5 kG and the factor two more power found in helical radiator.

REFERENCES

- [1] R. P. Walker, Proc. EPAC'99, 93.
- [2] G. De Ninno et al., *Nucl. Instrum. and Meth. A* **483** (2002) 177.
- [3] F. Curbis, G. De Ninno, Proc. FEL'05.
- [4] S. Reiche, *Nucl. Instrum. and Meth. A* **429** (1999) 243.
- [5] M. Danailov, Private Communication.
- [6] F. Iazzourene, Private Communication.

DESIGN AND PERFORMANCE OF THE FERMI AT ELETTRA FEL

G. De Ninno, E. Allaria, Sincrotrone Trieste, 34012 Trieste, Italy;

W. Fawley, G. Penn, LBNL, Berkeley, CA 94720-8211 USA.

Abstract

The FERMI at ELETTRA project will be comprised of two FELs, each based on the principle of seeded harmonic generation. The first undulator line, FEL-1, will operate in the 40-100 nm wavelength range relying upon one stage of harmonic up-conversion. The second undulator line, FEL-2, extends the output spectral domain to the 10-40 nm wavelength range and will use two harmonic stages operating as a cascade. We review the FEL studies that have led to the final design and present results of numerical simulations with GENESIS and GINGER codes including predicted output bandwidths and the effects of shot-to-shot fluctuations in multiple input parameters.

INTRODUCTION

The FERMI@ELETTRA project is based on the harmonic up-shifting of an initial radiation “seed” signal in a single-pass FEL amplifier employing multiple undulators. The basic principles which underlie this approach are: energy modulation of the electron beam via the resonant interaction with an external laser seed in a first undulator (modulator); use of a chromatic dispersive section to then develop a strong density modulation with large harmonic overtones; production of coherent radiation by the microbunched beam in a downstream undulator (radiator). The first stage of the project, FEL-1, aims at generating coherent output radiation in the 40-100 nm spectral range. For these wavelengths, users require short (< 100 fs) pulses with adjustable polarization together with high temporal and spatial reproducibility. The project’s second stage, FEL-2, will extend the spectral range down to 10 nm. Present users’ requirements for FEL-2 point to long (narrow-bandwidth) pulses with high peak brilliance and adjustable polarization. FEL-1 relies upon a single-stage scheme (i.e., modulator-dispersive section-radiator), similar to the one already operational at Brookhaven [1]. As for FEL-2, a two-stage harmonic cascade is necessary for reaching short wavelengths. The selected configuration is based on the so-called “fresh bunch” approach [2], in which the output radiation from the first radiator is used to energy-modulate in a subsequent modulator a part of the electron beam that did not interact in the first stage with the external seed.

In this paper we review the FEL studies that have led to the final design of FEL-1 and FEL-2 and present results of both time-independent and time-dependent numerical simulations with GENESIS and GINGER.

BASIC FEL OUTPUT REQUIREMENTS AND RELATED ISSUES

Table 1 summarizes the basic FEL output requirements for FEL-1 and FEL-2. At all wavelengths, both FEL-1 and FEL-2 are to have continuously tuneable output polarizations ranging from linear-horizontal to circular to linear-vertical. Consequently, the FEL-1 radiator and final radiator in FEL-2 have an APPLE-type configuration. Both FELs will operate at the accelerator repetition rate of 10-50 Hz.

At present it is believed that the major application for FEL-1 will involve time-domain experiments such as pump-probe interactions and possibly nonlinear phenomena. Consequently, the requirements for FEL-1 are more related to total photon number per pulse (i.e., $0.4 - 2 \times 10^{14}$) and pulse duration (20-100 fs) than they are to spectral bandwidth. A critical parameter affecting the needed electron beam duration is the timing jitter in the beam relative to that of the seed laser. In order that there be reasonable overlap between the seed and the electrons, the duration of the electron beam must be bigger than the duration of the seed pulse plus two times the RMS timing jitter. The expected RMS timing jitter from the accelerator is of order 130 fs [3], and therefore an electron-beam pulse duration of at least 600 fs is needed for 100-fs seed pulses. This timing jitter requirement may be one of the more difficult to satisfy in terms of the injector and accelerator subsystems.

Another important parameter associated with FEL-1 time domain experiments is shot-to-shot repeatability. Ideally, for nonlinear phenomena experiments, shot-to-shot RMS jitter in normalized photon number should be 5% or less. As reported in [3], we do not at present believe that such a low value is obtainable with the expected accelerator and injector parameters. Many FEL-1 experiments will be able to deal (via recording individual shot photon number for later post-processing) with values as high as 25% or greater.

In contrast to FEL-1 users, for whom timing and photon number jitter are critical parameters, most FEL-2 users are (presently) interested in the frequency domain experiments where longitudinal coherence and narrow bandwidth are crucial. The most important output goal for FEL-2 is $\geq 10^{12}$ photons/pulse/meV. Consequently, FEL-2 requirements favor long output pulses (≥ 200 fs) whose spectral properties are as close as possible to the transform limit. Although the total photon jitter is not critical for most experiments in the frequency domain, shot-to-shot central wavelength jitter is of concern. Consequently, in order not to increase the effective time-

averaged, output bandwidth as seen by the user, the wavelength jitter needs to be less than the individual shot bandwidth.

UNDULATOR DESIGN

In the FERMI case, wavelength tuning in the undulators will be done by changing the gap (and thus a_w) and not by changing the electron beam energy.

The FEL-1 undulator layout is shown in Fig. 1.

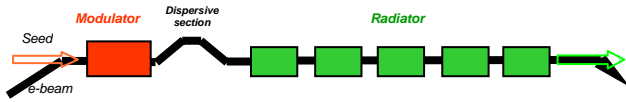


Fig. 1: FEL-1 undulator layout

For the first modulator which must satisfy FEL resonance over a nominal wavelength range of 240 to 360 nm, an undulator wavelength of 16 cm has been adopted. The modulator will be a standard planar undulator about 3-m long. In order to reach saturation over the whole spectral range, the necessary active radiator length for FEL-1 is about 16 m. For many reasons (e.g., magnetic forces, alignment, external focusing and diagnostic needs, possible tapering), this is far too long to construct as one continuous magnetic structure. Consequently, the radiators will be subdivided into six modules, each consisting of an active undulator segment (with a period of 6.5 cm and a length of about 2.3 m) and a break segment (about 1 m long), with the latter containing a number of items such as quadrupoles, a longitudinal phase shifter, beam position monitors, dipole correctors, and diagnostics. In order to produce light with variable polarization, the radiator modules will be APPLE-type. The FERMI design includes external quadrupole focusing to produce an average value of 10 m for the Twiss beta function in each plane.

Following the modulator is a break section (about 1 m long) that contains a magnetic chicane whose chromatic dispersion is used to develop a strong coherent microbunching from the energy modulation impressed upon the electron beam by the FEL interaction in the modulator. The undulator layout for FEL-2 is shown in Fig. 2.

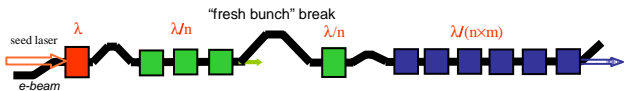


Fig. 2: FEL-2 undulator layout

The selected configuration is based on the so-called “fresh bunch” approach [2], in which the radiation from the first radiator is used to energy-modulate in a subsequent modulator a “fresh” part of the electron beam that did not interact with the external seed. The core design for the first stage of fresh-bunch FEL-2 is extremely similar to that described earlier for FEL-1.

Where the design for FEL-2 fresh bunch layout begins to differ significantly is that the first stage radiator is relatively short (i.e., 2-3 segments) and only brings the

radiation to a sufficient level to provide adequate coherent energy modulation in the following undulator. The basic parameters for the second stage modulator are the same as for the first stage radiator (i.e., 6.5-cm period; 2.3-m segment length). In general, the choice has been made to keep the first stage as short as possible, both for cost reasons and to minimize SASE growth which can increase the incoherent energy spread of the “fresh” portion of the e-beam to be used in the second stage modulator and radiator. The second-stage radiator has a shorter period (5 cm) and is subdivided into 2-m long active APPLE-type undulator segments separated by 1-m breaks. These breaks contain a quadrupole singlet for focusing, a phase shifter, dipole correctors, and diagnostics. The length of the final radiator is somewhat arbitrary; in general it has been presumed for the fresh bunch approach one would want sufficient length for power saturation, i.e., 6 segments at 10-nm wavelength. However, one could certainly increase the output power by adding more radiator segments and possibly also taper the undulator strength.

FEL-1 PERFORMANCE

Figure 3 displays the growth of power at 40-, 60-, and 100-nm wavelengths as predicted by the GENESIS and GINGER codes (each operated in time-independent mode). Electron-beam and seed parameters are reported in the figure caption.

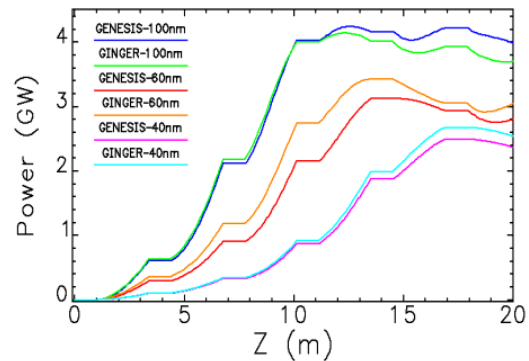


Fig. 3: Power growth as a function of radiator distance for FEL-1 tuned at 100-, 60-, and 40 nm, as predicted by Genesis and Ginger. Electron-beam parameters utilized for the simulation are: energy = 1.2 GeV; current = 800 A; incoherent energy spread (RMS) = 150 keV; normalized emittance = 1.5 mm mrad; input seed power = 100 MW; input seed wavelength = 240-300 nm.

As can be seen in Fig. 3, at the longer wavelengths power saturation is reached well before the end of the sixth section. The simulations show good basic agreement between the GENESIS and GINGER predictions. A factor of about two in output power can be gained by properly tapering the six radiator segments.

In order to get an estimate of output power sensitivity to electron beam and laser parameters, an extensive set of GENESIS and GINGER simulations has been performed varying single parameters at a time.

Parameter	FEL-1	FEL-2
Wavelength range [nm]	100 to 40	40 to 10
Output pulse length (rms) [fs]	≤ 100	> 200
Bandwidth (rms) [meV]	17 (at 40 nm)	5 (at 10 nm)
Polarization	Variable	Variable
Repetition rate [Hz]	50	50
Peak power [GW]	1 to >5	0.5 to 1
Harmonic peak power (% of fundamental)	~ 2	~ 0.2 (at 10 nm)
Photons per pulse	10^{14} (at 40 nm)	10^{12} (at 10 nm)
Pulse-to-pulse stability	$\leq 30\%$	$\sim 50\%$
Pointing stability [μ rad]	< 20	< 20
Virtual waist size [μ m]	250 (at 40 nm)	120
Divergence (rms, intensity) [μ rad]	50 (at 40 nm)	15 (at 10 nm)

Table 1: FEL-1 and FEL-2 expected performance

We present here time-independent calculations in which the input laser seed power and various electron beam quantities were allowed to vary independently around their individual design values (see Table 1) following Gaussian distributions characterized by the following RMS values: mean electron energy: 0.1%; current: 8%; emittance: 10%; energy spread: 10%; input seed power: 5%. Expected output fluctuations are about 22 % (see Fig. 4). The most limiting factor to output stability is represented by the 0.1% input energy fluctuation. Detailed time-dependent start-to-end simulations, including the impact on output stability of seed-bunch time jitter and beam distribution homogeneity, are reported in [3].

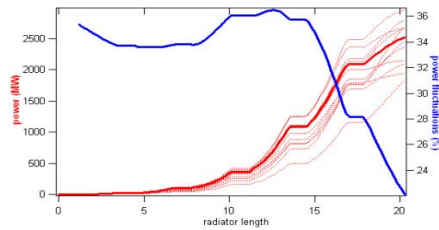


Fig. 4: Power growth for different initial random conditions (red curves, left vertical scale) and associated power fluctuation (blue curve, right vertical scale) vs. radiator distance.

A campaign of time-dependent start-to-end simulations has been performed making use of various electron-beam distributions provided by the FERMI gun and linac groups [4]. Figure 5 shows the GENESIS-predicted output temporal and spectrum profiles at 40-nm wavelength for an optimized (i.e., flat in both energy and current) input electron-beam distribution. The input seed was a 40-fs (RMS) Gaussian at a peak power of 100 MW.

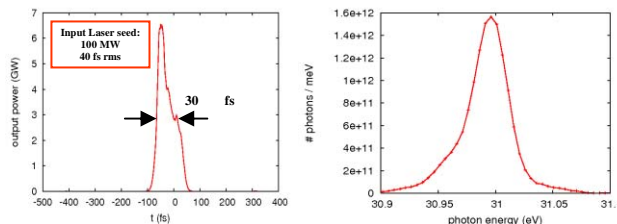


Fig. 5: FEL-1 temporal and spectrum profiles resulting from a GENESIS simulation in time-dependent mode.

The output number of photons per pulse is about $9 \cdot 10^{13}$ with $\sim 80\%$ in single transverse mode. The output pulse length is 30 fs and the spectral bandwidth 17 meV, about a factor of 2.5 above the transform limit

FEL-2 PERFORMANCE

Figure 6 displays the growth of power at 40-, 20-, and 10-nm wavelengths as predicted by the GENESIS and GINGER codes operated in time-independent mode. For a final radiator of six modules (see Fig. 2) deep saturation is reached only at 40 and 20 nm. At 10 nm, the output peak power is 1 GW for 800-A current and 0.35 GW for 500-A beam current (data not shown).

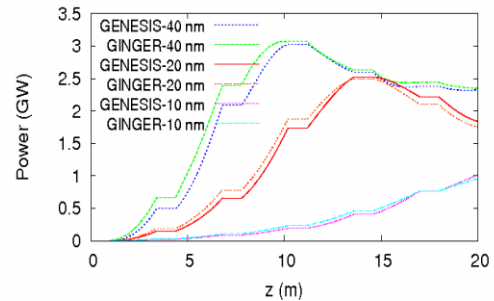


Fig. 6: GENESIS and GINGER time-independent simulations for the FEL-2 radiation power at various wavelengths versus radiator distance in the final radiator for the fresh bunch approach. These runs were done with 800-A beam current and 200-keV initial incoherent energy spread (for the other parameters see caption of Fig. 3).

FEL-2 is typically more sensitive to variations in input parameters than is FEL-1. This is largely due to the shorter wavelengths targeted for FEL-2, which leads to similar displacement errors translating into larger longitudinal phase errors, and there is the additional complexity of having two rather than one stage of harmonic conversion. Furthermore, at shorter wavelengths radiation diffraction is less important, which renders the FEL more sensitive to deviations in the electron orbit and to misalignments. However, it is presently believed that most applications for FEL-2 output will be in the spectral domain where reproducibility is less important and there is a premium for obtaining narrow bandwidth. Consequently, most of

our work on FEL-2 has concentrated utilizing a relatively long (~ 1 ps) electron-beam pulse with a moderate (~ 500 A) current. For the fresh bunch approach, such a long pulse is nearly essential given the practicalities of temporal jitter between the electron beam and input radiation seed. As discussed in [5], flatness of electron-beam phase space and homogeneity of current and energy spread distributions at undulator entrance are essential for obtaining the best output spectral resolution and shot-to-shot stability. An example of output temporal and spectrum profiles at 10 nm based on an optimized input electron-beam is shown in Fig. 7. The obtained number of photons per pulse is about 10^{13} (93% in single transverse mode). The output pulse length is 110 fs (rms) and the bandwidth 5 meV, about a factor of 1.5 above the transform limit. The peak brightness is about 10^{32} photons/ $\text{mm}^2/\text{mrad}^2/\text{sec}/0.1\%$ bandwidth.

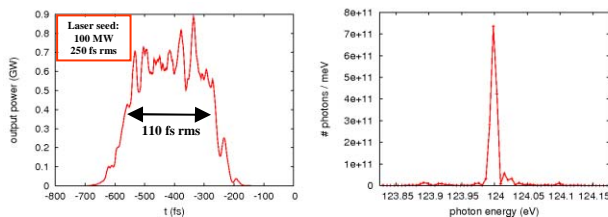


Fig. 7: FEL-2 temporal and spectrum profiles for fresh-bunch scheme resulting from a GENESIS simulation in time-dependent mode.

An alternative scheme we are considering for the FEL-2 is based on the so-called “whole-bunch” approach. Here, the entire electron beam pulse is energy-modulated by the external laser seed and, following the first radiator, there is neither a temporal delay section nor a second modulator. Instead, the electron beam immediately enters a weak dispersive section followed by a second radiator whose FEL resonant wavelength is tuned to an integer harmonic of the first radiator. Due to the relatively small harmonic microbunching at this new wavelength, this second radiator must operate deep in the exponential gain regime. Thus, to keep the exponential gain length and power saturation lengths acceptably small, the energy modulation produced by the first (and only) modulator must be relatively small compared to $\rho_2 \gamma$ where ρ_2 is the FEL parameter for the second radiator (generally $\sim 1 \times 10^{-3}$). This small energy modulation means that at entrance to the first radiator the e-beam will have a smaller microbunching level relative to that of the fresh bunch scheme.

Consequently, the whole bunch approach can essentially fail (in terms of the needed second radiator undulator length for saturation) if the initial energy spread becomes too large. Moreover, because the microbunching level is small at the beginnings of both the first and second radiator, the relative strength of the shot noise microbunching is much higher and the final SASE strength can be 2 or more orders of magnitude greater in the whole bunch approach than in the fresh bunch approach. The main advantage of such a scheme is that it

is less sensitive to shot-to-shot fluctuations of the relative timing between the e-beam and external seed laser. The output temporal profile and spectrum obtained at 10 nm using the whole bunch configuration are shown in fig. 8. The initial electron beam distribution is the same as for the fresh-bunch scheme (see Fig. 7).

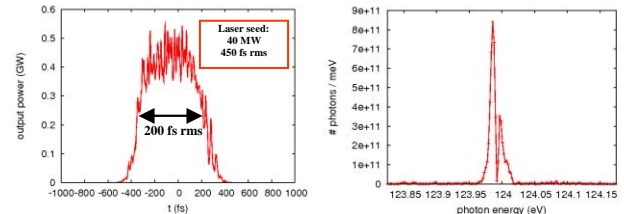


Fig. 8: FEL-2 temporal and spectrum profiles for whole-bunch scheme resulting from a GENESIS simulation in time-dependent mode.

In this case the obtained number of photons per pulse is about 10^{13} (93% in single transverse mode). The output pulse length is 200 fs (rms) and the bandwidth 4 meV. This gives a result which is a factor about 2.5 above the transform limit.

CONCLUSIONS

We have presented the current design configurations for both FELs of the FERMI@Elettra project. Design optimization has been driven by users’ requests (see table 1), i.e. short pulse and low shot-to-shot power fluctuations for FEL-1, and high energy resolution for FEL-2. We also give results derived from both time-independent and time-dependent simulations, using reference parameters and electron-bunch distributions as provided by the FERMI start-to-end group.

REFERENCES

- [1] L. H. Yu *et al.*, *Phys. Rev. Lett.* **91**, 074801 (2003).
- [2] I. Ben-Zvi, K.M. Yang, and L.H. Yu, *Nucl. Inst. Meth. A* **318**, 726 (1992).
- [3] E. Allaria, G. De Ninno, M. Trovo, these proceedings, Paper MOPPH058.
- [4] S. Dimitri *et al.*, these proceedings, Paper THBAU03.
- [5] W. Fawley, G. Penn, and A. Zholents, these proceedings, Paper THAAU01.

START-TO-END TIME-DEPENDENT STUDY OF FEL OUTPUT SENSITIVITY TO ELECTRON-BEAM JITTERS FOR THE FIRST STAGE OF THE FERMI@ELETTRA PROJECT

E. Allaria, G. De Nino, M. Trovó, Sincrotrone Trieste, 34012 Trieste, Italy.

Abstract

Sensitivity of the output laser pulse to electron-beam jitters is one of the major issues affecting the expected performance of both SASE and seeded FELs. Focusing on the first stage of the FERMI@Elettra project, in this paper we present results of time-dependent numerical simulations in which the codes GENESIS and GINGER have been used to run a large number of electron-beam distributions generated at the gun by the code GPT and propagated through the linac using the code ELEGANT.

INTRODUCTION

The FERMI@ELETTRA project is dedicated to the development of a FEL facility based on the principle of harmonic up shifting of an initial “seed” signal in a single pass [1]. The first stage of the project will be a single harmonic cascade tuneable in the 40-100 nm range. At present, it is believed that the major application for FEL-1 will involve time-domain experiments such as pump-probe interactions and possibly nonlinear phenomena. Consequently, the requirements for FEL-1 are more related to total photon number per pulse (*i.e.*, $0.4 - 2 \times 10^{14}$) and pulse duration (20-100fs) than they are to spectral bandwidth. Another important parameter associated with FEL-1 time-domain experiments is shot-to-shot repeatability [1]. Time-independent simulations of the FEL process based on the Fermi layout show a strong sensitivity of the output power with respect to many electron-beam parameters [2]. Jitter studies performed using jitter of input parameters as estimated by the linac group of the Fermi project provided fluctuation on the output power that can be greater than 20% for the radiation at 40nm. However, while time-independent simulations can give just an indication of the FEL performance, more accurate investigations should rely on “start-to-end” (S2E) simulations, that begin at the emitting cathode and end at the undulator exit.

In collaboration with the injector and linac groups of the Fermi project, dedicated simulations have been performed considering fluctuations on main machine parameters [3]. To examine the effects of injector and accelerator jitters upon the shot-to-shot, time-resolved properties of the output FEL-1 radiation, 100 individual files of 1M macroparticles were propagated starting from the injector (GPT code) through the linac (Elegant code). Nominal beam parameters are reported in the following table [3,4].

Table1: Nominal electron-beam parameters for the first stage (FEL-1) of the FERMI project

Parameter	Value	Units
Input Seed power	100	MW
Electron Beam Energy	1.2	GeV
Peak current	800	A
Uncorrelated energy spread (“slice” value)	150	KeV
Norm. Transverse Emittance (“slice” value)	1.5	mm-mrad
Electron Bunch Length (flat portion)	0.6	ps

Each file included the effects of random jitter in the individual injector and accelerator cell voltages. The jitter follows Gaussian distributions with variances set by the budget allowances allocated by the gun and linac groups.

GINGER and GENESIS time-dependent simulations for the FEL-1 lattice tuned at 40 nm were performed over a large time window with high resolution. For each jittered file, simulations were done using artificial macroparticles created from the time-dependent envelope quantities previously determined by the *elegant2genesis* code and also using directly the ELEGANT particles.

It is important to note that we here only consider the effect of the jitter on the electron bunches, without taking into account any jitter source on the seed laser.

ANALYSIS OF ELEGANT JITTERED FILES

The 100 jittered files have been produced starting from 100 GPT files that consider the possible jitter sources in the gun. Those files have been propagated through the linac with ELEGANT. Output distributions have been pre-processed in order to evaluate the resulting jitter in bunch arrival times (Fig.1).

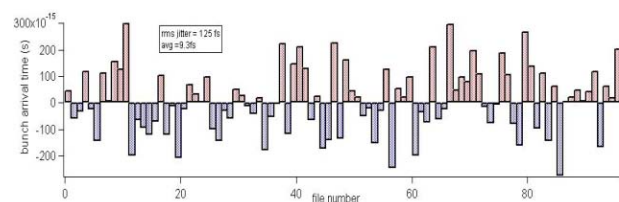


Figure 1: Arrival time jitter of the 100 elegant files with respect to the arrival time of the nominal file.

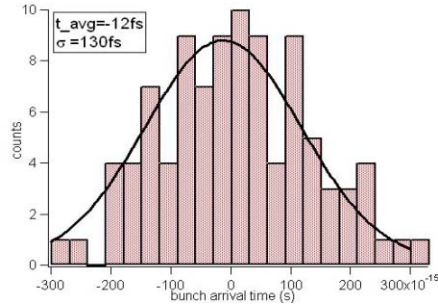


Figure 2: Distribution of the arrival time jitter reported in Fig.1; data can be fitted with a Gaussian distribution, whose sigma is about 130fs.

The analysis shows a distribution with an rms jitter of about 130 fs, which is close to the one predicted by LiTrack simulations [4]. These data can be fit with a Gaussian distribution (Fig.2).

By plotting the electron energy and current profiles of the 100 bunches taking into account of the arrival time (figs.3-6) it is evident that it exists a time window of the order of 400fs where the fluctuations of electron parameters due to the jitter arrival time are small. This is the “useful” part of the bunches to be used for the FEL process. We also report the analysis of the electron beam properties (electron energy, current, emittance, energy spread) on that window.

The electron mean energy, γ , in the useful part of the bunch (from -200fs to 200fs, see fig. 3,4,5) presents a distribution with an rms of 0.09%, in agreement with the values predicted by the linac group.

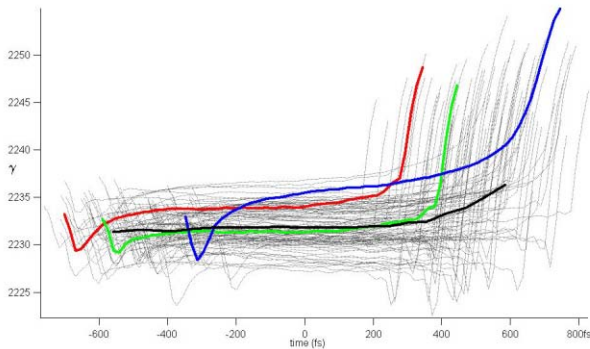


Figure 3: Temporal profile of the electron beam mean energy of the 100 jittered ELEGANT files.

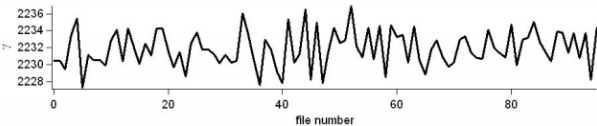


Figure 4: Average of the electron mean energy of the jittered electron bunch calculated in the useful time window (-200fs; 200fs).

The current distribution shows an rms value (6.6%) that is slightly lower than the one predicted by the linac group (8%).

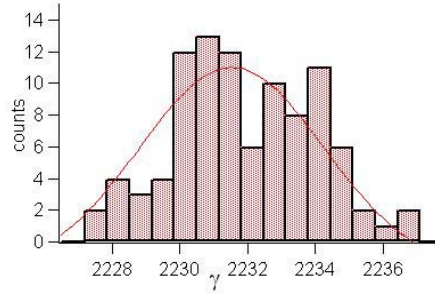


Figure 5: Distribution of the average electron mean energy of the useful part of the jittered bunches; data can be fitted with a Gaussian distribution whose sigma is 0.09%.

Similar analysis have been performed for other electron beam properties, (emittance, energy spread, ..). As for emittance, data show a distribution with an rms value which is close to the one predicted (about 12%). The energy spread, instead, is slightly affected by the temporal jitter of bunches and the rms distribution shows a larger value (almost 20% instead of 10%). Calculated electron-beam average values and corresponding standard deviations are reported in Table 2.

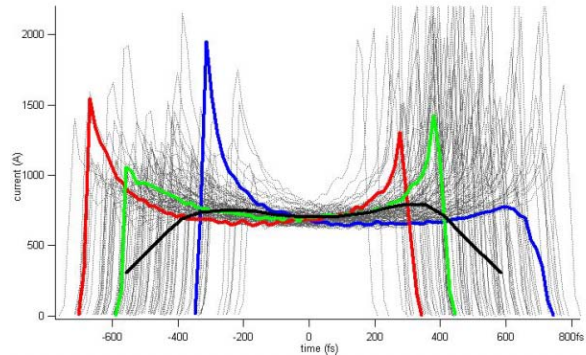


Figure 6: Temporal profile for current of the 100 jittered files.

Table 2: Average values and corresponding standard deviations for the main electron beam parameters extracted from time-dependent simulations.

Quantity	Mean Value	Std. Dev.
Gamma	2231.9	0.09%
Current (A)	718	6.6%
Incoherent energy spread	0.33	19.5%
Normalized emittance	1.35	12.4%

TIME-DEPENDENT FEL SIMULATIONS OF JITTERED FILES

For the FEL simulation we used the nominal setup of FEL1 [1] that has been optimized in terms of aw and R56 in order to maximize the output power extracted from an

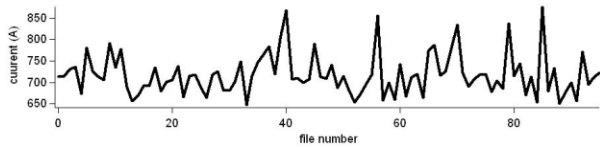


Figure 7: Average of the electron bunch current calculated on the useful part of the jittered files (from -200fs to 200 fs).

ideal bunch, whose parameters are equal to the average values reported in Table 2.

Time-dependent simulations using this optimized setup for the jittered files show a quite high sensitivity to beam jitters (e.g., about 50% of fluctuation in the output power), which is far from what it is predicted by time-independent simulations [2].

A new optimization has been necessary in order to find a setup that minimizes the effect of the beam jitters. In order to reduce the sensitivity of the FEL output power we slightly changed the tuning of the radiator, setting a smaller value of a_w .

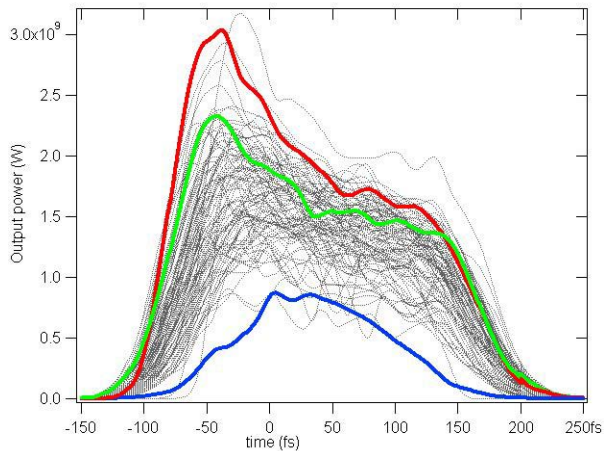


Figure 8: Temporal profiles for the FEL output radiation at 40 nm obtained from GINGER simulations using the jittered ELEGANT files; Red, Green and Blue curve refer to bunches reported with the same colors in figs. 3-6.

The setup utilized for simulations is the following: a seed laser of 100MW with a Gaussian temporal profile (100fs rms), the modulator tuned at 240nm, the dispersive section set with a $R56=19e-6$ and the radiator tuned at 40 nm.

Figure 8 displays the output power profiles obtained from the 100 jitter bunches, while Fig.10 shows the corresponding output spectra. Red, Green and Blue traces

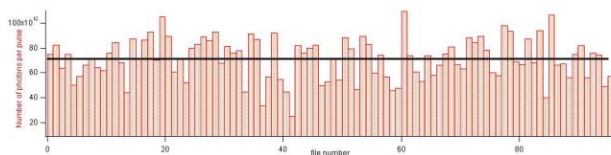


Figure 9: Number of photons per pulse obtained from the FEL simulation at 40 nm. Data show an average number of photons of the order of 70e12 with an rms fluctuation of about 23%.

in Fig.8,10 refers to the electron bunches reported in Red, Green, Blue in Figs. 3-6.

The analysis of the FEL output power has been performed by integrating the pulse profile in order to calculate the number of photons of each FEL pulse. Figure 9 report the number of photons of FEL output pulses for each of the 100 jittered electrons bunches. The statistical analysis of data shows a distribution which is close to a Gaussian centered at 70e12 photons per pulse with a standard deviation of about 23%.

By looking at the output spectra of the FEL pulses, one can see that the jitter of the input electron-beam parameters induces a fluctuation of the central wavelength. However, such a fluctuation is about a factor 3 smaller than the average bandwidth and, as a consequence, is not affecting too much the FEL performance (see Fig.10 and Tab.3). Considering the

$$\text{equation for the undulator resonance } \lambda = L_w \cdot \frac{(1 + a_w)}{2\gamma^2}$$

we can derive that, if the emission wavelength is defined by the resonance wavelength of the radiator, the jitter in wavelength, λ , should be two times that associated to the jitter in electron mean energy, γ . This is not true in a seeded FEL where the emission wavelength is defined by the seeding laser and only partially by the undulator resonance wavelength.

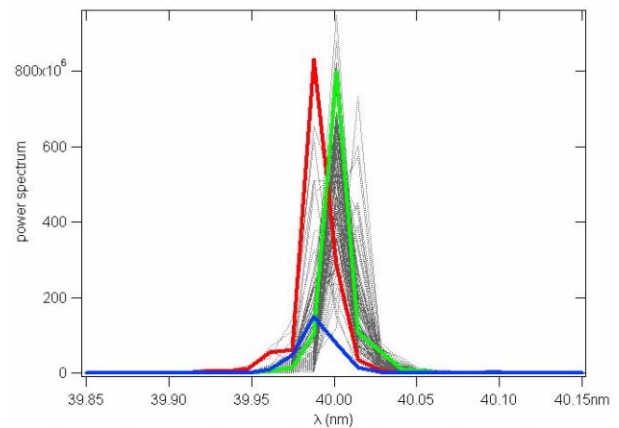


Figure 10: Output power spectra obtained from the FEL simulations of the jittered files.

Our results are in agreement with predictions and the obtained fluctuation for the wavelength is very lower compared to the fluctuation of the mean energy of the input jittered bunches.

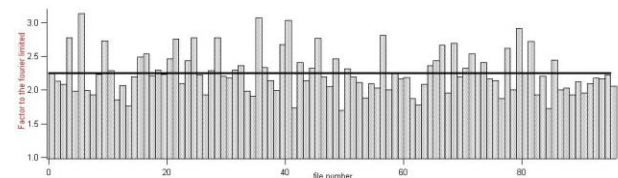


Figure 11: Factor to the Fourier transform limit of the FEL output pulses for the jittered ELEGANT files.

We also characterized the FEL output pulses in terms of how close they are to the Fourier limit. In Fig. 11 we report the distance of each FEL output pulse with respect to the Fourier limit for the 100 simulated jittered files. The average Fourier factor for the simulated data is 2.2 and the standard deviation of the distribution is about 13%.

Table 3: Statistics of the 100 FEL pulses.

Quantity	Mean Value	Std. Dev.
Average pulse width (fs)	73.2	
Average photon number	7.1e+13	23.3%
Average central wavelength (nm)	40.0019	0.013%
Average bandwidth	0.033%	
Fourier factor	2.2	13%

In order to verify the prediction of time independent simulations, which indicate the jitter in the mean electron energy as the most limiting factor for achieving a good output stability, in Fig. 12 we plot the number of photons per pulse vs the average electron-beam energy.

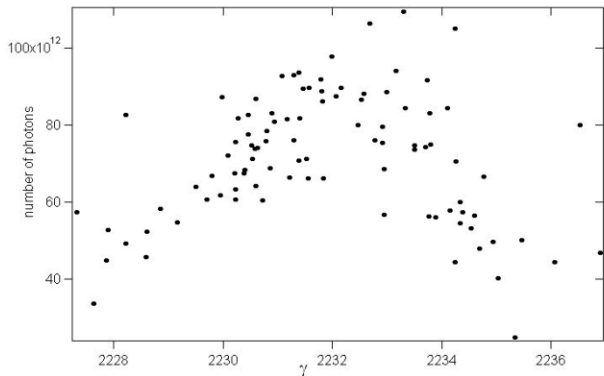


Figure 12: Number of photons per pulse vs the average electron mean energy of the corresponding electron bunch.

The good correlation between the two quantities clearly confirms the high sensitivity of the FEL output to the electron mean energy.

CONCLUSIONS

An extensive campaign of start-to-end simulations for the first stage of the FERMI@Elettra project has been presented. Results show a quite strong sensitivity of FEL characteristics to shot-to-shot jitters of electron-beam parameters.

The effect of the proposed strategies for the reduction of the output power fluctuation by means of sophisticated radiator configuration (tapering) or linear chirping of the electron bunches will be considered in a forthcoming work.

REFERENCES

- [1] C. Bocchetta *et al.*, MOPPH054 proceedings of this conference.
- [2] W. Fawley *et al.*, Sincrotrone Trieste tech. note, ST/F-TN-06/16.
- [3] P. Craievich, S. Dimitri, G. Penco, private communication.
- [4] M. Cornacchia *et al.*, Sincrotrone Trieste tech. note, ST/F-TN-06/15.

THE TEST FACILITY FOR HARMONIC GENERATION AT THE MAX-LAB INJECTOR LINAC *

Mathias Brandin, Tue Hansen, Sara Thorin, Sverker Werin, MAX-lab, Lund
 Michael Abo-Bakr, Johannes Bahrtdt, Kathrin Goldammer, BESSY GmbH, Berlin
 Jörgen Larsson, Anne L'Huillier, Anders Persson, Claes-Göran Wahlström, Department of Physics,
 Lund University.

Abstract

A test facility for harmonic generation is being built at MAX-lab. The third and fifth harmonic, at 90 and 53 nm respectively, will be created using a fs seed laser at 266 nm. The MAX-lab injector will be operated at 400+ MeV with a photo RF gun and the optics will be retuned to achieve compression. An optical klystron will be installed comprising of two undulators and a chicane.

OVERVIEW AND SCOPE

The BESSY FEL project [1] and the MAX IV proposal [2] are both focused on seeded FEL sources as part of the facilities. In the aim of improving the designs a decision was made to build a test facility for harmonic generation at MAX-lab.

The MAX injector system [3] is a recirculated linac with energy capabilities up to 500 MeV. Few other locations have this linac energy available for a test facility. The joint effort includes simulations, a new electron source, laser systems, an optical klystron and experimental activities.

The test facility is intended to use an electron beam of at least 400 MeV with an emittance of 3 μmRad and a bunch length around 500 fs. It will be injected into an optical klystron consisting of a modulator undulator, a chicane and a radiator undulator. A fs seed laser at 266 nm will be used and harmonic generation at 90 nm and later 53 nm will be studied.

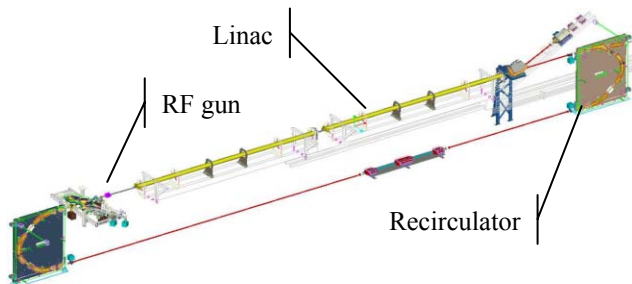


Fig 1. The MAX injector.

The FEL Principle

The FEL section consists of an Optical Klystron where in the first undulator, called modulator, the electron beam co-propagates with a strong seed laser of 266 nm

* This work has been partially supported by the Swedish Research Council and by the European Commission in the Sixth Framework Program, Contract No. 011935 – EUROFEL.

wavelength and is modulated in energy. The particles then pass through the magnetic chicane which serves as a dispersive element. It consists of four dipole magnets and introduces an energy-dependant longitudinal delay of the electrons: the unmodulated particles are bent into a longer trajectory than the higher energy particles so that the beam is redistributed longitudinally. The process is referred to as “(micro)bunching”. The bunching is tunable to achieve a maximal Fourier component at either the resonant frequency of the modulator or at higher harmonics. In the MAX-lab FEL experiment, the third harmonic will be used, thus efficiently shortening the output wavelength of the FEL to 88 nm. In the second undulator, called radiator, the bunched beam will then emit intense, coherent radiation at the shorter wavelength with an output power in the megawatt-range. Substantial development of this method, HGHG, has been done at BNL [4].

THE ACCELERATORS

While most of the accelerator systems are already at hand at MAX-lab some additions and alterations are necessary. These mainly regard a new photo cathode RF gun [5] and finding a new optics [6] which creates compression and transports the bunch to the optical klystron.

The Gun Pre Injector

In order to produce a transversely and energetically collimated electron beam, the electrons will be generated in a low emittance photocathode gun. The gun is a 3 GHz 1.6-cell cavity, mounted slightly off axis, with a copper cathode illuminated by a ten ps long laser pulse at 266 nm. This produces bunches with a total charge of 0.5 - 1 nC. The beam parameters at the exit from the gun can be seen in table 1.

Table 1: Beam parameters after the gun (simulated)

Energy	3.7 MeV
Energy spread	3 %
Normalized emittance ϵ_N	3 mm mrad
Charge	0.5 nC
Pulse length	11 ps
Peak current	45 A

The emittance compensation scheme adopted is similar to the LCLS [7]. Results of the tracking are shown in fig 2.

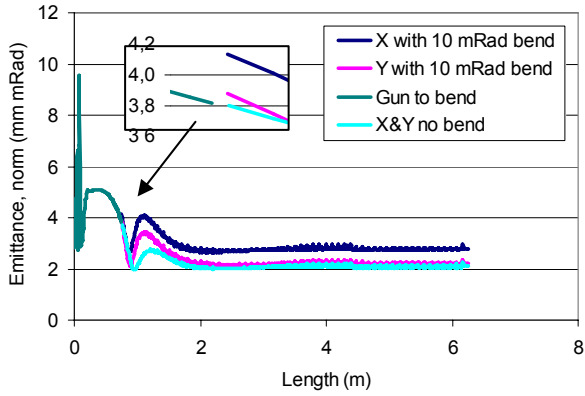


Figure 2: Emittance (normalised) (1 nC, 3.7 MeV, 10ps). off axis compensation (10mR) at 0.75 m and linac from 1m.

Linac and Recirculator

The linacs and recirculator system in the MAX-injector have been in operation for several years. They routinely deliver 380 MeV as injector for MAX I and II. They are currently being conditioned above 400 MeV.

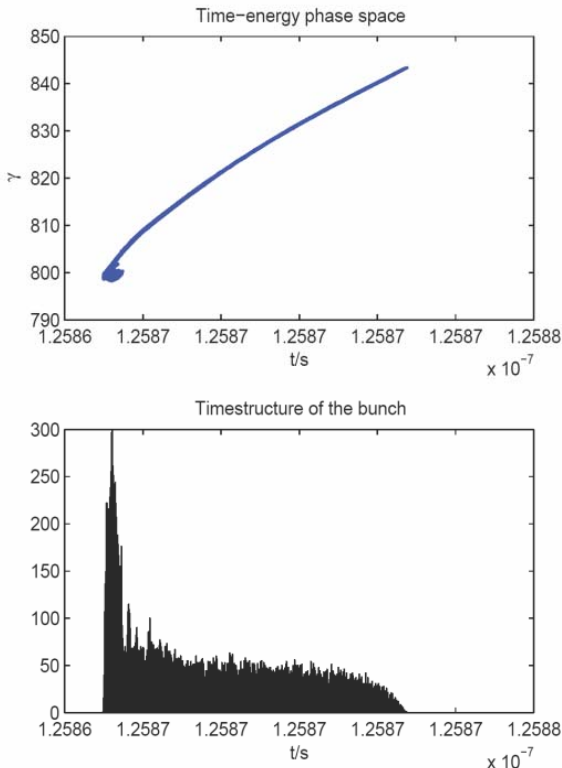


Figure 3: Electron bunch after the recirculator.

Since a high peak current is important for FEL efficiency, the electron bunches have to be compressed after the gun. Bunch compression is achieved using the linacs and the magnetic optics in the recirculator. The

electric field in the linac is given such a phase that an energy chirp is induced in the electron pulses. Through the quadrupoles and dipoles in the recirculator block, this chirp can then be rotated time wise to result in a very short pulse. Because of the sinusoidal shape of the accelerating field, the energy spread will not be completely linear, but some second order effects will occur. These second order effects can be compensated by the use of sextupole magnets which introduce second order corrections and straighten the energy chirp up to a line. In the MAX-injector sextupoles are incorporated in some of the quadrupoles in the recirculation blocks and are not separately tuneable. They can thus not be used to completely linearize the second order effects, but they do contribute a bit towards higher peak brilliances. With separately tuneable sextupoles linearization more corresponding to that of a higher order cavity can be done.

Approximately 25% of the bunch charge can be confined within the usable part of the bunch. This way bunch lengths shorter than 300 fs and peak currents of 300 A can be obtained. Table 2 and figure 3 show the beam at the exit of the recirculator.

Table 2: Beam parameters after the recirculator

Energy	400 MeV
Energy spread	0.1 %
Normalized emittance $\epsilon_{Nx}, \epsilon_{Ny}$	3 mm mrad, 8 mm mrad
Bunch charge in peak	0.12 nC
Pulse length	400 fs
Peak current	300 A

Transport

The transport from the injector to the undulator section is about 40 m and includes a vertical lift of the beam from the cellar to the ground floor. This lift is done with an achromatic dogleg [8] consisting of two 15 degree bends with 5 quadrupoles in between. The middle quad is used to control the beta-function while the two outer ones are used to close dispersion after the second bend. To avoid space charge effects in the centre of the dogleg, where the beta function can hit a very low minimum, the two quads on either side of the middle are used for modification of the beta function.

THE OPTICAL KLYSTRON

Existing magnet structures will be used to build the undulators. A pure permanent magnet (PPM) structure has been loaned from the ESRF to be used in the modulator. The radiator will be equipped with the APPLE structure of the BESSY UE56-1. The parameters are summarized in table 3.

Table3: Parameters of the undulators and the chicane

Modulator	
Period length	48 mm
Number of periods	30
Minimum gap	10 mm
Maximum K-parameter	4.3
Radiator	
Period length	56 mm
Number of periods	30
Minimum gap	12 mm
Maximum K-parameter	4.3
Chicane	
Number of magnets	4
Type of magnet	H-frame, electromagnet
Gap	15 mm
Maximum field	0.2 T
Distance between magnets	400 mm

Both undulators will have a motorized gap drive. The radiator provides also a motorized phase variation for polarization control. The modulator is moved only in case of an electron energy change whereas the radiator has to be tuned also when the harmonic number of the radiation or the state of polarization is changed.

The Chicane

The magnetic chicane converts the energy modulation of the electron beam into a spatial modulation. Optimum bunching is achieved if the energy modulation dominates the energy spread times the harmonic number n :

$$\Delta\gamma/\gamma \geq n \cdot \sigma_\gamma$$

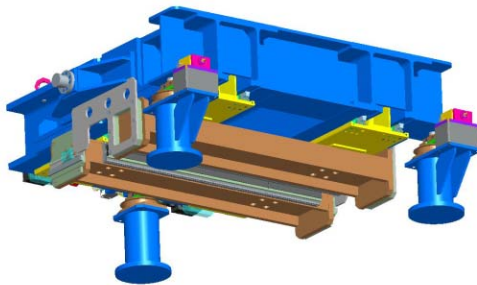


Figure 4: Modulator in operating position.

With a relative energy spread of $\sigma_\gamma = 5 \cdot 10^{-4}$ an energy modulation of at least $\Delta\gamma/\gamma = 1.5(2.5) \cdot 10^{-3}$ is needed to operate on the third (fifth) harmonic. This defines the laser power.

The maximum bunching appears for a path length difference of $\Delta L = \lambda_{\text{photon}}/4$ between modulated and non modulated electrons. The chicane is optimized such that $\Delta L = \lambda_{\text{photon}}^{1st}/4 = 67 \text{ nm}$ can be reached with 500 MeV electrons and an energy modulation of $\Delta\gamma/\gamma = 1.0 \cdot 10^{-3}$.

For higher harmonics (shorter wavelengths) $\Delta L \geq \lambda_{\text{photon}}/2$ can be produced and overbunching effects can be studied.

Mechanical Layout

The electron beam height at the HGHG-FEL is only 400 mm and conventional undulator carriages cannot be used. Therefore, a new carriage has been developed which can cope with this geometry (figure 4). The same structure is used for both undulators.

The two undulators will be measured and shimmed at the existing measurement bench at BESSY. For this purpose the undulators have to be flipped into upright orientation (figure 5). At MAX-lab the final magnetic measurements will be performed in the operating position using a pulsed wire system.

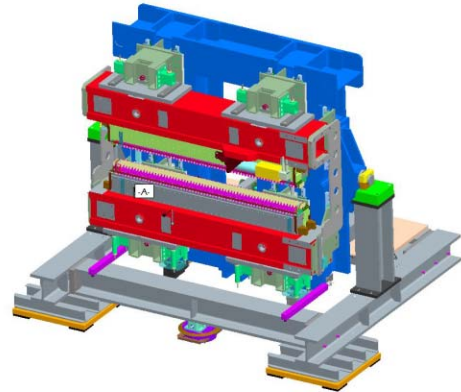


Figure 5: Radiator in measurement position.

LASER SYSTEMS

A combined laser system for the gun and the seeding of the HG-FEL has recently been sent out with an invitation to tender. We foresee a common system locked to the RF of the accelerators to better than 1 ps. The system should deliver 500 μJ in a 10 ps pulse at 266 nm to the RF gun and 100 μJ in a 300 fs pulse at 266 nm to the seeding. The solution is up to the supplier while the basic thought is a centrally located oscillator locked to the accelerator RF-system and an optical distribution to the amplifiers. (Due to the commercial actions the information is minimized. Please contact the authors for more information: sverker.werin@maxlab.lu.se)

DIAGNOSTICS

The diagnostics have two main duties. The first is to control the electron beam performance and the second to assure overlap in time and space of the laser and electrons. Table 4 shows the intended methods to be used to approach the different areas.

In a recent test set-up the uncompressed bunch length at the MAX injector was measured to $\sigma = 2.3$ ps. The technique used was detecting coherent transition radiation with an interferometer [9]. This set up will now be finalized to be able to diagnose sub ps pulses.

Table 4. Diagnostics

Feature	Method
Energy spread	Dispersive section
Emittance	Q scans
Bunch length	CTR and interferometer
Current/charge	Beam transformers, Faraday cage
X and y positions	YAG/OTR screens
Alignment	Apertures for spontaneous and laser beams
Synchronization/time	Electro-optical methods Energy spread
Beam loss	Cherenkov fibre

THE FEL SIMULATION

For realistic simulation of the FEL, the particles were tracked all the way through gun, linac, beam transport and the undulator section using ASTRA [10], elegant [11] and GENESIS [12]. In order to study time-dependant effects of FEL interaction, the 6-dimensional phase space file from elegant was converted into a GENESIS input file by cutting out the seeded part of the beam ± 50 fs and split it up into a collection of temporal slices. For each slice, the relevant beam parameters were calculated externally and delivered to a GENESIS compatible input file.

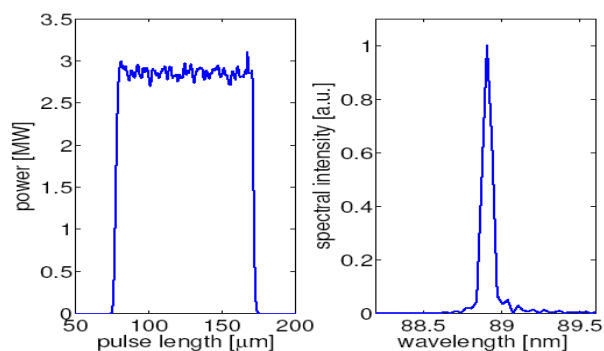


Figure 6: Temporal and spectral power distributions of FEL pulse at exit of radiator.

Simulation Results

Due to the fact that the simulation work is still ongoing, the results for the FEL section presented in this section were achieved without a formal start-to-end-transport of the original input bunch from ASTRA to GENESIS. However, the beam parameters gained by the slice analysis were used to perform fully time-dependant simulations taking into account the seed laser beam temporal profile. A 95%-emittance of 3 mm mrad (normalized) was assumed. The parameters used to model the undulator section and the magnetic chicane are listed in table 3.

Using a seed laser of 150 MW peak power and a FWHM flat top length of 300 fs, the necessary energy

modulation can reliably be established within the modulator. When optimizing the magnetic chicane for maximal bunching at the third harmonic, the radiator lases at 88 nm with a power level in the range of 1-10 MW. Figure 6 shows the temporal and spectral power distribution at the end of the radiator.

SUMMARY

A test facility for FEL and HGHG is currently being built at MAX-lab. The coming year will be spent on installation of undulators, the new pre injector, build up of the laser systems and finalizing the diagnostics. The aim of the facility is to test and develop the techniques, but also to already at an early stage of the BESSY FEL and MAX IV projects practically address the processes.

Simulations and development of beam optics are also part of this process.

An important side effect of this project is to start the process of joining forces between the accelerator and laser science. The future of accelerators lies in many ways in starting to use lasers as natural parts of accelerator installations.

The capabilities of this installation are also such that new ideas and a continuation after the initial generation of the 3rd harmonic are a natural continuation.

REFERENCES

- [1] BESSY TDR, D. Kraemer et al., 2004.
- [2] MAX IV Conceptual Design report, MAX-lab, 2006.
- [3] S. Werin et al., Commissioning of the 500 MeV Injector for MAX-lab, EPAC 2004
- [4] L. H. Yu, J. Wu, Nucl. Instr. and Meth. in Nucl. Res. A 483 (2002) 493.
- [5] S. Werin et al., "Design of a New Preinjector for the MAX Recirculator to be used in EUROFEL", EPAC 2006
- [6] S. Thorin et al., "Simulations for the FEL Test Facility at MAX-lab within EUROFEL", EPAC 2006
- [7] R. Boyce, D.H. Dowell, J. Hodgson, J.F. Schmerge, N. Yu, Design Considerations for the LCLS RF Gun, LCLS TN 04-4 (2004)
- [8] J. England et al., Sextupoles Correction of the Longitudinal Transport of Relativistic Beams in Dispersionless translating sections, Phys. Rev. ST Accel. Beams 8, 012801 (2005).
- [9] M. Brandin, B. Nelander, S. Werin, Measurement and diagnostics on the MAX recirculaor, EPAC 2006
- [10] K. Flöttman "ASTRA User Manual", September 18, 2000, www.desy.de/~mpyflo
- [11] M. Borland, "elegant: A Flexible SDDS-Compliant Code for Accelerator Simulation" Advanced Photon Source LS-287, September 2000.
- [12] S. Reiche, "Numerical Studies for a Single Pass High Gain Free-Electron Laser", PhD Thesis, Uni Hamburg, corona.physics.ucla.edu/~reiche/links.html

COHERENT X-RAY PRODUCTION BY CASCADING STAGES OF HIGH GAIN HARMONIC GENERATION FREE ELECTRON LASERS SEEDED BY IR LASER DRIVEN HIGH-ORDER HARMONIC GENERATION*

Juhao Wu[†] and Paul R. Bolton, SLAC, Menlo Park, CA 94025, USA.

Abstract

Coherent x-ray production achieved by a seeded free electron laser (FEL) with cascaded high gain harmonic generation (HG) is important for next generation development of synchrotron light sources. We examine the feasibility and some features of FEL emission seeded by a high order harmonic of an intense infrared conventional laser source (HHG). In addition to the intrinsic FEL chirp phenomenon, the longitudinal profile and spectral bandwidth of the HHG seed are modified significantly by the FEL interaction well before saturation occurs. This smears out original attosecond pulselet structure. As an example, we describe a cascaded HG scheme for coherent x-ray FEL generation that is seeded by the twenty-seventh harmonic of an ultrashort 800 nm laser pulse with 10 fs rms duration. By cascading two stages of HG, 15 GW peak power FEL emission at 0.3 nm can be produced with 90 MW peak power radiation at 0.1 nm via the non-linear harmonic generation.

INTRODUCTION

Short-wavelength Free-electron Lasers (FELs) are perceived as the next generation synchrotron light sources. Self-Amplified Spontaneous Emission (SASE) [1, 2, 3, 4], is the dominating approach to produce an x-ray FEL (XFEL). While it has good transverse coherence, the SASE FEL pulses are composed of a series of ultrashort spikes due to a short longitudinal coherent length. To improve the longitudinal coherence, various approaches have been proposed. Among them, a cascaded high gain harmonic generation (HG) FEL [5, 6, 7, 8, 9, 10] looks promising by invoking high order harmonic generation of an infrared (ir) laser (HHG) as the seed. In this paper, we study an HHG seeded FEL. This is of particular interest [11], since HHG can provide a uv to soft x-ray seed, making a coherent hard XFEL feasible.

HHG SEEDED HG FELS AT LCLS

HHG Seed: Attosecond Structure and Smearing Effect

HHG generates an electric field comprised of multiple harmonic orders, s and multiple time pulselets, n expressed

* The work was supported by the US Department of Energy under contract DE-AC02-76SF00515.

[†] jhwu@SLAC.Stanford.EDU

as the following double summation [12, 13]:

$$E_{\text{HHG}}(t, z) = \sum_s E_{s,0} e^{i(k_s z - \omega_s t)} e^{-i\mathcal{B}_s \omega_s^2 t^2} \times \sum_{n=-N}^N e^{-\frac{t_n^2}{4\sigma_{t,0}^2}} e^{-\alpha_s \omega_s^2 [(t-t_n) - z/c]^2}, \quad (1)$$

where for each order, s we sum over the temporal sequence of $2N + 1$ pulselets for which $n \in [-N, N]$. Because of temporal coherence of a group of harmonic orders, the pulselets can exhibit attosecond structure (with periodicity of $\tau/2$), limited by the relative amplitudes and phases of the different harmonic orders. The order dependent parameter, \mathcal{B}_s accounts for the small intrinsic chirp that characterizes each harmonic order [14]. In Eq. (1), $t_n = n\tau/2$ with τ being the period of the unchirped ir pulse (2.67 fs at 800 nm); $\sigma_{t,0}$ is the ir pulse rms duration; k_s and ω_s are the wavenumber and angular frequency of the s^{th} harmonic; and $\alpha_s = (4\sigma_{t,s}^2 \omega_s^2)^{-1}$ with $\sigma_{t,s}$ being the rms duration of each pulselet in the HHG pulse. Typically $\sigma_{t,0} \approx 10$ fs and $\tau/20 \leq \sigma_{t,s} \leq \tau/2$ for a single pulselet, where the lower limit assumes relative phase synchronization of a harmonics group [12, 15]. In this paper, we consider only a single harmonic order, s as the carrier frequency and for simplicity, we neglect the harmonic chirp ($\mathcal{B}_s \approx 0$). The HHG field expression then simplifies to:

$$E(t, z) = E_{s,0} e^{i(k_s z - \omega_s t)} \sum_{n=-N}^N e^{-\frac{t_n^2}{4\sigma_{t,0}^2}} \times e^{-\alpha_s \omega_s^2 [(t-t_n) - z/c]^2}, \quad (2)$$

which represents an attosecond pulselet train (APT) derived from the amplitude modulation of carrier frequency, ω_s . We use $\sigma_{t,0} = 10$ fs and $\sigma_{t,s} = \tau/8 \approx 334$ attosecond in the Fourier-transform limit. In this case, it is important to note that, although the central carrier frequency of the seed is a single harmonic, the transform limited seed spectrum also includes components from several neighboring harmonic orders [16]. A multi-pulselet HHG seed is the sum of many single pulselets. We address the single pulselet at $t_n = 0$ for $n = 0$ so that $E_s(t, z = 0) = E_{s,0} \exp(-i\omega_s t - \alpha_s \omega_s^2 t^2)$, assuming for simplicity that the single harmonic pulselet is transform-limited, *i. e.*, $\sigma_{t,s} \sigma_{\omega,s} = 1/2$, so that the rms bandwidth $\sigma_{\omega,s} = \sqrt{\alpha_s} \omega_s$. Since each pulselet is ultra short, the spectral bandwidth is broad. The seeded FEL solution reads [17]

$$E_{\text{FEL}}(t, z) = E_{0,\text{FEL}} e^{\rho(\sqrt{3}+i)k_w z} \quad (3)$$

$$\times e^{i(k_s z - \omega_s t)} e^{-[\alpha_{s,f}(z) + i\beta_{s,f}(z)]\omega_s^2(t-z/v_g)^2},$$

where $v_g = \omega_s/(k_s + 2/3k_w)$ is the group velocity of the FEL light,

$$\alpha_{s,f}(z) = \frac{1}{4\sigma_{t,s,f}^2(z)\omega_s^2}, \quad (4)$$

and

$$\beta_{s,f}(z)^2 = \alpha_{s,f}(z) \frac{\sigma_{\omega,s,f}^2(z)}{\omega_s^2} - \alpha_{s,f}(z)^2 \quad (5)$$

with

$$\left\{ \begin{array}{l} \sigma_{t,s,f}(z) = \sigma_{t,s} \sqrt{\frac{3+6R(z)^2+4R(z)^4}{3[1+R(z)^2]}} \\ \sigma_{\omega,s,f}(z) = \frac{\sigma_{\omega,s}}{\sqrt{1+R(z)^2}} \end{array} \right., \quad (6)$$

with

$$R(z) \equiv \frac{\sigma_{\omega,s}}{\sigma_{\omega,\text{GF}}(z)}, \quad (7)$$

and

$$\sigma_{\omega,\text{GF}}(z) \equiv \sqrt{\frac{3\sqrt{3}\rho\omega_s^2}{k_w z}}. \quad (8)$$

Here $\sigma_{\omega,\text{GF}}(z)$ is the rms bandwidth of the FEL Green function for a coasting electron beam with ρ being the Pierce parameter [1]. The transform limit also means that $\alpha_{s,f}(0) = \alpha_s$, $\beta_{s,f}(0) = \beta_s = 0$, $\sigma_{t,s,f}(0) = \sigma_{t,s}$, and $\sigma_{\omega,s,f}(0) = \sigma_{\omega,s}$. The FEL-interaction intrinsically generates a chirped FEL waveform,

$$\langle(t - \langle t \rangle)(\omega - \langle \omega \rangle)\rangle = \frac{\beta_{s,f}(z)}{2\alpha_{s,f}(z)} = \frac{R(z)^2}{2\sqrt{3}[1+R(z)^2]}. \quad (9)$$

The emittance of the FEL light at any position, z , is conserved, $\varepsilon \equiv \{ \langle(t - \langle t \rangle)^2 \rangle \langle(\omega - \langle \omega \rangle)^2 \rangle - \langle(t - \langle t \rangle)(\omega - \langle \omega \rangle)\rangle^2 \}^{1/2} = 1/2$, indicating that the FEL emission is fully coherent longitudinally [17].

We introduce the critical location, z_c , where the FEL Green function bandwidth reduces to the pulselet initial bandwidth, *i.e.*, $R(z_c) = 1$. Recall that, the power gain length $L_G = \lambda_w/(4\sqrt{3}\pi\rho)$, hence, if $\sigma_{\omega,s}/\omega_s > 3\sqrt{2}\rho$, then $z_c < L_G$. For large enough z , where $R(z) \gg 1$, the FEL has

$$\left\{ \begin{array}{l} \sigma_{t,s,f}(z) \rightarrow \frac{1}{\sqrt{3}\sigma_{\omega,\text{GF}}(z)} \\ \sigma_{\omega,s,f}(z) \rightarrow \sigma_{\omega,\text{GF}}(z) \\ \langle(t - \langle t \rangle)(\omega - \langle \omega \rangle)\rangle \rightarrow \frac{1}{2\sqrt{3}} \end{array} \right., \quad (10)$$

i.e., the final characteristics are determined by the FEL interaction. In accordance with Eq. (6), the FEL interaction rapidly reduces the seed pulselet bandwidth, extending its duration [16].

HHG-HGHG FELs at LCLS

Considering the feasibility of an HHG seeded HGHG XFEL, we use an ir laser at 800 nm with $\sigma_{t,0} = 10$ fs. We choose the 27th harmonic as the seed to interact with an LCLS-type high brightness electron bunch [18]. The

initial pulselet is assumed to have $\sigma_{t,s} = \tau/8$. Assuming a Fourier-transform limited single harmonic pulselet, we have $\sigma_{\omega,s} = 1/(2\sigma_{t,s})$. The relative rms bandwidth is $\sigma_{\omega,s}/\omega_s \approx 2.4\%$. Due to the FEL interaction, according to Eq. (7), the FEL bandwidth decreases. For the scheme shown in Fig. 1 with parameters in Table 1, we have $\rho = 0.54\%$ and $\lambda_w = 0.2$ m, we have $z_c \approx 1.6$ m. Considering that the first modulator is 25 m long and the power gain length is about 3 m, attosecond structure is smeared out within a short distance [16]. Consequently, the HHG seed resembles a conventional harmonic seed generated via wave-mixing in a solid such that we can ignore initial attosecond structure, at least as a good approximation.

In Fig. 1, we show the generic configuration of an HHG seeded cascaded HGHG FEL. It has the following features.

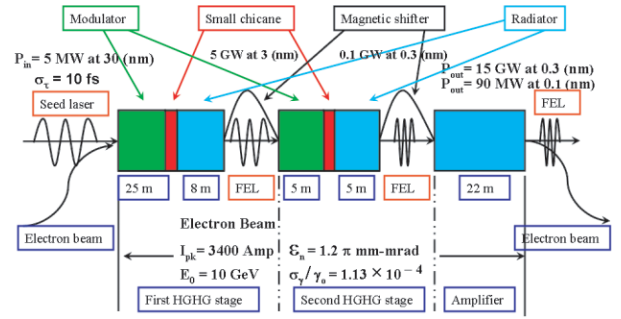


Figure 1: Schematics of an HHG seeded cascaded HGHG FEL. In this scheme an HHG seed of 30 nm is used. After two stages of HGHG and a final amplifier, we obtain 15 GW at 0.3 nm, and 90 MW at 0.1 nm.

1. We need multiple stages. During each stage the n th harmonic of the seed laser will be produced at the end of the radiator, and then this harmonic will be used as the seed for the next stage. In reality, n cannot be too large due to that stability consideration [7, 9]. In our paper we use $n = 10$ to achieve stable performance, and we need only two stages.

2. Conceptually, the device is composed of two parts: a converter [19] and an amplifier. The converter, consisting of several stages, converts the seed laser to the designed wavelength step by step. Then at the end, an amplifier exponentially amplifies the radiation obtained from the last stage to saturation.

3. Except for the first modulator and the last amplifier, each stage only converts the light to its n^{th} harmonic. Exponential growth is not required as long as the harmonic power is high enough to be used as the seed for the next stage.

4. The phase mixing induced by the emittance in the dispersion section is much smaller than that in an undulator. For an HGHG FEL, bunching is produced mainly in the dispersion section; while for a SASE FEL, bunching is produced in the undulator. Therefore, the emittance effect turns out to be less important in an HGHG FEL than in a SASE FEL [10].

5. Since we need to cascade several stages of HGHG, we need some extra components. Each stage will consist of one modulator, a dispersion section (a small chicane), and one radiator. The physics process in each stage will be the same as in Refs. [5, 6]. During the process, the output radiation has disturbed the coincident part of the e -bunch. Therefore, to achieve the best efficiency in the next stage of HGHG, we need use a fresh region of the e -bunch. To do this, the laser (i.e., the output radiation from the previous HGHG stage) is shifted to the front part of the same e -bunch, so that the laser will interact with a fresh part of the same e -bunch. *i.e.*, we use a magnetic shifter to relatively delay the electron bunch.

As mentioned above, this conceptual design uses the 27th harmonic of the 800 nm ir pulse with $\sigma_{t,0} = 10$ fs. Assuming the input seed peak power of 5 MW, with two stages of HGHG and a final amplifier, we obtain a 15 GW FEL at 0.3 nm, and 90 MW at 0.1 nm via nonlinear harmonic generation [20, 21]. In this example, the 27th harmonic pulselet interacts with an LCLS-type electron beam [18] (normalized emittance $\varepsilon_n = 1.2 \pi$ mm-mrad, relative energy spread $\sigma_\gamma/\gamma_0 = 1.13 \times 10^{-4}$, energy $E_0 = 10$ GeV, and peak current $I_{pk} = 3,400$ Amp). In the 25 m modulator of the first HGHG stage, the HHG seed is amplified, and simultaneously modulates the electron beam energy. A small chicane then converts the energy modulation into density microbunching at 30 nm. This microbunched electron beam then traverses the 8 m radiator which is resonant at 3 nm (the 10th harmonic of the original 30 nm seed). This microbunched electron beam first coherently radiates at 3 nm and then exponentially amplifies this 3 nm radiation to a peak power of 5 GW, which is used to seed the next HGHG stage. In the second stage, the 5 GW, 3 nm seed energy modulates the electron beam in the 5 m modulator. The energy modulation is converted into density microbunching at 3 nm via a second small chicane. This density modulated electron beam initially radiates coherently in the 5 m radiator, resonant at 0.3 nm (the 10th harmonic of the 3 nm seed). At the end of the 5 m radiator, the 0.3 nm radiation is amplified to 0.1 GW, which is further amplified in the 22 m final amplifier, resonant at 0.3 nm. At the amplifier exit, the FEL is well into saturation, and the system finally produces 15 GW, 0.3 nm radiation. Due to the microbunching at 0.3 nm, there are substantial harmonics. The third harmonic emission at 0.1 nm has a peak power of 90 MW.

As shown in Fig. 1, we consider an HHG seed with a wavelength of 30 nm, and a peak power of $P_{in} = 5$ MW. As we will discuss later, the corresponding start-up shot-noise power is only about $P_{noise} \approx 70$ W. Thus the input seed laser power dominates the shot-noise power. This dominance is necessary, because even though there is only negligible noise power in the initial stage, the signal-to-noise ratio of the final radiation at 0.3 nm can be degraded [22]. A simple estimate shows that the noise-to-signal (NTS) ratio at the seed will be amplified by n_{tot}^2 times for the n_{tot}^{th} harmonic generation. In this case, the two stage approach

Table 1: Parameters for the undulator, the dispersive section and the electron bunch.

	1 st stage		2 nd stage		Amplifier
λ_r (nm)	30	3	3	0.3	0.3
λ_w (cm)	20	6	6	3	3
$\frac{d\psi}{d\gamma}$	0.2		0.4		
$\frac{\sigma_\gamma}{\gamma_0}$	1.13×10^{-4}				
L_w (m)	25	8	5	5	22
L_G (m)	3	2	2	3	3

has an overall $n_{tot} = 100$, hence, the NTS ratio will be amplified by 10^4 times. Hence for the final radiation at 0.3 nm, the NTS ratio will be about 14 %.

After two HGHG stages, we have generated 0.3 nm radiation, and this 0.3 nm radiation is amplified to saturation with a peak power near 15 GW in a final amplifier stage. The parameters for the electron beam and the radiation are given in Fig. 1. The number in the first row stands for the output power and wavelength of the radiation of each stage. The output power of one stage is the input power of the next stage, though diffraction has been taken into consideration in the simulation. The e -beam parameters are printed below the schematic device. The relative local energy spread σ_γ/γ_0 given in Fig. 1 is the initial relative local energy spread before the e -beam enters the first modulator. This is increased by spontaneous radiation [23]. We take this into account in the simulation [21].

In Table 1, the first row gives the radiation wavelength λ_r ; the second row, the undulator period λ_w , and the third row the dispersion strength $d\psi/(d\gamma)$ with ψ being the ponderomotive phase in the radiator. The fourth row gives the initial relative local energy spread σ_γ/γ_0 . In our simulation, quantum diffusion [23] has been taken into account [21]. The fifth row gives the length of the undulators (modulators, radiators, and the amplifier) L_w . For example, the last amplifier has a length of 22 m. The sixth row gives the power gain length L_G in each undulator without energy modulation. The table has three boxes; the first two boxes are for the two convertor stages and the last one is for the amplifier. For the two convertor stages, the left column gives the parameters for the modulator and the right column those for the radiator; the numbers in the middle stand for the dispersion strength $d\psi/(d\gamma)$. For example, the left column in the second box stands for the modulator of the second stage. The table shows that in the modulator the resonant radiation has a wavelength of 3 nm, the modulator has a period of 6 cm, the length of the modulator is 5 m, and the corresponding power e -folding length without energy modulation is 2 m. The right column shows that the radiation in the radiator has a wavelength of 0.3 nm, the radiator has a period of 3 cm, the length of the radiator is 5 m, and the corresponding power e -folding length is 3 m. In the middle, *i.e.* 0.4, stands for the dispersion strength $d\psi/(d\gamma)$.

Start-up Noise Issue

First, we need to compute the effective start-up noise power for the fundamental SASE guiding mode [24, 9]

$$P_{\text{SASE}}^{\text{Start-up}} = C_1 \frac{2L_G}{L_w} \pi \left(\frac{2\lambda_r}{L_w} \right) \sqrt{\frac{3\sqrt{3}\rho}{N_w}} \quad (11)$$

$$\times \frac{eZ_0 I_{pk} N_w^2 \gamma^2}{4\pi} \frac{K^2}{\left(1 + \frac{K^2}{2}\right)^2} [JJ]^2 \omega_r,$$

where the coupling factor is found to be [24],

$$C_m(a) \approx \frac{\sqrt{3}}{\pi a^2} \exp \left[-\frac{1}{a\sqrt{1+a^2}} \left(\beta_{m,0} + \beta_{m,1} \frac{1}{a^2} \right) \right], \quad (12)$$

where, m is the index referring to a certain mode being excited; $a = \sqrt{4\rho k_w k_r} R_0$ is the scaled beam size with $k_w = 2\pi/\lambda_w$, $k_r = 2\pi/\lambda_r$, and R_0 the hard edge of an electron beam. The above formula is a good approximation, when $a > 0.25$. Within such range, $\beta_{m,0} = 1.093$, and $\beta_{m,1} = -0.02$ for the fundamental guiding mode. In Eq. (11), L_G is the power gain length; L_w the undulator length; λ_r the radiation wavelength; N_w the number of undulator period; Z_0 the vacuum impedance; I_{pk} the peak current; $\omega_r (= c2\pi/\lambda_r)$ the radiation angular frequency with c the speed of light in vacuum. The Bessel factor $[JJ] = J_0 \left[\frac{a_w^2}{2(1+a_w^2)} \right] - J_1 \left[\frac{a_w^2}{2(1+a_w^2)} \right]$, with $a_w = K/\sqrt{2}$, and J_0 and J_1 are the zeroth order and first order Bessel function, respectively. Approximately, $K \approx 93.4 B_w \lambda_w$ is the undulator parameter with B_w the peak field of the undulator in units of Tesla and λ_w in units of meter.

In the above SASE calculation, the bandwidth of the fundamental guided mode is $\sigma_{\omega, \text{GF}}$ for $z = 2L_G$ according to Eq. (8). However, the seeded FEL has a different bandwidth of $\sigma_{\omega, s, f}(z = 2L_G)$ according to Eq. (6). Hence, the true start-up noise power in the seeded FEL bandwidth is

$$P_{\text{Seeded}}^{\text{Start-up}} = P_{\text{SASE}}^{\text{Start-up}} \frac{\sigma_{\omega, s, f}(z = 2L_G)}{\sigma_{\omega, \text{GF}}(z = 2L_G)}. \quad (13)$$

Considering the first modulator, the Pierce parameter is $\rho \approx 5.4 \times 10^{-3}$; the scaled beam size is $a \approx 0.8$, which gives the coupling coefficient to be $C_1 \approx 0.3$. The SASE effective start-up noise power in the fundamental guided mode is $P_{\text{SASE}}^{\text{Start-up}} \approx 400$ W; however, since $\sigma_{\omega, s, f}(z = 2L_G) \approx 2.0 \times 10^{-3}$ and $\sigma_{\omega, \text{GF}}(z = 2L_G) \approx 1.2\%$, the true start-up noise power in the seeded FEL bandwidth is only about $P_{\text{Seeded}}^{\text{Start-up}} \approx 70$ W.

DISCUSSION

In this paper, we explored the details of an HHG seeded FEL. For simplicity, the HHG seed is modelled as an attosecond pulselet train (APT). Bandwidth reduction, intrinsic to the FEL interaction, smears out the initial attosecond structure of the seed within a very short distance, $z < L_G$. The seeded FEL remains coherent, if we do not

consider the accompanied noise power and electron beam non-uniformity [10]. The true start-up noise power in the seeded FEL bandwidth, $P_{\text{Seeded}}^{\text{Start-up}}$ is only about 70 W. Since the HHG seed has a power of $P_{\text{in}} = 5$ MW, the noise-to-signal ratio at the final radiation $\lambda_r = 0.3$ nm is still only about 14 %, even though it has $n_{\text{tot}}^2 = 10^4$ ($n_{\text{tot}} = 100$) times amplification, *i.e.*, the effective noise level is increased from the initial 70 W to 0.7 MW.

REFERENCES

- [1] R. Bonifacio, C. Pellegrini, L.M. Narducci, *Opt. Commun.*, **50**, 373 (1984).
- [2] J.-M. Wang and L.-H. Yu, *Nucl. Instr. and Meth.*, **A 250**, 484 (1986).
- [3] K.-J. Kim, *Nucl. Instr. and Meth.*, **A 250**, 396 (1986); *Phys. Rev. Lett.* **57**, 1871 (1986); Lawrence Berkeley National Laboratory Report No. 40672 (1997).
- [4] S. Krinsky and Z. Huang, *Phys. Rev. ST Accel. Beams* **6**, 050702 (2003); E.L. Saldin *et al.*, *Proc., 2005 Int. FEL Conf.*, p.258.
- [5] L.H. Yu, *Phys. Rev. A* **44**, 5178(1991).
- [6] L.-H. Yu, *et al.*, *Science*, **289**, 932(2000).
- [7] J. Wu and L.H. Yu, *Nucl. Instr. and Meth.*, **A 475**, 104 (2001).
- [8] L.H. Yu and J. Wu, *Nucl. Instr. and Meth.*, **A 483**, 493 (2002).
- [9] J. Wu and L.H. Yu, Stanford Linear Accelerator Center Report No. SLAC-PUB-10494 (2004).
- [10] J. Wu and L.H. Yu, Stanford Linear Accelerator Center Report No. SLAC-PUB-10495 (2004).
- [11] M.-E. Couprie *et al.*, *Proc., 2005 Int. FEL Conf.*, p.55.
- [12] R. López-Martens, *Phys. Rev. Lett.* **94**, 033001 (2005).
- [13] E.A. Gibson *et al.*, *IEEE J. of Selected Topics in Quant. Elec.* **10**, 1339 (2004).
- [14] J. Mauritsson *et al.*, *Phys. Rev. A* **70**, 021801(R) (2004).
- [15] P.M. Paul *et al.*, *Science* **292**, 1689 (2001).
- [16] J. Wu, P.R. Bolton, J.B. Murphy, and X. Zhong, Stanford Linear Accelerator Center Report No. SLAC-PUB-11891 (2006).
- [17] J.B. Murphy *et al.*, Brookhaven National Laboratory Report No. BNL-75807-2006-JA, and Stanford Linear Accelerator Center Report No. SLAC-PUB-11852 (2006); J. Wu *et al.*, Stanford Linear Accelerator Center Report No. SLAC-PUB-11985 (2006).
- [18] J. Arthur *et al.*, Stanford Linear Accelerator Center Report No. SLAC-R-593 (2002).
- [19] I. Boscolo and V. Stagno, *Nuovo Cimento B* **56**, 219(1980).
- [20] Z. Huang and K.J. Kim, *Phys. Rev. E* **62**, 7295 (2000).
- [21] J. Wu, *Proc., 2003 Particle Accel. Conf.*, p. 1035.
- [22] E.L. Saldin, E.A. Schneidmiller, and M.V. Yurkov, *Opt. commun.* **202**, 169 (2002).
- [23] E.L. Saldin, E.A. Schneidmiller, and M.V. Yurkov, *Nucl. Instrum. Methods Phys. Res. A* **381**, 545(1996).
- [24] L.H. Yu, *Phys. Rev. E* **58**, 4991(1998).

THE FIRST EXPERIMENTAL OBSERVATION OF FEL AMPLIFIER EFFICIENCY IMPROVEMENT USING ELECTRON BEAM ENERGY DETUNING AT THE NSLS SDL

T. Watanabe*, J.B. Murphy, J. Rose, Y. Shen, T. Tsang, X.J. Wang, BNL, Upton, NY 11973, USA
H.P. Freund, Science Applications International Corporation, McLean, VA 22102, USA

Abstract

The first experimental observation of efficiency enhancement using electron energy detuning in a single-pass laser seeded Free-Electron Laser (FEL) amplifier is reported. Our experiments show that it is possible to double the FEL efficiency by increasing the electron energy by +0.7 % relative to the resonance energy. The measurement of the laser seeded FEL spectra versus energy detuning shows that the peak wavelength of the FEL radiation is determined by the seed laser. The experimental results are discussed using FEL theory and a three-dimensional simulation code GENESIS1.3 [1].

INTRODUCTION

One of the advantages of the FEL is the ability to produce high power laser light without the conventional thermal issues associated with other laser systems [2]. In addition, the operating wavelength of the FEL can be adjusted according to the application. Because of the advantages, the FEL has been regarded as one of the promising approaches to generate Megawatt (MW) average power laser at 1 μm wavelength. Such an application is called directed energy application [3, 4].

In order for the FEL to realize the MW average power output, it is required to optimize the efficiency of the FEL process. Supposed that the interaction between the electron beam and the radiation is strong enough in the undulator, the radiation power grows exponentially as the electron beam goes through the undulator. According to the steady-state theory of a single-pass FEL, the radiation is saturated at ρP_e due to the deposition of the electron energy to the radiation. Here, ρ is the Pierce parameter and P_e is the input electron power. After the saturation, the electrons with lower energy no more resonate with the radiation as it does in the exponential gain regime. Instead, the mutual energy deposition between electrons and radiation is repeated.

To overcome the saturation, several schemes have been proposed and tested. One is to taper an undulator, in which the field strength of the undulator is gradually decreased after the saturation so that the electrons with lower energy can maintain the resonance with the radiation [5, 6]. Another is to detune the electron energy, in which the input elec-

trons with slightly higher energy can resonate with the radiation longer than the normal (resonant) case [3]. The detuning effect had been theoretically and numerically studied [7, 8, 9, 10]. The study indicates that the growth rate is deteriorated by the detuning, while the saturation power can be enhanced by optimizing the detuning. It is an advantage of the detuning scheme that the scheme does not require any modification of the experimental setup; only the requirement is to change electron beam energy. As far as authors know, however, the detuning effect in a single-pass FEL had not been experimentally verified.

In a self-amplified spontaneous emission (SASE) FEL, in which no external seed laser is supplied, the radiation wavelength is shifted when the electron energy is changed. Thus, the wavelength of the output radiation is inevitably resonated with the incident electron energy and no enhancement of FEL efficiency due to the detuning should be expected. In a seeded FEL, where an external laser is injected and then amplified via interaction with electrons, the wavelength of the radiation may be affected by both electron energy and the seed laser. Eventually, it may enhance the efficiency of the amplification to detune electron energy in terms of the wavelength of the seed laser.

In the paper, the experimental demonstrations of efficiency enhancement by the electron energy detuning is reported. The experimental results are compared with the numerical simulation and interpreted by FEL theory.

DETUNING EXPERIMENT

The experiments were conducted at the Source Development Laboratory (SDL) of National Synchrotron Light Source (NSLS), Brookhaven National Laboratory (BNL). The picosecond (ps) electron pulse generated by a photo-injector is compressed to 1.5 ps by a chicane-type bunch compressor. The compressed e-beam passes through a 10 m long planar undulator, of which period is 3.89 cm and the undulator parameter is $K=1.1$. The seed laser generated by a Ti:Sapphire laser system is compressed to 6 ps, with the frequency chirp being slightly negative. Passing through a bandpass filter, the seed laser has the central wavelength of 795 nm and the bandwidth of 1.5 nm at Full Width at Half Maximum (FWHM). The major experimental parameter are summarized in Table. 1.

* twatanabe@bnl.gov

Table 1: Major experimental parameters

Undulator parameter K	1.1
Undulator period	3.89 cm
Undulator length	10 m
Electron energy	98 - 102 MeV
Peak current	380 A
Electron bunch duration (FWHM)	1.5 ps
Energy spread (rms)	0.1 %
Normalized emittance	2-4 mm.mrad
Seed laser wavelength	795 nm
Seed laser bandwidth (FWHM)	1.5 nm
Seed laser pulse duration (FWHM)	6 ps
Seed laser energy	4 kW

Efficiency measurement

For a planar undulator, the wavelength of the FEL radiation, λ_r , is written as,

$$\lambda_r = \frac{\lambda_u(1 + K^2/2)}{2\gamma^2}, \quad (1)$$

where λ_u is the undulator period and γ is the electron energy normalized with its rest mass. In general seeded FEL experiments, the electron energy is adjusted to satisfy Eq.(1) for a given wavelength. In what follows, such an energy is called the energy on resonance. In our experiment, the energy on resonance was determined by measuring SASE spectrum without the seed laser.

In Fig. 1, the energy gains in the undulator on resonance and with two detuning cases are plotted; one is 0.7 % higher (+0.7 % detuning) and another is 0.5 % lower (-0.5 % detuning) relative to the energy on resonance. All the three data are shown with root-mean-squared (rms) error bars, but at most of points, the error bars are overlapped with the dots. In -0.5 % detuning case, the seed laser energy is dominant until 7.8 m, because both transversely and longitudinally the seed laser size is larger than the electron beam. The simulation results on resonance and with detuning were also presented in Fig. 1. The gain curve on resonance is shown by the solid curve, and those with +0.5 and -0.5 % detuning are respectively shown by dotted and dashed curves.

It is obvious in both experiment and simulation that the gains with detuning are asymmetric between positive and negative detuning; the negative detuning degrades the gain by more than one order of magnitude, while the positive detuning enhances it by factor of two. To interpret it, we recall one-dimensional steady-state theory [7, 8, 9, 10]. First, at the early stage of amplification, small-signal gain theory indicates that the direction of energy deposition between electrons and radiation is opposite depending on the direction of detuning. In Fig. 1, the radiation energy with negative detuning is deposited to electrons once, while that with positive detuning immediately gains energy from electrons. On resonance, there is no energy deposition, which is also

presented by the theory. Next, in a high gain regime, a cubic equation for time-dependent gain of FEL radiation in the form $\exp(i\lambda\tau)$ is written as,

$$\lambda^3 - \delta\lambda + 1 = 0, \quad (2)$$

where λ is an eigenvalue, of which negative imaginary part gives the growth rate, and δ is the normalized energy detuning $\delta = (\gamma^2 - \gamma_R^2)/2\gamma_R^2\rho$. In Eq.(2), the efficiency parameter is assumed to be small, $\rho \sim 0$. The preferable instability exists only when the detuning is smaller than the threshold, i.e., $\delta < \delta_{th} \sim 1.89$, where two of the three eigenvalues in Eq.(2) have imaginary part. The maximum growth rate, $Im\lambda = \sqrt{3}/2$, occurs at no detuning, $\delta = 0$. It has also been shown with the aid of numerical simulation that as the electron energy goes higher, the saturation energy becomes higher until it reaches the threshold, $\delta \sim \delta_{th}$. Since the efficiency parameter ρ of the experiment is in the range of 0.003 through 0.004, the threshold corresponds to the electron energy detuning of +0.55 to +0.75 % (shown grey in Fig.1). One can see in Fig. 1 that both experiment and numerical simulation represent the characteristics predicted by the theory and numerical simulation; the positive detuning in the range of threshold enhances the output energy, whereas the same amount of detuning but in negative direction just degrades the gain due to the combination of energy deposition to the electrons in small-signal gain regime and degraded gain in high gain regime.

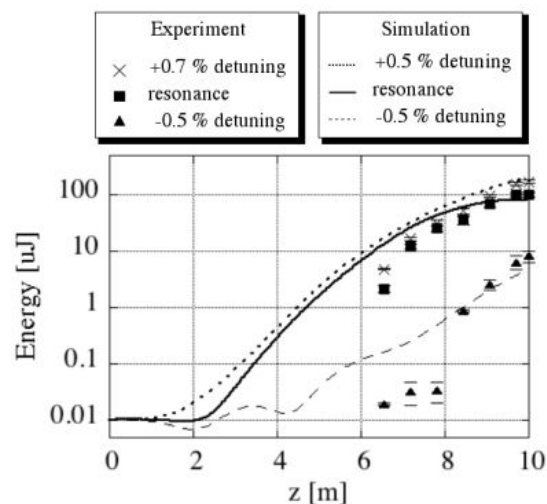


Figure 1: Gain curves on resonance and with detuning.

To see the detuning effect more clearly, the output energy of FEL radiation was plotted as a function of the electron gain in Fig. 2. The dots with peak-to-peak error bars are experimental data and the solid line is evaluated by the time-dependent simulation under the same condition as the experiment. The output radiation energies are normalized with those on resonance in both experiment and simulation results. The energy on resonance is 102 and 82 μJ respectively for the experimental and the numerical results. In

Fig. 2, the asymmetry between positive and negative detuning is again clearly observed. The negative detuning of 0.5 % deteriorates the FEL gain by one order of magnitude, while the positive detuning of 0.7 % enhances the gain by 70%. In addition, further detuning by a half percent in a positive direction, i.e., total detuning of +1.2 %, does no more enhance the gain, but suppresses it. It is because the detuning goes beyond the threshold δ_{th} (grey in Fig. 2). The experimental result agrees with the simulation result except for two things in detail; the enhancement of the energy in the experiment is lower than that of by simulation, and the amount of the detuning that gives the enhancement is +0.7 % in experiment and +0.5 % in simulation. It is because there was an electron energy jitter in the experiment, so the energy enhancement at the detuning was smoothed out by taking the average. In fact, the maximum energy given at the +0.7 % detuning was 206 μJ , which is more than 2 times higher than the average energy on resonance.

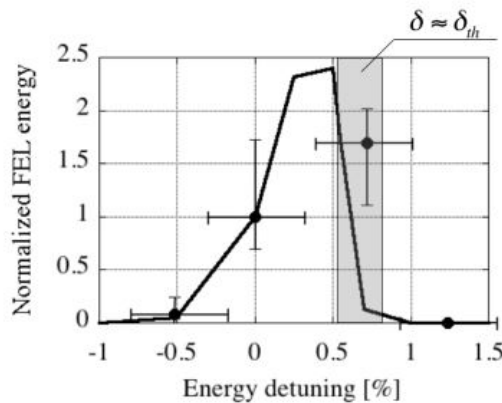


Figure 2: FEL output energy vs electron energy detuning. Solid line is simulation and dots are experimental result.

Spectral measurement

The spectra of the seeded FEL pulse were also measured. Figure 3 represents the example spectra of seeded FEL on resonance (solid line) and with the positive detuning at the threshold $\delta \sim \delta_{th}$ (dashed). The positive detuning in the experiment (Fig. 3 (a)) is +0.7 %, and that in the numerical simulation by GENESIS1.3 (Fig. 3 (b)) is +0.5 %.

It is both experimentally and numerically verified in Fig. 3 that the peak wavelength of output seeded FEL pulse is not notably shifted by detuning electron energy. In both cases, the difference of the peak wavelength between on resonance and with the positive detuning is much less than 1 nm. It follows that the seeded FEL spectrum with detuning is dominated by the seed laser, so the detuning scheme does not induce the undesirable frequency shift in the output pulse. Note that the detuning of +0.7 % in electron energy corresponds to the down-shift of SASE spectrum by as much as 11 nm.

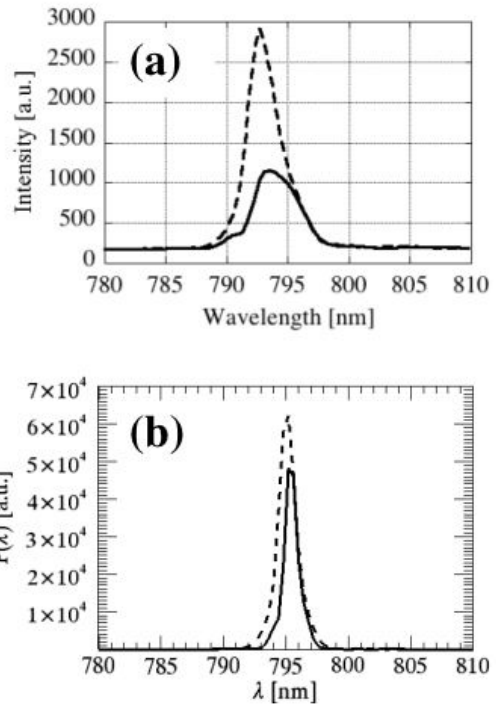


Figure 3: Spectra of laser seeded FEL on resonance (solid line) and with positive detuning at the threshold $\delta \sim \delta_{th}$ (dashed). (a) experiment and (b) GENESIS calculation.

CONCLUSION

We experimentally observed the efficiency enhancement by the electron energy detuning. By applying the energy detuning of +0.7 %, the efficiency was doubled. Both the further detuning and the opposite detuning significantly degrades the efficiency. The results were well consistent with one-dimensional steady-state theory as well as the three dimensional numerical simulation.

The spectra of seeded FEL pulses on resonance and with detuning were also measured. It was verified that the peak wavelength of seeded FEL with detuning was almost same as that on resonance both by the experimental result and the numerical simulation. It indicates that the detuning scheme works without modifying the seeded FEL spectrum substantially.

The study gives fundamental knowledge for implementing seeded FEL experiments as well as designing the high power FEL such as a directed energy application.

ACKNOWLEDGMENTS

We are grateful for support from the NSLS and BNL director's office and this work is supported by the Office of Naval Research and U.S. Department of Energy under contract No. DE-AC02-98CH1-886. The authors are pleased to acknowledge valuable technical contribution from Boyzie Singh.

REFERENCES

- [1] S. Reiche, Nucl. Instrum. Methods Phys. Res. A **429**, 243 (1999).
- [2] C.W. Roberson and P. Sprangle, *A review of free-electron lasers*, Phys. Fluides, **429**, 3, Jan. 1989.
- [3] P. Sprangle et al., IEEE J. Quantum Electronics, **40**, 1793 (2004).
- [4] T. Watanabe et al., Proc. of FEL2005, p.320 (2005).
- [5] T.J. Orzechowski et al., Phys. Rev. Lett. **57** 2172 (1986).
- [6] D.A. Jaroszynski et al., Phys. Rev. Lett. **74**, 2224 (1995).
- [7] P. Sprangle et al., Phys. Rev. A. **21**, 302 (1980).
- [8] R. Bonifacio et al., Opt. Commun. **50**, 373 (1984).
- [9] J.B. Murphy and C. Pellegrini, J. Opt. Soc. Am. B **2**, 259 (1985). J.B. Murphy and C. Pellegrini, NIM A **237**, 159 (1985).
- [10] J.B. Murphy and C. Pellegrini, *Laser Handbook Volume 6*, (Elsevier Science Pub., North-Holland, 1990), Chap. 2.

CHIRPED PULSE AMPLIFICATION EXPERIMENT AT 800 nm

L.H. Yu, T. Shaftan, D. Liu, T. Tsang, J. Rose, X.J. Wang, T. Watanabe
NSLS, BNL, Upton, NY 11973, USA.

Abstract

We report the chirped pulse amplification (CPA) experiment carried out using 800 nm direct seeding and NISUS undulator as free electron laser amplifier at SDL of BNL. The experiment indicated that due to saturation in the center part of the chirped electron bunch the output pulse shape has a dip in the middle, as result the edge of the bunch has higher power than the center. Hence the output spectrum also showed a dip in the center, resulting in a larger FWHM bandwidth than the seed. An interesting result is that the 800 nm chirped FEL output was compressed down to a pulse length shorter than what the seed pulse itself can be compressed to.

INTRODUCTION

Chirped pulse amplification (CPA) [1-4, 8] can be used to generate short high intensity pulse in FEL, and it has been shown theoretically possible to generate pulse shorter than what the seed can be used to generate [2]. Initial CPA experiment has been carried out in HGHG process at 266 nm but without the final compression of the pulse [5]. The experiment showed that by matching the electron bunch energy chirp with that of the seed pulse properly we were able to maximize the bandwidth of the output pulse while maintaining coherence. First SPIDER traces were measured and quadratic optical phase dependence along the pulse was obtained [7]. However, due to limited beam time, we were unable to finish the compression of the output pulse at 266 nm so far. In this paper, we report our preliminary result on the CPA at 800 nm with direct seeding.

EXPERIMENT SETUP AND CPA EXPERIMENT

A schematic diagram of the 788 nm experiment is

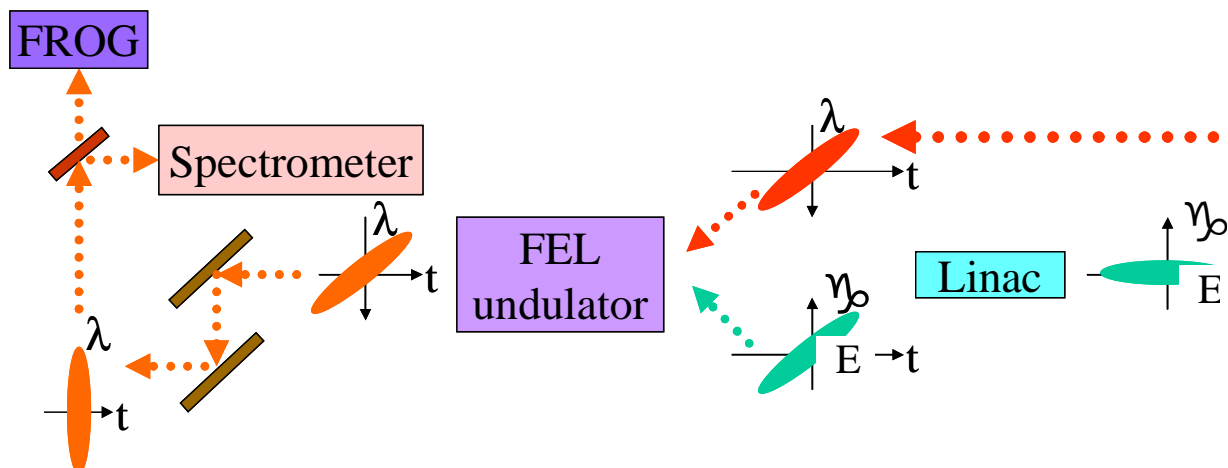


Figure 1: Layout of the experimental set-up.

shown in figure 1. The 788 nm seed pulse with pulse length of 2.5 ps and bandwidth of about 6 nm is chirped with the head of the pulse at longer wavelength. The 103 MeV electron bunch with charge of 500 pC is compressed down to about 2.5 ps and chirped using the last section of the linac to about 0.5% of projected energy spread with head at lower energy. During the experiment the chirp is adjusted to maximize the output bandwidth. The seed and the electron beam are sent into the FEL undulator NISUS and aligned to overlap in the first section of the undulator. The seed has a Rayleigh range of 1.95 m. We used first two pop-in monitors inside the NISUS undulator to carry out the alignment. Since the seed table where the seed is injected into the undulator beam line by a 45° mirror is 7 meters away from the entrance of the NISUS undulator, the physical limitation of the system made it impossible to match the seed beam size to the electron beam size at the beam waist of the seed, which is about 0.6 m inside of the entrance. As a result the laser beam size is much larger than the electron beam. This is illustrated in figure 2

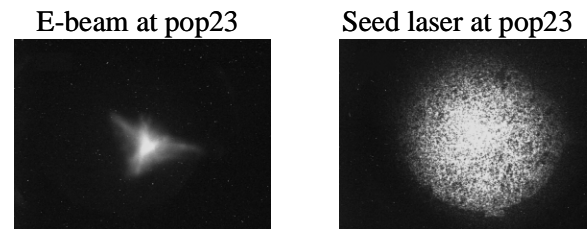


Figure 2: Images of the beam (left) and seed laser (right)

where we show the images of the seed and electron beam at the first pop in monitor in the NISUS. Thus this FEL amplifier setup is not very efficient. But it is sufficient to be used for a demonstration of the CPA process. The NISUS undulator has a period of 3.9cm with $K=1.126$.

The electron bunch length is measured by the zero-

phasing method using the dipole right after the last linac section as the energy spectrometer. The images of the measurement at 90 and -90 degree of the RF phase are shown in figure 3.

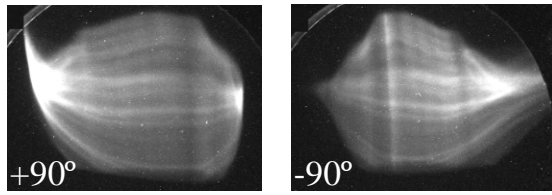


Figure 3: Measurement of bunch length

The synchronization between the electron bunch and the seed laser pulse is realized by observing the significant increase of energy spread when they temporally overlap. The energy spread is measured using the monitor after the beam passes through the undulator and the last dipole. This is shown in figure 4. The upper picture shows that the energy spread is adjusted to about 0.5% when the seed laser is turned off (the full screen corresponds to 1.5% of energy spread). When we turn on the seed laser and change the seed pulse time delay by an optical trombone so it overlaps with the electron bunch, the energy spread is increased significantly and hence the image of the electron beam occupies the full screen.

The seed laser pulse energy is 13.4 μ J before sent into the NISUS undulator during the CPA experiment. To ease the synchronization procedure before we achieve the overlap between the seed and the electron bunch, we remove the attenuation (which is 10 when the pulse energy is 13.4 μ J) so the energy spread increase will be more visible even when the tail of

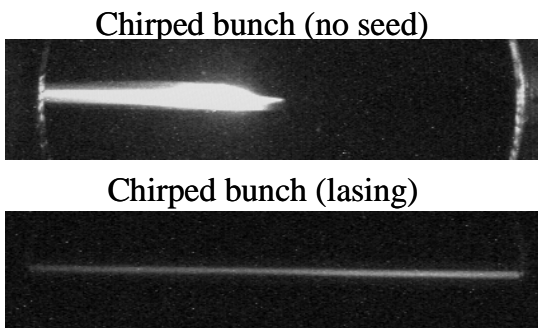


Figure 4: Electron beam energy spectra before (upper plot) and after (lower plot) interaction with electron beam

the electron bunch overlaps with the seed. This helps to increase the step size that we used to move the optical trombone and complete the synchronization procedure faster.

Due to energy and phase jitter and drift of the electron bunch (energy jitter is about 0.2% rms, time jitter about 140 fs rms), during the scan for synchronization for each trombone position we also scan energy within about 0.5% range then move to next position about 100 μ m apart. Once the synchronization is found, we send the amplified FEL output to the spectrometer to fine tune the synchronization. Since the seed laser is chirped, and the output wavelength is determined by the seed, if the tail of the electron bunch overlaps with the head of the laser pulse the output pulse wavelength is centered at longer wavelength of around 795 nm. When the head of the electron bunch overlaps with the tail of the seed, the wavelength moves to shorter wavelength of around 785

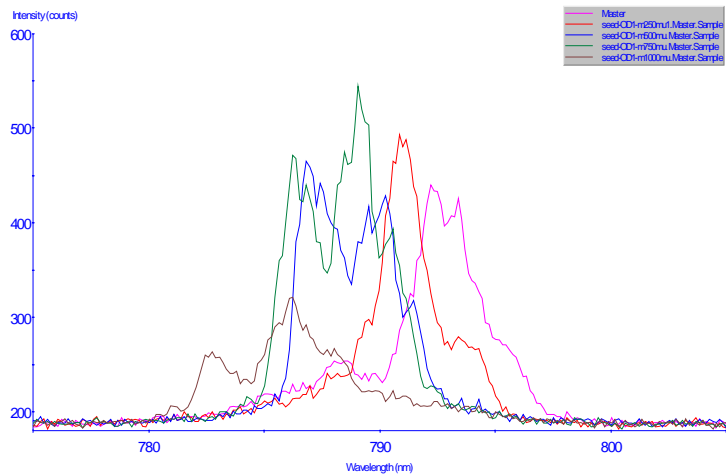


Figure 5: Measured FEL spectra

nm. This helps us to determine which direction and how much we should move the trombone to maximize the overlap. In figure 5 we show the measured FEL output spectrum at different positions of the optical trombone micrometer. The center of the spectrum is at 790 nm.

During the scan the FEL pulse central wavelength is

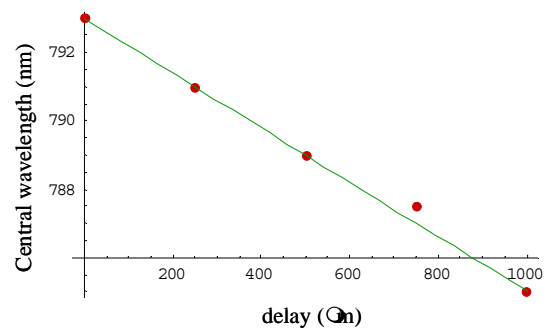


Figure 6 Central FEL wavelength for different delays between seed and electron bunch

also measured and plotted against the micrometer position, as shown in figure 6.

The figure 6 shows the wavelength has a linear dependence on the delay of electron bunch relative to the seed laser, as determined by the micrometer position. The slope of the curve (2.6 nm/ps) is the measured chirp of the

seed by FEL process. This is to be compared with the chirp setup by the seed laser compressor-stretcher system, which is 6 nm/2.5 ps=2.4 nm/ps, providing with a reasonable agreement.

The gain length of the FEL process is measured

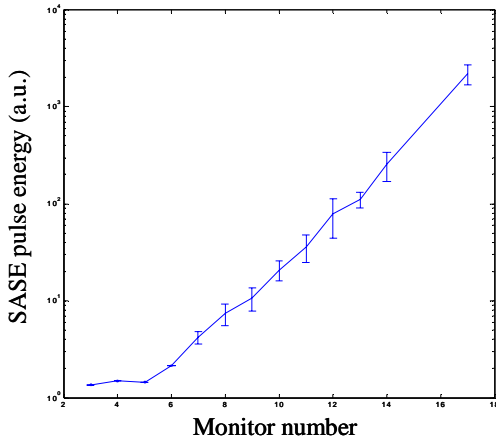


Figure 7: SASE gain length measurement

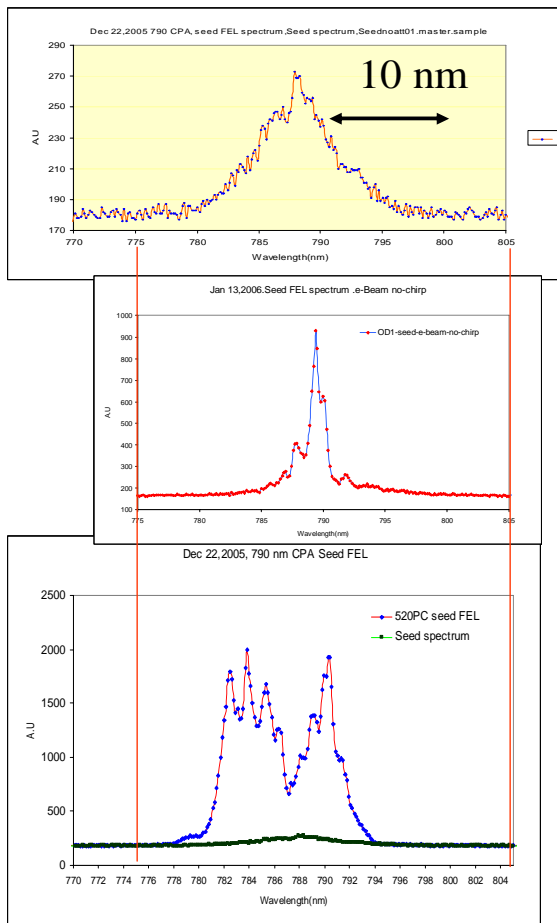


Figure 8: Measurements of seed (upper), unchirped FEL (middle) and FEL output with matched chirp (lower plot)

using SASE output pulse energy as function of distance in the NISUS by kicking the electron beam away from axis sequentially at different longitudinal locations inside the NISUS undulator with the horizontal trajectory correctors. The result is shown in figure 7. Considering the spacing between the monitor is 0.62 m, the power gain length is obtained from this plot as 1m.

The normalized emittance was measured to be 6 mmrad by fitting with the beam profile measurement in the NISUS undulator. Once the synchronization is achieved, we tune electron beam chirp by adjusting the last linac section to vary the energy spread and observing the bandwidth of the FEL output until we reach the maximum bandwidth. When the chirp is optimized and when the

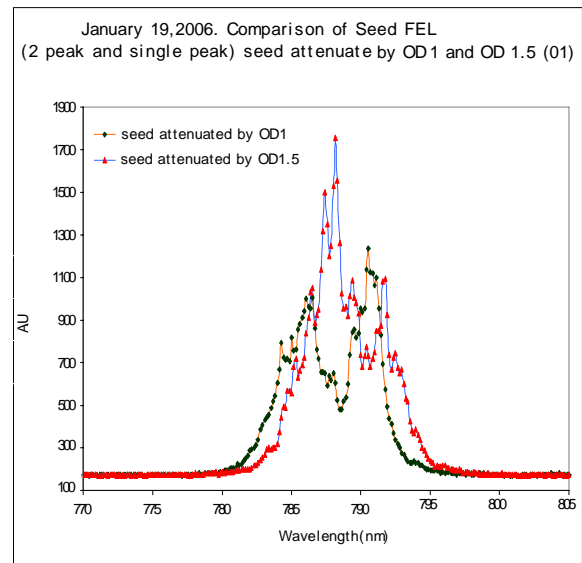


Figure 9: Spectra of the seeded FEL output for two values of attenuation 10 (OD1) and 30 (OD1.5)

seed laser is turned off, the image of the energy spread is shown in the top of the figure 4.

In the top plot of figure 8 we show the measurement of the seed spectrum. The middle plot of the same figure is the spectrum of the FEL output when the electron bunch is not chirped (when energy spread is minimized with the seed laser turned off). Lower plot shows the FEL radiation spectrum for the case when the chirp of the electron bunch is optimized. To be able to compare the bandwidth, we align the three plots vertically so that they use the same horizontal scale. It is seen that when the electron bunch is not chirped, the output bandwidth is narrower than the seed, showing that only the part of the seed pulse with the wavelength in resonance with the electron beam energy is amplified, and the width of the line is clearly determined by the bandwidth of the amplifier.

It is interesting to remark here that figure 8 shows when the energy chirped to match the seed chirp, the bandwidth increases to about 10 nm, significantly larger than the seed bandwidth of about 6 nm. And in particular there is a pronounced dip near the center of the FEL output spectrum. This can be explained by deep saturation in the

central part of the electron bunch. If the current at the central part of the electron bunch is and since the central part of the seed is also at peak, the FEL amplifier can be oversaturated so that power is lower than at the edge of the bunch where the FEL is just reaching saturation, thus creating a dip in the spectrum because due to linear chirp, the spectrum corresponds to time.

To further test this interpretation, we expect that when the seed power is lowered properly so that the central part of the bunch just reach saturation, the dip in the central part of the pulse will disappear, and hence the double peaks in the spectrum should be replaced by a single peak. And indeed, when we increase the attenuation from 10 to 30, we did observe that the double peaks are replaced by a single peak. This is shown in figure 9.

Because of the output bandwidth is larger than the seed bandwidth we expect that when compressed, the final pulse width can have a smaller pulse length than the fourier-transform-limited seed pulse length. This has been confirmed by our next step of the experiment, the compression and measurement of the compressed pulse.

MEASUREMENT OF THE COMPRESSED PULSE BY FROG

As shown in figure 1, the output FEL pulse is sent through a compressor, compressed and sent to a FROG (Frequency-Resolved Optical Gating) device [6]. This device is designed to measure spectral and temporal distribution of short laser pulse simultaneously, and generate the amplitude and phase as function of time for the pulse. It is compact and, in particular, easy to align. The schematic diagram of the arrangement of compressor, spectrometer and FROG is shown in figure 10. In figure 11, we show the FROG result of compressed chirped FEL output pulse. In the picture, the upper right one is the measured FROG image while the upper left one is the retrieved image from the reconstructed pulse shape, the agreement between these two pictures testifies the correctness of the FROG result. The lower left is the reconstructed temporal pulse while the lower right one is the reconstructed spectrum.

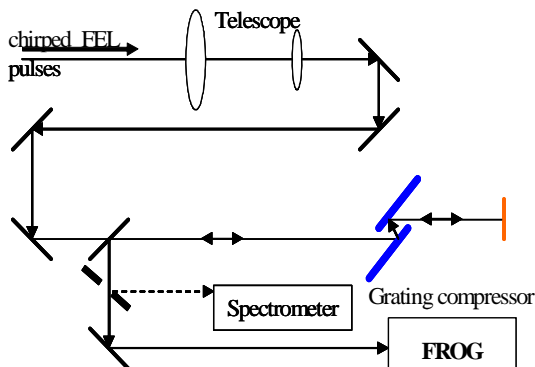


Figure 10: Time- and spectrum measurements set-up.

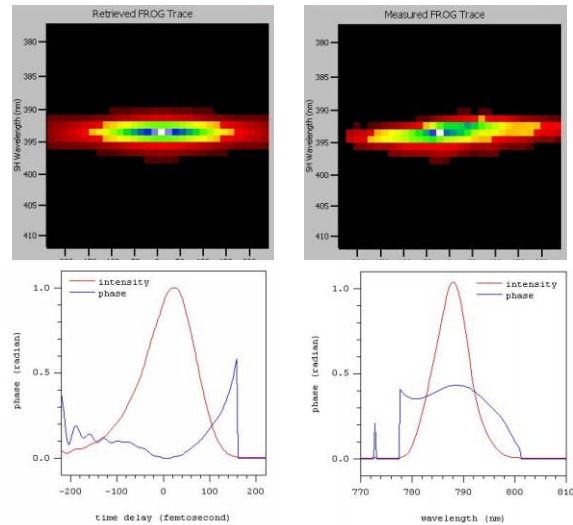


Figure 11: FROG traces of the compressed FEL pulse.

The result shows that pulse length is 122 fs FWHM. We remark that resolution of the spectrum obtained from the FROG is not as good as that of the spectrometer we used, so that in the reconstructed spectrum we could not see the double peaks feature as shown in figure 8 and 9.

This is to be compared with a fourier-transform-limited compressed seed. With the seed bandwidth of 6 nm at 800 nm, assuming minimum wave packet of Gaussian shape, the FWHM pulse length and FWHM bandwidth product is $\text{Log}(2)/\pi * 0.8 \mu\text{m}/(0.3 \mu\text{m}/\text{fs}) = 1.17$. So the pulse FWHM length should be $1.17 * 800 \text{ nm}/6 \text{ nm} = 156 \text{ fs}$. Hence even if the seed is fourier-transform-limited, it is still significantly longer than the CPA result.

In conclusion, we carried compressed CPA from FEL output at 800nm and obtained shorter pulse than what can be obtained from compressed seed. The result can be explained by the deep saturation of the FEL output. This illustrated the potential in the future to generate short pulse using CPA process in an FEL device.

REFERENCES

- [1] G.T. Moore, Nucl. Instrum. Methods in Phys. Res. A 272, p. 302 (1988).
- [2] L.H. Yu *et al.*, Phys. Rev. E 49, 5, p. 4480 (1994).
- [3] C. Pellegrini, Nucl. Instrum. Methods in Phys. Res. A 445, p. 124 (2000).
- [4] G. Andonian *et al.*, Phys. Rev. Lett. **95**, 054801 (2005).
- [5] A. Doyuran *et al.*, Nucl. Instrum. Methods in Phys. Res. A 528, p. 467 (2004).
- [6] R. Trebino *et al.*, Lithuanian Journal of Physics, v. 33, p. 247-252.
- [7] Z. Wu *et al.*, in Proc. of FEL-2004.
- [8] E. Saldin *et al.*, Phys. Rev. ST-SB, 9, 050702 (2006).

ISSUES IN HIGH HARMONIC SEEDING OF THE 4GLS XUV-FEL

B. Sheehy, Sheehy Scientific Consulting, New York, USA; J.A. Clarke, D. J. Dunning, N. R. Thompson, CCLRC, ASTeC, Daresbury Laboratory, Warrington, UK; B. W. J. McNeil, SUPA, Department of Physics, University of Strathclyde, Glasgow, UK

Abstract

Using High Harmonics (HH) as a seed for free electron lasers is currently under consideration in a number of proposed facilities. An HH seed source is independent of machine dynamics, and allows for extensive manipulation of the seed pulse using well-established techniques of ultrafast laser physics. These allow for rapid tuning, and may enable the extension of chirped pulse amplification and even pulse shaping for coherent control to short wavelengths. In addition, there are advantages in terms of noise and synchronization. There are a number of issues involved in the implementation of HH seeding: energy, tunability, coherence, temporal structure, etc. We discuss these issues and their application in the 4GLS XUV-FEL.

INTRODUCTION

The limitations of spontaneous sources have motivated a great deal of development in short-wavelength FEL design. For reasons of stability, coherence and bandwidth, SASE sources are disadvantageous relative to coherent alternatives. A number of seeding methods have been proposed, including high-gain harmonic generation, several self-seeding techniques, and using high harmonic generation to produce sufficient radiation at the fundamental resonant wavelength of the radiator to directly seed the FEL.

The attraction of seeding with high harmonics is that a great deal of control over the seed radiation can be had by using well-known ultrafast laser techniques to control the fundamental that drives the HH generation. Harmonic pulses can be made extremely short, down to a few femtoseconds, and tuning is relatively simple. Demands on timing and synchronization with the electron bunch are less stringent than in other techniques. Also, the coherent transfer of phase information from the HH pump to the harmonics opens the possibility of creating a chirped HH seed and performing chirped pulse amplification [1] in the FEL to achieve higher output energies, or even of pursuing more elaborate pulse shaping.

The efficiency of HH generation is currently too low for FEL seeding at soft X-ray energies. However, in the wavelength range planned for the 4GLS XUV-FEL (8-100 eV), available sources could provide sufficient energy for seeding at kHz repetition rates, and the available energy will increase with coming improvements in ultrafast laser technology.

A number of other issues must also be addressed. Tunability is required, and must be provided in a way that minimizes downtime and perturbations to timing and

synchronization. Other spectral and temporal properties have also been raised as issues. We address these issues and discuss the implementation of seeding in the 4GLS XUV-FEL.

ENERGY AND TUNABILITY

The 4GLS XUV-FEL will operate between 8-100 eV. We have simulated the XUV-FEL [2], using GENESIS 1.3 [3], using 100 kW peak seed power for output photon energies below 30 eV, and 30 kW for energies between 30 eV and 100 eV. For 30 fsec pulses, this is equivalent to 3 nJ and 1 nJ pulse energies respectively. This is three orders of magnitude above the spontaneous power generated in the first gain length due to intrinsic density fluctuations in the electron bunch, and, in simulations produces an output pulse with good contrast [2].

A number of groups have measured harmonic yields from Ti:Sapphire based systems, and we show a scaled synopsis of recent results [4-6] in Fig. 1. The experimental results represented here (unconnected points on the plot) were obtained using fundamental pulse energies from 3-50 mJ, and we have scaled the results to an energy of 14 mJ – the energy of the Ti:Sapphire system described below. These scaled yields exceed our requirements by over three orders of magnitude at the low energy end of the XUVFEL operating range, and by a factor of six at the high energy end.

The scaling energy of 14 millijoules was chosen because such a laser system has been demonstrated at kHz repetition rates [7]. This is conservative, as ultrafast laser technology is developing very rapidly, and extension to higher powers is not constrained by a fundamental limit. A number of recent developments, eg the use of optical parametric chirped pulse amplification [8], high power Yb:YAG lasers [9], and enhancement cavities [10-12], offer new opportunities for larger systems. Several 100-Watt kilohertz system designs have been proposed [13], and are likely to be demonstrated soon.

There is also considerable effort in the community focused on extending the wavelength range and yield of harmonics. Recent experiments [6] using two-color fields demonstrated an enhancement of over 2 orders of magnitude in the harmonic yield in Helium, producing 150 nanojoules in the 38th harmonic (59 eV), using only 2.8 mJ in the pump laser. Fig. 1 also shows the results of that experiment (scaled from the experimental energy of 2.8 mJ to 14 mJ). Since Helium is the least efficient of the rare gas targets used, it is reasonable to expect that when these techniques are extended to other gases and longer

pump wavelengths, available seed energies over the XUV-FEL operating range will increase substantially.

The simplest and most versatile way to tune between the harmonic orders is through control of the amplitude and phase of the fundamental. This can be as simple as a chirp [14-16], but more general adaptive pulse shaping [17-20] allows greater tuning range and greater control over the harmonic pulse width. This method presents minimal impact on synchronization during tuning, and is rapid once the system has been calibrated. The tuning range is of the order of $q\Delta\nu$, where q is the harmonic order and $\Delta\nu$ is the bandwidth of the fundamental, so the method does not work well at low harmonic orders. Reitze et al [18] demonstrated complete tunability (i.e. a tuning range exceeding the separation of adjacent harmonics) down to 40 eV in Argon using 28 fsec, 800 nm pulses, a tuning range of $2.2q\Delta\nu$. At some energy below 40 eV, complete tunability will be lost. For this reason in the current design, a tunable fundamental is used for the low-energy end of the XUV-FEL energy range.

Using a tunable fundamental entails a double loss, from the frequency conversion losses as well as the drop in harmonic efficiency at longer wavelengths [21]. Conversion to wavelengths shorter than 800 nm, where the harmonic efficiency is higher, is possible, but then the harmonic orders used to reach the very low end of the tuning range are smaller, and complete tunability cannot be obtained there. For an infrared source tunable from 1200 nm to 1475 nm, complete tunability would be obtained. Conversion efficiencies for commercial noncollinear phase-matched optical parametric amplifier (NOPA) systems in this range, pumped by a Ti:Sapphire system, are typically ~10%, while laboratory systems have reported efficiencies of 20% [22]. The harmonic efficiency drops as λ^{-3} [21,23,24], so it is 15-30% of the harmonic efficiency at 800 nm. Harmonic efficiencies are high enough at these lower energies that sufficient seed power can still be produced. Fig. 1 shows the projected range of the tunable source's harmonic yields in Xenon using the expected wavelength scaling of the harmonic efficiency, and assuming 15% conversion efficiency in the NOPA. Above 40 eV, tuning is done using adaptive control of the Ti:Sapphire fundamental

Developments in laser technology will probably make this two-track system unnecessary in the near future, as new high-power kilohertz ultrafast sources in the 1-2 micron wavelength range are developed [13]. Because the high energy cutoff of harmonic production increases with λ^2 [25], at longer wavelength, gases with higher harmonic efficiency can be used to generate higher photon energies, offsetting some of the wavelength-dependent drop in efficiency. A longer fundamental wavelength also increases the wavelength range over which adaptive tuning may be used, since the harmonic order q for a given wavelength increases and the harmonic spacing decreases. For example, assuming an adaptive tuning range of $2q\Delta\nu$, a source with a fixed wavelength of 1.8

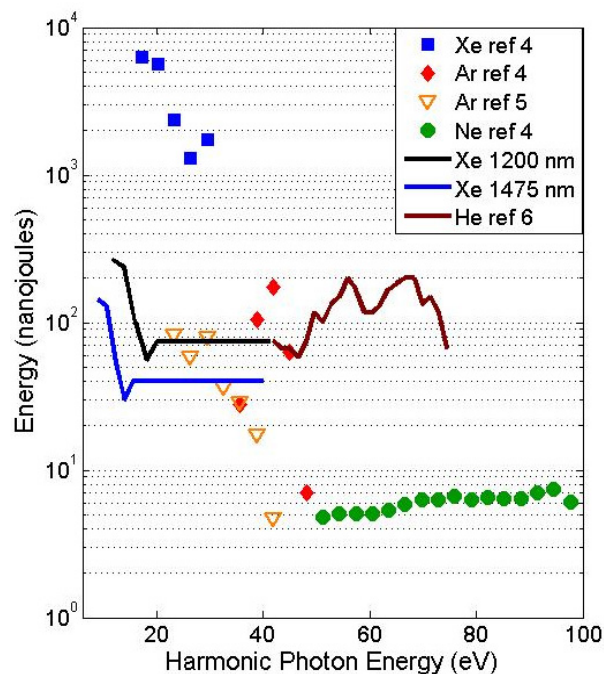


Figure 1. Recent high harmonic generation experimental results scaled by energy and wavelength. The unconnected points were taken with an 800 nm fundamental, and are scaled here to a pulse energy of 14 mJ. The solid Xe curves show the projected range of harmonic yields for the NOPA (2 mJ pulse energy), tuning between 1200 and 1475 nm. The solid He curve shows the results of a two-color experiment using 800 and 400 nm fundamentals, scaled to a 14 mJ pump energy. The minimum energy for seeding the XUV-FEL with a 30 fs pulse is 1 nJ.

microns and 20 fsec pulse width could cover the entire XUV-FEL energy range using only adaptive tuning.

COHERENCE, STRUCTURE AND CONTRAST

Other spectral and temporal qualities of the harmonics must also be considered. Over the design range of the XUV-FEL, the gain bandwidth of the FEL radiator is both larger than the bandwidth of individual harmonics, and much smaller than the separation between harmonics. This allows for efficient seeding without requiring the separation of harmonic orders in the seeding optics. The transverse spatial coherence of harmonics depends sensitively on the generation geometry, but very high coherent flux has been measured [26]. This concerns primarily the seeding efficiency, as the spatial coherence increases dramatically as the pulse is amplified to saturation.

Because harmonics are used to generate attosecond pulses, there is some question whether subfemtosecond temporal structure could affect seeding. There are, however, fundamental reasons for expecting little effect from this structure. Sub-femtosecond structure arises from the coherent superposition of multiple harmonics; it

is essentially an interference effect. Since the FEL radiator's bandwidth is restricted to a single harmonic order (the harmonic separation is ~ 3 eV, while the FWHM gain bandwidth of the radiator lies in the range of .04-.4 eV) it effectively acts as a filter, and the time profile of an individual harmonic, which is smooth [27], is the relevant temporal shape. Furthermore, the period of any sub-femtosecond structure is quite short – half of the fundamental optical cycle – so that, even if multiple harmonics could be amplified, slippage would tend to smooth out any short scale structure. We have considered the attosecond structure issue in our simulations however, and it is discussed in greater detail in Ref. [28].

An issue in all seeding techniques is the achievable contrast between the coherent output pulse and any incoherent background. This is of particular concern in experiments involving nonlinear interactions, as lower-order interactions with the background pedestal surrounding the main pulse can alter the target's initial state before the main pulse arrives or the product state after the main pulse is over, so that both the height of the background and the length of the window over which it persists are important. Our simulations [2,28] show that, for the minimal seed power, we obtain, over the XUV-FEL energy range, contrasts of 10^{-2} to 10^{-3} immediately beneath the main pulse, dropping to 10^{-5} to 10^{-7} within a picosecond on either side of the pulse.

The background consists of SASE evolving in the unseeded part of the bunch, and so the context of these numbers should also be considered carefully. First, the contrast improves with increasing seed power, as the length to saturation decreases and the ratio of the coherent seed power to spontaneous power in the wings of the pulse increases. The feasibility simulations were done with minimal seed power but, depending on the energy and tunability required, orders of magnitude more may be available. The simulations were also done with a Gaussian longitudinal electron bunch distribution with a FWHM pulse width of 625 fs; more sharply peaked distributions would also improve contrast, as the gain in the wings would drop accordingly. The full parameter space has not yet been explored with respect to contrast, and these aspects will be investigated further in future design work. A more detailed discussion and simulation results may be found in Ref [2].

IMPLEMENTATION

The current design for implementing HH seeding in the 4GLS XUV-FEL is shown schematically in Fig. 2. An ultrafast Titanium Sapphire oscillator producing 30 fsec, 800 nm pulses is synchronized at a subharmonic of the accelerator RF frequency. Pulses are selected at 1 kHz and amplified to 14 mJ. Amplifier chains capable of this power presently exist [7], and systems with higher output are expected to appear soon.

After amplification, the pulse is switched into one of two paths, depending on the FEL photon energy. For low

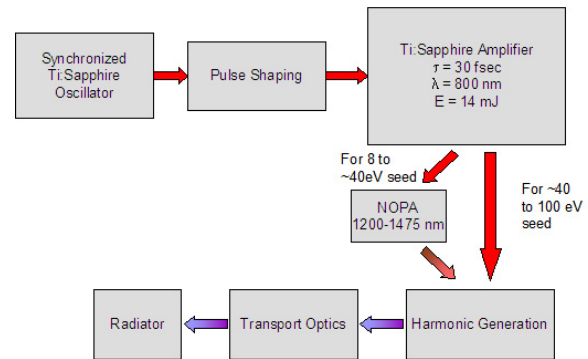


Figure 2. Block diagram of high harmonic seeding for the 4GLS XUV-FEL.

energies (8 to approximately 40 eV), a tunable pump pulse is generated using a noncollinear optical parametric amplifier (NOPA) operating between 1200-1475 nm. At higher energies (40 - 100 eV), the 800 nm light is used for HH generation, and adaptive tuning is used. Pulse shaping for the adaptive tuning can be done either before the amplifier, as shown here, or afterwards.

The geometry for the HH generation is still under study. A loose focusing geometry in a variable length cell is the simplest to implement over the entire range of the XUV-FEL and is equivalent to waveguide geometries at sufficiently high power [29]. Waveguide geometries [30] may be beneficial for the low photon energies, where the pump pulse energy is lower, Modulated waveguide geometries [31] may provide greater efficiency, but it may be difficult to implement multiple configurations to cover the entire wavelength range. Efficient materials (eg SiC) for grazing incidence optics are available for the optics coupling the HH seed into the radiator.

SUMMARY

We have developed a design to establish the feasibility of seeding the 4GLS XUV-FEL with high harmonics. Currently available technology is capable of supplying sufficient seed energy, and tuning may be accomplished with a tunable fundamental at the low-energy end of the XUV-FEL operating range, and with pulse shaping of a fixed-frequency fundamental at higher energies. Technological improvements are expected to increase the available power and simplify the implementation. Spectral and temporal properties of the harmonics appear to be commensurate with the requirements for seeding.

REFERENCES

- [1] L. H. Yu et al., Physical Review E 49 (1994) 4480.
- [2] *4GLS Conceptual Design Report*. (Council for the Central Laboratory of the Research Councils, UK, <http://www.4gls.ac.uk/>, 2006)

- [3] S. Reiche, Nuclear Instruments and Methods A 429 (1999) 243.
- [4] E. J. Takahashi et al., IEEE Journal of Selected Topics in Quantum Electronics 10 (2004) 1315.
- [5] J. F. Hergott et al., Physical Review A 66 (2002) 021801.
- [6] I. Jong Kim et al., Physical Review Letters 94 (2005) 243901.
- [7] Y. Nabekawa et al., Optics Letters 23 (1998) 1384.
- [8] A. Dubietis et al., Optics Communications 88 (1992) 437.
- [9] D. J. Ripin et al., IEEE Journal of Quantum Electronics 41 (2005) 1274.
- [10] R. Jones and J. Ye, Optics Letters 27 (2002) 1848.
- [11] R. Jones and J. Ye, Optics Letters 29 (2004) 2812.
- [12] F. Ö. Ilday and F. X. Kärtner, "Cavity-Enhanced Optical Parametric Chirped-Pulse Amplification," Joint Conference on Ultrafast Optics V and Applications of High Field and Short Wavelength Sources XI, Nara, Japan, 2005,
- [13] F. X. Kärtner et al., "Experiments in Laser Seed Generation," MIT Workshop on the Physics of Seeded FELs, Boston, MA, June 2004,
- [14] J. Zhou et al., Physical Review Letters 76 (1996) 752.
- [15] D. G. Lee et al., Physical Review Letters 87 (2001) 243902.
- [16] H. T. Kim et al., Physical Review A 67 (2003) 051801.
- [17] R. Bartels et al., Nature 406 (2000) 164.
- [18] D. H. Reitze et al., Optics Letters 29 (2004) 86.
- [19] T. Pfeifer et al., Optics Letters 30 (2005) 1497.
- [20] T. Pfeifer et al., Appl Physical B 80 (2005) 277.
- [21] M. Lewenstein et al., Physical Review A 49 (1994) 2117.
- [22] V. Yakovlev, B. Kohler, and K. Wilson, Optics Letters 19 (1994) 2000.
- [23] B. Shan and Z. Chang, Physical Review A 65 (2002) 011804.
- [24] A. Gordon and F. X. Kärtner, Optics Exp 13 (2005) 2941.
- [25] J. L. Krause, K. J. Schafer, and K. C. Kulander, Physical Review Letters, 68 (1992) 3535.
- [26] L. Le Deroff et al., Physical Review A 61 (2000) 043802.
- [27] I. P. Christov, M. M. Murnane, and H. C. Kapteyn, Physical Review Letters 78 (1997), 1251.
- [28] B. W. J. McNeil et al. "The Use of HHG at 4GLS", These proceedings MOCAU03
- [29] S. Kazamias et al., Physical Review Letters 90 (2003) 193901.
- [30] C. G. Durfee III et al., Physical Review Letters 83 (1999) 2187.
- [31] A. Paul et al., Nature 421 (2003) 51.

ATTOSECOND PULSES FROM X-RAY FEL WITH AN ENERGY-CHIRPED ELECTRON BEAM AND A TAPERED UNDULATOR

E.L. Saldin, E.A. Schneidmiller, and M.V. Yurkov
Deutsches Elektronen-Synchrotron (DESY), Hamburg, Germany.

Abstract

We present a new scheme for generation of attosecond pulses in X-ray SASE FEL. A short slice in the electron beam is strongly modulated in energy by a few-cycle laser pulse in a short undulator, placed in front of the main undulator. Gain degradation within this slice is compensated by an appropriate undulator taper while the rest of the bunch suffers from this taper and does not lase. Three-dimensional simulations with the code FAST predict that short (200 attoseconds) high-power (up to 100 GW) pulses can be produced in Angstrom wavelength range with a high degree of contrast. A possibility to reduce pulse duration to sub-100 attosecond scale is discussed.

INTRODUCTION

Generation of attosecond pulses would significantly increase scientific potential of future hard X-ray FELs such as European XFEL [1] and Linac Coherent Light Source [2]. Up to now several schemes for generation of attosecond pulses from X-ray SASE FELs have been proposed [3, 4, 5, 6, 7, 8]. In this paper we study a new scheme making use of energy chirp in the electron beam and a tapered undulator. The impact of energy chirp on SASE FEL performance was studied in details in [9]. It was found that FEL gain degradation can be perfectly compensated by undulator tapering. An application of the compensation effect for generation of attosecond pulses from X-ray FELs was conceptually proposed in [9]. In this paper we present the results of numerical simulations demonstrating that the scheme works very well in a realistic situation. We also discuss a possible extension of this scheme that can allow to generate high-power, high-contrast hard X-ray pulses with a duration in 10-100 attosecond range.

ENERGY CHIRP AND UNDULATOR TAPERING

The energy chirp parameter [9]

$$\hat{\alpha} = -\frac{d\gamma}{dt} \frac{1}{\gamma_0 \omega_0 \rho^2} \quad (1)$$

is defined such that, for positive sign of $\hat{\alpha}$, particles in the head of the bunch have larger energy than those in the tail. Here $\rho = \lambda_w \Gamma / (4\pi)$ is the efficiency parameter, $\Gamma^3 = \pi j_0 K^2 A_{JJ}^2 / (I_A \lambda_w \gamma_0^3)$, j_0 is the beam current density, $I_A = mc^3/e \simeq 17$ kA, γ_0 is relativistic factor, $K = e\lambda_w H_w / (2\sqrt{2}\pi mc^2)$ is rms undulator parameter, $A_{JJ} = J_0(Q) - J_1(Q)$ is the Bessel function factor, $Q = K^2 / [2(1 + K^2)]$, Relativistic factor γ_0 and reference

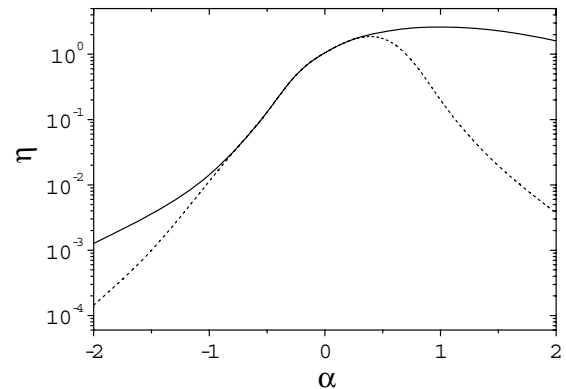


Figure 1: Normalized output power versus parameter $\hat{\alpha}$. Solid: $\hat{z} = \hat{z}_{\text{sat}}(\hat{\alpha})$; dash: $\hat{z} = \hat{z}_{\text{sat}}(0) = 13$.

frequency ω_0 are connected by the FEL resonance condition: $\omega_0 = 2ck_w \gamma_0^2 / (1 + K^2)$. It is also useful to define normalized detuning [11]: $\hat{C} = [k_w - \omega(1 + K^2) / 2c\gamma_0^2] / \Gamma$.

A high-gain linear regime of a chirped SASE FEL operation was studied in [10, 9]. The main results of the simulations of the nonlinear regime [9] with 1-D version of the code FAST [11, 12] are presented in Fig. 1. Saturation length and power are functions of two parameters, $\hat{\alpha}$ and N_c . For our simulations we have chosen $N_c = 3 \times 10^7$ - a typical value for VUV SASE FELs. Note, however, that the results, presented in Fig. 1, very weakly depend on N_c . In Fig. 1 the output power is plotted versus chirp parameter for two cases: when undulator length is equal to a saturation length for a given $\hat{\alpha}$ and when it is equal to the saturation length for the unchirped beam case ($\hat{z} = 13$). One can see sharp reduction of power for negative $\hat{\alpha}$ while a mild positive chirp ($\hat{\alpha} < 0.5$) is beneficial for SASE.

Let us consider now the case when there is no energy chirp ($\hat{\alpha} = 0$) and the detuning parameter changes linearly along the undulator [11]: $\hat{C}(\hat{z}) = \hat{b}_1 \hat{z}$. This change can be due to variation of undulator parameters ($K(\hat{z})$ and/or $k_w(\hat{z})$), or due to an energy change $\gamma_0(\hat{z})$.¹ We have found from numerical simulations [9] that in such case the effect on FEL gain is exactly the same as in the case of energy chirp and no taper if $\hat{\alpha} = 2\hat{b}_1$ for any value of $\hat{\alpha}$ (Figure 2 shows an example).

A symmetry between two considered effects (energy chirp and undulator tapering) can be understood as follows.

¹An effect of undulator tapering (or energy change along the undulator) on FEL gain was studied in [13] in the limit $\hat{b}_1 \ll 1$.

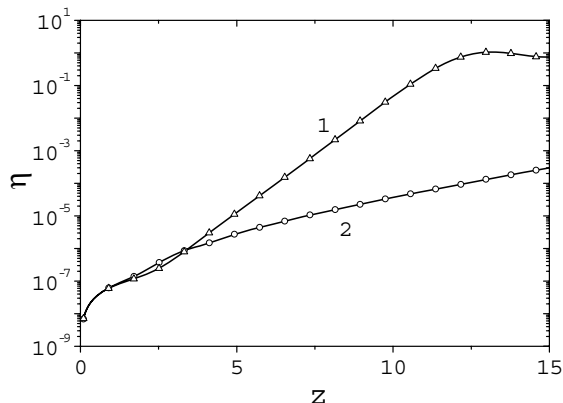


Figure 2: Normalized power versus undulator length. Solid line 1: $\hat{\alpha} = 0$, $\hat{b}_1 = 0$; triangles: $\hat{\alpha} = 4$, $\hat{b}_1 = -2$; solid line 2: $\hat{\alpha} = 4$, $\hat{b}_1 = 0$; circles: $\hat{\alpha} = 0$, $\hat{b}_1 = 2$.

If we look at the radiation field acting on some test electron from an electron behind it, this field was emitted at a retarded time. In the first case a back electron has a detuning due to an energy offset, in the second case it has the same detuning because undulator parameters were different at a retarded time. The question arises: can these two effects compensate each other? We give a positive answer based on numerical simulations (see Fig. 2 as an example): by setting $\hat{b}_1 = -\hat{\alpha}/2$ we get rid of gain degradation, and FEL power at any point along the undulator is the same as in the case of unchirped beam and untapered undulator. This holds for any value of $\hat{\alpha}$. For instance, if one linearly changes magnetic field H_w of the undulator, the compensation condition can be written as follows (nominal values of parameters are marked with subscript '0'):

$$\frac{1}{H_{w0}} \frac{dH_w}{dz} = -\frac{1}{2} \frac{(1 + K_0^2)^2}{K_0^2} \frac{1}{\gamma_0^3} \frac{d\gamma}{cdt} \quad (2)$$

Of course, in such a case we get frequency chirped SASE pulse. Since compensation of gain degradation is possible also for large values of $\hat{\alpha}$ (there is no theoretical limit on the value of chirp parameter, except for above mentioned condition $\rho\hat{\alpha} \ll 1$), one can, in principle, organize a regime when a frequency chirp within an intensity spike is much larger than the natural FEL bandwidth (given by $\rho\omega_0$).

GENERATION OF ATTOSECOND PULSES

A new scheme looks similar to those considered in [5, 6] making use of energy modulation of a short slice in the electron bunch by a high-power few-cycle optical pulse in a two-period undulator. Due to energy modulation the frequency of SASE radiation in X-ray undulator is correlated to the longitudinal position within the few-cycle-driven slice of the electron beam. The largest frequency offset corresponds to a single-spike pulse in time domain (about

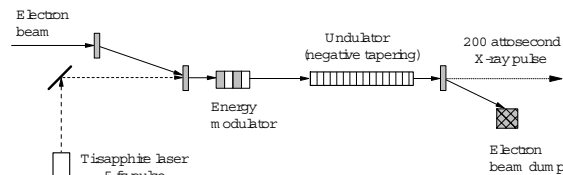


Figure 3: Schematic diagram of attosecond X-ray source. Energy modulator performs slice energy modulation of the electron bunch (see Fig. 5). Undulator tapering leads to complete suppression of the amplification process in the most fraction of the electron bunch, and output X-ray pulse has 200 attosecond pulse duration.

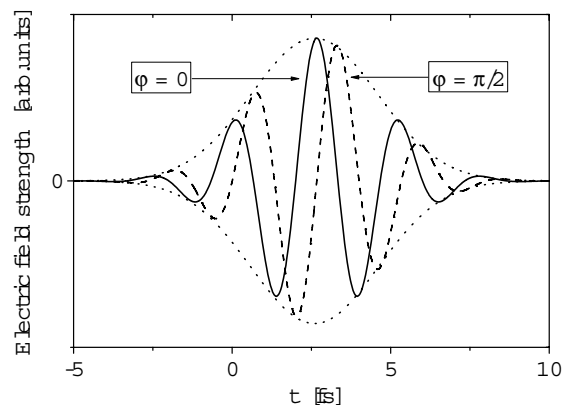


Figure 4: Possible evolutions of the electric field in the 5-fs pulse, carried at a wavelength 800 nm for two different pulse phases ($\phi = 0, \pi/2$)

300 attoseconds). The selection of single-spike pulses is achieved by using a crystal monochromator after the X-ray undulator [5], or with the help of the other undulator tuned to the offset frequency [6].

In this paper we consider a new scheme (see Fig. 3) that makes use of the compensation effect, described in the previous Section. Indeed, there is a strong energy chirp around zero-crossing of energy modulation. If one uses appropriate undulator taper then only a short slice around zero-crossing produces powerful FEL pulse. The main part of the bunch is unmodulated and suffers from strong negative undulator tapering (see Fig. 1). One should also note that for large negative taper the SASE FEL gain is very sensitive to longitudinal velocity spread. Therefore, a high-contrast attosecond pulse is directly produced in the undulator.

Operation of attosecond SASE FEL is illustrated for the parameters close to those of the European XFEL operating at the wavelength 0.15 nm [1]. The parameters of the electron beam are: energy 15 GeV, charge 1 nC, rms pulse

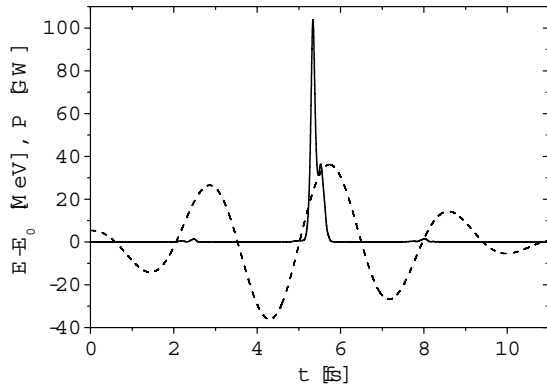


Figure 5: Energy modulation of the electron beam at the exit of the modulator undulator (dotted line) and a profile of the radiation pulse at the undulator length 100 m

length $25 \mu\text{m}$, rms normalized emittance 1.4 mm-mrad, rms energy spread 1 MeV. Undulator period is 3.65 cm, and the rms K-value is 2.5.

The parameters of the seed laser are: wavelength 800 nm, energy in the laser pulse 3 mJ, and FWHM pulse duration 5 fs (see Fig. 4). The laser beam is focused onto the electron beam in a short undulator resonant at the optical wavelength of 800 nm. Optimal conditions of the focusing correspond to the positioning of the laser beam waist in the center of the modulator undulator. It is assumed that the phase of laser field corresponds to "sine" mode (dashed line with $\varphi = \pi/2$, see Fig. 4). Parameters of the modulator undulator are: period length 50 cm, peak field 1.6 T, number of periods 2. The interaction with the laser light in the undulator produces a time-dependent electron energy modulation as it is shown in Fig. 5. This modulation corresponds to the energy chirp parameter $\hat{\alpha} \simeq 2$ at zero crossing ($t = 5$ fs in Fig. 5).

Optimization of the attosecond SASE FEL has been performed with the three-dimensional, time dependent code FAST [12] taking into account all physical effects influencing the SASE FEL operation (diffraction effects, energy spread, emittance, slippage effect, etc.). Three-dimensional simulations confirmed the predictions of the one-dimensional model: the energy chirp and the undulator tapering compensate each other, there is strong suppression of the amplification in the case of uncompensated negative taper.

Undulator tapering is performed by changing the gap of undulator modules [1] such that magnetic field increases linearly along the undulator length ($\hat{b}_1 < 0$). We performed the scan of tapering depth \hat{b}_1 in order to maximize the power in the main peak on one hand, and to minimize contribution of the background, on the other hand. We ended up with the value of taper which is about 20 % smaller than that required for a perfect compensation of chirp at $t = 5$

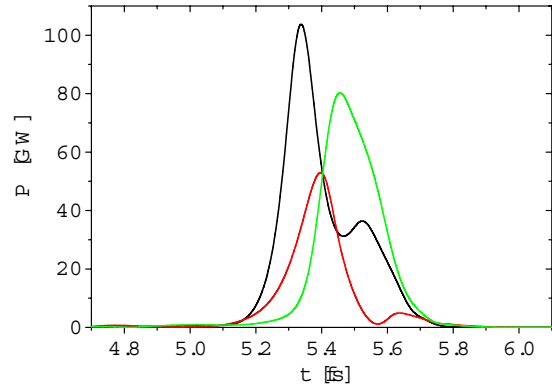


Figure 6: Temporal structure of the radiation pulse (three different shots) at the undulator length 100 m.

fs. Note that the chirp is not linear in the region of interest. In addition, a mild net positive chirp is beneficial for SASE, as it was discussed above (see Fig. 1).

A typical radiation pulse at the undulator length 100 m is shown in Fig. 5. One can see a high-power spike in the region where the energy chirp is well compensated by the taper and two weak side peaks at $t \simeq 2$ fs and $t \simeq 8$ fs where the net effect is negative taper. In the rest of the bunch a large negative taper together with velocity spread and 3-D effects completely suppresses amplification. In Fig. 6 we present three different shots illustrating the properties of the main peak. Typical pulse duration is about 200 attoseconds (FWHM) and peak power ranges from several tens up to hundred GW. To estimate the contrast (which we define as the ratio of energy in the main peak to the total radiated energy at the experiment) we assume that an angular collimation is used in order to reduce spontaneous emission background. A collimator with half-angle $3 \mu\text{rad}$ allows the entire intensity in the main peak to be transmitted. The contrast is influenced by SASE intensity in two side peaks and by spontaneous emission in the first harmonic from the rest of the bunch. For the charge of 1 nC, as in our numerical example, the contrast is about 95 %. Higher harmonics of undulator radiation (if they disturb an experiment) can be cut, for instance, by a multilayer monochromator with a bandwidth of the order of 1 %.

BEYOND "FUNDAMENTAL LIMIT"

It is generally accepted that the shortest pulse, that can be obtained from a SASE FEL, is given by a duration of intensity spike in time domain, i.e. it is defined by inverse FEL bandwidth $(\rho\omega_0)^{-1}$. However, the fact that a SASE FEL can operate with a strong chirp parameter (in combination with undulator tapering) without gain degradation, opens up a possibility of a conceptual breakthrough: one can get from SASE FEL a radiation pulse which is much

shorter than the inverse FEL bandwidth. Indeed, in the case of $\hat{\alpha} \gg 1$, the frequency chirp inside an intensity spike is much larger than FEL bandwidth. Thus, one can use a monochromator to reduce pulse duration. By an appropriate choice of the monochromator bandwidth one can select an X-ray pulse that is shorter by a factor of $\sqrt{2\hat{\alpha}}$ than the inverse FEL bandwidth. The only theoretical limit in this case is given by the condition $\rho\hat{\alpha} \ll 1$. Note that for hard X-ray FELs the parameter ρ is in the range $10^{-4} - 10^{-3}$.

To illustrate a possible technical realization of this idea, we can suppose that the energy modulation by a few-cycle optical pulse is increased by a factor 3 so that $\hat{\alpha} \simeq 6$. In combination with undulator tapering and a monochromator, this would allow to obtain sub-100-GW coherent X-ray pulses with a duration below 100 attoseconds and a contrast above 90 %. Note that the contrast remains high because the spectrum of spontaneous emission from the rest of the bunch gets broader due to the stronger taper.

REFERENCES

- [1] M. Altarelli et al. (Eds.): XFEL: The European X-Ray Free-Electron Laser. Technical Design Report, Preprint DESY 2006-097, DESY, Hamburg, 2006.
- [2] J. Arthur et al.: Linac Cherenkov Light Source (LCLS). Conceptual Design Report, SLAC- R593, Stanford, 2002.
- [3] E.L. Saldin and E.A. Schneidmiller and M.V. Yurkov, Opt. Commun. **212**(2002)377.
- [4] A.A. Zholents and W.M. Fawley, Phys. Rev. Lett. **92**(2004)224801.
- [5] E.L. Saldin, E.A. Schneidmiller, M.V. Yurkov, Opt. Comm. **237**(2004)153.
- [6] E.L. Saldin, E.A. Schneidmiller, M.V. Yurkov, Opt. Comm. **239**(2004)161.
- [7] P. Emma, Z. Huang and M. Borland, Proc. of the 2004 FEL Conference, p. 333.
- [8] A.A. Zholents and G. Penn, Phys. Rev. ST Accel. Beams **8**(2005)050704.
- [9] E.L. Saldin, E.A. Schneidmiller, M.V. Yurkov, Proc. of the 2005 FEL Conference, p. 258.
- [10] S. Krinsky, Z. Huang, Phys. Rev. ST Accel. Beams **8**(2003)050702.
- [11] E.L. Saldin, E.A. Schneidmiller, M.V. Yurkov, *The Physics of Free Electron Lasers* (Springer-Verlag, Berlin, 1999).
- [12] E.L. Saldin, E.A. Schneidmiller, M.V. Yurkov, Nucl. Instr. and Methods **A 429**(1999)233.
- [13] Z. Huang and G. Stupakov, Phys. Rev. ST Accel. Beams **8**(2005)040702.

TRANSVERSE AND LONGITUDINAL COHERENCE PROPERTIES OF THE RADIATION FROM X-RAY SASE FELS

E.L. Saldin, E.A. Schneidmiller, and M.V. Yurkov
Deutsches Elektronen-Synchrotron (DESY), Hamburg, Germany

Abstract

We present a comprehensive analysis of coherence properties of the radiation from X-ray free electron laser (XFEL). We consider practically important case when XFEL is optimized for maximum gain. Such an optimization allows to reduce significantly parameter space. Application of similarity techniques to the results of numerical simulations allows to present all output characteristics of the optimized XFEL as functions of the only parameter, ratio of the emittance to the radiation wavelength, $\hat{\epsilon} = 2\pi\epsilon/\lambda$. Our studies show that optimum performance of the XFEL in terms of transverse coherence is achieved at the value of the parameter $\hat{\epsilon}$ of about unity. At smaller values of $\hat{\epsilon}$ the degree of transverse coherence is reduced due to strong influence of poor longitudinal coherence on a transverse one. At large values of the emittance the degree of transverse coherence degrades due to poor mode selection. Comparative analysis of existing XFEL projects, European XFEL, LCLS, and SCSS is presented as well.

INTRODUCTION

In the X-ray FEL the radiation is produced by the electron beam during single-pass of the undulator [1]. The amplification process starts from the shot noise in the electron beam. Any random fluctuations in the beam current correspond to an intensity modulation of the beam current at all frequencies simultaneously. When the electron beam enters the undulator, the presence of the beam modulation at frequencies close to the resonance frequency initiates the process of radiation. The FEL collective instability in the electron beam produces an exponential growth (along the undulator) of the modulation of the electron density on the scale of undulator radiation wavelength. The fluctuations of current density in the electron beam are uncorrelated not only in time but in space, too. Thus, a large number of transverse radiation modes are excited when the electron beam enters the undulator. These radiation modes have different gain. As undulator length progresses, the high gain modes start to predominate more and more. For enough long undulator, the emission will emerge in a high degree of transverse coherence.

The first analysis of the problem of transverse coherence has been performed in [2]. It has been found that even after finishing the transverse mode selection process the degree of transverse coherence of the radiation from SASE

FEL visibly differs from the unity. This is consequence of the interdependence of the longitudinal and transverse coherence. First studies of the evolution of transverse coherence in the nonlinear regime of SASE FEL operation have been performed in [3]. It has been found that the degree of transverse coherence reaches maximum value in the end of the linear regime. Further increase of the undulator length leads to its decrease. Despite output power of the SASE FEL grows continuously in the nonlinear regime, maximum brilliance of the radiation is achieved in the very beginning of the nonlinear regime. Due to limited computing power available at that time we limited our study with a specific numerical example just illustrating the general features of coherence properties of the radiation produced by the SASE FEL operating in the nonlinear regime.

In this paper we present general analysis of the coherence properties (longitudinal and transverse) of the radiation from SASE FEL. The results have been obtained with time-dependent, three-dimensional FEL simulation code FAST [4] performing simulation of the FEL process with actual number of electrons in the beam. Using similarity techniques we present universal dependencies for the main characteristics of the SASE FEL covering all practical range of X-ray FELs.

BASIC RELATIONS

Design of the focusing system of XFEL assumes nearly uniform focusing of the electron beam in the undulator, so we consider axisymmetric model of the electron beam. It is assumed that transverse distribution function of the electron beam is Gaussian, so rms transverse size of matched beam is $\sigma = \sqrt{\epsilon\beta}$, where $\epsilon = \epsilon_n/\gamma$ is rms beam emittance and β is focusing beta-function. In the case of negligibly small effects of the space charge and energy spread, operation of the FEL amplifier is described by the diffraction parameter B and the betatron motion parameter \hat{k}_β : [5]:

$$B = 2\Gamma\sigma^2\omega/c, \quad \hat{k}_\beta = 1/(\beta\Gamma), \quad (1)$$

where $\Gamma = [I\omega^2\theta_s^2 A_{JJ}^2 / (I_A c^2 \gamma_z^2 \gamma)]^{1/2}$ is the gain parameter. When describing shot noise in the electron beam, one more parameter appears, the number of electrons in the volume of coherence: $N_c = I/(e\omega\rho)$, where $\rho = c\gamma_z^2\Gamma/\omega$ is the efficiency parameter. The following notations are used here: I is the beam current, $\omega = 2\pi c/\lambda$ is the frequency of the electromagnetic wave, $\theta_s = K_{\text{rms}}/\gamma$, K_{rms} is the rms

undulator parameter, γ is relativistic factor, $\gamma_z^{-2} = \gamma^{-2} + \theta_s^2$, $k_w = 2\pi/\lambda_w$ is the undulator wavenumber, $I_A = 17$ kA is the Alfvén current, $A_{JJ} = 1$ for helical undulator and $A_{JJ} = J_0(K_{\text{rms}}^2/2(1 + K_{\text{rms}}^2)) - J_1(K_{\text{rms}}^2/2(1 + K_{\text{rms}}^2))$ for planar undulator. Here J_0 and J_1 are the Bessel functions of the first kind.

Target value of interest for XFEL optimization is the field gain length of the fundamental mode. For this practically important case the solution of the eigenvalue equation for the field gain length of the fundamental mode and optimum beta function are rather accurately approximated by [6]:

$$\begin{aligned} L_g &= 1.67 \left(\frac{I_A}{I} \right)^{1/2} \frac{(\epsilon_n \lambda_w)^{5/6}}{\lambda^{2/3}} \frac{(1 + K^2)^{1/3}}{K A_{JJ}} \\ \beta_{\text{opt}} &\simeq 11.2 \left(\frac{I_A}{I} \right)^{1/2} \frac{\epsilon_n^{3/2} \lambda_w^{1/2}}{\lambda K A_{JJ}}, \end{aligned} \quad (2)$$

Accuracy of this fit is better than 5% in the range of parameter $\hat{\epsilon} = 2\pi\epsilon/\lambda$ from 1 to 5. It follows from (1) and (2) that diffraction parameter B and parameter of betatron oscillations, \hat{k}_β are functions of the only parameter $\hat{\epsilon}$. FEL equations written down in the dimensionless form involve an additional parameter N_c defining the initial conditions for the start-up from the shot noise. Note that the dependence of output characteristics of the SASE FEL operating in saturation is slow, in fact logarithmic in terms of N_c .

SIMULATION ALGORITHM

Rigorous studies of the nonlinear stage of amplification is possible only with numerical simulation code. Typically FEL codes use an artificial ensemble of macroparticles for simulating of the FEL process when one macroparticle represents large number of real electrons. Thus, a natural question arises if macroparticle phase space distributions are identical to those of actual electron beam at all stages of amplification. Let us trace typical procedure for preparation of an artificial ensemble [7, 8]. The first step of particle loading consists in a quasi-uniform distribution of the macroparticles in the phase space. At this stage an ensemble of particles with random distribution is generated which occupies a fraction of the phase space. Then this ensemble is copied on the other parts of the phase space to provide pseudo-uniform loading of the phase space. Pseudo-uniformity means that initial microbunching at the fundamental harmonic (or for several harmonics) is equal to zero. Also, phase positions of the mirrored particles are correlated such that microbunching does not appear due to betatron oscillations, or due to the energy spread. Finally, artificial displacements of the macroparticles are applied to provide desired (in our case gaussian) statistics of microbunching at the undulator entrance. We note that it is not evident that such an artificial ensemble reflects actual physical situation for a short wavelength SASE FEL. Let us consider an example of the SASE FEL operating at the radiation wavelength of 0.1 nm. With the peak current of 5 kA we find

that the number of electrons per wavelength is about 10^4 . On the other hand, it is well known that properties of an artificial ensemble (even at the first step of pseudo-uniform loading) converge very slowly to the model of continuous media. In fact, even with the number of macroparticles per radiation wavelength 6.4×10^4 the FEL gain still visibly deviates from the target value. Introducing of an artificial noise makes situation with the quality of an ensemble preparation even more problematic. The only way to test the quality of an artificial ensemble is to perform numerical simulations with actual number of electrons in the beam. We constructed such a version of three-dimensional, time-dependent FEL simulation code FAST [4]. Comparison of the results with direct simulations of the electron beam and with an artificial distributions has shown that artificial ensembles are not adequate to the problem. Artificial effects are pronouncing especially when calculating such fine features as transverse correlation functions. Thus, all the simulations presented in this paper have been performed with code FAST using actual number of electrons in the beam.

GENERAL DEFINITIONS

The first-order transverse correlation function is defined as

$$\gamma_1(\vec{r}_\perp, \vec{r}'_\perp, z, t) = \frac{\langle \tilde{E}(\vec{r}_\perp, z, t) \tilde{E}^*(\vec{r}'_\perp, z, t) \rangle}{\left[\langle |\tilde{E}(\vec{r}_\perp, z, t)|^2 \rangle \langle |\tilde{E}(\vec{r}'_\perp, z, t)|^2 \rangle \right]^{1/2}},$$

where \tilde{E} is the slowly varying amplitude of the amplified wave. For a stationary random process γ_1 does not depend on time, and the degree of transverse is:

$$\zeta = \frac{\int |\gamma_1(\vec{r}_\perp, \vec{r}'_\perp)|^2 I(\vec{r}_\perp) I(\vec{r}'_\perp) d\vec{r}_\perp d\vec{r}'_\perp}{\left[\int I(\vec{r}_\perp) d\vec{r}_\perp \right]^2}, \quad (3)$$

where $I(\vec{r}_\perp) = \langle |\tilde{E}(\vec{r}_\perp)|^2 \rangle$. The first order time correlation function, $g_1(t, t')$, is calculated in accordance with the definition:

$$g_1(\vec{r}, t - t') = \frac{\langle \tilde{E}(\vec{r}, t) \tilde{E}^*(\vec{r}, t') \rangle}{\left[\langle |\tilde{E}(\vec{r}, t)|^2 \rangle \langle |\tilde{E}(\vec{r}, t')|^2 \rangle \right]^{1/2}}, \quad (4)$$

For a stationary random process time correlation functions are functions of the only argument, $\tau = t - t'$. The coherence time is defined as

$$\tau_c = \int_{-\infty}^{\infty} |g_1(\tau)|^2 d\tau. \quad (5)$$

If one traces evolution of the brilliance of the radiation along the undulator length there is always the point, which we define as the saturation point, where the brilliance reaches maximum value [9]. In the following we present characteristics of the radiation at the saturation point which

are universal functions of the only parameter, $\hat{\epsilon}$. In fact, the brilliance is proportional to the degeneracy parameter δ , i.e. the number of photons in a single pulse which are transversely and longitudinally coherent. We introduce a notion of normalized degeneracy parameter

$$\hat{\delta} = \hat{\eta} \zeta \hat{\tau}_c .$$

Here normalized FEL efficiency is defined as $\hat{\eta} = P/(\rho W_b)$ where P is radiation power, and $W_b = \gamma mc^2 I/e$ is electron beam power. Normalized coherence time is defined as $\hat{\tau}_c = \rho \omega \tau_c$. Parameter $\hat{\delta}$ and the degeneracy parameter δ are simply related as:

$$\delta = \frac{W_b}{\hbar \omega^2} \hat{\delta} = 2.7 \times 10^7 \times \lambda[\text{\AA}] \times I[\text{kA}] \times E[\text{GeV}] \times \hat{\delta} .$$

PROPERTIES OF THE RADIATION

Simulations of the FEL process have been performed for the case of a long bunch with uniform axial profile of the beam current. Such a model provides rather accurate predictions for the coherence properties of the XFEL, since typical radiation pulse from the XFEL is much longer than the coherence time. Calculations has been performed with FEL simulation code FAST using actual number of electrons in the beam. The value of parameter $N_c = 8 \times 10^5$ corresponds to the parameter range of XFEL operating at the radiation wavelength about 0.1 nm.

A series of simulation runs have been performed in the range of the parameter $\hat{\epsilon} = 0.25 \dots 4.5$. Application of similarity techniques described above allowed us to extract universal parametric dependencies of the main characteristics of the optimized XFEL operating in the saturation (see Figs. 1-3).

Figure 1 shows the dependence of the saturation length $\hat{z}_{\text{sat}} = \Gamma z_{\text{sat}}$ on parameter $\hat{\epsilon}$. Analysis of the curve shows that the saturation length scales as $\hat{z}_{\text{sat}} \propto \hat{\epsilon}^{5/6}$. Such dependence directly follows from the optimization procedure of the gain length given by (2). The normalized coherence

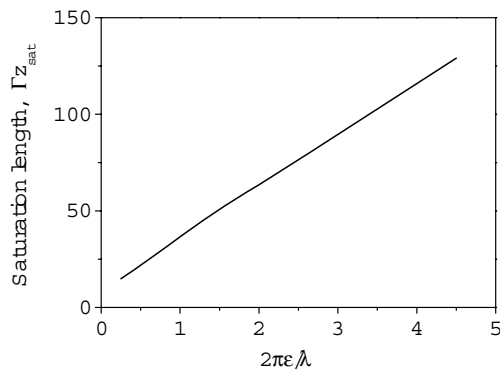


Figure 1: Saturation length Γz_{sat} versus parameter $\hat{\epsilon}$.

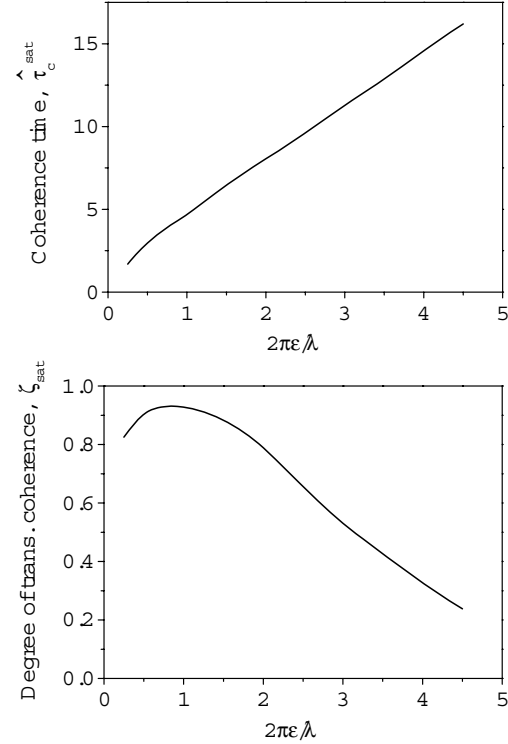


Figure 2: Degree of transverse coherence, ζ_{sat} , and normalized coherence time, $\hat{\tau}_c^{\text{sat}}$ in saturation versus parameter $\hat{\epsilon}$.

time in the saturation, $\hat{\tau}_c^{\text{sat}}$ is also proportional to $\hat{\epsilon}^{5/6}$ (see Fig. 2).

The dependence of the degree of transverse coherence in the saturation on the parameter $\hat{\epsilon}$ exhibits rather complicated behavior (see Fig. 2). It reaches maximum value in the range of $\hat{\epsilon}$ values about of unity, and drops at small and large values of $\hat{\epsilon}$. Actually, the degree of transverse coherence is formed due to two effects. The first effect takes place due to interdependence of the poor longitudinal coherence and transverse coherence [2]. Due to the start-up from shot noise every radiation mode is excited within finite spectral bandwidth. Actually this means that in the high gain linear regime the radiation of the SASE FEL is formed by many fundamental TEM_{00} modes with different frequencies. The transverse distribution of the radiation field of the mode is also different for different frequencies. Smaller value of the diffraction parameter (i.e. smaller value of $\hat{\epsilon}$) corresponds to larger deviation of the radiation mode from the plane wave. This explains a decrease of the transverse coherence at small values of $\hat{\epsilon}$. When the parameter $\hat{\epsilon}$ increases, the diffraction parameter increases as well thus leading to the degeneration of the radiation modes. Amplification process in the SASE FEL passes limited number of the field gain lengths, and starting from some value of $\hat{\epsilon}$ the linear stage of amplification becomes too short to provide mode selection process. When amplification process enters nonlinear stage, the mode content of

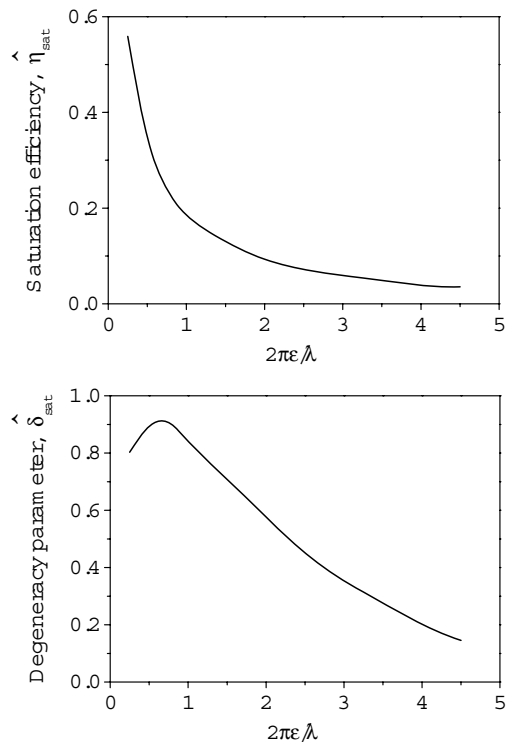


Figure 3: Efficiency, $\langle \hat{\eta}_{\text{sat}} \rangle$, and normalized degeneracy parameter, $\hat{\delta}_{\text{sat}}$, in the saturation versus parameter $\hat{\epsilon}$.

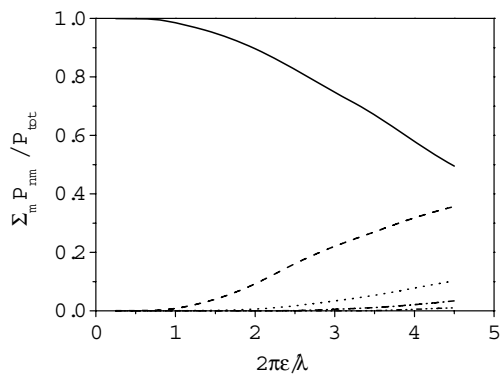


Figure 4: Partial contributions of the modes with azimuthal index $m = 0 \dots 4$ into the total power versus parameter $\hat{\epsilon}$. SASE FEL operates in the saturation.

the radiation becomes even more rich due to independent growth of the radiation modes in the nonlinear medium (see Fig. 4). Thus, at large values of $\hat{\epsilon}$ the degree of transverse coherence is limited by poor mode selection. Analytical estimations presented in [9] show that in the limit of large emittance, $\hat{\epsilon} \gg 1$, the degree of transverse coherence scales as $1/\hat{\epsilon}^2$.

We present in Fig. 3 the plots for normalized efficiency and degeneracy parameter for optimized XFEL. Normalized efficiency in saturation has simple scaling, it falls in-

Table 1: Parameter space of XFEL projects

	European XFEL		LCLS	SCSS
	SASE1	SASE2		
λ , nm	0.1	0.15	0.15	0.1
E , GeV	17.5	17.5	14.35	6.135
ϵ_n , mm-mrad	1.4	1.4	1.2	0.85
$\hat{\epsilon}$	2.6	1.7	1.8	4.5
ζ	0.65	0.85	0.83	0.24

versely proportional to the parameter $\hat{\epsilon}$. Taking into account that the value of the coherence time $\hat{\tau}_c^{\text{sat}}$ scales proportional to $\hat{\epsilon}^{5/6}$, we find that the normalized degeneracy parameter of the radiation is nearly proportional to the degree of transverse coherence, $\hat{\delta} \propto \zeta/\hat{\epsilon}^{1/6}$.

Finally, in Table 1 we present comparison of existing XFEL projects, the European XFEL, LCLS and SCSS in terms of degree of transverse coherence [10–12]. We see that the European XFEL and LCLS are in the same range of parameter space. These projects assume conservative value of the emittance, and relatively high degree of transverse coherence is achieved by increasing the energy of the driving accelerator. Project SCSS assumes much smaller energy of the driving accelerator. However, despite much smaller value of the normalized emittance it falls in the range of parameters for the output radiation with poor transverse coherence.

REFERENCES

- [1] Ya.S. Derbenev, A.M. Kondratenko and E.L. Saldin, Nucl. Instrum. and Methods **193**(1982)415.
- [2] E.L. Saldin, E.A. Schneidmiller, and M.V. Yurkov, Opt. Commun. **186**(2000)185.
- [3] E.L. Saldin, E.A. Schneidmiller, and M.V. Yurkov, Nucl. Instrum. and Methods **A 507**(2003)106.
- [4] E.L. Saldin, E.A. Schneidmiller, and M.V. Yurkov, Nucl. Instrum. and Methods **A 429**(1999)233.
- [5] E.L. Saldin, E.A. Schneidmiller and M.V. Yurkov, Nucl. Instrum. and Methods **A475**(2001)86.
- [6] E.L. Saldin, E. A. Schneidmiller, and M.V. Yurkov, Opt. Commun. 235(2004)415.
- [7] W.M. Fawley, Phys. Rev. STAB 5(2002)070701.
- [8] S. Reiche, Nucl. Instrum. and Methods **A429**(1999)243.
- [9] E.L. Saldin, E.A. Schneidmiller and M.V. Yurkov, Preprint DESY 06-137, Hamburg, 2006.
- [10] M. Altarelli et al. (Eds.), XFEL: The European X-Ray Free-Electron Laser. Technical Design Report, Preprint DESY 2006-097, DESY, Hamburg, 2006 (see also <http://xfel.desy.de>).
- [11] J. Arthur et al., Linac Coherent Light Source (LCLS). Conceptual Design Report, SLAC- R593, Stanford, 2002 (see also <http://www-ssrl.slac.stanford.edu/lcls/cdr>).
- [12] SCSS X-FEL: Conceptual design report, RIKEN, Japan, May 2005. (see also <http://www-xfel.spring8.or.jp>).

DESIGN STATUS OF PAL-XFEL*

T.-Y. Lee[†], Y. S. Bae, J. Choi, J. Y. Huang, H. S. Kang, C. B. Kim, D. E. Kim, M. G. Kim,
Y. J. Kim^a, I. S. Ko, J. S. Oh, Y. W. Parc, and J. H. Park

Pohang Accelerator Laboratory, San 31, Hyoja-dong, Pohang, Kyungbuk 790-784, KOREA

^aFree Electron Laser Laboratory, Duke University, N.C. 27708-0319, USA

Abstract

Pohang Accelerator Laboratory has a plan to build an X-ray FEL machine. This new machine will utilize the existing 2.5 GeV injection linac to the storage ring by upgrading its energy up to 3.7 GeV or more. The target wavelength will be 3-4.5 Å and its third harmonic 1-1.5 Å will also be used. The project will proceed in two stages: In the first stage, a VUV SASE machine with 320 MeV will be constructed and tested for the proof-of-principle. The full X-ray machine will be constructed in the next stage.

INTRODUCTION

PAL-XFEL is the name of new project of Pohang Accelerator Laboratory (PAL) to build a new X-ray FEL machine based on SASE (self amplified spontaneous emission) scheme. This new machine will utilize the existing 2.5 GeV electron linac by increasing its energy to 3.7 GeV and upgrading the performance. The linac is currently used for injection to the 2.5 GeV storage ring of Pohang Light Source (PLS). The new linac energy will be 3.7 GeV. The overview of the PAL-XFEL project was reported previously [1]. For readers unfamiliar with the project, fundamental parameters of PAL-XFEL are listed in Table 1 and the machine layout is displayed in Fig. 1. At the moment, detailed design study and machine R& D are going on. In the figure, K2,...,K12 denote the currently used accelerating columns and X1,...,X9 denote the new accelerating columns that will be added to the existing linac. X3X denotes the X-band high harmonic cavity. We are going to build the new part of PAL-XFEL while still running PLS.

However, there have been a few modifications in the PAL-XFEL project. The first important modification is the target wavelength that will be used mainly. The X-ray community, which is the biggest synchrotron user community in Korea, has demanded that the target wavelength be in 1-1.5 Å range, which put quite a challenge for the PAL-XFEL design. Since the available linac energy of PAL is limited, we decided to utilize the high harmonic radiation of SASE. It is well known that the high harmonic radiations are also amplified to FEL by the so called nonlinear harmonic generation [2, 3]. The existence and usefulness of SASE higher harmonic radiation was verified experimentally in VUV-FEL at DESY [4]. According to calculation based on [5], the third harmonic radiation power is approximately 1% of the fundamental one.

* Work supported by Korean Ministry of Science and Technology

[†] tylee@postech.ac.kr

The fundamental wavelength of PAL-XFEL was determined to be 3 Å in which case the third harmonic becomes 1 Å. These wavelengths are achieved by using an in-vacuum undulator of 4 mm gap. Recently, we are considering an alternative choice in which the fundamental wavelength is 4.5 Å and the third harmonic wavelength is 1.5 Å. In this case, wider undulator period and gap (and thus out-vacuum undulator) are allowed and the undulator wakefield is smaller. Currently, we are estimating the two designs and the final decision is not made yet. Below, comparison of the two choices is given briefly.

Another important modification is the procedure of PAL-XFEL construction. The PAL-XFEL project will proceed in two stages. In the first stage, only a small 320 MeV SASE machine will be constructed. The purpose of this machine is to test and prove the design strategy of PAL-XFEL. Hence, this test machine (TM) will use the same undulator as PAL-XFEL. Only in the second stage, the full PAL-XFEL will be constructed. The design of TM is under active study. Brief introduction to the TM design will be given below. This status report will describe major modifications of the PAL-XFEL design briefly. The PAL-XFEL photo-injector status has been prepared separately [6, 7].

ALTERNATIVE UNDULATOR DESIGN

The point of the alternative undulator design is to relax the original design slightly and make the whole scheme safer. For the purpose, the fundamental radiation wavelength is changed from 3 Å to 4.5 Å, which makes the third harmonic wavelength 1.5 Å. This change makes some difference. The comparison of the two undulator designs is given in Table 2.

What advantages do we get from this alternative design over the original one? First of all, the undulator gap is relaxed from 4 mm to 7.8 mm, which is wide enough to allow an out-vacuum undulator. With out-vacuum undulator, the chamber inner gap would be 6.8 mm which gives wakefield 40 % smaller. The longitudinal wakefield induces relative energy spread in the bunch, which is inversely proportional to the electron energy E . The relatively low energy, 3.7 GeV, of PAL-XFEL as a hard X-ray FEL machine may make the undulator wakefield particularly serious. Hence 40% reduction of wakefield is not negligible.

Another advantage is related to the transversal coherence of the SASE radiation and explained by a number B =gain length/Rayleigh length. B measures how fast the transversal higher modes diffract out of the electron beam. One of the advantages of the SASE FEL radiation is the transver-

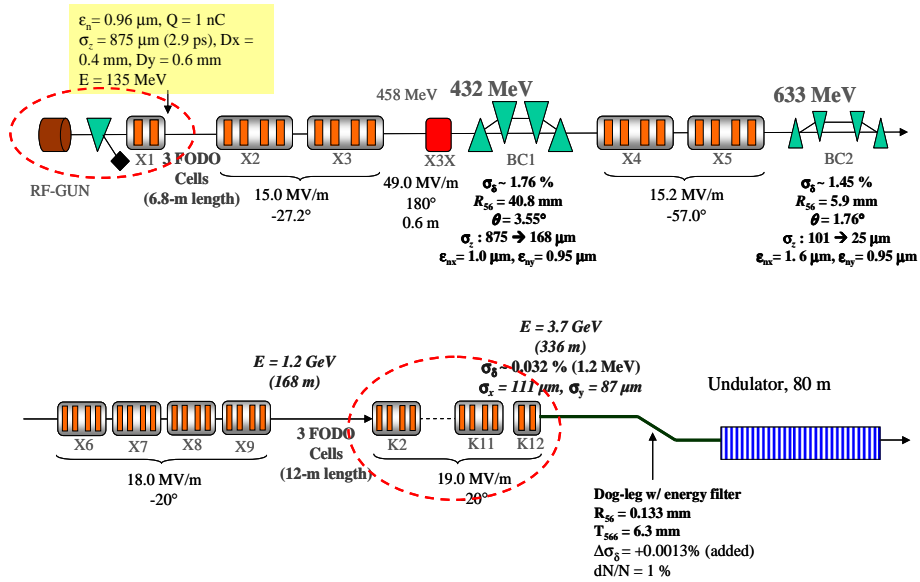


Figure 1: Layout of the PAL-XFEL injector and linac. K2,....,K12 denote the currently used accelerating columns and X1,....,X9 denote the new accelerating columns that will be added.

Table 1: Parameters of PAL-XFEL

Beam Parameters	Value	Unit
Electron energy	3.7	GeV
Peak current	3	kA
Normalized slice emittance	1	mm mrad
RMS slice energy spread	0.01 %	
Full bunch length	270	fs
Undulator Parameters		
Undulator period	1.5	cm
Segment length	4.5	m
Full undulator length	80	m
Peak undulator field	1.19	T
Undulator parameter, K	1.49	
Undulator gap	4	mm
Average β -function	10	m
FEL Parameters		
Radiation wavelength	3	Å
FEL parameter, ρ	5.7×10^{-4}	
Peak brightness	5×10^{31}	*
Peak coherent power	1	GW
Pulse repetition rate (Max.)	60	Hz
1D gain length	1.2	m
Saturation length, L_{sat}	45	m

* photon/(sec mm² mrad² 0.1%BW)

sal coherence. However, the transversal coherence is not an intrinsic property of the undulator radiation but acquired by the amplification process in which all the transversal higher modes diffract out of the beam while only the fundamental mode keeps growing. The bigger B is, the faster the higher modes diffract. It is true that B values of both the original design and the alternative design are not big enough compared with other machines such as LCLS. Figure 2 shows

Table 2: Comparison of the two undulator designs

Design	Original	Alternative
Wavelength	3 Å	4.5 Å
Third harmonic	1 Å	1.5 Å
Undulator	in-vacuum	out-vacuum
Undulator period	1.5 cm	2.2 cm
Undulator gap	4 mm	7.8 mm
Undulator parameter, K	1.49	1.52
FEL parameter	5.8×10^{-4}	6.6×10^{-4}
1-D gain length	1.2 m	1.5 m
Gain Length/Rayleigh length	0.04	0.07
Saturation length	45 m	48 m
Peak power	2 GW	4 GW

the power gain of the original design, while Fig. 3 shows that of the alternative design.

It is hard but possible to see that the power gain in Fig. 2 is not in a straight line but slightly over it. This indicates that the transversal higher modes do not diffract out fast enough and thus a small portion of it might remain at the final stage. Figure 3 shows a better case.

The third advantage of the alternative design is that its radiation power is bigger than that of the original design. As shown in Figs. 2 and 3, the peak radiation power of the original design is almost 2 GW while that of the alternative design is almost 4 GW.

The disadvantage of the alternative design compared with the original design is that its third harmonic radiation is 1.5 Å not 1 Å that is preferred by scientists working on organic samples. Those scientists include material scientists, biologists, organic chemists, and the number grows rapidly. The alternative design can provide 0.9 Å radiation

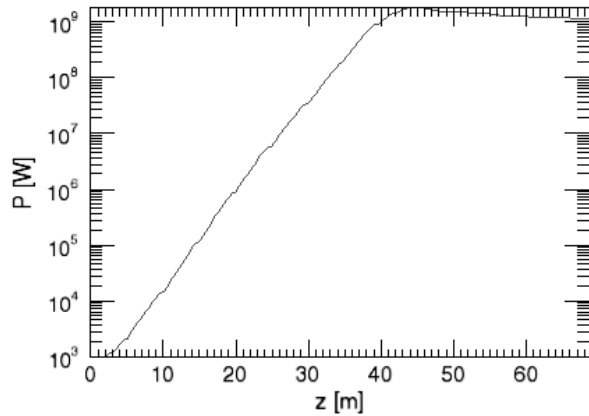


Figure 2: Power gain of the original undulator design.

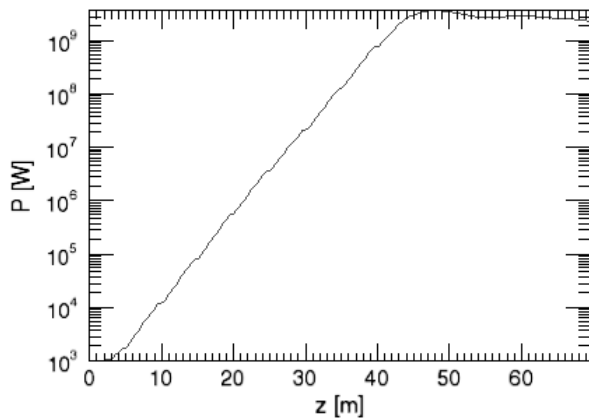


Figure 3: Power gain of the alternative undulator design.

as a fifth harmonic but its power is approximately 1/10 of the third harmonic radiation.

BUNCH COMPRESSOR DESIGN

The bunch compressor design is not fixed yet. There are a few issues still to be examined. One of the issues is the space charge in the bunch compressors. The ELEGANT code that is used in the linac design does not include the space charge effect and thus the space charge effect has not been checked seriously. It has been suggested that the second bunch compressor be in the higher energy region to make the space charge effect unimportant. A simulation study to estimate the space charge effect in the bunch compressors is going on.

Another important issue is the coherent synchrotron radiation (CSR). According to simulation, the electron distribution in the phase space is shifted slightly in the x, x' direction by CSR. This has to be fixed for the successful SASE FEL. A start to end simulation from the gun to the undulator was carried out. In case the CSR effect is off, the final radiation profile is very good as shown in Fig. 4, which was obtained with the alternative undulator design.

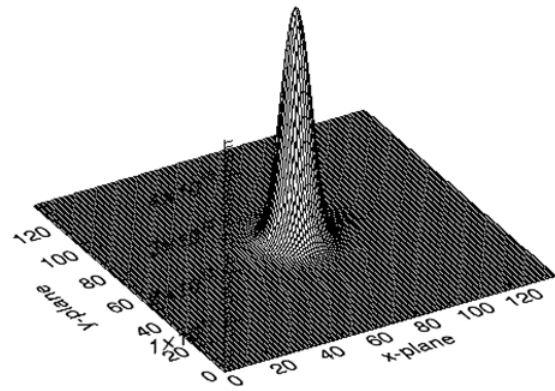


Figure 4: Radiation beam profile obtained from start to end simulation.

TEST MACHINE

The purpose of TM is to prove, in the low energy, that PAL-XFEL is achievable. It will not be used as a user facility. The reason why we need TM is that PAL-XFEL is challenging. It is challenging to generate hard X-ray (3 - 4.5 Å) SASE radiation with 3.7 GeV electron beam. The validity of the PAL-XFEL scheme will be proved by TM. TM will have a low energy of 320 MeV, lower than a tenth of PAL-XFEL energy, but the undulator will be the same as in PAL-XFEL except the total length. It will still adopt a pair of bunch compressors, but X-band higher harmonic cavity is not planned to be used at the moment. Beam parameters are chosen to give comparable magnitude of energy spread to the PAL-XFEL case. The optimal average β function of the undulator lattice is reduced from 10 m of PAL-XFEL to 5 m. A few fundamental parameters of TM are shown in Table 2.

Table 3: Parameters of the test machine

Parameters	Value	Unit
Electron energy	0.32	GeV
Peak current	0.7	kA
Normalized slice emittance	0.8	mm mrad
RMS slice energy spread	0.01 %	
Full undulator length	8	m
Average β -function	5	m
Radiation wavelength	28	nm
FEL parameter, ρ	3.4×10^{-3}	
1D gain length	0.2	m
Saturation length, L_{sat}	6	m

Since the high harmonic cavity is not used, the compressed bunch has a different shape from the PAL-XFEL case. The layout of TM is displayed in Fig. 5 and Fig. 6 shows the current distribution in a bunch at the test linac end.

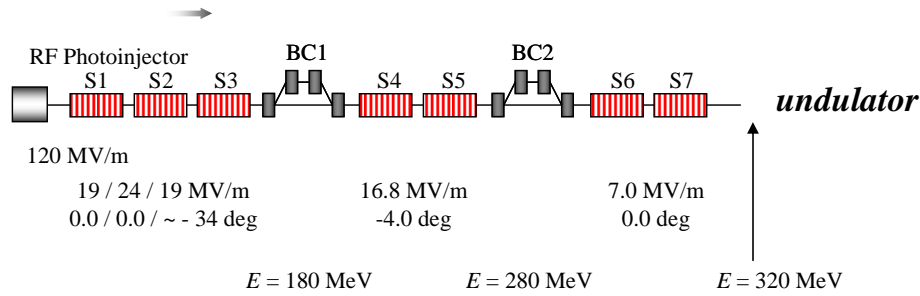
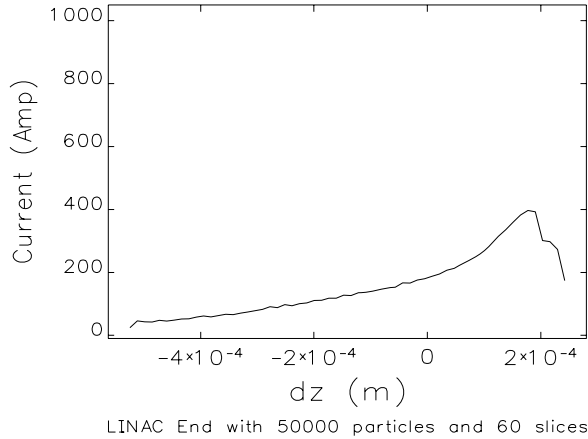


Figure 5: Layout of the test machine.



- [5] E. L. Saldin, E. A. Schneidmiller, and M. V. Yurkov, Phys. Rev. ST Accel. Beams, 9 (2006) 030702.
- [6] Y. W. Parc et al., In this proceedings.
- [7] J. H. Park et al., In this proceedings.

Figure 6: Current distribution in the linac end of the test machine.

SUMMARY

The progress of the PAL-XFEL design since the previous report [1] has been described. The bunch compressor design needs to be examined further with respect to the CSR and space charge effect. As for the undulator design, an alternative design has been described in comparison with the original design. The alternative design gives 4.5 Å fundamental radiation and 1.5 Å third harmonic, while the original design gives 3 Å fundamental and 1 Å third harmonic. The final decision for the undulator is not made yet. Also, an important change of the PAL-XFEL construction plan has been described. PAL-XFEL will be constructed in two stages. In the first stage, 320 MeV test machine will be constructed and the full 3.7 GeV machine will be constructed only in the second stage.

REFERENCES

- [1] I. S. Ko, Proceedings of the 27th International Free Electron Laser Conference, SLAC, USA (2005) 216.
- [2] R. Bonifacio, L. D. Salvo, and P. Pierini, Nucl. Instrum. Methods Phys. Res. A 293 (1990) 627.
- [3] Z. Huang and K.-J. Kim, Phys. Rev. E 62 (2000) 7295.
- [4] S. Schreiber, Proceedings of the 27th International Free Electron Laser Conference, SLAC, USA (2005) 12.

ULTRA HIGH BRIGHTNESS ACCELERATOR DESIGN

R.J. Bakker, A. Adelman, A. Anghel, M. Dehler, R. Ganter, S. Leemann, K. Li, M. Pedrozzi, J.-Y. Raguin, L. Rivkin, V. Schlott, F. Wei, A. Wrulich
Paul Scherrer Institut, Villigen CH 5232, Switzerland.

Abstract

The PSI FEL Project at the Paul Scherrer Institute in Switzerland incorporates the development of a low emittance gun as a driver for a cost-effective X-ray free-electron laser user facility ($\lambda_s \geq 0.1$ nm, $\hbar\omega_s \leq 12.4$ keV). We investigate sources based on field-emitter technology and photoemission, followed by high gradient ($\mathcal{F} \geq 0.25$ GV/m) acceleration up to 1 MeV. We present a concept to preserve the emittance in the acceleration process where the first 250 MeV of acceleration is the most delicate. Experimentally we intend to verify the validity of ultra-high brightness acceleration over this energy range in the period 2008-2011.

INTRODUCTION

In a free-electron laser (FEL) the resonant wavelength (λ_s) is given by:

$$\lambda_s = \frac{\lambda_u}{2\gamma^2} (1 + K^2) \quad (1)$$

where λ_u is the undulator period, γ the Lorentz factor corresponding to the beam energy ($\gamma = E$ [MeV]/0.511), and K the dimensionless undulator strength ($K \approx 0.66 \lambda_u \cdot B_u$ [cm] [T]). It follows that the X-ray regime (0.1 nm) is accessible with conventional undulator technology ($\lambda_u \geq 0.8$ cm) and a beam-energy as low as 4 GeV. Lasing at such a wavelength is more restrictive, however, since it is fundamental to control the transverse emittance (ε), the energy spread (σ_γ) and the current (I) of the electron-beam. An estimate for the critical wavelength limit λ_{cr} for sufficient gain in the FEL is [1]:

$$\lambda_{cr} \approx 18\pi \varepsilon_n \frac{\sigma_\gamma}{\gamma} \sqrt{\frac{1}{\gamma} \frac{I_A}{I}} \quad (2)$$

where ε_n , σ_γ/γ , and I_A are the normalized emittance, the relative energy-spread, and the Alfén current (≈ 17 kA) respectively. For typical electron beam parameters for short wavelength operation ($Q = 1$ nC, $\varepsilon_n \approx 1$ mm mrad) λ_{cr} is then reduced by increasing beam-energy combined with an increased undulator period and length.

As a future alternative, the PSI-FEL project at the Paul Scherrer Institute in Switzerland attempts to develop an electron source with a significantly lower transverse emittance as a basis to develop a cost-effective X-ray FEL user facility [2] by pushing the beam-energy as low as technological possible. That is, for the case with $\varepsilon_n \leq 0.1$ mm mrad, parameter studies [2] suggest that the beam energy and peak current may be limited to 6 GeV and 1.5 kA, respectively.

In this paper we present a concept for an ultra-high brilliance 6-GeV accelerator. Starting point is the performance expectations of the Low Emittance Gun (LEG) [3], which is under construction at PSI. The first 250 MeV deserves special attention since emittance preservation proves to be most challenging in this part of the machine. It is our intention to test the concept of emittance conservation in this part of the machine experimentally. If successful, it should then serve as an injector for a linac that feeds a cost-effective X-FEL. An outlook follows at the end of this paper.

Table 1. Electron Source Parameters for the PSI FEL.

Peak current	I	≥ 5	A
Bunch charge	Q	0.2	nC
Bunch length (full width)	τ	≤ 40	ps
Bunch shape	-	uniform	-
Normalized emittance*	ε_n	≤ 0.05	mm mrad
Repetition rate [#]	f	10	Hz

* Slice parameter of a field-emitter at $E=1$ MeV and a slice-charge of 1 pC, i.e., the charge in the FEL-corporation length [2].

[#] Limited by high-gradient pulser technology.

THE ELECTRON SOURCE

In a linac the emittance is limited by the intrinsic emittance at the electron source, which can be expressed as [4]:

$$\varepsilon_n = \frac{R}{2} \sqrt{\frac{2 E_{kin}}{3 mc^2}} \quad (3)$$

where R is the beam radius in the case of a uniform radial distribution and E_{kin} is the mean kinetic energy of emitted electrons. With Eq. (3) in mind two strategies are pursued: laser assisted Field Emission and photo-emission. Both technologies rely on laser-illumination to shape the temporal profile of the pulse.

With field emission electrons are drawn from sharp tips that are exposed to high gradient electric fields ($\mathcal{F} \approx 6$ GV/m). Normally the emitting radius is small ($R \leq 5$ μ m) and the field-emission process keeps the kinetic energy of the emitted electrons low ($E_{kin} \approx 0.15$ eV), which suggests a normalized emittance below 10^{-3} mm mrad. However, with increasing current the required electrical field-strength goes up followed by increased space-charge forces. This makes the combination of high-current and low-emittance challenging, both from technological and operational point of view. To reach ultra-low emittance two types of field emitters (FE) are under investigation: (i) a macroscopic single-tip FE and (ii) Field-Emitter Arrays (FEA). Construction of the former is technologically less demanding but the latter permits a reduction of the current density and most likely a lower

emittance. The status and performance are discussed in detail in [3]. Target specifications are summarized in Tab. 1, where the emittance refers to the slice-value after acceleration up to 1 MeV.

The transverse emittance of a photo-cathode for a 1 nC electron bunch typically is $\epsilon_n \approx 1$ mm mrad. This value may become smaller with a reduced bunch-charge, a reduced peak-current, combined with an appropriate choice of cathode material. Optimizations based on Eq. (3) suggest that the slice emittance can reach $\epsilon_n \leq 0.1$ mm mrad for a Cu cathode with beam parameters as quoted in Tab. 1 and an initial transverse radius $R = 0.25$ mm.

Since the fabrication and operation of a photo-cathode is less challenging than field emission, we anticipate commencing with a photo-cathode. A second stage based on field emission should then permit a lower initial emittance, which should permit a final value of 0.1 at the entrance of the undulator section of the FEL. Note that we have chosen the beam parameters identical for both types of cathodes such that the choice of cathode does not affect the design of the following accelerator structure.

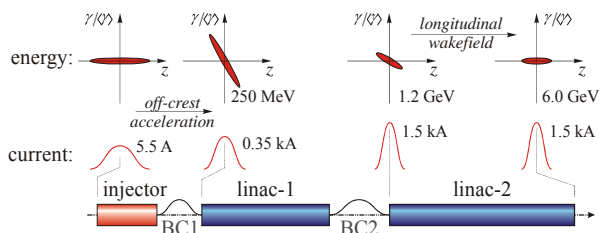


Figure 1. Functional layout of a low-emittance linac for an X-FEL. See text for details on the longitudinal shaping of the electron bunch.

ACCELERATOR CONCEPT

The performance parameters specified in Tab. 1 have, compared to more conventional RF photo-cathode designs, a low beam current and bunch charge at the cathode. This is beneficial to reduce the initial emittance and its dilution due to space charge in the region where the electron beam is sub-relativistic. The obvious drawback is the increased bunch compression ratio, which is required to obtain sufficient current for lasing. E.g., the LCLS [5] and the European X-FEL at DESY [6] have a total compression ratio of 70 and 100, respectively. The PSI-FEL aims for a ratio of 270.

The concept shown in Fig. 1 enables the increased compression ratio as it focuses on the control of the longitudinal phase-space. This is possible because we do not expect a significant emittance dilution in the bunch-

compressors BC1 and BC2 [7]. Hence, the difficulties related to the emittance preservation are transferred to the design of the injector, which follows in the next section.

In terms of functionality the injector and BC1 accommodate most of the shaping of the longitudinal phase-space (γ, z). Similar to the design of the LCLS [5], linac-1 and linac-2 serve to boost the energy and allow of adiabatic damping of the emittance and relative energy spread. Deformation of the longitudinal phase-space, caused by wakefields in the linac structures, is controlled by off-crest acceleration in the injector and linac-1. In the present design both linac sections consist of 3-GHz room temperature (RT) traveling wave structures. We did not consider super-conducting technology because of the low repetition rate of the injector. Higher frequency RT will be considered later as an option to reduce the accelerator length.

THE INJECTOR

Fig. 2 shows a schematic of the injector. Details of the low-energy section are presented in Fig. 3.

Low Energy Acceleration

To minimize the initial blow-up of the emittance by space-charge, the cathode is positioned in a high-gradient field. The necessity of such a field is illustrated in Fig. 4, which shows a CAPONE [9] simulation of the slice-emittance of an ideal uniform beam with parameters as presented in Tab. 1. To obtain the gradient, the cathode is followed by a pulsed diode configuration as illustrated in Fig. 3. A 500 kV pulser has been constructed, which allows for initial tests with gradients up to 125 MV/m (top curve in Fig. 4). After sufficient operational experience the pulser will be upgraded to 1 MV to reach gradients up to 250 MV/m.

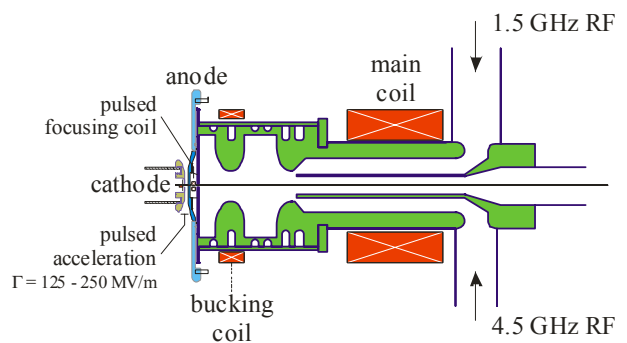


Figure 3. Layout of the high-gradient accelerating section followed by the initial RF acceleration [8].

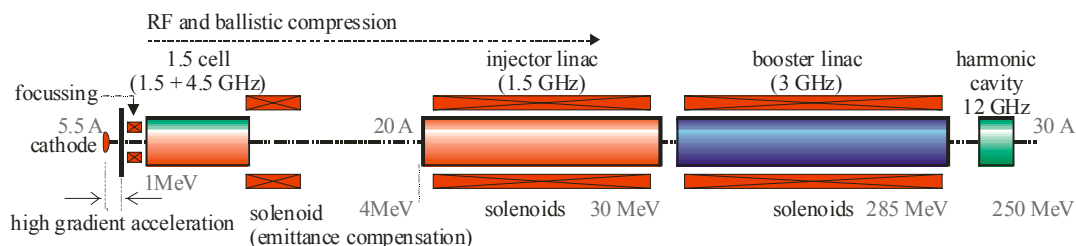


Figure 2. Schematic layout of the injector.

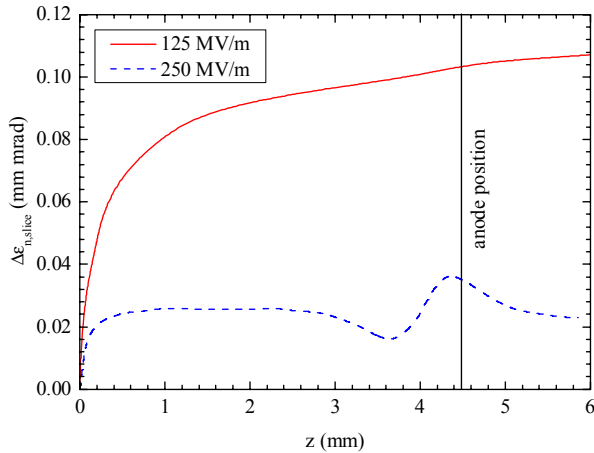


Figure 4. CAPONE [9] simulation of the slice emittance growth of a uniform electron bunch (Tab. 1) in a DC accelerator field (1 pC slice with an initial radius of 0.25 mm).

For further acceleration we have chosen an initial RF frequency of 1.5 GHz as a compromise between a high accelerating gradient (≥ 40 MV/m) and a large acceptance window to collect sufficient charge in a single bunch. A specially designed double-frequency 1.5-cell cavity [8] behind the diode further increases acceptance, see Fig. 3. Additional advantages of the double-frequency are: (i) a reduction of the emittance dilution caused by non-linear RF fields [8] and (ii) optimized RF compression. The latter is incorporated to reduce the bunch-length, see Fig. 2. We note that RF-compression is, in this part of the machine, the preferred choice as compared to magnetic compression since it maintains the cylindrical symmetry of the beam. That is, it avoids a break-up of the horizontal and vertical beam-optics in the space-charge dominated regime. For the similar reasons there are no quadrupoles included in the injector design.

During RF acceleration, it is important to control the transverse beam size since non-linear off-axis fields in the RF cavity may dilute the emittance otherwise. This is especially true in the first RF-structures where the beam-size may be blown up by a strong defocusing field as the beam passes the anode. For this reason, we plan to install a pulsed coil behind the anode to control the beam-size. We note that the pulsed technology has the advantage that the eddy-currents in the anode naturally shield the magnetic field from the cathode area.

Energy Booster

The RF compression is finalized in a 3-m long 1.5 GHz traveling wave structure. As soon as the electron bunches are short enough they enter a 3-GHz structures. A 12-GHz harmonic cavity at the end of the booster linearizes the longitudinal phase-space before further compression. All linac structures require additional focusing to control the electron beam-size. The final energy is 250 MeV. At this energy, the influence of space charge on the beam-optics is sufficiently reduced to permit the use of a chicane to reduce the bunch length.

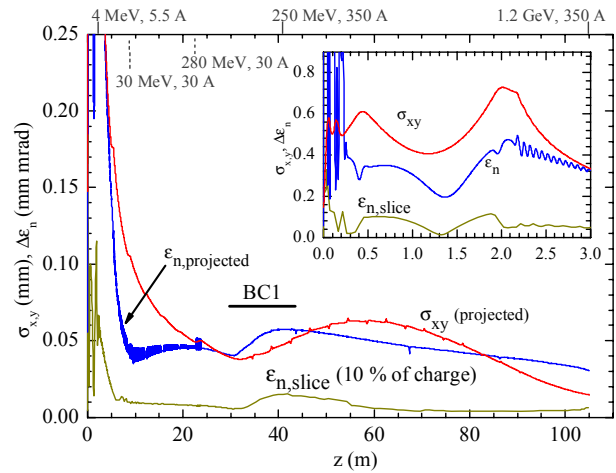


Figure 5. HOMDYN [10] simulation of the beam envelope and emittance dilution for the PSI FEL linac up to BC2, see Fig. 1. The inset is a zoom of the first 3 m.

Performance

As a first step, the emittance dilution has been tracked over the initial 1 GeV of acceleration (up to BC2) with HOMDYN [10], see Fig. 5. Initial conditions were an electron beam with the parameters presented in Tab. 1 with zero emittance at the cathode. It follows that a low emittance can be maintained during compression and acceleration. Verification of these results with more sophisticated codes is still in progress. Here we use MAFIA [11] to simulate the configuration presented in Fig. 3. Calculations are complemented with PARMELA [12] and GPT [13] simulations for tracking of the electron beam behind the diode. As a next step we will use IMPACT [14] for more elaborate calculations and tolerance studies.



Figure 6. Installation of the 500-kV pulser in the test-bunker OBLA.

STATUS AND OUTLOOK

The status of the field emitter development and the associated test stands are reported in [3]. As a first step towards the preservation of the emittance a 500 kV, 200-

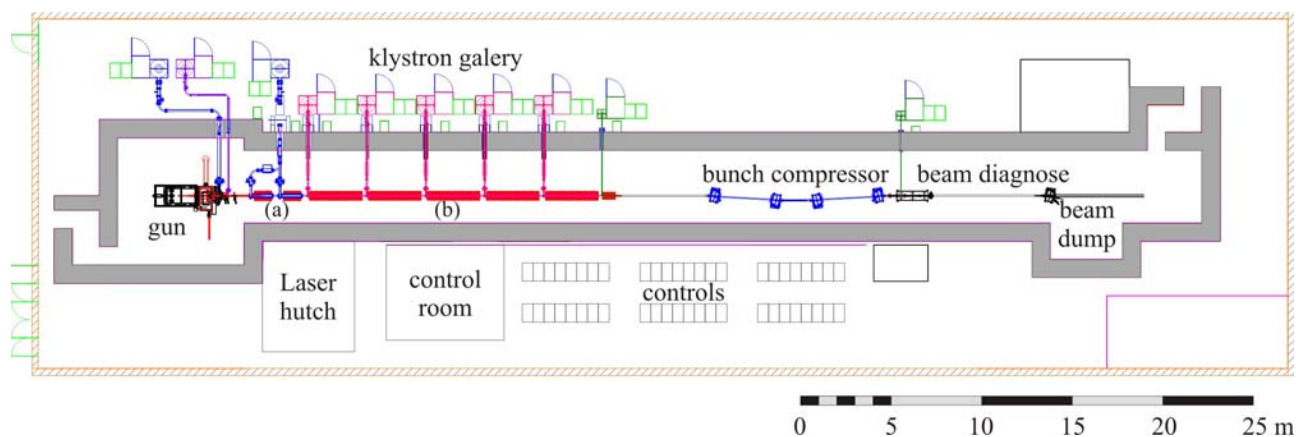


Figure 7. Layout of the 250 MeV test injector. The areas (a) and (b) mark the injector linac and booster linac as depicted in Fig. 2. The designed tunnel is sufficiently long to house the first bunch compressor (BC1 in Fig. 1).

ns pulser has been installed in a bunker at the PSI. It permits the operation of a diode configuration with a variable gap from 30 mm to 2 mm. A photo of the pulser is shown in Fig. 6. In fall of 2006 the pulser will be complemented with a diagnostic station for current and emittance measurements. First tests with pure field emitters (without laser illumination) are then foreseen for the end of the same year. In 2007 the experimental setup will be upgraded to permit laser assisted field emission and photo-emission combined with 1.5 cell RF cavity as depicted in Fig. 3. We note here the different laser systems. Laser assisted field emission has a high quantum efficiency (≈ 1) and requires a photon energy below the work function ($\lambda > 400$ nm). This can be a sub-system of the laser required for photo-emission, which typically has to deal with a low quantum efficiency at a wavelength of 266 nm.

In parallel surface cleaning techniques are studied to optimize the operation at high gradient and to minimize the occurrence of breakdowns in the high-gradient accelerator structure.

We plan to extend the experimental capabilities to a 250 MeV accelerator in the period 2008-2011. This linac should demonstrate low-emittance acceleration and bunch compression to reach a beam current of 350 A. In addition, it should serve as a test environment for the development of diagnose for an X-FEL. A possible layout is presented in Fig. 7. It includes the injector sketched schematically in Fig. 2 as well as the first bunch compressor, which is shown in Fig. 1.

REFERENCES

- [1] J. Rossbach, E.L. Saldin, E.A. Schneidmiller, M.V. Yurkov, "Interdependence of parameters of an X-ray FEL", Nucl. Instr. Meth. In Physics Research, A374, 401 (1996)
- [2] [http://leg.web.psi.ch/public/publications/2005/ESFRI 20PSI-FEL.pdf](http://leg.web.psi.ch/public/publications/2005/ESFRI%20PSI-FEL.pdf)
- [3] R. Ganter, R.J. Bakker, M. Dehler, J. Gobrecht, C. Gough, E. Kirk, S.C. Leemann, K. Li, M. Paraliiev, M. Pedrozzi, F. Le Pimpec, J.-Y. Raguin, L. Rivkin, V. Schlott, H. Sehr, S. Tsujino, "High Current

- Electron Emission from Microscopic Tips", THCAU04, this conference
- [4] S. Humphries, Charged Particle Beams (John Wiley & Sons, 1990).
- [5] LCLS CDR, SLAC Report No. SLAC-R-593, 2002.
- [6] TESLA TDR, DESY Report No. DESY-2001-011, 2001.
- [7] K. Li, A. Adelman, A. Anghel, R.J. Bakker, A. Candel, M. Dehler, R. Ganter, G. Ingold, S. Leemann, M. Pedrozzi, J.-Y. Raguin, L. Rivkin, V. Schlott, A. Streun, A. Wrulich, "Low Emittance X-FEL Development", Proc. of the 27th FEL Conf., Stanford (CA), USA, p. 483 (2005).
- [8] J.-Y. Raguin, R. J. Bakker, K. Li, M. Pedrozzi, "A Two-Frequency RF Cavity for the PSI Low Emittance Gun", Proc. of the 27th FEL Conf., Stanford (CA), USA, p. 324 (2005).
- [9] A.E. Candel, M.M. Dehler, S.C. Leemann, "Electron Beam Dynamics Simulations for the Low Emittance Gun", Proc. of EPAC2004, Lucerne, Switzerland, p. 2505 (2004)
- [10] M. Ferrario, J.E. Clendenin, D.T. Palmer, J.B. Rosenzweig, L. Serafini, "HOMDYN study for the LCLS photoinjector", SLAC-PUB-8400 (2000).
- [11] CST GmbH, Bad Nauheimer Strasse 19, D-64289 Darmstadt, <http://www.cst.com>
- [12] L.Young, PARMELA, LA-UR-96-1835, LANL (1996)
- [13] Pulsar Physics, De Bongerd 23, NL-3762 XA Soest, <http://www.pulsar.nl/>
- [14] J. Qiang, S. Lidia, R. Ryne, C. Limborg, "A 3D Parallel Beam Dynamics Code for Modeling High Brightness Beams in Photoinjectors", Proc. of the 2005 Particle Accelerator Conference, Knoxville, USA, p. 3316 (2005)

AN ENHANCED GINGER SIMULATION CODE WITH HARMONIC EMISSION and HDF5 IO CAPABILITIES*

William M. Fawley[†], LBNL, Berkeley, CA 94720, USA

Abstract

GINGER [1] is an axisymmetric, polychromatic ($r-z-t$) FEL simulation code originally developed in the mid-1980's to model the performance of single-pass amplifiers. Over the past 15 years GINGER's capabilities have been extended to include more complicated configurations such as undulators with drift spaces, dispersive sections, and vacuum chamber wakefield effects; multi-pass oscillators; and multi-stage harmonic cascades. Its coding base has been tuned to permit running effectively on platforms ranging from desktop PC's to massively parallel processors such as the IBM-SP. Recently, we have made significant changes to GINGER by replacing the original predictor-corrector field solver with a new direct implicit algorithm, adding harmonic emission capability, and switching to the HDF5 IO library [2] for output diagnostics. In this paper, we discuss some details regarding these changes and also present simulation results for LCLS SASE emission at $\lambda = 0.15$ nm and higher harmonics.

INTRODUCTION

Over the past 25 years, there has been a steady advance in the use of numerical simulation codes to explore FEL physics, analyze experimental results, and to help design elaborate and expensive projects such as the LCLS. As the underlying computer hardware has grown both faster and often more complex (*i.e.*, massively parallel environments), FEL codes have similarly become more complex both in terms of the underlying physical phenomena they model (*e.g.*, wakefield losses) and the more realistic forms of simulation they attempt (*e.g.*, importation of massive macroparticle files for start-to-end tracking runs). Moreover, the amount of information the codes utilize and produce has increased by several orders of magnitude with multi-GB output and/or particle restart files becoming necessary for full time-dependent simulations of x-ray FEL's and multi-stage harmonic cascades.

This paper present recent changes to the GINGER simulation code [1] which originally was designed in the mid-1980's to study sideband growth in single-pass FEL amplifiers and which has steadily evolved since to study more and more elaborate configurations such as SASE devices, harmonic cascades and oscillators. The Fortran90 base currently underlying GINGER has proven very useful both in

terms of modularization and in the number of useful language features (*e.g.*, array syntax and built-in operators, type definitions, memory management). The code structure has proven very amenable to efficient multiprocessing in which the different longitudinal slices are assigned to different processors with MPI [3] handling the necessary interprocessor communication. In the past year, we have replaced the original predictor-corrector field solver by a new implicit solver and also have extended the code to calculate radiation emission at multiple harmonics; the next section gives details on these changes. We then present results from a GINGER calculation for predicted harmonic emission from the LCLS.

With the addition of calculations of harmonic emission, typical GINGER output file sizes doubled or more. Based upon file compactness, IO speed, and flexibility in data layout, the output file format was changed from simple ASCII to HDF5 [2]. In part because we believe that the FEL simulation community should become aware of the usefulness of HDF5 IO, the last section of this paper gives details concerning its implementation into GINGER.

THE NEW FIELD SOLVER AND IMPLEMENTATION OF HARMONICS

Adopting the slowly-varying envelope approximation (SVEA) with $E(r, z, t) \equiv \tilde{E}(r, z, t) \times \exp i(k_o z - \omega_o t)$, the field equation becomes

$$2ik_s \frac{\partial \tilde{E}}{\partial Z} = -\nabla_{\perp}^2 \tilde{E} - \left(\frac{\omega_0}{c^2} - k_o^2 \right) \tilde{E} - \frac{4\pi i}{c^2} \omega_0 J_{\perp} \quad (1)$$

where $\partial/\partial Z$ is the Lagrangian derivative in the forward (*i.e.*, positive z) direction, and J_{\perp} is the microbunched transverse current at angular frequency ω_0 . The original GINGER field solver used a Gear predictor-corrector scheme [4] which automatically controlled step size to maximize computational speed for a given error allowance, but had negative aspects regarding algorithmic complexity and non-trivial coding difficulties with regards to adding additional dimensions such as harmonics and (eventually) non-axisymmetric modes. Consequently, we developed a completely new field solver based upon a backward-biased, implicit solution of the heat flow equation ("Case 5" in table 8.1 of [5]). This solution is always stable for arbitrary step size ΔZ and the chosen default bias factor makes the scheme equivalent to the Crank and Nicholson algorithm with errors scaling as Δr^2 and ΔZ^2 . Tests of simple vacuum Gaussian mode propagation over multiple Rayleigh ranges show normalized energy conservation to better than 10^{-3} for $\Delta r/R_0 \leq 0.1$ where R_0 is the mode waist size.

* Work performed in support of the LCLS project at SLAC under US DOE Contract DE-AC02-76SF00515 (SLAC) and also supported under Contract DE-AC02-05CH11231 (LBNL).

[†] WMFawley@lbl.gov

Sec. 8.5 of Ref. [5] gives an elegant (and simple to code) solution method based upon a Gaussian elimination procedure where one first sweeps outward in r and then back to the axis. Extension of the field solver to include higher harmonics is simple with (k_o, ω_o) being replaced by $(hk_o, h\omega_o)$ and use of the appropriate current source term. For the latter, GINGER uses wiggler-period averaging and follows the standard formulation (see, e.g., [6]) for odd harmonic emission that depends only upon the local harmonic microbunching amplitude (and ignores even harmonic emission arising from transverse gradients in the electron beam density). Tests by Z. Huang comparing the predicted 3rd harmonic power from nonlinear microbunching with that computed by GINGER for a simple $\lambda_0 = 0.15$ nm, steady-state amplifier with LCLS parameters show excellent agreement (e.g., 10% or better) for sufficient macroparticle number (e.g., $\geq 65K$ per slice). Use of smaller macroparticle number tends to lead to an overestimation of the harmonic power, perhaps because the longer Rayleigh length (and thus less radial smoothing in Z) at 0.05 nm makes the effective source term “grid noise” (i.e., in higher radial modes) much worse than that corresponding to the fundamental (for which 8K macroparticles appear more to be than sufficient).

The original macroparticle longitudinal mover also used a Gear-scheme (which was extreme computational overkill given the slow evolution of particle phase and energy) and was replaced by a simple second-order Runge-Kutta solver in which only the fundamental radiation field acts back upon the particles. Within this limitation one can study nonlinear harmonic generation (the dominant emission term for most SASE and harmonic cascade devices) but not linear amplification. As shown in Ref. [7], ignoring the harmonic emission feedback is an extremely good approximation for SASE x-ray FELs and essentially all FELs in which gain at the fundamental wavelength is much larger than that at the harmonics, as is the usual case.

In fall 2006 we expect to add the harmonic field feedback terms to the mover and also a fourth-order Runge-Kutta scheme as an option. Lastly, we note that Eq. (1) is separable by azimuthal mode and thus the new field solver can be easily extended (as is hopefully planned for 2007) to solve for $\vec{E}(r, \varphi, z, t)$.

AN EXAMPLE LCLS HARMONIC EMISSION CALCULATION

Nonlinear harmonic emission from the LCLS is potentially extremely useful, both for experimentalists and as a diagnostic of FEL performance. Adopting design parameters (3.4 kA, $\gamma = 26693$, 1.2 mm-mrad, $B_w = 1.25$ T, $\sigma_\gamma/\gamma = 10^{-4}$), and a quad FODO focusing lattice that produces an average Twiss β -function of 28 m, we simulated a LCLS 9.2-fs segment at 6-attosecond temporal resolution with 32768 macroparticles per slice. The calculation was run on 128-POWER 5 (1.9 GHz) processors of the “BASSI” IBM p575 system at NERSC and required ≈ 40

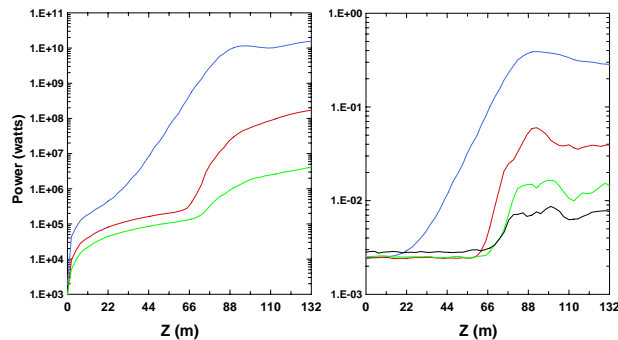


Figure 1: Time-averaged SASE power (left) and microbunching fraction (right) vs. z for an LCLS pulse at the 0.15-nm fundamental (blue curve) and also the 3rd, 5th, and 7th harmonics (bunching only) (red, green, black curves).

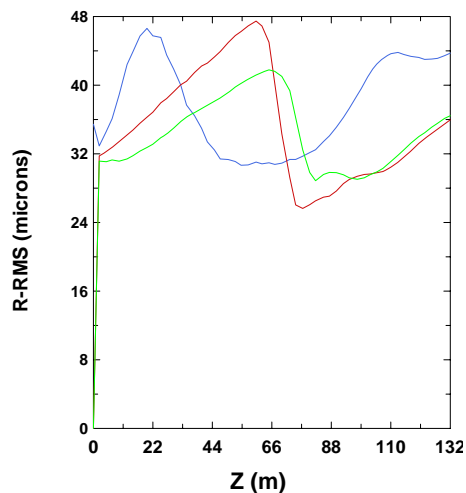


Figure 2: RMS transverse size vs. z for SASE emission from an LCLS pulse at the 0.15-nm fundamental wavelength (blue curve) and also the 3rd and 5th harmonics (red and green curves).

minutes of wall-clock time. Figure 1 plots the power at the fundamental wavelength of 0.15 nm and also the 3rd and 5th harmonics as functions of z . One sees that the plateau region (on this semi-log plot) for small z where spontaneous emission dominates the coherent FEL component lasts much longer for the harmonics than the fundamental; in reality the plateau region would extend even further because these calculations do not include non-axisymmetric spontaneous emission. While the third harmonic grows more rapidly with z than the fundamental in the region $60 \leq z \leq 85$ m, it saturates at a low ($\sim 1\%$) relative power level.

Comparing the behavior of the on-axis far-field power (not displayed) with the total near-field power (Fig. 1) reveals that the plateau region is much smaller for the fundamental but there is essentially no change for the harmonics. This is likely related both to the short gain length for the

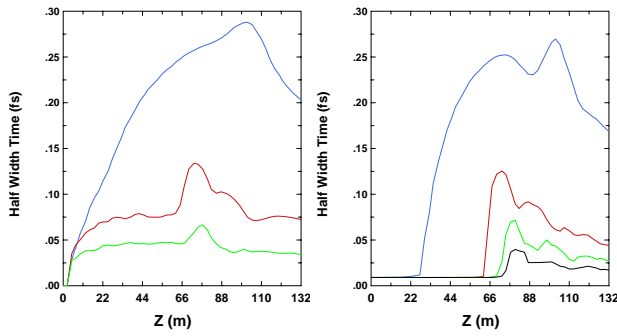


Figure 3: Plots of $C_{1/2}(\tau)$ for the on-axis far field emission (left) and microbunching (right) for the fundamental and harmonics (same color scheme as Fig. 1).

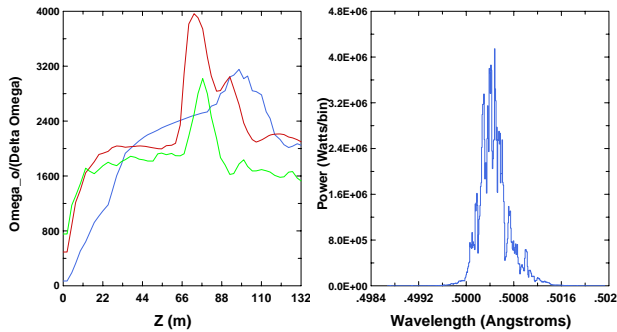


Figure 4: Plots of RMS spectral width for on-axis far field emission at the fundamental and harmonics (left) and the 3rd harmonic output (near-field) spectrum (smoothed with a 5-bin average) (right).

harmonics $L_{g,h} \approx L_{g,1}/h$ and the smaller mode size (see Fig. 2) for the coherent harmonic emission which reduces some of the far-field contrast *vis-a-vis* the spontaneous harmonic emission. Near power saturation, the RMS transverse sizes of the 3rd and 5th harmonic emission are $\sim 20\%$ smaller than that of the fundamental (Fig. 2). However, after saturation, they also grow with z despite a greater Rayleigh range, indicating perhaps that optical guiding effects are far more important for the fundamental.

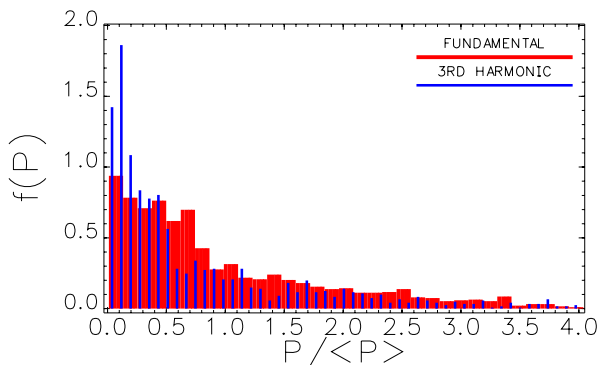


Figure 5: Histogram of the probability distribution of $P(t)/\langle P \rangle$ at the fundamental and 3rd harmonic at the undulator exit.

Standard SASE theory (*e.g.*, Ref. [8]) predicts that the inverse spectral bandwidth $\omega/\Delta\omega$ and autocorrelation time $C_{1/2}(\tau)$ (the point at which the temporal autocorrelation function drops to 0.5) for FEL radiation increase as $z^{1/2}$. Such behavior is demonstrated by radiation at the fundamental (blue curves in Fig. 3). For the harmonics, the coherent component of $C_{1/2}(\tau)$ suddenly dominates over the spontaneous emission (for the radiation) and shot noise (for the microbunching) at two-thirds of a saturation length, reaches a maximum within a gain length, and then begins declining with z , in contrast to the fundamental which reaches a maximum somewhat later in z (right plot in Fig. 1) and only drops in the last 20-m or so. Presumably, debunching due to the development of a large energy spread is responsible for the greater sensitivity of the harmonics.

An autocorrelation function and power spectrum can be similarly calculated for microbunching by using the complex average computed over the macroparticles corresponding to each longitudinal electron beam slice. In contrast to the radiation quantities, the microbunching $C_{1/2}(\tau)$ (right plot in Fig. 3) has a slow but steady linear decay from its maximum which is perhaps associated with the temporal variation of Ω_{syn} over the individual microspikes. Ideally, in a near time-steady situation with essentially no variation in radiation eikonal phase, $C_{1/2}(\tau)$ would be constant with harmonic. However, in the SASE regime, Saldin *et al.* [7] have predicted from 1-D numerical studies that $C_{1/2}^{h=3}(\tau)/C_{1/2}^{fund.}(\tau) \approx 0.65$; the GINGER LCLS results show a ratio $\simeq 0.5$, a reduction attributable perhaps to non-zero emittance effects not included in the 1-D study.

Figure 4 plots the inverse spectra width versus z together with the output spectrum at the third harmonic. Another diagnostic of radiation field correlation, the ratio $[\omega/\Delta\omega]/[1.18\omega C_{1/2}(\tau)]$ ($\equiv 1$ for a Gaussian power spectrum), is 0.76 for the fundamental and drops to 0.69 and 0.65 for the third and fifth harmonics at the position of maximum inverse bandwidth.

Another apparent difference with the Saldin *et al.* 1-D results concerns the probability distribution for $P(t)$. In Fig. 5 we plot the normalized histogram for the fundamental and third harmonic of the output (near-field) radiation. One sees that in accord with the earlier study, the third harmonic emission is more peaked toward $P = 0$. However, the peak is more extreme and the first order moment is much smaller, evidently because of large temporal regions of relatively low harmonic power. The probability distribution for the fundamental is also more peaked toward $P = 0$ whereas Ref. [7] found a peak near $P = \langle P \rangle$. Because our data is taken somewhat deeper in saturation than the z point chosen by Saldin *et al.*, it is possible (albeit unlikely) that the distribution function reverts back to a negative exponential corresponding to the exponential gain regime. or that this particular SASE run does not have sufficient statistics in terms of slice number to clearly resolve the distribution shape. However, it may also be possible that inclusion of true transverse effects actually change the nature of

the distribution function in the saturation regime. Consequently, this topic may warrant some additional study.

IMPLEMENTATION OF HDF5 IO

As is true for most large-scale simulation tools, an FEL code must have numerous IO capabilities. On the input side, the user must be able to specify a number of beam and run parameters. Depending upon the run complexity, additional input might be required, *e.g.*, 6D macroparticle phase space information from a tracking particle output file or a “restart” file from a previous FEL code run (as might be true for a harmonic cascade); a time-dependent input radiation field; an undulator “lattice” including $a_w(z)$, possible pole error field and dipole corrector information, and possible vacuum chamber longitudinal wake field input. Output information can be very extensive: spatially- and temporally-resolved radiation field information including harmonics; 5D macroparticle phase space snapshots at different z - and t - locations for later use in scatterplots; z - and t - resolved “scalar” information such as total radiation power and macroparticle microbunching (at multiple harmonics), energy spread, on-axis far field complex amplitude; and possible full 6D macroparticle and/or 2D (r, t) radiation field information for a subsequent downstream undulator run. As the raw binary size of this information can exceed 100 MB for fields and 1 GB for particles, simple ASCII formats are unattractive both due to their size ($\sim 3X$ larger than pure binary) and slow IO transfer speed. Moreover, unless one designs a very clever and robust self-describing data structure and/or divides the heterogeneous output into many separate files per run, it is difficult to have an output file system that is reasonably easy to analyze (and which maintains good backward compatibility as the simulation code inevitably evolves in complexity).

In answer to the above requirements and problems, the HDF5[2] IO system offers a strong set of attractive features: (1) self-describing data format, including optional dataset attributes (2) Unix-like directory trees including soft links (3) compact data storage with little additional overhead relative to binary (4) multiplatform data file portability (*e.g.*, little- to big-endian, 32- to 64-bit native) (5) a rich class of native data types range from simple strings to 1-D integer arrays to many dimensional real arrays (6) user-definable data types (7) MPI-based parallel IO on platforms such as the IBM-SP. The HDF5 development group also provides a set of useful tools for HDF5 file data visualization and data dumping of individual structures. Many projects in the high performance computing community have embraced HDF5 as well as a number of 3rd party visualization tools vendors (*e.g.*, IDL). I note that the GENESIS code [9] also has a growing HDF5 IO capability and would suggest that other FEL and tracking code developers consider this option.

Currently, the GINGER HDF5 output file has 5 main top directories: `/base_param` to pass simulation run variables such as the central wavelength, number of slices, etc.;

`/grids` which have the r - and z - locations of grid points; `/input` which has the complete ASCII input and template files for the run; `/radiation` which contains all scalar and vector radiation field information; and `/particles` which has all particle-derived information including scatterplot dumps, if any. Separately, particle restart files can also be written in HDF5 format and the extension to radiation restart files (as is needed for multistage harmonic cascades) will be done in the near future. Knowledge of the exact “path” of a given data set (*e.g.*, `/radiation/scalar_data/...`) is completely sufficient for a HDF5 utility (and GINGER post-processor) to access the data set; the exact disk address within the HDF5 file is not needed by external programs but is provided by a low-level look-up table in the HDF5 file. This massively simplifies data access. With the migration to HDF5 format, we believe it will be relatively straight-forward and painless to extend the GINGER output file to handle fully “3D” field information (*i.e.*, $[r, z, t] \rightarrow [r, \varphi, z, t]$) and variable spatial resolution (*e.g.*, relative finely z -resolved scalar quantities such as radiation power and microbunching but coarser resolution of vector quantities such as $E(r, z, t)$) as needed by future code upgrades.

ACKNOWLEDGEMENTS

I am pleased to acknowledge many useful discussions with numerous individuals including A. Adelman, E. Al-laria, M. Borland, W. Graves, Z. Huang, H.-D. Nuhn, G. Penn, E. Pourmal (HDF5 group/NCSA), and S. Reiche. I also thank the LCLS project office at SLAC for financially supporting much of the work presented here and also the US DOE National Energy Supercomputer Center for providing Computational resources.

REFERENCES

- [1] W.M. Fawley, “A User Manual for GINGER ...”, LBNL-49625-Rev.1 (2004); see also http://www-ssrl.slac.stanford.edu/lcls/lcls_tech_notes.html/LCLS-TN-04-3.pdf.
- [2] National Center for Supercomputing Applications (U. Ill.), “HDF5 Home Page”, <http://hdf.ncsa.uiuc.edu/HDF5/>
- [3] Message Passing Interface Forum, “MPI: A Message-Passing Interface standard”, Int. J. Supercomputer Applications and High Perf. Comp. **8** (1994); see also: <http://www.mpi-forum.org/docs/docs.html>.
- [4] C.W. Gear, Comm. ACM **14**, 176 (1971).
- [5] R.D. Richtmeyer and K.W. Morton, “Difference Methods for Initial-Value Problems”, (Interscience, New York), 2nd. Ed., 1967.
- [6] Z. Huang and K.-J. Kim, Phys. Rev. E **62**, 7295 (2000).
- [7] E.L. Saldin, E.A. Schneidmiller, and M.V. Yurkov, *Proc. 27th Int. FEL Conf.* (2005, Stanford, CA), 51.
- [8] K.-J. Kim, Phys. Rev. Lett. **57**, 1871 (1986).
- [9] S. Reiche, Nucl. Inst. Meth. Phys. Res. A **429**, 243 (1999).

SIMULATIONS OF HIGH POWER-FEL AMPLIFIERS*

J. Blau, D. Burggraff, T.Y. Voughs and W.B. Colson
 Physics Department, Naval Postgraduate School
 333 Dyer Road, Monterey, CA 93943.

Abstract

FEL amplifier simulations have been updated and parallelized, and system vibration effects have been added. The simulations are used to study proposed high-power amplifier FELs at LANL and BNL. We look at the single-pass gain and output power, including the effects of wiggler tapering, electron beam pinching, and shifting and tilting of the electron beam.

INTRODUCTION

At the Naval Postgraduate School over the past several years, we have made significant changes to our simulations of FEL oscillators, including an improved light propagation method using expanding coordinates [1], cavity and electron beam stability effects [2], better diagnostics such as optical mode analysis [3], and parallelizing the codes to run on a cluster computer. These same improvements have now been incorporated into our FEL amplifier simulations. In this paper, we discuss the results of using these simulations to study several existing and proposed high-power FEL amplifiers at Brookhaven and Los Alamos National Labs. We look at the effects of tapering the undulator, as well as shifting, tilting, and focusing of the electron beam. We consider how each of these affect the single-pass gain, energy extraction, and optical beam quality.

SIMULATION METHOD

We represent the optical field using a Cartesian coordinate system, following the amplitude and phase at each (x, y) grid point as it evolves through the undulator. The initial field has a Gaussian transverse profile, focused at the beginning of the undulator. The electron and optical pulse lengths are assumed to be much longer than the slippage distance $N\lambda$, where N is the number of undulator periods and λ is the optical wavelength. We use a large number of sample electrons, with an initial position and angular distribution determined by the transverse emittance, and an initial energy spread determined by the longitudinal emittance. To study stability effects we can include an initial shift or tilt in the electron beam, and we can also adjust the beam focus position along the undulator.

At each time step within the undulator, the electrons evolve according to the Lorentz force equation, including betatron focusing. The optical field evolves self-consistently according to Maxwell's wave equation. At the

end of the undulator, the field is propagated to the first optical element using an expanding coordinate system [1] to handle the large scale change due to diffraction.

In our simulations, we use dimensionless parameters, with longitudinal lengths normalized to the undulator length L , transverse lengths normalized to $\sqrt{L\lambda/\pi}$, and time normalized to L/c , where c is the speed of light. Graphical output from the simulations shows the evolution of the optical field, bunching of the electrons in phase space, and the structure of the optical wavefront at the end of the undulator and at the first optical element.

SIMULATION RESULTS

Brookhaven SDL FEL

At the Source Development Lab (SDL) at Brookhaven National Lab (BNL), they have an FEL amplifier based on the NISUS undulator [4], with $N = 256$ periods, each $\lambda_0 = 3.9$ cm long, for a total length $L = N\lambda_0 \approx 10$ m. The undulator parameter is $K_{rms} = 0.78$. The electron beam has an energy of 102 MeV, with a bunch length of 1 ps and a bunch charge of 0.35 nC. The optical wavelength is $\lambda = 0.79 \mu\text{m}$, and the distance to the first optic is 20 m.

Figure 1 shows results from a simulation of this FEL. On the top, a cross-section of the dimensionless optical field amplitude $|a(y)|$ is represented as it evolves from the be-

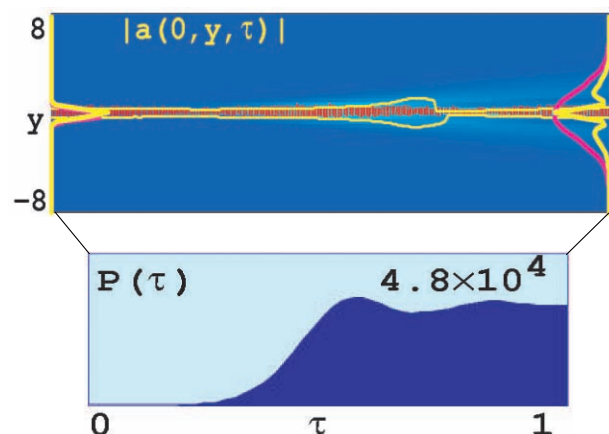


Figure 1: Simulation results for the SDL FEL with no taper. On the top is the evolution of the amplitude profile $|a(y)|$, as described in the text. On the bottom is the evolution of the dimensionless optical power $P(\tau)$ from the beginning ($\tau = 0$) to the end ($\tau = 1$) of the undulator. The maximum value of the power is indicated in arbitrary units.

*Work supported by JTO, ONR, and NAVSEA.

ginning (dimensionless time $\tau = 0$) to the end ($\tau = 1$) of the undulator. The narrow yellow contour line marks the $1/e$ value of the field amplitude at each time step, while the bold yellow curves on the left and right plot the field profile at $\tau = 0$ and $\tau = 1$. A few sample electrons are shown in red. The simulation predicts high gain, $G \approx 1000$, which leads to optical mode distortion and guiding [5]. Without the gain medium, the field would maintain a Gaussian profile and diffract out to a large radius, as shown in purple on the right; the actual field profile shown in bold yellow is much narrower and distorted. The simulation predicts an extraction of $\eta = 0.6\%$ (extraction is defined as the ratio of the output optical power to the input electron beam power). In the actual experiment, an extraction of about 0.4% was measured. The difference is likely due to pulse slippage effects, which are not included in the simulation.

The lower half of Fig. 1 shows the power saturating about halfway down the undulator, so we consider tapering the magnetic field to enhance the extraction. Figure 2 shows the simulation results with a linear taper rate $\Delta K/K \approx -5\%$ over the last 2.4 m of the undulator. Now the power continues growing, and the extraction is increased to $\eta = 1.2\%$. The final electron phase space on the lower left shows about half of the electrons trapped in closed orbits [5]. The electron phase ζ roughly corresponds to the position of an electron within an optical wavelength, while $\nu = d\zeta/d\tau$ is the phase velocity. The induced spread in phase velocities $\Delta\nu$ translates to an electron beam energy spread $\Delta E/E = \Delta\nu/4\pi N = 3.7\%$, compared to 2.5% for the untapered case. The final optical wavefront $|a(x, y)|$ at the output mirror is shown in the lower right.

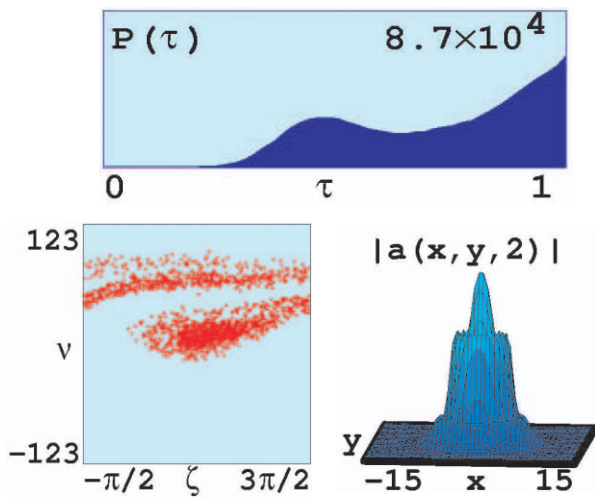


Figure 2: Simulation results for the SDL FEL with a -5% taper rate over the last 2.4 m of the undulator. On the top is the evolution of the optical power, $P(\tau)$. On the lower left is the final electron phase space as described in the text, with sample electrons shown in red. On the lower right is the final optical wavefront, $|a(x, y)|$, at the output mirror.

Another factor of two improvement in extraction could be achieved by starting the taper earlier at $\tau_s = 0.5$, near the onset of saturation for the untapered FEL. Figure 3 shows the results of many simulations, plotting extraction η versus phase acceleration δ for this latter case. The phase acceleration [5] is related to the undulator taper rate by

$$\delta = -4\pi N \frac{K^2}{1 + K^2} \frac{(\Delta K/K)}{1 - \tau_s}. \quad (1)$$

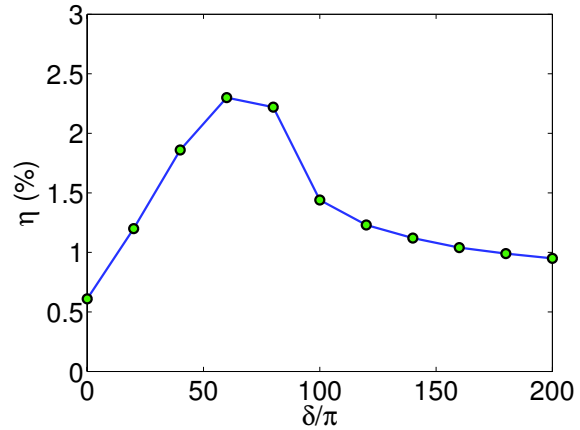


Figure 3: Extraction η versus phase acceleration δ for the SDL FEL, with a linear taper over the last 5 m of the undulator. The maximum extraction $\eta = 2.3\%$ is achieved for $\delta = 60\pi$, which corresponds to $\Delta K/K \approx -7\%$.

Figure 4 shows the results of simulating the SDL FEL with a taper rate of -7% over the last 5 m of the undulator, corresponding to the peak extraction value of 2.3% in Fig. 3. The optical power $P(\tau)$ grows significantly in the second half of the undulator, and the phase space plot shows good bunching. The induced energy spread is 5% .

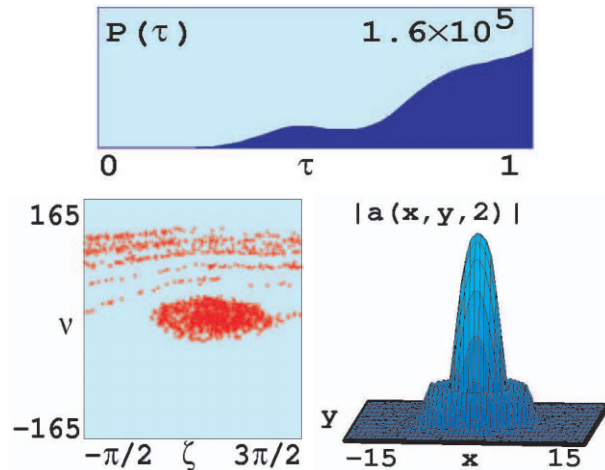


Figure 4: Simulation results for the SDL FEL, with a -7% taper rate over the last 5 m of the undulator.

Brookhaven proposed FEL

Another high-power amplifier FEL has been proposed at BNL [6]. This system would use an 80 MeV electron beam with a bunch length of 2.8 ps and a bunch charge of 1.4 nC. The undulator would have $N = 120$ periods, each $\lambda_0 = 3.25$ cm long, for a total length $L = 390$ cm, with $K_{rms} = 0.7$. The optical wavelength would be $\lambda = 1 \mu\text{m}$, with the first optic at a distance of 27 m.

Figure 5 shows simulation results for this FEL. Again we see guiding of the optical field (top), and the power is near saturation at the end of the undulator (center). The simulation predicts gain $G \approx 800$ and corresponding extraction $\eta \approx 1\%$; the design goal for this system is $\eta = 0.25\%$. In the lower left, the electron phase space shows bunching, and an induced electron beam energy spread of 3.5%. In the lower right, the final optical wavefront has a nearly top-hat shape.

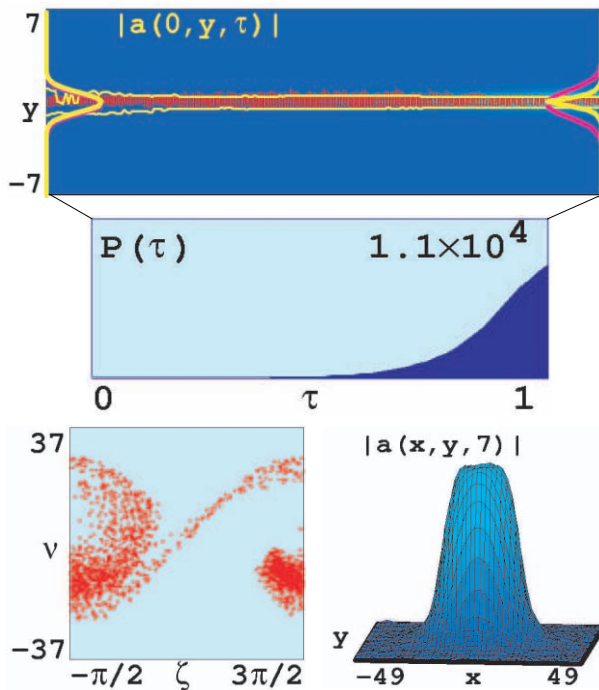


Figure 5: Simulation results for the proposed BNL FEL.

We also studied electron beam stability effects for this system. Figure 6 shows the results of many simulations, with the electron beam shifted off-axis in the plane of the undulator magnetic field. The extraction drops as the beam is shifted, but the design goal of $\eta = 0.25\%$ is still achieved for $y_0 < 1.2$ mm, about 5 times the electron beam radius ($r_b = 0.25$ mm, indicated on the graph). Figure 7 shows how guiding enables the optical mode to follow the shifted electron beam over about half of a betatron oscillation, for a beam shift of $y_0 = 1$ mm.

Figure 8 shows the effect of tilting the electron beam about the center of the undulator. The simulations predict that the system can tolerate a beam tilt of $\theta_y \approx 0.9$ mrad, well beyond the beam angular spread of $\Delta\theta = 0.1$ mrad.

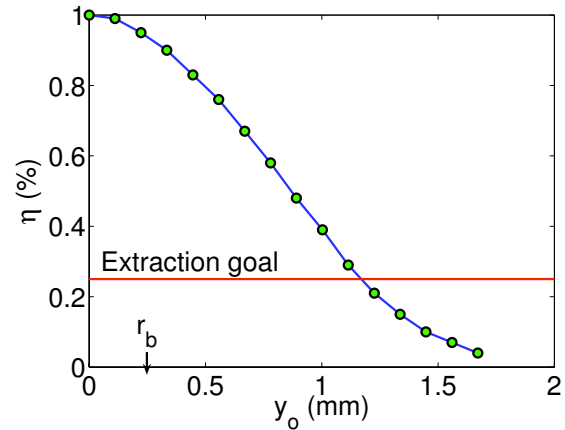


Figure 6: Extraction η vs. electron beam shift y_0 for the proposed BNL FEL. The extraction goal is exceeded for all values of $y_0 < 1.2$ mm, well beyond a typical experimental tolerance of $\approx 50 \mu\text{m}$, and much greater than the electron beam radius $r_b = 0.25$ mm.

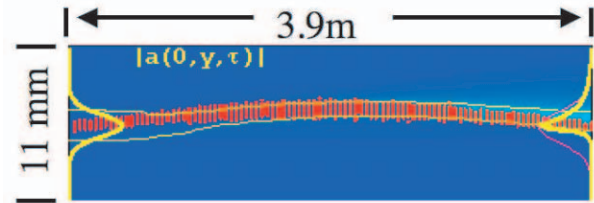


Figure 7: Optical field evolution for the proposed BNL FEL. Initial conditions are chosen so that the electron beam (shown in red) is shifted off-axis by $y_0 = 1$ mm at the center of the undulator. Betatron focusing bends the beam back towards the axis at the ends of the undulator. The horizontal and vertical axis scales are quite different, as indicated. Notice how guiding enables the optical mode (narrow contour line) to follow the electron beam as it shifts off axis.

Again, this is due to the guiding effect, as shown in Fig. 9. Our simulations predict good extraction for electron beam shifts x20 and tilts x100 greater than the experimental tolerance of existing FELs [7].

Los Alamos proposed FEL

At Los Alamos National Lab (LANL), they have proposed a somewhat different design for a high-power FEL amplifier [8]. This system would use an 81 MeV electron beam with a bunch length of 1 ps and a bunch charge of 1 nC. The undulator would have $N = 110$ periods, each $\lambda_0 = 2.18$ cm long, for a total length of $L = 240$ cm, with $K_{rms} = 1.2$. The optical wavelength would be $\lambda = 1.05 \mu\text{m}$, with the first optic at a distance of 24 m.

Our simulations of this design predict that it would achieve a gain of $G \approx 240$, corresponding to extraction of $\eta = 0.74\%$, with induced energy spread of about 5%.

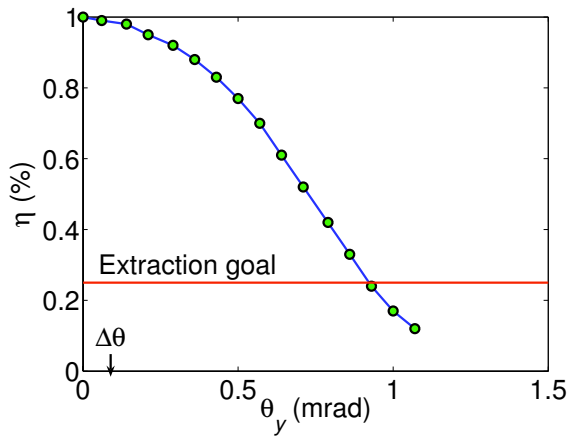


Figure 8: Extraction η vs. electron beam tilt θ_y for the proposed BNL FEL. The extraction goal is obtained for all values of $\theta_y < 0.9$ mrad, well beyond a typical experimental tolerance of $10 \mu\text{rad}$, and much greater than the electron beam angular spread, $\Delta\theta = 0.1$ mrad.

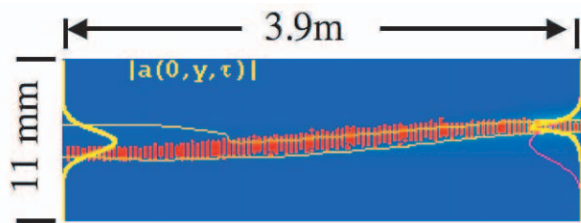


Figure 9: Optical field evolution for the proposed BNL FEL. Initial conditions are chosen so that the electron beam is tilted by $\theta_y = 0.9$ mrad at the center of the undulator. The tilt appears exaggerated due to the different horizontal and vertical scales. Notice that the optical mode (narrow yellow contour line) follows the tilted electron beam (red).

However, the design goal for this system is $\eta = 1.2\%$. We find that by tapering the undulator, $\Delta K/K \approx -18\%$ over the last 40 undulator periods, they could increase the gain to $G \approx 500$ and the extraction to $\eta = 1.7\%$, while only inducing an energy spread of about 6%.

We studied stability effects for the LANL amplifier design; our simulations predict that it will still achieve the desired extraction with beam shifts up to 0.4 mm, or beam tilts up to 0.4 mrad. These results are again well beyond the experimental tolerance of existing FELs.

We also tried varying the electron beam focus for this FEL. Figure 10 is a plot of the extraction versus the beam focus position, τ_β . The peak extraction $\eta \approx 1.9\%$ is at $\tau_\beta = 0.15$ or 0.75 , rather than at $\tau_\beta = 0.5$ as one might expect. This is due to the betatron motion of the electrons, in both cases focusing the beam near the end of the undulator, where the tapering enhances the extraction. This "scalped" shape of the electron beam, as seen in the inset plots in Fig. 10, leads to focusing of the optical wavefront at

the undulator exit, thus allowing it to rapidly diffract afterwards, which should reduce the intensity at the first optic.

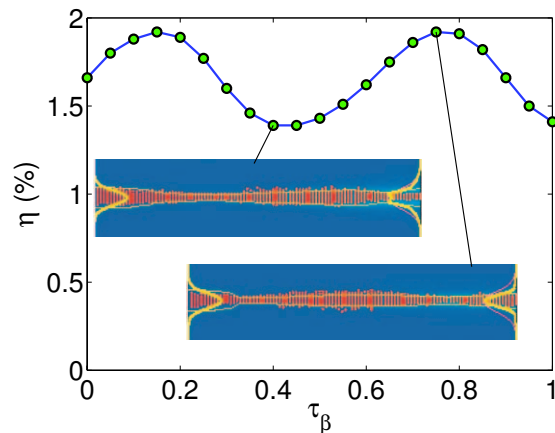


Figure 10: Extraction η vs. electron beam focus position τ_β for the proposed LANL FEL. The inset plots show the evolution of the electron beam and the optical mode at $\tau_\beta = 0.4$ (top) and $\tau_\beta = 0.75$ (bottom).

REFERENCES

- [1] R.L. Armstead, J. Blau, and W.B. Colson, "Short Rayleigh length free electron laser simulations in expanding coordinates", Proceedings of the 26th International Free Electron Laser Conference (2004), p. 274. <http://www.JACoW.org>.
- [2] P.P. Crooker, J. Blau, and W.B. Colson, "Stability of a short-Rayleigh length laser resonator", Phys. Rev. ST-AB, 8, 040703 (2005).
- [3] R. Vigil, "Hermite-Gaussian modes and mirror distortions in the free electron laser", M.S. Thesis, Naval Postgraduate School, June 2006.
- [4] T. Watanabe, et. al., "An experimental test of superradiance in a single pass seeded FEL", Proceedings of the 27th International Free Electron Laser Conference (2005), p. 526, <http://www.JACoW.org>.
- [5] W.B. Colson, C. Pellegrini, A. Renieri (Eds.), Free Electron Laser Handbook, North-Holland Physics, Elsevier Science Publishing Co. Inc., The Netherlands, 1990 (Chapter 5).
- [6] I. Ben-Zvi, D. Kayran and V. Litvinenko, "High average power optical FEL amplifiers", Proceedings of the 27th International Free Electron Laser Conference (2005), p. 232, <http://www.JACoW.org>.
- [7] S. Benson, priv. comm.
- [8] D. C. Nguyen, W. B. Colson and H. Freund, "Scalloped electron beam FEL", Proceedings of the 28th International Free Electron Laser Conference (2006), p. xxx, <http://www.JACoW.org>.

THE BESSY SOFT X-RAY FEL: A SEEDED HGHG FEL *

A. Meseck[†] for the BESSY FEL team
 BESSY GmbH, Albert-Einstein-Str.15, Berlin, Germany.

Abstract

Reproducibility, high power and short pulse length combined with variable polarization and tunable wavelength are required to open new frontiers for the soft X-ray users. To provide radiation with such extraordinary properties, BESSY has been designing a seeded FEL based on the high-gain harmonic-generation (HGHG) concept [1]. The seeding with an external tunable laser ensures the reproducibility of the full-coherent radiation. The combination of so-called HGHG stages, used to down-convert the seed wavelength, and a final amplifier provides for the high power and superior spectral properties. Furthermore, the HGHG concept and the fresh bunch technique planned for the BESSY FEL mitigate the effects of parameter variation along the bunch which are expected from realistic assumptions of the Gun and LINAC structure. The design concept of the BESSY soft X-ray FEL will be presented and the stabilizing effect of HGHG stages and the benefits from the fresh bunch technique and the final amplifier will be discussed.

INTRODUCTION

The BESSY Soft X-Ray FEL is designed as a multi-user facility consisting of three independent FEL lines based on HGHG-concept. Each line is seeded by a tunable laser covering the spectral range of 230 nm to 460 nm. The target wavelength ranges from 51 nm to 1.24 nm with peak powers up to a few GWs and pulse lengths less than 20 fs (rms). The polarization of the fully coherent radiation will be variable.

In the HGHG-FEL approach the light output is derived from a coherent subharmonic seed field. Consequently the optical properties of the HGHG-FEL output reflect the characteristics of the high-quality seed. The benefit is a pulse with selectable short duration, a high degree of stability and control of the central wavelength and bandwidth. Cascades of two to four HGHG stages are planned to reduce the existing laser wavelength to the target range of the BESSY-FEL. The planned “fresh bunch” technique [2] prevents the final output from the electron beam heating effect of FEL interaction in the upstream stages, ensuring the high output power and the spectral quality.

The optimization of an HGHG-line includes the proper choice of the seeding radiation, the electron beam parameters, the harmonic cascade, the undulator parameters and the strength of the dispersive section. In the following

the steps taken during the optimization process will be described.

All calculations have been performed with the time-dependent 3D simulation code GENESIS [3].

THE HIGH-GAIN-HARMONIC GENERATION

Several HGHG stages are necessary to reduce the seed laser wavelengths available today to the desired spectral range. Each stage consists of an undulator - dispersion - undulator structure. In the first undulator, the so called modulator, the interaction with a radiation field (e.g. provided by an external laser) leads to an energy modulation of the electron beam with the period of the seeding wavelength. The following dispersive section converts this energy modulation into a spatial modulation, or bunching, that includes bunching on higher harmonics of the seeding frequency. The fundamental of the second undulator, the so called radiator, is set in resonance with the chosen harmonic. The prebunched beam then radiates at the harmonic wavelength with high efficiency. The radiator output is used as the seed for the next stage. The last radiator is followed by the so called final amplifier. It is seeded at the desired wavelength and the amplification process is brought to saturation.

In a cascaded HGHG scheme the necessary seeding power for each stage is produced by adjusting the output power of the previous stage. The output power of the radiator is proportional to the square of the bunching factor, b_n , of the entering electron beam [4]:

$$p_{out} \sim b_n^2.$$

The bunching factor for the n^{th} harmonic of the seed laser is given by:

$$\begin{aligned} b_n &= \langle \exp(i n \theta_j) \rangle^2 \\ &= \exp\left(\frac{-1}{2} n^2 \sigma_\gamma^2 \left(\frac{d\theta}{d\gamma}\right)^2\right) J_n\left(n \Delta\gamma \frac{d\theta}{d\gamma}\right) \\ &= \exp\left(\frac{-1}{2} \sigma_\gamma^2 \left(\frac{d\psi}{d\gamma}\right)^2\right) J_n\left(\Delta\gamma \frac{d\psi}{d\gamma}\right), \end{aligned}$$

where θ is the ponderomotive phase of the electron beam in the modulator, $\psi = n\theta$ is the phase in the radiator, $\Delta\gamma$ is the maximum energy modulation generated in the modulator, σ_γ is the energy spread of the electron beam, $\frac{d\theta}{d\gamma}$ is the strength of the dispersive section and J_n is the n^{th} order Bessel function.

* Work funded by the Bundesministerium für Bildung und Forschung and the Land Berlin

[†] meseck@bessy.de

Large bunching factors can be achieved when the energy modulation impressed by the seed dominates the energy spread of the electron beam. Hence, for a reasonable performance of an HGHG stage the energy modulation induced by the seed should fulfill the following inequality [4]:

$$\Delta\gamma \geq n\sigma_\gamma. \quad (1)$$

When the radiation size at the entrance of the modulator and the transverse size of the electron beam are matched, the energy modulation of the electron beam scales with the seed power, p_{seed} , seed wavelength, λ_s , the modulator length, L_{mod} , the electron beam energy, γ , and the undulator parameter, K , as [4]:

$$\Delta\gamma \sim \frac{K}{\gamma} L_{mod} \sqrt{\frac{p_{seed}}{\lambda_s}}. \quad (2)$$

The modulator length should not exceed twice its power gain length in order to avoid an increase in energy spread due to the spontaneous radiation. For given electron beam energy and seed wavelength, and a fixed modulator length, the energy modulation, $\Delta\gamma$, can be controlled by the undulator parameter, or the seeding power, p_{seed} , both of which have their technical limits. The dispersive section has to be adjusted according to the energy modulation, reached in the modulator, taking the effective dispersion in the modulator and radiator into account. The total dispersive strength is given by [4, 5]:

$$\frac{d\psi}{d\gamma} \approx -\frac{n 2\pi L_{mod}}{\lambda_{um} \gamma} + \left(\frac{d\psi}{d\gamma}\right)_{dis.sec.} - \frac{4\pi L_{rad}}{\lambda_{ur} \gamma}, \quad (3)$$

where λ_{um} and λ_{ur} are the modulator and radiator period length, and L_{rad} is the length of the radiator.

Due to the interaction of the electron beam with the seed, the effective energy spread of the electron beam entering the radiator is given by

$$\sigma_{\gamma eff} = \sqrt{\sigma_\gamma^2 + \frac{(\Delta\gamma)^2}{2}}. \quad (4)$$

An increased energy spread causes an enhanced gain length and therefore extends the necessary length of the radiator. The ‘‘fresh bunch’’ technique is employed to limit the growth of energy spread from stage to stage in a cascaded HGHG FEL. In this approach the seeding pulse is significantly shorter than the electron bunch. As a result the harmonic generation process, and with it the enlargement of the energy spread applies only to a fraction of the bunch. After passing the first HGHG-stage the resulting radiation is shifted to a ‘‘fresh’’ part of the bunch which was not affected by the seed. A theoretical treatment of the HGHG-scheme can be found in [4, 5].

SEEDING RADIATION AND ELECTRON BEAM PROPERTIES

Contrary to a continuous seed pulse as used for the DUV-FEL [6, 7], in the case of a Gaussian-shaped pulse the

electrons do not experience the seed peak power during the whole transition through the modulator. Since the integrated power experienced by electrons should be in the same order of magnitude to induce the same amount of bunching, the Gaussian-shaped seed pulse needs a higher peak power. For example, the 30 MW continuous power with a wavelength of 800 nm used for the DUV-FEL where the modulator has 10 periods, corresponds, according to equation 2, to a seed power of 90 MW for a seed wavelength of 266 nm, and the same number of modulator periods. A Gaussian-shaped seed with 266 nm wavelength and 15 fs rms pulse duration would require a peak power of 1.3 GW in a 10 periods modulator to induce the same bunching. Since the modulator can be chosen longer for the 266 nm seed radiation, using a proper modulator of 18 periods a peak power of 400 MW is sufficient. Note, to suppress the noise degradation effects [8] a higher peak power should be preferred.

The wavelength of the seed radiation within the range provided by the laser is deduced from the desired final wavelength and the harmonic cascade. Out of the several combinations of harmonics that can be used to provide the desired wavelength range in each particular HGHG-line, the one requiring the minimal number of stages is chosen. The accessible harmonic content in the bunching drops off with rising harmonic numbers and photon energies, limiting the usable harmonics to the first five. The fifth harmonic is used in the early stages, where, due to the long wavelength, enough power and thus bunching can be obtained with acceptably short radiator lengths. Later stages use the third harmonics. The harmonic combination can change when the gaps are moved and the resonant wavelengths vary.

The planned tunable seed laser covers the spectral range of 230 nm to 460 nm with a Gaussian profile, a peak power of 500 MW and a pulse length of about 15 fs (rms), for more details see [1].

The energy of the electron beam has to fulfill the resonance condition, equation 5, for the whole HGHG-line with the minimum possible gain length. The nominal values of the electron beam parameters, extracted from start-to-end simulations, are listed in Table 1. The electron beam at the entrance of the HGHG-lines has a normalized transverse emittance of 1.5 mm mrad, a relative energy spread less than 0.02%, and an average current of about 2 kA at the ‘‘flat top’’. The duration of the flat top amounts to 730 fs. For the presented calculation an electron bunch with transverse Gaussian distributions is assumed.

OPTIMIZATION OF UNDULATOR PARAMETERS

The resulting resonant wavelength of the FEL, λ , depends on the undulator period length, λ_U , the K-value and the electron beam energy γ in units of the electron’s rest

Parameter	High-energy	Medium-energy	Low-energy
ϵ_n [mm mrad]	1.5	1.5	1.5
I_{peak} [kA]	1.75	1.75	1.75
E [GeV]	1.63-2.3	2.3	1.02
$\Delta E/E$ [%]	0.01-0.014	0.01	0.02
Δt [fs]	730	730	730

Table 1: The nominal electron beam parameters at the entrance of the first modulator used in the simulation studies.

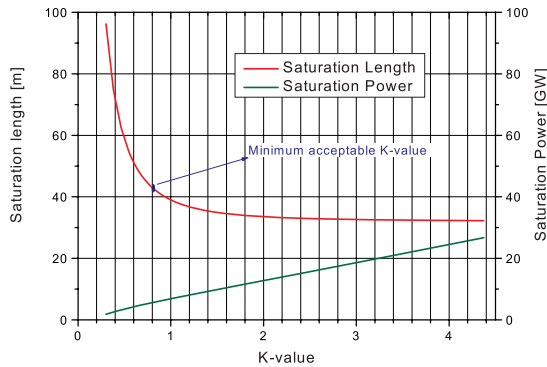


Figure 1: Saturation length and power as functions of the K-value for the final amplifier of the medium-energy HGHG-FEL. The FEL performance deteriorates with decreasing K-value.

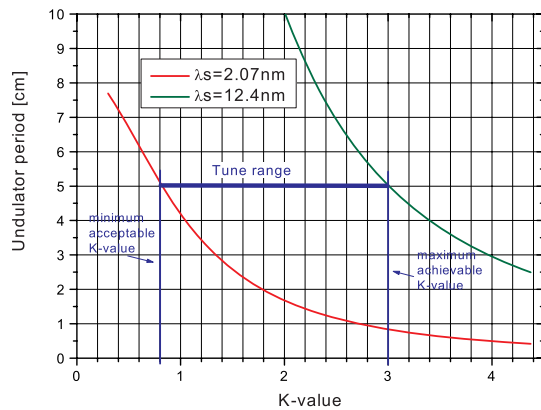


Figure 2: The undulator period as function of K-value for the final amplifier of the medium-energy HGHG-FEL. The tune range is limited by the minimum acceptable and maximum achievable K-value. With an undulator period of 5 cm the desired wavelength range can be covered by gap variation.

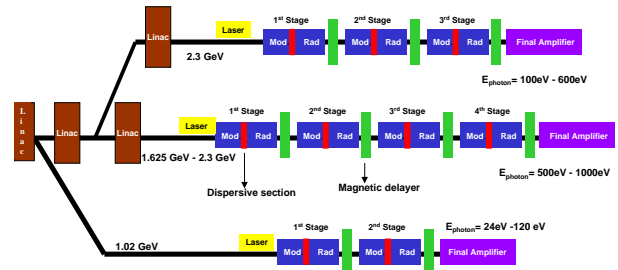


Figure 3: The BESSY HGHG multi user FEL-facility will consist of three HGHG-lines to cover the target wavelength range.

mass:

$$\lambda = \frac{1}{2\gamma^2} \lambda_U (1 + K^2). \quad (5)$$

The maximum achievable K-value is limited by the permanent magnet undulator technology. The minimal gap is set to 10.4 mm according to impedance considerations.

The minimum acceptable K-value is set to 0.8 as the interaction between the radiation field and the electron beam suffers from too small K-values. Figure 1 shows the saturation length and power as functions of the K-value for the final amplifier of the medium-energy HGHG-FEL. The deterioration of the FEL performance with decreasing K-parameter is obvious.

The undulator period length is chosen such, that the desired wavelength range can be completely covered within the given range of K-parameter. Figure 2 shows the tune range for the medium-energy HGHG-FEL as an example. With an undulator period of 5 cm the desired wavelength range can be covered. Once the period length, λ_U , is fixed, the resonant wavelength can be altered by adjusting the gap of the undulator.

LAYOUT OF THE HGHG UNDULATOR SECTION

The BESSY HGHG multi user FEL-facility will consist of three undulator-lines to cover the target photon energy range from 24 eV to 1 keV ($51 \text{ nm} \geq \lambda \geq 1.2 \text{ nm}$). The “low-energy” HGHG-FEL operates in two stages at a beam energy of 1.02 GeV delivering photons in a spectral range of 24 eV to 120 eV. An energy of 2.30 GeV is chosen for the “medium-energy” HGHG-FEL. A cascade of three stages covers the energy range of 100 eV to 600 eV. The “high-energy” HGHG-FEL operates at variable electron beam energies of 1.625 GeV to 2.30 GeV. It delivers in four stages photon energy ranges from 500 eV to 1000 eV. Figure 3 shows a schematic view of the BESSY HGHG multi user FEL-facility. A description of the electron source, linac and compressor scheme providing electron beams with the required properties can be found in [1].

Each of the three HGHG-lines consist of several stages and a final amplifier. In order to optimize an HGHG-stage

Table 2: High Energy HGHG-FEL

Stage	MODULATOR			RADIATOR		
	λ_U [mm]	P #	L [m]	λ_U [mm]	P #	L [m]
1	122	18	2.196	92	40	3.680
2	92	22	2.024	70	86	6.020
3	70	30	2.100	50	180	9.000
4	50	69	3.450	28.5	225	6.413
Final				28.5	630	17.955

Table 3: Medium Energy HGHG-FEL

Stage	MODULATOR			RADIATOR		
	λ_U [mm]	P #	L [m]	λ_U [mm]	P #	L [m]
1	122	18	2.196	92	40	3.680
2	92	22	2.024	70	104	7.280
3	70	30	2.100	50	231	11.550
Final				50.	393	19.650

Table 4: Low Energy HGHG-FEL

Stage	MODULATOR			RADIATOR		
	λ_U [mm]	P #	L [m]	λ_U [mm]	P #	L [m]
1	80	20	1.600	62	56	3.472
2	62	26	1.612	50	69	3.450
Final				50	162	8.100

the lengths of the modulator und radiator as well as the strength of the dispersion section has to be adjusted. The modulator has to be long enough to imprint the necessary energy modulation according to the equation 1. The strength of the dispersion has to be adjusted according to the energy modulation with respect to the total dispersion given in equation 3. The radiator length has to be chosen suitable to deliver the required power for the next stage. Note, that the effective energy spread generated in the modulator determines the efficient of the radiator according to equation 4. The main parameter of the modulators and radiators for each HGHG-line are listed in tables 2, 3 and 4. Listed are undulator period length, λ_u , number of periods, P , and undulator length, L .

Magnetic delayers shift the electron bunch with respect to the radiation field between the HGHG stages and ensure that the radiation field interacts always with a undisturbed part of the bunch in the modulator. Quadrupoles and phase shifters are planned between the stages as well as between the undulator segments of the radiators and the final amplifier to focus and match the electron beam.

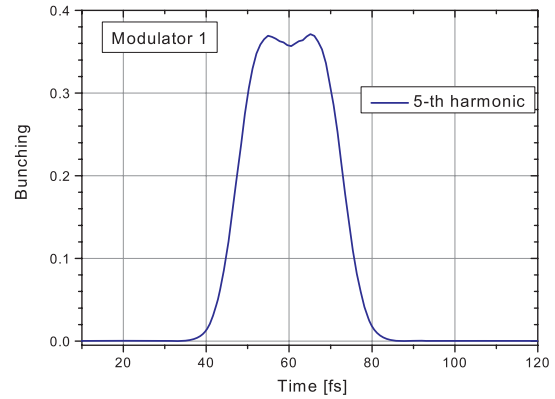


Figure 4: Bunching on the fifth harmonic after the first dispersion section for the high energy HGHG

POWER AND SPECTRUM OPTIMIZATION

For the optimization of the HGHG-FEL performance, the adjustment of the bunching, by setting the modulator length and the dispersion strength, is of major importance. The laser seed interacts with electrons at the rear of the bunch. Due to the slippage effect only a part of the interacting electrons experience the full power of the Gaussian shaped seed. Optimizing the modulator length and dispersive section to a somewhat reduced power level the output of the following radiator can be maximised. In this case the electrons at the center, which experience the full power sufficiently long are somewhat overbunched.

Figure 4 shows the bunching after the first dispersion section for the high energy HGHG. The overbunching causes a power dip in the radiation pulse provided by the first radiator, as shown in figure 5a. Figure 5b shows the corresponding radiation spectrum. The overbunched electrons fulfill synchrotron oscillations in the ponderomotive bucket. The resulting modulation of the emitted radiation frequency causes the side spikes (sidebands) [9].

The more electrons are overbunched the stronger is the growth of the sidebands. This effect is repeated in the following stages, where the slippage shifts the sidebands to one side. In this way the number of sidebands in the spectrum adds up from stage to stage. The higher the harmonic numbers in the cascade the stronger are the sidebands. For example in the case of the medium-energy HGHG-FEL the sidebands for $\lambda_s = 2.07 \text{ nm}$ with harmonic numbers $5 \times 5 \times 5$, figure 7, are much stronger than for $\lambda_s = 12.4 \text{ nm}$ with harmonic numbers $3 \times 3 \times 3$, see figure 6.

The side spikes can be avoided by optimizing the stages for the seed peak power. In this case the output of the following radiator is reduced. The bunching is of more Gaussian shape. The resulting radiation power and pulse length are reduced compared to the overbunched case. An example of such a spectrum purity optimized case is shown in

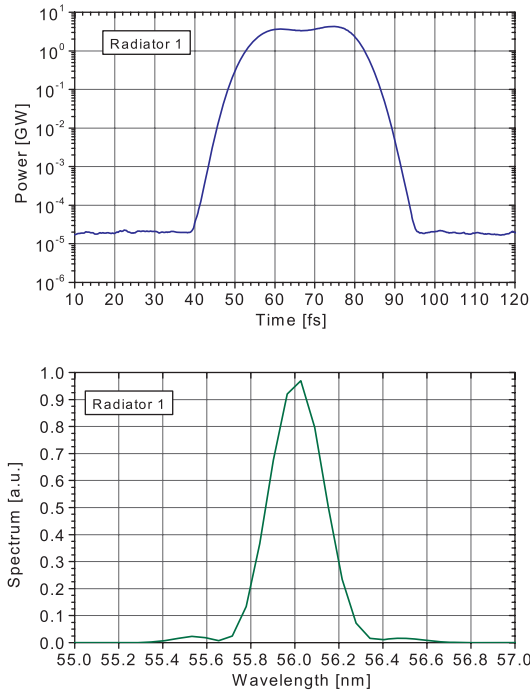


Figure 5: Simulation results for the first radiator of the high-energy HGHG-FEL a) the time resolved power distribution (top) and b) the spectral power distribution (bottom).

figure 8, where the power and spectral distribution of a purity optimized and a power optimized case are displayed in the same graph for comparison.

The details of the cascades for the boundary wavelengths of each HGHG-line are summarised in [1].

PERFORMANCE CALCULATIONS

For the performance calculations the seeding radiation properties and electron beam parameters are chosen according to the considerations of the previous sections.

In order to obtain reliable results, the slippage effects in the undulators and the radiation diffraction in the fresh bunch sections have to be taken into account. The first effect lengthens the pulse, whereas the second one reduces the power density on axis which is relevant for the energy modulation in the following modulator. The time-dependent mode of GENESIS [3] used for the simulation allows an adequate treatment of these effects.

In spite of the short lengths of the modulators and radiators, see Tables 2-4, the degradation of the unseeded part of the bunch due to the emission of incoherent radiation can not be neglected. The resulting increase of the energy spread and decrease in the central energy from stage to stage are shown in figure 9 for the high-energy case.

The relative increase of the energy spread at the entrance of the second modulator is only 0.2%, but it increases to

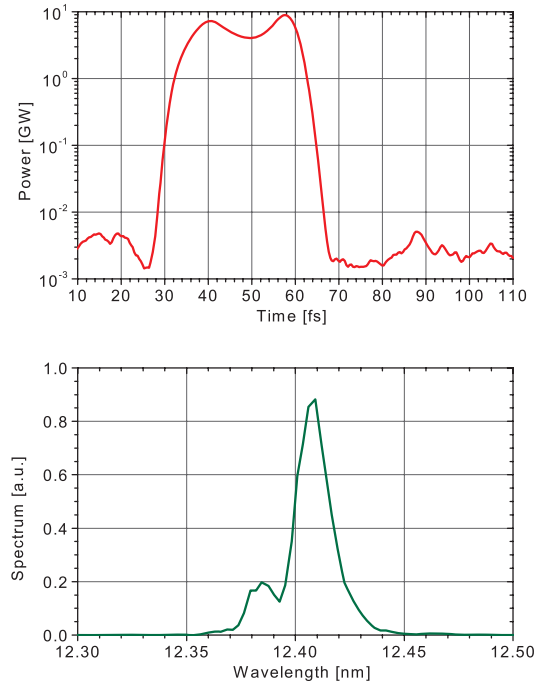


Figure 6: Simulation results for the medium-energy HGHG-FEL, $\lambda_s = 12.4 \text{ nm}$ the time resolved power distribution (top) and the spectral power distribution (bottom) are calculated.

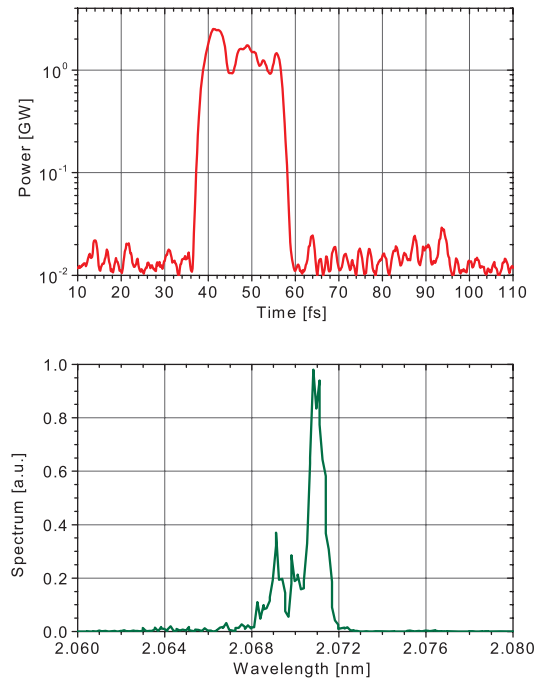


Figure 7: Simulation results for the medium-energy HGHG-FEL, $\lambda_s = 2.07 \text{ nm}$ the time resolved power distribution (top) and the spectral power distribution (bottom) are calculated.

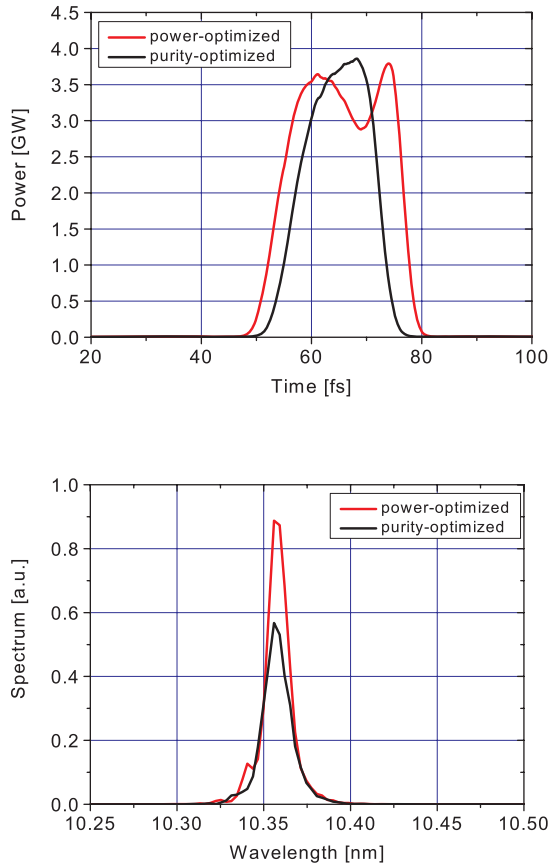


Figure 8: Simulation results for the low-energy HGHG-FEL, the power and spectral distributions of a purity-optimized case and a power-optimized case.

Table 5: The performance of the three HGHG-line for the boundary wavelengths

	<i>LE-FEL</i>		<i>ME-FEL</i>		<i>HE-FEL</i>	
λ [nm]	10.33	51.00	12.40	2.07	2.48	1.24
Power [GW]	3.5	14.0	9.0	1.5	1.3	1.5

4% at the fourth modulator. The loss in the central energy at the entrance of the fourth modulator is about 0.45% which is larger than the bandwidth of about 0.2% of the fourth radiator and the final amplifier. This means that the following radiator and amplifier have to be readjusted to meet the resonance condition for the lower central energy.

This loss of the electron beam quality causes a reduction in the maximum bunching and a deterioration of the spectral properties of the radiation. Tracking the electrons through all the previous undulators, this effect has been taken into account. The performance of the three HGHG-lines for the boundary wavelengths are summarised in the

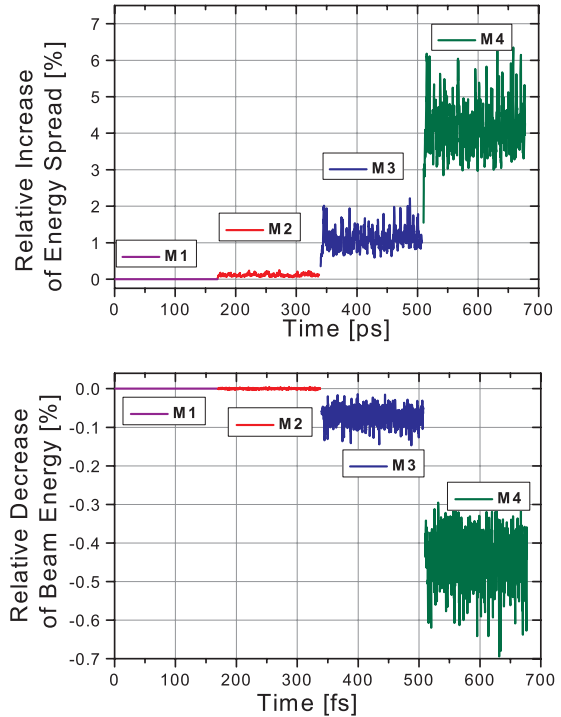


Figure 9: Degradation of the unseeded part of the bunch for the high-energy HGHG-FEL, the relative changes in energy spread (top) and the central energy (bottom) at the entrance of modulators, M1 to M4, are shown.

Table 5.

S2E BUNCHES AND SELF-STABILIZING

Start-to-end simulations for the BESSY FEL show variation of the electron beam parameter along the bunch [10]. The possibility to adjust the undulator gaps and the strengths of the dispersive sections independently, mitigates the effects of the parameter variations [11]. Each stage can be optimized according to the particular parameters of the interacting part.

Furthermore, the concept of the final amplifier allows to use the asymmetry of the detuning curve to reduce the output degradation due to the combination of the energy chirp and the arrival-time jitter of the bunch [12]. The energy chirp, induced for the bunch compression, combined with the arrival-time jitter, due to gun and LINAC errors, causes a mismatch between the central energy of the interacting part of the bunch and the resonance energy. This leads to a fluctuation of the FEL output power. Adjusting the final amplifier to a somewhat reduced K-value, stabilizes the output power, as the average energy of the interacting electrons is somewhat higher than the resonance energy.

CONCLUSION

BESSY has been designing a seeded FEL based on a cascaded high-gain harmonic-generation concept. Simulations with start-to-end bunches including all relevant effects show that the BESSY FEL meets the user requirements with respect to pulse duration, tunability, spectral purity and power. Furthermore, simulation studies including errors in the gun and LINAC attest to the advantages of the HGHG concept planned for the BESSY FEL.

REFERENCES

- [1] The BESSY Soft X-ray Free Electron Laser, Technical Design Report March 2004, eds.: D.Krämer, E. Jaeschke, W. Eberhardt, ISBN 3-9809534-08, BESSY, Berlin (2004).
- [2] L. Yu, "High-gain harmonic generation of soft X-ray with the "fresh bunch" technique", NIM A 393 (1997) 96.
- [3] S. Reiche, GENESIS 1.3, NIM A 429(1999) 243.
- [4] L. Yu, "Theory of high gain harmonic generation: an analytical estimate", NIM A 483 (2002) 493.
- [5] J. Wu, "Coherent X-ray production by cascading stages of a high-gain harmonic generation free electron laser", Thesis, May 2002.
- [6] L.H. Yu, L. DiMauro, A.Doyuran, W. Graves, R. Heese, E.D. Johnson, S. Krinsky, H. Loos, J.B. Murphy, G. Rakowsky, J. Rose, T. Shaftan, B. Sheehy, Y. Shen, J. Skaritka, X.J. Wang, Z. Wang, "First Ultraviolet High-Gain Harmonic-Generation Free-Electron Laser", Phys. Rev. Lett. 91, 074801 (2003).
- [7] A.Doyuran, L. DiMauro, W. Graves, R. Heese, E.D. Johnson, S. Krinsky, H. Loos, J.B. Murphy, G. Rakowsky, J. Rose, T. Shaftan, B. Sheehy, Y. Shen, J. Skaritka, X.J. Wang, Z. Wang, L.H. Yu, "Saturation of the NSLS DUV-FEL at BNL", PAC 2003, Proceedings.
- [8] E.L. Saldin et al., "Study of a noise degradation of amplification process in a multistage HGHG FEL", Opt. Commun. 202. (2002) 169.
- [9] E.L. Saldin, E.A. Schneidmiller, M.V. Yurkov, The physics of free electron lasers, Springer-Verlag Berlin Heidelberg.
- [10] M. Abo-Bakr et al., "Start to end simulations for BESSY FEL", Proceeding of the FEL 2003 Conference, Japan, published in NIM-A, **258** (2004), 476.
- [11] B. Kuske, M. Abo-Bakr, A. Meseck, "Impact of Realistic Bunch Profiles and Timing Jitter on the Output of the BESSY Low Energy FEL Line", Proceedings of the FEL 2005, Stanford, USA.
- [12] B. Kuske, M. Abo-Bakr, A. Meseck, "Start-to-End Simulations for the BESSY Low and Medium Energy FEL Line Including Errors", proceedings of the FEL 2005, Stanford, USA.

THE CHALLENGES OF SEEDED FELS

G. De Ninno, ELETTRA, Basovizza, Trieste

Abstract

Basic users' expectations for the light produced by next generation FELs are:

- much higher peak brilliance than conventional synchrotron radiation and complete tunability in the VUV/X-ray spectral range;
- full transverse and longitudinal coherence of the radiation pulse;
- possibility of controlling pulse duration and spectral bandwidth;
- high shot-to-shot reproducibility, i.e. low power fluctuations, good pointing stability and reduced temporal jitter.

Seeded schemes appear nowadays as a way to satisfy all the above mentioned requirements. However, this achievement relies on the solution of several open technological and physical issues. In this paper we give a review of some of these challenges and discuss the expected performance of future seed-based FELs.

**PAPER NOT
AVAILABLE**

THE USE OF HHG AT 4GLS

B.W.J. McNeil, SUPA, Department of Physics, University of Strathclyde, Glasgow, UK
 D. Dunning and N.R. Thompson, ASTeC, CCLRC Daresbury Laboratory, UK
 B. Sheehy, Sheehy Scientific Consulting, New York, USA.

Abstract

4GLS is a facility proposed for the Daresbury Laboratory in the UK which will offer users a suite of high brightness synchronised sources from THz frequencies into the XUV [1]. In the current design, photon energies from 8-100eV will be generated in a variable polarisation FEL amplifier directly seeded by a High Harmonic Gain system. The reasoning behind this choice will be discussed and characterisation of the sources based on the present design presented.

INTRODUCTION

The Conceptual Design Report for the 4GLS project to be based at UK's Daresbury Laboratory has been published [1]. A suite of synchronised coherent variably polarised radiation sources covering the spectrum from THz frequencies to photons energies of ~ 100 eV will provide the scientific community with a tool that will enable new windows of scientific exploration to be opened and thereafter exploited. Initially, the major themes of the 4GLS science programme will lie in time-resolved measurements and nanoscience. Details of the science case driving the need for 4GLS were first published in [2] and more recently updated in [1].

A major component of 4GLS will be the XUV-FEL. The current design for this component is for a seeded FEL amplifier that operates in the 8-100 eV photon energy range to provide peak powers between approximately 1-10 GW allowing very high field intensities of up to 10^{17} W/cm² to be achieved. In order to tune over the spectral range both the electron beam energy and the undulator magnetic field are variable. Because the FEL acts as an amplifier the seed sources also need to be continuously tunable.

There are several potential benefits in operating a FEL as an amplifier of an injected seed as opposed to allowing the FEL to self-seed from inherent noise to generate Self Amplified Spontaneous Emission. An important benefit is the potential improvement in the temporal coherence of the FEL output over that of SASE. This increases the spectral brightness. Shot-to-shot reproducibility and stability are also improved. The amplified pulse width, being determined by that of the seed, may be significantly shorter than that of the electron pulse, and indeed there is the potential to amplify more exotic pulses for post-amplification manipulation. Finally, the length of FEL interaction required to achieve saturation may be shortened, thereby reducing space requirements and ultimately costs. All of these bene-

fits require that the seed power be significantly greater than the spontaneous power due to the inherent noise.

XUV-FEL OVERVIEW

The design of the 4GLS XUV-FEL has undergone several iterations [3]..[6]. The XUV-FEL branch of the 4GLS conceptual design is shown in schematic form in Fig. 1. Typical operating parameters and specification for the conceptual design are given in Table 1.

Table 1: XUV-FEL conceptual design parameters

General	
FEL design	High Gain Amplifier
Seeding mechanism	HHG source
Photon output	
Tuning Range	$\sim 8 - 100$ eV
Peak Power	$\sim 8 - 2$ GW
Repetition rate	~ 1 kHz
Polarisation	Variable elliptical
Min Pulse length FWHM	< 50 fs
Typical $\Delta f \Delta t$	~ 0.6
Max pulse energy	$400 \mu\text{J}$
Electron beam parameters	
Energy	750 - 950 MeV
Bunch Charge	1 nC
RMS bunch length	266 fs
Normalised emittance	2π mm mrad
RMS energy spread	0.1%
Undulator parameters	
Undulator Type	PPM & APPLE-II
No of Modules	8 & 5
Module lengths	~ 2 m
Period	45 mm & 51 mm
Focusing	FODO
Minimum magnetic gap	~ 10 mm

The work of [6] describes some detail of the undulator and focusing lattice choices based upon studies using the design formulae of Xie [7] and steady state 3-D simulations using Genesis [8]. Undulator module lengths of ≈ 2 m were chosen with a simple FODO quadrupole focusing lattice inserted between modules along with BPMs and phase matching units. This solution requires a shorter total undulator length to achieve saturation than the longer module options considered in [5], which require a more complex quadrupole doublet or triplet focusing system. However,

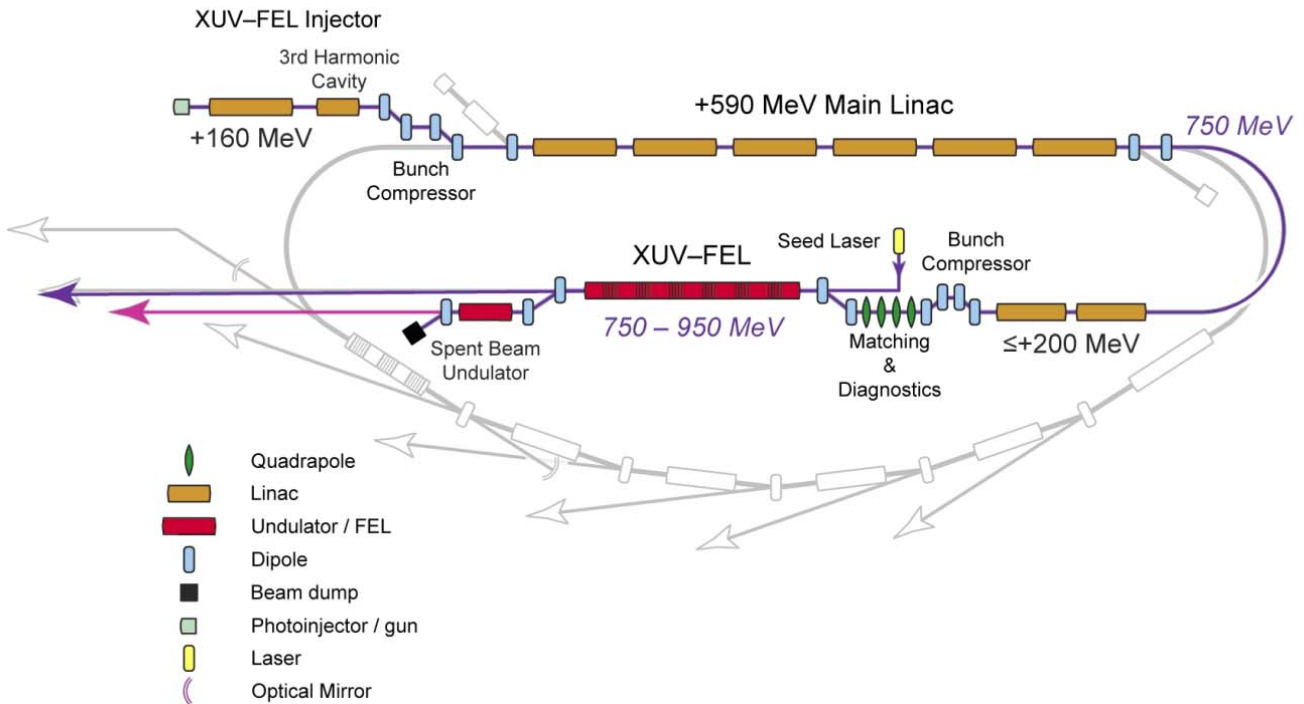


Figure 1: Schematic layout of the XUV-FEL conceptual design.

when gaps between modules are included, the total overall length of modules plus gaps is slightly longer for the shorter module option. The ability to monitor and optimise the electron beam transverse position at regular intervals to ensure optimal radiation-electron beam coupling throughout the FEL and the relative simplicity of the design ensured the shorter 2 m module length with FODO focusing was chosen.

A schematic for the undulator/focusing lattice is shown in Fig. 2. Also shown are the injected radiation seed fields focused to the beginning of the first resonant undulator module, for each of the cases. The undulator length is therefore controlled so that saturation always occurs in the final variable undulator module VU5. In this way, variable polarised photons may be generated across the full operational range of the FEL and it acts as a fixed source simplifying the optical transport system of the output to the final user experimental areas.

It can be seen from Fig. 2 that planar undulator module PU1 is only required to ensure saturation at ~ 100 eV and that its magnetic gap will be at the operational maximum of ~ 28 mm. This module will not be required to operate at gaps very much smaller than this, and therefore the vacuum vessel aperture containing both electron beam and radiation seed can be relatively large at this point. Similar considerations show that module PU2 will operate with minimum magnetic gap slightly smaller again, and so on for the rest of the modules PU3..PU8. Use of a step-tapered

vacuum vessel has therefore been proposed that gradually decreases in aperture from module to module. The two advantages of this approach are that firstly resistive wall and surface roughness wakefields are much reduced compared to a constant minimum aperture, and secondly, as discussed later, the tapered internal aperture allows optimal focusing of the seed pulse across the whole wavelength range.

HIGH HARMONIC GENERATION SOURCES

Peak pulse powers due to intrinsic noise at the beginning of the FEL interaction for the XUV-FEL parameters of Table 1 are typically 30..50 W across the photon energy range 10..100 eV. Any seed source for the XUV-FEL must therefore generate significantly greater power than this if it is to dominate the evolution of the noise to saturation. In addition, these seed sources must be continuously tunable over 10-100 eV. Fortunately, High Harmonic Generation (HHG) sources now exist that meet these seed requirements, or are readily foreseeable within the very near future [1]. Indeed, it can be expected that the rapid advances in this field will be able to easily surpass present 4GLS design requirements for seed sources over the next few years, so this is an area of research that must be closely observed and the XUV-FEL design modified accordingly. Here the method of HHG generation is summarised and the properties of the HHG seed fields described to enable simulation by the 3-D FEL

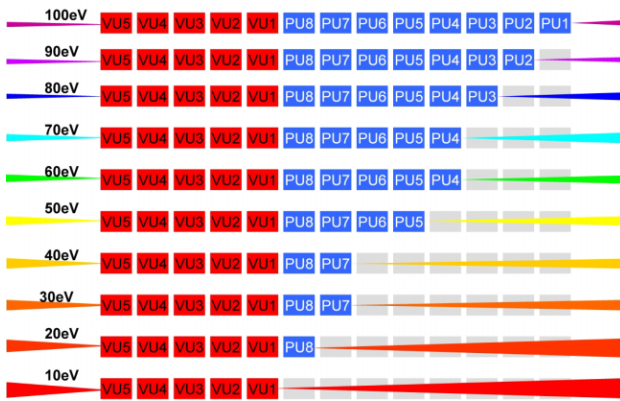


Figure 2: Schematic of the modular undulator system and focusing lattice of the XUV-FEL demonstrating the different modes of operation across the photon energy range 10-100 eV. Electron beam transport is right to left. Undulator modules marked in grey have large magnetic gaps $\bar{a}_u \approx 0$ and are effectively absent for the purposes of the FEL interaction. The minimum required undulator gap (and vacuum vessel internal aperture) decrease in gradual steps from 28 mm (25 mm) for PU1 down to 10 mm (7 mm) for PU8 and the variable polarisation modules VU1-VU5. Radiation beam waists of the seed and output are shown from 100 eV (violet)..10 eV (red).

code Genesis [8]. Further detail and references regarding the HHG sources systems may be obtained from [1, 9].

The HHG sources are based upon samples of Noble gases driven by a high-energy drive laser [10]. A typical drive laser is a linearly polarised Ti:Sapphire system operating at ~ 800 nm generating several to tens of mJ per pulse of FWHM duration of a few tens of fs. For the 4GLS conceptual design, 14 mJ pulses of width 30 fs FWHM are assumed. The high fields generated by such lasers is the key to harmonic generation. The process can be understood semiclassically at the atomic level in terms of ionization and recombination steps occurring within an optical cycle, with the energy gained by the electron from the laser field between these steps going into the harmonics [11, 12], and the phase of the harmonics being related to the trajectories in the field between steps. By macroscopic phase matching, single trajectory lengths for each harmonic can be selected, and a coherent output, with well-defined phases between the harmonics obtained.

The experimentally observed shape of the HHG yield curve is of a rapid decline of the lower order harmonics followed by a plateau-region, in which the harmonic yield falls relatively slowly. An intensity dependent cut-off harmonic is then reached, beyond which the yield drops quickly to zero [13]. This model is used to construct an HHG field to simulate seed injection into the XUV-FEL in the simulations of later sections - see Fig. 4.

Tuning of the HHG sources may be achieved by suitably modifying the drive laser, for example by introducing a chirp or more generally by adaptive pulse shaping. Contin-

uous tuning between adjacent harmonics is possible above about the 25th harmonic or a photon energy of ~ 40 eV (31 nm). Below this photon energy it is proposed to introduce an intermediate noncollinear phase-matched optical parametric amplifier (NOPA) between Ti:Sapphire laser and the gas, which will give continuously tunable output between 1200 nm to 1475 nm. For the 14 mJ specification of the Ti:Sapphire laser this gives ~ 2 mJ output from the NOPA. Although introducing this further efficiency loss, the system will enable more than sufficient continuously tunable power for XUV-FEL seeding for 8-40 eV operation.

Summarising, the powers available from HHG sources exceed 4GLS requirements. In the XUV-FEL modelling that follows, for 10 eV (100 eV) operation a Gaussian input seed of peak power $P_{pk} = 100$ kW (30 kW) in 30 fs FWHM pulses are assumed. The repetition rate of ~ 1 kHz is well matched to the XUV-FEL seed requirements.

MODELLING SEEDING OF THE XUV-FEL

Seed injection

For effective seeding, the seed pulse should be injected coincident with the electron pulse at the start of the undulator and focused to a waist, w_0 , of approximately the same transverse dimensions as the electron pulse. (The waist minimum w_0 is defined as the radius at which the radiation power is $1/e^2$ of its peak value.) Focusing should not be so tight that the seed diffracts rapidly within a gain length at the start of the FEL interaction (i.e. when the Rayleigh length $Z_R = \pi w_0^2/\lambda \ll L_g$.) The relation for the radiation waist size

$$w(z) = w_0 \sqrt{1 + \left(\frac{z - z_0}{Z_R} \right)^2},$$

where z_0 is the position of the focus along the axis of the undulator lattice, restricts the minimum aperture size of the vacuum vessel that will allow transmission of the seed to its focus. As the focal size is determined by the electron beam radius, which is nearly constant for all seed wavelengths, the vacuum vessel's minimum transverse dimensions are determined by the longest wavelength seed (10 eV photons) which must be focused furthest from the FEL entrance as shown in Fig. 2. As the minimum operational undulator gap decreases with undulator module PU1..PU8, as discussed for Fig. 2, the vacuum vessel may be tapered to accommodate the focusing of the 10 eV photon energy seed. This is demonstrated in Fig. 3, where the seed field is injected at the entrance of undulator module PU1 and focused to the optimal waist (as shown in following simulations) of $w_0 = 200 \mu\text{m}$ at the entrance of module VU1 approximately 21 m downstream. It is seen that the vacuum vessel inner wall dimension at $z = 0$ is 25 mm to accommodate wall thickness and clearance for the 28 mm undulator magnetic gap. The walls are at least two beam

waists away from the peak power on axis at all positions up to the start of the FEL interaction region at $z \approx 21$ m. Thus the tapered vacuum vessel should provide sufficient clearance for injection of this (worst case) 10 eV seed injection.

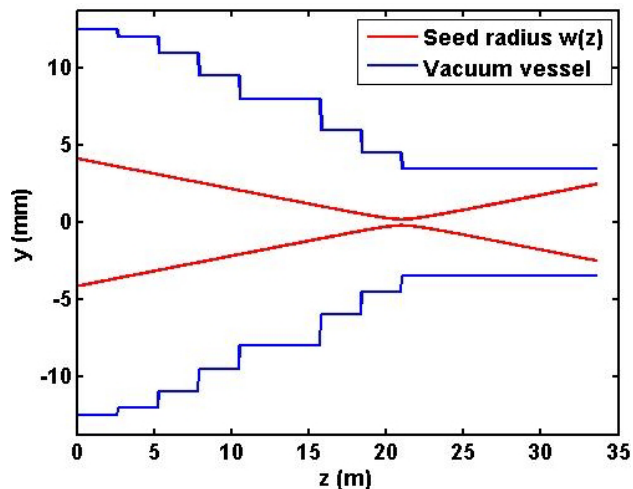


Figure 3: Plot of the dimension of the inner vacuum vessel wall (blue) which has been step-tapered to enable the undulator module tuning ranges of Fig. 2. The waist size $w(z)$ (red) for a 10 eV seed is also shown, focused at the entrance to VU1 at $z = 21$ m.

Seed with full harmonic content

The method of seed generation and specification across the XUV-FEL spectral range is summarised in the previous section and described in more detail in [1, 9]. The HHG seed has interesting spectral and temporal properties, being composed of a large number of narrow, phase-coherent odd harmonics of a fundamental drive laser. This forms a comb structure in frequency-space. Such a phase correlated comb in frequency space has a similar comb-like structure in the temporal domain, resulting in a series of atto-second pulse structures each separated by one half the drive laser period. For a drive laser such as the Ti:Sapphire laser with wavelength of ~ 800 nm, the 65th harmonic corresponds to the maximum XUV-FEL photon energy of 100 eV. If the complete frequency content of a HHG pulse were to be injected into the XUV-FEL it would be preferable if only one of the harmonics, say the n th harmonic, interact resonantly with the electrons. The HWHM gain bandwidth $\Delta\lambda/\lambda \approx \rho$ should then be less than the spacing between harmonics. This gives the condition $\rho < 1/n$. A typical value of $\rho \approx 2 - 3 \times 10^{-3}$ for 100 eV operation so that $\rho < 1/65 \approx 1.5 \times 10^{-2}$ is easily satisfied. Thus, it should be possible to inject all of the seed radiation, including all non-resonant harmonics, into the XUV-FEL without the need for band-pass pre-filtering of the seed, as all non-resonant harmonics will simply become negligible relative to the resonant harmonic as the FEL interaction proceeds through the undulator. For the purposes

of investigating the effects a typical HHG radiation field was generated for use with the 3-D code Genesis. The full HHG spectral power is shown in Fig. 4. However, Gen-

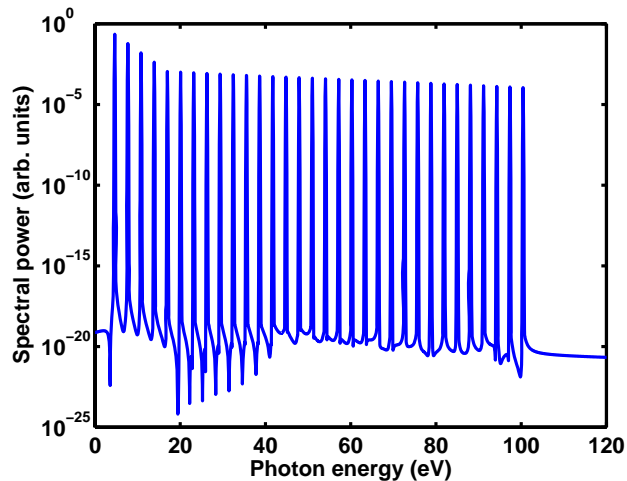


Figure 4: Simulated power spectrum from an HHG source.

esis is a time-averaged code with a minimum interval between sample points of the field of one radiation period so the sampling rate is $\Delta t_s = f_r^{-1}$, the inverse of the resonant frequency. The Nyquist frequency, $f_N = 1/2\Delta t_s$ determines the bandwidth of frequencies that the field can contain without the effects of aliasing. Hence the range of frequencies that can be simulated by Genesis without aliasing effects is $f_r/2 < f_r < 3f_r/2$. Thus from Fig. 4 it is seen that if simulating 100 eV photon energy generation in the XUV-FEL, only the 50-100 eV components of the HHG spectrum should contribute to the Genesis input file using its 'RADFILE' option.

A Genesis simulation was performed for 100 eV operation with the limited spectral range HHG seed pulse as described above. A uniform current of 1.5 kA was assumed. Due to the relatively short slippage experienced at these photon energies, this is very close to that experienced by a short pulse coincident with the Gaussian peak current of the XUV-FEL. All 13 undulator modules were assumed to be the planar type modules PU1..8. The seed at the beginning of the FEL interaction at $z = 0$, the entrance to PU1, is plotted in Fig. 5. Both the atto-second structure in the pulse power and the comb of odd-harmonic wavelengths (inset) are clearly visible. The peak power of the resonant 100 eV (~ 12.3 nm) component is approximately 22 kW.

On propagating through the amplifier to $z = 16.2$ m, Fig. 6 shows that the fine atto-second structure is beginning to be 'washed out' due to the selective amplification of the resonant wavelength at 12.3 nm (inset). All non-resonant harmonics of the seed appear unaffected by the resonant FEL interaction. This is further confirmed by Fig. 7 which shows the output at saturation at $z = 32.4$ m, the end of the interaction region. The radiation pulse shows none of the atto-second structure of the input seed and the spectral power density shows a single high power emission at

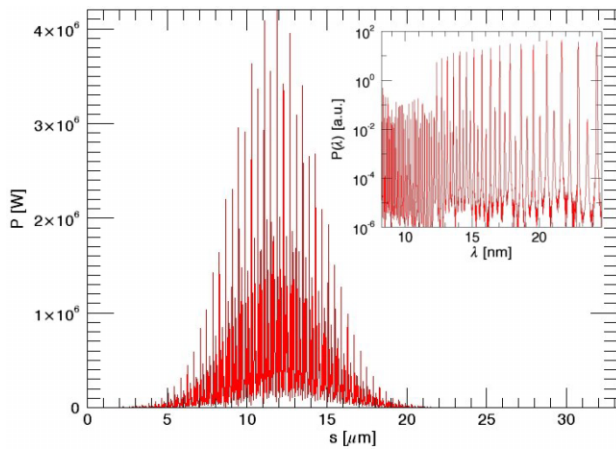


Figure 5: Radiation seed power at the beginning of the amplifier $z = 0$ m as a function of local distance, s . The spectral power content of this pulse is shown as a function of radiation wavelength in the inset.

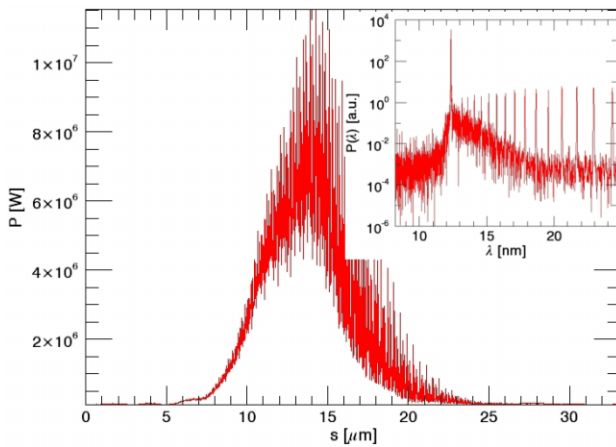


Figure 6: Radiation power as a function of local distance, s , at $z = 16.2$ m through the amplifier. The spectral power content of this pulse is shown as a function of radiation wavelength in the inset.

the resonant wavelength 12.3 nm. It is concluded that, at least for these three-dimensional simulations, the injection of the (Nyquist limited) harmonic content of the HHG seed appears to have no adverse effects in the FEL evolution, or in the saturated emission. The same conclusion may be drawn for lower photon energy XUV-FEL operation where the condition to enable neglect of non-resonant HHG content, $\rho < 1/n$, is more easily satisfied. Thus in all subsequent simulations only the resonant harmonic of the HHG seed content is used in the simulation input.

XUV-FEL 100eV simulations

A complete simulation of the design for the XUV-FEL operating at 100 eV is now demonstrated, using the parameters as given in Table 1. Full details of all parameters may be obtained in [1]. The system modelled is that of Fig. 2

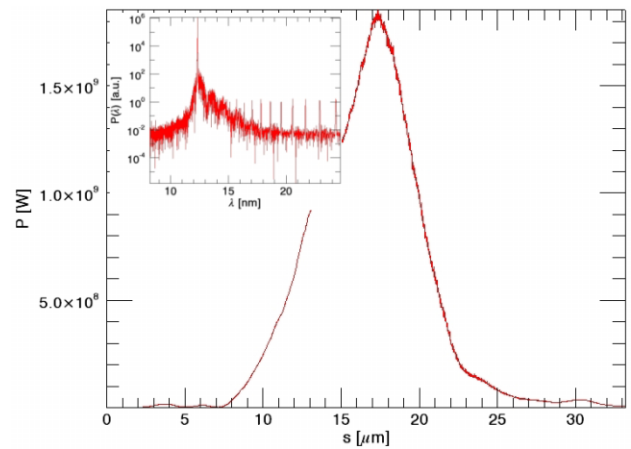


Figure 7: Radiation power as a function of local distance, s , at the end of the amplifier, $z = 32.4$ m. The spectral power content of this pulse is shown as a function of radiation wavelength in the inset.

which, for 100 eV operation, uses the full set of planar and variable undulator modules with the FODO lattice incorporated between modules. The variable APPLE-II undulator modules VU1..5 are set to helical mode so that circularly polarised radiation is generated. The radiation power is plotted in a spatial window that travels along the undulator axis at the speed of light. Fig. 8 plots the power distribution of the seed pulse of peak power $P_{pk} = 30$ kW and duration 30 fs FWHM at the entrance to the first undulator section, PU1. The seed is assumed to have only the resonant har-

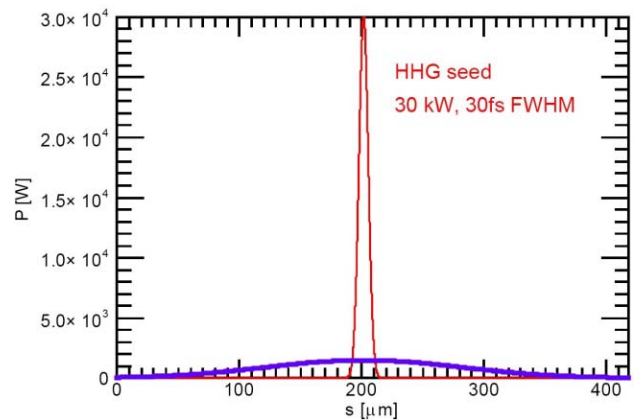


Figure 8: Input radiation seed power (red) to PU1 as a function of local distance, s . The electron beam current profile (blue) is also shown against the same numerical scale.

monic component so that none of the atto-second structure discussed above is present. Also plotted to scale is the electron beam current, here assumed Gaussian, of peak current $I_{pk} = 1.5$ kA and duration 626 fs FWHM. At the exit of the planar undulator modules, it can be seen from Fig. 9 that the peak radiation power has increased to ≈ 70 MW with little change in the pulse structure or width. This pulse

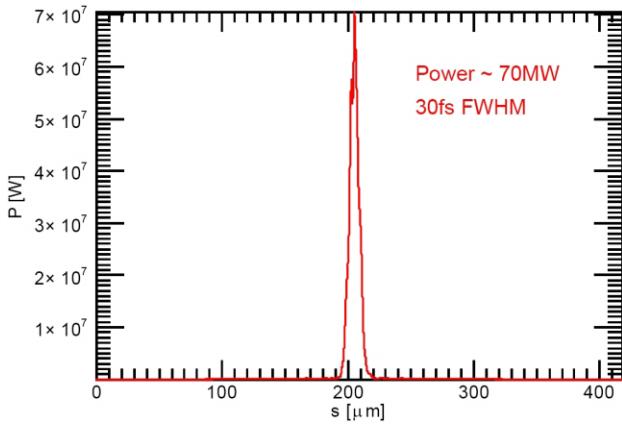


Figure 9: The radiation power at the exit of PU8 as a function of local distance, s.

and the co-propagating electrons are then injected into the set of APPLE-II undulators, VU1 to VU5. By the end of this set of undulator modules, it is seen from Fig. 10 that the FEL interaction has saturated, achieving a peak power of $P_{pk} \approx 2.5$ GW and of duration $\Delta t \approx 60$ fs FWHM. Fourier analysis gives the bandwidth of the spectrum as

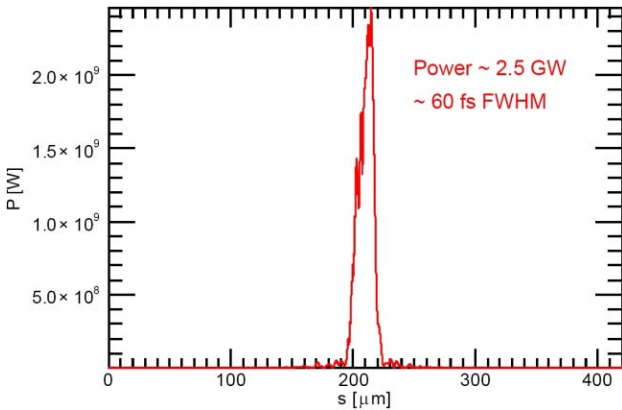


Figure 10: The radiation power at the exit of VU5 as a function of local distance, s.

$\Delta\nu/\nu \approx 5.6 \times 10^{-4}$ which gives a time-bandwidth product of $\Delta f \Delta t \approx 0.8$ which compares favourably with that for a transform limited Gaussian pulse of $\Delta f \Delta t \approx 0.44$. A log-plot of the same data clearly shows in Fig. 11 the relatively clean central seeded region upon a noisier pedestal. This pedestal is the amplified SASE radiation which remains well below saturation because of the smaller initial spontaneous noise radiation (typically a few tens of watts), compared with the initial peak seed power of 30 kW. The shape of the saturated pulse power envelope is not quite as Gaussian as may be expected which suggests that the FEL interaction may have progressed just past saturation. Taking the output power at the end of the previous undulator module, VU4, and plotting it in a similar log plot in Fig. 12, a cleaner Gaussian shape can be seen, with a slightly reduced peak power of $P_{pk} \approx 1.5$ GW. The improved pulse

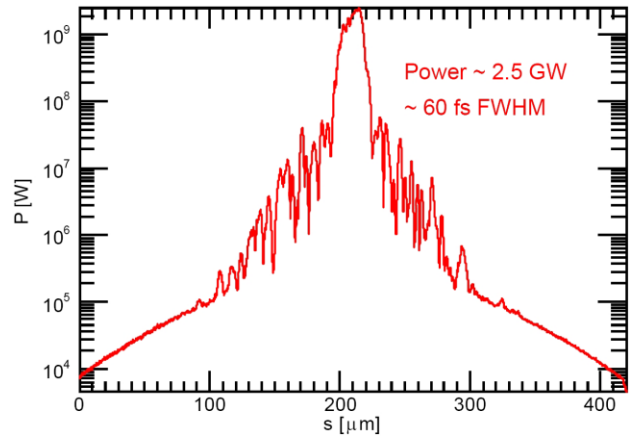


Figure 11: A log-plot of the radiation power at the exit of VU5 as a function of local distance, s.

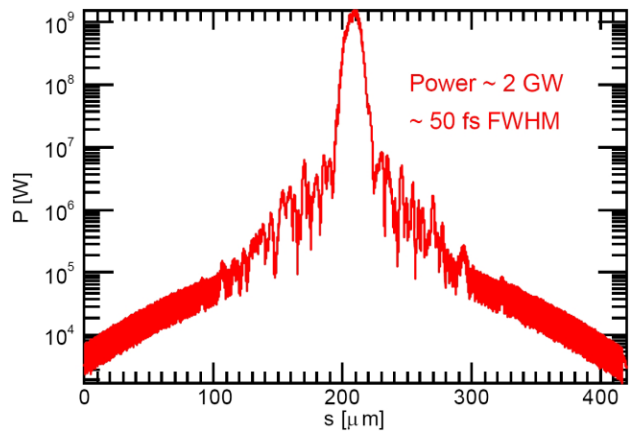


Figure 12: A Log-plot of the radiation power at the exit of VU4 as a function of local distance, s.

shape is confirmed from the pulse duration of $\Delta t \approx 43$ fs FWHM and spectral bandwidth of $\Delta\nu/\nu \approx 6 \times 10^{-4}$ giving an improved time-bandwidth product of $\Delta f \Delta t \approx 0.63$. An improved contrast between the peak power and that of the SASE pedestal is also evident.

XUV-FEL 10eV simulations

Similar simulations to those at 100 eV were carried out for the case of 10 eV operation of the XUV-FEL. Now only the APPLE-II undulator modules VU1 to VU5 are required to achieve saturation as shown schematically in Fig. 2. The input seed power is Gaussian with a peak power $P_{pk} = 100$ kW and duration 30 fs FWHM. The electron pulse current will have the same Gaussian distribution as that for the 100 eV case of Fig. 8.

Radiation power output at the end of undulator module VU5 is shown in Fig. 13 using a log scale. Pulse quality is very good with a peak power of ≈ 6 GW and pulse time-bandwidth product very close to that of a transform-limited Gaussian ($\Delta t \Delta f \approx 0.44$). If the radiation is instead extracted at the end of undulator VU4, the radi-

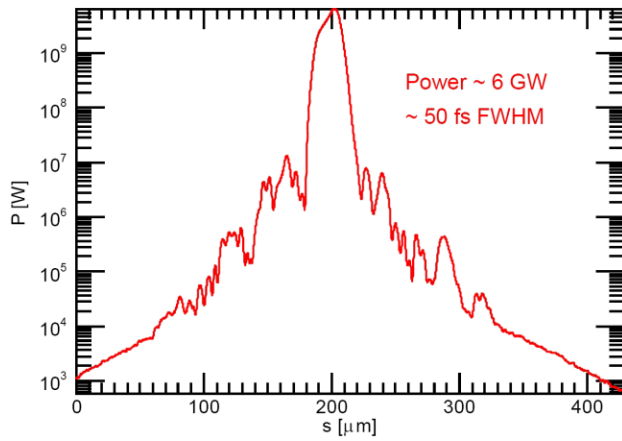


Figure 13: Log-plot of the radiation power for 10 eV operation at the end of undulator module VU5, as a function of local distance, s .

tion power output is shown in Fig. 14. A better contrast

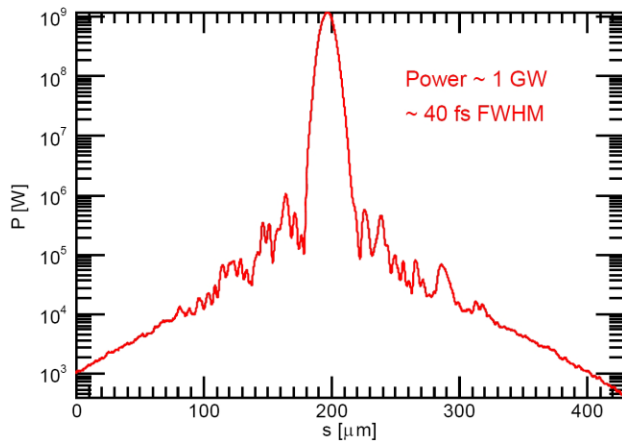


Figure 14: Log-plot of the radiation power for 10 eV operation at the end of undulator module VU4, as a function of local distance, s .

between the peak power of $P_{pk} \approx 1$ GW and the SASE pedestal power is seen from the case of Fig. 13, indicating that the FEL had already saturated before the end of VU5. The time-bandwidth product is approximately the same at $\Delta t \Delta f \approx 0.48$.

Time dependent Genesis 1.3 simulations have also been used to assess the sensitivity of the XUV-FEL output power to the seeding geometry. It is assumed that the most difficult photon energy to achieve optimum geometry will be 10 eV because of the relatively long distance of ≈ 21 m between the seed injection point (before PU1) and the first operational undulator (VU1). The peak seed power of 100 kW was focused to a waist at the beginning of VU1. Fig. 15 shows the effect of varying the size of the focal point waist. An optimum waist of $\approx 200 \mu\text{m}$ yields a peak output power of $P_{pk} \approx 7.5$ GW. The corresponding Rayleigh length for this focus is ≈ 1.0 m. The Xie formulae [7] estimate the

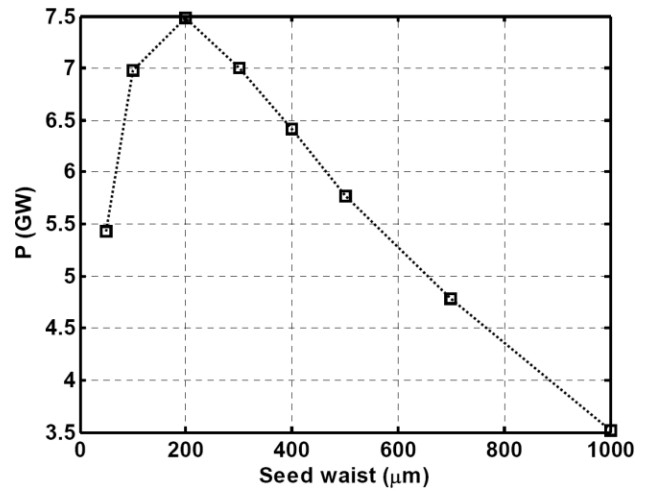


Figure 15: Radiation peak power for 10 eV operation at the end of undulator module VU5, as a function of seed beam waist at the entrance to VU1.

gain length at 10 eV for these parameters to be ≈ 0.5 m. The optimum Rayleigh length for a seed focused at the undulator entrance is therefore found to be $Z_{R\ opt} \approx 2L_g$. For this optimum focusing the seed beam waist at the injection point, $z = 0$ (beginning of PU1), is 4.1 mm. If it is assumed that a full aperture at the injection point of six times the beam radius is required to minimise diffraction effects, then a vacuum vessel aperture of ≈ 25 mm (magnetic gap minus 3mm) is sufficient. This is achieved with the step-tapered vacuum vessel design, as discussed above.

The above results show that the output power at the end of VU5 reduces as the seed waist size at the entrance to VU1 increases. (Consequently the seed radius at the injection point also decreases.) The reduced coupling between radiation and electrons with increasing radiation waist means that saturation is not achieved in the fixed undulator length. Nevertheless, it may be beneficial to use a larger seed waist size than the optimum value of $200 \mu\text{m}$ and compensate for the increased saturation length by focusing the seed into the previous module PU8 for example. (This will have no effect on the saturation power which is independent of seed.) A larger waist size will reduce output power fluctuation due to seed source pointing stability. While this will be investigated further in future design work, the current conclusion shows that the optimum seed focusing geometry may be obtained with the use of the proposed step-tapered vacuum vessel.

Variable polarisation

As has been noted above, the HHG seed sources are linearly polarised. However, this should not present problems in generating variable polarisation. When the HHG seed is injected into a planar undulator it causes the electrons to bunch in the axial (\hat{z}) direction. The polarisation of the radiation emitted is determined by the electron trajectory. Hence, if the electron bunching is initiated in a planar

undulator and subsequently transferred into an elliptically polarised undulator, the electrons will emit elliptically polarised radiation and progress via the FEL interaction to saturation. If the linearly polarised HHG seed is injected with the electrons directly into an elliptically polarised undulator then coupling between seed and electrons will occur in the plane of the radiation electric field and will begin to bunch the electrons. The bunching electrons will then emit with the elliptical polarisation determined by the undulator. Optimal coupling will occur when the major axis of the elliptically polarised undulator is co-incident with that of the electric field polarisation of the seed.

Timing

Detailed discussion of synchronisation and timing jitter effects between the seed and electron pulse at the entrance to the XUV-FEL are summarised here and presented in more detail in [1, 14]. A relation between a timing offset Δt and the peak electron current has been used with the Xie formulae [7] to estimate the effects of timing offset upon the saturation length and saturation power of the XUV-FEL operating at 100 eV. From these estimates a 50 fs offset increases the saturation length by $\sim 1.3\%$, and decreases the saturation power by $\sim 4\%$. A 100 fs offset increases the saturation length by $\sim 5\%$, and decreases the saturation power by $\sim 13\%$. Genesis simulations have also been used to investigate the effect of timing offset and are in very good agreement. While timing jitters of ~ 100 fs should be readily achievable, it is projected that this figure may be reduced to the low tens of femto-second level. It may be possible to offset the effect of the increase in saturation length by allowing the amplifier sufficient length to oversaturate. In this way the saturated power will nearly always be attained. This area is the subject of future design and research effort.

CONCLUSIONS

The main use of HHG in 4GLS is to act as a seed source for the XUV-FEL. These sources have enabled a robust conceptual design for the XUV-FEL to be developed. Established theory and simulation codes predict this FEL will generate photons of giga-watt power levels in pulses of duration 40-60 fs FWHM. The design specification presented here is optimised for 10-100 eV operation but it has been demonstrated [1] that extension to a revised photon energy range of 8-100 eV requires only small parameter changes. The quality and tunability of the HHG seed ensures the FEL remains continuously tunable generating pulses that will have very good temporal and spatial coherence with time-bandwidth products close to the Fourier transform limit for a Gaussian pulse. The XUV-FEL interaction here is acting as a simple, bandwidth limited amplifier - so long as the radiation input seed pulses have sufficient spectral purity, the output radiation is very nearly a simple amplified version of the input.

HHG sources have also been included in the 4GLS conceptual design as user sources in their own right. This has not been discussed, but is of significant importance to the overall concept of 4GLS as a facility providing multi-colour synchronised sources to the user.

It has been demonstrated that the multi-harmonic content of the HHG seed need not be filtered before injection as the gain-bandwidth of the FEL interaction ensures that only the resonant harmonic affects the FEL output.

The most critical aspect to ensuring the success of the XUV-FEL design is in the spatio-temporal synchronisation between electron pulses and HHG seed at the beginning of the FEL interaction region. While initial study suggests this is feasible, this and other aspects will now be the subject of greater scrutiny as the 4GLS project enters the technical design phase.

REFERENCES

- [1] *4GLS Conceptual Design Report*, Council for the Central Laboratory of the Research Councils, UK (2006), available from: <http://www.4gls.ac.uk/documents.htm#CDR>
- [2] *The Science Case for 4GLS* (2001), available from: http://www.4gls.ac.uk/Documents/EPSC-Dec2001/Science_Case.pdf
- [3] M.W. Poole and B.W.J. M^cNeil, Nucl. Inst. Meth. Phys. Res. A **507**, 489 (2003)
- [4] M.W. Poole and B.W.J. M^cNeil, Proceedings of the 25th International Free Electron Laser Conference, Tsukuba, Japan (2003)
- [5] B.W.J. M^cNeil, G.R.M. Robb, N.R. Thompson, J. Jones, M.W. Poole and C.K.M. Gerth, Proceedings of the 27th International Free Electron Laser Conference, Stanford, JA-CoW / eConf C0508213 (2005)
- [6] B.W.J. M^cNeil, N.R. Thompson, and B. Sheehy, *The Conceptual Design of the 4GLS XUV-FEL*, *ibid.*
- [7] Ming Xie, Proc. Of 1995 Part. Accel. Conf., 183 (1996)
- [8] S. Reiche, Nucl. Inst. Meth. Phys. Res. A, **429**, 243, (1999)
- [9] B. Sheehy, J.A. Clarke, D.J. Dunning, N.R. Thompson, and B.W.J. M^cNeil, Proceedings of the 37th ICFA Advanced Beam Dynamics Workshop on Future Light Sources, Hamburg, Germany (2006)
- [10] See e.g. Eiji J. Takahashi et al., IEEE Journal of Selected Topics in Quantum Electronics **10**, 1315 (2004)
- [11] K.J. Schafer, B. Yang, L.F. DiMauro, and K.C. Kulander, Phys. Rev. Lett. **70**, 1599 (1993)
- [12] P.B. Corkum, Phys. Rev. Lett. **71**, 1994 (1993)
- [13] See e.g. Pascal Salieres, Anne LHuillier, Philippe Antoine and Maciej Lewenstein, Adv. At. Mol. Opt. Phys. **41**, 83 (1999)
- [14] D. Dunning et al., *First Tolerance Studies for the 4GLS FEL Sources*, *ibid.*

FOCAL POINT LASER-FIELD AS OPTICAL SEEDER

Tsumoru Shintake, RIKEN/SPring-8, 679-5148 Japan.

Abstract

Focusing laser beam in wavelength size, passing electron beam at focal point in normal direction to the laser axis, we may apply periodic velocity modulation on the electron beam at optical wavelength. With energy chirp, the electron bunch is longitudinally compressed in the magnetic chicane. With appropriate depth of optical modulation and energy chirp, we may obtain micro-bunching at compressed wavelength after the chicane. If the slice energy spread of incoming electron beam is very low, we may compress the optical modulation down to X-ray wavelength, in principle. For example, using 2nd harmonic YAG-laser at 532 nm (green), the resulting optical modulation becomes 266 nm, then compressing bunch length by 1/60 and 1/30 in two stage bunch compressors, we may obtain 1 Å. The energy chirp will be compensated due to single bunch wake field in the linear accelerator. Sending the beam into undulator line, the density modulation will provide seeding, which will be strongly amplified and create single longitudinal mode with full coherence. If we use femto-second laser, such as TiSa in the optical modulator, we can obtain atto-second pulse of X-ray after the compression.

MOTIVATION

SASE-FEL: Self-amplified Spontaneous Emission Free Electron Laser, as it was named the spontaneous radiation (noise power) is amplified along with long undulator line, and reaches to saturation level. Since its power level is extremely higher than conventional X-ray sources, even higher than 3rd generation light sources, many new

scientific applications are expected. Also the short pulse feature in femto-sec range is expected to be an important feature for analysing fast chemical and physical properties of condensed matter.

However, since SASE-FEL process starts from the spontaneous radiation at upstream undulator, the resulting saturated radiation power varies by shot-to-shot. And most importantly, there are many longitudinal modes, same as ruby laser does, temporal profile has many spikes, thus longitudinal coherence is quite limited.

If we seed a coherent signal from upstream undulator, whose power level has to be higher than spontaneous radiation, only the seeding signal will be amplified and saturated, thus it becomes (1) fully coherent, (2) temporally single-mode, and (3) stable energy in pulse-to-pulse. These features are favourable to all kind of scientific applications. Therefore, various proposals have been made on seeding schemes, including HGHG, HHG and wavelength shift [1, 2, 3]. They are promising approach to generate coherent radiation at VUV and also X-ray region. All of them use non-linear higher harmonic generation in high gain FEL, which requests high density electron beam.

In this paper, the author will propose a new approach: seeding density modulation at optical wavelength using conventional laser, and compress the bunch length together with wavelength of optical modulation down to X-ray wavelength. It does not rely on higher harmonic generation. Operational principle is simple. But there are many technical difficulties. However, the author believes that with extensive R&D efforts, in near future using this scheme we will be able to reach the X-ray wavelength with clean seeding signal after compressing bunch by factor of 1000 times. What we do is writing wave or coding signal on the electron beam, and transfer to the X-ray world.

BASIC CONFIGURATION

Figure 1 shows the basic configuration of this seeding scheme. We apply energy chirp on the incoming electron bunch, and add energy modulation at optical wavelength in the laser modulator, then compress the bunch length in the magnetic chicane. At the same time the velocity modulation is converted into density modulation at compressed short wavelength. The compression factors for the bunch length and the modulation wavelength are exactly same. After accelerating the beam up to higher energy, and sending into undulator, the bunch will radiate coherent signal. If the

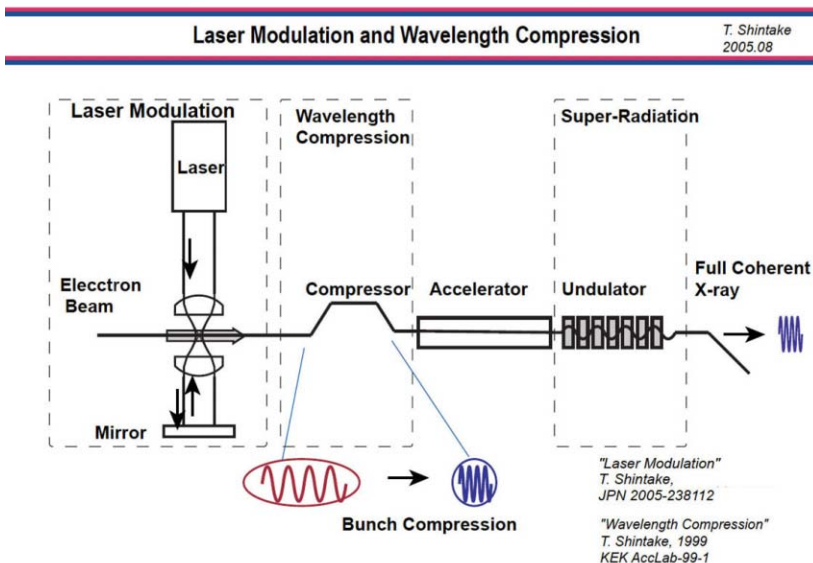


Fig. 1 Laser optical modulation and wavelength compression. Energy chirp after the compressor can be corrected by single bunch wake field and off crest acceleration in the linear accelerator.

#shintake@spring8.or.jp

wavelength of undulator radiation meets with the density modulation on the bunch, the undulator will radiate coherent radiation at super radiant mode.

In case of SASE-FEL of X-ray wavelength, we need 1/1000 times compression. Any kind of non-linear effect in magnetic chicane or wake-field will smear the optical modulation. However, if the residual density modulation exceeds the Schottky noise level, which is usually a few kW level only, the density modulation will provide coherent seeding signal to the SAS-FEL.

Similar approach was discussed independently by T. Shaftan and experimentally demonstrated using DUV FEL at BNL [3], where the tuning range that can be achieved is full range through a 10% tuning around each harmonic and switching between different harmonics.

APPLYING LASER MODULATION ON THE CATHODE

We may apply laser field directly on the cathode and create modulation on electron beam. If the electric field intensity of the laser field is strong enough, the accelerating field initially applied on the electron gun will be controlled, thus the current flow can be switch ON-OFF at the speed of the optical frequency. However, the thermal motion of electron erases the modulation at optical wavelength during acceleration as discussed below.

Fig. 2 shows electron trajectory in a constant accelerating field of E . The kinetic energy increases along its trajectory as

$$W_k(z) = eE_z \cdot z + W_{th} \quad (1)$$

Where W_{th} is the initial kinetic energy on the cathode, which is given by the thermal energy,

$$\left\langle \frac{1}{2} m_e v_z^2 \right\rangle = \frac{1}{2} kT \quad (2)$$

Solving eq. (1) under initial condition of eq. (2), we can compute thermal effect on the trajectory. Here we graphically estimate the thermal effect, refer Fig. 2. An electron starts from the cathode with zero initial energy, which follows curved line **A**, and reaches to the final position z_f at time t_f , where the velocity is very close to the speed of light. If the electron starts from the cathode with finite initial velocity, it follows trajectory **B**, at time t_f it runs more Δz , which smears out the modulation. This effect can be graphically estimated as follows. In the trajectory **A**, near the cathode, electron reaches to the point (t_1, z_1) where the kinetic energy becomes equal to the initial energy of trajectory **B**:

$$ct_1 = \frac{m_0 c^2}{eE_z} \sqrt{\frac{2W_i}{m_0 c^2}}, \quad z_1 = \frac{W_i}{E_z}, \quad (3)$$

Trajectory **B** is exactly same as **A** if we shift the point (t_1, z_1) to origin $(0, 0)$. Assuming the final energy is relativistic, the distance Δz is given by

$$\Delta z = ct_1 - z_1 \quad (4)$$

As an example, we assume accelerating field of 10 MV/m, and thermionic cathode operating at 1800 K, thermal energy in z-direction is 74 meV, and we find:

$$\begin{aligned} t_1 &= 61 \text{ femto-sec.} \\ z_1 &= 7.4 \text{ nm} \\ ct_1 &= 19 \mu\text{m} \\ \Delta z &= 19 \mu\text{m} \end{aligned} \quad (5)$$

Δz is much longer than the optical wavelength, thus the modulation will be totally smeared out.

In case of RF-gun, the cathode temperature is room temperature, and cathode field is much higher, thus thermal diffusion becomes smaller. Assuming a very high acceleration field such as 100 MV/m, the diffusion distance becomes $\Delta z = 1.1 \mu\text{m}$. They are summarized in Table 1. If we use CO₂ laser at 10 μm wavelength, the modulation will remain. Tuneable infrared radiation from OPO (Optical Parametric Oscillator) will also be a candidate.

Table 1: Thermal diffusion effect for electrons starting from the cathode

Physical Parameter	Thermionic Gun	Photo-cathode rf-gun
Field Gradient: E	10 (MV/m)	100 (MV/m)
Temperature: T	1800 (K)	300 (K)
Thermal energy: W_{th}	74 (meV)	12 (meV)
Equivalent point: t_1	61 fs	3.8 fs
z_1	7.4 nm	0.12 nm
ct_1	19 μm	1.1 μm
Diffusion length: Δz	19 μm	1.1 μm

In case of the photo-cathode rf-gun, the laser beam is introduced on the cathode from normal direction, and the electric field of the laser is oriented paralleled to the cathode surface, which takes minimum on the cathode

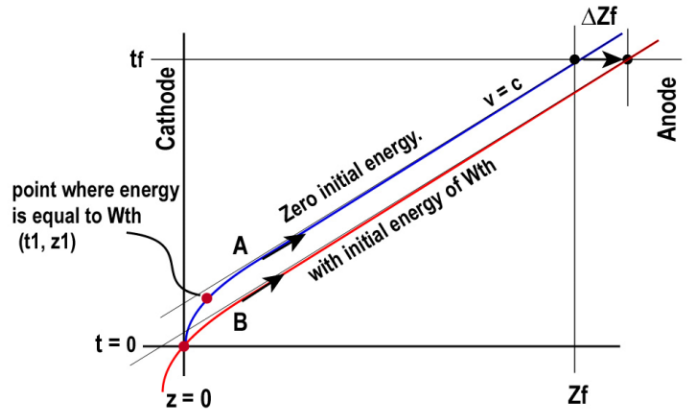


Fig. 2 The electron trajectory in the constant acceleration field. Starting from the cathode ($z = 0$), reaches to final position z_f at the time of t_f . With initial energy, the electron runs more: Δz , which smears out the modulation.

because the cathode is electric conductor, thus the laser field does not directly modulate velocity of emitting electron. However, in case of pulsed laser, if it is not seeded with coherent beam there are multi-modes in longitudinal direction, resulting in temporal variation. If the period of this variation is longer than ΔZ , the produced electron bunch from the rf-gun will contain density modulation. This will be a possible source of CSR instability in the magnetic chicane. Tiny density fluctuation on electron beam is amplified due to negative slope of energy (energy loss at bunch head, opposite to the wake-fields), which is amplified through dispersion in the bunch compressor, results in higher CSR radiation and positively feedbacks to the energy modulation on the electron bunch, cause CSR instability.

THRESHOLD ENERGY

Reason why such a small thermal energy causes diffusion on accelerating electron in high gradient is that the electron remains near the cathode when the speed is not high enough. It can be shown by the following equations.

$$v = \sqrt{\frac{2eE_z}{m_0}} \cdot z \quad (6)$$

$$dt = \frac{1}{v} dz \propto \frac{1}{\sqrt{z}} \cdot dz \quad (7)$$

Near the cathode, z is small, thus it takes long time to travel. Once the electron departs from the cathode and increases speed, the travelling time for unit distance becomes shorter, and it becomes independent from initial thermal energy.

The diffusion distance during acceleration between point-1 and point-2 is given by

$$\Delta z_{th} = \frac{\Delta \gamma_{th}}{\gamma'} \left(\frac{1}{\beta_1} - \frac{1}{\beta_2} \right)$$

$$\gamma' = eE_z / m_0 c^2 \quad (8)$$

$$\Delta \gamma_{th} = kT / 2m_0 c^2$$

For example, to accelerate beam up to 8 GeV ($\beta_2 = 1$) on 20 MV/m field gradient ($\gamma' = 39.1/\text{m}$), assuming thermionic gun (74 meV, $\Delta \gamma_{th} = 1.4 \times 10^{-7}$), to make the diffusion distance being lower than quarter wavelength of 4th harmonic of YAG: $\Delta Z < 60 \text{ nm}$, we find

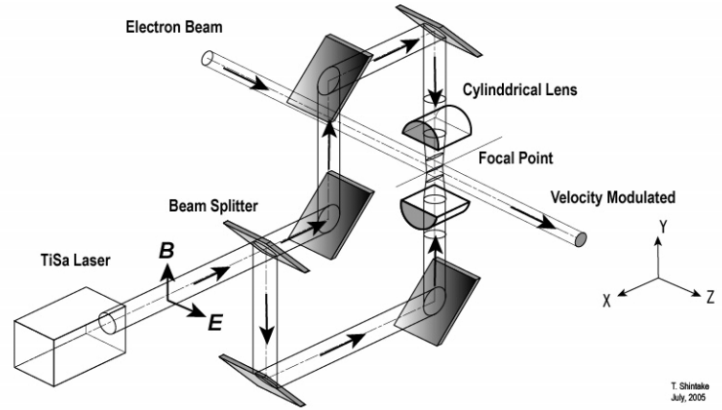


Fig. 3 Laser modulation, using focal point field in the standing wave of the laser beam. To make interaction area wider, the cylindrical lens is employed rather than spherical lens. Polarization is chosen as to make the electric field being oriented to the electron path.

$$\frac{1}{\beta_1} - 1 > 16.7 \quad (9)$$

Thus, $\beta_1 > 0.056$, or the beam energy has to be higher than 810 eV. If we apply the laser modulation at this energy or at higher energy, the modulation will be kept up to relativistic energy.

At high energy, eq. (8) becomes

$$\Delta z_{th} = \frac{\Delta \gamma_{th}}{\gamma'} \cdot \frac{1}{2\gamma_1^2} \left[1 - \left(\frac{\gamma_1}{\gamma_2} \right)^2 \right] \quad (10)$$

For example, if we compress the bunch into 1 Å at 1 GeV and accelerate to 10 GeV with 30 MV/m accelerating gradient, the diffusion due to thermal energy becomes $\Delta Z = 0.3 \text{ femto-meter}$, this is much smaller than 1 Å, thus the modulation will be kept.

The betatron oscillation of each electron inside the bunch causes path difference and smearing effect. Average path difference can be estimated by

$$\Delta z_{\beta} = \frac{2\varepsilon_n}{\pi^2 \gamma} \cdot \frac{L}{\langle \beta \rangle} \quad (11),$$

Assuming, $\varepsilon_n = 1 \times 10^{-6} \pi \text{ mm} \cdot \text{mrad}$, $L = 300 \text{ m}$, $\beta = 30$ m, the path difference becomes 2 Å. Therefore, simple betatron oscillation contributes to erase micro bunching. But inside the bunch, near the core, betatron oscillation amplitude is lower, thus the modulation pattern will remain. This is ideal case, there is only accelerating static field, and no magnetic component which will create dispersion and cause path length difference inside the bunch and will smear the modulation pattern. Further careful study is required.

LASER MODULATION

When an electron beam passes through a laser beam in free space, usually there is no energy transfer with relativistic electron beam. This is because the laser field is transverse electro-magnetic field, and no longitudinal electric field exists. “The laser acceleration” technology uses dispersive media, such as gas or plasma, to obtain longitudinal electric field propagating with speed of electron.

When we pass an electron in an undulator, the electron transversely oscillates. We inject laser beam from behind of the electron, where longitudinal drift velocity of electron is slower than speed of light even in relativistic case due to transverse velocity component, and the electron delays from laser beam. With optimum tuning condition, for each one period of undulation, the electron delays one wavelength on laser field, thus recover phase and continue to exchange energy through $v_i \cdot E_i$ coupling.

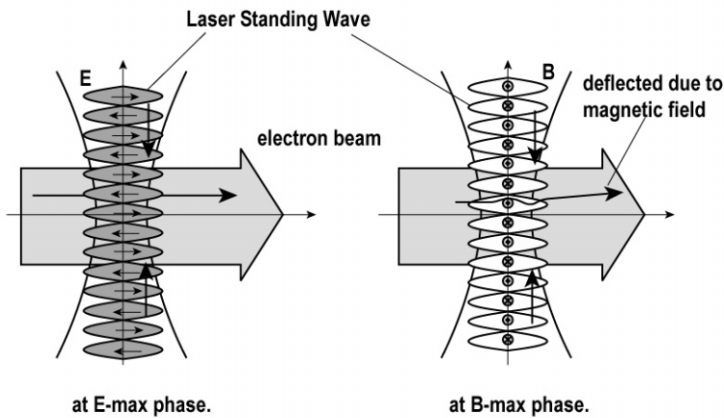


Fig. 4 Overlapping two laser beams create standing wave. At the electric field maximum location, electron receives velocity modulation. In between these maximums, the magnetic field deflects beam, which deteriorate beam emittance, also cause Compton scattering with laser photon and generate gamma-ray, which contributes to energy spread.

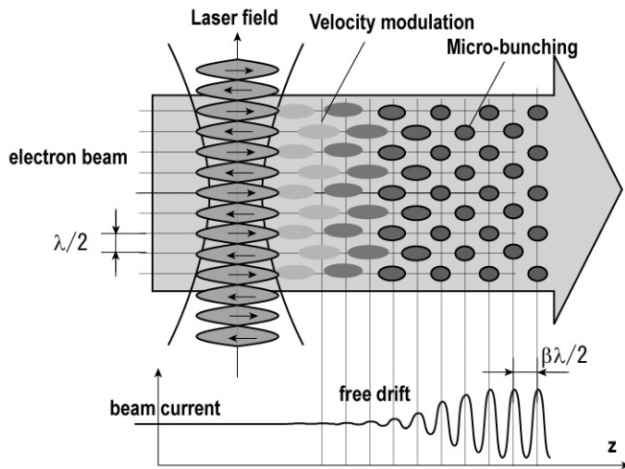


Fig. 5 Standing wave laser beam adopts velocity modulation and generate density modulation pattern at double frequency.

This type of laser modulator is so called “inverse FEL”, and experimentally demonstrated elsewhere. However the system becomes complicated.

Here we introduce new scheme, which uses transverse electric field at focal point as illustrated in Fig. 3. This scheme uses same configuration as the spot size monitor tested at FFTB SLAC [4], but in this case we utilize the electric field. Since two laser beam overlap at the focal point, the standing wave is created. By choosing polarization of the laser beam as the electric field being oriented to the electron beam path at the focal point, the electron beam receives energy modulation through $v_z \cdot E_z$ coupling at each electric field maximum points with $\lambda/2$ apart as Fig.4 left. In between them, there are magnetic field maximum points, where electron receives transverse kick from the magnetic field as shown in Fig. 4 right. This transverse coupling provides Compton scattering of laser photon, which causes increase of energy spread.

If the spot depth is much larger than laser wavelength, $v_z \cdot E_z$ oscillates along its trajectory and integration becomes zero, thus the electron does not receive energy gain. If we focus the laser beam into very small spot, the integral becomes non zero.

Here we assume Gaussian laser beam, and focus into a long elliptical spot using cylindrical lens as shown in Fig. 3. Here we define the coupling coefficient as follows.

$$T = \frac{\int_{-\infty}^{+\infty} E_z(z, t = z/c) \cdot dz}{\int_{-\infty}^{+\infty} E_z(z, t = 0) \cdot dz} = e^{-(k\sigma_z)^2/4} \quad (12)$$

Function T is plotted in Fig. 6. To obtain substantial coupling, we need to focus the laser spot very small close to the laser wavelength. From Fig. 6 we find that in order to obtain coupling of 0.1 or higher we have to focus the spot size $\sigma_z < 0.5\lambda$.

Can we focus the laser into such a small spot? The answer is yes. The CD player uses photopickup, where a short focal lens is used to focus laser beam into small spot in wavelength dimension to fit with the micron-size pits, and read out the reflection from those. The relation between the lens aperture, focal length and minimum spot size is given by

$$\begin{aligned} \sigma_z &= \frac{\lambda}{\pi\theta} \\ NA &= n \cdot \sin \theta \\ F &= \frac{f}{D} \approx \frac{1}{2NA} \end{aligned} \quad (13)$$

Where NA is called ‘‘Numerical Aperture’’ and higher NA provides smaller spot size, but it technically limited less than 1. One of the most advanced lens system is employed in the lithography system in Si-process, for example, NA of 0.85 has been realized in 157 nm F₂-laser lithography and 70-nm line width has been achieved[5].

From eq. (13), in order to obtain $\sigma_z < 0.5\lambda$, we need $\theta = 2/\pi = 0.64$, and $NA = 0.59$. There are commercially available products of cylindrical lenses having NA value 0.5 or even higher.

Using pulsed laser of 2nd harmonic of YAG-laser at 532 nm, assuming 1 mJ pulse and 10 nsec duration, this is small class laser oscillator in commercial production line, we may obtain 170 MV/m of peak electric field at the focal point, and 16 eV of modulation energy. This is quite enough for our purpose.

Table-2: Example laser system and modulation energy.

YAG-Laser 2nd			
wavelength	λ	532	nm
Output power	100 kW, 10 nsec, 1 mJ		
Focusing	Cylindrical lens		
Focusing length	f	5	mm
Numerical aperture	NA	0.6	
Matched laser beam size	$\sigma \sim 0.5D$	3	mm
Focused spot size	σ_{z0}	266	nm
Transverse width	σ_{x0}	3	mm
Field intensity	E_{z0}	170	MV/m
Modulation period	λ_{mod}	266	nm
Coupling Constant	T	0.1	
Modulation Energy		16	eV

REQUIRED ENERGY CHIRP AND OPTIMUM MODULATION

In the magnetic chicane, the bunch length is compressed according to its initial energy chirp: bunch head is lower energy and higher at tail, so that head part delays and tail catches up, results in compressing bunch length. If the optical modulation system is located upstream of the bunch compressor, the energy modulation will overlap with the linear energy chirp. After bunching,

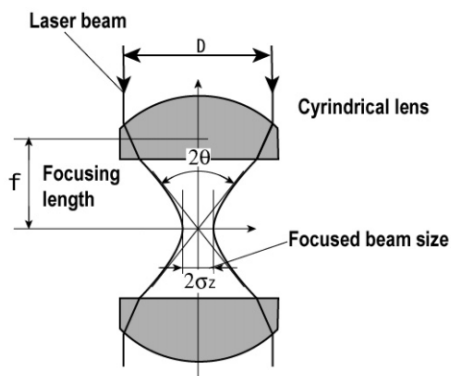


Fig. 7 High-NA focusing optics.

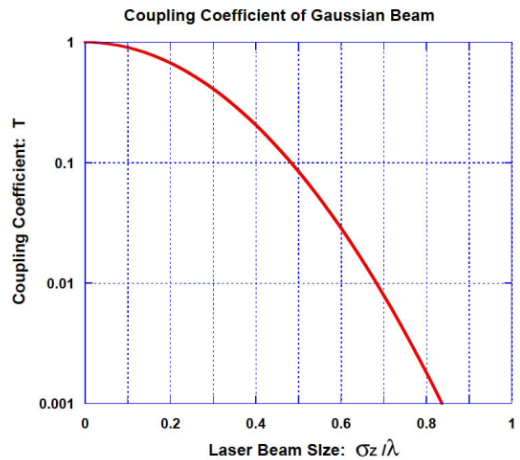


Fig. 6. Coupling coefficient as a function of the laser beam spot size.

the energy modulation will be converted into density modulation with shorter wavelength. If the energy modulation is too strong, the micro bunching will be over compressed and modulation contrast becomes lower. Thus there is certain relation between linear energy chirp and micro energy modulation. As shown in Fig. 8 left, there are three energy components: the initial energy chirp, optical modulation and energy spread:

$$E = E_0 - V_{I,RF} \cdot k_{RF} z - V_{mod} \sin(2\pi z / \lambda_{mod}) + \sigma_e, \quad (13)$$

Where $V_{I,RF}$, k_{RF} is the RF cavity voltage to produce energy chirp (off crest component), V_{mod} is the optical modulation voltage, λ_{mod} is modulation wavelength before compression and σ_e is the energy spread. In the chicane, the bunch length is compressed according to $z_f = z_i + R_{56} \delta_i$. Optimum bunching condition is illustrated in Fig. 8 right, where the longitudinal spread of bunched beam becomes minimum, which is given by the following condition. Note the no space charge effect is considered in this discussion.

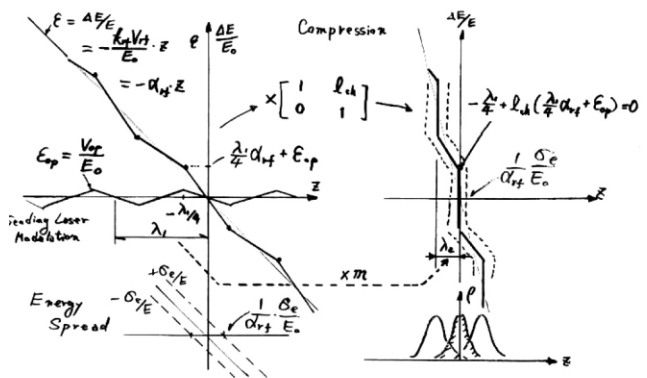


Fig. 8. Phase diagram of electron bunch before and after the compression.

$$\left. \frac{\partial z_2}{\partial \delta_2} \right|_{z=0} = 0, \quad (14)$$

$$\frac{V_{LRF}}{E_0} k_{RF} + \frac{V_{mod}}{E_0} k_{mod} = R_{56}^{-1}, \quad (15)$$

The bunch compression factor is

$$m = \sigma_{zf} / \sigma_{zi} = 1 - \frac{V_{LRF}}{E_0} k_{RF} R_{56} \quad (16)$$

At high compression ratio, i.e., we can approximate

$$\frac{V_{LRF}}{E_0} = (k_{RF} R_{56})^{-1} \quad (17)$$

For the optical modulation the optimum condition is,

$$\frac{V_{mod}}{E_0} = m \cdot (k_{mod} R_{56})^{-1}. \quad (18)$$

For example, if we compress bunch length by 1000 times at 3 GeV, $m = 0.001$, with $R_{56} = 40$ mm, and $\lambda_{mod} = 266$ nm, the required modulation becomes $V_{mod} = 1 \times 10^{-9} E_0$, that is optical velocity modulation becomes 3 eV. This value will be easily provided by the laser modulation as shown in Table 2.

If the energy spread is large, the modulation pattern will be smeared out. The energy spread has to be smaller than modulation energy. If the electron energy spread is still as low as the thermal energy: 74 meV, the modulation will be kept through the bunch compression process. The wavelength of the micro-bunching after the compressor becomes $\lambda = m \cdot \lambda_{mod}$. If we use 532 nm wavelength, the modulation period becomes 266 nm, then, after the compression with $m = 0.001$, the modulation wavelength becomes 0.27 nm.

If we use femto-second laser, such as TiSa to optical modulator, we will be able to obtain atto-second pulse of X-ray after the compression.

CONCLUSIONS

New optical modulation scheme has been proposed in this paper. If we apply velocity modulation at optical wavelength, and compress it with bunch length, we will have density modulation at X-ray wavelength range. At least in an ideal case, mathematics shows possible parameter set. If we assume 1000 times compression ratio, we will have direct seeding source at X-ray wavelength.

Further studies will be required on non-linear field in bunch compressor, non uniform velocity distribution in bunch, energy spread due to radiation excitation, etc.

In year of 2007, we will install a laser modulator in our test accelerator to demonstrate velocity modulation, and compress the wavelength by ten times in bunch compression to seed FEL at 50 nm range.

REFERENCES

- [1] L.-H. Yu, Phys. Rev. A44 (1991) 5178.
- [2] Timur Shaftan and Li Hua Yu, "High-gain harmonic generation free-electron laser with variable wavelength", Phys. Rev. E 71, 046501 (2005).
- [3] Timur Shaftan et al., "Experimental Demonstration of Wavelength Tuning in High Gain Harmonic Generation Free Electron Laser", Proc. FEL 2004, pp. 282-284, Trieste Italy.
- [4] T. Shintake, "Proposal of nano-meter beam size monitor for e+e- linear colliders", NIM A311, (1992) pp. 453-464.
- [5] Toshiro Itani et al., "Effect of high numerical aperture lens on lithographic performance in 157 nm lithography", J. Vac. Sci. Technol. B 20(6), Nov/Dec 2002.

ANALYSIS OF THE PROCESS OF AMPLIFICATION IN A SINGLE PASS FEL OF HIGH ORDER HARMONICS GENERATED IN A GAS JET

L. Giannessi, M. Quattromini, ENEA C.R. Frascati, Frascati (Roma) Italy

P. Musumeci, INFN Sez. Roma I, Roma, Italy

G. Sansone, S. Stagira, M. Nisoli, S. De Silvestri, Politecnico di Milano, Milano, Italy.

Abstract

We have studied the amplification of high harmonics generated by a short infrared pulse in a gas jet, injected in a free electron laser amplifier. The high-order harmonic spectra have been simulated using a 3D non-adiabatic model that includes both the single atom response and the effect of the propagation of the XUV field inside the gas jet. The response of a single atom to the IR field is calculated in the framework of the Strong Field Approximation (SFA); The nonlinear polarization associated to this process is evaluated as the acceleration of the nonlinear dipole moment. This term is used as source term in the propagation of the harmonic field inside the gas jet. The propagation effect are extremely relevant for the temporal structure of the XUV field as the coherent interference of the dipole emission of the different atoms leads to the selection of only one XUV pulse for each semi-cycle of the driving IR field. The amplification in the free electron laser has been simulated with GENESIS 1.3. The effects of filtering the seed spectrum have been analyzed and the coherence properties of the light are considered.

INTRODUCTION

The FEL amplification in the SASE regime [1] leads to a longitudinal pulse shape and amplitude governed by the stochastic properties of the electron beam shot noise. The result is a reduced longitudinal coherence and intrinsic pulse to pulse energy fluctuations [2]. A single pass FEL, seeded with an external source, shows a number of advantages with respect to SASE, as the control over the pulse shape better coherence properties which are determined by the seed [3,4]. Intense seed sources are available in the visible and UV region of the spectrum based on reliable solid state laser technology. The FEL operating range may be extended to shorter wavelengths with cascaded schemes, i.e. taking advantage of the harmonic generation process in the FEL dynamics[5]. On the other hand high harmonic multiplication factors in a multi-stage cascade FEL are limited by the energy spread induced in each stage by the FEL process and these configurations are affected by stability issues associated to the fluctuation of one or more of the large number of parameters defining the configuration [6,7]. An alternative to a multi-stage cascade with a high harmonic multiplication factor is that of seeding the FEL amplifier directly at short wavelengths with the high order harmonics of an intense Ti:Sa laser pulse generated in a

Gas Jet [8]. Such a possibility is considered in the scheme of several proposed facilities [9,10,11] and experiments are planned in the next future [12,13]. The high frequency field produced in the interaction with the gas jet has some very peculiar features. The pulse has a spiky structure, with attosecond pulses separated by half of the drive laser wavelength [14]. The spectrum contains the odd harmonics of the Ti:Sa drive laser and extends to short wavelengths with a cut-off depending on the nature of the gas used. The energy per pulse drops rapidly at the shortest wavelengths, where the combination of this seed source with an FEL amplifier would be more appealing. We are interested in understanding what is the minimum energy required by an FEL amplifier in order to overcome the electron beam shot noise and amplify the harmonic pulse. A threshold intensity was obtained in the case of a seed constituted by a uniform plane wave [15], but it is not clear whether that threshold remains valid when the pulse has the time/spectral structure of the harmonics produced in gas and whether filtering the input seed is required despite of the fact that the FEL has a limited bandwidth proportional to the FEL parameter ρ [1,2]. Start to end simulations of the electron beam dynamics in a single pass FEL have been widely used to understand the dynamics of the coupled system of electrons and fields undergoing the FEL process. In order to answer the previous questions we have implemented a start-to-end simulation from the radiation point of view, starting with the process of harmonic generation in the gas jet and injecting the field distribution in a widespread and reliable FEL simulation code as GENESIS 1.3 [16]. The paper is organized as follows: in the next section we study the generation of the high harmonics field in the gas jet. In the last section we select the field at the target wavelength of 29.6 nm corresponding to the 27th harmonic of the Ti:Sa and we analyse the results of simulations of the seeded FEL amplifier.

HIGH ORDER HARMONICS IN GAS

The high-order harmonic spectra have been simulated using a 3D non-adiabatic model that includes both the single atom response and the effect of the propagation of the XUV field inside the gas jet. The response of a single atom to the IR field is calculated in the framework of the Strong Field Approximation (SFA); in this model the atom is ionized via tunnelling by the IR field and the freed electron is then accelerated by the electric field of the driving pulse. For particular emission instant the

electron can be driven back to the parent ion and can recombine with the ground state emitting the exceeding energy as a photon in the extreme ultraviolet region or soft x ray region. The nonlinear polarizability associated to this process is evaluated as the acceleration of the nonlinear dipole moment:

$$d_{nl}(t) = 2 \operatorname{Re} \left\{ i \int_{-\infty}^t dt' \left\{ \left(\frac{\pi}{\varepsilon + i(t-t')/2} \right)^{3/2} \exp[-iS_{st}(t,t')] \right\} \right. \\ \left. \left\{ E(t') d^*(p_{st}(t,t') - A(t)) d(p_{st}(t,t') - A(t')) \right\} \right. \\ \left. * \exp \left(- \int_{-\infty}^t w(t') dt' \right) \right\} \quad (1)$$

In this equation $E(t)$ and $A(t)$ are respectively the electric field and the vector potential of the driving field; $p_{st}(t,t')$ is the stationary value of the momentum of the freed electron, $S_{st}(t,t')$ is the phase accumulated by the electron wave packet, $d(p)$ and $d^*(p)$ are the dipole matrix element for transitions from the ground state to a continuum state characterized by momentum p . The last term of equation (1) takes into account ground state depletion through the term ionization rate $w(t)$ calculated using the ADK model. The nonlinear dipole moment is used as source term in the propagation of the harmonic field inside the gas jet. The wave propagation equations for the driving and the harmonic field are solved in cylindrical symmetry in the framework of the paraxial approximation. The harmonic power spectrum is obtained integrating over the radial profile the harmonic electric field at the output of the gas jet.

Propagation effects are extremely relevant for a correct simulation of the time structure of the harmonic radiation. Indeed usually the single atom response is characterized by a complex time structure (usually two attosecond pulses for each half optical cycle), whereas the macroscopic time structure of the XUV radiation is characterized by a single attosecond pulse for each semi optical cycle. The origin of this difference is related to the phase matching mechanism operating during the propagation of the XUV field inside the gas jet.

In the process of high order harmonic generation, the electron can follow two different paths in order to recombine with the parent ion. These two paths are usually referred to as the “short” and the “long” path, as they are characterized by different times spent by the electron in the continuum of energy states. For the short path this time is usually less than half the optical period T_0 , while for the long paths this time is typically of the order of the laser period. The coherent superposition of the contributions of these two paths leads to the generation of two attosecond pulses for each half optical cycle of the driving laser field. The coherent interference of the dipole emission of the different atoms inside the gas jet leads to different phase-matching conditions for the two paths. The relative contribution of the two paths

to the harmonic spectra can be enhanced or reduced changing the relative position of the gas jet with respect the laser focus. The phase-matching condition in the HHG process are indeed determined by the geometric phase of the driving pulse and by the phase accumulated by the electron wave packet during his motion. In particular conditions, gas jet positioned few millimeters after the laser focus, it is possible to efficiently select on the contribution of the short path, leading to the selection of only one XUV pulse for each semi cycle of the driving IR field[17].

In other experimental condition (gas jet before or close to the laser focus), the contribution of the long paths increases and therefore also the time structure of the generated XUV radiation is more complex.

For our simulation we considered a Gaussian beam with a beam waist of $w_0 = 50 \mu\text{m}$ (in the focus), and focused 3mm before a Neon gas jet with a thickness of 1mm. The pulse duration is FWHM=30 fs with a peak intensity in the focus of $1 \times 10^{14} \text{W/cm}^2$. The high frequency portion of the spectrum, in the range 20 nm – 60 nm of the on axis radiation is shown in Fig. 1. The spectrum contains the odd harmonics of the Ti:Sa resonant wavelength (800 nm).

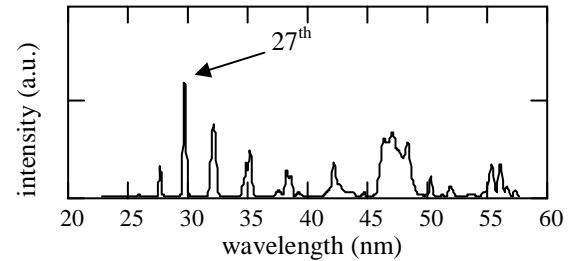


Fig. 1 Short wavelength spectrum of the HHG seed field.

The slowly varying envelope approximation (SVEA) has not been used in the model, but the FEL dynamics studied with GENESIS 1.3 rely on this approximation.

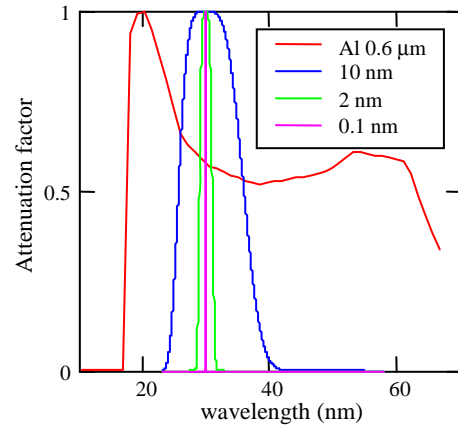


Fig. 2 Attenuation factor as a function of the wavelength of the different filters used in the simulations. The red line correspond to 600 nm layer of Aluminium.

For this reason we have to limit the bandwidth of the input signal by filtering the seed field and define the

slowly varying field as $\tilde{E}(z) = E(z)\exp(-ik_0z)$ where k_0 is the FEL central resonant wave vector. In our example we consider filtering with different bandwidth as shown in Fig.2 centered at the resonant wavelength $\lambda_0 = 2\pi/k_0 = 29.66\text{nm}$ corresponding to the 27th harmonic of the Ti:Sa (Fig.1).

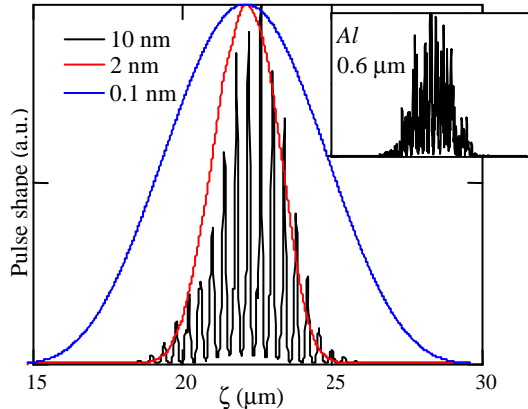


Fig. 3 Longitudinal pulse profile of the input seed after filtering. The plot in the upper right corner is the pulse shape filtered only with the Al broadband filter.

The effect of filtering on the seed temporal profile is shown in Fig. 3. The 10nm bandwidth is wide enough to preserve the attosecond structure of the input field. At 2nm the bandwidth preserves the pulse envelope, but overrides the fine structure. The 0.1nm filter induces an increase of the pulse length.

THE FEL SIMULATION

The FEL configuration considered is based on the parameters shown in Tab. 1. The FEL parameter is $\rho \sim 10^{-3}$ and an estimate of the seed intensity necessary to override the e-beam shot noise as calculated in ref.[15] is about $I_0 \approx 0.3\text{MW}/\text{cm}^2$.

Table 1: FEL configuration parameters

Beam Energy (GeV)	1
Peak current (A)	1000
Energy Spread (%)	0.06
Emittance (mm-mrad)	1
Average β_T (m)	6
Undulator period (cm)	4.2
K (peak)	2.97
Periods per section	58
Sections	7

The field spot size and divergence have been matched to the e-beam optical functions by propagation through a drift+lens+drift optical system. The field phase and amplitude at the undulator entrance are shown in Fig.4.

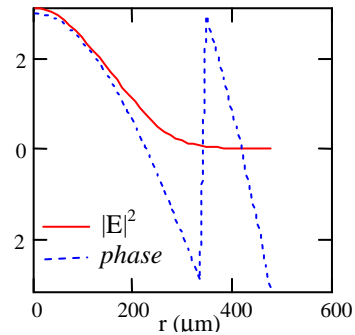


Fig. 4 Transverse field at the undulator entrance averaged over z .

The radiation power as a function of the longitudinal coordinate in the electron beam frame (horizontal) and position along the undulator at the coordinate z (vertical) is shown in Fig.5. The power is normalized at each z . The plots have been obtained by different filtering of the seed. The input seed energies, 2.5nJ@10nm, 1nJ@2nm and 0.5nJ@0.1nm have been chosen in order the energy in a bandwidth 2ρ to be roughly the same (0.5nJ) in the three cases.

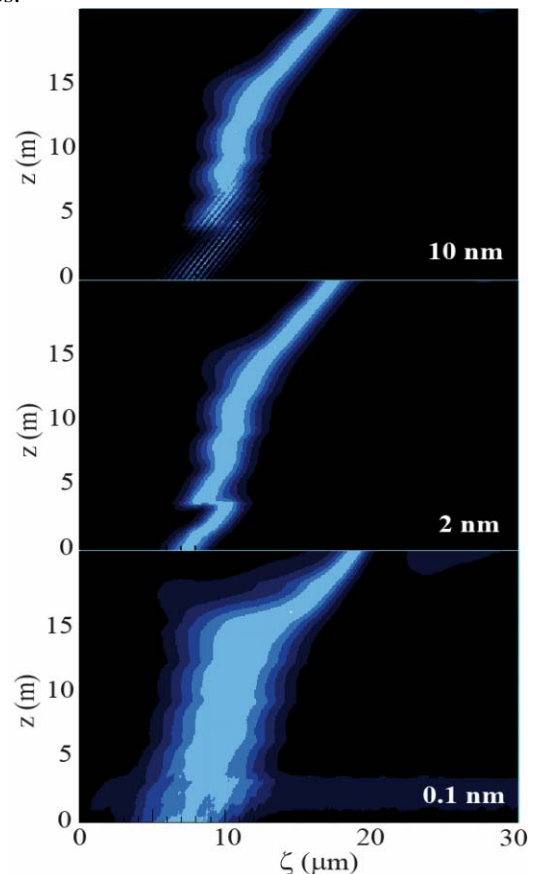


Fig. 5 Normalized longitudinal profile of the radiation power as a function of the longitudinal coordinate in the electron beam frame as it evolves along the undulator with coordinate z . The seed has been filtered at different bandwidths.

The fine structure present in the 10nm case is wiped out by the finite bandwidth of the FEL. The different filtering

affects the pulse shape only before saturation, which occurs at about 15m in all cases. Thereafter the pulse enters the superradiant regime where the pulse length is related to the peak power and is the same in all cases. The

The input seed intensity is $15\text{MW}/\text{cm}^2@10\text{nm}$, $8.5\text{MW}/\text{cm}^2@2\text{nm}$, and $4\text{MW}/\text{cm}^2@0.1\text{nm}$ averaged over z , always much larger than I_0 . In Fig. 6, the simulation corresponding to 0.1nm has been repeated with input energies 0.05nJ and 0.01nJ, corresponding to intensities slightly above and below the threshold I_0 respectively. In both cases SASE is clearly visible at the beginning. In the latter case a structure in the pulse with loss of longitudinal coherence is present and SASE spikes compete with the seeded signal until saturation.

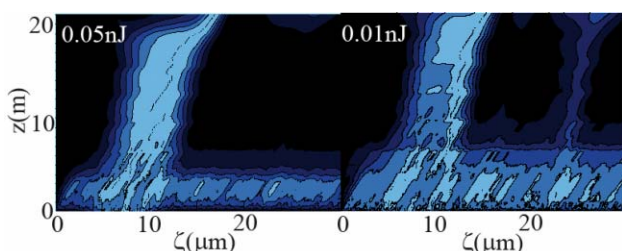


Fig. 6 Same as in Fig.5, case with 0.1nm BW above (left) and below (right) the threshold I_0 .

The input energy levels considered are however very conservative. In fact recent results [18] have demonstrated the feasibility of pulses with energies up to several hundreds nanojoules at the considered photon wavelength. In Fig. 7 the power vs. ζ and z as in Figs. 5 and 6 (left) and the spectrum (right) are shown for the $100\text{nJ}@10\text{nm}$ case. Saturation is reached after only 8m. The splitting of the spectrum typical of the superradiant regime is clearly visible at the end of the undulator.

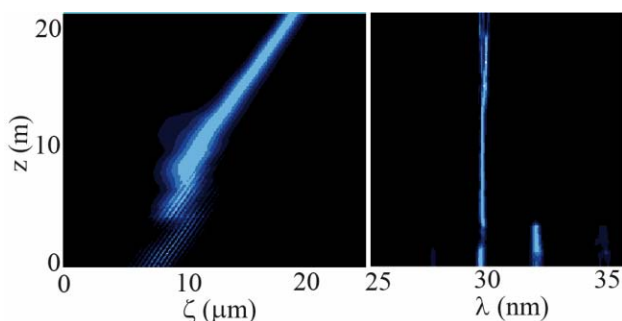


Fig. 7 Normalized longitudinal profile of the radiation power as a function of the longitudinal coordinate in the electron beam frame as it evolves along the undulator with coordinate z (upper plot). Corresponding wavelength spectrum as a function of z .

CONCLUSIONS

In this paper we have presented an analysis of the dynamics of a FEL seeded with the high order harmonics generated in gas. The minimum seed energy has been estimated in a specific FEL configuration with the resonance at the 27th harmonic of the Ti:Sa drive laser.

The results are in reasonable agreement with the threshold estimation in [15]. Currently available sources in the XUV appears to be sufficiently intense to implement such a scheme. The analysis in the frequency domain, suggests that filtering the seed it is not necessary unless a line-width smaller than the natural FEL line-width is required.

This work was partially supported by the EU Commission in the Sixth Framework Programme, Contract No. 011935-EUROFEL.

REFERENCES

- [1] R. Bonifacio, C. Pellegrini, and L. M. Narducci, Opt. Commun. 50, 373 (1984)
- [2] E. L. Saldin, E. A. Schneidmiller, M. V. Yurkov, Opt. Commun. 148, 383 (1998)
- [3] L. H. Yu et al., Science 289, 932 (2000)
- [4] L. H. Yu et al. Phys. Rev. Lett. 91, 074801 (2003)
- [5] G. Dattoli et al. Journal of Appl. Phys. 97, 113102 (2005)
- [6] B. Kuske et al. Development of Figures of Merit to Evaluate the Output of FEL HGHG Cascades, MOPPH051, these proceedings
- [7] G. De Ninno et al. Start-to-end Time-Dependent Study of FEL Output Sensitivity to Electron-beam Jitters for the First Stage of the FERMI@Elettra Project, MOPPH058, these proceedings
- [8] D. Garzella *et al.*, Nucl. Instrum. Methods Phys. Res. Sect. A 528, 502 (2004).
- [9] C. Bruni, The Arc En Ciel FEL proposal, MOPPH048, these proceedings
- [10] B. McNeil et al, The Conceptual Design of the 4GLS XUV-FEL, MOPPH012, these proceedings
- [11] C. Vaccarezza et al., Status of the SPARX FEL project , MOPCH028 in procs. of the 2006 EPAC conference (2006).
- [12] G. Lambert, Seeding the FEL of the SCSS Phase I Facility, MOPPH046 these proceedings
- [13] O. Tcherbakoff et al, MOPPH047 these proceedings, see also L. Giannessi, Future seeding experiments at SPARC, MOPPH028 these proceedings
- [14] P. Salieres, M. Lewenstein, Meas. Sci. Technol. 12, 1818 (2001)
- [15] L. Giannessi, Harmonic generation and linewidth narrowing in seeded FEL, in Proc. of the 26th FEL conference, Trieste 2004 JACoW (Joint Accelerator Conference Website) at <http://www.JACoW.org>, p. 37 (2004)
- [16] S. Reiche, Nuclear Instrum. & Meth. A429, 243 (1999)
- [17] P. Salieres, B. Carré, L. Le Déroff, F. Grasbon, G. G. Paulus, H. Walther, R. Kopold, W. Becker, D. B. Milosevic, A. Sanpera, M. Lewenstein, Science 292, 902 (2001).
- [18] E.J. Takahashi et al. IEEE J. of Sel. Topics in Q.Elec. 10, 1315 (2004)